FINAL REPORT

THERMAL PERFORMANCE OF

MULTILAYER INSULATIONS

prepared for

NATIONAL AERONAUTICS AND SPACE ADMINISTRATION

5 April 1974

Contract NAS 3-14377

NASA Lewis Research Center
Cleveland, Ohio 44135

William R. Johnson, Project Manager
Propulsion Technology Branch

LOCKHEED MISSILES & SPACE COMPANY. INC.
A   SUBSIDIARY   OF   LOCKHEED   AIRCRAFT   CORPORATION

FINAL REPORT

THERMAL PERFORMANCE OF MULTILAYER INSULATIONS

by

C. W. Keller, G. R. Cunnington, and
A. P. Glassford

LOCKHEED MISSILES & SPACE COMPANY
Sunnyvale, California 94088

Prepared for

NATIONAL AERONAUTICS AND SPACE ADMINISTRATION

5 April 1974

CONTRACT NAS 3-14377

NASA Lewis Research Center
Cleveland, Ohio 44135

William R. Johnson, Project Manager
Propulsion Technology Branch

LOCKHEED MISSILES & SPACE COMPANY

FOREWORD

The Lockheed Missiles and Space Company, Inc. (LMSC)
is submitting this Final Report in completion of the
requirements of Contract NAS 3-14377, Thermal Perform-
ance of Multilayer Insulation, dated 23 June 1971. The
total scope of work, data, results, and conclusions
pertinent to this program are presented herein. The
program was conducted under the technical direction
of Mr. William R. Johnson, Propulsion Technology Branch,
Chemical Propulsion Division of the NASA Lewis Research
Center.

PRECEDING PAGE BLANK NOT FILMED

LOCKHEED MISSILES & SPACE COMPANY

CONTENTS

LOCKHEED MISSILES & SPACE COMPANY

CONTENTS (Cont'd)

CONTENTS (Cont'd)

LOCKHEED MISSILES & SPACE COMPANY

ILLUSTRATIONS

ILLUSTRATIONS (Cont'd)

viii

LOCKHEED MISSILES & SPACE COMPANY

ILLUSTRATIONS (Cont'd)

ix

LOCKHEED MISSILES & SPACE COMPANY

ILLUSTRATIONS (Cont'd)

ILLUSTRATIONS (Cont'd)

ILLUSTRATIONS (Cont'd)

TABLES

LOCKHEED MISSILES & SPACE COMPANY

ABSTRACT

Experimental and analytical studies were conducted in order to extend previous knowledge of the thermal performance and gas evacuation characteristics of three selected multilayer insulation (MLI) composites. Flat plate calorimeter heat flux measurements were obtained for 20- and 80- shield specimens using three representative layer densities over boundary temperatures ranging from $39^{\circ}K$ ($70^{\circ}R$) to $389^{\circ}K$ ($700^{\circ}R$). Laboratory gas evacuation tests were performed on representative specimens of each MLI composite after initially purging them with helium, nitrogen, or argon gases. In these tests, the specimens were maintained at temperatures between $128^{\circ}K$ ($230^{\circ}R$) and $300^{\circ}K$ ($540^{\circ}R$). Based on the results of the laboratory-scale tests, a composite MLI system consisting of 112 unperforated, double-aluminized Mylar reflective shields and 113 water preconditioned silk net spacer pairs was fabricated and installed on a 1.22-m-(4-ft-) diameter calorimeter tank. Heat flux and gas evacuation tests were performed for hot boundary temperatures of $278^{\circ}K$ ($500^{\circ}R$), $319^{\circ}K$ ($575^{\circ}R$), and $361^{\circ}K$ ($650^{\circ}R$) with LH_2 used to establish a cold boundary temperature of $21^{\circ}K$ ($37^{\circ}R$). The outer layers of this MLI system were then removed to yield a 56-shield configuration, and both a gas evacuation and a heat flux test were performed with a nominal hot boundary temperature of $361^{\circ}K$ ($650^{\circ}R$). Experimental heat flux values correlated with those predicted by analysis within $\pm$ 8 percent, and gas evacuation rates agreed well with those predicted by the analysis. This excellent performance correlation was attributed to pre-test vacuum-drying of the MLI, improved knowledge and control of layer density values which existed during test, and development of an improved analytical model based on a wider range of test variables in conjunction with a more thermally reproducible composite.

xv

LOCKHEED MISSILES & SPACE COMPANY

Section 1
SUMMARY

The primary goal of the NAS 3-14377 contract program was to extend pre-
viously-obtained basic knowledge of the thermal performance and gas
evacuation characteristics of the following composite multilayer in-
sulation (MLI) systems:

o   double-aluminized Mylar/Tissuglas
o   double-aluminized Mylar/silk net
o   crinkled, single-aluminized Mylar

Specifically, it was desired to: (1) improve the previously-derived
analytical heat transfer models for an extended range of boundary tem-
peratures, for smaller temperature differences, and for a higher number
of shields in a given sample; (2) establish baseline thermal performance
and thermal reproducibility for the double-aluminized Mylar/silk net
composite system using water-preconditioned rather than "as received"
silk net spacers; and (3) evaluate the influence of perforated reflective
shields on both thermal performance and gas evacuation mechanisms.

In Task 1, heat flux measurements were obtained using a flat plate calor-
imeter for boundary temperatures ranging from $39^{O}K$ ($70^{O}R$) to $389^{O}K$ ($700^{O}R$),
with temperature differences from $28^{O}K$ ($50^{O}R$) to $350^{O}K$ ($630^{O}R$). Composite
layer density values were varied within the range of 28 layers/cm (71
layers/in.) to 91 layers/cm (230 layers/in.). Specimens were composed of
either 20 or 80 shields each, whereas the existing previously derived
analytical heat transfer model was based on tests of specimens which con-
tained a maximum of 20 shields each. Heat transfer model equations were
updated, based on the test results, and although gas conduction heat
transfer could be neglected in Task 1 due to the low interstitial gas
pressures encountered, a gas conduction term was developed for analytically

1-1

LOCKHEED MISSILES & SPACE COMPANY

predicting the Task 3 thermal performance.

Gas evacuation tests were conducted on a laboratory apparatus in Task 2. The parameters varied in these tests included specimen temperatures from 128°K (230°R) to 300°K (540°R), flow path lengths from 19.1 cm (7.5 in.) to 34.3 cm (13.5 in.), and layer density values within the same range studied in Task 1. Again, there were either 20 or 80 shields used in any given specimen. In these tests, helium, nitrogen, and argon initial purge gases were used to study the influence of a variable interstitial gas molecular weight.

In Task 3, one composite MLI system consisting of 112 unperforated, double-aluminized Mylar reflective shields with 113 water-preconditioned silk net spacer pairs was fabricated and installed on a 1.22-m-(4-ft-) diameter calorimeter tank. The system selected was based on the results of Tasks 1 and 2 in that it offered the best compromise of heat transfer and gas evacuation characteristics with the maximum degree of thermal reproducibility, as well as ease of fabrication and installation. A similar system with perforated shields was also fabricated and stored for future use. Heat flux and gas evacuation tests were performed to correlate the data obtained for this relatively thick, tank-installed MLI system with those predicted by the updated analytical models. These tests were conducted for nominal hot boundary temperatures of 278°K (500°R), 319°K (575°R), and 361°K (650°R) with a cold boundary temperature of 21°K (37°R) using liquid hydrogen as the calorimetric fluid. The outer layers of this MLI system were then re-moved to yield a 56-shield configuration, and both a gas evacuation and a heat flux test were performed with a hot boundary temperature of 361°K (650°R). The experimentally-obtained heat flux values correlated with those predicted by the analysis within $\pm$ 8 percent. It was shown in the post-test analysis that this remarkable performance correlation was due to a combination of factors including (1) thorough vacuum-drying of water vapor from the MLI prior to filling the cryogen tank, (2) improved knowledge and control of layer density, (3) greater reproducibility of the composite thermal performance, and (4) an improved analytical heat transfer model.

1-2

With vacuum preconditioning (item 1), long-term outgassing of water vapor and interstitial frost formations were precluded. Also, initial purge gases were readily evacuated as predicted by the analysis. The use of button-pin MLI blanket attachments and water-preconditioned silk net spacers resulted in more precise control of layer density (item 2), thus reducing the scatter of the solid conduction heat transfer data (item 3). Finally, the revised heat transfer model (item 4) benefited from the relatively large number of heat transfer test data points obtained for specimens with a greater number of layers over a wider range of boundary temperatures, as compared to the previously derived model developed during the NAS 3-12045 contract program (Ref 1).

Section 2

INTRODUCTION

Heat transfer characteristics of four promising multilayer insulations, while exposed to a high-vacuum environment, were previously investigated and evaluated by analytical and experimental studies conducted under Contract NAS 3-12025. These systems were: (1) double-aluminized Mylar/silk net, (2) double-goldized Mylar/silk net, (3) crinkled, single-aluminized Mylar, and (4) double-aluminized Mylar/Tissuglas. Mathematical expressions, based on experimental data, were developed for prediction of heat flux values for each of these systems for a wide range of variable design parameters. These design parameters included compressive pressure, layer density, shield and spacer optical properties, number of layers, and environmental boundary temperatures.

The objective of the work performed under Contract NAS 3-14377 was to extend the previous analytical and experimental studies in order to more accurately predict thermal performance and gas evacuation characteristics of systems (1), (3), and (4) as described above. Much of the data obtained for the double-aluminized Mylar/silk net system can also be applied to the double-goldized Mylar/silk net system since the only significant difference in these two systems is shield emittance and, consequently, radiative heat transfer. For system (1), pre-conditioned silk net spacers were used in an effort to further improve the good thermal reproducibility of this system. Current knowledge of all three systems was extended by (1) verification of the analytical heat transfer model over a much wider range of boundary temperatures, and for a higher number of shields in a given specimen, (2) assessment of the magnitude of multilayer interstitial gas pressures as a function of time during evacuation and steady-state operation, and (3) assessment of the magnitude of changes in insulation layer density induced by gas flow pressures during evacuation and repressurization cycles.

2-1

The Task 1 heat transfer tests were performed using a 61-cm-(24-in.-) diameter flat plate heat transfer apparatus developed previously under a Lockheed Independent Research Program. Task 2 evacuation tests were performed using the 40.6-cm-(16-in.-) diameter flat plate calorimeter, used previously for the NAS 3-12025 heat transfer tests, and modified under this program to test gas evacuation characteristics of specimens up to 68.6-cm-(27-in.-) in diameter. Data obtained from the Task 1 and Task 2 tests were used to select the double-aluminized Mylar/silk net material system for further tests under Task 3 using a 1.22-m-(4-ft-) diameter tank calorimeter. In the latter tests, an 8-blanket, 112-shield system of the selected material candidate was fabricated, installed on the tank, and tested in a 4.9-m-(16-ft-) diameter vacuum chamber.

LOCKHEED MISSILES & SPACE COMPANY

Section 3
MLI SPECIMEN MATERIAL REQUIREMENTS

Multilayer insulation (MLI) reflective shield and spacer materials which were required in order to fabricate test specimens for all three tasks of the contract program are described in this section. The composite MLI systems for which materials were procured and tests were conducted are: (1) unperforated, double-aluminized Mylar/preconditioned, double silk net; (2) perforated, double-aluminized Mylar/preconditioned, double silk net; (3) unperforated, double-aluminized Mylar/Tissuglas; (4) perforated, double-aluminized Mylar/ Tissuglas; and (5) crinkled, single-aluminized Mylar.

In general, reflective shield and spacer materials were procured from the same suppliers who had previously furnished them for the NAS 3-12025 contract program. The purchase specification that was developed under the previous program (Ref 1, Appendix A) for unperforated Mylar reflective shields was expanded under this contract to cover perforated double-aluminized Mylar shield materials. The revised specification is included as Appendix A of this report. Descriptions of the shield and spacer materials used during this contract program are presented in Table 3-1.

3.1 REFLECTIVE SHIELDS

3.1.1 Double-Aluminized Mylar

All of the double-aluminized Mylar material used during the program was procured in 1.52-meter-(5-ft-) wide rolls from the supplier (see Table 3-1). The quality of the aluminized film was certified by the supplier, and then a portion of the run was shipped directly to LMSC for use as unperforated shields. The balance of the run was shipped initially to the perforator who provided the five perforation patterns used in this program. The perforated

LOCKHEED MISSILES & SPACE COMPANY

Table 3-1

MLI MATERIALS DESCRIPTION

Designation	Use	Source	Nominal Thickness mm (mils)	Average Specific Weight, kg/m^2 (lbm/ft^2)
Unperforated, double-aluminized 0.0064-mm (0.25-mil) Mylar (a)	Shield	National Metallizing Division, Standard Packaging Corp.,Cranbury, N.J.	0.0064 (0.25)	8.8×10^{-3} (1.8×10^{-3})
Perforated, double-aluminized 0.0064-mm (0.25-mil) Mylar (b)	Shield	Same as above (c)	0.0064 (0.25	8.8×10^{-3} (1.8×10^{-3})(d)
Crinkled, single-aluminized 0.0064-mm (0.25-mil) Mylar	Shield with integral spacer	Same as above	0.0064 (0.25)	9.3×10^{-3} (1.9×10^{-3})
"Illusion silk net", approx. 0.159-cm (1/16-in.) hexagonal mesh	Spacer	John Heath-Coat Co., New York,N.Y.	0.13 (5.0)	7.3×10^{-3} (1.5×10^{-3})
"Tissuglas", Style 60G	Spacer	Pallflex Products Co., Putnam,Conn.	0.015 (0.6)	3.9×10^{-3} (8.0×10^{-4})

Notes: (a) E.I. DuPont
         (b) See Fig. 3-1 for description of perforation patterns
         (c) Perforating services by Perforated Specialties Company, Inc., 351
              West 35th Street, New York, N.Y., under subcontract to National
              Metallizing Division
         (d) Nominal specific weight value shown neglects weight loss due to
              open area. Exact values can be obtained from the equation

$$\begin{array}{c} \text{Exact Specific} \\ \text{Weight} \end{array} = \left[\begin{array}{c} \text{Nominal Specific} \\ \text{Weight} \end{array} \right] \left[1 - \frac{\text{Percent Open Area}}{100} \right]$$

3-2

stock was returned to the metallizer for reinspection and rerolling before shipment to LMSC. Receiving inspection at LMSC consisted of the following:

o Visual inspection to ensure that there were no significant tears, areas of metal removal, or punched pieces of the film (slugs) still partially attached.

o Spot dimensional checks of hole sizes and center-to-center spacings.

o Room temperature reflectance measurements using the Gier-Dunkle DB-100 reflectometer (Ref 1, Section 3.1.3). For patterns having a hole spacing smaller than the instrument aperature (i.e., S-604), the samples were backed with a first surface aluminum mirror. Measurements were made at the beginning, middle, and end of each roll supplied. Upon receipt of the initial shipment of material at LMSC, a room temperature total hemispherical emittance measurement was made on a single sample of the unperforated double-aluminized Mylar. The LMSC Calorimetric Emittance Apparatus was used (Ref 1, Section 3.1.2). The total hemispherical emittance measured at $297^{\circ}K$ ($535^{\circ}R$) was 0.031 ± 0.001. The corresponding near-normal reflectance (DB-100) measurement was 0.977. These measurements verified the metallizer's certification, and the material was accepted for this program.

Nominal dimensions for the five perforation patterns used in the program are shown in Fig. 3-1. Actual measurements of the spacing dimensions were made on the material during receiving inspection and these values, which varied slightly from the perforator's data, are presented in Table 3-2. Small variations in hole spacing, on the order of 0.08 cm (0.03 in.), were observed over a large area of several patterns, but the average spacing values conformed to the requirements for percent open area. The percent open area values were determined by dividing each pattern into rectangles of equal area, each containing a single hole, and then by dividing the area per hole times 100 by the area of the rectangle. The actual material measurements were used to compute the open area values given in Table 3-2.

3-3
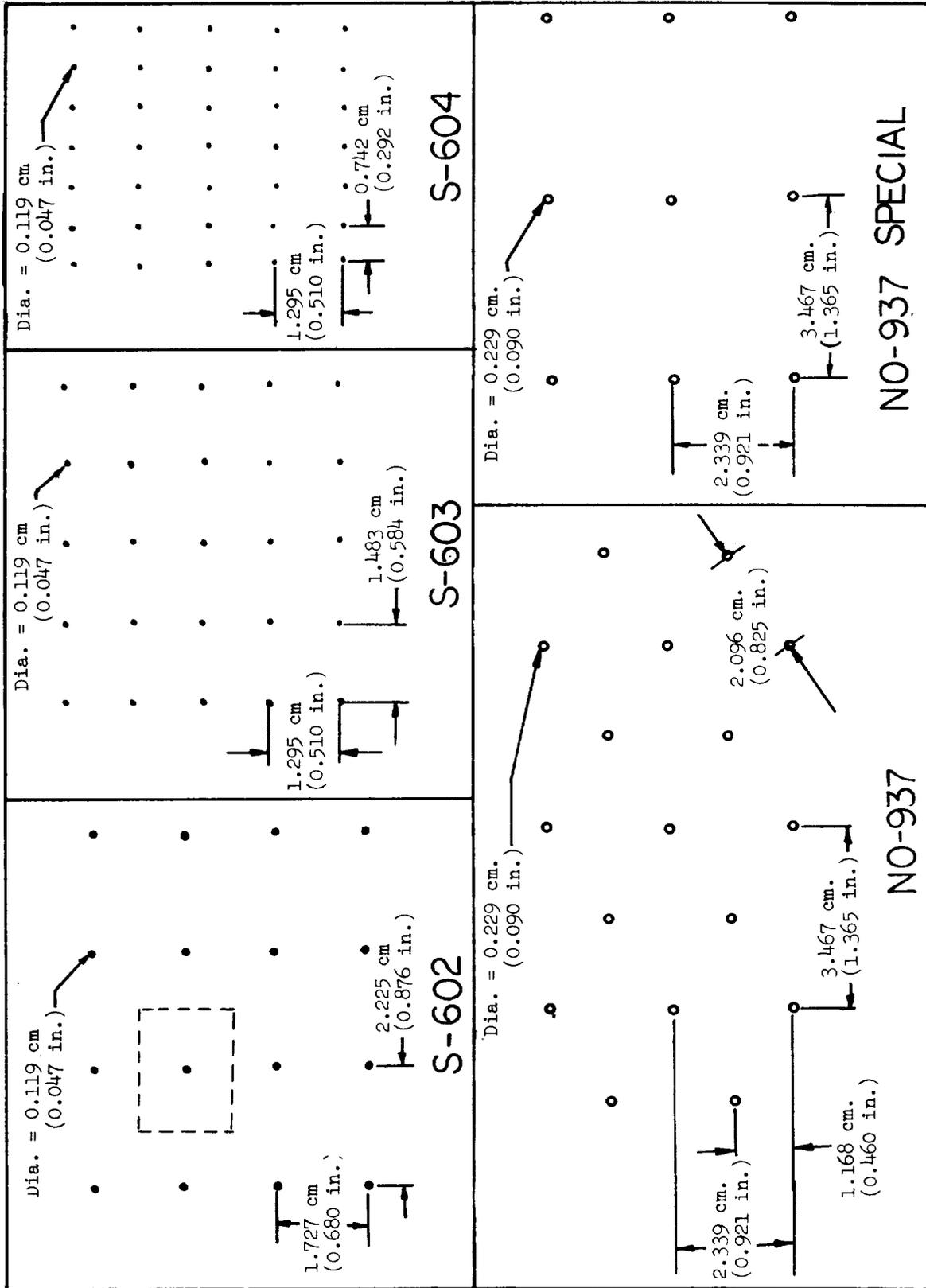
Fig. 3-1 Replicas of Selected Perforation Patterns

S-604

Dia. = 0.119 cm
(0.047 in.)

0.742 cm
(0.292 in.)

1.295 cm
(0.510 in.)

S-603

Dia. = 0.119 cm
(0.047 in.)

1.483 cm
(0.584 in.)

1.295 cm
(0.510 in.)

S-602

Dia. = 0.119 cm
(0.047 in.)

2.225 cm
(0.876 in.)

1.727 cm
(0.680 in.)

NO-937 SPECIAL

Dia. = 0.229 cm.
(0.090 in.)

3.467 cm.
(1.365 in.)

2.339 cm.
(0.921 in.)

NO-937

Dia. = 0.229 cm.
(0.090 in.)

2.096 cm.
(0.825 in.)

3.467 cm.
(1.365 in.)

1.168 cm.
(0.460 in.)

2.339 cm.
(0.921 in.)

3-4

Table 3-2

DIMENSIONAL AND OPEN AREA MEASUREMENTS ON PERFORATED MYLAR

Perforators' Pattern Designation	Hole Dia. cm (in.)	Hole Spacings,cm (in.)		Percent Open Area
		Horizontal	Vertical	
S-602	0.119(0.047)	2.24(0.88)	1.93(0.76)	0.26
S-603	0.119(0.047)	1.47(0.58)	1.37(0.54)	0.55
S-604	0.119(0.047)	0.74(0.29)	1.42(0.56)	1.07
937	0.229(0.090)	3.48(1.37)	1.19(0.47)	0.99
937 Special	0.229(0.090)	3.48(1.37)	2.49(0.98)	0.48

Visual inspection of the material did not reveal any tears, irregular openings, or removal of the metal film. Reflectance measurements were made at four locations near the beginning and end of each roll. The reflectance values obtained from the measurements are tabulated in Table 3-3. The relatively low values obtained for the S-604 pattern were most likely caused by the relationship of the close spacing of the perforations and the size of the reflectometer entrance apperature (1.5 cm or 0.59 in.). The S-604 specimens were backed by a rigid, first surface aluminum mirror with a reflectance of 0.98 (as measured using the DB-100 reflectometer). However, the exposed edges of the perforations in the Mylar decrease the reflectance of the surface viewed through the instrument aperature, and the resulting value is less than that of the unperforated metallized surface. For the large-hole-spacing patterns, the reflectance values obtained ranged from 0.96 to 0.97 which shows some degradation over typical values of 0.97 to 0.98 for unperforated double-aluminized Mylar. This decrease in reflectance is attributed to the handling encountered in the perforation process. Total hemispherical emittance measurements were also made on perforated samples during the heat transfer testing to verify emittance.

LOCKHEED MISSILES & SPACE COMPANY

Table 3-3

REFLECTANCE MEASUREMENTS ON PERFORATED MYLAR

Pattern Designation	Near-Normal Reflectance
S-602	0.965, 0.962, 0.959, 0.968 (0.963 av.)
S-603	0.961, 0.964, 0.960, 0.951 (0.959 av.)
S-604	0.945, 0.952, 0.949, 0.954 (0.950 av.)
937	0.958, 0.963, 0.958, 0.962 (0.960 av.)
937 Special	0.968, 0.970, 0.965, 0.965 (0.967 av.)

3.1.2 Crinkled, Single-Aluminized Mylar

The crinkled, single aluminized Mylar material used to fabricate gas evacuation
test specimens in Task 2 was also procured in 1.52-meter-(5-ft-) wide rolls
from the supplier (see Table 3-1). Although the quality of this aluminized
film was again certified by the supplier, no emittance or reflectance measure-
ments were obtained at LMSC since the material was not used for heat transfer
testing. As for the double-aluminized Mylar material, visual inspection re-
vealed that there were no tears or areas where the metal film had been removed
from the crinkled, single-aluminized Mylar material.

LOCKHEED MISSILES & SPACE COMPANY

3.2 SPACERS

3.2.1 Preconditioned Silk Net

As a result of studies performed for the NASA/LeRC by the Boeing Company, LMSC was directed to implement a water-preconditioning process for the silk net spacers in order to improve uniformity of layer density as well as to facilitate fabrication of MLI for contoured surfaces. This process consisted of wetting the silk net material, smoothing out the wrinkles and surface irregularities, and then drying it to provide a wrinkle-free layer. Developmental studies were conducted which demonstrated that adequate wetting of the net could be accomplished by water-spraying 10 to 20 layers stretched one over the other on a frame rather than by soaking each layer individually. Also, it was shown that air-drying was adequate for the removal of excess moisture and yielded a smooth layer of netting. The preconditioning process was applied during fabrication of the double-aluminized Mylar/silk net MLI specimens for heat transfer and gas evacuation tests conducted in Tasks 1, 2, and 3.

3.2.1.1 Experimental Procedures.

The initial tests conducted during the net preconditioning study were performed to evaluate the effects of the wetting technique on moisture content and removal of sizing. It was found that soaking of the net in water removed most of the sizing (which has fire retardent properties), but did not improve the layer flatness characteristics over those achieved by spraying the net with water. The latter method leaves most of the sizing in the net, thus imparting stiffness to the material and resulting in better handling characteristics for blanket layup procedures. Amounts of moisture and sizing were determined from a series of weight change measurements on 0.093-m^2 (1.0-ft^2) specimens of net.

The moisture content of the "as received" material (after storage in a laboratory environment at $22 \pm 2°C$, $72 \pm 3.6°F$, and 50 ± 10 percent relative humidity for seven days) was determined by weight measurements before and after oven drying as shown in Table 3-4. A forced-convection oven was used, weight measurements were obtained hourly, and at $100°C$ ($212°F$) equilibrium

LOCKHEED MISSILES & SPACE COMPANY

weight (i.e., < 1 percent change per hour) was achieved in four hours. The initial moisture content determined for two specimens was 4.7 and 4.4 percent. These values are in agreement with an independent Thermogravimetric Analysis (TGA) conducted during an earlier program study on a specimen of "as received" net which showed a weight loss of 4.9 percent at 100°C (212°F) and 5.3 percent at 150°C (302°F). Following oven drying, one of the two current-study specimens was again weighed after a 42-hour period in the laboratory at 22 to 24°C (72 to 75°F) and a relative humidity of 40 to 50 percent. After this period, the specimen weight was nearly the same as the initial weight indicating a moisture content gain to achieve equilibrium with the environment conditions.

Table 3-4

WEIGHTS OF SILK NET AS FUNCTION OF WETTING AND DRYING
PROCEDURE

Water Treatment	Specimen Weight, gm (oz)[a]			
	As received	Soak or Spray	Oven Dry 4 hrs at 100°C (212°F)	Air Dry or Store at 22°C to 24°C (72°F to 75°F)
None	0.643 (0.0227)	--	0.613 (0.0216)	0.641 (0.0226) after 42 hr
None	0.639 (0.0225)	--	0.611 (0.0215)	-- -
Soak	0.650 (0.0229)	1.667 (0.0588) after 5 rinses	--	0.429 (0.0151) after 20 hr
				0.428 (0.0151) after 42 hr
				0.427 (0.0151) after 66 hr
Soak	0.642 (0.0226)	5 rinses	0.408 (0.0144)	0.417 (0.0147) after 42 hr
				0.417 (0.0147) after 66 hr
Spray	0.631 (0.0223)	1.140 (0.0402) after spray	0.577 (0.0204)	0.585 (0.0206) after 42 hr
Spray	0.634 (0.0224)	1.160 (0.0409) after spray	--	0.598 (0.0211) after 16 hr
				0.590 (0.0208) after 42 hr

(a) Surface area of each specimen 0.093 m^2 (1.0 ft^2). Sequence of measurements from left to right.

3-8

Two additional specimens of the silk net were soaked in distilled water at 23°C (73°F) and, after five rinses each, an increase in the initial weight of approximately 156 percent was observed. One of these specimens was air dried in the laboratory while the other was oven dried and then stored at laboratory conditions until an equilibrium weight was observed. The difference between initial and final weight values, with the latter obtained after 42 hours of air drying or storage after oven drying, indicated a net weight loss of approximately 34.7 percent for each of these specimens. Since it had been shown by the prior specimen tests that the moisture content after oven drying and storage for 42 hours at laboratory conditions was virtually the same as it had been initially, it was concluded that the entire weight loss observed for the two water-soaked specimens was due to removal of the sizing.

A third pair of specimens was preconditioned by spraying them with a fine water mist. Immediately after spraying, an increase of approximately 82 percent of the initial weight value was observed for each specimen. One specimen was then oven dried and subsequently stored at laboratory conditions for 42 hours. The net loss in the initial weight for this specimen was 7.3 percent after storage. The second specimen exhibited a similar weight loss of 6.9 percent after air drying in the laboratory for 42 hours.

Results of the laboratory tests described above indicate that air drying of the wetted net material in a nominal room environment for 42 hours or longer is adequate to remove the excess moisture absorbed during the water-soak or water-spray preconditioning processes. No apparent benefit results from oven drying, unless the material is then to be continuously stored and handled in a dry atmosphere, since it appears that the net moisture content will equilibrate with that of the local environment within a 42-hour period. Based on study results, the average specific weight obtained for two water-soaked specimens, after air drying (or oven drying and storage) for 42 hours, was 4.55×10^{-3} kg/m^2 (9.32×10^{-4} lbm/ft^2). Also, the water content was found to be approximately 6.9 percent, based on final specimen weights, and the sizing content was estimated to be negligible for netting preconditioned in

3-9

this manner. Similarly, the average specific weight for two water-sprayed specimens, after 42 hours of drying and/or storage, was 6.33×10^{-3} kg/m^2 (1.30×10^{-3} lbm/ft^2). For these specimens, calculations show that the sizing content was approximately 29.7 percent and the water content was approximately 4.9 percent based on final specimen weights.

The procedure selected for water-spray preconditioning of the net material for Tasks 1 and 2 required initial placement of twenty layers of net over a wooden frame 1.37 m by 1.37 m (4.5 ft by 4.5 ft) inside dimensions. Each layer was stretched individually over the frame until the total of twenty was reached. The edges of each layer were held by a double row of pins, staggered on 2.54 cm (1-in.) centers. Wetting of the net was accomplished by spraying water over both sides of the lay-up using a Binks No. 15 spray gun held 0.46 to 0.61 m (1.5 to 2.0 ft) from the net. The material was then allowed to air dry in the frame for 48 hours. After removal from the frame, each layer of the preconditioned net was stored flat until it was used.

In order to compare the layer density and compressive pressure characteristics of the preconditioned material, additional 0.093-m^2 (1.0-ft^2) multilayer specimens were prepared and subjected to a test to measure specimen thickness as a function of applied load. Four specimens each of preconditioned net and smooth double-aluminized Mylar were prepared with 10, 20, and 80 shields (22, 42, and 162 layers of net, respectively). Also, one specimen of each number of layers was prepared using the "as received" net material to serve as a baseline for evaluation of the preconditioning treatment.

Data on thickness and layer density as a function of applied compressive pressure at room temperature were obtained by loading the specimens in a compression testing machine. The specimens were placed between parallel 0.093-m^2 (1.0-ft^2) rigid metal plates. Uncompressed thicknesses were determined by visually observing contact of the insulation with the upper plate. Compressive loads were then applied incrementally at 0.556, 1.11, 2.22, 4.45, 8.90, 13.3, 22.2, 35.6, 48.9, and 62.3 N (0.125, 0.25, 0.5, 1, 2, 3, 5, 8, 11, and 14 lbf). The resulting compressive pressure values range from 1.17 N/m^2 (1.70×10^{-4} psi),

3-10

for zero external load applied to the 10-shield specimens, to 679 N/m² (985x10⁻² psi) for a 62.3-N (14-1bf) external load applied to the 80-shield specimens. Compressive load was maintained constant at each value for one minute, and plate separation was recorded continuously using a linear variable differential transducer (LVDT) calibrated to obtain an accuracy of 2.5 x 10⁻² mm (1.0 mil). The applied force was monitored using a load cell having an accuracy of 0.2 N (0.05 lb) over the range of test loads. After maximum compression, the load values were reduced using the same increments with continuous recording of plate separation. Subsequently, the loading-unloading cycle described above was repeated once and the final uncompressed thickness value was determined.

3.2.1.2 Results. The results of the tests conducted to determine the compressive loading response of the double-aluminized Mylar/preconditioned silk net composite material are summarized in Table 3-5. The uncompressed values of layer density for all sets of specimens were within 10 percent and, with exception of the 10-shield specimen set, generally good specimen-to-specimen uniformity was observed under all loads for a given set. Post-test inspection of the 10-shield specimens did not reveal any reason for the anomalous behavior of this set such as wrinkled or creased shields or spacers. Also, all spacers used for these four specimens were taken from a single preconditioning batch so that batch-to-batch variables in the preconditioning process cannot be considered as a possible explanation. For the 10-shield case, and especially at the large layer density values, specimen thicknesses are small and any misalignment of the loading plates could result in appreciable errors in thickness and subsequent layer density determinations. However, parallelism of the plates was checked prior to each test and no discrepancies were noted.

The second loading cycle for each specimen using as-received silk net spacers showed little deviation from the initial cycle as shown by the 80-shield set data in Table 3-6. A layer density increase was observed after the initial unloading, but under an applied external load the response was essentially identical for both cycles.

A comparison of the layer density-compressive pressure relationship for composites using preconditioned and "as received" silk net is presented in Table

3-11

Table 3-5a

SUMMARY OF LAYER DENSITY DATA AS A FUNCTION OF COMPRESSIVE PRESSURE
FOR DOUBLE-ALUMINIZED MYLAR WITH WATER-PRECONDITIONED SILK NET SPACERS (a)

Compressive Pressure, N/m^2 (b)	Layer Density, No./cm				
	Specimen No. 1	Specimen No. 2	Specimen No. 3	Specimen No. 4	Average
10 Shield, 22 Net; Specimen Weight = 0.022 kg					
1.17 (c)	28.9	28.9	28.9	29.9	29.1
7.16	36.9	34.6	37.0	39.8	37.1
13.1	43.3	39.4	39.4	42.0	41.0
25.1	47.1	44.2	43.3	45.6	45.0
49.1	56.3	49.8	48.1	49.2	50.8
96.9	61.9	57.0	53.5	52.8	56.1
145	66.6	61.9	56.3	55.5	60.1
241	69.8	66.6	59.3	59.3	63.8
384	78.7	72.2	64.6	63.7	69.8
528	86.6	78.7	69.8	68.7	76.0
672	92.1	83.3	74.7	72.2	80.6
20 Shields, 42 Net; Specimen Weight = 0.043 kg					
2.27 (c)	25.8	27.6	27.6	28.5	27.4
8.26	33.3	38.8	39.6	39.4	38.7
14.2	36.3	41.3	41.8	43.5	40.7
26.2	42.4	44.4	47.0	46.5	45.1
50.2	47.2	48.1	49.2	49.5	48.7
146	53.0	53.3	56.6	54.8	54.4
242	55.9	56.3	59.1	55.9	56.8
385	59.1	59.1	62.2	61.3	60.4
529	61.3	60.4	65.1	63.6	62.6
673	64.6	64.6	67.8	65.6	65.7
80 Shields, 162 Net; Specimen Weight = 0.168 kg					
8.88 (c)	28.7	29.6	28.0	27.9	28.5
14.9	35.3	35.6	35.0	34.7	35.2
20.9	39.1	39.2	39.7	38.7	39.2
32.8	41.6	41.9	42.1	40.9	41.6
56.8	43.5	43.7	43.5	42.8	43.4
105	46.7	47.0	47.1	45.4	46.6
153	48.0	48.3	48.4	47.1	48.0
248	50.3	50.4	50.6	49.1	50.1
392	52.4	52.7	52.6	51.5	52.3
536	54.1	54.3	54.1	53.5	54.0
679	55.5	55.7	55.5	54.8	55.4

Notes: (a) Data shown are for the initial loading cycle
(b) Applied load plus one-half of specimen weight per unit area
(c) Based on one-half of specimen weight per unit area (unloaded condition)

LOCKHEED MISSILES & SPACE COMPANY

Table 3-5b

SUMMARY OF LAYER DENSITY DATA AS A FUNCTION OF COMPRESSIVE PRESSURE
FOR DOUBLE-ALUMINIZED MYLAR WITH WATER-PRECONDITIONED SILK NET SPACERS (a)

Compressive Pressure (psi)[b]	Layer Density (No./in.)				
	Specimen No. 1	Specimen No. 2	Specimen No. 3	Specimen No. 4	Average
10 Shields, 22 Net; Specimen Weight = 0.049 lbm					
1.70×10^{-4} (c)	73.5	73.4	73.3	76.0	74.0
1.04×10^{-3}	93.7	88.0	94.0	101.2	94.3
1.91×10^{-3}	110.0	100.0	100.0	106.8	104.2
3.64×10^{-3}	119.6	112.2	110.0	115.8	114.4
7.11×10^{-3}	142.9	126.4	122.2	125.0	129.1
1.41×10^{-2}	157.1	144.7	135.8	134.1	142.6
2.10×10^{-2}	169.2	157.1	142.9	141.0	152.6
3.49×10^{-2}	177.4	169.2	150.7	150.7	162.0
5.57×10^{-2}	200.0	183.3	164.2	161.8	177.3
7.66×10^{-2}	220.0	200.0	177.4	174.6	193.0
9.74×10^{-2}	234.0	211.5	189.7	183.3	204.6
20 Shields, 42 Net; Specimen Weight = 0.095 lbm					
3.30×10^{-4} (c)	65.6	70.1	70.0	72.3	69.5
1.20×10^{-3}	84.5	98.5	100.7	100.0	98.2
2.07×10^{-3}	92.1	105.0	106.1	110.5	103.4
3.80×10^{-3}	107.7	112.9	119.3	118.0	114.5
7.27×10^{-3}	120.0	122.1	125.0	125.7	123.6
2.12×10^{-2}	134.6	135.5	143.8	139.1	138.3
3.51×10^{-2}	141.9	142.9	150.0	141.9	144.2
5.59×10^{-2}	150.0	150.0	157.9	155.6	153.4
7.67×10^{-2}	155.6	153.3	165.4	161.6	159.0
9.76×10^{-2}	164.1	164.1	172.1	166.7	166.8
80 Shields, 162 Net; Specimen Weight - 0.371 lbm					
1.29×10^{-3} (c)	72.8	75.3	71.2	70.8	72.5
2.16×10^{-3}	89.6	90.3	89.0	88.1	89.3
3.02×10^{-3}	99.4	99.6	100.9	98.3	99.5
4.76×10^{-3}	105.6	106.3	106.9	103.9	105.7
8.23×10^{-3}	110.4	110.9	110.6	108.7	110.2
1.52×10^{-2}	118.6	119.3	119.7	115.4	118.3
2.21×10^{-2}	122.0	122.7	122.9	119.7	121.8
3.60×10^{-2}	127.8	128.1	128.4	124.6	127.2
5.68×10^{-2}	133.0	133.9	133.7	130.9	132.9
7.77×10^{-2}	137.3	137.9	137.5	135.8	137.1
9.85×10^{-2}	140.9	141.4	140.9	139.1	140.6

Notes: (a) Data shown are for the initial loading cycle
(b) Applied load plus one-half of specimen weight per unit area
(c) Based on one-half of specimen weight per unit area (unloaded condition)

3-13

Table 3-6

SUMMARY OF LAYER DENSITY DATA AS A FUNCTION OF COMPRESSIVE PRESSURE
FOR DOUBLE-ALUMINIZED MYLAR WITH AS-RECEIVED
SILK NET SPACERS

Compressive Pressure N/m² (psi) (a)		Layer Density, No./cm (No./in.)			
		First Cycle		Second Cycle	
		Loading	Unloading	Loading	Unloading
		80 Shields, 162 Net			
8.88	(1.29×10^{-3}) (b)	20.9 (53.0)	21.7 (55.2)	23.1 (58.6)	23.6 (60.0)
14.9	(2.16×10^{-3})	25.9 (65.8)	27.4 (69.7)	26.3 (66.8)	28.4 (72.1)
20.9	(3.02×10^{-3})	26.9 (68.3)	29.1 (73.9)	26.9 (68.2)	30.4 (77.1)
32.8	(4.76×10^{-3})	29.8 (75.7)	31.4 (79.8)	29.6 (75.3)	32.0 (81.3)
56.8	(8.23×10^{-3})	33.2 (84.3)	34.6 (88.0)	33.1 (84.2)	35.0 (89.0)
105	(1.52×10^{-2})	36.4 (92.5)	37.6 (95.6)	36.4 (92.5)	38.4 (97.5)
153	(2.21×10^{-2})	38.7 (98.3)	40.3 (102.3)	38.7 (98.2)	40.4 (102.5)
248	(3.60×10^{-2})	41.5 (105.4)	42.7 (108.4)	41.6 (105.6)	42.8 (108.6)
392	(5.68×10^{-2})	43.3 (110.0)	44.5 (113.0)	43.7 (111.0)	44.6 (113.3)
536	(7.77×10^{-2})	45.3 (115.0)	45.6 (115.7)	45.2 (114.9)	45.7 (116.2)
679	(9.85×10^{-2})	46.5 (118.0)	-	46.5 (118.2)	-

Notes: (a) Applied load plus 1/2 specimen weight per unit area

(b) Based on 1/2 specimen weight per unit area (unloaded condition)

3-7 and Fig. 3-2 for 80-shield sets. By inspection of these data it is seen
that the water-spray preconditioning procedure resulted in a higher layer
density for any given value of compressive pressure. However, the specimen-
to-specimen layer density variation (i.e., data scatter) was much less for
the specimens containing the preconditioned net spacers than it was for those
using "as received" net. A maximum variation of 6 percent, based on the mini-
mum layer density value for any given compressive pressure, was observed for
the preconditioned-net specimens, whereas a 26 percent maximum difference was
noted for the specimens with as-received net material. These variations de-
creased with increased compressive pressure to values of approximately 2 and
10 percent, respectively.

Table 3-7

COMPARISON OF LAYER DENSITY DATA AS A FUNCTION OF COMPRESSIVE PRESSURE
FOR DOUBLE-ALUMINIZED MYLAR WITH
AS-RECEIVED AND WATER-PRECONDITIONED SILK NET SPACERS (a)

Compressive (b) Pressure N/m^2(psi)	Layer Density No./cm (No./in.)			
	Specimen No. 1	Specimen No. 2	Specimen No. 3	Specimen No. 4
Preconditioned Net				
8.88 (1.29 x 10^{-3})	28.7(72.8)	29.6(75.3)	28.0(71.2)	27.9(70.8)
14.9 (2.16 x 10^{-3})	35.3(89.6)	35.6(90.3)	35.0(89.0)	34.7(88.1)
20.9 (3.02 x 10^{-3})	39.1(99.4)	39.2(99.6)	39.7(100.9)	38.7(98.3)
32.8 (4.76 x 10^{-3})	41.6(105.6)	41.9(106.3)	42.1(106.9)	40.9(103.9)
56.8 (8.23 x 10^{-3})	43.5(110.4)	43.7(110.9)	43.5(110.6)	42.8(108.7)
105 (1.52 x 10^{-2})	46.7(118.6)	47.0(119.3)	47.1(119.7)	45.4(115.4)
153 (2.21 x 10^{-2})	48.0(122.0)	48.3(122.7)	48.4(122.9)	47.1(119.7)
248 (3.60 x 10^{-2})	50.3(127.8)	50.4(128.1)	50.6(128.4)	49.1(124.6)
392 (5.68 x 10^{-2})	52.4(133.0)	52.7(133.9)	52.6(133.7)	51.5(130.9)
536 (7.77 x 10^{-2})	54.1(137.3)	54.3(137.9)	54.1(137.5)	53.5(135.8)
679 (9.85 x 10^{-2})	55.5(140.9)	55.7(141.4)	55.5(140.9)	54.8(139.1)
As Received Net				
8.88 (1.29 x 10^{-3})	20.9(53.0)	25.5(64.8)	24.1(61.2)	
14.9 (2.16 x 10^{-3})	25.9(65.8)	32.0(81.3)	27.1(68.9)	
20.9 (3.02 x 10^{-3})	26.9(68.3)	33.9(86.1)	29.0(73.7)	
32.8 (4.76 x 10^{-3})	29.8(75.7)	36.3(92.2)	36.2(92.0)	
56.8 (8.23 x 10^{-3})	33.2(84.3)	38.7(98.2)	38.5(97.8)	
105 (1.52 x 10^{-2})	36.4(92.5)	41.6(105.6)	41.0(104.1)	
153 (2.21 x 10^{-2})	38.7(98.3)	43.3(110.0)	43.6(110.8)	
248 (3.60 x 10^{-2})	41.5(105.4)	45.7(116.2)	45.2(114.7)	
392 (5.68 x 10^{-2})	43.3(110.0)	48.1(122.2)	47.2(120.0)	
536 (7.77 x 10^{-2})	45.3(115.0)	49.8(126.4)	49.1(124.6)	
679 (9.85 x 10^{-2})	46.5(118.0)	51.1(129.8)	50.3(127.8)	

(a) Data shown are for 80-shield specimens and the initial loading cycle

(b) Applied load plus one half specimen weight per unit area

3-15

LOCKHEED MISSILES & SPACE COMPANY
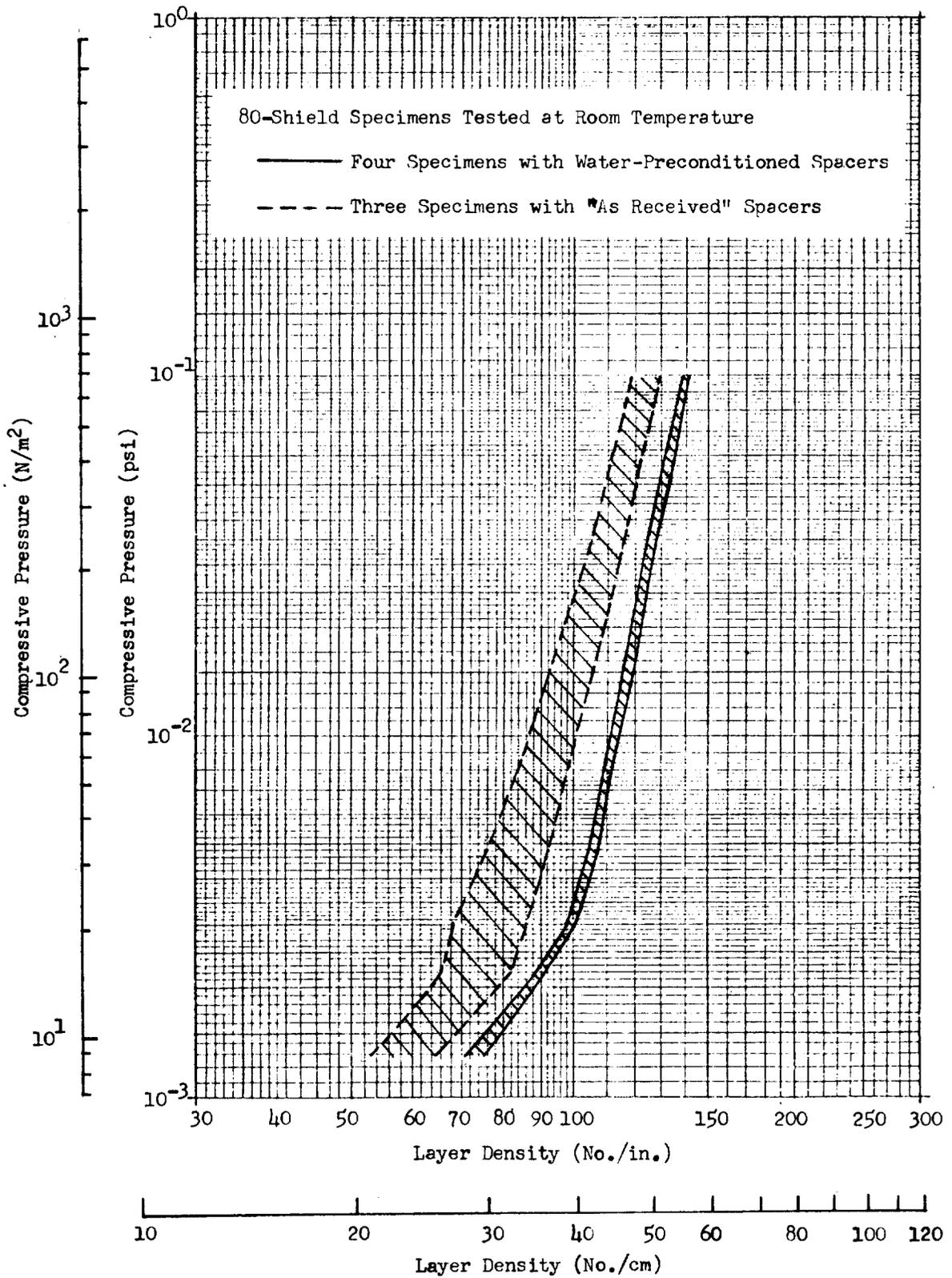
Fig. 3-2 Compressive Pressure as a Function of Layer Density for Double-
Aluminized Mylar/Silk Net

LOCKHEED MISSILES & SPACE COMPANY

While the influence of layer density uniformity cannot be evaluated in an absolute sense, it can be qualitatively shown that the preconditioning should significantly reduce the uncertainty in the thermal performance characteristics of this insulation. For example, the heat flux attributed to conduction typically varies approximately as the third power of layer density. If the composite is such that 15-percent variations are expected in layer density this would then result in a 50-percent uncertainty in conduction. The effect on total heat transfer would be dependent upon the boundary temperatures, but for a 300°K to 40°K (540°R to 72°R) case conduction accounts for approximately one-half of the total heat transfer so a 20 to 25 percent penalty is incurred due to lack of layer density reproducibility. If layer density variations can be held to 5 percent, the total heat flux uncertainty reduces to less than 10 percent which is a significant reduction in the insulation thermal performance uncertainty value.

3.2.2 Tissuglas

The Tissuglas spacer material used to prepare test specimens for Tasks 1 and 2 was procured from the supplier (Ref Table 3-1) in 0.9-m-(3-ft-) wide rolls. Single layer spacers were then cut from the roll and alternated with the reflective shields using the procedures developed during the NAS 3-12025 contract program. The Tissuglas spacer material was used in the "as received" condition.

Section 4

TASK I - HEAT TRANSFER EVALUATIONS

In this program task, the heat transfer characteristics of three MLI composites were evaluated in terms of boundary temperature, number of shields, and layer density. The three basic composite systems investigated were:

- o unperforated, double-aluminized Mylar reflective shields with Tissuglas paper spacers.
- o unperforated, double-aluminized Mylar reflective shields with water-preconditioned, double silk net spacers.
- o perforated, double-aluminized Mylar reflective shields with water-preconditioned, double silk net spacers.

Parallel experimental and analytical efforts were conducted in this task. From the experimental heat transfer data, mathematical models were developed and modified so that they could be used to predict the performance of the tank-installed insulation systems for a wide range of boundary temperatures, numbers of layers, layer densities, and interstitial gas pressures.

The specimens and test conditions selected for the heat transfer evaluation were chosen to (1) supplement the data for silk net and Tissuglas spacers obtained under Contract NAS 3-12025 (Ref 1) in terms of increased number of layers and boundary temperature conditions, (2) establish the thermal per-formance of the preconditioned silk net composite, and (3) evaluate the influence of perforated reflective shields on composite thermal performance. Boundary temperature effects from 40° K (72°R) to 390°K (702°R) were investigated for both small and large temperature differences of 30°K (54°R) to 350°K (630°R), respectively, in conjunction with varying layer density for both silk net and Tissuglas spacers for 20-and 80-shield specimens. The influence of perforated shields was studied for two perforation sizes of

0.119 cm (0.047-in.) and 0.229-cm (0.090-in.) diameter and three open area percentages of 0.3 percent, 0.5 percent, and 1.0 percent for the silk net spacer system only. Initially, it was intended that the perforation study would also include the Tissuglas spacer, but on the basis of gas flow test results from Task 2 this portion of the program was deleted. As discussed in Section 5, the experiments with this spacer showed that broadside pumping with perforated shields resulted in relatively high interstitial pressure values and damage to the specimen. Thus, it is not an effective method by which to evacuate a blanket made up of these material components.

During the analytical phase, the heat transfer models developed under Contract NAS 3-12025 were modified, using the experimental data, to consider interstitial gas pressure, to consider the influence of perforated reflective shields, and to more accurately reflect the temperature dependence of the solid conduction term of the total heat transfer equation at low hot boundary temperatures (i.e., less than 100°K or 180°R). Using the modified mathematical model, predictions of Task 3 insulation system performance were made for comparison with the actual tank system performance data.

A summary of the heat transfer tests which were conducted in Task 1 is given in Table 4-1. The experimental results are discussed in Section 4.1, and the analytical studies are presented and discussed in Section 4.2.

4.1 HEAT TRANSFER TESTING

4.1.1 Experimental Method

During the earlier NAS 3-12025 contract program, heat flux values ranging from 0.5 to 63 w/m^2 (0.16 to 20 Btu/hr ft^2) were measured on a 40.6-cm-(16-in.-) diameter flat plate apparatus using boiloff calorimetry. During this NAS 3-14377 contract program, however, measurements of values approximately an order of magnitude lower than the previous minimum were required for the Task 1 testing. The boiloff flow rates resulting from heat flux values of this low magnitude are too small for practical measurement using

Table 4-1

SUMMARY OF TASK 1 HEAT TRANSFER TESTS

Insulation Composite	Specimen No. (Perforation Pattern)	No. of Shields	Perf. Dia., cm (in.)	Open Area, percent	Nominal Boundary Temperatures, °K(°R) T_C	T_H	Layer Density, No./cm (No./in.)
Unperforated, Double-Aluminized Mylar/ Tissuglas	1	20	–	–	40 (72) 95 (171)	75, 170, 300, 390 (135),(306),(540),(702) 125,300,390 (225),(540),(702)	52,60,91 (132),(152),(230) 52,91 (132),(230)
	2	80	–	–	40 (72) 95 (171) 300 (540)	70,225,300,370 (126),(405),(540),(666) 125,300,370 (225),(540),(666) 370 (666)	52,60,91 (132),(152),(230) 52,60,91 (132),(152),(230) 52,91 (132),(230)
Unperforated, Double-Aluminized Mylar/ Double Preconditioned Silk net	3	20	–	–	40 (72) 95 (171)	75,225,300,370 (135),(405),(540),(666) 125,300,370 (225),(540),(666)	28,48 (71),(122) 28,48 (71),(122)
	4	80	–	–	40 (72) 95 (171) 330 (594)	75,250,300,370 (135),(450),(540),(666) 250,300,370 (450),(540),(666) 370 (666)	28,39,48 (71),(99),(122) 28,39,48 (71),(99),(122) 28 (71)
Perforated Double-Aluminized Mylar- Double Preconditioned Silk Net	5(S-602)	80	0.119 (0.047)	0.26	95 (171)	250,300,370 (450),(540),(666)	28,39,48 (71),(99),(122)
	6(S-603)	80	0.119 (0.047)	0.55	95 (171)	250,300,370 (450),(540),(666)	28,39,48 (71),(99),(122)
	7(S-604)	80	0.119 (0.047)	1.07	95 (171)	250,300,370 (450),(540),(666)	28,39,48 (71),(99),(122)
	8(937Sp)	80	0.229 (0.090)	0.48	95 (171)	250,300,370 (450),(540),(666)	28,39,48 (71),(99),(122)
	9(937)	80	0.229 (0.090)	0.99	95 (171)	250,300,370 (450),(540),(666)	28,48 (71),(122)

the 40.6-cm-(16-in.-) diameter apparatus with the instrumentation system that was used previously. Consequently, it was necessary to select a more suitable apparatus and test method with which to accurately measure heat flux values down to 0.03 W/m^2 (0.01 Btu/hr ft^2).

The method selected for this task is an electrical power input difference method in which the cryogens are used only to maintain constant sink temperatures. Reasonably accurate heat flux values can be determined from measurements of the electrical power dissipated in a 15.2-cm-(6-in.-) diameter measuring section located in the center of a 61-cm-(24-in.-) outside diameter guard heater. Specimens to 3.8-cm-(1.5-in.-) thick, with boundary temperature differences as low as $30^\circ K$ ($54^\circ R$) can be accurately evaluated. Measurements can also be obtained with relative ease for a wide range of boundary temperatures including very large temperature differences.

A physical model of the measuring system is shown schematically in Fig. 4-1. The boundary surface plates are thermally connected to heat sinks which are reservoirs filled with a cryogen. Electrical power, P_C, is applied to the measuring area heater to increase the plate temperature to the desired cold boundary value, $T_1 = T_C$, which is higher than the sink temperature, T_S. Power is also applied to the guard plate heater, to the edge guard ring heater (not shown in Fig. 4-1) and to the warm boundary plate heater such that $T_1 = T_2 = T_3 = T_E = T_C$. In this calibration condition, the heat transfer through the insulation specimen at equilibrium is nominally zero, since the hot and cold boundary temperatures are the same. All of the energy dissipated in the measuring section is transferred to the cryogen sink through the thermal link and through the insulation placed between the plate and the sink. After steady-state conditions have been achieved, the measuring section power, P_C, is determined and recorded. Then the hot boundary temperature is increased to the desired level for test, $T_3 = T_H$. Concurrently, the edge guard ring temperature, T_E, is increased to the average of T_H and T_C, while T_1 and T_2 are maintained at T_C. Again, after steady-state conditions have been attained, the power to the main (measuring) heater,

4-4
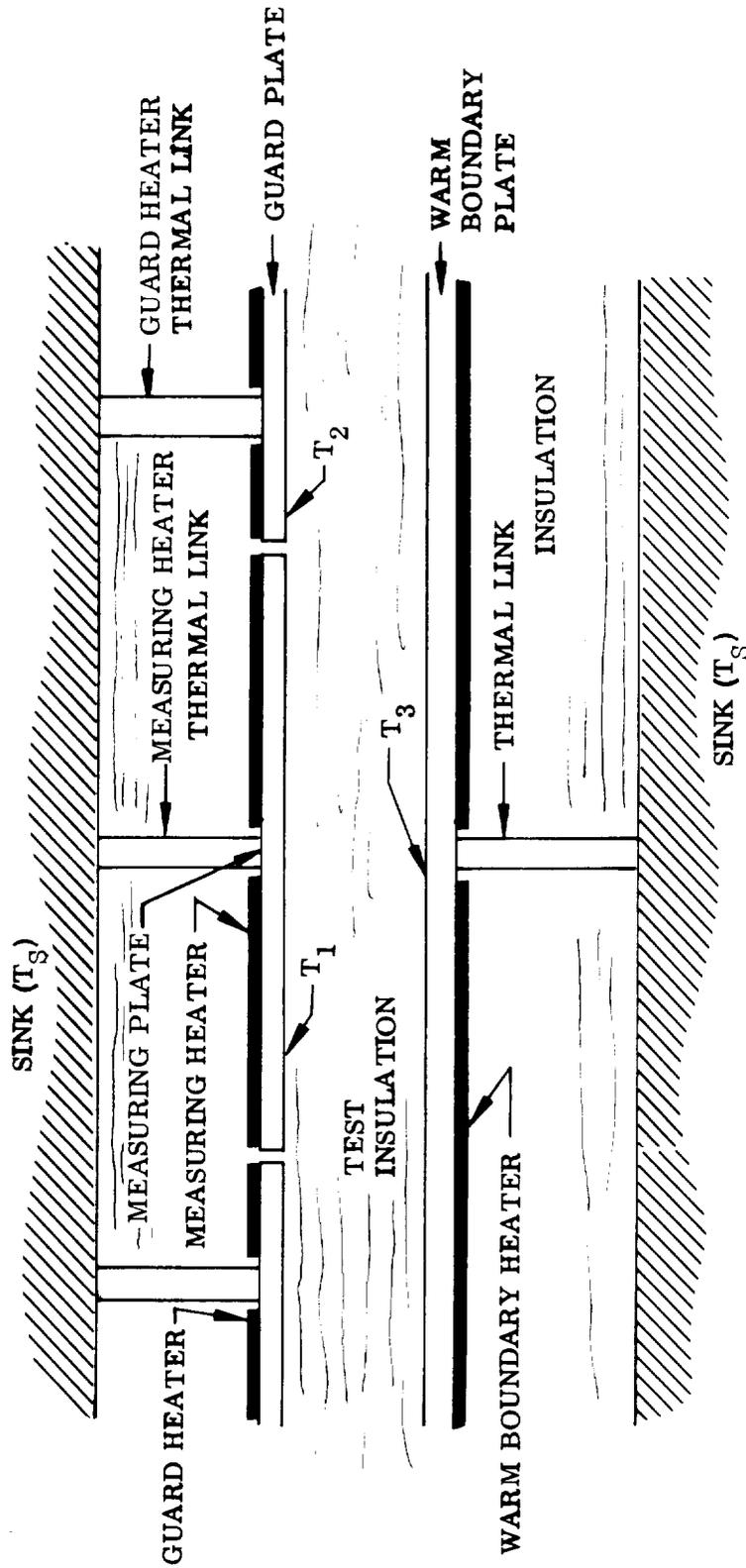
Fig. 4-1   Physical Model of Measuring System

LOCKHEED MISSILES & SPACE COMPANY

P_H, is measured and recorded. Under this test condition, heat transfer occurs through the insulation specimen, and the electrical power required to maintain the measuring plate at the constant temperature T_C is less than it was for the calibration condition with zero heat flow through the specimen (i.e., $P_H < P_C$). The heat flow through the measuring section of the insulation for a given temperature difference is equal to the difference in measuring plate heater power for the two equilibrium conditions.

Temperature and power relationships for the calibration equilibrium condition can be expressed as

$$T_1 = T_2 = T_3 = T_E = T_C \tag{4-1}$$

and

$$P = P_C \tag{4-2}$$

Similarly, for the test equilibrium condition

$$T_1 = T_2 = T_C \tag{4-3}$$

$$T_3 = T_H \tag{4-4}$$

$$T_E = (T_H + T_C)/2 \tag{4-5}$$

and

$$P = P_H \tag{4-6}$$

The insulation heat flux, q_i, for a temperature difference of $(T_H - T_C)$ is given by

$$q_i = \frac{P_C - P_H}{A_m} \tag{4-7}$$

where A_m is the measuring plate area.

In addition to the heat transfer measurements described above, measurements of total hemispherical emittance and reflectance were obtained in Task 1. These values were used to determine the radiation heat flux component during analytical evaluation of the heat flux data.

Total hemispherical emittance at room temperature was measured on one reference shield from each heat transfer test specimen. These measurements were obtained using the Calorimetric Emittance Apparatus used previously for the NAS 3-12025 contract work (Ref 1, Section 3.1.2). Near-normal infrared reflectance at room temperature was measured on all shields for each test specimen. The reflectance measurements were obtained using a Gier Dunkle DB100 Infrared Reflectometer (Ref 1, Section 3.1.3) at the center and at three equally-spaced locations approximately 10.2 cm (4 in.) inward from the edge on each side of each shield.

Approximate values of total hemispherical emittance were calculated from the reflectance data using the relationships

$$\epsilon_{TH} = 1.33 \ \epsilon_{TN} \qquad\qquad (4\text{-}8)$$

and

$$\epsilon_{TN} = 1 - \rho_N \qquad\qquad (4\text{-}9)$$

where ϵ_{TN} is the total normal emittance and ρ_N is the near-normal reflectance. The values computed for the reference shield in each specimen were compared with those measured directly, and these results were used to correct the computed values when required.

4.1.2 Experimental Apparatus

The flat plate heat transfer apparatus consists essentially of a vacuum chamber and pumping system, a cold boundary measuring plate with heater, a cold boundary guard plate with heater, an edge guard ring with both a heater and a cryogen heat exchanger, a hot boundary plate with heater, two insulated

4-7

cryogen reservoirs for heat sinks, and a mechanism for remotely raising and lowering the hot boundary (lower) surface plate. The overall apparatus and the insulated cryogen reservoirs are shown in Figs. 4-2 and 4-3, respectively. A schematic cross-section showing the general arrangement is presented in Fig. 4-4. Letter callouts used in describing the apparatus in the following paragraphs refer to this figure.

The vacuum chamber is 91.4 cm (36 in.) in diameter by 91.4 cm (36 in.) high and is constructed of 316 stainless steel. Two 3.8-cm-(1.5-in.-) diameter view-ports are located in the cylindrical wall of the chamber, approximately 90 degrees apart, for visual observation and measurement of hot and cold boundary plate separation using telemicroscopes. The chamber rests on a stainless steel base plate which contains plumbing ports for vacuum pumping, electrical feedthroughs for instrumentation and power leads, vacuum gauges, reservoir fill and vent lines (D and E) and the operating mechanism for moving the hot boundary plate-lower cryogen reservoir assembly. The vacuum pumping system consists of a cold-trapped 15.2-cm (6-in.) oil diffusion pump, a 7.1-ℓ/sec (15-cfm) mechanical fore pump, and a 2.4-ℓ/sec (5-cfm) mechanical holding pump. Chamber pressure is measured with thermocouple and ionization gauges located in the base plate below the lower support plate (J).

The hot boundary surface is provided by a 61-cm-(24-in.-) diameter by 0.95-cm-(0.375-in.-) thick copper plate. A silicone-insulated wire mesh heater* is bonded to the lower surface** (back side) of the plate. At maximum heater power, the applied heat flux is approximately 775 w/m^2 (246 Btu/hr-ft^2) uniformly dissipated across the plate area. Four stainless steel tubular supports (F) thermally link the plate to the cryogen reservoir. The reservoir is a stainless steel tank 61 cm (24 in.) in diameter by 15.2 cm (6 in.) in height which is braced internally to maintain flatness of the upper and lower surfaces. The stainless steel thermal links are attached to copper rods which extend vertically through the reservoir. Crinkled, single-aluminized Mylar multi-layer insulation (B) is placed in the space between the upper surface of

---

* Watlow Company

** Dow Corning 93-046 silicone adhesive with DC 1200 primer
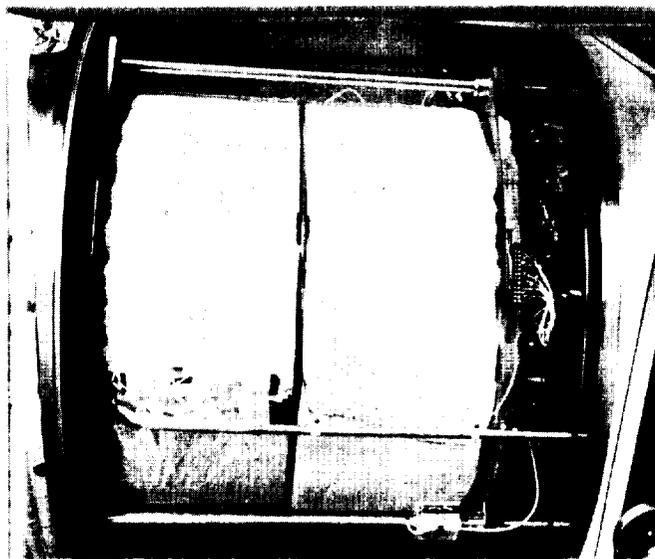
Fig. 4-3 Closeup View of the Apparatus
          Showing the Insulated Cryogen
          Reservoirs
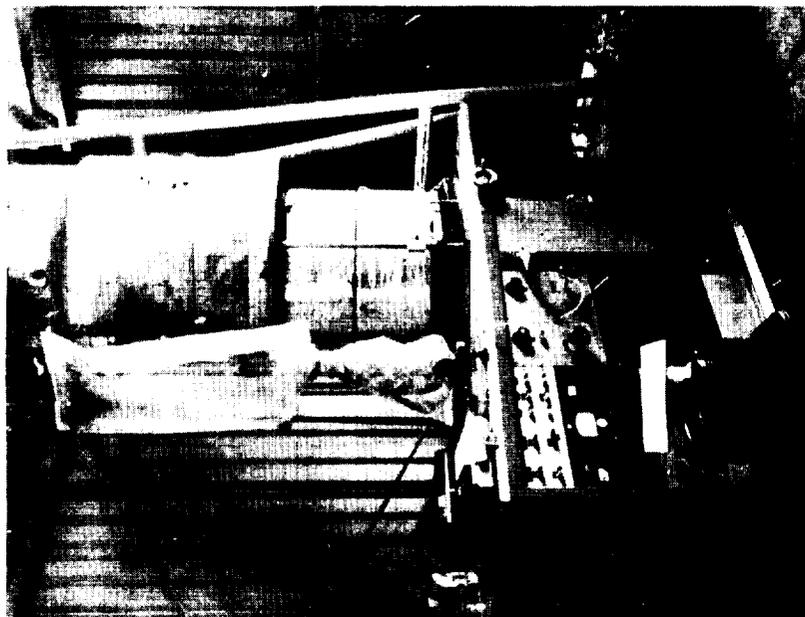
Fig. 4-2 View of the Flat Plate
          Heat Transfer Apparatus With
          the Vacuum Jacket Removed

4-9
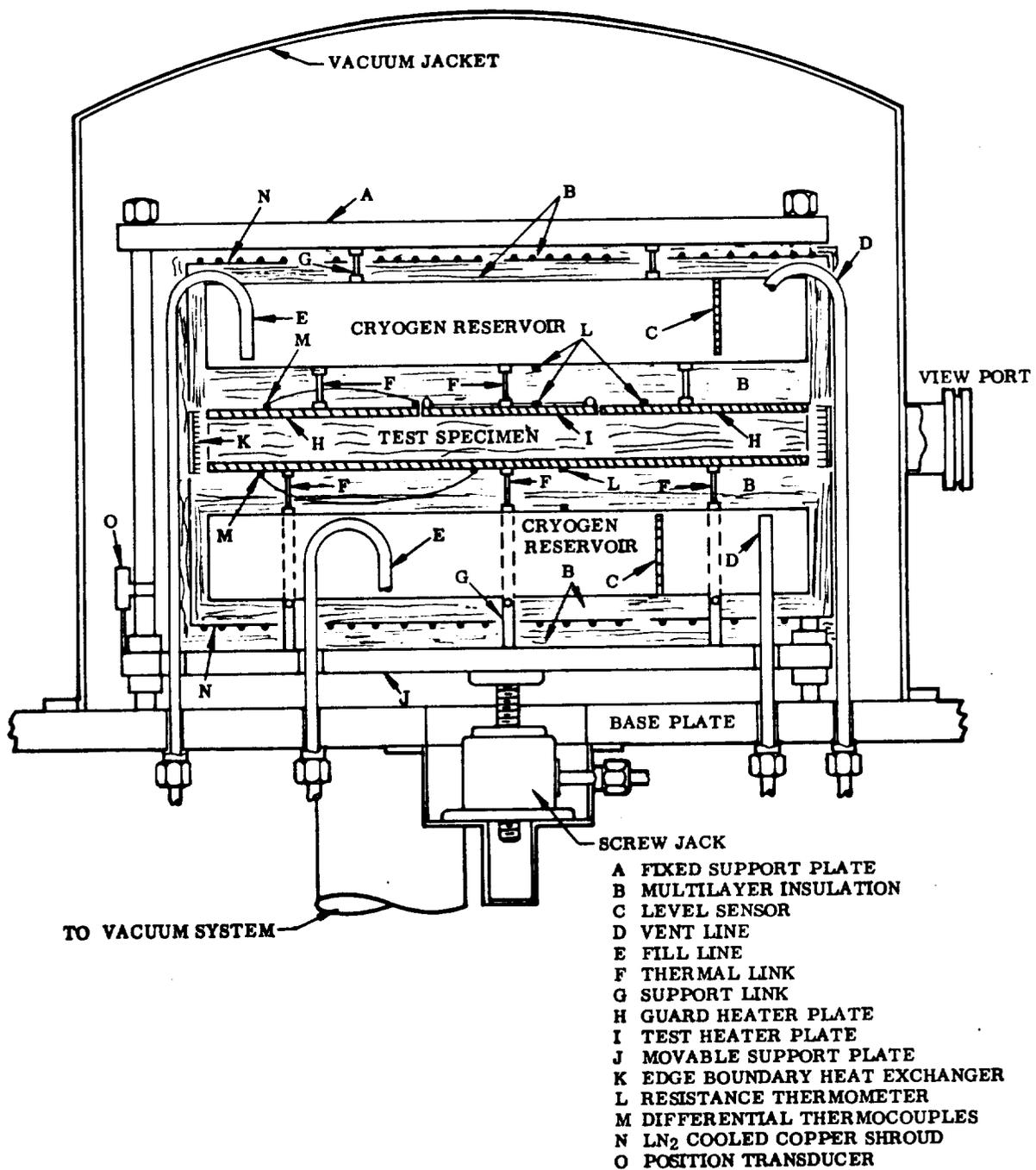
Fig. 4.4   Schematic of the Flat Plate Heat Transfer Apparatus

Labels in figure:

VACUUM JACKET

CRYOGEN RESERVOIR

VIEW PORT

TEST SPECIMEN

CRYOGEN RESERVOIR

BASE PLATE

SCREW JACK

TO VACUUM SYSTEM

A FIXED SUPPORT PLATE
B MULTILAYER INSULATION
C LEVEL SENSOR
D VENT LINE
E FILL LINE
F THERMAL LINK
G SUPPORT LINK
H GUARD HEATER PLATE
I TEST HEATER PLATE
J MOVABLE SUPPORT PLATE
K EDGE BOUNDARY HEAT EXCHANGER
L RESISTANCE THERMOMETER
M DIFFERENTIAL THERMOCOUPLES
N LN$_2$ COOLED COPPER SHROUD
O POSITION TRANSDUCER

LOCKHEED MISSILES & SPACE COMPANY

the lower cryogen reservoir and the hot boundary heater plate. In addition, the reservoir is insulated around the lower surface and cylinder section with double-aluminized Mylar/silk net multilayers which extend up to the edge of the hot boundary plate. A cryogen-cooled copper shroud (N) encloses this insulation, and a second multilayer blanket is installed between the shroud and the vacuum chamber wall including the base plate (Fig. 4-4). The lower reservoir-hot boundary plate assembly is supported above a 2.54-cm-(1-in.-) thick stainless steel plate (J) by three stainless steel tubes (support links). These tubes are separated from the cryogen reservoir by pyrex ball-joints to reduce heat leaks into the cryogen from the support assembly. Each tube is provided with a screw adjustment for leveling of the plate-reservoir assembly. The 2.54-cm-(1-in.-) thick support plate (J) is mounted on three ball bushings guided by ground stainless steel rods, and the entire assembly is moved vertically by a remotely-operated screw jack located below the support plate.

In the upper region of the apparatus, the measuring section plate (I) is a 15.2-cm-(6-in.-) diameter by 0.159-cm-(0.0625-in.-) thick copper plate which is spirally-wound on the upper (back side) surface with Evanohm* heater wire in a pattern to provide uniform power dissipation. This plate is thermally linked to the upper cryogen reservoir, similar in size and construction to the lower reservoir, through a single, centrally-located tubular support. A 61-cm-(24-in.-) diameter by 0.318-cm-(0.125-in.-) thick copper plate (H), with a 15.7-cm-(6.188-in.-) cutout in the center to accommodate the measuring plate, provides the cold boundary guard surface.

An electrically-conductive film heater** is bonded to the upper surface of the guard plate which is supported by six tubular links from the upper cryo-gen reservoir. This assembly is insulated (B) in the same manner as the lower plate-cryogen reservoir assembly, and also includes an intermediate cryogen-cooled shroud (N). The upper cryogen reservoir is supported from an

---

*   Driver-Harris Company

** Electrofilm, Inc.

4-11

upper rigid plate (A) by three tubular struts (support links) which are joined to the support plate through pyrex spheres to minimize heat leaks. The upper support plate (A) is rigidly attached to the three support rods which guide the moveable lower assembly.

An edge guard ring (K) is provided between the upper and lower boundary plate assemblies to control the radiation environment around the exposed edge of the test specimen. Both an electric heater and a cryogen heat exchanger are installed on the outside of this ring in order to achieve any desired temperature within the operational range of the apparatus. Two rectangular cutouts in the ring, approximately 2.54-cm-(1-in.-) wide by 3.8-cm-(1.5-in.) high, provide visual access to the test specimen area through the viewports.

Resistance thermometers are attached to each of the three plates which form the hot and cold boundaries and provide measurements of absolute temperature. These thermometers are clamped to the back-side plate surfaces (i.e., the side opposite the insulation specimen space) using indium foil between the sensor and plate surfaces. In addition, copper constantan thermocouples, referenced to the ice point or LN_2, are attached to the back side of each plate, the shrouds, the cryogen reservoirs, and several of the thermal links for monitoring of apparatus temperatures. Differentially-connected gold-colbalt copper thermocouples are attached to the back side of each boundary surface plate for measurement of center-to-edge temperature gradients. The guard-to-measuring plate temperature difference is controlled using a gold-cobalt copper thermopile with junctions at the outer edge of the measuring plate and the inner edge of the guard plate.

The main (measuring plate) heater is connected to a manually-controlled, 0.001-percent regulation DC power supply. Heater current is measured through a precision resistor in series with the heater, and the voltage drop across the heater is measured through potential leads attached to the heater windings at the plate. These potential leads are connected to a voltage

4-12

divider for potential drop measurements using a precision potentiometer. The guard plate heater temperature is controlled automatically to the temperature of the main (measuring plate) heater by the thermopile output which is fed into a Leeds and Northrup Model M variable set point controller. Power for this heater is supplied by a Silicon Controlled Rectifier (SCR) power supply operated by the control unit. The hot boundary plate heater is controlled using a resistance thermometer which provides the input to a second Leeds and Northrup Model M controller with a second SCR power supply. Edge guard ring temperature is controlled in a similar manner using a third Leeds and Northrup controller and an SCR power supply.

Separation of the hot and cold boundary plates is measured optically using two Gaertner Model M101AT telemicroscopes mounted at the two viewports. Also, a Bourns linear position transducer (0) is rigidly mounted on one of the guide rods with the spring-loaded probe in contact with the lower support plate (J). The output of this transducer is used to monitor plate separation during chill-down and testing. However, the optical measurements are used for primary plate separation data.

Instrumentation used for data acquisition includes a Leeds and Northrup K-5 potentiometer with electronic null detector which is used for all voltage measurements (thermometer and thermocouple signals as well as main heater voltage drop). All current measurements are obtained using Leeds and Northrup standard type resistors. Thermocouple and main heater voltage outputs are monitored continuously using four strip chart recorders. A digital millivolt meter is also included for periodic readout of all temperature signals prior to the measurement of steady-state data.

4-13

4.1.3 Experimental Uncertainties

The major uncertainty in the heat flux measurement is due to the uncertainties in the electrical power difference measurement and in the heat storage within the measuring plate caused by small perturbations of temperature during the "steady-state" measurement period. For the power measurement, the maximum uncertainty is equivalent to a heat flux of 3×10^{-4} W/m^2 (1×10^{-4} Btu/hr ft^2). This is the sum of the uncertainties in voltage measurements, current resistor value, and power supply stability. The uncertainty in the heat storage term is a function of the ability to detect and control small changes in the temperature of the measuring plate during the steady-state period. This temperature is measured with a platinum resistance thermometer (PRT) having an absolute calibration within $\pm$ 0.1°K ($\pm$ 0.18°R) by the LMSC primary standards laboratory. However, the sensitivity of the PRT measurement is such that temperature changes of 0.01°K (0.018°R) can easily be detected. By assuming an uncertainty of this order in the plate temperature change as a function of time, the uncertainty in heat flux from the storage term varies from 3.5×10^{-3} W/m^2 at 30°K to 2.3×10^{-2} W/m^2 at 360°K (1.1×10^{-3} Btu/hr ft^2 at 54°R to 7.3×10^{-3} Btu/hr ft^2 at 648°R). For the 20-layer specimens, this corresponds to an uncertainty in heat flux ranging from 3 percent for the 370°K to 95°K (666°R to 171°R) test conditions to 9 percent for the 250°K to 95°K (450°R to 171°R) test. For the small temperature difference tests, the uncertainty is nearly 30 percent for 125° to 95°K (225°R to 171°R), 20 percent for 75°K to 40°K (135°R to 72°R), and then decreases to 10 percent for 370°K to 330°K (666°R to 594°R).

The uncertainty in controlling the guard-to-measuring plate temperature difference is 0.01°K, (0.018°R) and the uncertainty of the hot boundary plate temperature, using a calibrated resistance thermometer, is 0.5°K (0.9°R). The uncertainty in plate separation measurements is 1.27×10^{-2} mm (5×10^{-3} in.), including deviations in flatness of the plate surfaces.

4-14

4.1.4 Experimental Procedure

Prior to installation of the specimen in the Flat Plate Apparatus, the "as assembled" height of the specimen is measured on a flat horizontal surface using a dial-gauge at six points around the periphery (2 to 5 cm, 0.8 to 2.0 in., in from the edge) and at the center. The specimen is then installed into the Flat Plate heat transfer apparatus, and a second uncompressed thickness measurement is made by raising the lower plate until contact is visually observed in the test area. This observation is made by shining a light across the upper surface of the insulation. Plate separation is then increased by 0.5 cm (0.2 in.) and the test chamber is evacuated. After a chamber pressure of 5×10^{-6} torr is achieved and maintained for 16 to 24 hrs., the reservoirs are filled with cryogen and the plate separation is set to the initial test value. After chilldown, the heater power values for the measuring plate and guard plate are adjusted to maintain the desired cold boundary temperature. Similarly, the hot boundary plate and the edge guard ring heaters are used to adjust the temperatures of these surfaces to the same temperature. After steady-state conditions are achieved for this calibration run, the measuring plate heater power is recorded. The hot boundary temperature is then increased to the desired test value, while maintaining the measuring and guard plates at the initial cold boundary temperature. Concurrently, power is changed to the edge guard heater to adjust the edge boundary temperature to the average of the hot and cold boundary temperatures. The measuring plate heater power is again recorded at equilibrium, and the heat flux computed from the difference of the calibration and test equilibrium power values.

This procedure is repeated for other desired boundary temperatures at the initial specimen thickness. After completion of all boundary temperature conditions at the initial thickness, the specimen thickness is changed to the next desired value and the entire procedure is repeated until all of the planned test conditions are completed.

LOCKHEED MISSILES & SPACE COMPANY

4.1.5 Specimen Preparation

In order to be sure that all Task 1 test specimens were uniform in configuration and quality, the following preparation and handling procedure was developed and used:

o Shield and spacer materials were visually inspected so that disks were cut from areas free from defects, wrinkles, or creases.

o The materials were cut to proper size using an electric shears and a template. Reflective shields were cut to a 58.5 - cm-(23-in.-) diameter, and spacers were cut to a 61.1-cm-(24-in.-) diameter.

o Total near-normal reflectance of each shield was measured at two points on each side. The reflective shields were stacked with alternate layers of a kraft-type paper. The stack was then subjected to a uniform compressive pressure of approximately 1.7×10^3 N/m^2 (0.25 psi) for 24 hours in an attempt to remove inherent wrinkles in the Mylar. While this procedure was partially successful, not all of the wrinkles were removed.

o A spacer layer was included at each exterior boundary.

o The assembled specimen was weighed and the weight was recorded.

o The specimen was installed in the Flat Plate Apparatus within one hour after preparation was completed.

o At the conclusion of the calorimeter testing, the specimens were stored in the laboratory environment. One shield at or near the middle of the specimen was removed, and a sample was prepared for room temperature calorimeter emittance tests.

4.1.6 Experimental Results

The experimentally-determined values of heat flux as a function of insulation materials, boundary temperatures, and layer density are described in this section for the nine different MLI specimens tested. Mathematical

4-16

models which were derived for correlation of the experimental results are presented, but details of the analysis are discussed in Section 4.2. Since the 61-cm-(24-in.) diameter flat plate apparatus did not have the capability for measurement of specimen compressive loading during testing, all of the data obtained are in terms of layer density rather than compressive pressure. A relationship between pressure and layer density can be obtained from the data presented in Section 3 of this report for the composites using the preconditioned silk net. For the Tissuglas system, the reader is referred to the previous work (Ref 1, Section 4.3.4) for the pressure-layer density relationships. The lack of compressive pressure data from this program is not a deficiency, however, since the only measureable parameter applicable to an actual insulation system is the layer density as installed on a tank or structure.

4.1.6.1 <u>Unperforated, Double-Aluminized Mylar/Tissuglas</u>. The heat transfer characteristics of this system were investigated using two specimens, one consisting of 20 shields and 21 spacers while the others contained 80 shields and 81 spacers (Ref Table 4-1). Heat flux measurements were obtained at layer densities of 52, 60, and 91 layers/cm (132, 152, and 230 layers/in., respectively). These layer densities correspond to compressive pressure values of 0.34, 6.9, and 69 N/m^2 ($5x10^{-4}$, $1x10^{-3}$, and $1x10^{-2}$psi) based upon the data of Ref 1. Cold boundary temperatures were established at $40^{\circ}K$, $95^{\circ}K$, and $300^{\circ}K$ ($72^{\circ}R$, $171^{\circ}R$, and $540^{\circ}R$) whereas warm boundary temperatures were varied from $69^{\circ}K$ to $370^{\circ}K$ ($125^{\circ}R$ to $666^{\circ}R$). The experimental data obtained for the two specimens are presented in Tables 4-2 and 4-3, and they are shown graphically in Figs. 4-5 through 4-8. The curves shown in each figure represent two analytical models developed to describe the performance of this system. Equation (4-10) is based upon the data of Ref 1. The curves designated Equation (4-11) are derived from a revised model which includes the temperature dependence of the spacer material. The derivation of this equation is discussed in Section 4.2.1. The two equations are

LOCKHEED MISSILES & SPACE COMPANY

Table 4-2

SUMMARY OF TEST DATA FOR SPECIMEN NO. 1 COMPOSED OF 20 SHIELDS OF
UNPERFORATED, DOUBLE-ALUMINIZED MYLAR WITH 21 TISSUGLAS SPACERS

| Layer Density, $\overline{N}$ | | T_H | T_C | Heat Flux, q |
No./cm	(No./in.)	$^{\circ}K$ ($^{\circ}R$)	$^{\circ}K$ ($^{\circ}R$)	w/m^2 (Btu/hr ft^2)
52	(132)	124 (224)	93 (168)	0.032 (0.010)
52	(132)	301 (542)	95 (171)	0.860 (0.273)
52	(132)	391 (703)	95 (171)	2.20 (0.698)
52	(132)	390 (702)	42 (75)	2.37 (0.752)
52	(132)	301 (542)	41 (73)	0.952 (0.302)
52	(132)	168 (302)	39 (71)	0.183 (0.0580)
52	(132)	79 (142)	39 (71)	0.0353 (0.0112)
60	(152)	301 (542)	42 (75)	1.22 (0.387)
60	(152)	167 (301)	40 (72)	0.303 (0.096)
60	(152)	78 (141)	40 (72)	0.058 (0.0183)
60	(152)	391 (703)	41 (74)	2.97 (0.941)
91	(230)	76 (136)	40 (72)	0.252 (0.080)
91	(230)	168 (302)	41 (74)	1.53 (0.484)
91	(230)	302 (544)	43 (78)	5.42 (1.72)
91	(230)	388 (698)	43 (78)	8.35 (2.65)
91	(230)	125 (225)	94 (170)	0.356 (0.113)
91	(230)	301 (541)	96 (173)	4.82 (1.53)
91	(230)	389 (700)	97 (174)	8.79 (2.79)

LOCKHEED MISSILES & SPACE COMPANY

Table 4-3

SUMMARY OF TEST DATA FOR SPECIMEN NO. 2 COMPOSED OF
80 SHIELDS OF UNPERFORATED, DOUBLE-ALUMINIZED MYLAR
WITH 81 TISSUGLAS SPACERS

Layer Density, $\bar{N}$ No./cm (No./in.)	T_H $^\circ K$ ($^\circ R$)	T_C $^\circ K$ ($^\circ R$)	Heat Flux, q w/m^2 (Btu/Hr.Ft.^{2})
52(132)	69(124)	40(72)	0.006(0.002)
52(132)	226(406)	40(72)	0.112(0.0355)
52(132)	301(542)	41(73)	0.268(0.0850)
52(132)	367(660)	41(74)	0.504(0.160)
52(132)	129(232)	95(171)	0.016(0.005)
52(132)	300(540)	96(172)	0.229(0.0727)
52(132)	367(660)	94(170)	0.479(0.152)
52(132)	369(664)	301(541)	0.250(0.0794)
60(152)	69(124)	41(73)	0.009(0.003)
60(152)	224(404)	40(72)	0.159(0.0505)
60(152)	300(540)	40(72)	0.372(0.118)
60(152)	366(658)	42(75)	0.640(0.203)
60(152)	129(233)	95(171)	0.025(0.008)
60(152)	301(542)	96(172)	0.344(0.109)
60(152)	367(660)	94(170)	0.624(0.198)
91(230)	70(126)	39(71)	0.054(0.0172)
91(230)	227(409)	41(74)	0.734(0.233)
91(230)	302(543)	41(73)	1.28(0.407)
91(230)	367(661)	43(78)	2.01(0.639)
91(230)	129(232)	95(171)	0.111(0.0351)
91(230)	300(540)	96(173)	1.21(0.385)
91(230)	368(663)	96(172)	1.92(0.608)
91(230)	369(664)	300(540)	0.750(0.238)
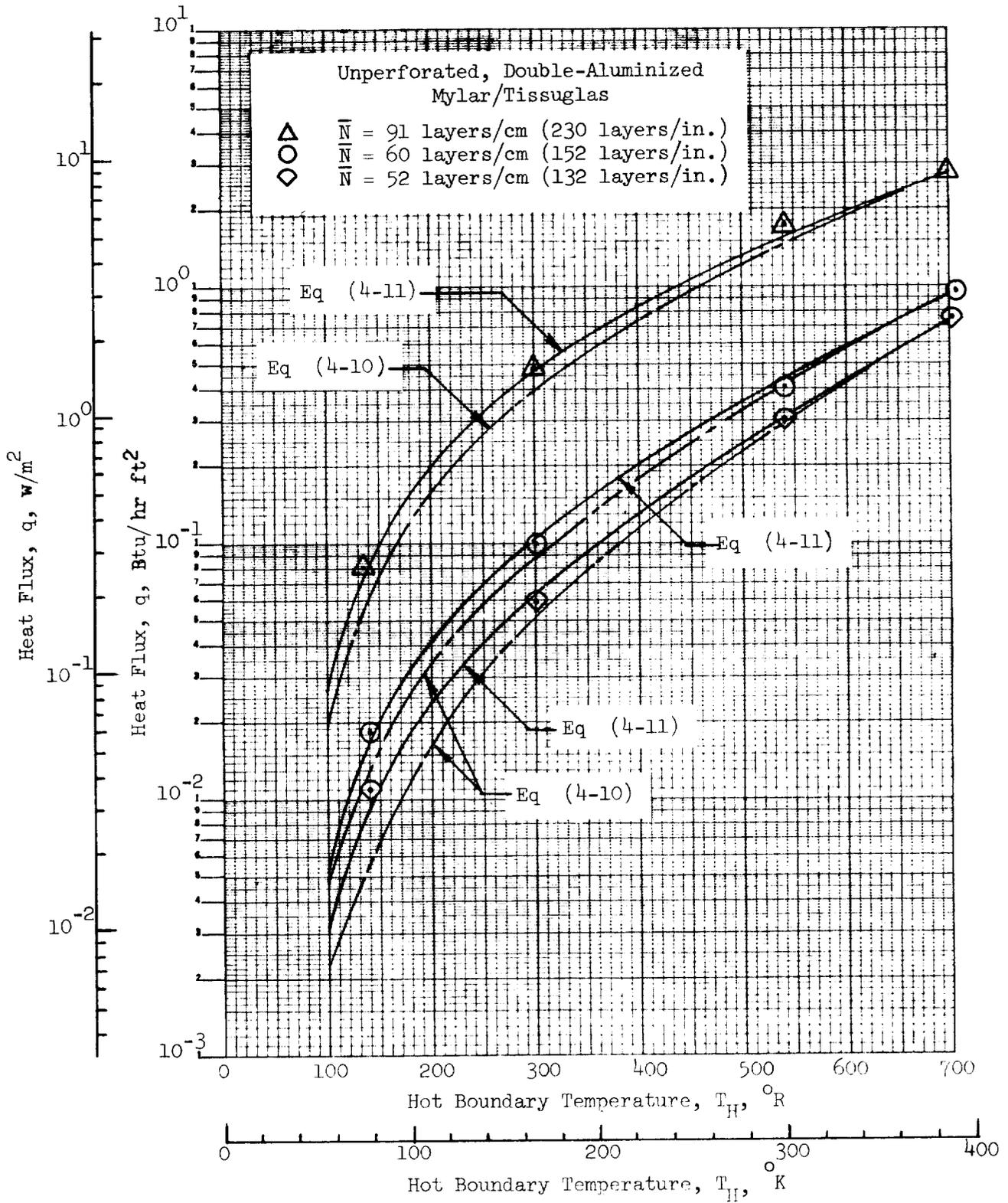
Fig. 4-5 Heat Flux as a Function of T_H and $\overline{N}$ for Specimen No. 1 with $T_C = 39°K$ ($70°R$)
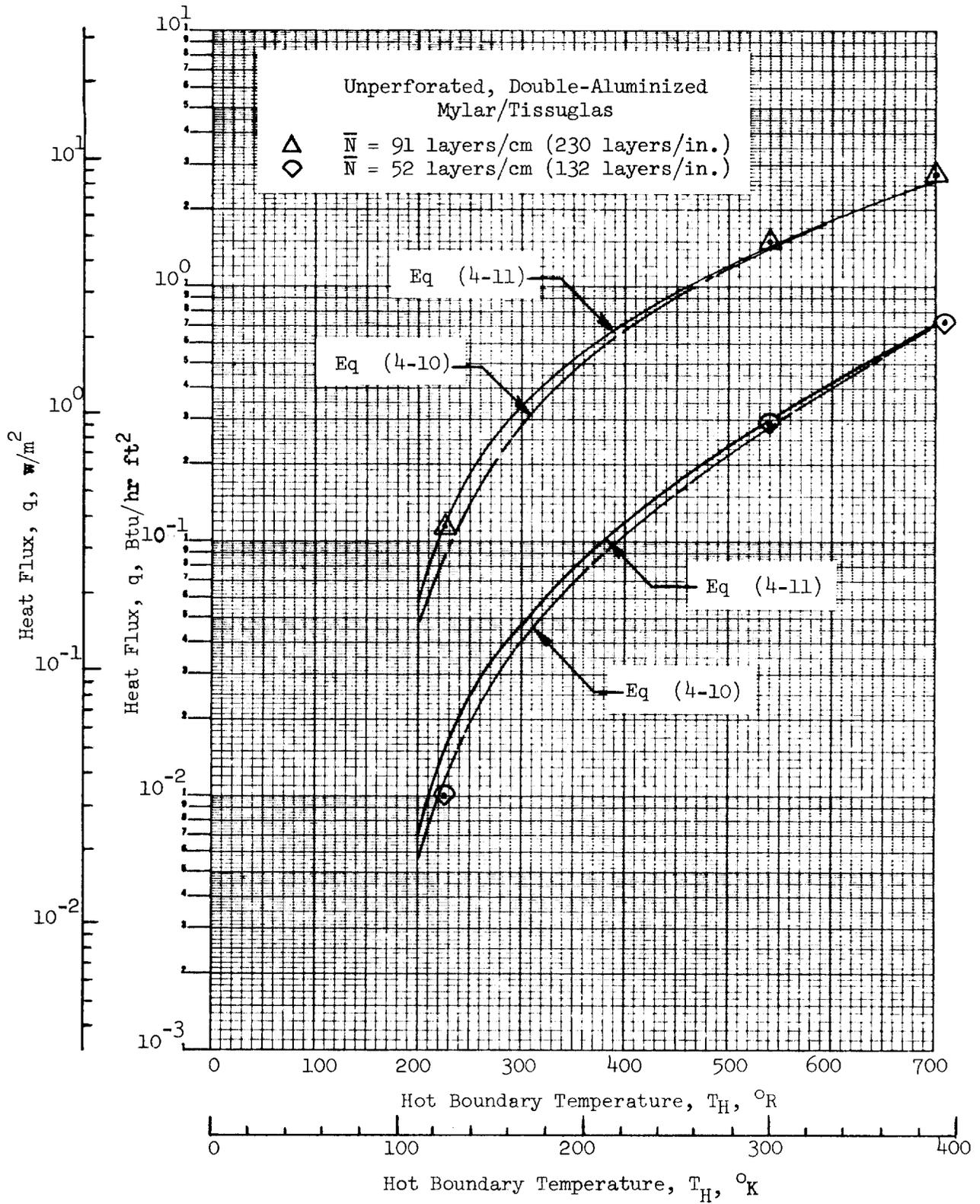
Fig. 4-6 Heat Flux as a Function of T_H and $\overline{N}$ for Specimen No. 1 with T_C = 94°K (170°R)

LOCKHEED MISSILES & SPACE COMPANY
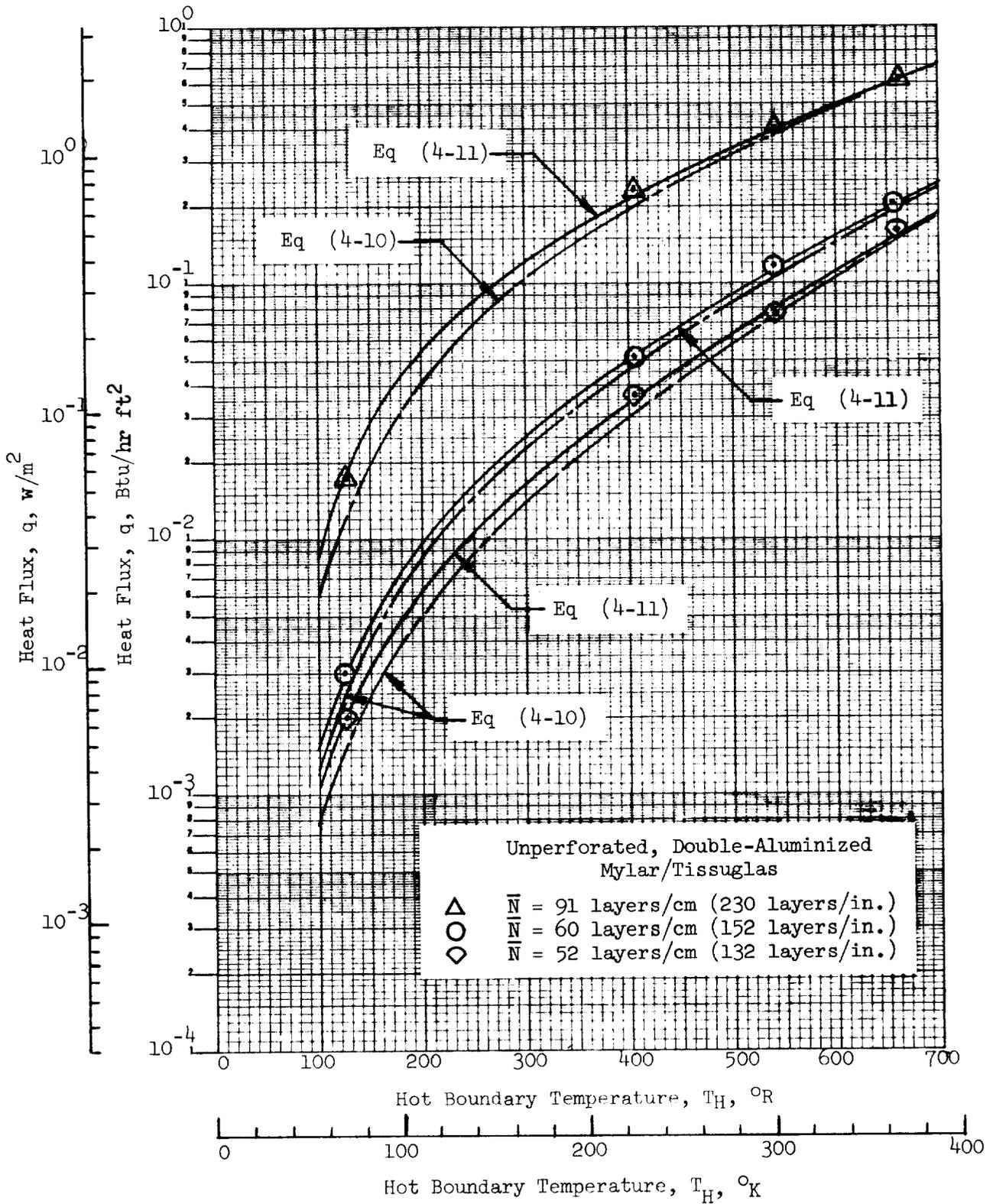
Fig. 4-7 Heat Flux as a Function of T_H and $\overline{N}$ for Specimen No. 2 with $T_C = 39^\circ K$ ($70^\circ R$)

Fig. 4-8 Heat Flux as a Function of T_H and $\overline{N}$ for Specimen No. 2 with $T_C = 94°K$ (170°R)

$$q = \frac{C_s(\bar{N})^{3.91}T_m}{N_s + 1}(T_H - T_C) + \frac{C_r \, \epsilon_{TR}}{N_s}(T_H^{4.67} - T_C^{4.67}) \qquad (4\text{-}10)$$

$$q = \frac{\left[C_{s1}(T_H^2 - T_C^2) - C_{s2}(T_H^3 - T_C^3)\right]\bar{N}^{3.91}}{N_s + 1} + \frac{C_r \, \epsilon_{TR}}{N_s}(T_H^{4.67} - T_C^{4.67}) \qquad (4\text{-}11)$$

where: $C_s = 4.43 \times 10^{-11}$, $C_{s1} = 3.07 \times 10^{-11}$, $\quad\}$ for $\bar{N}$ in layers/cm, T in
$C_{s2} = 2.13 \times 10^{-14}$, and $C_r = 8.03 \times 10^{-10}$ $\quad\}$ $^{\circ}$K, and q in w/m^2

or: $C_s = 1.13 \times 10^{-13}$, $C_{s1} = 7.85 \times 10^{-14}$, $\quad\}$ for $\bar{N}$ in layers/in., T in
$C_{s2} = 3.03 \times 10^{-17}$, and $C_r = 1.63 \times 10^{-11}$ $\quad\}$ $^{\circ}$R, and q in Btu/hr ft^2

From an inspection of Figs. 4-5 through 4-8, it is apparent that Equation (4-11) yields a better fit to the experimental data. In evaluating the equation, a value of 0.031 was used for the room temperature total hemispherical emittance, ϵ_{TR}. This was the average value measured for one shield from each specimen. As discussed in Section 4.2, Equation (4-11) is considered to be a better model of the conduction heat transfer process because it includes the approximate temperature dependency of the thermal conductivity of the glass fibers which make up the spacer material. This model predicts a higher conduction heat transfer value at lower temperatures because of the non-linear variation of the glass thermal conductivity with temperature. On the other hand, Equation (4-10) was originally developed with the assumption that the thermal conductivity was a linear function of temperature. This assumption is reasonable for the higher warm boundary temperature region ($T_H > 200^{\circ}$K or 360°R) because the larger fraction of spacer material is at a sufficiently high temperature where the glass thermal conductivity does indeed behave in a nearly linear manner with temperature.

The agreement between the 20- and 80-shield specimens is quite good when considered in terms of the analytical model. No non-linear dependence of heat flux and number of layers is evident in the 20- to 80-shield range.

This is in agreement with the findings of Contract NAS 3-12025 when comparing the data for 20- and 40-shield specimens investigated under that program.

4.1.6.2 Unperforated, Double-Aluminized Mylar/Preconditioned Silk Net.

Heat transfer measurements were performed on two specimens of this composite to evaluate the effect of the preconditioned silk net on insulation performance. All of the past thermal performance testing with the silk net spacers had been performed using net in the "as received" condition. Because of the significant change in the layer density - compressive pressure characteristics between composites with the "as received" and the preconditioned net, it was necessary to conduct heat transfer tests with the latter material so that the conduction term of the previously developed mathematical model for silk net spacers could be modified to reflect the performance of the pre-conditioned net system.

The two specimens investigated contained 20 and 80 reflective shields, respectively. Each spacer layer was made up of two layers of the preconditioned netting. Total hemispherical emittance measurements, performed on one shield from each insulation specimen, yielded a value of ϵ_{TR} of 0.031 ± 0.001. The average value of ϵ_{TR}, based upon reflectance measurements made on each shield, was 0.033 with a range of + 0.002 - 0.003. Thus, the value of 0.031 adequately describes the optical properties of the shield material for each specimen, and this value was incorporated into the heat transfer equation developed for this composite system.

The experimental data obtained for the two specimens are given in Tables 4-4 and 4-5. Heat flux values as a function of temperature and layer density are shown in Figs. 4-9 and 4-10. A single equation describing the heat flux in terms of layer density and boundary temperature was formulated from the experimental data. The general form of this equation was taken from the work performed under Contract NAS 3-12025 (Ref 1), and the experimental data were used to reevaluate the coefficient and exponent of the conduction term of the total heat flux equation. Evaluation of the coefficient was accomplished

LOCKHEED MISSILES & SPACE COMPANY

by using the experimental data in the form

$$\frac{q_{total} (N_s + 1)}{T_m (T_H - T_C)} = a (\bar{N})^n + \frac{b (N_s + 1)}{N_s T_m (T_H - T_C)} \sigma (T_H^{4.67} - T_C^{4.67}) \quad (4-12)$$

, and for a constant value of $\bar{N}$, this becomes

$$\frac{q_{total} (N_s + 1)}{T_m (T_H - T_C)} = Y = A + B \frac{(T_H^{4.67} - T_C^{4.67})}{T_m (T_H - T_C)} \quad (4-13)$$

The A and B terms were computed by simultaneous solution of Equation (4-13) as evaluated for the different boundary temperatures for each particular value of $\bar{N}$. Then, since $a(\bar{N})^n = A$, values of the coefficient a and the exponent n were obtained from considering the variation of $\bar{N}$ for each fixed set of boundary temperatures. Using this procedure, the following equation

Table 4-4

SUMMARY OF TEST DATA FOR SPECIMEN NO. 3 COMPOSED OF 20 SHIELDS OF UNPERFORATED, DOUBLE-ALUMINIZED MYLAR WITH 42 WATER-PRECONDITIONED SILK NET SPACERS

Layer Density, $\bar{N}$ No./cm (No./in.)	T_H °K (°R)	T_C °K (°R)	Heat Flux, q w/m^2 (Btu/Hr.Ft.^{2})
28.2 (71.6)	128 (231)	96 (173)	0.091 (0.029)
28.2 (71.6)	301 (542)	96 (173)	1.22 (0.388)
28.2 (71.6)	367 (660)	96 (173)	2.20 (0.699)
48.6 (123.5)	130 (234)	79 (142)	0.448 (0.142)
48.6 (123.5)	301 (542)	99 (178)	3.75 (1.19)
48.6 (123.5)	368 (663)	104 (188)	6.37 (2.02)
28.2 (71.6)	252 (454)	41 (74)	0.838 (0.266)
28.2 (71.6)	301 (541)	41 (73)	1.34 (0.424)
28.2 (71.6)	367 (660)	42 (75)	2.37 (0.751)
48.0 (122.0)	251 (452)	43 (78)	2.72 (0.862)
48.0 (122.0)	300 (540)	45 (81)	3.78 (1.20)
48.0 (122.0)	368 (663)	49 (88)	6.30 (2.00)
48.0 (122.0)	79 (143)	41 (73)	0.217 (0.069)

LOCKHEED MISSILES & SPACE COMPANY

Table 4-5

SUMMARY OF TEST DATA FOR SPECIMEN NO. 4 COMPOSED OF 80 SHIELDS OF UNPERFORATED, DOUBLE-ALUMINIZED MYLAR WITH 162 WATER-PRECONDITIONED SILK NET SPACERS

Layer Density, $\overline{N}$ No./cm (no./in.)	T_H $^\circ$K ($^\circ$R)	T_C $^\circ$K ($^\circ$R)	Heat Flux, q w/m^2 (Btu/Hr.Ft.^{2})
28.2 (71.6)	250 (450)	94 (170)	0.202 (0.064)
28.2 (71.6)	301 (541)	94 (170)	0.303 (0.096)
28.2 (71.6)	368 (662)	95 (171)	0.583 (0.185)
39.0 (99.0)	251 (452)	95 (171)	0.400 (0.127)
39.0 (99.0)	301 (542)	96 (172)	0.659 (0.209)
39.0 (99.0)	367 (660)	96 (172)	1.02 (0.324)
48.0 (122.0)	249 (448)	95 (171)	0.687 (0.218)
48.0 (122.0)	301 (541)	96 (172)	1.10 (0.350)
48.0 (122.0)	368 (662)	96 (173)	1.65 (0.524)
28.2 (71.6)	369 (664)	329 (593)	0.161 (0.051)
28.2 (71.6)	251 (452	41 (73)	0.227 (0.072)
28.2 (71.6)	301 (541)	41 (73)	0.353 (0.112)
28.2 (71.6)	367 (660)	42 (75)	0.615 (0.195)
28.2 (71.6)	86 (155)	39 (71)	0.025 (0.008)
39.3 (99.8)	251 (451)	39 (71)	0.514 (0.163)
39.3 (99.8)	300 (540)	41 (73)	0.756 (0.240)
39.3 (99.8)	367 (661)	42 (76)	1.23 (0.391)
48.0 (122.0)	83 (150)	41 (73)	0.079 (0.025)
48.0 (122.0)	257 (462)	41 (73)	0.829 (0.263)
48.0 (122.0)	302 (543)	42 (75)	1.19 (0.378)
48.0 (122.0)	366 (658)	44 (79)	1.84 (0.583)

LOCKHEED MISSILES & SPACE COMPANY
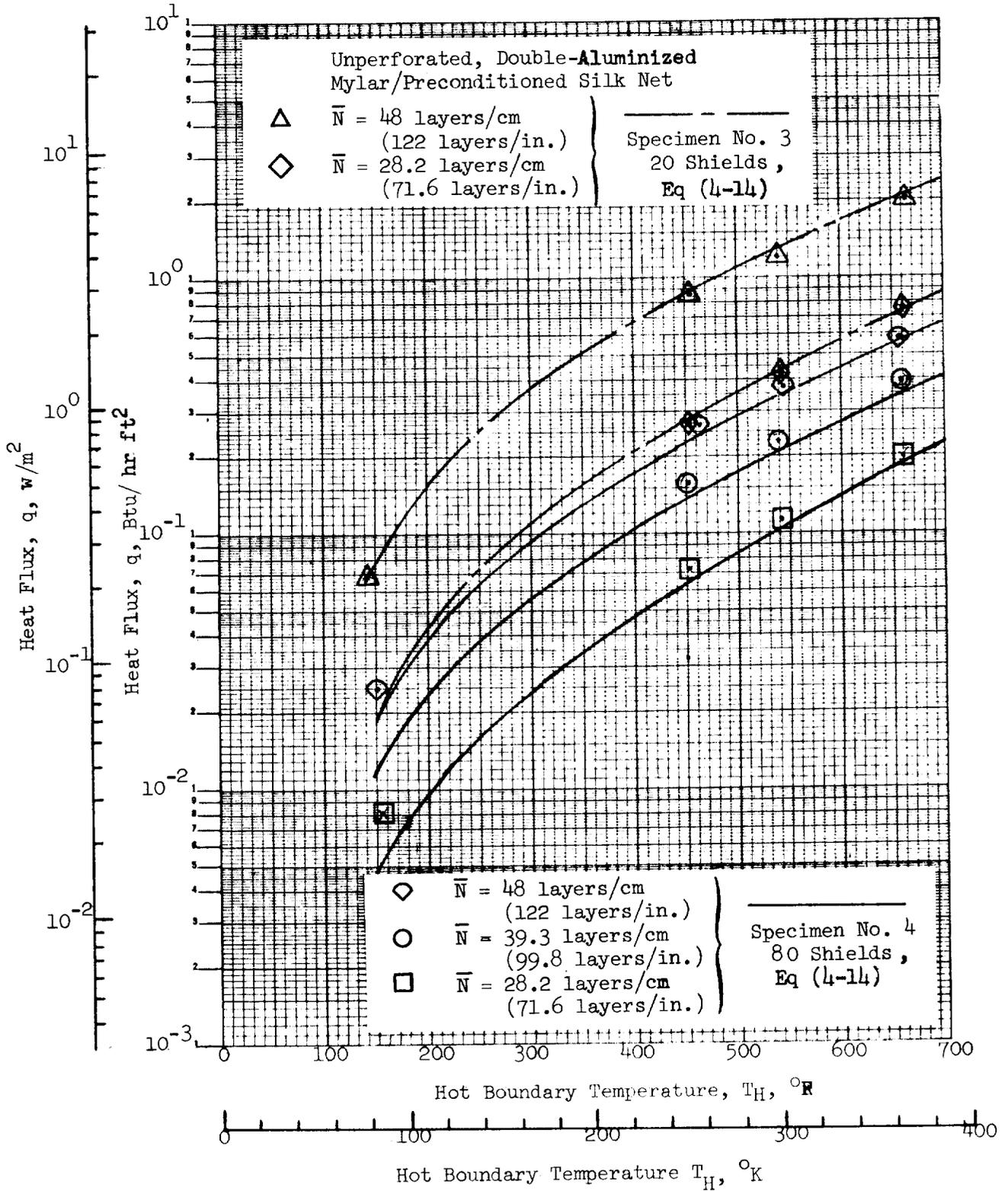
Fig. 4-9   Heat Flux as a Function of T_H and $\overline{N}$ for Specimens No. 3 and 4 with $T_C = 42°K$ (75°R)

LOCKHEED MISSILES & SPACE COMPANY
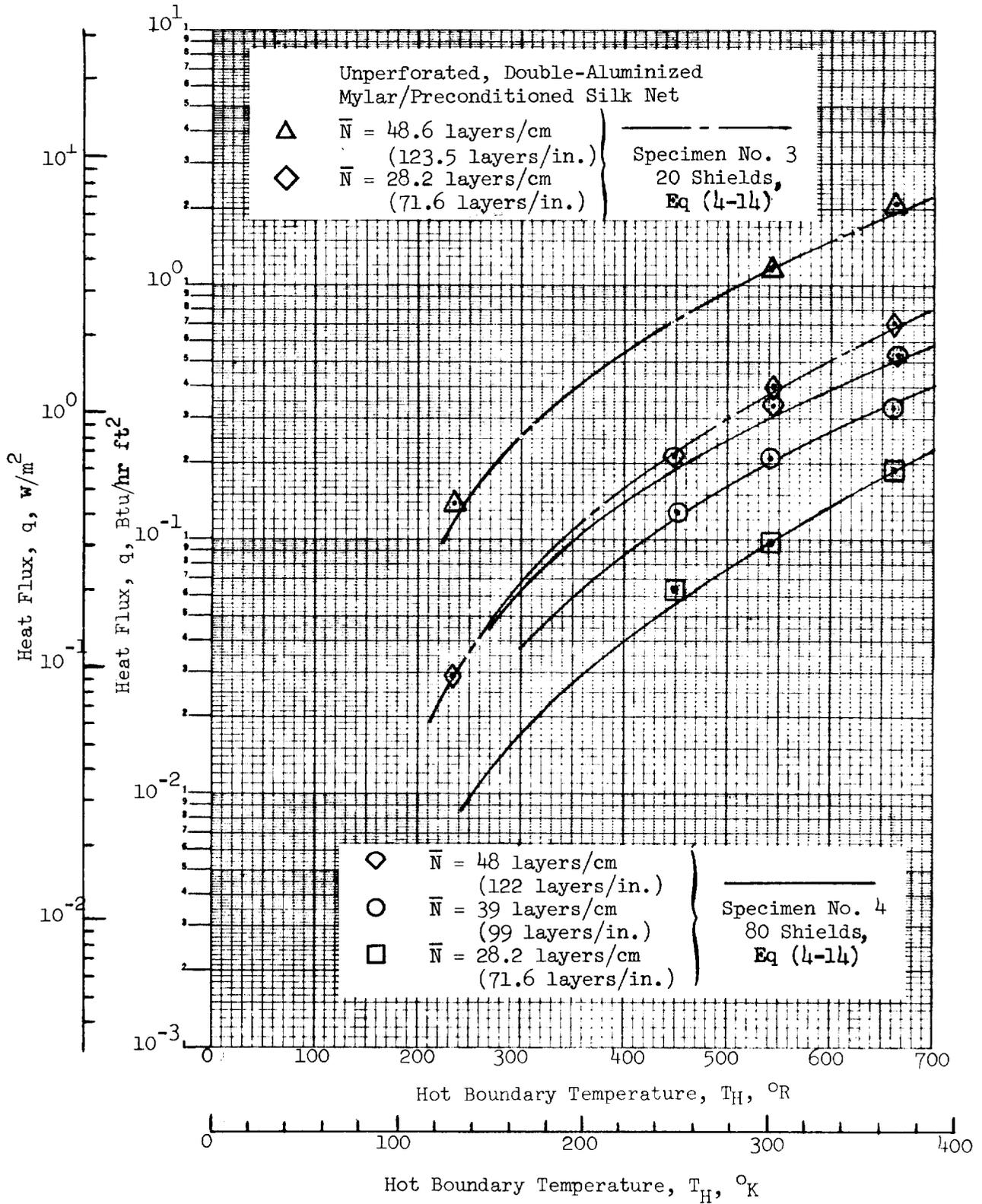
Fig. 4-10   Heat Flux as a Function of T_H and $\overline{N}$ for Specimens No. 3 and 4 with $T_C = 97°K$ (175°R)

was generated to describe the thermal performance of the preconditioned silk net spacer system.

$$q = \frac{C_s(\bar{N})^{2.56}T_m}{N_s+1}\,(T_H-T_C) + \frac{C_r\,\epsilon_{TR}}{N_s}\,(T_H^{4.67}-T_C^{4.67}) \tag{4-14}$$

where: $C_s = 8.95 \times 10^{-8}$ and $C_r = 5.39 \times 10^{-10}$

for $\bar{N}$ in layers/cm, T in °K, and q in w/m²

or: $C_s = 8.06 \times 10^{-10}$ and $C_r = 1.10 \times 10^{-11}$

for $\bar{N}$ in layers/in., T in °R, and q in Btu/hr ft²

In evaluating this equation, the average measured value of $\epsilon_{TR} = 0.031$ was used.

The comparable equation for the "as received" silk net system from Ref 1, Eq (4.22), for $\epsilon_{TR} = 0.031$ is

$$q = \frac{C_s(\bar{N})^{3.56}T_m}{N_s+1}\,(T_H-T_C) + \frac{C_r\,\epsilon_{TR}}{N_s}\,(T_H^{4.67}-T_C^{4.67}) \tag{4-15}$$

where: $C_s = 2.11 \times 10^{-9}$ and $C_r = 5.39 \times 10^{-10}$

for $\bar{N}$ in layers/cm, T in °K, and q in w/m²

or: $C_s = 7.46 \times 10^{-12}$ and $C_r = 1.10 \times 10^{-11}$

for N in layers/in., T in °R, and q in Btu/hr ft²

The radiation terms for both systems are the same, of course, since preconditioning does not alter the radiative behavior of the system. However, the conduction heat transfer varies because of changes in contact geometry for the preconditioned spacer layers. Comparing the conduction terms of Equations (4-14) and (4-15), it can be seen that Equation (4-15) for "as received" net systems yields a value of the conduction term which is 35 percent smaller than that obtained from Equation (4-14) for preconditioned net systems at a layer density of 28 layers/cm (70 layers/in.). At a layer density of 43 layers/cm (110 layers/in.), both equations show approximately equal conduction heat transfer, and at a layer density of 51 layers/cm (130 layers/in.) Equation (4-15) exhibits a conduction term which is approximately 20 percent

4-30

greater than that obtained from Equation (4-14). It is hypothesized that this cross-over in the magnitude of conduction heat transfer as a function of layer density is due to differences both in flatness and relative stiffness of the "as received" and water-preconditioned net materials. The change in flatness occurs as initial wrinkles are removed, whereas the relative stiffness (i.e., springrate) is reduced as the material sizing content is decreased. However, the interaction of these factors is not completely understood and analytical correlations with test results are not possible, since no adequate contact geometry model exists for MLI systems.

A comparison of Equation (4-14) and the experimental data obtained for the two test specimens is shown in Figs. 4-9 and 4-10. The solid lines represent the equation, whereas the experimental values are presented as single data points. Considering both cold boundary temperature conditions, the equation generally fits the experimental data to within $\pm$ 10 percent. For the two data points where the greatest scatter was observed, the measured values exceed those predicted by the analysis. In one case, for boundary temperatures of 86°K (155°R) and 39°K (71°R) and for a layer density of 28.2 layers/cm (71.6 layers/in.), the measured heat flux value was found to be 48 percent higher than that predicted. In the other case, the measured value was found to be 33 percent higher than that predicted for boundary temperatures of 83°K (150°R) and 41°K (73°R) and for a layer density of 48 layers/cm (122 layers/in.). For both cases, it should be noted that the hot boundary temperature value was very low (i.e., approximately 83°K or 150°R) so, consequently, both the temperature difference and the measured heat flux values were also very small. On the basis of the very limited data available, no definite conclusion can be reached regarding temperature dependence. However, in view of the 20-shield specimen data, and considering the small values of heat flux (with inherently greater inaccuracies) for the 80-shield specimen, it is recommended that the present linear dependence form of the model be used.

4-31

4.1.6.3 <u>Perforated, Double-Aluminized Mylar/Preconditional Silk Net</u>. Heat flux measurements were performed on five 80-shield specimens using the preconditioned silk net, two layers per spacer, in conjunction with perforated, double-aluminized Mylar reflective shields. Descriptions of the five perforation patterns selected were presented previously (Ref Section 3.1.1). Perforation diameters were 0.119 cm (0.047 in.) and 0.229 cm (0.090 in.), while the percent of open area varied within the range of 0.26 to 1.07. The heat flux measurements were obtained at a constant cold boundary temperature of 95°K (170°R) and with hot boundary temperatures of 250°K (450°R), 300°K (540°R) and 367°K (661°R). These measurements were performed at layer densities which varied from 28.2 layers/cm (71.6 layers/in.) to 48.0 layers/cm (122 layers/in.). The parameter values given above were chosen to be consistent with those used in the investigation of the unperforated, double-aluminized Mylar system (Ref Section 4.1.6.2) so that a direct comparison could be made of the effect of perforations on the insulation heat transfer.

The experimental results for this test series are summarized in Table 4-6, and the heat flux data as a function of layer density and hot boundary temperature are shown graphically in Figs. 4-11 through 4-15. For each specimen, the coefficient and exponent of the conduction term and the coefficient of the radiation term of the total heat flux equations were determined from a fit of the experimental data using the same procedure discussed in Section 4.1.6.2. The resulting equations are:

$$S\text{-}602: \quad q = \frac{C_s (\bar{N})^{2.84} T_m}{N_s + 1} (T_H - T_C) + \frac{C_r \, \epsilon_{TR}}{N_s} (T_H^{4.67} - T_C^{4.67}) \qquad (4\text{-}16)$$

where: $C_s = 2.98 \times 10^{-8}$ and $C_r = 5.86 \times 10^{-10}$
         for $\bar{N}$ in layers/cm, T in °K, and q in w/m^2

or: $C_s = 2.07 \times 10^{-10}$ and $C_r = 1.20 \times 10^{-11}$
         for $\bar{N}$ in layers/in., T in °R and q in Btu/hr ft^2

and: $\epsilon_{TR} = 0.043$ (See Table 4-8)

LOCKHEED MISSILES & SPACE COMPANY

Table 4-6

SUMMARY OF TEST DATA FOR SPECIMENS NO. 5 THROUGH 9 COMPOSED OF 80 SHIELDS OF PERFORATED, DOUBLE-ALUMINIZED MYLAR WITH 162 WATER-PRECONDITIONED SILK NET SPACERS

Specimen No. (Perforation Pattern)	Hole Dia., cm (in)	Open Area, percent	Layer Density No./cm(No./in.)	T_H °K (°R)	T_C °K (°R)	Heat Flux w/m² (Btu/hr ft²)
5 (S-602)	0.119 (0.047)	0.26	28.2 (71.6)	251 (451)	94 (170)	0.208 (0.066)
			28.2 (71.6)	301 (542)	94 (170)	0.340 (0.108)
			28.2 (71.6)	367 (660)	95 (171)	0.649 (0.206)
			38.6 (98.0)	251 (451)	94 (170)	0.340 (0.108)
			38.6 (98.0)	302 (543)	96 (172)	0.646 (0.205)
			38.6 (98.0)	367 (660)	96 (172)	1.08 (0.344)
			47.6 (121)	251 (451)	96 (172)	0.665 (0.211)
			47.6 (121)	301 (542)	97 (174)	1.10 (0.349)
			47.6 (121)	367 (661)	97 (174)	1.81 (0.575)
6 (S-603)	0.119 (0.047)	0.55	28.2 (71.6)	251 (451)	94 (170)	0.217 (0.069)
			28.2 (71.6)	302 (544)	94 (170)	0.369 (0.117)
			28.2 (71.6)	366 (658)	94 (170)	0.722 (0.229)
			38.6 (98.0)	250 (450)	95 (171)	0.394 (0.125)
			38.6 (98.0)	367 (660)	95 (171)	1.19 (0.379)
			47.6 (121)	251 (451)	95 (171)	0.652 (0.207)
			47.6 (121)	302 (543)	96 (173)	1.11 (0.351)
			47.6 (121)	368 (663)	96 (173)	1.94 (0.614)
7 (S-604)	0.119 (0.047)	1.07	28.2 (71.6)	250 (450)	94 (170)	0.230 (0.073)
			28.2 (71.6)	301 (541)	94 (170)	0.397 (0.126)
			28.2 (71.6)	367 (661)	94 (170)	0.785 (0.249)
			38.6 (98.0)	251 (452)	95 (171)	0.416 (0.132)
			38.6 (98.0)	300 (540)	96 (172)	0.687 (0.218)
			38.6 (98.0)	367 (660)	96 (172)	1.27 (0.402)
			47.6 (121)	251 (452)	97 (174)	0.668 (0.212)
			47.6 (121)	302 (543)	97 (174)	1.13 (0.359)
			47.6 (121)	367 (660)	97 (174)	2.00 (0.636)
8 (937-S)	0.229 (0.090)	0.48	28.3 (71.8)	251 (451)	94 (170)	0.224 (0.071)
			28.3 (71.8)	299 (538)	94 (170)	0.375 (0.119)
			28.3 (71.8)	368 (662)	94 (170)	0.709 (0.225)
			38.6 (98.0)	251 (452)	94 (170)	0.407 (0.129)
			38.6 (98.0)	302 (543)	96 (172)	0.599 (0.190)
			38.6 (98.0)	368 (662)	97 (174)	1.21 (0.384)
			48.0 (122)	252 (454)	96 (173)	0.665 (0.211)
			48.0 (122)	302 (543)	97 (174)	1.12 (0.354)
			48.0 (122)	368 (663)	97 (175)	1.95 (0.619)
9 (937)	0.229 (0.090)	0.99	28.2 (71.6)	250 (450)	95 (171)	0.224 (0.071)
			28.2 (71.6)	301 (542)	94 (170)	0.400 (0.127)
			28.2 (71.6)	368 (663)	95 (171)	0.740 (0.235)
			47.6 (121)	249 (449)	96 (173)	0.637 (0.202)
			47.6 (121)	301 (541)	97 (174)	1.11 (0.351)
			47.6 (121)	367 (660)	97 (174)	1.98 (0.627)

4-33
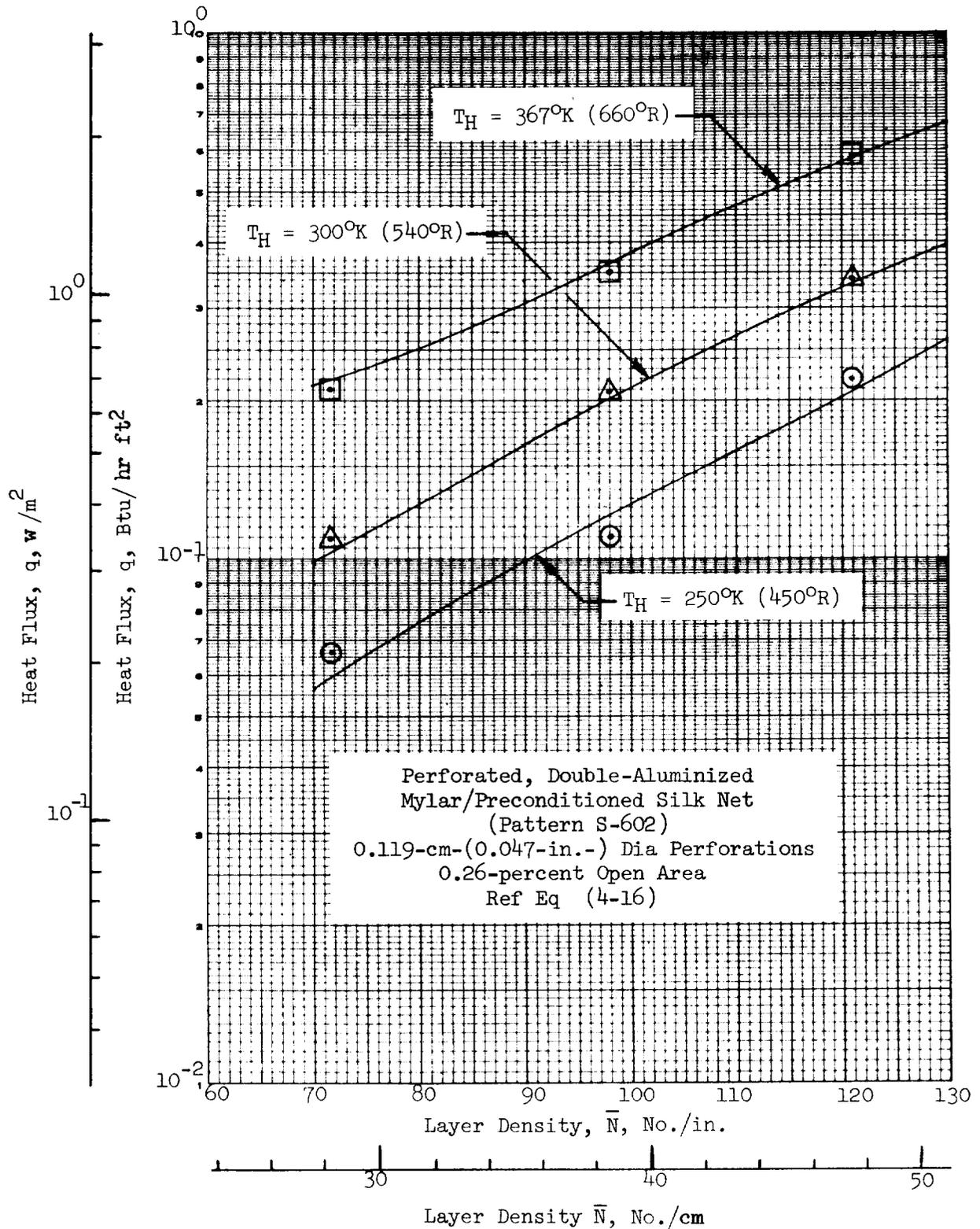
Fig. 4-11 Heat Flux as a Function of $\overline{N}$ and T_H for Specimen No. 5 with $T_C = 94^\circ K$ (170°R)

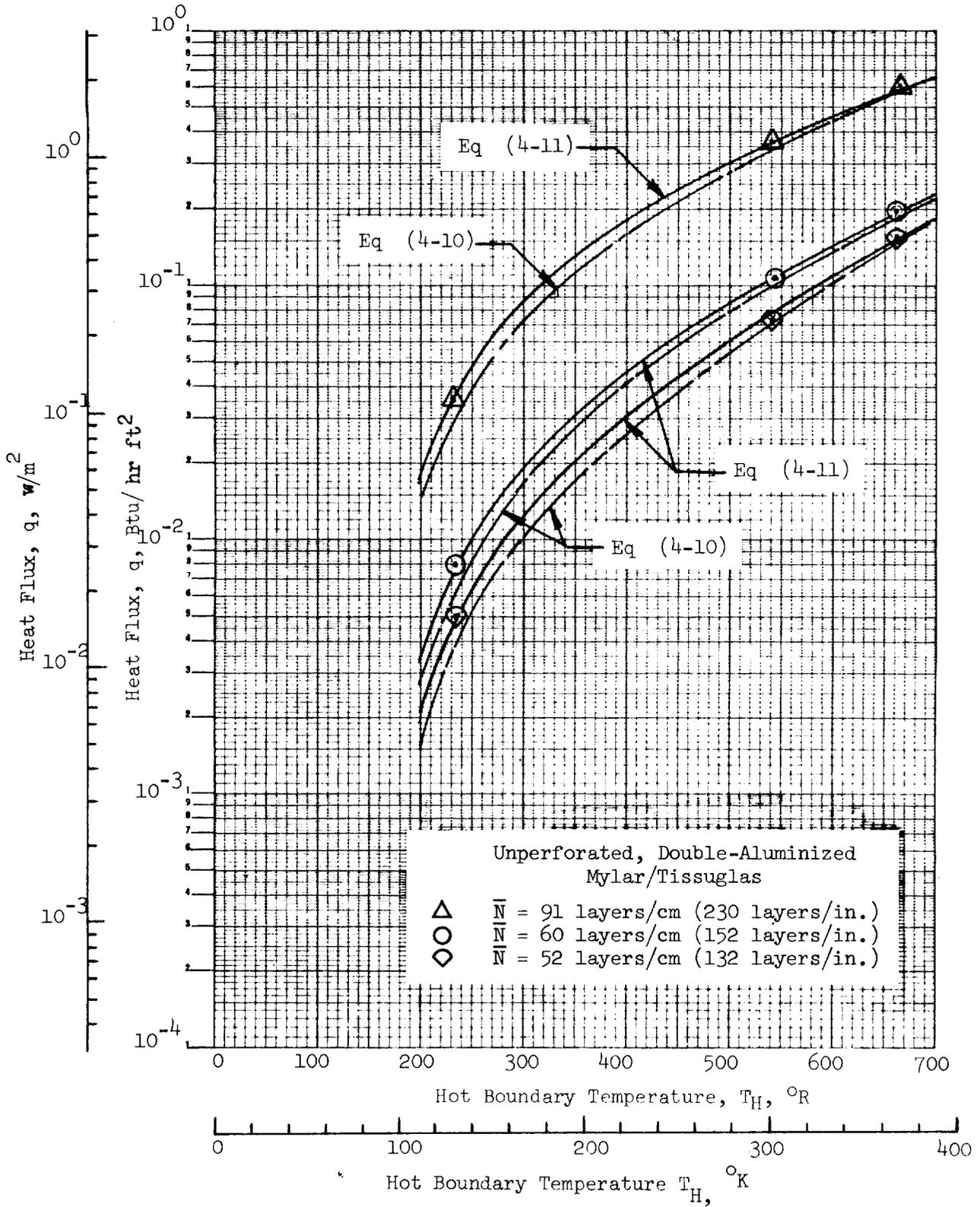Fig. 4-12 Heat Flux as a Function of $\bar{N}$ and T_H for Specimen No. 6 with $T_C = 94^\circ K$ ($170^\circ R$)
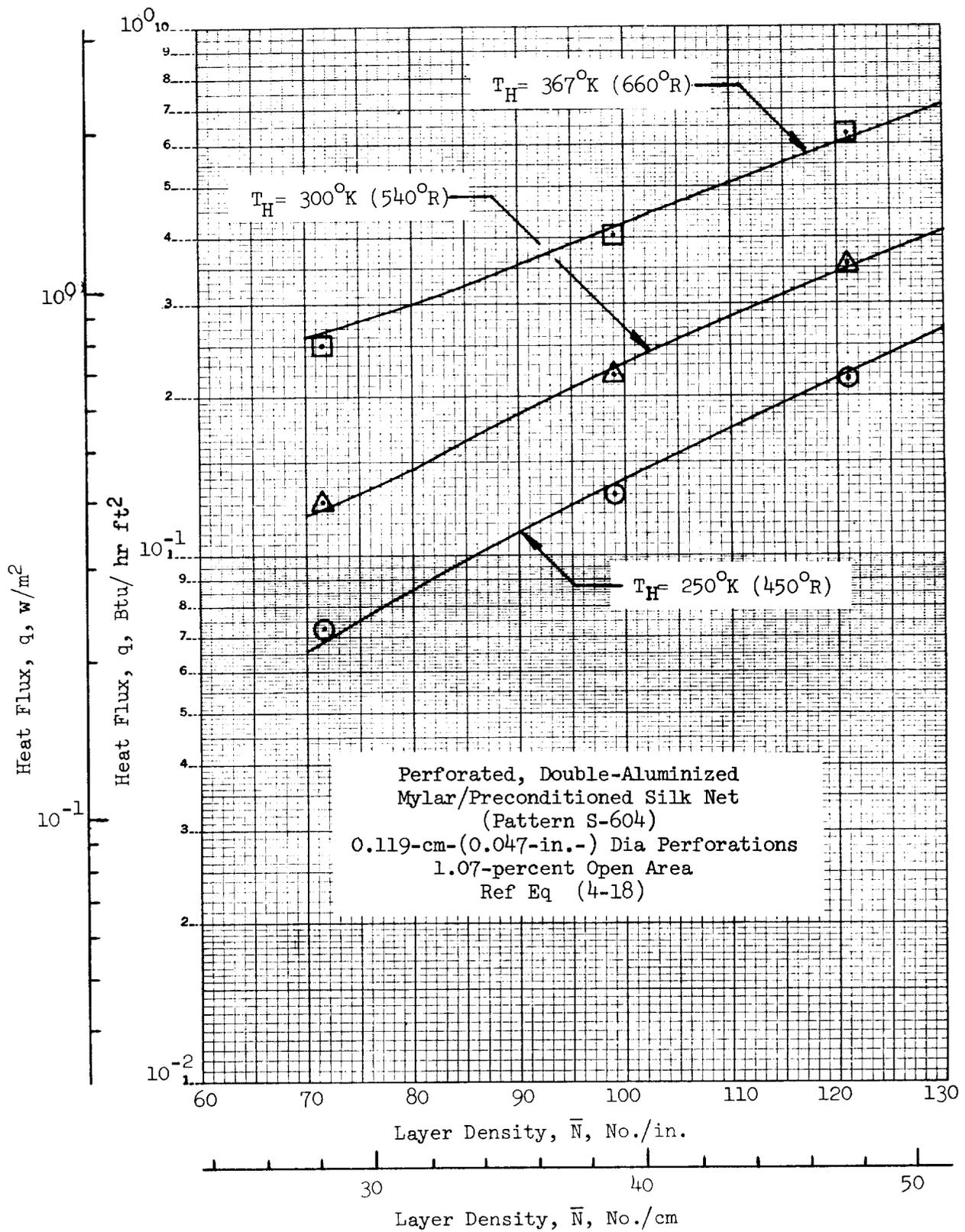
Fig. 4-13 Heat Flux as a Function of $\overline{N}$ and T_H for Specimen No. 7 with $T_C = 94°K$ (170°R)
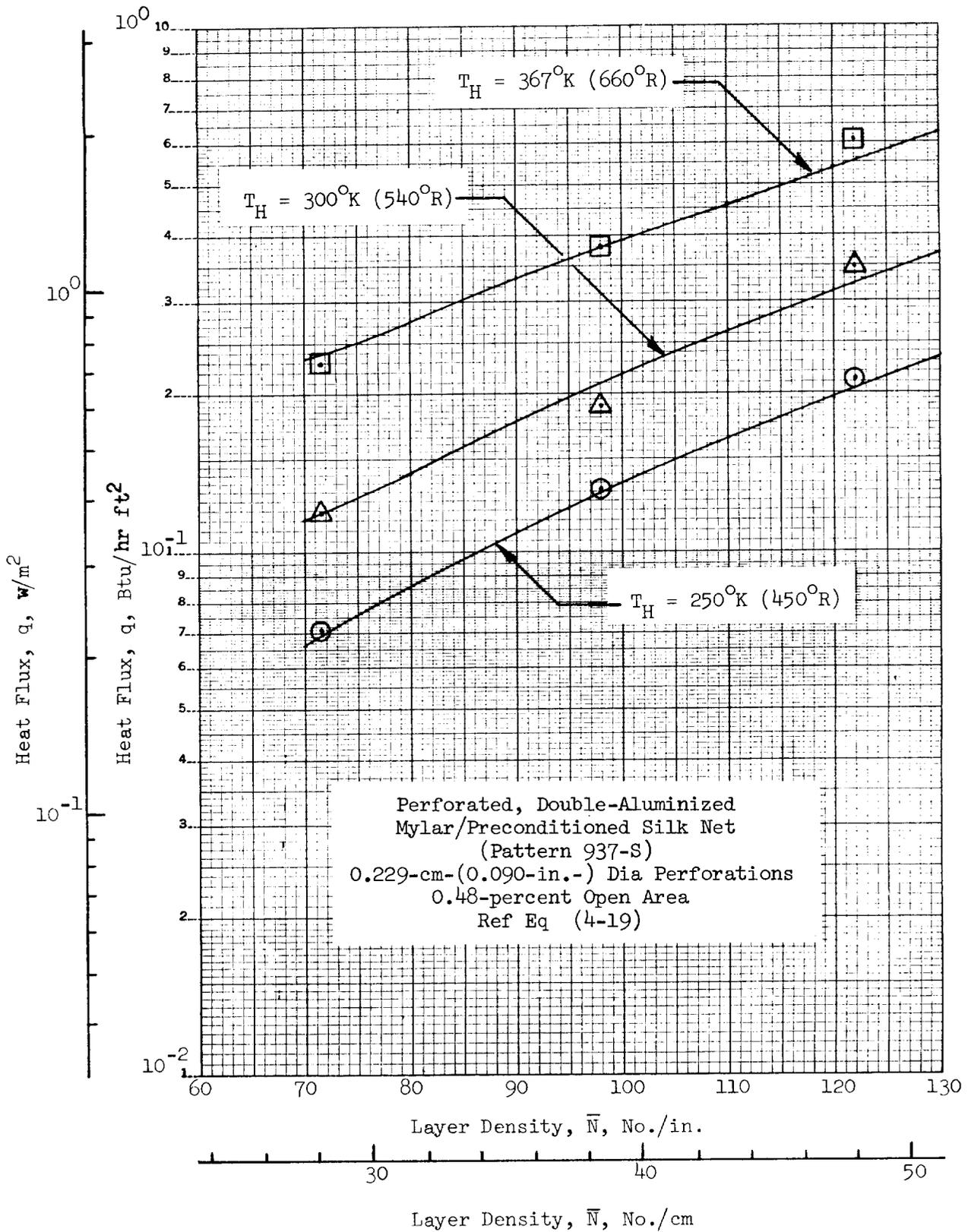
Fig. 4-14 Heat Flux as a Function of $\overline{N}$ and T_H for Specimen No. 8 with $T_C = 94^{\circ}K$ (170°R)

4-37

Fig. 4-15 Heat Flux as a Function of $\bar{N}$ and T_H for Specimen No. 9 with $T_C = 94°K$ (170°R)

S-603: $\quad q = \dfrac{C_s(\bar{N})^{2.63}T_m}{N_s+1}\,(T_H - T_C) + \dfrac{C_r\,\epsilon_{TR}}{N_s}\,(T_H^{\,4.67} - T_C^{\,4.67})$ $\qquad$ (4-17)

where: $\quad C_s = 7.04 \times 10^{-8}$ and $C_r = 6.32 \times 10^{-10}$
$\qquad$ for $\bar{N}$ in layers/cm, T in $^\circ$K, and q in w/m^2

or: $\quad C_s = 5.93 \times 10^{-10}$ and $C_r = 1.29 \times 10^{-11}$
$\qquad$ for $\bar{N}$ in layers/in., T in $^\circ$R, and q in Btu/hr ft^2

and: $\quad \epsilon_{TR} = 0.044$ (See Table 4-8)

S-604: $\quad q = \dfrac{C_s(\bar{N})^{2.63}T_m}{N_s+1}\,(T_H - T_C) + \dfrac{C_r\,\epsilon_{TR}}{N_s}\,(T_H^{\,4.67} - T_C^{\,4.67})$ $\qquad$ (4-18)

where: $\quad C_s = 7.30 \times 10^{-8}$ and $C_r = 7.07 \times 10^{-10}$
$\qquad$ for $\bar{N}$ in layers/cm, T in $^\circ$K, and q in w/m^2

or: $\quad C_s = 6.15 \times 10^{-10}$ and $C_r = 1.44 \times 10^{-11}$
$\qquad$ for $\bar{N}$ in layers/in., T in $^\circ$R, and q in Btu/hr ft^2

and: $\quad \epsilon_{TR} = 0.043$ (See Table 4-8)

937-S: $\quad q = \dfrac{C_s(\bar{N})^{2.35}T_m}{N_s+1}\,(T_H - T_C) + \dfrac{C_r\,\epsilon_{TR}}{N_s}\,(T_H^{\,4.67} - T_C^{\,4.67})$ $\qquad$ (4-19)

where: $\quad C_s = 1.99 \times 10^{-7}$ and $C_r = 6.10 \times 10^{-10}$
$\qquad$ for $\bar{N}$ in layers/cm, T in $^\circ$K, and q in w/m^2

or: $\quad C_s = 2.18 \times 10^{-9}$ and $C_r = 1.25 \times 10^{-11}$
$\qquad$ for $\bar{N}$ in layers/in., T in $^\circ$R, and q in Btu/hr ft^2

and: $\quad \epsilon_{TR} = 0.042$ (See Table 4-8)

937: $\quad q = \dfrac{C_s(N)^{2.70}T_m}{N_s+1}\,(T_H - T_C) + \dfrac{C_r\,\epsilon_{TR}}{N_s}\,(T_H^{\,4.67} - T_C^{\,4.67})$ $\qquad$ (4-20)

where: $\quad C_s = 6.22 \times 10^{-8}$ and $C_r = 6.65 \times 10^{-10}$
$\qquad$ for N in layers/cm, T in $^\circ$K, and q in w/m^2

or: $\quad C_s = 4.90 \times 10^{-10}$ and $C_r = 1.36 \times 10^{-11}$
$\qquad$ for $\bar{N}$ in layers/in., T in $^\circ$R, and q in Btu/hr ft^2

and: $\quad \epsilon_{TR} = 0.043$ (See Table 4-8)

With respect to the solid conduction term, a single best fit of all of the data for the five specimens with perforated shields was obtained by subtracting the computed radiative heat flux for each specimen from the measured value of total heat flux, and by then plotting this remainder as a function of layer density. To account for the number of layers and the several boundary temperature conditions, the equation was rearranged to the form

$$\Phi = (q_t - q_r) \left[\frac{N_s + 1}{T_m(T_H - T_C)} \right] = A\,(\overline{N})^n \tag{4-21}$$

The best fit of all of the data was obtained with $A = 7.77 \times 10^{-8}$ for $\overline{N}$ in layers/cm and T in $^{\circ}$K ($A = 6.59 \times 10^{-10}$ for $\overline{N}$ in layers/in. and T in $^{\circ}$R) and $n = 2.62$, as shown in Fig. 4-16. The solid curve depicts the best-fit equation, and the bars represent the spread of the values of Φ at the several layer densities investigated. All of the values fell well within the $\pm$ 20 percent bands shown, indicating that the preconditioning of the silk net resulted in a system having good reproducibility for solid conduction heat flux in terms of layer density.

A comparison of conduction heat flux values, based upon evaluation of all of the data obtained for the five specimens having perforated shields with those obtained for the two specimens with unperforated shields, is presented in Table 4-7. It can be seen that the scatter of data is within a 10 percent band, which is typical for multiple specimens of either system considered independently. Consequently, it was concluded that, as expected, no significant differences exist in the conduction heat transfer mechanism for the perforated-shield and the unperforated-shield systems.

An evaluation of the influence of reflective shield perforations on radiative heat transfer was accomplished by examining the coefficient, C_r, in the radiative term of the heat flux equations. Values of the radiative heat flux ratio, q_r/q_{ro}, were computed as the ratio of C_r for each perforated-shield system (Ref Equations 4-16 through 4-20) to that for the unperforated-shield system (Ref Equation 4-14). Since room temperature total hemispherical surface emittance, ϵ_{TR}, is an independent variable in each of these equations, the

4-40
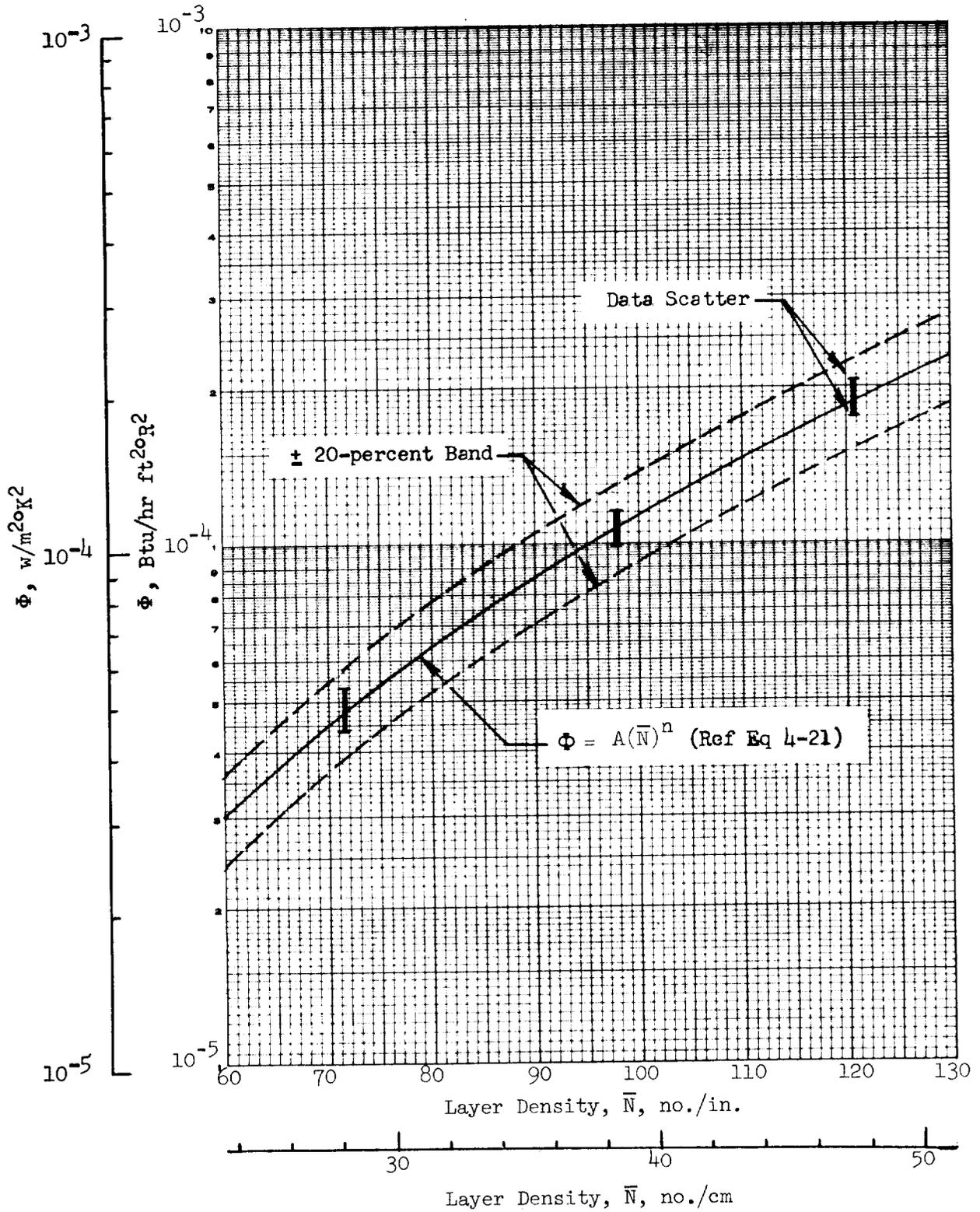
Fig. 4-16 Solid Conduction Parameter as a Function of Layer Density for Five
Specimens with Preconditioned Silk Net Spacers

4-41

resulting radiative heat flux ratio is based upon a constant emittance value for all of the systems. The computed radiative heat flux ratio values are presented in Table 4-8, together with other shield parameters, and are plotted as a function of open-area fraction in Fig. 4-17. The vertical bars shown in the figure illustrate the uncertainty band of q_r/q_{ro} for an uncertainty of $\pm$ 0.002 in the emittance value.

Table 4-7

COMPARISON OF SOLID CONDUCTION HEAT FLUX COMPUTED FROM EQUATIONS FOR UNPERFORATED AND PERFORATED MYLAR/PRECONDITIONED SILK NET

Layer Density		q_{sp}/q_{su} [a]
No./cm	(No./in.)	
23.6	(60)	1.05
35.4	(90)	1.07
47.2	(120)	1.10

[a] $q_{sp} \propto 7.77 \times 10^{-8} (\bar{N})^{2.62}$, $q_{su} \propto 8.95 \times 10^{-8} (\bar{N})^{2.56}$ (Ref Eq 4-14 and 4-21)

The solid curve shown in Fig. 4-17 represents a theoretical behavior of the heat flux ratio as a function of fractional open area, τ, shield emittance, ϵ, and spacer transmittance, t. Transmittance measurements were made for the spacer layer only and for hole-spacer layer combinations. Because of the possibility of scattering by the spacer, hemispherical rather than normal transmission data were obtained. For the two layers of net, spacer transmittance ranged from 0.55 to 0.67. The scatter of these measurements was due to the random arrangement of the overlapping patterns in the net material. Transmittance of a single layer of net was approximately 0.85. The data for the spacer plus hole combination are considered in a qualitative sense only because of measurement problems encountered with this arrangement. For the 0.119-cm-(0.047-in.-) diameter perforation with net, the range of effective transmittance was 0.7 to 1.0, and for the 0.229- cm -(0.090-in.-) diameter perforation with net, the effective transmittance was 0.6 to 0.7. For the curve plotted on

Fig. 4-17, a spacer transmittance value of 0.8 was used since it is the average of the measured transmittances for the two hole sizes. The analysis of perforations is discussed in more detail in Section 4.2.2.

Table 4-8

COMPARISON OF THE EFFECT OF PERFORATIONS ON RADIATIVE HEAT FLUX

Perforation Pattern	Hole Dia , cm(in.)	Fractional Open Area	ϵ_{TR}	q_r/q_{ro}(c)
S-602	0.119(0.047)	0.0026	0.043(a)	$1.09 \pm .05$
S-603	0.119(0.047)	0.0055	0.044(a)	$1.17 \pm .05$
S-604	0.119(0.047)	0.0107	0.043(b)	$1.31 \pm .07$
937-S	0.229(0.090)	0.0048	0.042(a)	$1.13 \pm .05$
937	0.229(0.090)	0.0099	0.043(b)	$1.23 \pm .06$

(a) Calorimetric value.

(b) Computed from reflectance data since perforation spacing precluded calorimetric measurements; ϵ_{TR} from reflectance data is 0.040; however, this corresponds to reflectance values for S-602, S-603 and 937-S so 0.043 used in computations of q.

(c) Range based upon 0.002 uncertainty in ϵ_{TR} for perforated material.

The hole size effect reported in Refs 2 and 3 is not apparent in these data. The two points for the 0.229-cm-(0.090-in.-) diameter perforations both fall below the values for 0.119-cm-(0.047-in.-) diameter openings, but considering the uncertainty in the data no definite conclusion can be drawn in this regard. For the hole sizes and open area range investigated in this work, one would conclude that, for the purpose of engineering calculations, the radiative heat transfer is independent of the diameter of the perforations.

$$q_r/q_{ro} = \frac{2(1-\epsilon)(1-\tau)\,\tau\,t^2 + \epsilon(1-\tau)}{\epsilon}$$

Legend within figure:
- O 0.119-cm(0.047-in.) Dia. Holes
- △ 0.229-cm(0.090-in.) Dia. Holes
- t = 0.8 (spacer transmittance)

Axis labels: q_r/q_{ro} (vertical), Fractional Open Area, τ (horizontal)
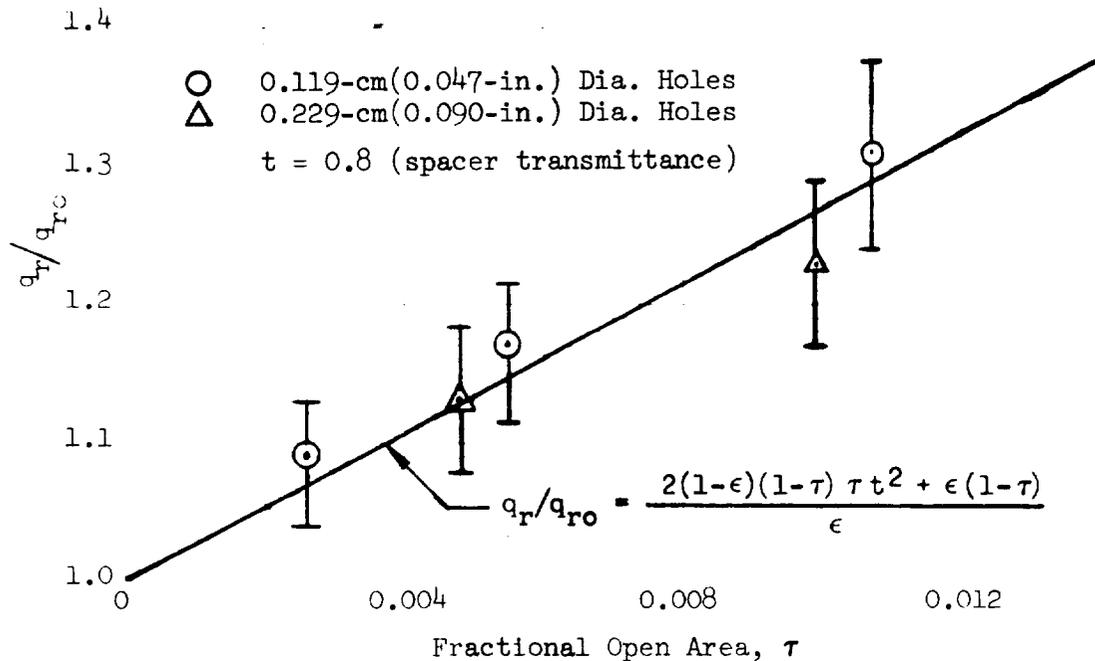
Fig. 4-17 Ratio of Radiative Heat Fluxes for Perforated Double-Aluminized Mylar as a Function of Fractional Open Area for Five Specimens.

4.2 HEAT TRANSFER ANALYSIS

In addition to the analysis of the basic experimental data, several parallel analytical studies were conducted in Task 1 in order to provide a basis for interpretation of the experimental results. In these studies, the effects of (1) the temperature dependence of solid conduction, (2) shield perforations on radiative heat transfer, and (3) interstitial gas conduction were assessed. Finally, the equation for the prediction of the Task 3 tank-installed MLI heat flux was developed with the incorporation of an interstitial gas conduction term into the total energy transport model.

4.2.1 Temperature Dependency of Solid Conduction

By inspection of the experimental heat flux data for the Tissuglas system, it was observed that at hot boundary temperatures below approximately 140°K (252°R) the original analytical heat transfer model developed in Ref 1

LOCKHEED MISSILES & SPACE COMPANY

significantly underpredicted the measured heat flux (see Figs. 4-5 through 4-8). The source of this anomaly was believed to be the solid conduction term because at low temperatures the radiative transport is very small and, consequently, should not constitute a significant portion of the transfer. The earlier model assumed a linear temperature dependence (i.e., $\propto T_m$) for the thermal conductivity of the glass fibers from which the Tissuglas paper is manufactured. However, if this assumption is not valid at low temperatures, the heat flux will not be a linear function of temperature, since the conduction term is directly proportional to the fiber thermal conductivity.

The heat transfer due to solid conduction through an evacuated multilayer insulation is limited by the low thermal conductivity of the spacer material and by the contact resistance between adjacent layer surfaces. In systems using fibrous spacers (e.g., Tissuglas), the heat flow paths are long and tortuous. Moreover, the heat flow is constricted by numberous fiber-to-fiber and fiber-to-shield contact points. Since the layers are free to move, the number and shape of the microscopic contract areas varies significantly with the application of compressive loads. Because of these variables, the development of an exact analytical model that precisely describes the physical characteristics of contact resistance in such a system is not feasible. However, a semi-empirical expression can be developed and used to approximate the variation of conductance with temperature in terms of the important physical parameters of conductivity, k, modulus of elasticity, E, and Poisson's ratio, μ, of the spacer material.

To evaluate the effect of temperature on these parameters, consider first the case of a single contact point. The constriction resistance for circular contacts as first suggested by Holms (Ref 4 , is given by

$$R_c = \frac{1}{2k_s \ r_c} \tag{4-22}$$

where k_s is the thermal conductivity of the material and r_c is the radius of the contact area. The radius r_c depends upon the mechanical properties of

the contacting materials as well as upon the geometry of the contact. For
the simple case of elastic deformation of two identical spherical surfaces
in contact, the radius is defined by the Hertz equation (Ref 5)

$$r_c = a \left[\frac{(1 - \mu^2)}{E} F \, r_s \right]^{1/3} \tag{4-23}$$

where a is a constant, μ is Poisson's ratio, E is Young's modulus, F is the
force acting on the contacting elements, and r_s is the spherical radius.
For other contact configurations, the exponents will vary but the general
form of the equation is applicable so that the contact resistance is given
by

$$R_c = \frac{1}{a' k_s (\frac{1 - \mu^2}{E})^m (F)^n (r)^o} \tag{4-24}$$

where r is a characteristic dimension of the contact. It can also be shown
that the thermal resistance of the heat path along a spacer fiber is directly
proportional to the distance between the contact points, ℓ, and inversely
proportional to the fiber thermal conductivity and cross-sectional area.

The total resistance of a spacer layer is then the sum of the resistances
for the series-parallel paths between the adjacent shields. In each case,
the resistance is a function of the thermal conductivity of the contacting
materials and, for the constriction resistance, the elastic properties of
the materials. Thus, a relationship between the conductive heat transfer
and these parameters can be expressed as $q_s \propto (\bar{k}_s)$, $(\bar{\mu})$, $(1/\bar{E})$, (P), (ℓ)
where $\bar{k}$, $\bar{\mu}$, and $\bar{E}$ are representative of the properties of both materials
in contact, P is the equivalent pressure on each contact, and ℓ is a char-
acteristic dimension of the contact geometry. Although it is not feasible
to develop a physical model that would accurately predict contact resistance,
the temperature dependence of the solid conduction heat transfer mechanism
can be evaluated by examining the effect of temperature on the important
properties. Modulus of elasticity and Poisson's ratio vary with temperature,
but these changes are generally small over the temperature range of interest.
Glass, for example, shows a small increase of both modulus and Poisson's
ratio with increasing temperatures. Aluminum, on the other hand, shows

4-46

a slight decrease in modulus and Poisson's ratio is essentially constant over the insulation temperature range. Typical values for a borosilicate glass (such as is used for Tissuglas) and pure aluminum are given in Table 4-9.

Table 4-9

ELASTIC PROPERTIES OF BOROSILICATE GLASS* AND ALUMINUM
AS A FUNCTION OF TEMPERATURE

Material	Property	Temperature $^\circ K(^\circ R)$				
		56(100)	139(250)	222(400)	306(550)	389(700)
Glass	$E, N/m^2 \times 10^{-10}$	6.1	6.1	6.2	6.3	6.3
	(psi $\times 10^{-6}$)	(8.8)	(8.9)	(9.0)	(9.1)	(9.2)
Glass	μ	0.190	0.194	0.197	0.204	0.205
Aluminum	$E, N/m^2 \times 10^{-10}$	7.7	7.7	7.4	7.3	---
	(psi $\times 10^{-6}$)	(11.2)	(11.2)	(10.8)	(10.5)	
Aluminum	μ	---	0.30	---	0.30	---

* Corning 7740 glass.

Since the variations in elastic properties with temperature are small, and since their influence is of the form $(\frac{1 - \mu^2}{E})^m$ where m is on the order of 1/3, this term can be considered to be essentially independent of temperature. Thermal conductivity, however, may vary by a factor of 2 to 5 over the test temperature range, and, therefore, it is considered to be the major contributor to a temperature dependence of the solid conduction heat flux term.

For thin metal films, such as those deposited on plastic reflective shields, the thin film thermal conductivity is not the same as that of the bulk metal. For film thicknesses typical of those used on metallized reflective shields (i.e., 500 Å), the electron mean free path is on the order of the metal thickness. This results in a reduced conductivity because some of the electron free paths are shortened due to termination at the boundary surfaces. Since phonon excitation is reduced and electron-phonon interaction increases as

4-47

LOCKHEED MISSILES & SPACE COMPANY

the temperature decreases, the thin film effect is more pronounced at cryo-
genic temperatures. Thermal conductivity of a thin metal film, k_f, can be
expressed in the following manner (Ref 6)

$$\frac{k_f}{k_b} = f \left(\frac{t}{l_k}, p \right) \tag{4-25}$$

where k_b is the bulk metal conductivity, t is the film thickness, l_k is the
electron mean free path for thermal conductivity, and p is the probability
of specular electron reflection at the boundary. At room temperature, l_k
for aluminum is on the order of 400 $\overset{o}{A}$, and increases as T^{-3}. Typical
conductivity data for a thin aluminum film (i.e., t = 500 $\overset{o}{A}$) and for glass
fibers, which are representative for Tissuglas, are presented in Fig. 4-18.
It can be seen that the glass material exhibits a non-linear temperature
dependence, but that the thin aluminum conductivity is relatively independent
of temperatures.

In order to evaluate the effect of temperature on the solid conduction heat
transfer term for multi-layer insulations, the aluminum surface is neglected
for cases in which glass paper spacers are used since the conductivity of
the aluminum film is markedly greater than that of the glass fibers and
since many more fiber-to-fiber contacts are present than aluminum-to-fiber
interfaces. Since the temperature dependence of the elastic properties can
be neglected, the conduction heat transfer between adjacent shields is
$q_{i-j} = \frac{\Delta T}{2R_c + R_s}$ where R_c is defined by Eq (4-24) and R_s is the spacer layer
resistance, $R_s \equiv \frac{h}{k}$. The total resistance between adjacent shields is then
$R_T = \frac{1}{k} \left[\frac{1}{C(F)^n} + h \right]$ where C describes the elastic and geometric properties
of the contact, F is the force and h is the spacer thickness. As $h \ll 1$,
this reduces to $R_T = \frac{1}{kC(F)^n}$. To treat a composite of many layers as a
continuous media (Ref 1), the resistance is expressed as an effective
conductivity $K \equiv h/R_T$, and the conductive heat transfer is

$$q_s = K \; dT/dx = hk \; C(F)^n \; dT/dx \tag{4-26}$$

4-48
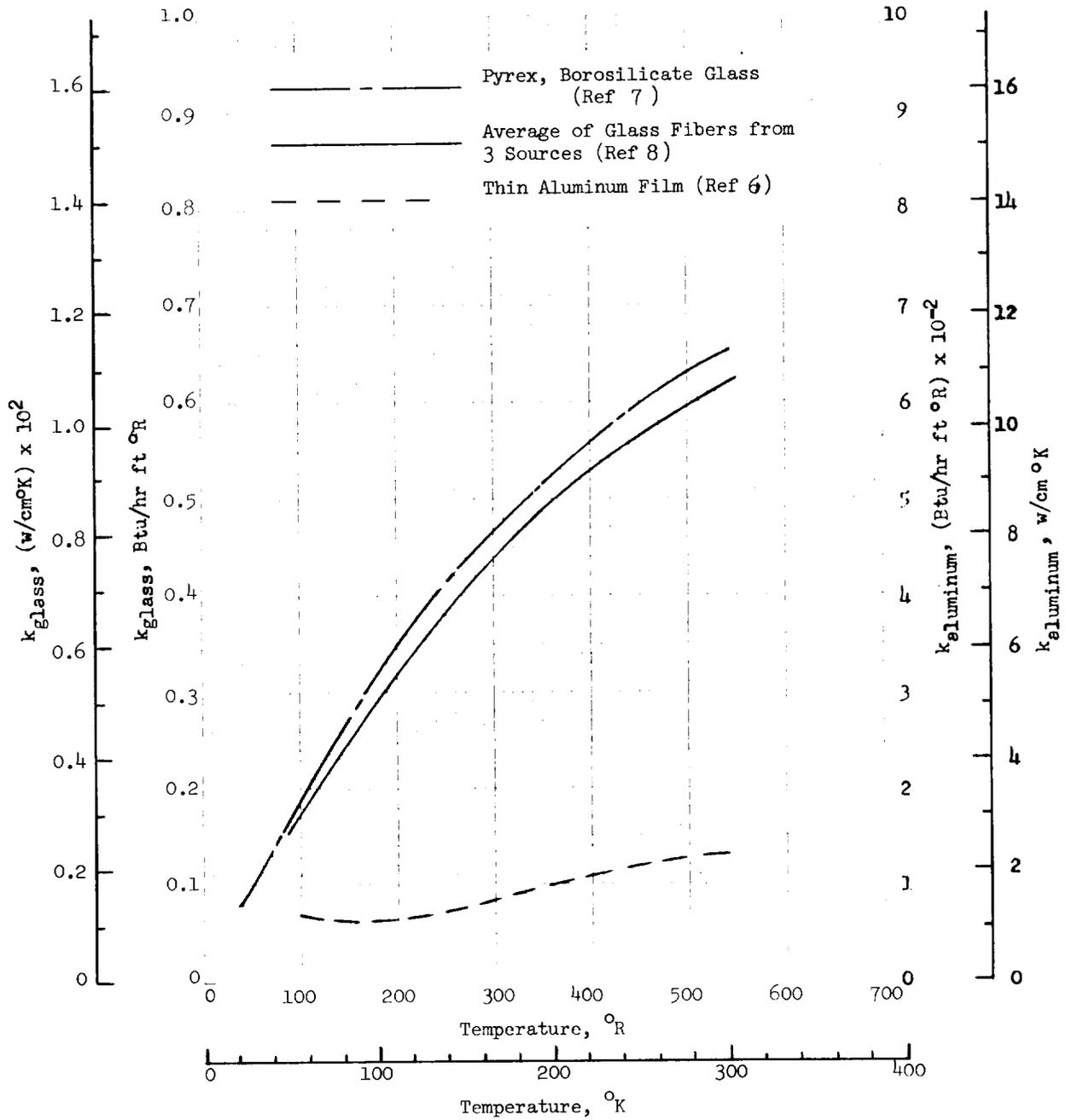
Fig. 4-18 Thermal Conductivity as a Function of Temperature for Glass Fibers and Thin Aluminum Film.

From the data of Fig. 4-18, a good approximation for the temperature dependent thermal conductivity of the fibers is $k_{(T)} = aT - bT^2$. Substituting this expression for $k(T)$ into Equation (4-26) together with $h = \ell/N$, where ℓ is the composite thickness and N is the total number of layers, and integrating between the limits $T = T_H$ at $X = X_1$ and $T = T_C$ at $X = X_2$ yields

$$q_s = \frac{\ell C(F)^n}{N(X_1 - X_2)} \left[\frac{a}{2} (T_H^2 - T_C^2) - \frac{b}{3} (T_H^3 - T_C^3) \right] \qquad (4\text{-}27)$$

and, since $\ell = (X_1 - X_2)$, the thickness terms cancel each other in this equation.

The contact force is proportional to the compressive pressure on the composite, which in turn is a function of layer density (Ref. 1). Thus,

$$q_s = \frac{C(\overline{N})^m}{N} \left[\frac{a}{2} (T_H^2 - T_C^2) - \frac{b}{3} (T_H^3 - T_C^3) \right] \qquad (4\text{-}28)$$

Constants a, b and C are combined and evaluated together with the exponent m from the experimental heat flux data in terms of $\overline{N}$ and T to yield the conductive term of the heat transfer equation (Ref Equation 4-11). The $(N_s + 1)$ term replaces N of Equation (4-28) because of the additional layer imposed by the boundary plates of the Flat Plate apparatus.

From Figs. 4-5 through 4-8, it can be seen that the above form of the heat transfer equation is in good agreement with the experimental data over the entire range of temperatures investigated in this program. However, for very low temperatures, i.e., 4°K to 20°K (7.2°R to 36°R), the thermal conductivity term should be further examined to evaluate its temperature function in this region. Since the test data for the silk net systems were in close agreement with the previous heat transfer model using a linear dependence form of conduction, it is assumed that the thermal conductivity of the silk fiber over the test temperature range is essentially linear with respect to temperature, although no actual conductivity data are available.

4.2.2 Radiative Heat Transfer with Perforated Shields

In a recent analysis (Ref 9), a resistance network method was used to eval-
uate the effect of perforated reflective shields on the radiation heat trans-
fer for the silk net multilayer insulation system. The influence of perfor-
ation open area, shield emittance, and spacer transmittance was investigated.
Also, the effect of perforation diameter was examined qualitatively.

The physical system considered was a set of n gray perforated shields of
emissivity ϵ equally spaced between black or gray boundaries as shown in
Fig. 4-19. Because the holes in the shields are staggered randomly from
shield to shield, radiation from any given shield falls on no more than
two shields on either side of it. Consequently, only four interactions for
each shield are used in the analysis. It is assumed that spacers of trans-
missivity t are placed between the shields. It is also assumed that the
emittance ϵ and the transmittance (or fractional open area) τ of the shields
are small (typically in practice, $\tau \cong 0$ to 0.1, $\epsilon \cong 0.02$ to 0.10) and that
the spacer transmittance t is relatively high (typically t $\cong$ 0.6 to 0.8) so
that several appropriate simplifications can be made.

When the holes are small, the radiosity can be approximated as a constant
and the resistance network method (Ref 10) can be applied to solve the problem.
The network for the system is shown in Fig. 4-20. The letters a, b, c, d,
and e refer to the resistance values which are defined in the figure.

A numerical step-by-step procedure was employed for the solution of this
network problem. Initially, the case of one interstitial gray shield
between black plates was solved. Then, as the number of interstitial shields
was increased one at a time, the resistances so obtained were found to involve
increasingly lengthy expressions. However, by plotting the resistance per
shield, R_n/n, versus n, it was shown that the resistance per shield very
quickly approaches an asymptotic value (n $\geq$ 3) for all cases having values
of ϵ and τ which are practical for multilayer insulations.

4-51

NOTE: -Numbers 1 through n indicate surface of shields facing T_0 boundary, whereas those numbered 1' through n' indicate shield surfaces facing T_∞ boundary
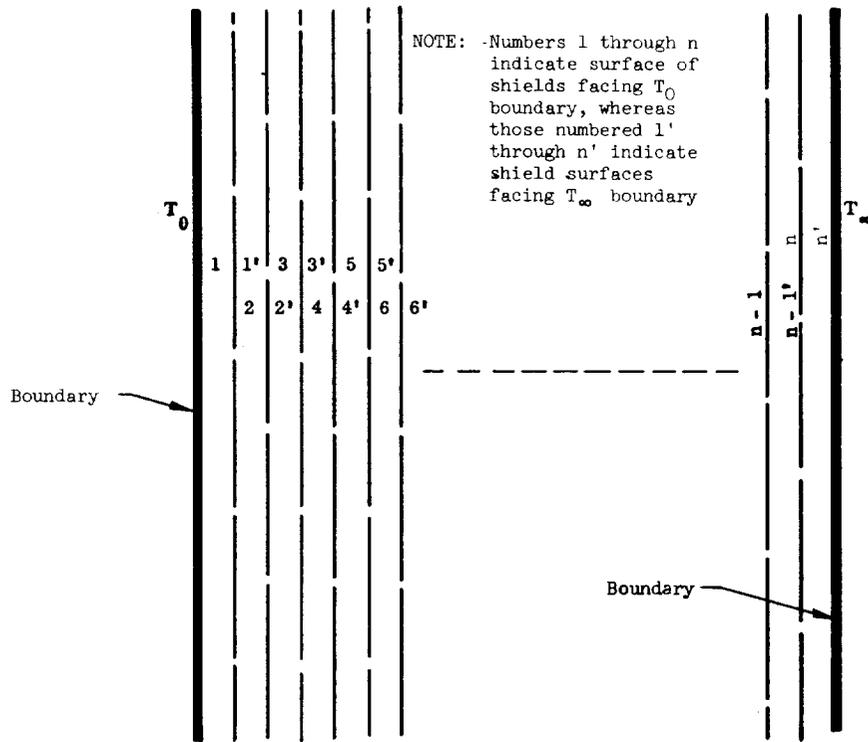
Fig. 4-19   Physical Model of a System of Perforated Reflective Shields Between Gray Boundaries
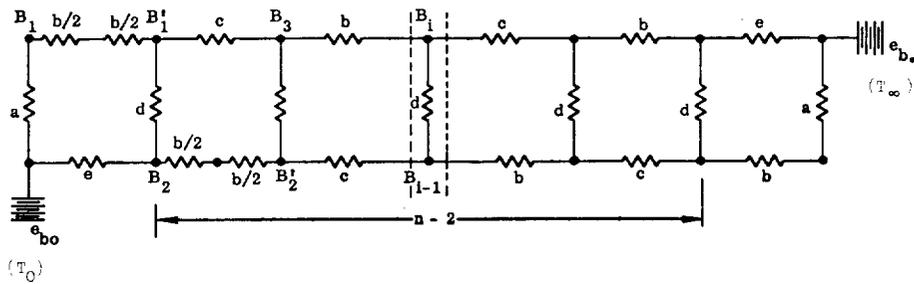
Fig. 4-20   Schematic of Resistance Network

4-52

The network solution is simplified by neglecting resistances a and d since these are more than an order of magnitude smaller than b. For $\epsilon \leq 0.1$ and $t > 0.6$, both a and d < 3, whereas b > 50 to $\epsilon \leq 0.04$. The circuit then consists of n resistances of (b-c) in parallel to each other (assuming $\epsilon \cong e$ if n is large). The resistance per shield becomes

$$\frac{R_n}{n} = \frac{bc}{b+c} = \frac{2(1-\epsilon)}{2(1-\epsilon)(1-\tau)\tau t^2 + \epsilon(1-\tau)} \tag{4-29}$$

and this is approximately $2(1-\epsilon)/(2\tau t^2 + \epsilon)$ for small values of ϵ and τ. This is shown plotted in Fig. 4-21 where it is compared with the asymptotic value of the more exact formulation that was discussed above. The agreement is good (within 5 percent) because the error in neglecting d is approximately compensated for by assuming $c \cong e$. As n increases, the end effect error disappears, and calculations show that this expression always underestimates the resistance. If the end plates are gray instead of black, a resistance of $(1-\epsilon)/\epsilon$ is added at each end of the circuit. If n is very large and τ is small these additional resistances can be neglected. The network results are also compared on the same figure with the "large hole" and "small hole" results of Ref 2 . The resistance values per shield (for large values of n) are

$$R_n/n = \frac{2-\epsilon}{\epsilon + 2\epsilon\tau} \quad \text{(large holes)} \tag{4-30a}$$

$$R_n/n = \frac{2-\epsilon-2\tau+\epsilon\tau}{2\tau+\epsilon-\epsilon\tau} \quad \text{(small holes)} \tag{4-30b}$$

The radiation heat transfer between boundaries can be expressed as $q = \frac{E_o - E_n}{R_{o-n}}$, where E is defined as the emissive power of the boundary surfaces. Then, since R_{o-n} is $R_n n$ from Eq (4-29), the heat transfer equation can be expressed as

$$q_{o-n} = \left[\frac{2(1-\epsilon)(1-\tau)\tau t^2 + \epsilon(1-\tau)}{2n(1-\epsilon)} \right] (E_o - E_n) \tag{4-31}$$

which, for $\tau = 0$, reduces to $q_{o-n} = \frac{\epsilon}{2n(1-\epsilon)} (E_o - E_n)$. The ratio of radiative heat flux values for systems with perforated shields to those for systems with unperforated shields simply becomes the expression shown earlier on Fig. 4-17.

4-53
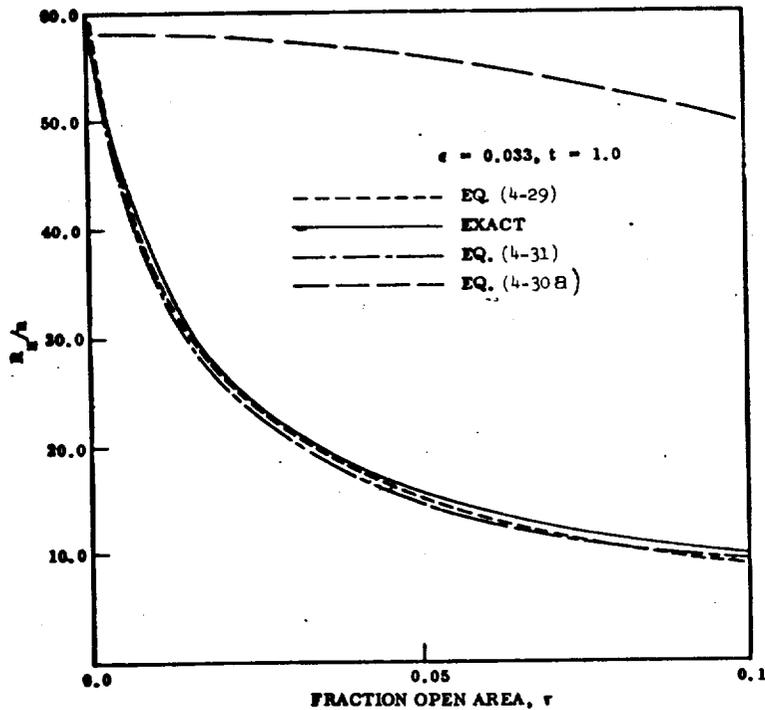
Fig. 4-21   Comparison of Unit Shield Resistance as a Function of Fractional
Open Area

The agreement of the network formulation with the small-hole (two-flux model)
case is extremely good at low values of ϵ and τ, but differs up to 20 percent
where ϵ = 0.1 and τ = 0.1.   The large-hole expression yields much higher re-
sistances, especially at low emissivities; however, the validity of the large-
hole equation is highly questionable.   The close agreement between the small-
hole results, which are based on a two-flux model, and the network method was
expected since both are based on a uniform radiosity model (i.e., no dis-
continuity at the holes).   The resistance expressions for these two methods
are very nearly identical, except for second order terms, although two basic
differences exist between them.   One difference is that the two-flux model
considers radiosities (or heat fluxes) per unit area in space (adjacent to
the plate), whereas the network method considers heat fluxes per unit area
of solid surface.   Thus the q in the two-flux model is not the heat flux at
the interstitial shield but that at the end plates.   The other basic difference

LOCKHEED MISSILES & SPACE COMPANY

is that the network method considers interaction of each plate with only four other plates, whereas the two-flux model considers a continuous interaction between all of the plates. Thus, from a fundamental viewpoint, the network formulation is more appropriate than the two-flux model for this problem.

It is clear that neither the two-flux model nor the network method take into account the actual size of the holes or perforations since both are based on a uniform radiosity model. As the hole size gets larger, accuracy of the present prediction could be affected due to non-uniform distribution of irradiation, radiosity, and temperature over the shields. However, this effect should be small for the typical value of τ = 0 to 0.1.

As discussed in Section 4.1.6.3, the experimental data obtained in Task 1 are in good agreement with the analysis for the small-diameter perforations and small fractional open areas investigated under this program. To extend the analysis to larger holes and larger values of τ, a comparison was made with the data of Ref **3**. These data, which were obtained for 10-shield systems using silk net spacers, are shown in Table 4-10. For values of τ = 0.01 and 0.0107, they are in good agreement with the Task 1 data for the 80-shield specimens (Ref Table 4-8).

Table 4-10

EXPERIMENTAL DATA FOR 10-SHIELD SPECIMENS WITH SILK NET SPACERS*

Perforation Geometry	Fractional Open Area, τ	Measured Heat Flux, w/m^2 (Btu/hr ft^2)		Computed Radiation Heat Flux, w/m^2 (Btu/hr ft^2)		q_r/q_{r_o}
None	0.000	4.135	(1.312)	1.485	(0.471)	1.0
0.318-cm(0.047-in.-) Dia, 2.54-cm (1.0-in.) rectangular spacing	0.0118	4.550	(1.444)	1.90	(0.603)	1.29
0.660-cm-(0.260-in.-)Dia, 5.08-cm (2.0-in.) rectangular spacing	0.0123	4.46	(1.42)	1.81	(0.574)	1.23
0.660-cm-(0.260-in.-) Dia, 2.54-cm (1.0-in.) rectangular spacing	0.0514	5.22	(1.66)	2.57	(0.815)	1.74
0.228-cm-(0.090-in.-) Dia	0.0100	5.44	(1.73)	2.795	(0.887)	1.28
0.120-cm-(0.047-in.-) Dia	0.0107	5.51	(1.75)	2.86	(0.907)	1.31

* Data shown are for $\bar{N}$ = 28 layers/cm(71 layers/in.) and for boundary temperatures of 372°K(670°R) to 77°K(139°R).

The experimental results from Table 4-10 are compared with approximate network analysis results and with those for the large hole model in Fig. 4-22. The influence of spacer transmittance and that of shield emittance are illustrated by the broken and solid line curves. At a 0.01 fractional open area, the data are in good agreement with the theory for hole sizes from 0.12-cm-(0.047-in-) to 0.318-cm-(0.125-in.-) diameter. The two smaller holes correspond to the spacer transmittance of 0.8 and shield emittance of 0.040. Similarly, there is good agreement between the 0.318-cm-(0.125-in.-) diameter hole results and those for t = 0.6 and ϵ_s = 0.027, indicating that there is a hole-size effect. A larger discrepancy between the experimental data and the theory is evident for the 0.660-cm-(0.260-in.-) diameter hole size at τ = 0.0514.
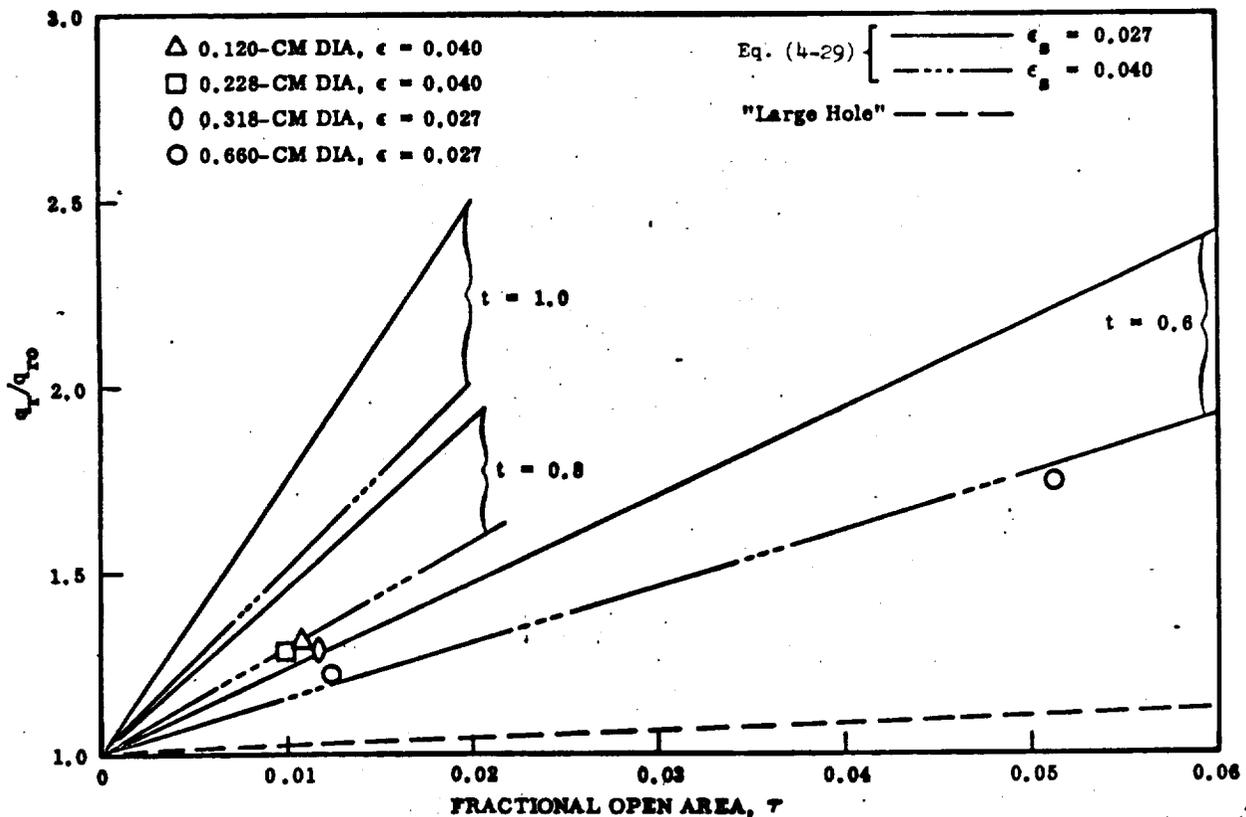
Fig. 4-22 Comparison of Experimental and Predicted Radiation Heat Flux Ratios

The discrepancy in hole size effect between the analysis and the experimental data can be attributed to three possible causes: (a) assumption of uniform temperature across the shields, (b) non-uniform distribution of irradiation and radiosities over the surfaces, and (c) the fact that the surfaces are specular rather than diffuse. The problem of specular surfaces was not analyzed because of its complexity, but the effect is not expected to be substantial, particularly when τ is small. Also, a simplified one-dimensional analysis of the problem of the non-uniformity of temperature, considering the thermal conductivity of aluminized Mylar, did not show this to be a significant effect either. This is borne out by the consistency of the experimental data between that for the aluminized Mylar shields and for aluminum foil shields (Ref 2).

The problem of non-uniformity of irradiance and radiosities was examined, again using a one-dimensional model to simplify the analysis, and a very small dependence was noted for hole diameter, shield spacing, and open area. Although this effect was in the right direction, it was not of sufficient magnitude to explain the experimental data. However, it did suggest a possibility for obtaining some correlation of the experiment in terms of the above parameters. An empirical correlation of the data was obtained in a qualitative sense by considering a modification of resistance c in the network model. This was accomplished by modifying the configuration factor in terms of τ (which is a function of the hole-diameter-to-hole-spacing ratio), separation between adjacent shields, and hole diameter. This empirical relationship serves to increase the value of resistance c with increasing hole size and τ and with decreasing shield separation.

4.2.3 Interstitial Gas Conduction

All of the Task 1 tests were performed with relatively small disk-shaped specimens and the insulation was exposed to a hard vacuum environment (i.e., 10^{-7} torr or less) so it is reasonable to assume that any heat flux due to conduction through trapped interstitial gases was negligible. However, at early times during the Task 3 tests, the interstitial pressure within the

4-57

multilayers was found to be two or more orders of magnitude higher than chamber pressure. For this case, the gas conduction component contributed a significant portion of the total heat transfer. Consequently, it was necessary to perform an analysis to determine what the magnitude of the gas conduction component might be for this material system as a function of interstitial pressure in order to predict thermal performance for the Task 3 testing. Details of the analysis are described below, and the resulting thermal performance equations are presented and discussed in Section 4.2.4.

Heat transfer in a direction normal to the reflective shields has been studied extensively for highly-evacuated systems and conduction through any residual gas phase has been neglected because of the assumption of very low interstitial gas pressures (10^{-6} torr or less) within the void spaces. However, for larger and/or thicker insulation blankets, as applied to storage vessels, the gas pressure within the insulation may be higher than that of the outer vacuum space due to outgassing from the insulation materials, tank wall permeability, and/or poor flow conductances from the interstitial spaces to the exterior of the system. In order to evaluate the influence of the presence of an interstitial gas on the insulation performance, the gas conduction problem was studied in terms of pressure, temperature, and gas species.

Heat conduction in gases is normally considered in four separate molecular regimes: namely, free-molecule ($Kn > 10$), transition ($10 > Kn > 0.1$), temperature-jump (slip) ($0.1 > Kn > 0.01$), and continuum ($Kn < 0.01$), where Kn is the Knudsen number ($Kn = \ell/L$), ℓ is the mean free path of molecular collisions, and L is the characteristic length of the gas layer (e.g., the vacuum spacing). The various regimes have been under extensive investigations in the field of rarefied gas dynamics (Ref 11) but these studies are mostly restricted to linearized problems (i.e., $[(T_1/T_2) - 1] \ll 1$) where T_1 and T_2 are temperatures of the two bounding surfaces. In extending these results to heat transfer calculations for cryogenic insulations, however, care must be exercised since the boundary temperatures are often quite different,

rendering the linearization condition invalid. A general discussion of gas-conduction calculations in cryogenic insulations is given by Corruccini (Ref 12). A brief discussion of the current status is presented in the following paragraphs.

To characterize the mode of gas conduction, the mean free path of molecular collisions must be known. The mean free path can be obtained from kinetic theory (Ref 13), and a convenient relation in terms of macroscopic properties is given as

$$\ell = 8.6 \left(\frac{\mu}{P} \right) \left(\frac{T}{M} \right)^{1/2} \tag{4-32}$$

where ℓ is in cm, μ is viscosity in poise, P is pressure in torr, T is temperature in $^{\circ}$K, and M is molecular weight. At a one-micron pressure and 77°K, for example, $\ell = 0.9$ cm (0.35 in.) for nitrogen, 1.9 cm (0.75 in.) for hydrogen, and 3.1 cm (1.22 in.) for helium.

Under free-molecule conditions (Kn > 10), the conduction heat flux for parallel plates, coaxial cylinders, and concentric spheres can be estimated by Knudsen's formula (Ref 12) as

$$q_{FM} = \frac{Q_{FM}}{A_1} = \alpha \left(\frac{\gamma + 1}{\gamma - 1} \right) \left(\frac{R^{\circ}}{8 \pi MT} \right)^{1/2} P(T_2 - T_1) \tag{4-33}$$

In the expression, A_1 is the area of the surface corresponding to T_1, γ is the specific heat ratio of the gas, R° is the molar gas constant, $T = (T_1 + T_2)/2$, and α is the overall thermal accommodation coefficient, defined as

$$\alpha = \frac{\alpha_1 \alpha_2}{\alpha_2 + \alpha_1 (1 - \alpha_2) A_1 / A_2} = \frac{\alpha_1 \alpha_2}{\alpha_1 + \alpha_2 - \alpha_1 \alpha_2} \tag{4-34}$$

for finite parallel planes, and subscripts 1 and 2 refer to the inner and outer surfaces, respectively. The thermal accommodation coefficient is a measure of the efficiency of thermal energy interchange that occurs when a gas molecule collides with the surface. It may vary between 1 (complete accommodation, diffuse re-emission) and 0 (specular re-emission). Its exact

4-59

value depends upon the kind of gas molecule, the surface temperature, and most importantly the exact condition of the surface. As far as is now known, α can only be regarded as an empirical parameter that must be determined from measurements. Values of α under various conditions have been reported by a number of investigators (Refs. 11, 12, 14 and 15) and, in most cases, increase with decreasing cleanliness, heavier gas molecules, and decreasing temperature. Some experimental results (Ref 16) for the accommodation coefficient of hydrogen gas to aluminized Mylar are given in Fig. 4-23 to illustrate the temperature dependence. Values of α for several gases to platinum at nominally $300^{\circ}K$ ($540^{\circ}R$) and hydrogen and helium at various temperatures are also shown in this figure.

One notable feature of the free-molecule regime is that the conductive heat flux is independent of the gas-layer thickness L (i.e., the vacuum gap spacing). This is analogous to the radiative transport between two surfaces separated by a nonradiating medium. The parameter L, however, is important here in defining the free-molecule regime (i.e., $\ell/L > 10$). For spacing on the order of 1 cm at an average temperature of $200^{\circ}K$ ($360^{\circ}R$) with N_2, the vacuum pressure required for the onset of free-molecule conduction is about 3×10^{-4} torr. For the same pressure level, if n shields of identical surface accommodation characteristics are separately spaced in the gap region, the conductive heat flux will be reduced by a factor (n + 1). In other words, the same vacuum insulation effectiveness can be achieved with lesser vacuum requirement when more shields are used. Thus, the shielding concept in insulation applies to residual gas conduction as well as to radiation. Conduction shielding, however, is often overlooked because in many situations either the natural surrounding is at such a high vacuum (e.g., outer space) or it is very convenient to reduce the gas pressure to such a level that gas conduction is negligibly small compared to radiation.

Gas conduction in the transition and slip regimes is a rather complicated subject and has been under numerous recent investigations (Ref 11). For practical calculations for parallel plates, coaxial cylinders, and

LOCKHEED MISSILES & SPACE COMPANY
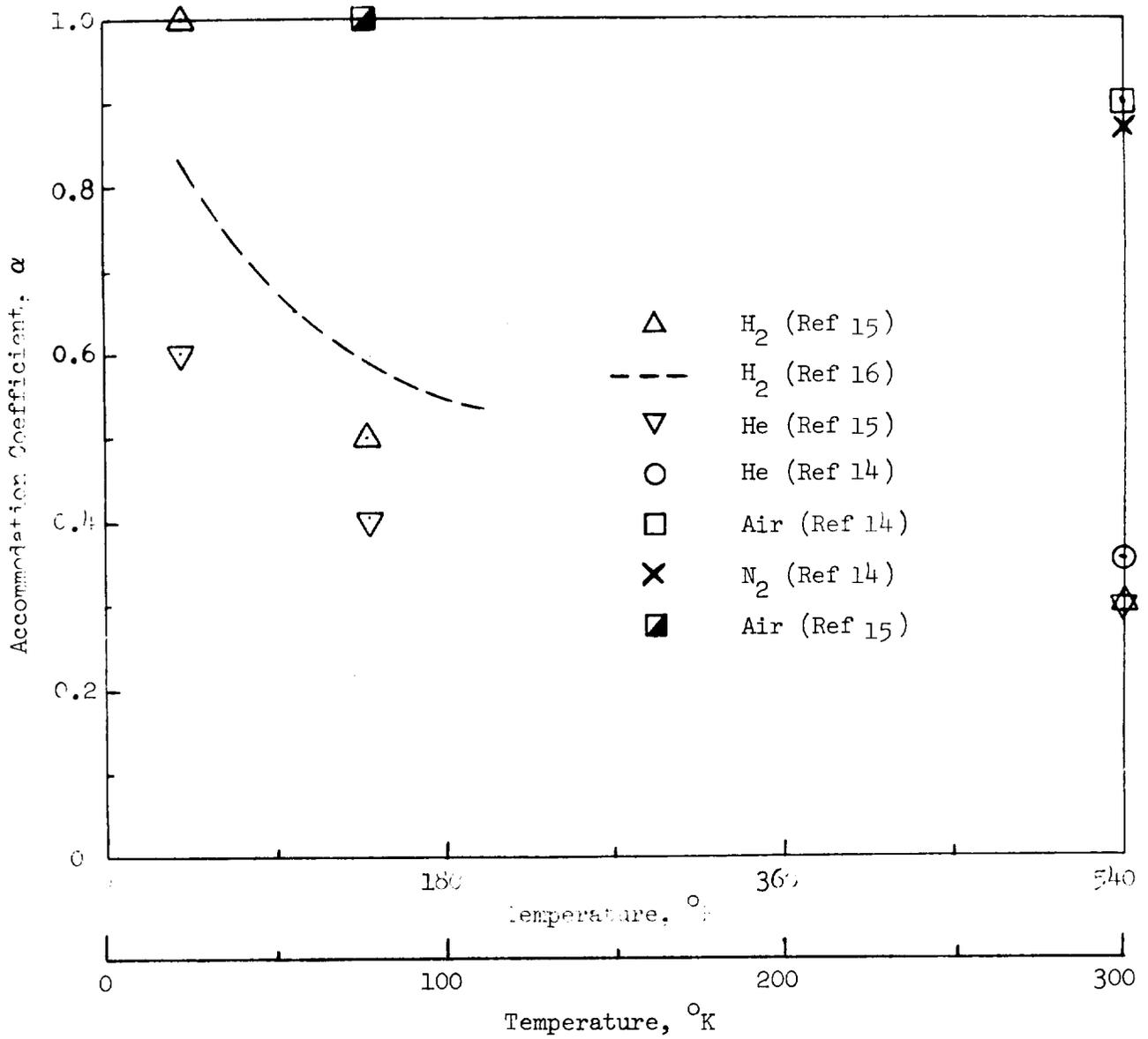
Fig. 4-23   Temperature Dependence of Accommodation Coefficients of Several
Gases to Clean Metal Surfaces

4-61

concentric spheres, it is recommended that the following simple interpolation formula be used

$$q/q_{FM} = \left[1 + (q_{FM}/q_C) \right]^{-1} = \left[1 + (KL/\ell) \right]^{-1} \qquad (4\text{-}35)$$

where q_C is the continuum heat flux. For instance, for a plane layer, q_C can be written from the simple kinetic theory (Ref 12) as,

$$q_C = k_g (T_3 - T_1)/L = \left[(9\gamma - 5)\, \mu\, c_v/4 \right]\ (T_2 - T_1)/L \qquad (4\text{-}36)$$

In these expressions, c_v is the constant-volume specific heat and the constant K can be obtained through simple manipulations of Equations (4-32, (4-33), (4-35), and (4-36).

The thermal conductivity of a gas at ordinary temperature and pressure conditions can be expressed in terms of density, ρ, and mean free path, ℓ, as

$$k_g \propto \bar{c}\, \rho\, C_v\, \ell$$

where $\bar{c}$ is the mean molecular speed and C_v is the molar specific heat. For a free or unrestricted gas, the thermal conductivity is independent of pressure as density varies directly with pressure while the mean free path is inversely proportional to pressure, as indicated in Eq (4-32). For a contained or restricted gas, however, the dimensions of the void (such as the spacing between shields in multilayer insulation) may become much smaller than the gaseous mean free path at low pressures, resulting in free-molecular conduction. A convenient semi-empirical technique for computing the effective thermal conductivity of a contained gas over a wide range of pressures is based on the use of an effective mean free path (Ref 17) which takes into account both the molecule-to-molecule and the molecule-to-wall collisions. An effective mean free path is defined as

$$\ell' = \ell \left(\frac{L}{L + \ell} \right) \qquad (4\text{-}37)$$

where L is a characteristic dimension of the void. The effective thermal conductivity of the contained gas at reduced pressures is then

$$k_g' = \alpha \, k_g \left(\frac{L}{L + \ell} \right) \qquad (4\text{-}38)$$

In this expression, α is the accommodation coefficient as defined by Eq (4-34)

To evaluate the multilayer insulation case, first consider a single element composed of one reflective shield and one spacer layer as shown below.
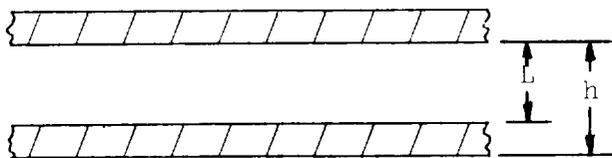
The heat flux between adjacent shields is then

$$q = \alpha \, k_g \left(\frac{L}{L + \ell} \right) \left(\frac{T_1 - T_2}{L} \right) \qquad (4\text{-}39)$$

For typical multilayer systems using 0.0064-mm-(0.25-mil-) thick Mylar reflective shields, the value of h ranges from 5×10^{-3} to 2.5×10^{-3} cm, which corresponds to layer densities of 20 to 40 layers/cm (51 to 102 layers/in.), so $L \cong h$.

When a system is composed of many elements, and the temperature difference between adjacent shields is small compared to the total temperature difference between system boundaries, the elemental heat transfer may be expressed by differentials which results in a continuum approximation to the segmented system.

$$q_x \cong \alpha \, k_g \left(\frac{h}{h + \ell} \right) \frac{dT}{dx} \qquad (4\text{-}40)$$

The properties α, k_g and ℓ are, in general, temperature dependent so that Eq (4-40) becomes

4-63

$$q_x \cong \left\{ \alpha(T) \, k_g(T) \left[\left(\frac{h}{h+\ell}\right)(T) \right] \right\} \frac{dT}{dx} \tag{4-41}$$

and, if the temperature dependences can be expressed in simple forms, equation (4-41) is easily integrated over appropriate boundary conditions to result in a closed form solution for the conduction heat transfer.

Consider first the accommodation coefficient. For heavier gases such as air and nitrogen it is essentially independent of temperature and reasonably approximated by a value of unity for engineering heat transfer calculations. For the lower molecular weight gases such as hydrogen and helium, α may be expressed in the form $\alpha = a(T)^{-n}$. Assuming that $\alpha_1 = \alpha_2$, because of small temperature differences between adjacent surfaces, an approximation for an effective accommodation coefficient is $a_0 T^n$ from Eq (4-34). From this and the data of Fig. 4-23, the values of α for hydrogen and helium are:

$$\begin{aligned} \bar{\alpha}_{H_2} &= 2.66 \, (T)^{-0.42} \quad \text{for T in } {}^\circ K \\ &= 3.40 \, (T)^{-0.42} \quad \text{for T in } {}^\circ R \end{aligned} \tag{4-42}$$

$$\begin{aligned} \bar{\alpha}_{H_e} &= 1.17(T)^{-1/3} \quad \text{for T in } {}^\circ K \\ &= 1.43(T)^{-1/3} \quad \text{for T in } {}^\circ R \end{aligned} \tag{4-43}$$

Next, consider the conductivity of the gas, k_g, which can be expressed as a simple power function over the cryogenic temperature range, $k_g = a_1 T^m$, ($T > 20 {}^\circ K$ or $36 {}^\circ R$). The values of k_g which were used for H_2, He, and N_2, respectively, are evaluated as follows:

$$\begin{aligned} k_g(H_2) &= 9.71 \times 10^{-6} \, (T)^{0.92} \text{ for T in } {}^\circ K \text{ and } k_g \text{ in w/cm } {}^\circ K \\ &= 3.25 \times 10^{-4} \, (T)^{0.92} \text{ for T in } {}^\circ R \text{ and } k_g \text{ in Btu/hr ft } {}^\circ R \end{aligned} \tag{4-44}$$

$$\begin{aligned} k_g(H_e) &= 2.35 \times 10^{-5} \, (T)^{0.74} \text{ for T in } {}^\circ K \text{ and } k_g \text{ in w/cm } {}^\circ K \\ &= 8.83 \times 10^{-4} \, (T)^{0.74} \text{ for T in } {}^\circ R \text{ and } k_g \text{ in Btu/hr ft } {}^\circ R \end{aligned} \tag{4-45}$$

$$\begin{aligned} k_g(N_2) &= 1.38 \times 10^{-6} \, (T)^{0.92} \text{ for T in } {}^\circ K \text{ and } k_g \text{ in w/cm } {}^\circ K \\ &= 4.62 \times 10^{-5} \, (T)^{0.92} \text{ for T in } {}^\circ R \text{ and } k_g \text{ in Btu/hr ft } {}^\circ R \end{aligned} \tag{4-46}$$

and the results are plotted in Fig. 4-24.

4-64

A similar expression, $\mu = a_2(T)^o$, can be used to express the temperature dependence of the viscosity term appearing in the equation for mean free path, Eq (4-32), as shown in Fig. 4-25.

Substitution of the temperature dependent properties into Eq (4-41) yields

$$q_x = \left[\frac{a_o(T)^{-n} a_1(T)^m h}{\dfrac{8.6 \, a_2(T)^o(T)^{1/2}}{P(M)^{1/2}} + h} \right] \frac{dT}{dx} \tag{4-47}$$

which reduces to

$$q_x = \left[\frac{A(T)^N h}{B(T)^M(P)^{-1} + h} \right] dT/dx \tag{4-48}$$

A further simplification may be made for the free molecular regime, as the interlayer spacing h is now much less than the mean free path ℓ and may be deleted from the denominator of Equation (4-48) to yield

$$q_x = \left[C(T)^S Ph \right] dT/dx \tag{4-49}$$

where C and S are the combined coefficients and exponents of T.

For steady-state one dimensional heat transfer across a multilayer insulation with the boundary conditions $x = 0$, $T = T_C$, and $x = N_o h$, $T = T_H$, where N_o is the total number of layers and subscripts H and C denote temperature of the exterior surfaces, integration of Eq (4-49) yields

$$q_g = \frac{CP}{N_o(S+1)} \left[T_H^{(S+1)} - T_C^{(S+1)} \right] \tag{4-50}$$

Calculations of the heat flux due to the presence of a gas in an 80-layer insulation as a function of pressure were performed for helium at $20^o K$ ($36^o R$) to $300^o K$ ($540^o R$), and for helium and nitrogen at $77^o K$ ($139^o R$) to $300^o K$ ($540^o R$). The results are shown in Fig. 4-26. At a pressure of 10^{-3} torr, or less,
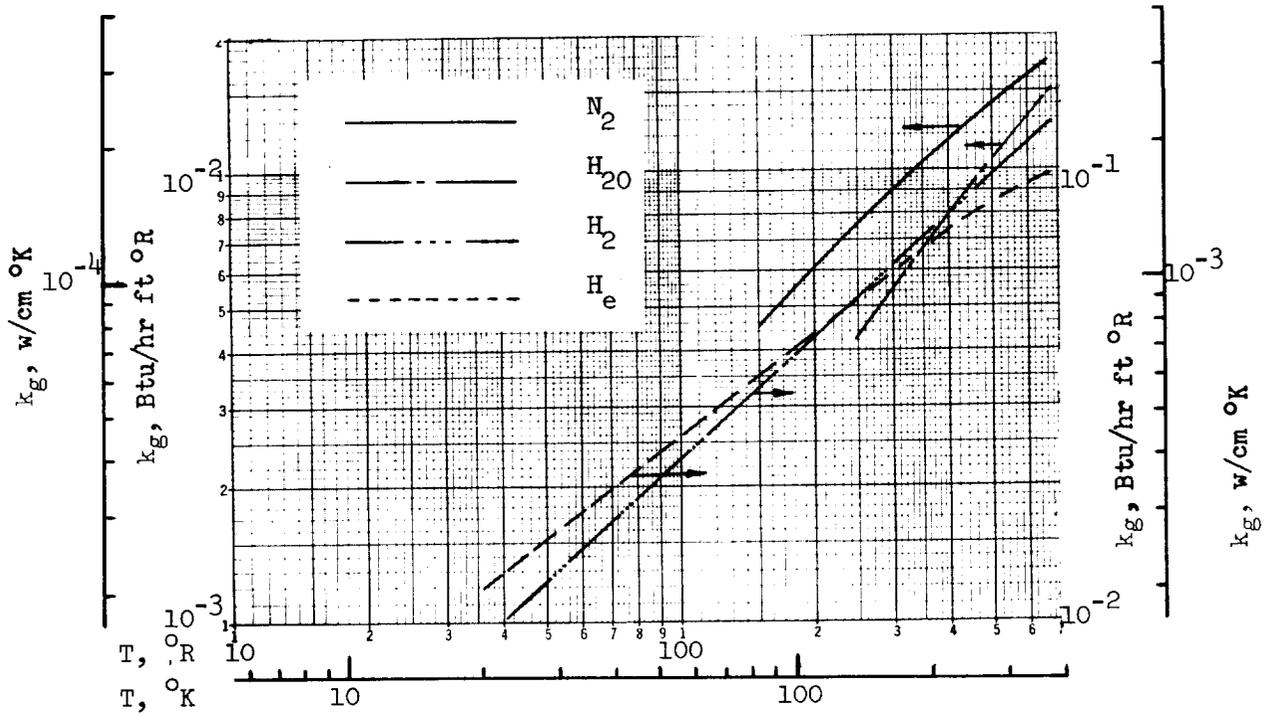
Fig. 4-24 Thermal Conductivity of Several Gases as a
Function of Temperature
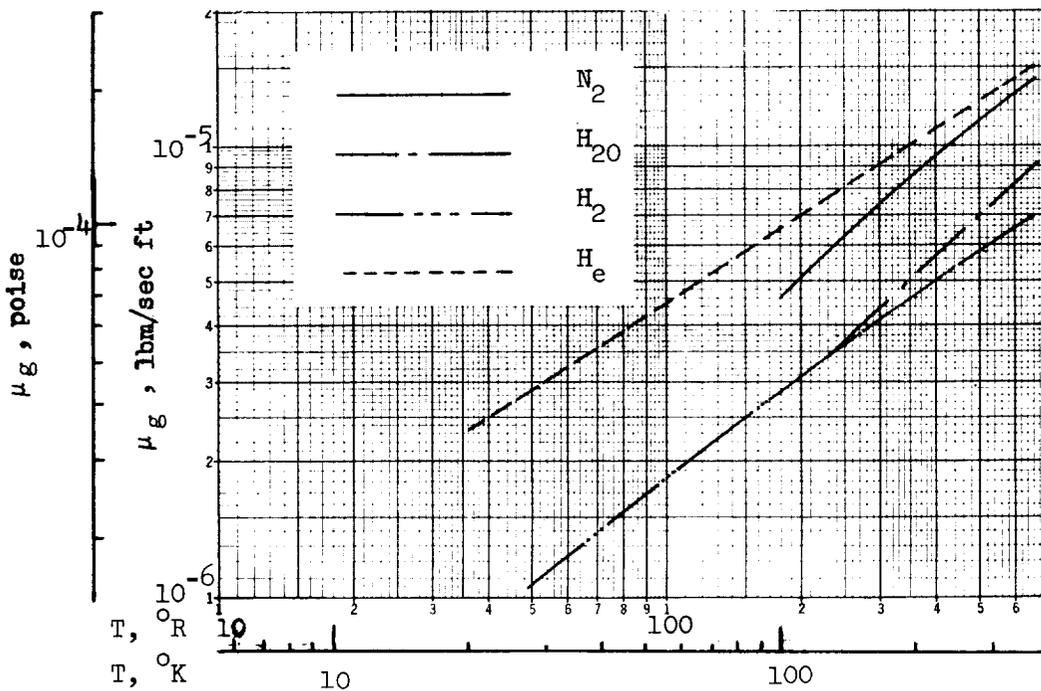
Fig. 4-25 Viscosity of Several Gases as a Function of
Temperature

4-66
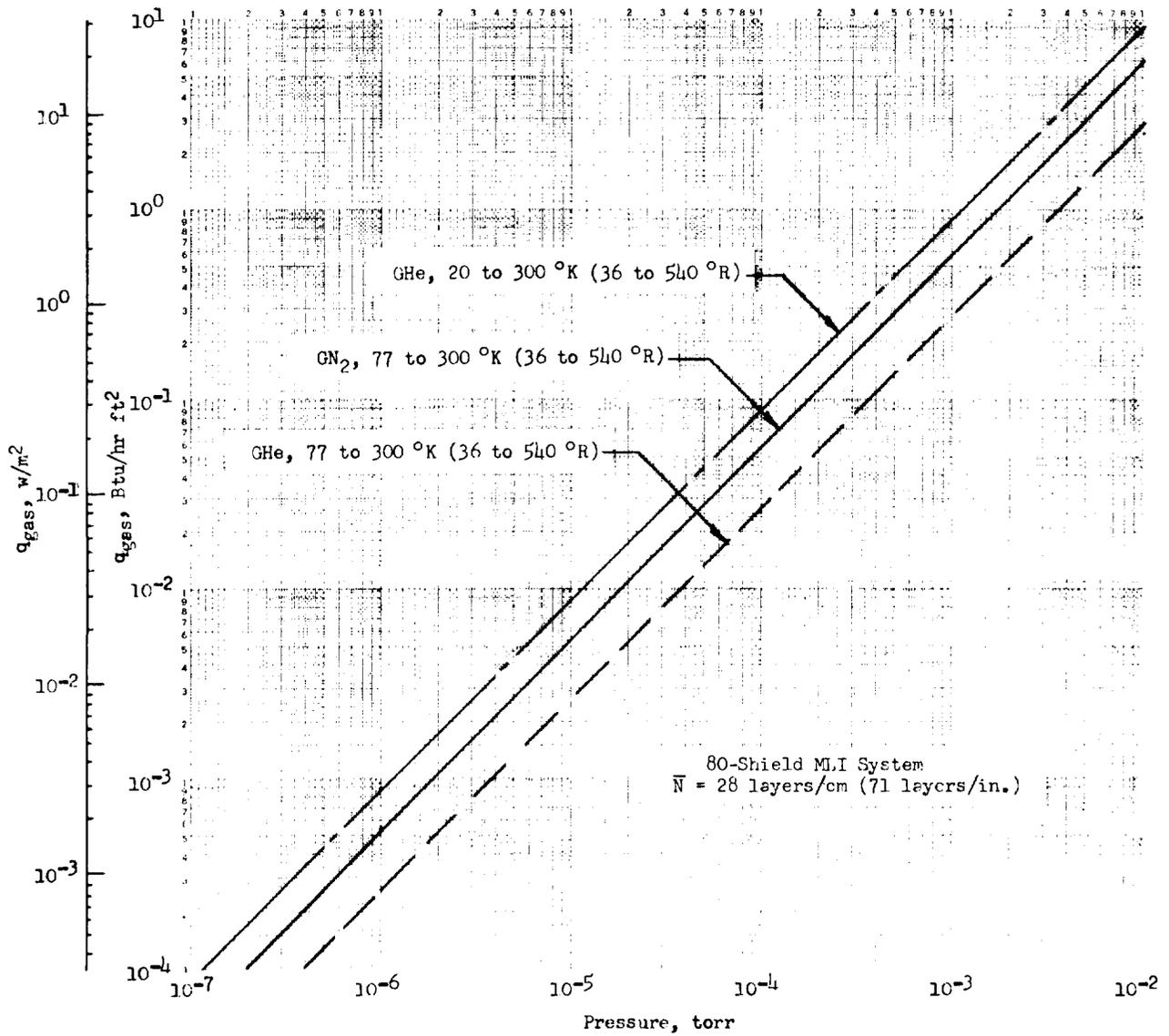
Fig. 4-26   Heat Flux from Gaseous Conduction as a Function of Pressure for
Two Temperature Conditions and Two Gases

4-67

the mean free paths for helium and nitrogen at $150^\circ K$ ($270^\circ R$) are much greater than the layer spacing, h, so that Eq (4-50) is valid (ℓ_{He} = 6.8 cm, 2.7 in., and ℓ_{N_2} = 2 cm, 0.8 in., for h = 0.036 cm, 0.014 in., which corresponds to a layer density of 28 layers/cm, 71 layers/in.). The heat flux for helium at the $20^\circ K$ ($36^\circ R$) condition is greater than that for the $77^\circ K$ ($139^\circ R$) case because of the strong temperature dependence of the accommodation coefficient. Similarly, the heat flux for nitrogen is greater than that for helium from $77^\circ K$ ($139^\circ R$) to $300^\circ K$ ($540^\circ R$) because of the smaller value of $\bar{\alpha}$ for helium in this temperature region.

The gas conduction heat transfer term can be added to those for radiation and solid conduction to result in the following equation for total heat transfer

q = gas conduction + solid conduction + radiation

$$q = \frac{CP(x,T)\,(T_H^{m+1} - T_C^{m+1})}{(N_s + 1)\,(m + 1)} + \frac{A(N)^n\,T_m\,(T_H - T_C)}{N_s + 1} + \frac{B\sigma\,(T_H^{4.67} - T_C^{4.67})}{N_s} \quad (4\text{-}51)$$

where $P(x,T)$ is the pressure within the insulation as a function of position and local temperature, and coefficients, A, B, and C as well as the exponents m and n are derived for the particular insulation system and interstitial gas.

4.2.4 Thermal Performance Prediction Equations

In the application of Eq (4-51) to the Task 3 tests, the denominators of the two conduction terms become N_s rather than (N_s +1) because the exterior shield temperature was established as the warm boundary temperature. The equations for the prediction of the Task 3 tank insulation heat flux were derived from the flat plate data for the S-604 and the unperforated Mylar systems.* These are, respectively,

---

* The rationale for selecting the S-604 perforation pattern for the Task 3 work was based primarily on a consideration of gas evacuation capability. It was shown in Task 2 (See Section 5.3.1.6) that a small improvement in gas evacuation characteristics for combined edge – and broadside-pumping was achieved for this pattern, whereas the improvement was negligible for other patterns. However, since a significant penalty was incurred in terms of increased radiation heat transfer for all perforated systems investigated (Ref Table 4-8), only the unperforated-shield system was tested in Task 3. This is discussed further in Section 6.1.1.

$$q = \frac{C_s(\bar{N})^{2.63}T_m}{N_s}(T_H - T_C) + \frac{C_r \epsilon_{TR}}{N_s}(T_H^{4.67} - T_C^{4.67}) \qquad (4-52)$$

where: $C_s = 7.40 \times 10^{-8}$ and $C_r = 7.07 \times 10^{-10}$

for $\bar{N}$ in layers/cm, T in $^{\circ}$K, and q in w/m^2

or: $C_s = 6.15 \times 10^{-10}$ and $C_r = 1.44 \times 10^{-11}$

for $\bar{N}$ in layers/in., T in $^{\circ}$R, and q in Btu/hr ft^2

and: $\epsilon_{TR} = 0.043$

and $q = \frac{C_s(\bar{N})^{2.56}T_m}{N_s}(T_H - T_C) + \frac{C_r \epsilon_{TR}}{N_s}(T_H^{4.67} - T_C^{4.67}) \qquad (4-53)$

where: $C_s = 8.95 \times 10^{-8}$ and $C_r = 5.39 \times 10^{-10}$

for $\bar{N}$ in layers/cm, T in $^{\circ}$K, and q in w/m^2

or: $C_s = 8.06 \times 10^{-10}$ and $C_r = 1.10 \times 10^{-11}$

for $\bar{N}$ in layers/in., T in $^{\circ}$K, and q in Btu/hr ft^2

and: $\epsilon_{TR} = 0.031$

for conditions when the interstitial gas pressure is 10^{-7} torr or less. If the pressure within the layers is greater than 10^{-7} torr, a third term representing the gas conduction is added to the right side of each equation. For the high-vacuum case, the calculated values of heat flux for 56- and 112-shield MLI systems are shown in Figs. 4-27 and 4-28 as a function of layer density for the three warm boundary test conditions. A comparison of heat fluxes for the perforated and unperforated shields, neglecting that due to gas conduction, is given in Table 4-11.

The significance of the gas conduction is illustrated in Figs. 4-29 and 4-30 which show total heat flux (solid + gas + radiation) for the unperforated- and perforated-shield insulations, respectively. In these figures, the total heat flux is plotted as a function of insulation pressure, with nitrogen assumed to be the interstitial gas, for the nominal design case of 28 layers/cm (70 layers/in.). The coefficient and exponent of the gas conduction term were derived as discussed previously (Ref Equations 4-47 through 4-49). The

4-69

	N_s	T_H	
		°K	(°R)
————————	56	361	(650)
——— — ——— —	56	319	(575)
——————— · ——————	56	278	(500)
— — — — — — — —	112	361	(650)
——— · · · ———	112	319	(575)
——————— · · ———————	112	278	(500)

$P \leq 10^{-7}$ torr, T_C = 22 °K (40 °R),
S-604 Perforations, Ref Eq(4-52)
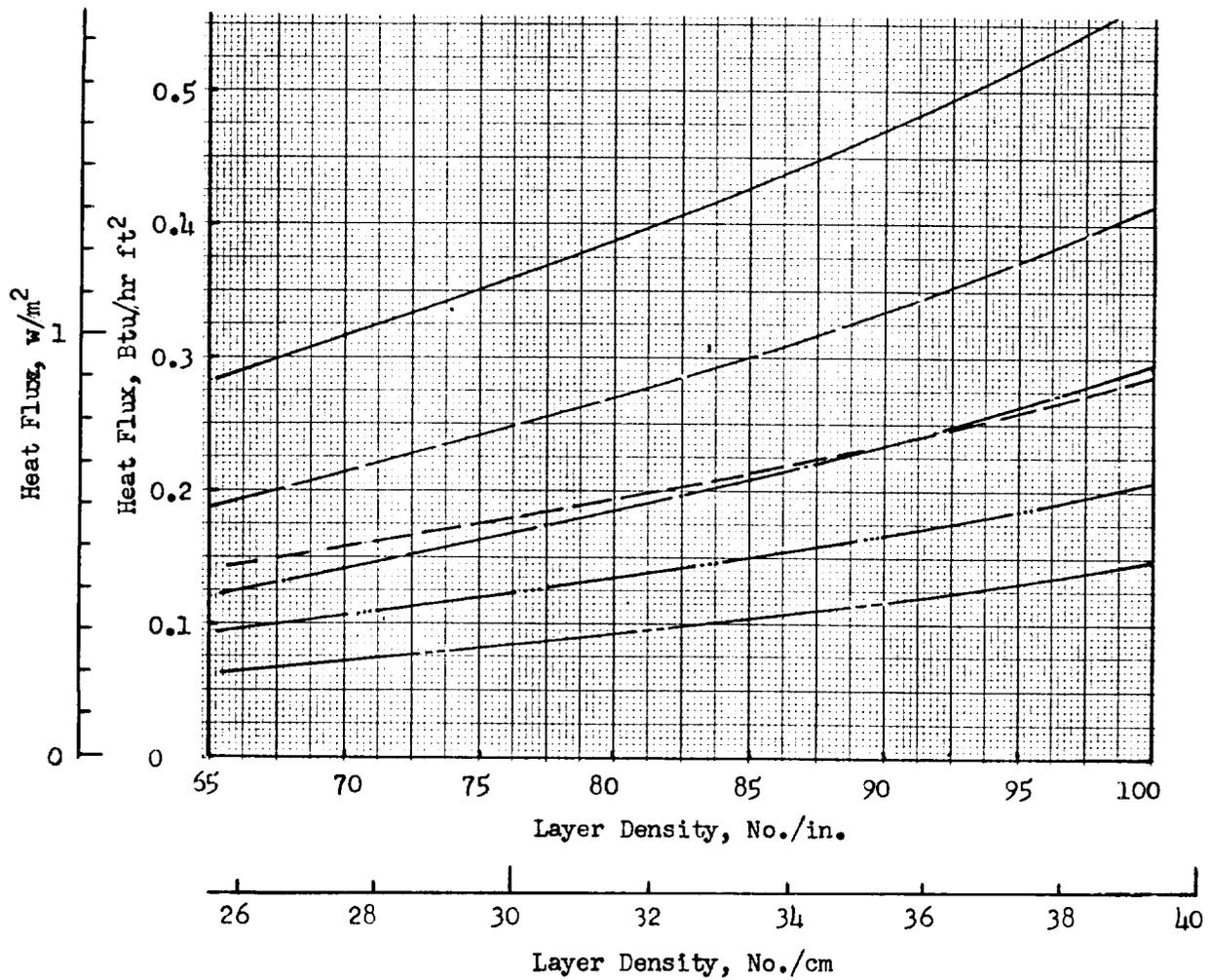
Fig. 4-27 Calculated Total Solid Conduction and Radiation Heat
Flux as a Function of Layer Density and Hot Boundary
Temperature for the Perforated-Shield MLI System

4-70

N_s	T_H	
	$°K$	$(°R)$
56	361	(650)
56	319	(575)
56	278	(500)
112	361	(650)
112	319	(575)
112	278	(500)

$P \leq 10^{-7}$ torr, $T_C = 22 °K$ (40 °R),
Ref Eq (4-53)
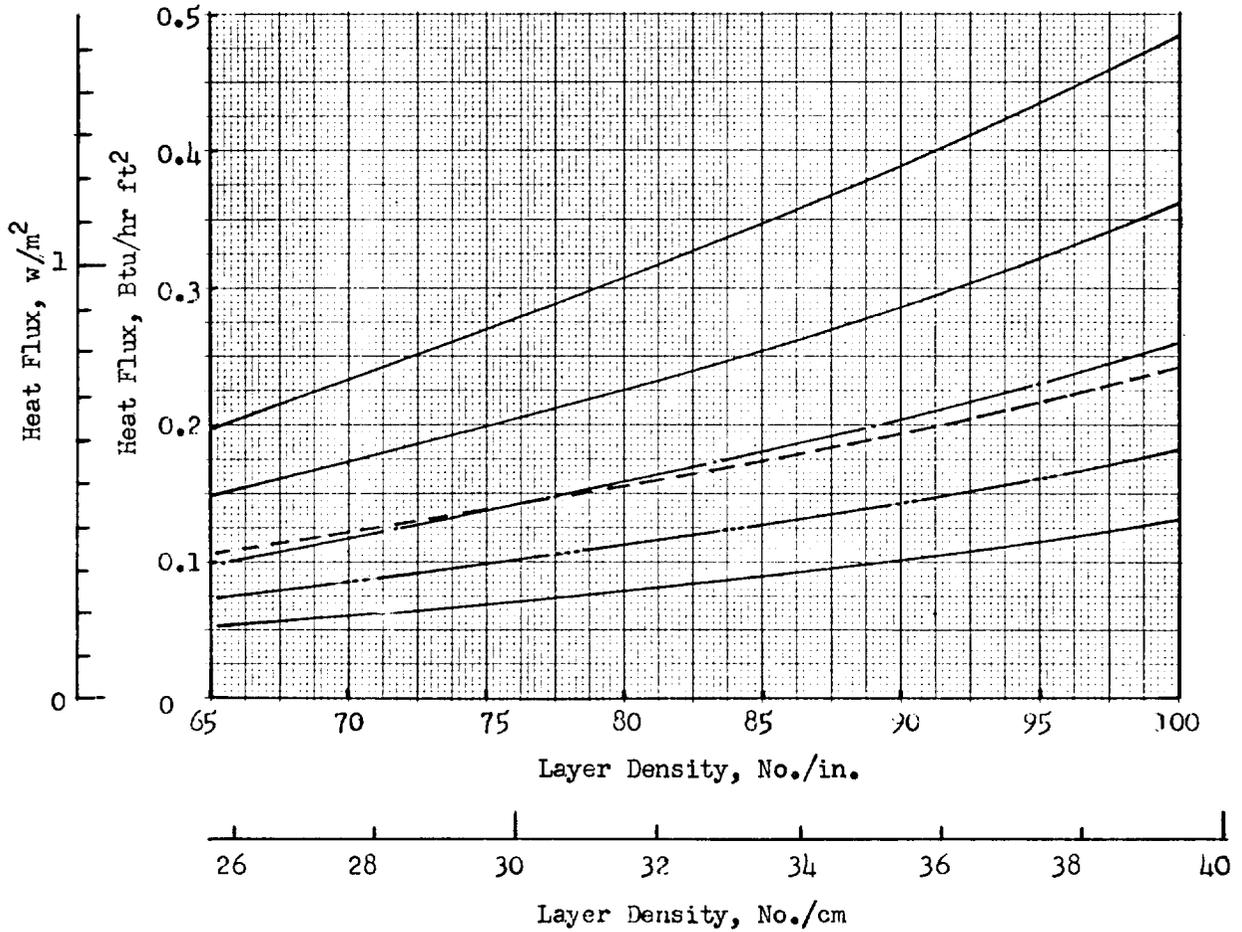
Fig. 4-28   Calculated Total Solid Conduction and Radiation Heat Flux as
a Function of Layer Density and Hot Boundary Temperature for
the Unperforated-Shield MLI System

4-71

gas conduction term varies directly with interstitial pressure and, if the interstitial gas specie is assumed to be helium, becomes

$$q_g = \frac{C_g P}{N_s} (T_H^{0.26} - T_C^{0.26}) \qquad (4\text{-}54)$$

where: $C_g = 4.89 \times 10^4$ for P in torr, T in $^\circ K$, and q_g in w/m^2

or: $C_g = 1.33 \times 10^4$ for P in torr, T in $^\circ R$, and q_g in $Btu/hr\ ft^2$

Table 4-11

COMPARISON OF SOLID CONDUCTION PLUS RADIATION HEAT FLUXES
FOR PERFORATED-AND UNPERFORATED-SHIELD SYSTEMS

Layer Density, $\overline{N}$		T_H $^\circ K$ ($^\circ R$)	$\dfrac{q_{perforated}}{q_{unperforated}}$
No./cm	(No./In.)		
28	(70)	361 (650) 319 (575) 278 (500)	1.30 1.24 1.19
33	(85)	361 (650) 319 (575) 278 (500)	1.23 1.19 1.15
39	(100)	361 (650) 319 (575) 278 (500)	1.18 1.15 1.13

Because of the smaller exponent of temperature, the magnitude of this term is about one-half that for nitrogen. From Figs. 4-29 and 4-30, it can be seen that gas conduction becomes a significant heat transport mechanism at pressures greater than 10^{-5} torr for both the unperforated- and perforated-shield systems. Ratios of gas conduction to the sum of solid conduction and radiation are shown in Table 4-12 for both systems for several interstitial pressures and warm boundary temperatures.
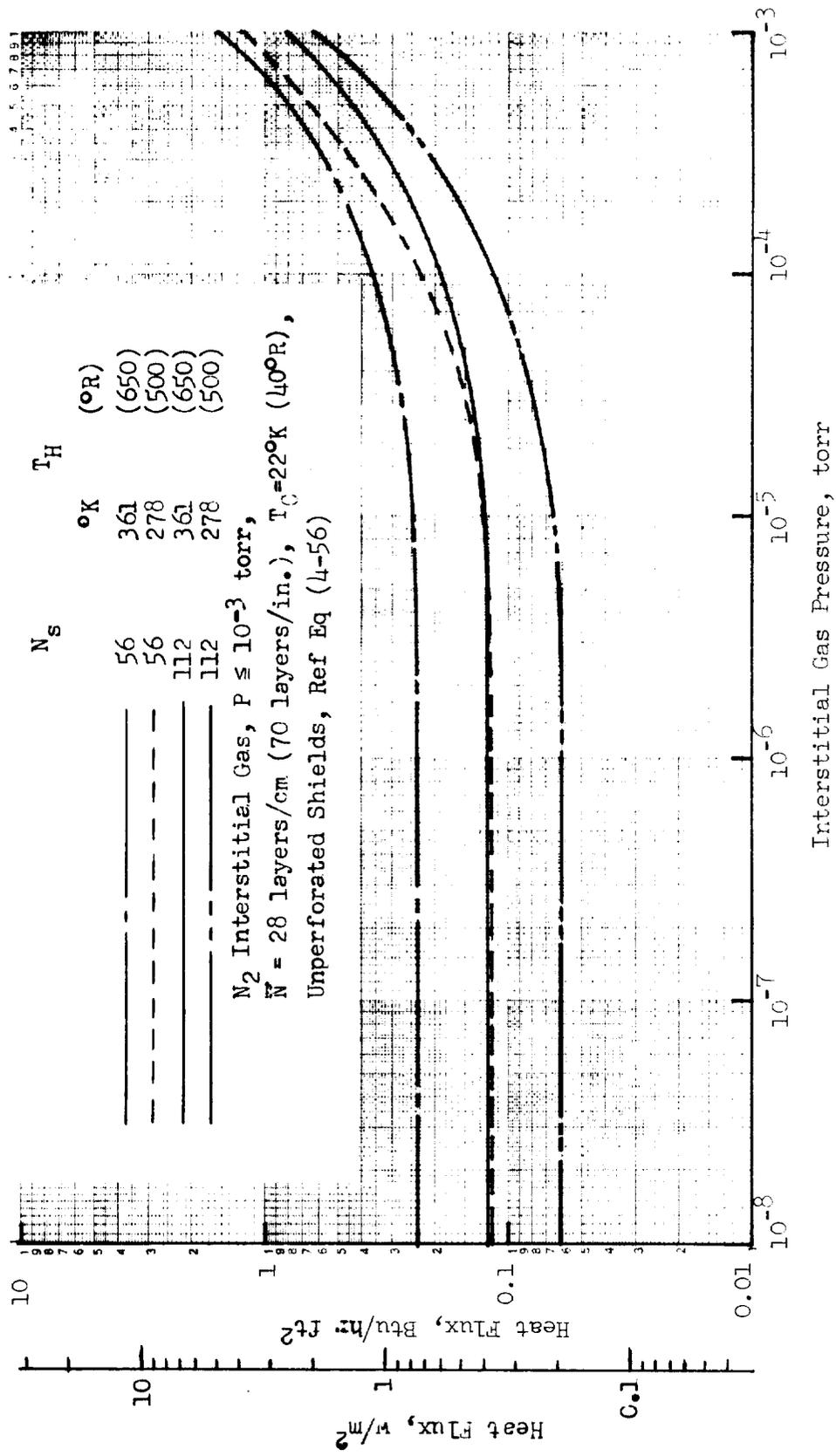
Fig. 4-29 Calculated Total Heat Flux as a Function of Interstitial Gas Pressure and Hot Boundary Temperature for the Unperforated Double-Aluminized Mylar/Water-Preconditioned Double Silk Net Spacer System

N_s	T_H	
	°K	(°R)
56	361	(650)
56	278	(500)
112	361	(650)
112	278	(500)

N_2 Interstitial Gas, $P \leq 10^{-3}$ torr,
$\bar{N} = 28$ layers/cm (70 layers/in.), $T_C = 22°K$ (40°R),
S-604 Perforations, Ref Eq (4-55)
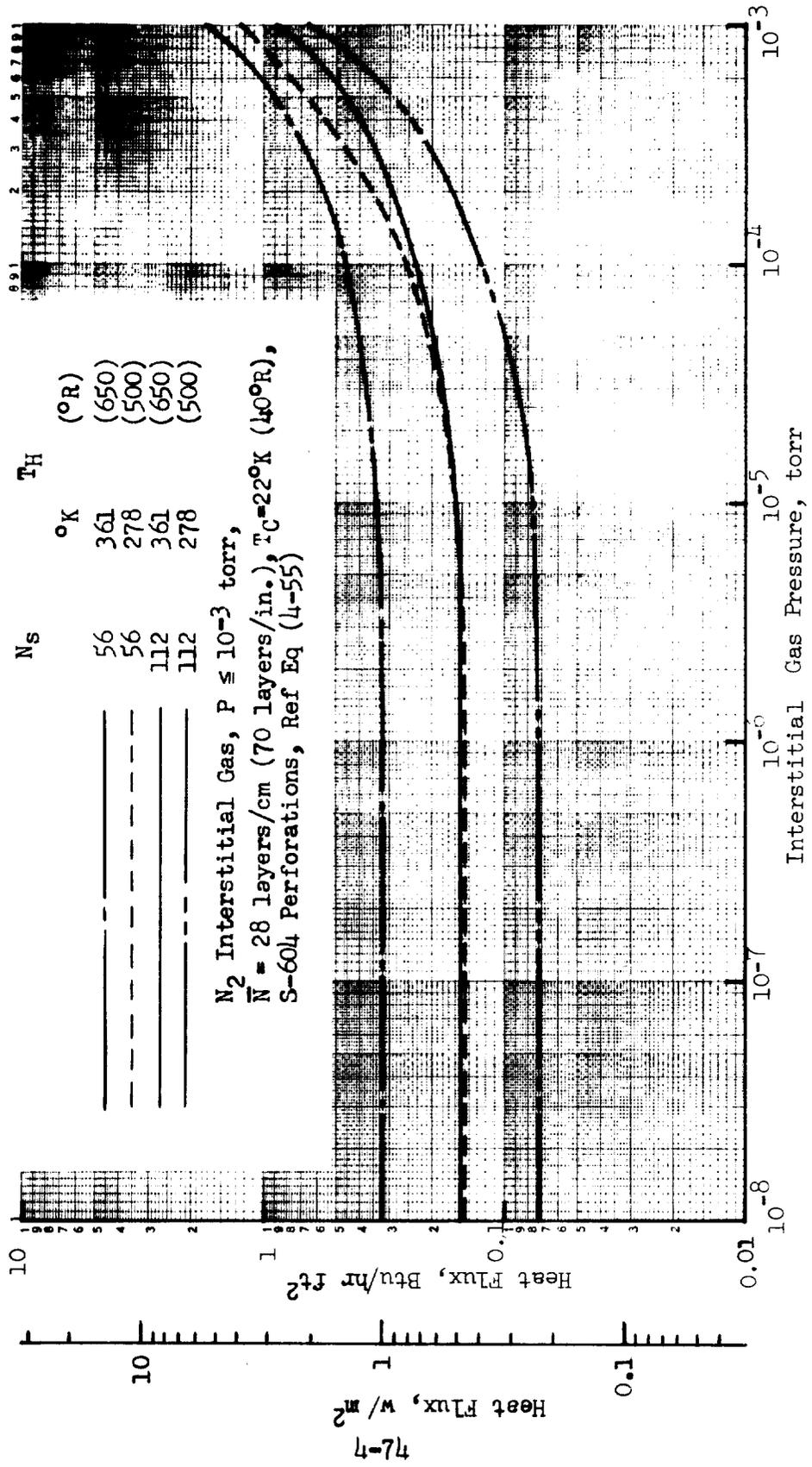
Fig. 4-30   Calculated Total Heat Flux as a Function Of Interstitial Gas Pressure and
Hot Boundary Temperature for the Perforated Double-Aluminized Mylar/Water-
Preconditioned Double Silk Net Spacer System

Table 4-12

RATIO OF GAS CONDUCTION TO SOLID PLUS RADIATION HEAT FLUXES
FOR THE PERFORATED-AND UNPERFORATED-SHIELD SYSTEMS

Insulation	Gas	Layer Density, $\bar{N}$		T_H	$q_g/(q_s + q_r)$ at P = (torr):			
		No./cm	(No./in.)	°K(°R)	10^{-3}	10^{-4}	10^{-5}	10^{-6}
S604 Perforation	N_2	28	(70)	361(650)	4.35	0.435	0.044	0.004
	He	28	(70)	361(650)	2.08	0.208	0.21	0.002
	N_2	28	(70)	319(575)	5.94	0.594	0.059	0.006
	He	28	(70)	319(575)	2.88	0.288	0.029	0.003
	N_2	28	(70)	278(500)	8.08	0.808	0.081	0.008
	He	28	(70)	278(500)	4.07	0.407	0.041	0.004
Unperforated	N_2	28	(70)	361(650)	5.67	0.567	0.057	0.006
	He	28	(70)	361(650)	2.71	0.271	0.027	0.003
	N_2	28	(70)	319(575)	7.38	0.738	0.074	0.007
	He	28	(70)	319(575)	3.57	0.357	0.036	0.004
	N_2	28	(70)	278(500)	9.62	0.962	0.096	0.010
	He	28	(70)	278(500)	4.85	0.485	0.049	0.005

The final equations used to predict thermal performance prior to initiation of the Task 3 tests are as follows:

Perforated S-604) Shields:

$$q_T = \frac{C_s(\bar{N})^{2.63}T_m}{N_s}(T_H - T_C) + \frac{C_r \epsilon_{TR}}{N_s}(T_H^{4.67} - T_C^{4.67}) \qquad (4-55)$$

$$+ \begin{cases} \dfrac{C_g P}{N_s}(T_H^{0.52} - T_C^{0.52}) \text{ for } GN_2, \text{ or} \\[2em] \dfrac{C_g P}{N_s}(T_H^{0.26} - T_C^{0.26}) \text{ for } GHe \end{cases}$$

where: $C_s = 7.30 \times 10^{-8}$, $C_r = 7.07 \times 10^{-10}$, $C_g(GN_2) = 1.46 \times 10^4$, and $C_g(GHe) = 4.89 \times 10^4$ for $\bar{N}$ in layers/cm^2, T in °K, P in torr, and q in w/m^2

or: $C_s = 6.15 \times 10^{-10}$, $C_r = 1.44 \times 10^{-11}$, $C_g(GN_2) = 3.44 \times 10^3$, and $C_g(GHe) = 1.33 \times 10^4$ for $\bar{N}$ in layers/in., T in °R, P in torr, and q in Btu/hr ft^2

and: $\epsilon_{TR} = 0.043$

Unperforated Shields:

$$q_T = \frac{C_s (\bar{N})^{2.56} T_m}{N_s}(T_H - T_C) + \frac{C_r \epsilon_{TR}}{N_s}(T_H^{4.67} - T_C^{4.67}) \qquad (4\text{-}56)$$

$$+ \begin{cases} \dfrac{C_g P}{N_s}(T_H^{0.52} - T_C^{0.52}) \text{ for } GN_2, \text{ or} \\[3ex] \dfrac{C_g P}{N_s}(T_H^{0.26} - T_C^{0.26}) \text{ for GHe} \end{cases}$$

where: $C_s = 8.95 \times 10^{-8}$, $C_r = 5.39 \times 10^{-10}$, $C_g(GN_2) = 1.46 \times 10^4$, and $C_g(GHe) = 4.89 \times 10^4$ for $\bar{N}$ in layers/cm, T in °K, P in torr, and q in w/m^2

or: $C_s = 8.06 \times 10^{-10}$, $C_r = 1.10 \times 10^{-11}$, $C_g(GN_2) = 3.44 \times 10^3$, and $C_g(GHe) = 1.33 \times 10^4$ for $\bar{N}$ in layers/in., T in °R, P in torr, and q in Btu/hr ft^2

and: $\epsilon_{TR} = 0.031$

4-76

Section 5

TASK 2 - GAS EVACUATION EVALUATIONS

Test data obtained from previous programs have indicated that for relatively thick multilayer insulations the measured thermal performance has not improved in proportion to the thickness as predicted by heretofore existing heat transfer models. One of the explanations suggested for this apparent anomaly is that the residual interstitial gas pressure in the thick MLI systems is high enough to cause significant gas conduction heat transfer (Ref Section 4.2.3). The residual gas could remain in the layers from the original interstitial purge gas, and/or could be generated by desorption (outgassing) of the insulation materials. The magnitude of the interstitial gas pressure at any point in the insulation as a function of time and temperature is dependent upon the rate of decay of the gas pressure outside of the insulation system, the flow resistance between the particular interstitial point and the exterior, the volume of gas filling the void spaces of the insulation, and the outgassing rate of the insulation materials. It was the object of Task 2 of this program to investigate the variation of interstitial gas pressure as a function of time and other significant parameters by both experimental and analytical means. As a result of these investigations, it was planned to develop the analytical and experimental tools necessary to predict in advance, and then to determine experimentally, the interstitial gas pressures for the full-scale insulated tank tests of Task 3. A particular goal of this task of the program was to generate reliable interstitial gas pressure data for inclusion in the thermal performance analysis of Tasks 1 and 3, and thereby to assist in resolving the anomalous behavior problem for relatively thick MLI systems.

During the program, MLI systems with both unperforated and perforated reflective shields were investigated in order to determine whether or not the perforations could significantly enhance the outgassing process. It was postulated that, should gas conduction heat transfer prove to be the source of the anomalous

5-1

behavior for thick MLI systems, the perforations might result in an increased
gas evacuation rate and, thereby, provide at least a partial solution to the
problem.

For an MLI system with unperforated reflective shields, the evacuation process
is commonly defined as edge pumping, since the gas molecules must flow parallel
to the shields for some distance until they can escape through the joints between
adjacent blankets. On the other hand, for a perforated-shield MLI composite,
the evacuation mechanism is normally described as broadside pumping. In this
instance, the gas molecules also flow parallel to the layers, but only for
relatively short distances until they reach one of the numerous shield per-
forations and can then escape outward to the next adjacent interlayer cavity.
However, for any practical tank-installed MLI system using perforated re-
flective shields, the actual gas evacuation process will be a combination of both
broadside pumping (through the perforations) and edge pumping (through joints
between adjacent blankets).

5.1 GAS EVACUATION ANALYSIS

5.1.1 Analytical Model

The goals of the analysis for broadside and edge pumping are identical. The
problem is to assess the gas pressure distribution within a multilayer in-
sulation system as a function of time for certain particular boundary con-
ditions. At time zero, for any given evacuation, the pressure within the
insulation is uniform and equal to that of its environment. At times greater
than zero the pressure outside the insulation is reduced at some specified
rate. The gas molecules within the layers flow out to the environment due
to the induced pressure difference. At the beginning of the evacuation pro-
cess, the gas between the layers will be air or some selected purge gas. As
the interlayer pressure is reduced, additional molecules will be desorbed
from the surfaces of the insulation, constituting a second source of gas.

The desorbed gas and the original purge gas probably will not be of the same species, so the problem involves at least two different gases.

In order to determine the gas pressure within the layers as a function of time and space, it is necessary to write a series of equations, one of which is a non-linear first order partial differential equation which cannot be solved by any simple closed-form method. From the outset of this analysis, it was accepted that numerical techniques would be essential for its solution, and so the equations describing the flow were written with this end in mind. Also, although it would be of interest to know the spatial distribution of pressure within the insulation as a function of time, the maximum interstitial pressure is of prime importance. Considerations of symmetry usually indicate where this will occur, and the equations were set up specifically to calculate the pressure at this point. Because the pressure differentials can be very small by comparison with local absolute pressures, the equations were written so as to determine the maximum pressure differential across the insulation rather than the absolute maximum pressure within the insulation.

The simple Newtonian method, used widely and successfully to solve heat transfer problems (Ref 18), was selected for application to the Task 2 analysis. The basis for using this technique was to divide the continuum flow path length into finite nodal volumes with gas capacity but no flow resistance, interconnected by flow passages with flow resistance but no gas capacity.

For experimental reasons, a circular edge pumping sample was selected. In this case the maximum pressure during evacuation occurs at the center of the insulation specimen, and the equations were set up in polar coordinates to describe the purely radial gas flow. For broadside evacuation, the overall sample shape in the plane of the multilayers is of no consequence, since the evacuation flow is primarily in the transverse direction. Circular samples were in fact used so as to interface with the same apparatus as the edge pumped samples. Further inspection of the broadside pumping process reveals that the flow pattern is approximately radially inward to each perforation

5-3

hole, and approximately radially outward from each hole, so that the flow pattern around each hole is assumed to be purely radial for the purposes of the analysis. Thus the analyses for each type of evacuation are both based on radial flow fields.

5.1.2 Nodal Model Development

The nodal model used for both edge and broadside evacuation is shown in Fig. 5-1. The flow path between the point of maximum pressure and the exterior is divided into N nodal volumes. The maximum pressure occurs in nodal volume 1, as determined by symmetry. The pressure in nodal volume N is equal to that of the environment and is given as a function of time. The volumes of the nodes are V_1, V_2 . . . V_i . . . V_N. These volumes are interconnected by (N-1) flow paths whose conductances are functions of the distance between the centers of adjacent nodal volumes. The conductances have magnitudes C_1, C_2 . . . C_i . . . C_{N-1}. The conductance, C, is defined as

$$C = \frac{\dot{m}}{P} \qquad (5-1)$$

Thus, C is the mass flow induced by unit pressure drop.
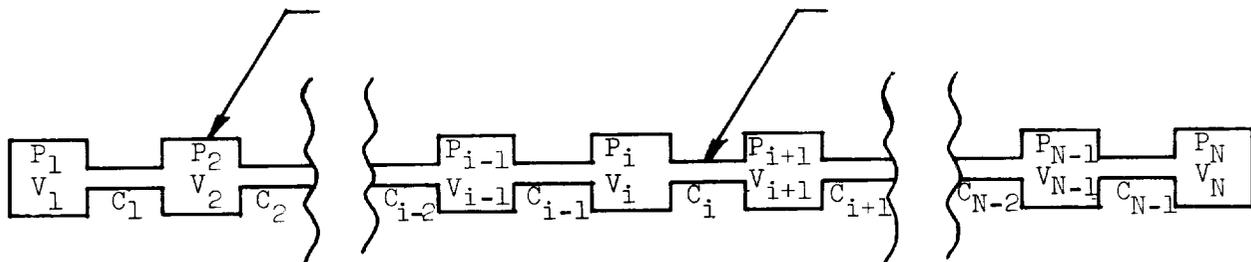
P_1 = Maximum Pressure $\Delta P(t) = P_1(t) - P_N(t)$ where $P_N(t)$

P_N = Minimum Pressure   is determined experimentally

Fig. 5-1 Basic Nodal Model for Gas Evacuation Analysis

LOCKHEED MISSILES & SPACE COMPANY

Additional gas molecules can be generated within a nodal volume due to out-gassing. The mass generation rate in the ith node is Q_i. Q_i is equal to the local outgassing rate per unit area, Q, times the total surface area within the node. The following continuity equation, written in finite difference form, describes the rise of pressure within the ith node during time Δt in terms of conditions within this and adjacent nodes at time t.

$$\frac{V_i M}{R^o T} \frac{(P_i' - P_i)}{\Delta t} \cong (P_{i-1} - P_i)C_{i-1} - (P_i - P_{i+1})C_i + Q_i \qquad (5\text{-}2)$$

where P_{i-1}, P_i, and P_{i+1} are the pressures at time t and P_i' is the pressure at time $t+\Delta t$. As Δt approaches O, the equation can be expressed in differential form. However, it is not possible to solve the equation for this condition because C_{i-1} and C_i are functions of pressure and Q_i is a function of time and pressure, making the equation non-linear. Hence the need for a numerical solution technique.

A complication is introduced because the gas may be composed of two or more species. To treat this case, two continuity equations are written similar to Eq (5-2); one for the purge gas and one for the desorbed gas. The equations thus determine partial pressures for these two components. The conductances, C, are determined assuming an average bulk velocity which is the same for each gas and is evaluated using mixture properties. The mixture properties are determined as follows (subscripts p, d and t refer to the purge gas, the desorbed gas, and the mixture, respectively):

Molecular weight, $M_t = \dfrac{M_p P_p + M_d P_d}{P_p + P_d}$ $\qquad (5\text{-}3)$

Total pressure, $P_t = P_p + P_d$ $\qquad (5\text{-}4)$

Viscosity (Ref 19), $\mu_t = \dfrac{\mu_p}{1 + (P_p/P_d)\,\phi_{pd}} + \dfrac{\mu_d}{1 + (P_d/P_p)\,\phi_{dp}}$ $\qquad (5\text{-}5)$

LOCKHEED MISSILES & SPACE COMPANY

where

$$\phi_{pd} = \left[1 + (\mu_p/\mu_d)^{0.5} (M_d/M_p)^{0.25} \right]^2 \Big/ \left[2^{1.5}(1 + M_p/M_d)^{0.5} \right] \quad (5\text{-}6)$$

$$\phi_{dp} = \left[1 + (\mu_d/\mu_p)^{0.5} (M_p/M_d)^{0.25} \right]^2 \Big/ \left[2^{1.5}(1 + M_d/M_p)^{0.5} \right] \quad (5\text{-}7)$$

In order to solve the continuity equations, a value must be assigned to the outgassing rate Q_i.

Outgassing is the process by which the sorption concentration of a gas on or in a solid adjusts from an equilibrium value consistent with an initial set of environmental pressure and temperature conditions to an equilibrium value for another set of conditions. Sorption concentration is a function of a particular solid and its previous manufacturing and storage history, the solid geometry and temperature, and the gas pressure and temperature. Outgassing rate is a function of all these parameters plus time. Its magnitude cannot be predicted analytically with the accuracy required for engineering analysis, so experimental data are required. It is customary to obtain these data under experimental conditions similar to those recommended by the American Vacuum Society (Ref 20), which call for constant temperature and an experimental gas pressure low enough to be neglected, rendering the outgassing data independent of pressure. In the insulation evacuation application, the gas pressure will not always be negligible. Thus outgassing experiments which include pressure as a parameter would be desirable. Such experiments would require considerably more complex apparatus than standard experiments, and as far as is now known, have not yet been attempted. An alternate approach to obtaining pressure dependence is to add an analytic pressure-dependent term to conventional data. Rigorous derivation of such a term requires knowledge of the sorption isotherm for the system of interest and is outside the scope of the present work. Therefore, for the purposes of this analysis, existing experimental outgassing data were fitted by an exponential series to obtain the following type of expression.

$$Q = \sum_{j=1}^{n} a_j e^{k_j t} \qquad (5-8)$$

where a_j and k_j are constants, t is time, and j and n are integers.

Pressure dependence can be introduced to Eq (5-8) as follows

$$Q = \left(\frac{P_o - P}{P_o}\right) \sum_{j=1}^{n} a_j e^{k_j t} \qquad (5-9)$$

Here P_o is the initial pressure of the system (usually one atmosphere) and P is the instantaneous pressure during evacuation. The equation is correct at $P = P_o$ and $P \ll P_o$ and, thus, seems to represent a reasonable first order approximation. Later, in Section 5.2, it is shown that the validity of this type of expression can be verified at least qualitatively, in that with its help certain characteristics of the data can be explained.

5.1.3 Computation Techniques

The basic equation used for the numerical solution is Eq (5-2). Expressions for V_i and C_i are developed in Sections 5.1.4 and 5.1.5. The pressures in all nodal volumes at evacuation time zero are assumed to be identical and equal to some specified pressure, usually one atmosphere. The pressure in the Nth node, P_N, at the edge of the insulation is set equal to the chamber pressure and is specified as a function of time. The time is advanced an amount Δt, causing P_N to decay, and the response of the interlayer pressure to this reduction is determined. The time is advanced by successive steps, using the pressures and conductances at time t to determine pressures at time t + Δt, until the evacuation is completed. The flow diagram for this calculation is shown in Fig. 5-2. The diagram is not exact, since its purpose is simply to show the calculation sequence.

A critical step in the calculation is to determine the time step, Δt. In the Newtonian type of solution, the time step is usually selected according to the

```
            Choose Number of Nodes, N

            Calculate Nodal Volumes, $V_i$

            Set Up Initial Pressures
            at Time Zero, $P_{io}$

            Calculate Mixture Properties

            Calculate Conductances, $C_i$

            Determine Time Step, $\Delta t$

            Advance Time, $t = t + \Delta t$

            Calculate New Pressures, $P_i'$

            Calculate Pressure
            Differential

            Write Output

            Set $P_i = P_i'$

            Repeat Calculation if $t < t_{max}$
```
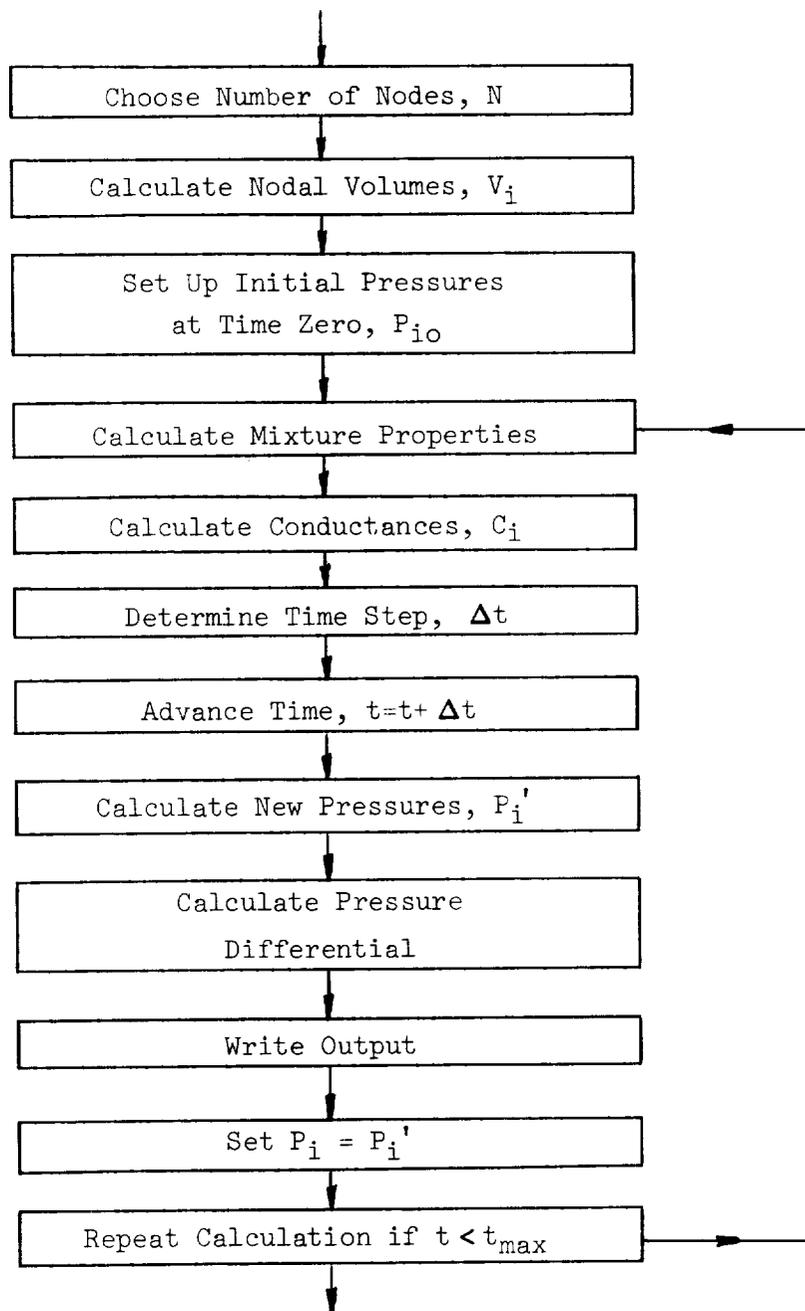
Fig. 5-2 Outline of Flow Diagram for Computer Program

LOCKHEED MISSILES & SPACE COMPANY

following criterion

$$\Delta t \leq 0.5 \times \left(\frac{\text{Nodal Capacitance}}{\text{Internodal Conductance}}\right) \qquad (5\text{-}10)$$

If Δt is greater than the value given by Eq (5-10), the solution is unstable
For this application, the criterion can be expressed as

$$\Delta t \leq 0.5 \; \frac{V_i \, M_t}{R^o \, T \, C_i} \qquad (5\text{-}11)$$

Tests were made to verify this criterion for the present application. The
constant (i.e., 0.5) in Eq (5-11) was assigned values of 0.6, 0.5, and 0.4
in successive solutions. The value of 0.5 was found to be the correct upper
limit for stability.

Increasing the number of nodal volumes decreases the volume per node, V_i, and
also increases the internodal conductance, C_i, because of the shorter flow path
length between adjacent nodes. It can be seen from Eq (5-11) that this will
reduce the maximum time step and thereby slow down the computation. Additional
nodal subdivisions will increase the accuracy of the calculation, however. It
was found that, for the 68.6-cm-(27-in.-) diameter test specimens, six or more
nodes were necessary in order to obtain a solution within approximately five
percent of the asymptotic value for an infinite number of nodes.

The only problem encountered in the Task 2 numerical analysis was a basic
limitation of the Newtonian procedure. This procedure uses data at time t
to calculate data for time t+ Δt. Eq (5-11) indicates that Δt must
not exceed a certain value for this technique to be valid. This places a
lower limit on the number of time steps that must be considered in order to
achieve a solution. It was found that, for layer densities lower than
approximately 39 layers/cm(100 layers/in.), the number of time steps required
became excessive, thus requiring a computer run time on the order of several
minutes. At a layer density of 28 layers/cm (72 layers/in.), the computer
time required was approximately ten minutes. This requirement precluded a

detailed study of the evacuation history of low density insulation systems. However, it was possible to compare predictions at early times in the evacuation process quite satisfactorily.

It would be possible to use other numerical integration techniques in order to reduce the computation time considerably. For example, instead of using only data for time t to predict data for $t + \Delta t$, those for several time steps earlier than t could be used in addition. The use of data at additional earlier times would permit a more accurate prediction of future data. Alternatively, for a given accuracy, a longer range forecast could be made. However, since it was not within the scope of this program to develop advanced numerical techniques, such a modification was not undertaken.

5.1.4 Determination of Nodal Volumes

5.1.4.1 Edge Evacuation. For the case of edge evacuation, the interstitial gas flows radially outward and has circular symmetry. The maximum pressure is at the center. For numerical analysis, the radial path is broken into N annular volumes. Normally, for a problem of this nature, the nodal volumes are established equal to each other. In the case of radial flow, however, this procedure would result in a series of annular volumes whose radial thickness would decrease as their mean radius increased. One of the important considerations in a numerical analysis is to maintain a relatively constant ratio of capacitance to conductance for the nodal system. Since both conductance and capacitance increase with radius, it was decided to use a constant radial step width for all nodal volumes. This approach proved to be successful.

The selected nodal breakdown is shown in Fig. 5-3. The mean radius of the ith node is denoted r_{Mi}. The inner radius and outer radius of the ith node are denoted r_{Ii-1} and r_{Ii}, respectively. The nodal volume, V_i, is thus equal to $(\pi)(2 z_o)(r_{Ii}^2 - r_{Ii-1}^2)$, where $2z_o$ is the distance between adjacent layers, and the volume of the insulation material is neglected. The flow conductance between nodes is based on radial flow between mean radii r_{Mi-1} and r_{Mi}.

5-10

LOCKHEED MISSILES & SPACE COMPANY
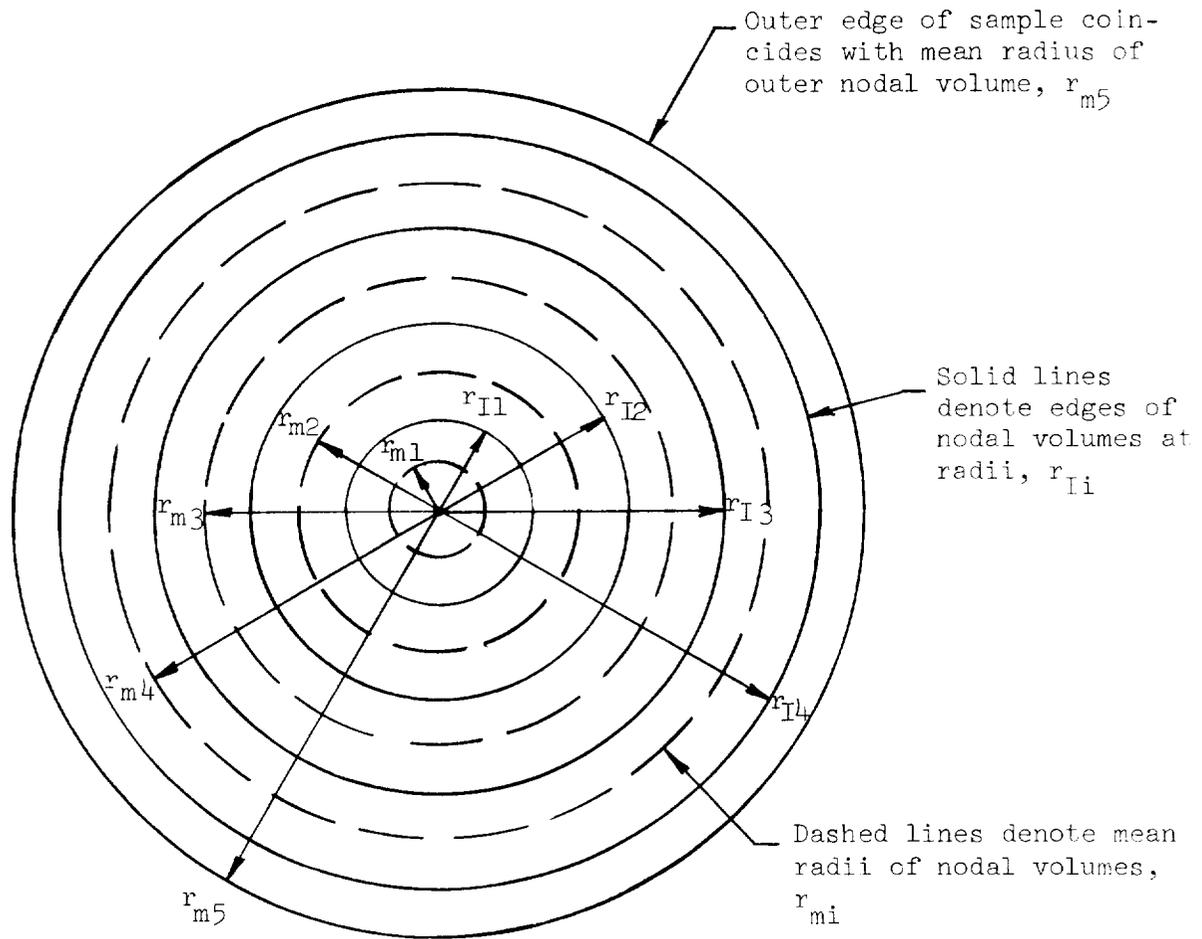
Fig. 5-3 Typical 5-Node Model for Edge Evacuation

5.1.4.2 <u>Broadside Evacuation</u>. In the case of broadside evacuation, the gas molecules follow a tortuous path from the inner layers to the outer layers by flowing successively and repeatedly through perforations in a given shield and then parallel to the shields until they reach a perforation in the next outer shield. A fixed area of unperforated shield is associated with each perforation. If the perforation diameter is d_h and the fraction of open area is F_o, then the total projected area of shield per perforation is $\pi d_h^2 / 4 F_o$.

Because of the interlayer separation, $2 z_o$, this creates an associated void volume per perforation of $2z_o \pi d_h^2/4F_o$. All of the shields have the same perforation density so that, on the average, the mass flow through a given perforation is equal to the evacuation flow of this associated volume plus the flow from all similar upstream volumes (i.e., one volume per upstream shield).

For the purposes of analysis, therefore, the nodal volume model is a linear succession of volumes, each equal to the volume associated with one perforation in each successive shield, $2z_o \pi d_h^2/4F_o$. In the actual solution, these volumes are lumped together in equal groups to reduce the total number of nodes. If N_L successive layers are lumped as a single node (i.e., $N_L = N_{LT}/N$), the volume of this node is $2z_o N_L \pi d_h^2/4F_o$.

5.1.5 Determination of Flow Conductance

5.1.5.1 Edge Evacuation. By definition, the conductance of a flow path between adjacent nodes is given by

$$C_i = \frac{\dot{m}_i}{P_i - P_{i+1}} \tag{5-12}$$

In the case of edge pumping this conductance must be calculated for a flow path whose cross-sectional area is proportional to the radius. Consequently, for flow from one annular volume node to the next, the following expression also applies

$$\dot{m}_i = (2\pi r_i)(2z_o)\left(\frac{\overline{P} M}{R^o T} \overline{v}_r\right) = 4\pi r_i z_o \overline{v}_r \frac{\overline{P} M}{R^o T} \tag{5-13}$$

where $\overline{v}_r$ is the average flow velocity in the channel at any radius r_i, and $\overline{P}$ is the average pressure for the two nodes. Determination of C therefore requires determination of average flow velocity.

5-12

The flow velocity is obtained from the Navier-Stokes momentum equations as written for cylindrical coordinates (Ref 21). Since the form of the Navier-Stokes equations is very complex, it is not practical to present them here. However, several conditions exist for this application which permit the equations to be greatly simplified. First, the flow has circular symmetry, so there is no change in fluid properties or in flow parameters, in the θ-direction (i.e., circumferentially). Second, the distance between the plates is very small compared with the radial flow path length, so that fluid property and flow parameter variations in the z-direction (i.e., normal to the layers) can be neglected. Third, the Navier-Stokes equations are in effect a statement of Newton's Second Law in that they equate the algebraic sum of inertia, viscous, pressure, and body forces to zero. The body forces are zero for this application where the gas flow pressures are low. The inertia forces may be neglected by comparison with pressure and viscous forces.

With these assumptions, the Navier-Stokes equations for the z-and θ-directions are eliminated, and that for the r-direction becomes

$$- \frac{\partial P}{\partial r} + \mu \left[\left(\frac{\partial^2 v_r}{\partial r^2} \right) + \frac{1}{r} \left(\frac{\partial v_r}{\partial r} \right) - \frac{v_r}{r^2} + \frac{\partial^2 v_r}{\partial z^2} \right] = 0 \qquad (5\text{-}14)$$

Here P is the gas pressure, v_r is the velocity in the radial direction, and μ is the gas viscosity.

Since the radial flow path is very long by comparison with the separation between the plates, the first three terms are negligible by comparison with the fourth term. Omitting these terms, the final equation becomes

$$- \frac{\partial P}{\partial r} + \mu \left(\frac{\partial^2 v_r}{\partial z^2} \right) = 0 \qquad (5\text{-}15)$$

5-13

The mean gas flow velocity, $\bar{v}_r$, can be determined for flow in the continuum, transition, and free molecule flow regimes from a slip-flow modified laminar flow equation as follows. The momentum equation for flow in the r-direction is

$$-\frac{\partial P}{\partial r} + \mu \left(\frac{\partial^2 v_r}{\partial z^2}\right) = 0 \qquad (5\text{-}16)$$

Eq (5-16) can be integrated in accordance with the boundary conditions $(\partial v_r / \partial z) = 0$ at $z = 0$ and $v_r = v_o$ at $z = \pm z_o$, where the coordinate z is zero midway between the adjacent layers.

In pure laminar continuum flow, v_o is zero. In pure free molecule flow, v_o is equal to the velocity at the center line. In transition flow, v_o assumes some intermediate value. The following velocity distribution equation is obtained

$$v_r = \frac{-1}{2\mu} \left[z_o^2 - z^2 \right] \frac{\partial P}{\partial r} + v_o \qquad (5\text{-}17)$$

The assumption is now made that the shear stress at the wall, τ , is equal to a constant, ϵ , times the wall velocity, v_o. Since, by definition, τ is equal to $\mu(\partial^2 v_r / \partial z^2)$ at $z = z_o$, the expression obtained for v_o is

$$v_o = \frac{\mu}{\epsilon} \left(\frac{\partial^2 v_r}{\partial z^2}\right)_{z = z_o} \qquad (5\text{-}18)$$

Eq (5-17) can be integrated to determine the average flow velocity, $\bar{v}_r$, and v_o can be replaced according to Eq (5-18) to yield

$$\bar{v}_r = \frac{-z_o^2}{3\mu} \left(1 + \frac{3\mu}{\epsilon z_o}\right) \frac{\partial P}{\partial r} \qquad (5\text{-}19)$$

The ratio μ/ϵ is known as the slip coefficient, ξ , and is given by (Ref 22)

$$\frac{\mu}{\epsilon} = \zeta = \frac{\mu}{P} \left(\frac{\pi v_a}{4} \right) \left(\frac{2-f}{f} \right) \qquad (5\text{-}20)$$

where v_a is the mean molecular velocity given by (Ref 23)

$$v_a = \left(\frac{8R^o T}{\pi M} \right)^{1/2} \qquad (5\text{-}21)$$

and f is the specular reflection coefficient. This coefficient is equal to that fraction of the total molecules incident upon the channel walls which are reflected diffusely. The value of f must be determined experimentally, but is usually slightly less than unity. Substitution of these quantities into Eq (5-19) yields

$$\bar{v}_r = \frac{-z_o^2}{3\mu} \left(1 + \frac{3\mu}{z_o P} \frac{\pi v_a}{4} \frac{2-f}{f} \right) \frac{\partial P}{\partial r} \qquad (5\text{-}22)$$

At high pressures, the second term in the parentheses of Eq (5-22) becomes negligible and the familiar Poissieulle equation is obtained. At very low pressures, free molecule flow will occur and the expression for $\bar{v}_r$ reduces to

$$\bar{v}_r = \left(\frac{-\pi}{4} \right) \left(\frac{2-f}{f} \right) \left(\frac{z_o}{P} \right) \left(v_a \frac{\partial P}{\partial r} \right) \qquad (5\text{-}23)$$

Knudsen derived an expression for mass flow in the free molecule flow regime which, when rearranged, defines the average velocity as follows (Ref 24).

$$\bar{v}_r = \left(-\frac{4z_o}{3P} \right) \left(v_a \frac{\partial P}{\partial r} \right) \qquad (5\text{-}24)$$

Eq (5-23) and (5-24) agree parametrically, confirming the qualitative validity of the slip flow model for transition. The constant would agree if

$$\frac{4}{3} \equiv \frac{(2-f)}{f} \left(\frac{\pi}{4} \right) \qquad (5\text{-}25)$$

5-15

or

$$f \cong 0.75 \tag{5-26}$$

However, this value of f is somewhat lower than would be expected from past experimental work.

Further investigation of the literature reveals that in fact f is not constant and depends upon some independent variables such as surface finish, in addition to those already discussed. The explanation for this apparent discrepancy is that in reality the conductance of a flow passage, which is proportional to the product $\bar{v}_r P$, does not decrease monotonically from the viscous regime values to the constant free molecule flow value, but instead passes through a small minimum over a relatively narrow pressure range at the high-pressure end of the free molecule regime. This is because in the viscous slip and much of the transition flow regimes, the flow is dependent upon momentum exchange within the fluid, whereas in the free molecule regime momentum is exchanged only with the tube walls. This characteristic conductance minimum is an indication of the regime over which the principal momentum interactions change from one type to the other. It is difficult, if not impossible, to represent it analytically because of the shift of flow mechanisms. Knudsen (Ref 25) proposed use of an empirical constant, Z, to account for the minimum. Using this constant in a general form, Eq (5-22) can be rewritten as

$$\bar{v}_r = \frac{-z_o{}^2}{3\mu} \left[1 + \left(\frac{4\mu v_a}{z_o P} \right) Z \right] \frac{dP}{dr} \tag{5-27}$$

For the specific case of round tubes, Knudsen also proposed an empirical expression for Z given by

$$Z_t = \frac{1 + \frac{2a}{\mu} \left(\frac{M}{R^o T} \right)^{1/2} P}{1 + \frac{2.7a}{\mu} \left(\frac{M}{R^o T} \right)^{1/2} P} \tag{5-28}$$

where a is the tube radius.

5-16

No equivalent expression has been developed heretofore for the case of flow between flat plates. However, it was found in the early Task 2 analysis that evaluation of Eq (5-27) using Z as computed from Eq (5-28), with the tube diameter, 2a, replaced by the equivalent hydraulic diameter, $4z_o$, did produce the characteristic minimum in $\bar{v}_r$ with decreasing pressure at the high-pressure end of the free molecule regime. Moreover, the resulting equation also reduces to Knudsen's expression, Eq (5-24), at very low pressures. During the succeeding analysis in Task 2, two alternate techniques were evaluated for correcting the slip-flow modified expression given by Eq (5-22). These were to: (1) assume Z = unity, and (2) assume a value for Z calculated from Eq (5-28) with a = $2z_o$ as described above. The results of these alternate techniques are compared in Table 5-1 with the reference case where the uncorrected slip-flow modified equation, Eq (5-22), was used. This comparison was made on the basis of a term, B, which represents the pressure dependence of the conductance. This term is equal to the product of area, density, and velocity. Values of B for the three cases compared are given by

$$B_1 = P \left[1 + (\frac{3\mu}{z_o P}) (\frac{\pi v_a}{4}) (\frac{2-f}{f}) \right] \tag{5-29}$$

$$B_2 = P \left[1 + (\frac{4\mu v_a}{z_o P}) z \right] \tag{5-30}$$

$$B_3 = P \left[1 + \frac{4\mu v_a}{z_o P} \right] \tag{5-31}$$

In the first of these expressions, B_1 is determined from the slip flow analysis and is accurate for viscous, early transition flow but, as noted earlier, does not adequately represent low pressure transition flow and free molecule flow. B_2 is obtained from Knudsen's equation for free molecule flow, Poissieulles equation for viscous flow and Knudsen's impirical Z factor to account for the transition minimum. B_3 is simply B_2 evaluated for Z = 1.0. In computing the comparative B factors shown in the table, helium gas at 300°K (540°R), an f value equal to 0.85, and an insulation layer density of 39.4 layers/cm (100 layers/in.) were assumed.

Table 5-1

COMPARISON OF ALTERNATE CONDUCTANCE FACTORS AS A FUNCTION OF PRESSURE

Absolute Pressure Torr	Conductance Factor		
	B_1	B_2	B_3
1000	1004.27	1004.85	1005.95
100	104.27	104.85	105.95
10	14.27	14.85	15.95
8	12.27	12.85	13.95
6	10.27	10.85	11.95
4	8.27	8.88	9.95
2	6.27	6.94	7.95
1	5.27	6.00	6.95
0.8	5.07	5.90	6.75
0.6	4.87	5.73	6.55
0.4	4.67	5.57	6.35
0.2	4.47	5.60	6.15
0.1	4.37	5.65	6.05
.08	4.35	5.70	6.03
.06	4.33	5.78	6.01
.04	4.31	5.80	5.99
.02	4.29	5.84	5.97
.01	4.28	5.90	5.96
.001	4.27	5.95	5.95

Note: B_1 is obtained from the slipflow modified Poissieulle equation.

B_2 is obtained from the sum of Poissieulle and Knudsen conductances with a Z factor equal to correct empirically-determined expression.

B_3 is obtained from the sum of Poissieulle and Knudsen conductances with a Z factor equal to unity.

From inspection of Table 5-1, it can be seen that by assuming Z = 1, a systematic error on the order of 5 to 15 percent is incurred. For the purpose of the Task 2 analysis, it was decided to use this approximation since it would simplify the analysis. However, it is clear that a Z factor could be added for future applications if the additional accuracy was required.

The expression for $\bar{v}_r$ thus selected for the Task 2 analysis is

$$\bar{v}_r = \frac{-z_o^2}{3\mu} \left[1 + \frac{4\mu v_a}{z_o P} \right] \frac{dP}{dr} \qquad (5\text{-}32)$$

Substituting Eq (5-32) into Eq (5-13) yields

$$\dot{m}_i = -\left(\frac{4\pi r z_o^3}{3\mu}\right)\left(\frac{PM}{\bar{R}^oT}\right)\left[1 + \frac{4\mu v_a}{z_o P}\right]\frac{dP}{dr} \tag{5-33}$$

Rearranging,

$$\frac{dr}{r} = -\left(\frac{4\pi z_o^3}{3\mu}\right)\left(\frac{PM}{\bar{R}^oT}\right)\left[1 + \frac{4\mu v_a}{z_o P}\right]\frac{dP}{\dot{m}_i} \tag{5-34}$$

Integrating between nodes with average radii of r_{Mi} and r_{Mi+1} yields

$$\ln\left(\frac{r_{Mi+1}}{r_{Mi}}\right) = \left(\frac{4\pi z_o^3}{3\mu}\right)\left(\frac{\bar{P}M}{\bar{R}^oT}\right)\left[1 + \frac{4\mu v_a}{z_o P}\right]\frac{(P_i - P_{i+1})}{\dot{m}_i} \tag{5-35}$$

and

$$\frac{\dot{m}_i}{(P_i - P_{i+1})} = \left(\frac{4\pi z_o^3}{3\mu}\right)\left(\frac{\bar{P}M}{\bar{R}^oT}\right)\frac{\left[1 + \frac{4\mu v_a}{z_o P}\right]}{\ln(r_{Mi+1}/r_{Mi})} \tag{5-36}$$

Then, by comparison with Eq (5-12),

$$C_i = \left(\frac{4\pi z_o^3}{3\mu}\right)\left(\frac{\bar{P}M}{\bar{R}^oT}\right)\left[1 + \frac{4\mu v_a}{z_o P}\right]\Big/\ln(r_{Mi+1}/r_{Mi}) \tag{5-37}$$

5.1.5.2 Broadside Evacuation. At the outset of the analysis, the major
assumption was made that the flow resistance during broadside evacuation is
due to radial flow between shields from hole to hole, rather than to the
orifice effect of the holes themselves. This assumption was found to be
valid in the viscous flow regime, but could be questionable in the free
molecule regime. However, it was not possible within the scope of the pro-
gram to develop expressions for orifice flow in the free molecule regime.

Based on the assumptions noted above, the problem of analyzing broadside
evacuation flow through the perforated shields is essentially similar in
nature to the edge pumping situation. The basic difference lies in the
establishment of the geometric model. In this regard, two basic problems

arise. First, the perforation patterns are basically rectangles or parallelograms. Consequently, the exact geometry of the gas flow path through the holes in one layer, between the layers, and then out through the holes in the next layer is quite complex. Second, insulation shields are normally stacked randomly, so it is not possible to specify in advance exactly how the holes will match up between adjacent layers. In order to proceed with the analysis, some simplifying assumptions were made as follows:

(1) The flow field around a given perforation has circular symmetry, and the flow path is thus pure radial inflow towards a given perforation or pure radial outflow from the perforation.

(2) Since the perforation patterns in adjacent layers are identical, the mass flow rate through each perforation in a given layer is identical.

(3) The gas flowing radially inward toward any given perforation includes some fraction of the flow through adjacent perforations in the preceding layer (i.e., point sources). The flow from these sources is distributed uniformly circumferentially, and the total flow rate is equal in magnitude to that from all of the point sources combined.

(4) The random relative orientation between the perforation patterns of adjacent shields results in a "most probable" separation between any two given perforations of the adjacent shields equal to the first moment about its centroid of the effective (circular) shield area per perforation divided by that effective area.

The resulting geometric model for broadside evacuation is shown in Fig. 5-4. For each hole in each layer, gas flow is assumed to proceed radially and uniformly inward between flat circular disks. The diameter of the disks is found in two steps. First, for each perforation there is an associated effective shield area, A_s, given by

$$A_s = \frac{\pi d_h^2}{4F_o} \tag{5-38}$$

5-20

Holes in Nth Layer

Holes in (N+1)th Layer

Model Gas Flow in the Form of Uniformly Distributed Flow Around Circumference of Equivalent Circle

Gas Flow from Holes in Nth Layer to Holes in (N+1)th Layer

Hole Diameter, d_h

Fraction Open Area, F_o

Effective Area Per Hole

$$= \frac{\pi d_h^2}{4 F_o}$$

Model Area in the Form of an Equivalent Circle

Diameter of Circular Area

$$d_A = \frac{d_h}{\sqrt{F_o}}$$

d_A
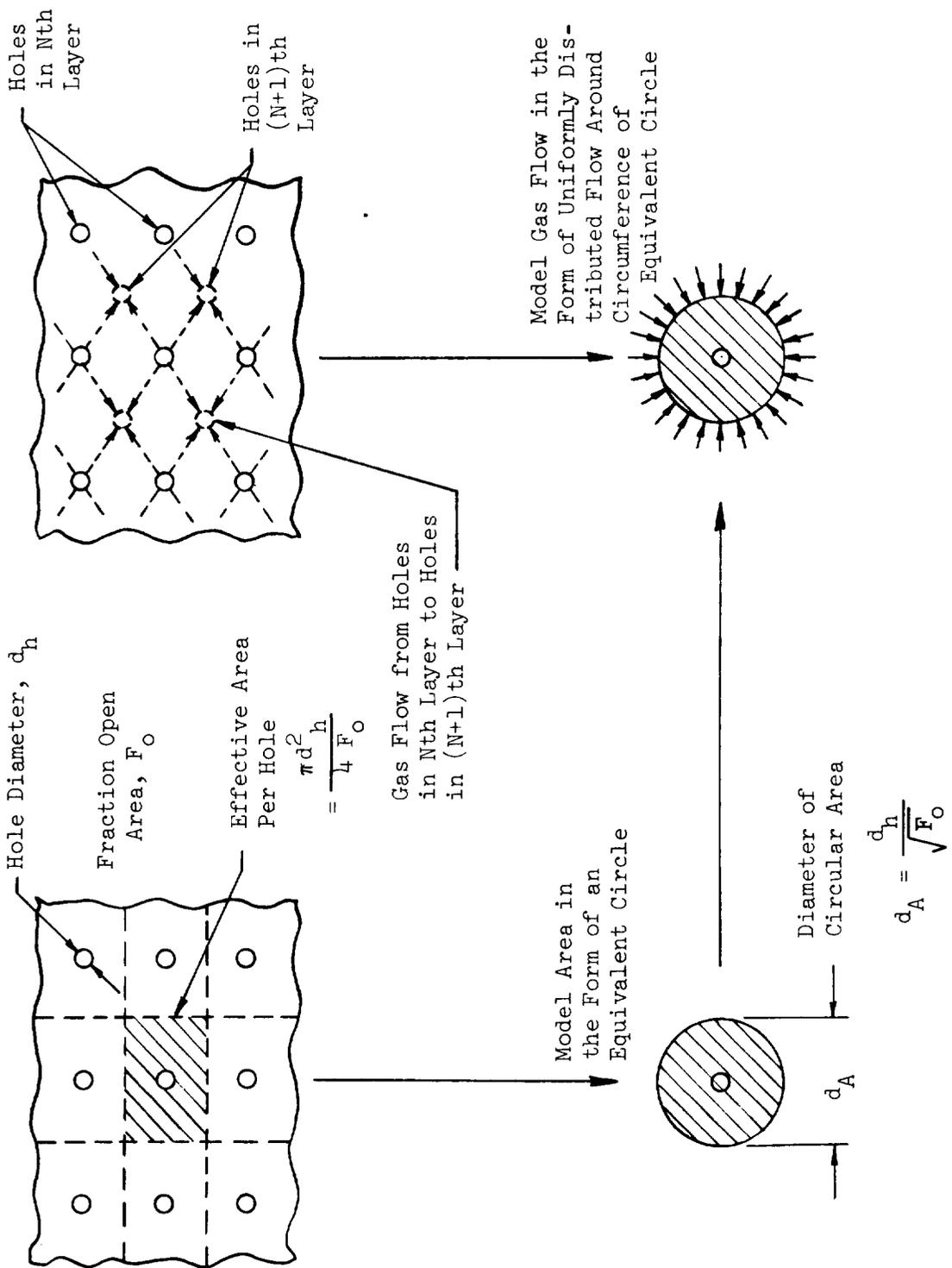
Fig. 5-4 Geometry and Flow Model for Broadside Evacuation

5-21

where d_h is the perforation diameter. This area is rectangular in shape because of the rectangular perforation patterns. As an approximation A_s is assumed to be circular, having a diameter d_A where

$$d_A = \sqrt{\frac{4A_s}{\pi}} = \frac{d_h}{\sqrt{F_o}} \tag{5-39}$$

In analyzing broadside evacuation, the insulation was considered to consist of a set of nodal volumes of diameter d_A and height $2z_o$, connected in series. The flow resistance between nodes was assumed to be that of the radial flow path length. This path length could be zero, for coincident perforation patterns, or $(d_A - d_h)/2$, for maximum staggering. For random stacking, the most probable radial path flow length is given by the first moment of the effective area about its centroid divided by the effective area, which for $d_A \gg d_h$ is equal to $d_A/3$.

With the geometry of the flow model thus established, the flow equation for broadside evacuation can now be determined. By analogy with the edge pumping of circular specimens as discussed in section 5.1.5.1, the average flow velocity between the plates is given by Eq (5-32). Assuming constant mass flow within the node, the continuity equation at radius r yields

$$\dot{m} = (2\pi r)\,(2z_o)\,(\rho\,\overline{v}_r) \tag{5-40}$$

Assuming perfect gas behavior, Eq (5-32) can be rewritten as

$$\frac{dr}{r} = \left(\frac{-4\pi z_o^3}{3\mu\dot{m}}\right)\left(\frac{\overline{P}M}{R^o T}\right)\left[1 + \frac{4\mu v_a}{z_o P}\right] dP \tag{5-41}$$

Integrating Eq (5-41) between $r = \dfrac{d_h}{2}$ and $r = \dfrac{d_A}{3}$ yields

$$\ln\,(2d_A/3d_h) = \left(\frac{4\pi z_o^3}{3\mu\dot{m}}\right)\left(\frac{\overline{P}M}{R^o T}\right)\left[1 + \frac{4\mu v_a}{z_o P}\right](P_2 - P_1) \tag{5-42}$$

and, solving for $\dot{m}$ yields

$$\frac{\dot{m}}{P_2 - P_1} = \left(\frac{4\pi z_o{}^3}{3\mu}\right) \left(\frac{\bar{P}M}{R^oT}\right) \left[1 + \frac{4\mu v_a}{z_o P}\right] \Big/ \ln\left(\frac{2}{3}\sqrt{\frac{1}{F_o}}\right) \qquad (5\text{-}43)$$

This equation represents the flow conductance for one layer. It should be divided by the number of layers to give the conductance of N_L layers in series. By comparison with Eq (5-12),

$$C = \left(\frac{4\pi z_o{}^3}{N_L 3\mu}\right) \left(\frac{\bar{P}M}{R^oT}\right) \left[1 + \frac{4\mu v_a}{z_o P}\right] \Big/ \ln\left(\frac{2}{3}\sqrt{\frac{1}{F_o}}\right) \qquad (5\text{-}44)$$

5-23

5.2   GAS EVACUATION TESTING

5.2.1   Experimental Method

The basic experimental approach used in Task 2 was to place various MLI sys-
tem specimens in a vacuum chamber, evacuate the chamber, and then measure
both the chamber pressure and the interstitial differential pressure as func-
tions of time. This experiment was repeated for many combinations of multi-
layer system type, layer density, flow path length, temperature, and purge
gas species. A summary of the gas evacuation tests conducted in Task 2 is
presented in Table 5-2. Because the difference between the interstitial
and the chamber pressure is characteristically very small, this parameter,
rather than absolute interstitial pressure, was measured in these experiments.
When desired, absolute pressure was then obtained simply as the sum of the
chamber and differential pressure values.

Tests were performed on both unperforated and perforated samples. The unper-
forated samples were, of course, evacuated by edge pumping only. The perfora-
ted samples were evacuated both by broadside pumping alone, and by a combina-
tion of edge and broadside pumping.

In order to avoid experimental and analytical problems associated with flow
asymmetry, circular-shaped specimens were used. Thus, the evacuation flow was
radial, from the center to the edge of the specimen, and there was no net
force acting on the specimen during the pumpdown. The differential pressure
was measured between the center and the circumference of the specimen. In
the case of broadside evacuation, circular-shaped specimens again were used,
but edge sealing was necessary, as explained in the following section.

LOCKHEED MISSILES & SPACE COMPANY

Table 5-2a

SUMMARY OF TASK 2 GAS EVACUATION TESTS

Insulation Composite	Specimen No. (Perforation Pattern)	No. Of Shields	Perf. Dia., cm	Open Area percent	Spec. Dia., cm	Test Temp., °K	Purge Gas Species	Boundary Plate Separation cm	Layer Density, No./cm
Unperforated Double-Aluminized Mylar/Tissuglas (c)	1A	20	-	-	68.6	300	He,N₂,A	0.406	46.8(a)
	1B	20	-	-	68.6	300	He,N₂,A	0.348	54.6(a)
	1C	20	-	-	68.6	300	He,N₂,A	0.229	83.0(a)
	2	20	-	-	50.8	300	N₂	0.348	54.6(a)
	3	20	-	-	38.1	300	N₂	0.348	54.6(a)
	4	80	-	-	68.6	128, 182	He	1.392	56.8(a)
	4	80	-	-	68.6	213, 239	He	1.392	56.8(a)
	4	80	-	-	68.6	287, 300	He	1.392	56.8(a)
Perforated, Double-Aluminized Mylar/Double Preconditioned Silk Net (d)	5 (S-602)	80	0.119	0.26	68.6	300	N₂	2.855	28.4(b)
	6 (S-603)	80	0.119	0.55	68.6	300	N₂	2.855	28.4(b)
	7 (S-604)	80	0.119	1.07	68.6	300	N₂	2.855	28.4(b)
	8 (937-S)	80	0.229	0.48	68.6	300	N₂	2.855	28.4(b)
	9 (937)	80	0.229	0.99	68.6	300	N₂	2.855	28.4(b)
	10 (S-604)(e)	80	0.119	1.07	68.6	300	N₂	2.855	28.4(b)
Perforated, Double-Aluminized Mylar/Tissuglas (d)	11 (S-602)	80	0.119	0.26	68.6	300	N₂	1.392	58.2(b)
	12 (S-603)	80	0.119	0.55	68.6	300	N₂	1.392	58.2(b)
	13 (S-604)	80	0.119	1.07	68.6	300	N₂	1.392	58.2(b)
	14 (937-S)	80	0.229	0.48	68.6	300	N₂	1.392	58.2(b)
	15 (937)	80	0.229	0.99	68.6	300	N₂	1.392	58.2(b)
	16 (S-604)(f)	80	0.119	1.07	68.6	300	N₂	1.392	58.2(b)
Unperforated, Double-Aluminized Mylar/Double Preconditioned Silk Net (c)	17A	20	-	-	68.6	300	N₂	0.742	28.4(b)
	17B	20	-	-	68.6	300	N₂	0.544	38.6(b)
	17C	20	-	-	68.6	300	N₂	0.442	47.5(b)
	18	20	-	-	50.8	300	N₂	0.544	38.6(b)
	19	20	-	-	38.1	300	N₂	0.544	38.6(b)
	20	80	-	-	68.6	131,266,	He	2.098	38.6(b)
	20	80	-	-	68.6	272, 276,	He	2.098	38.6(b)
	20	80	-	-	68.6	300	N₂,He,A	2.098	38.6(b)
Unperforated, Crinkled Single-Aluminized Mylar (c)	21A	20	-	-	68.6	300	N₂	0.726	28.9(b)
	21B	20	-	-	68.6	300	N₂	0.597	35.2(b)
	21C	20	-	-	68.6	300	N₂	0.363	57.9(b)

Notes:
(a) Values shown correspond to specimens with one less spacer layer than the number of shields shown.
(b) Values shown correspond to specimens with one more spacer layer than the number of shields shown.
(c) Specimens of this MLI system tested in edge-pumping mode only.
(d) Specimens of this MLI system tested in broadside-pumping mode with edges sealed, except as noted otherwise.
(e) This specimen tested in combined edge-pumping and broadside-pumping modes.
(f) This specimen test deleted.

5-25

Table 5-2b

SUMMARY OF TASK 2 GAS EVACUATION TESTS

Insulation Composite	Specimen No. (Perforation Pattern)	No. Of Shields	Perf. Dia., in.	Open Area, percent	Spec. Dia., in.	Test Temp, °R	Purge Gas Species	Boundary Plate Separation, in.	Layer Density, No./in.
Unperforated, Double-Aluminized Mylar/ Tissuglas (c)	1A	20	-	-	27	540	He,N₂,A	0.160	119(a)
	1B	20	-	-	27	540	He,N₂,A	0.137	139(a)
	1C	20	-	-	27	540	He,N₂,A	0.090	211(a)
	2	20	-	-	20	540	N₂	0.137	139(a)
	3	20	-	-	15	540	N₂	0.137	139(a)
	4	80	-	-	27	230, 328	He	0.548	144(a)
	4	80	-	-	27	384, 430	He	0.548	144(a)
	4	80	-	-	27	517, 540	He	0.548	144(a)
Perforated, Double-Aluminized Mylar/ Double Preconditioned Silk Net (d)	5 (S-602)	80	0.047	0.26	27	540	N₂	1.124	72(b)
	6 (S-603)	80	0.047	0.55	27	540	N₂	1.124	72(b)
	7 (S-604)	80	0.047	1.07	27	540	N₂	1.124	72(b)
	8 (937-S)	80	0.090	0.48	27	540	N₂	1.124	72(b)
	9 (937)	80	0.090	0.99	27	540	N₂	1.124	72(b)
	10 (S-604)(e)	80	0.047	1.07	27	540	N₂	1.124	72(b)
Perforated, Double-Aluminized Mylar/ Tissuglas (d)	11 (S-602)	80	0.047	0.026	27	540	N₂	0.548	148(b)
	12 (S-603)	80	0.047	0.55	27	540	N₂	0.548	148(b)
	13 (S-604)	80	0.047	1.07	27	540	N₂	0.548	148(b)
	14 (937-S)	80	0.090	0.48	27	540	N₂	0.548	148(b)
	15 (937)	80	0.090	0.99	27	540	N₂	0.548	148(b)
	16 (S-604)(f)	80	0.047	1.07	27	540	N₂	0.548	148(b)
Unperforated, Double-Aluminized Mylar/ Double Preconditioned Silk Net (c)	17A	20	-	-	27	540	N₂	0.292	72(b)
	17B	20	-	-	27	540	N₂	0.214	98(b)
	17C	20	-	-	27	540	N₂	0.174	121(b)
	18	20	-	-	20	540	N₂	0.214	98(b)
	19	20	-	-	15	540	N₂	0.214	98(b)
	20	80	-	-	27	236, 479	He	0.826	98(b)
	20	80	-	-	27	490, 497	He	0.826	98(b)
	20	80	-	-	27	540	N₂, He,A	0.826	98(b)
Unperforated, Crinkled, Single-Aluminized Mylar (c)	21A	20	-	-	27	540	N₂	0.286	73(b)
	21B	20	-	-	27	540	N₂	0.235	89(b)
	21C	20	-	-	27	540	N₂	0.143	147(b)

Notes:
(a) Values shown correspond to specimens with one less spacer layer than the number of shields shown.
(b) Values shown correspond to specimens with one more spacer layer than the number of shields shown.
(c) Specimens of this MLI system tested in edge-pumping mode only.
(d) Specimens of this MLI system tested in broadside-pumping mode with edges sealed, except as noted otherwise.
(e) This specimen tested in combined edge-pumping and broadside-pumping modes.
(f) This specimen test deleted.

5.2.2   Experimental Apparatus

The evacuation experiments were conducted in a 76.2-cm- (30-in.-) diameter
by 55.9-cm- (22-in.-) high vacuum chamber. The chamber was fitted with a
very high capacity mechanical pump, capable of reducing the chamber pressure
from one atmosphere to a few microns in about two minutes. A 15.2-cm (6-in.)
diffusion pump was also fitted to the chamber. The general arrangement and
some details of the basic apparatus are shown in Figs. 5-5 through 5-7.

The insulation specimens were suspended from the cover of the vacuum chamber,
as shown in Fig. 5-5. For the edge pumping experiments, the specimens were
held between two 71-cm-(28-in.-) diameter, 1.3-cm-(0.5-in.-) thick aluminum
plates. The plates were bolted together at one of several selected spacings
by eight equally-spaced attachments. Accurately machined 0.635-cm-(0.25-in.-)
diameter spacers were used to establish and maintain the selected plate separa-
tion. The circular insulation specimens were cut to a 68.6-cm (27-in.) diame-
ter. When a specimen was installed between the plates, there was a nominal
0.318-cm (0.125-in.) radial clearance between the circumferential edge and
the 8 attachment bolts. However, in view of the difficulty of assembling
an MLI specimen with all layers exactly concentric, the effective outside
diameter of the specimen was usually near 69.2-cm (27.25-in.-) and, thus,
the stack was conveniently centrally located by the spacers. The edge-pumped
specimens were provided with a central 0.318-cm-(0.125-in.-) diameter hole,
passing through all of the MLI layers. This hole coincided with a central
pressure tap hole located in the upper aluminum boundary plate. One side
of a differential pressure transducer, which is described below, was attached
to this tap hole. The total assembly with the two plates, the sandwiched
insulation sample, and the pressure transducer was inserted into the evacua-
tion chamber. It was suspended from the top cover plate by low thermal con-
ductance rods as shown in the figures. The reference side of the pressure
transducer was opened to the chamber, so that the transducer would measure
directly the pressure differential between the center and the periphery of
the sample due to radially outward gas flow. Because of the plenum created
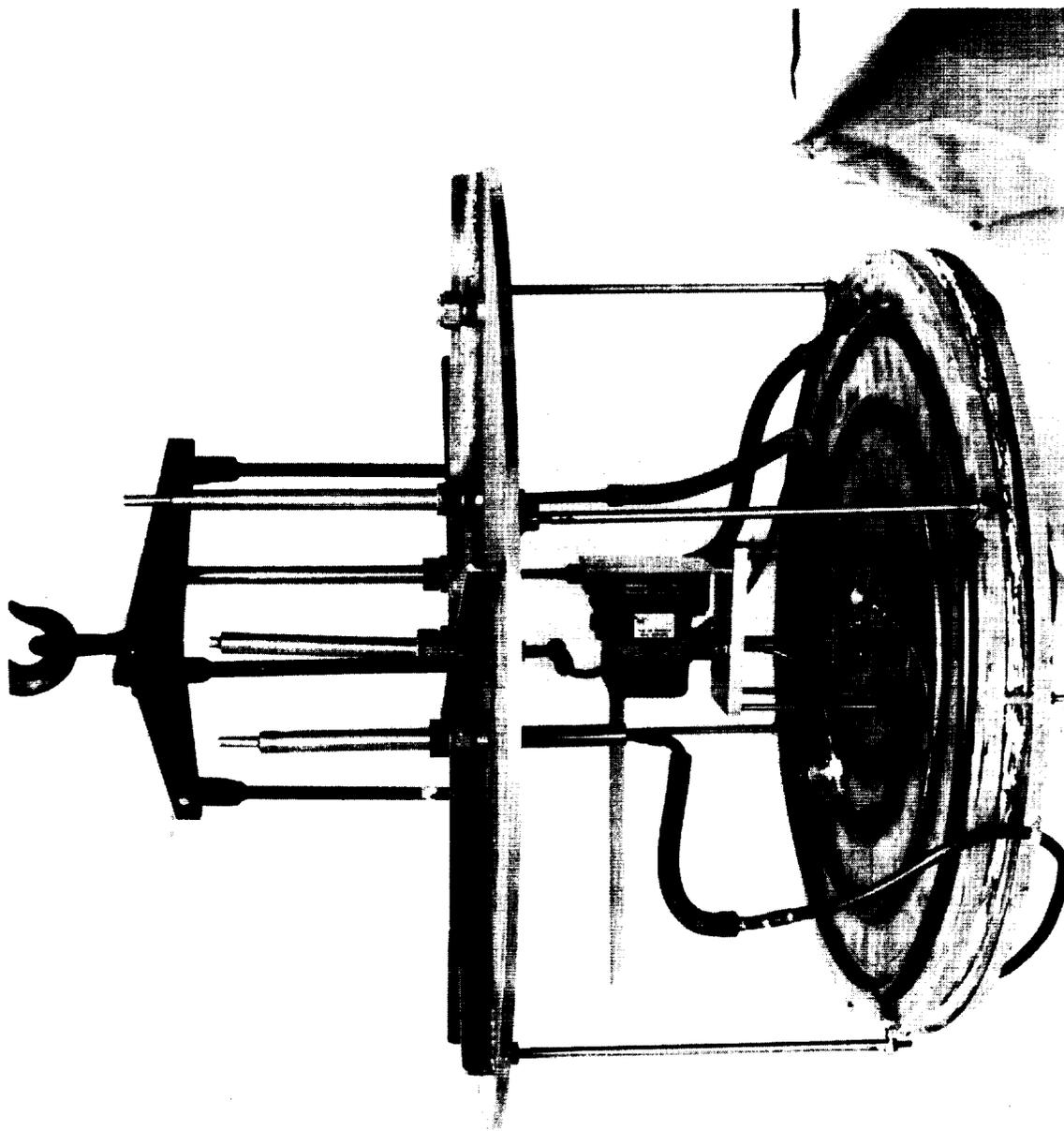
Fig. 5-5 Side View of Gas Evacuation Apparatus
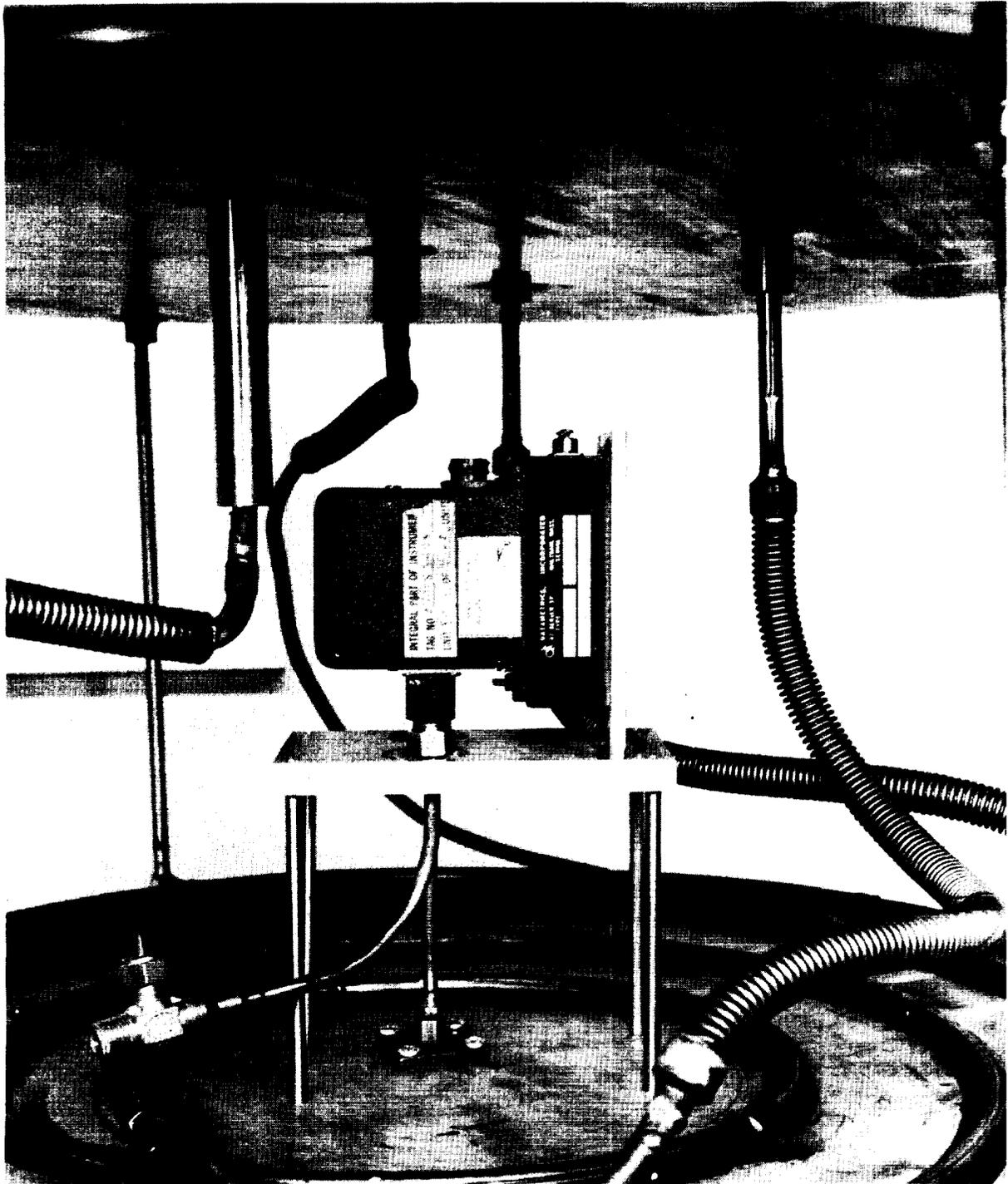
Fig. 5- 6 Side View of Pressure Transducer Installation

5-29

Fig. 5-7   View of Lower Boundary Plate and Heat Exchanger

LOCKHEED MISSILES & SPACE COMPANY

by the 0.318-cm-(0.125-in.-) diameter central hole in the specimen, the up-stream pressure was always common to all MLI layers.

During testing, the temperature of the two plates and the specimen was established and maintained at any desired value between ambient and approximately $230^{\circ}K$ ($414^{\circ}R$) by flowing cold gaseous or liquid nitrogen through copper coils epoxy-bonded to the outer sides of the boundary plates. These heat exchanger coils can be seen in Figs. 5-5 through 5-7.

For the broadside evacuation tests, the lower solid aluminum plate with its cooling coils was removed from the chamber. The broadside evacuation samples were then cut to a 68.6-cm-(27-in.-) diameter, and were clamped circumferentially to the under side of the upper plate using the eight mounting bolts. An aluminum clamping ring was used which was 1.27-cm-(0.5-in.) thick, 71.1-cm (28-in.) outside diameter, and 66-cm (26-in.) inside diameter. In the clamped position, the edges of the insulation specimen were tightly sealed, thus preventing edge flow. The central portion of the sample sagged somewhat as shown in Fig. 5-8. To compress the central portion back to the required thickness, a screen support was installed as shown in Fig. 5-9. This support consisted of a 20 mesh/cm (50 mesh/in.) sheet of stainless steel screen attached to a support ring of similar dimensions to the clamping ring. As shown, the central portion of the screen was maintained in a flat configuration by several stiffening webs. The screen support was attached to the upper plate using the eight mounting bolts, and was maintained at a selected distance from the upper plate by spacers. The screen support thus served to establish a desired layer density value, but was sufficiently porous to permit broadside evacuation.

The primary measurements required in these tests were absolute chamber pressure and sample differential pressure as a function of time from the beginning of evacuation. In addition, it was necessary to determine the temperature of the insulation. A number of copper-constantan thermocouples were bonded to the plates and, for the cold tests, to selected insulation layers for this purpose.

5-31
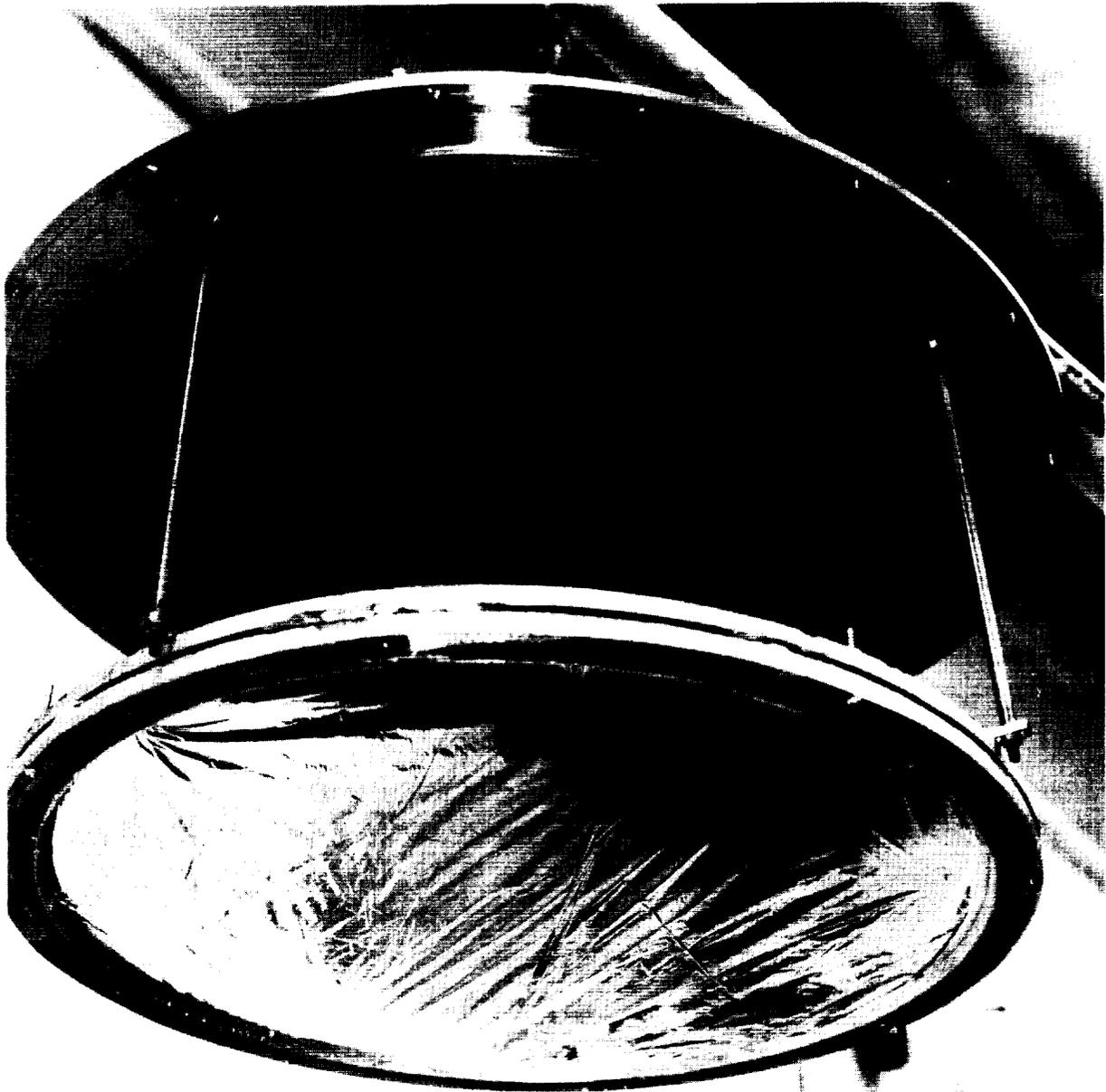
Fig. 5-8   Broadside Evacuation Specimen Installed Without Support Screen

LOCKHEED MISSILES & SPACE COMPANY
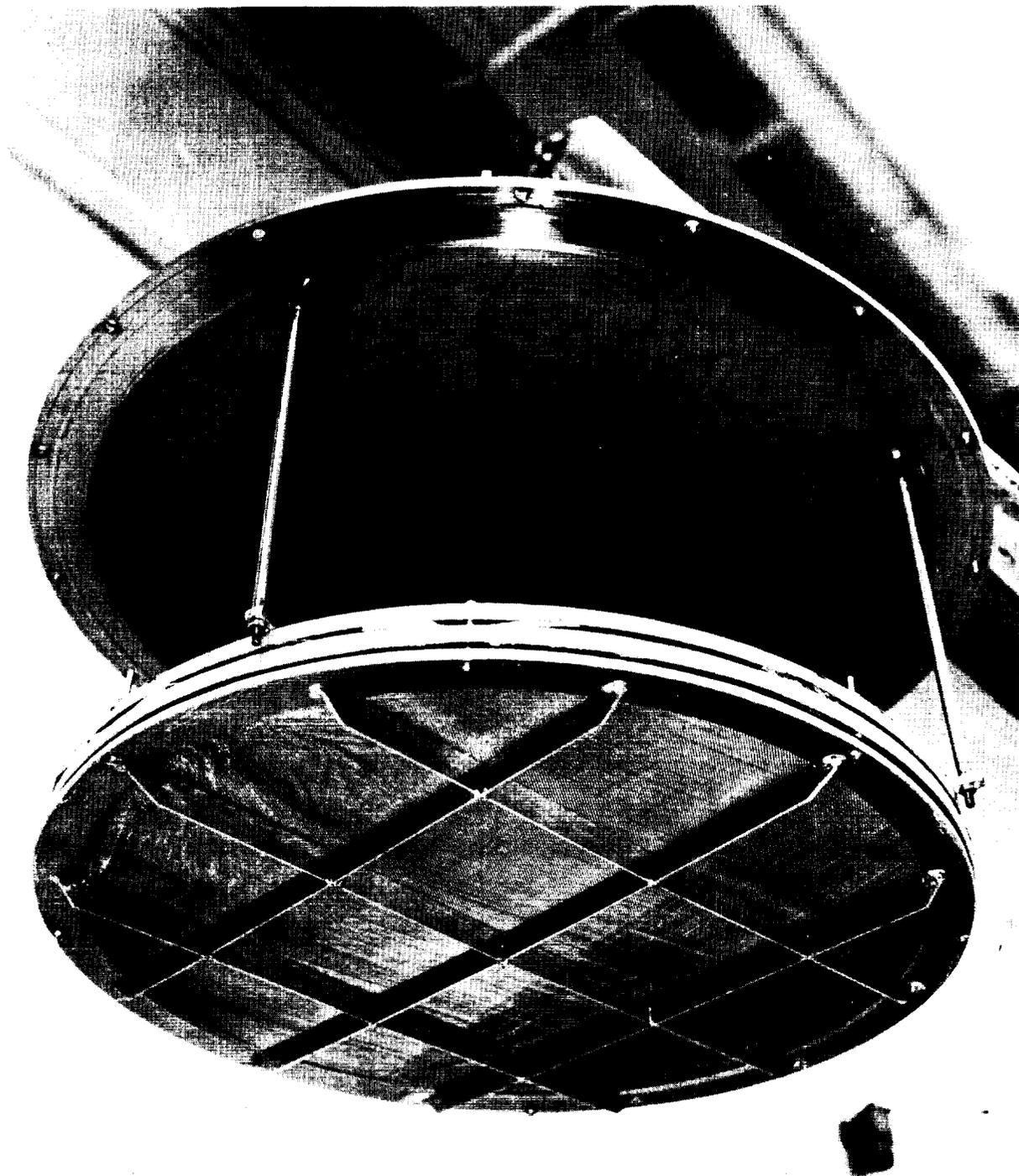
Fig. 5-9 Broadside Evacuation Specimen Installed With Support Screen

5-33

Both absolute and differential pressure measurements were obtained using Barocel transducers. The Barocel is a differential pressure measurement device which detects the deflection of a highly sensitive stainless steel diaphragm in response to an imposed pressure differential. The steel diaphragm is a plate common to two opposed electrical condensers, in turn attached to an a.c. bridge circuit. A movement of the diaphragm increases the capacitance of one condenser and decreases that of the other, thereby unbalancing the a.c. bridge and creating an output signal. The signal is processed through a control box which also provides a meter and an a.c. analog output. Fig. 5-10 shows a Barocel control box with a single transducer head and a temperature control base.

Absolute pressure was measured using a system of two Barocel transducers mounted outside of the vacuum chamber such that both were connected to a single control box. The two transducers had ranges of 0-1000 torr and 0-10 torr, respectively, thus permitting continuous measurement of chamber pressures from one atmosphere down to approximately 10^{-4} torr.* Pressures below 10^{-4} torr were determined using an NRC ionization gauge. During early evacuation times, the absolute pressure was recorded on a Varian stripchart recorder, which also provided the time base. Subsequent to evacuation times of approximately 3 minutes, when the pressure changes occurred much more slowly, the recorder was stopped and thereafter both pressure and time were recorded manually. Since the Barocel is a differential instrument, one side of each of the transducers must be referenced to a known or negligible pressure source in order to obtain absolute readings. For absolute measurements in Task 2, the reference side was connected to the inlet of a separate diffusion pumping system and was thus maintained at about 10^{-6} torr or less. As shown in the schematic of Fig. 5-11, the absolute pressure Barocel system was provided with valves to permit the two sides of the transducer to be isolated from external pressure sources and connected together for zeroing purposes.

---

* Since the 0-10 torr transducer was able to withstand the substantial over-pressure at 1 atmosphere, both transducers were maintained in continuous communication with the vacuum chamber.
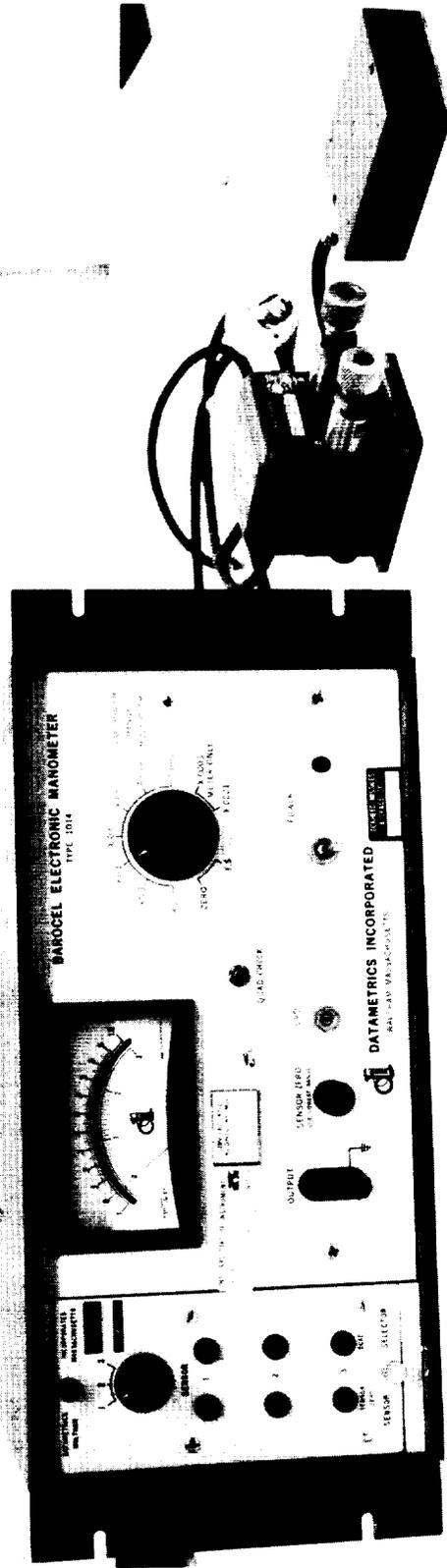
Fig. 5-10 Barocell Control Box, Transducer, and Thermal Control Base

LOCKHEED MISSILES & SPACE COMPANY
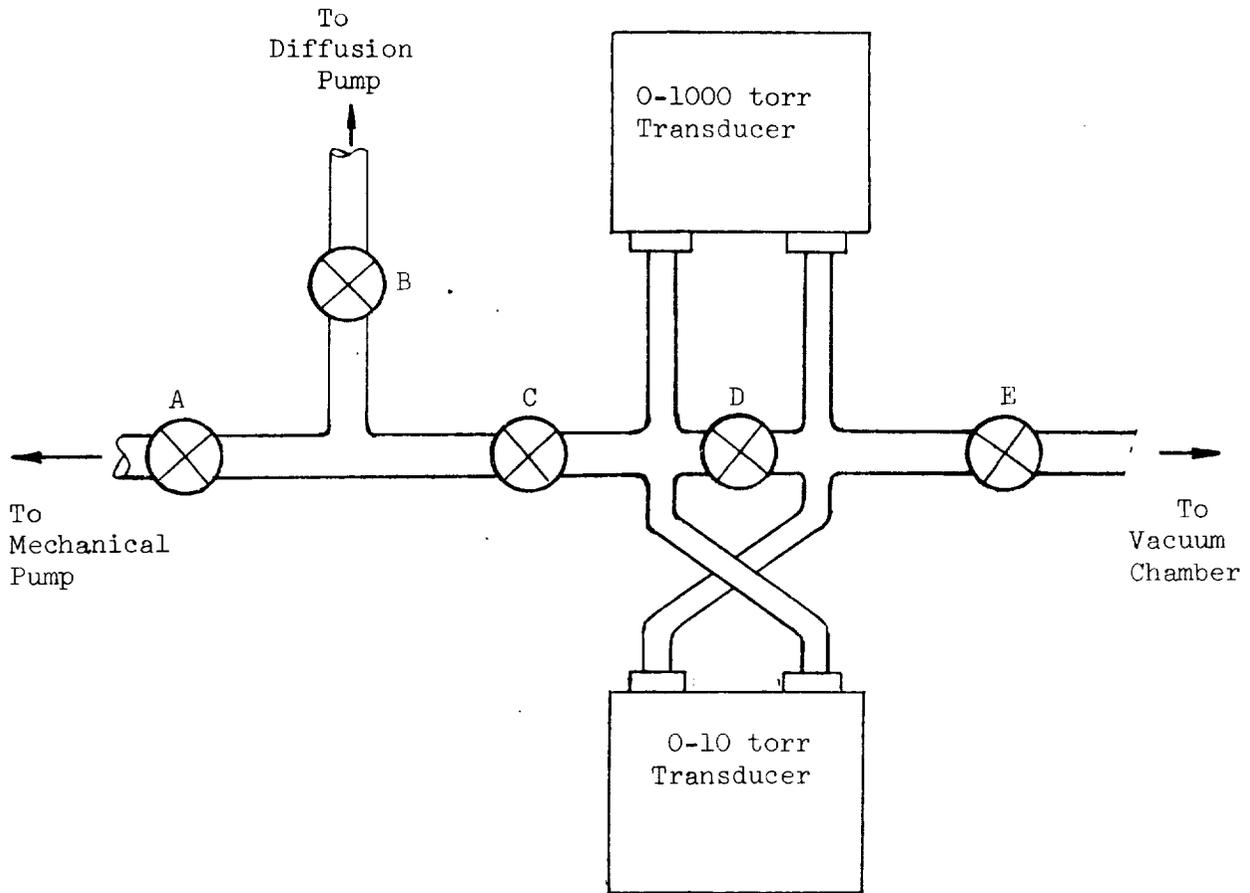
Normal Operation: B, C, and E Open
                   A and D Closed

Zeroing Operation: D Open
                   C and E Closed

Fig. 5-11 Schematic of Absolute Pressure Measurement System

Differential pressure across the insulation specimen was measured by a 0-10 torr Barocel transducer mounted inside of the vacuum chamber in order to keep the connecting lines as short as possible and thus achieve good pressure response in the free molecule regime. The transducer was mounted on a plate supported approximately 15.2-cm (6-in.-) above the sample assembly by four low-thermal-conductance supports. This thermal isolation was necessary in order

5-36

to achieve the desired operating temperature of approximately $46^{\circ}C$ ($115^{\circ}F$), while the sample was cooled to about $128^{\circ}K$ ($230^{\circ}R$) for some of the tests. One of the transducer ports was connected to the pressure tap hole in the center of the upper sample plate by a 0.159-cm- (0.0625-in.-) I.D. stainless steel tube approximately 15.2-cm (6-in.-) long. The other port was set up to communicate with the vacuum chamber through a short length of tubing and a needle valve. The flow resistance of this tube-valve combination was adjusted using a trial and error procedure in order to balance that of the measuring tube and thereby eliminate flow-induced pressure errors under dynamic conditions.

5.2.3 Experimental Procedures and Uncertainties

5.2.3.1 <u>Checkout Procedures</u>. Prior to initiation of the Task 2 test program, a number of preliminary system checkout tests were performed. First, the integrity of the vacuum chamber was verified and the evacuation rate produced by the pumping system was investigated. The chamber was evacuated by the mechanical pump several times in succession after back filling with each of the three purge gases to be used in the tests (i.e., argon, helium, and nitrogen). Because of the short, large-diameter line which connects the chamber with the pump, the evacuation rate was found to be virtually identical for all three purge gases, as shown in Fig. 5-12. Also, it was determined that initiation of the evacuation process by hand-opening of the valve in the pumping line did not introduce significant variations in the pressure-time history. Opening of the valve requires approximately 1.5 sec. It was found from this preliminary test that the measured chamber pressure at any point in time was reproducible with ± 1 percent. Also, it was determined that the mechanical pump could reduce the chamber pressure to a value less than 0.010 torr in approximately 2.5 minutes. When the rate of pressure decay appeared to be decreasing, the valve connecting the diffusion pump with the system was opened. The ultimate evacuated chamber pressure was approximately 10^{-5} torr. This value was achieved soon after connecting the diffusion pump, and was probably limited by leakage into the system rather than by outgassing.

5-37
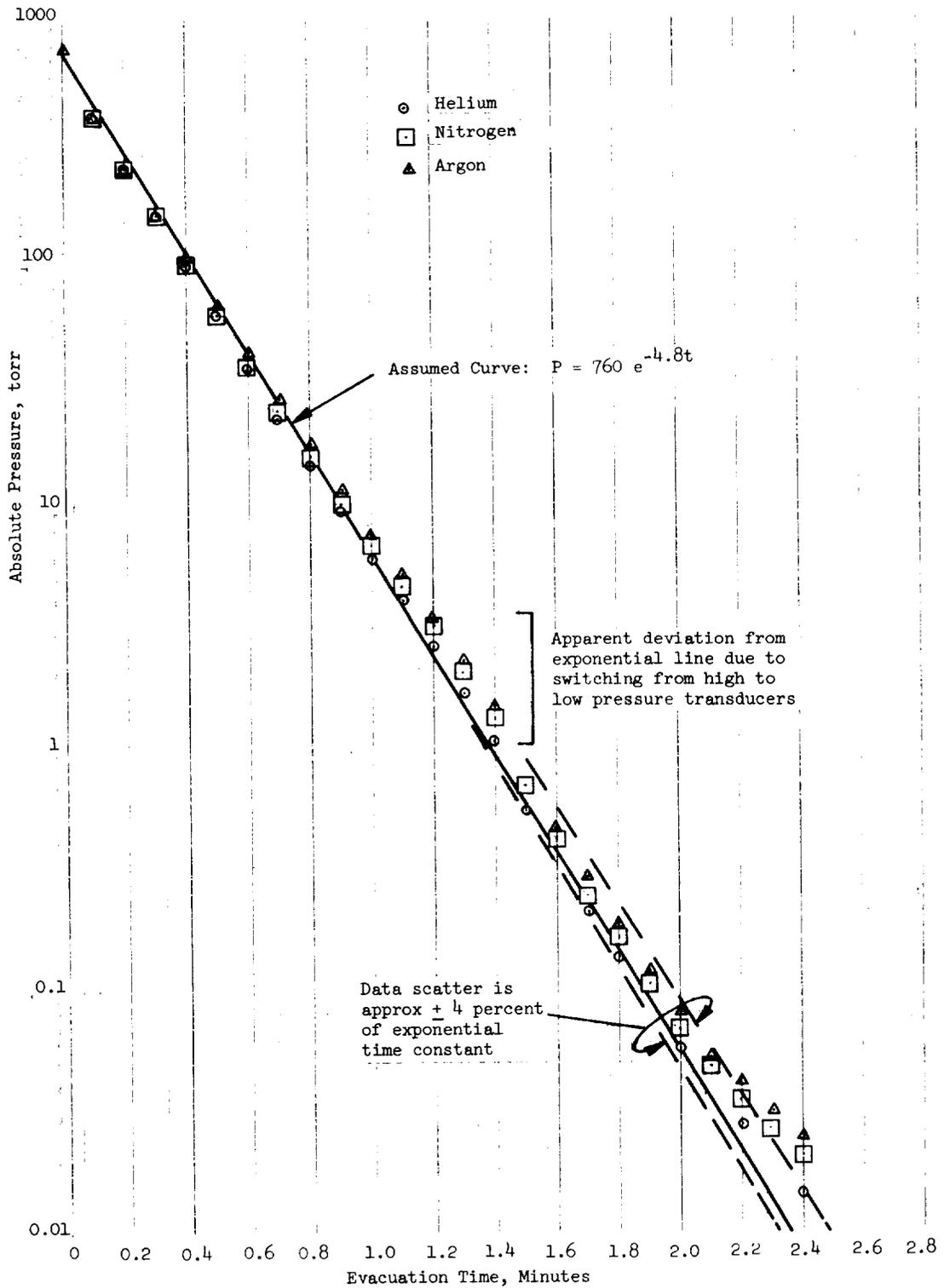
Fig. 5-12 Empty Vacuum Chamber Pressure History During Pumpdown

LOCKHEED MISSILES & SPACE COMPANY

Pressure data below 0.010 torr were not plotted in Fig. 5-12, although these data are contained in Appendix B. Since the primary objective of the Task 2 work was to compare analytical predictions with experimental data, and since these comparisons can all be made for pumping times less than 2.5 minutes, predictions for longer times or lower pressures (where flow conductance becomes constant) are unnecessary.

It was found that some adjustments were necessary in order to match the d.c. analog output from the Barocel transducer control box to the requirements of the stripchart recorder. A voltage divider was used for this purpose. In addition, a procedure was developed for recording the chamber pressure history during the early portion of the evacuation when the rate of pressure decay was high. Prior to pumping, the transducers were balanced and zeroed with the chamber pressure at 760 torr. Before an evacuation was initiated, the stripchart was operated in order to check the ink flow. The evacuation was then initiated by rapidly opening the hand valve to the mechanical pump. During the pumpdown, it was necessary for an operator to stand by the control box in order to select the proper output scale as the pressure was reduced. The Barocel has output scales of X1, X0.3, X0.1, X0.03, X0.01, X0.003 and X0.001. Thus, to obtain the maximum output signal (and accuracy) the scale was reduced whenever the signal fell below approximately 1/3 of full scale on the meter. The recorded output on the stripchart thus describes a saw-tooth pattern. When the pressure was reduced below 10 torr, the control box was switched from the 1000-torr transducer to the 10-torr transducer, necessitating that the scale switch be returned to the X1 scale. Since the absolute pressure-time history was a nearly perfect exponential curve, it was not difficult to determine which scale and/or transducer corresponded to any given portion of the trace. The NRC ionization gauge was used to measure pressures below 10^{-4} torr. When adjusted independently, according to the manufacturer's instructions, the ionization gauge indicated approximately 85 percent of the Barocel reading for pressures near 10^{-3} torr. Because the ion gauge is dependent on the gas species, it was decided to adjust its reading to coincide with that of the Barocel at a pressure of approximately 10^{-3} torr in order to read and record consistent data.

5-39

The most significant measurement obtained in Task 2 was the differential pressure across the insulation. Therefore, considerable effort was devoted to an investigation of the performance of the Barocel differential transducer for this application.

The transducer is usually operated with the body at atmospheric pressure. Two tests were conducted to compare the behavior of the transducer when exposed to atmospheric and high-vacuum environments. For these tests, the two ports of the transducer were manifolded together and a short tube was connected through a tee fitting into the manifold midway between the ports. Thus, the flow paths from either port along the manifold and through the tube were identical. In the first of these tests, the transducer and manifolding were placed outside of the vacuum chamber with the connecting tube passing into the chamber using a regular o-ring feedthrough. The transducer was initially zeroed and the chamber was evacuated. The output data of the transducer as obtained from this test are plotted as a function of absolute pressure in Fig. 5-13, curve A. Assuming that the two flow paths from the transducer ports were identical, this output is due either to a pressure-dependent zero shift or to a difference in void volume on the two sides of the diaphram. Whatever the explanation, the effect is systematic and will remain constant so long as the evacuation rate does not change. In the second test, the transducer, including manifolding, was placed entirely within the chamber and the evacuation was repeated. In this second case, the interior of the transducer diaphragm assembly experienced the same effects as those imposed during the first test, but the exterior of the body and the electronic components were subjected to the lower pressure environment. The data obtained from this test are shown in Fig. 5-13, Curve B. From these data, it can be seen that (a) the zero shift is minimal in both case, decreasing to less than 10^{-3} torr below an absolute pressure of approximately 5 torr, and (b) the effect of locating and operating the transducer totally within the vacuum chamber is to displace the zero error by a nearly-constant negative 0.001 torr over the entire pressure measurement range.

5-40
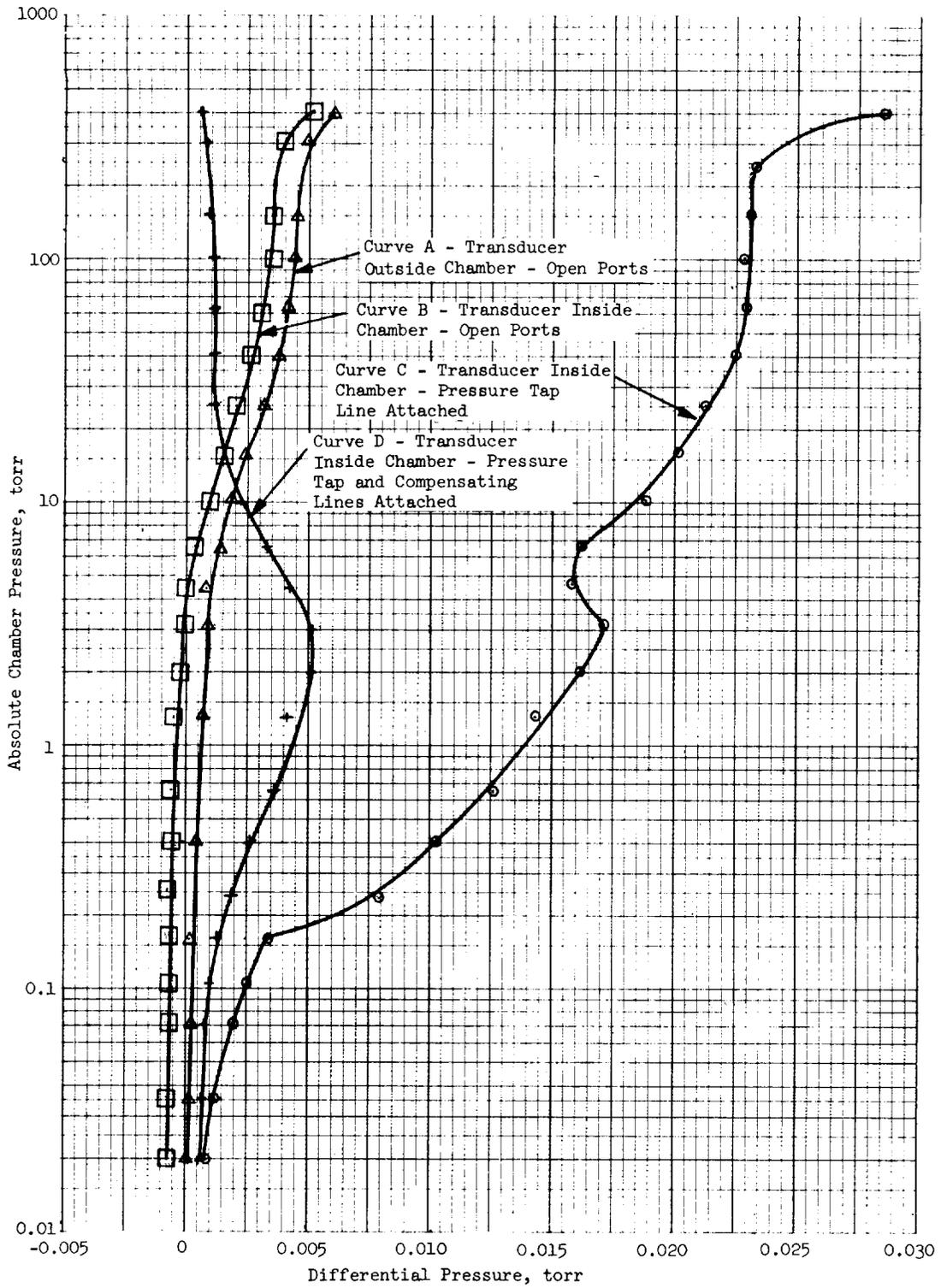
Fig. 5-13 Comparison of Differential Pressure Transducer Zero Offset with
No Sample in Place

5-41

From these two preliminary tests, it was concluded that the basic pressure-dependent zero shift was minimal, and that the effect of operation within a vacuum environment was also minimal and, in fact, tended to reduce the effect of the zero shift.

During the next preliminary test, the transducer was installed in its intended position on the upper boundary plate with the 15.2-cm-(6-in.-) long sensing line connected between the high-pressure transducer port and the tap hole in the center of the plate. Again, the chamber was evacuated and the data obtained are plotted in Fig. 5-13, Curve C. It can be seen that the influence of the sensing line resistance is considerable, introducing an apparent zero error on the order of ten times greater than that of the inherent zero shift. In order to minimize this effect, a compensating line was attached to the low-pressure side of the transducer. Because of the practical difficulty of precisely matching the two lines, the compensating line was cut slightly short, and a needle valve was installed in order to permit adjustment of the flow resistance and thereby achieve a better balance. This needle valve was adjusted by trial and error until a minimum transducer imbalance was observed at the beginning of the evacuation. After making this adjustment, the empty chamber was again evacuated. The data obtained from this test are shown in Fig. 5-13, Curve D. It can be seen that the flow resistance of the compensating tube did, in fact, adequately match the resistance of the pressure tap (measuring tube) at both high and low pressure values. However, it did not completely compensate for the resistance of the measuring tube over the entire pressure range because the geometric dependence of orifice and tube resistances are different from each other in the continuum and free molecule flow regimes. Thus, it was not possible to balance the resistance of the compensating tube plus the orifice such that it was equal to the resistance of the measuring tube throughout both flow regimes. For the setup used in Task 2, a good balance was achieved in the continuum regime, with the mismatch occurring at the onset of free molecule flow. In retrospect, it would have been better to adjust the orifice for equality in the free molecule range. However, since the method used did achieve the major goal of reducing the imbalance to a negligible value, no further modification was required.

The basic adjustment required in order to operate this type of pressure transducer is the zero setting. With the pressure-sensing and reference-pressure ports interconnected in order to equalize pressures on the two sides of the diaphragm, the control box output is brought to zero using successively more sensitive scales. In using these transducers during Task 2, this adjustment was made prior to evacuation, with both sides at 760 torr. The pressure level was then reduced during the evacuation with the result that the zero position shifted. It would have been desirable to reset the zero at some lower pressure value. This could not be done by bringing the entire test chamber to pressure equilibrium since this would have defeated the purpose of the tests (i.e., to obtain data for a continuous, dynamic pumpdown). Two alternatives were considered: (1) to determine and perhaps tolerate the zero error which appeared at low pressures after zeroing the gauge at high pressure, or (2) to devise and construct a system for isolating the two sides of the transducer from the remainder of the apparatus at low pressure, and then to use it to bring them into communication to equalize the pressures and permit rezeroing during the evacuation. In the Task 2 tests, the first alternative was selected with regard to the internally-mounted differential transducers, since the primary goal of this task was to correlate the analytical flow model with the test data, and this could be accomplished in this manner without difficulty. The second alternative was used in the case of the absolute pressure transducer, which was mounted external to the vacuum chamber. It was concluded at that time, however, that it would be necessary to develop a low-pressure rezeroing device to use with the internal transducers during the Task 3 tests, since these tests would be of longer duration with a greater chance of zero drift, and greater accuracy would be required.

Inspection of the data obtained in Task 2 indicates that at high and medium pressures there was a very high degree of reproducibility between the differential pressures for nominally identical evacuations. This reproducibility was limited only by the accuracy with which data could be extracted from the recorder chart paper. As the pressure was reduced further, a divergence of the data appeared between these nominally identical cases. This scatter was consistently within the range of ±0.0005 torr. This is to say, the indicated

differential pressure after long evacuation times was within the range of
0.0 $\pm$0.0005 torr. For a transducer used in this manner (i.e., one zeroed
only at high pressure), the manufacturer claims an accuracy of 0.1 percent
of the reading plus 0.01 percent of the transducer full range. Thus, for
a differential pressure transducer with a full range of 10 torr, the manu-
facturer claims an accuracy at 10^{-3} torr of approximately $\pm$0.001 torr. The
data obtained in Task 2 shows that the accuracy attained was better than that
claimed by the manufacturer by a factor of approximately two. This accuracy
was quite adequate for the Task 2 work where the primary emphasis was upon veri-
fication of the analytical model.

5.2.3.2 <u>Test Procedure</u>. For each of the selected MLI test specimens (Ref
Table 5-2), the experimental procedure employed in Task 2 was virtually identi-
cal. This procedure consisted of the following steps:

(1) Subsequent to an initial evacuation (or following a previous test),
the vacuum chamber pressure was increased to one atmosphere using
the particular purge gas (i.e., argon, nitrogen, or helium) speci-
fied for the next planned test.

(2) The chamber was opened, if a new specimen was to be installed or
if the layer density of a specimen already installed was to be
adjusted, and the necessary operations were performed. This part
of the procedure nominally required from 15 to 30 minutes, during
which time all portions of the chamber, the apparatus, and the
specimen were exposed to the ambient atmosphere.

(3) Both the absolute and the differential pressure transducer systems
were then zeroed. The two stripchart recorders were checked and
adjusted to obtain zero and fullscale deflections in accordance
with the control box output. The recorders were switched on to
verify proper ink flow through the pens. Both control box scale
multipliers were adjusted so as to obtain a suitable deflection (i.e.,
between one-third and full scale) for the values anticipated at the
beginning of the test. A notation was made directly on each of the
strip charts indicating the date, the specimen number, the purge

gas, and the number of the particular pumpdown for that specimen (e.g., 1st, 2nd, 3rd).

(4) The test was initiated with the vacuum pumps operating and with both recorders in motion. The main valve connecting the mechanical pump with the chamber was opened, and a timer was started simultaneously. (This timer was used to record evacuation times greater than 2 to 3 minutes after which the stripcharts were stopped). The test operator was positioned directly in front of the control boxes for both the absolute and differential measurement systems so that he could adjust the scale multipliers as required during the pumpdown. After approximately two to three minutes of evacuation, the absolute pressure in the chamber was decreased to the low-pressure limit of the mechanical pump. The procedure subsequent to this point in time depended upon whether the particular test was the first pumpdown of a newly-installed sample, or was the second or subsequent pumpdown of a specimen previously evacuated.

(5) If the test was the first evacuation of a newly-installed sample, the gas flow in the multilayers after approximately two minutes of pumping time was due entirely to outgassing. For this case, the rate of decrease of the differential pressure was governed primarily by the rate of decrease in outgassing. At this point, the valve connecting the diffusion pump with the system was opened, and the stripchart recorders were switched to a low operating speed. Evacuation was continued in this manner for approximately 24 hours. However, shortly after the diffusion pump was activated, the absolute pressure nominally decreased to a value below 10^{-3} torr, and the ionization gauge was switched on. At this point in time the Barocel absolute pressure measurement system was switched off and further absolute pressure readings were obtained manually from the ionization gauge.

(6) If the test was a second or subsequent pumpdown, the insulation was ordinarily outgassed sufficiently already so that the pressure

5-45

differential due to the remaining outgassing load was less than 10^{-3}torr. Thus, it was not detectable by the differential Barocel transducer, without rezeroing, and the evacuation test was then terminated.

(7) Subsequent to completion of each particular test run, the chamber pressure was raised back to one atmosphere with the appropriate purge gas (i.e., that selected for the next evacuation). Particular combinations of purge gas, specimen number, and temperature were repeated until two consecutive tests produced essentially coincident data. Generally, this required three separate evacuations; the first in the off-shelf condition, the second in a degassed or outgassed condition, and the third also in a degassed condition to confirm the second.

5.2.4 Specimen Preparation

For most of the Task 2 experiments, the multilayer shields and spacers were cut individually to obtain 68.6-cm- (27-in.-) diameter circular specimens. For two particular edge-pumping test series during which the effect of diameter was investigated, the samples were cut to obtain 50.8-cm (20-in.) and 38.1-cm (15-in.) diameters. A 0.318-cm-(0.125-in.-) diameter hole was punched at the center of each edge-pumping specimen layer. Test specimens were then assembled by stacking the desired number of alternate reflective shields and spacers, taking great care to maintain concentricity. In the case of the edge-pumped samples, a central guide pin was used to assist in this process. After stacking, several light spring clips and pads were placed around the edges of the stack in order to maintain geometry while the sample was transported and mounted between the boundary plates within the vacuum chamber. Where possible, shields and spacers were reused in succeeding specimens in order to conserve material.

No special storage procedures were used for the insulation stock or for the prepared samples. Using the test procedure described previously, the samples

5-46

were subjected to several recorded evacuations. The first of these evacuations thus relates to "as received" insulation stored and handled in a normal laboratory atmosphere.

5.2.5 Experimental Results

The basic experimental data obtained during the Task 2 tests were chamber absolute pressure and differential pressure across the insulation, measured as functions of time. As noted previously, during early evacuation times, these measurements were obtained using stripchart recorders. At later times, when the pressure variation rate had diminished, the data were taken manually. Typical stripchart output records are presented in Fig. 5-14. These charts are for Specimen No. 4 at $300^{\circ}K$ ($540^{\circ}R$). The purge gas was helium. Fig. 5-14(a) shows the absolute pressure-time history. The 1000-torr absolute pressure transducer was set on the X1 scale at the beginning of the test. As the evacuation proceeded, the scale multiplier was switched successively to the X0.3, X0.1, X0.03, X0.01 and X0.003 scales. At this point, the 1000-torr transducer was replaced by the 10-torr transducer, and the scale multiplier was switched back to X0.3. Again, as the pressure decreased below 1 torr, the scale multiplier was switched to the 0.1, 0.03, 0.01, 0.003 and 0.001 scales. No data are shown in the figure for pumping times after approximately 1.6 minutes, when the absolute pressure had been reduced to a value of approximately 0.38 torr. However, the actual stripchart record was not terminated until after the absolute pressure was reduced to a value below 0.01 torr. At this point in time, the stripchart recorder was stopped, the diffusion pump was connected to the system, and further data were obtained manually.

Fig. 5-14(b) shows the differential pressure-time history for the specimen in the off-shelf condition (i.e., during its first evacuation). The 10-torr differential pressure transducer was set on the X0.1 scale before initiating the evacuation. Here, the multiplier range was selected on the basis of prior experience. At the beginning of the evacuation, the differential pressure rose rapidly to a peak and then decayed to a nearly constant but

5-47
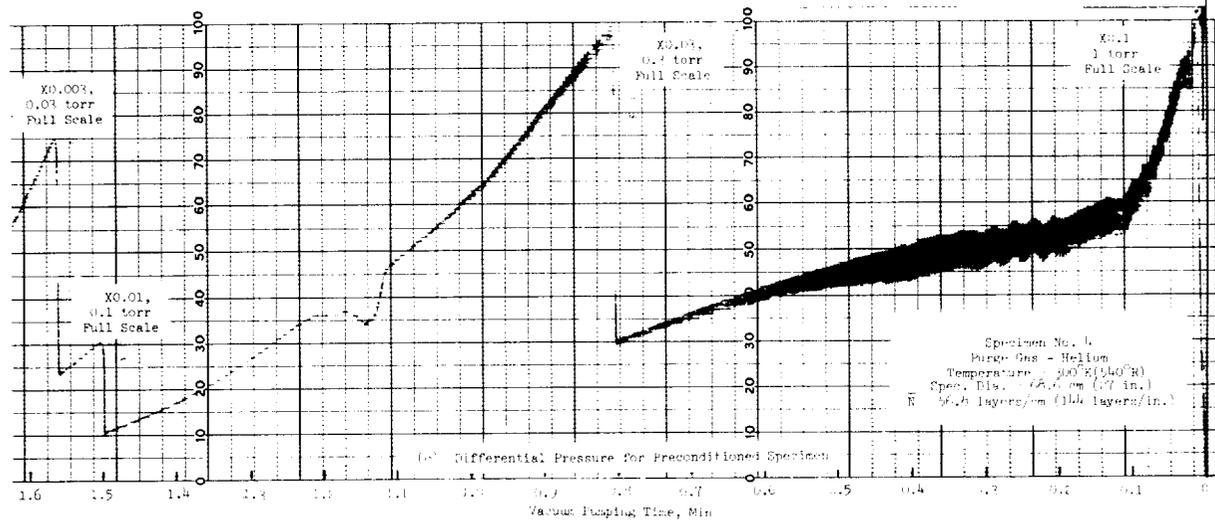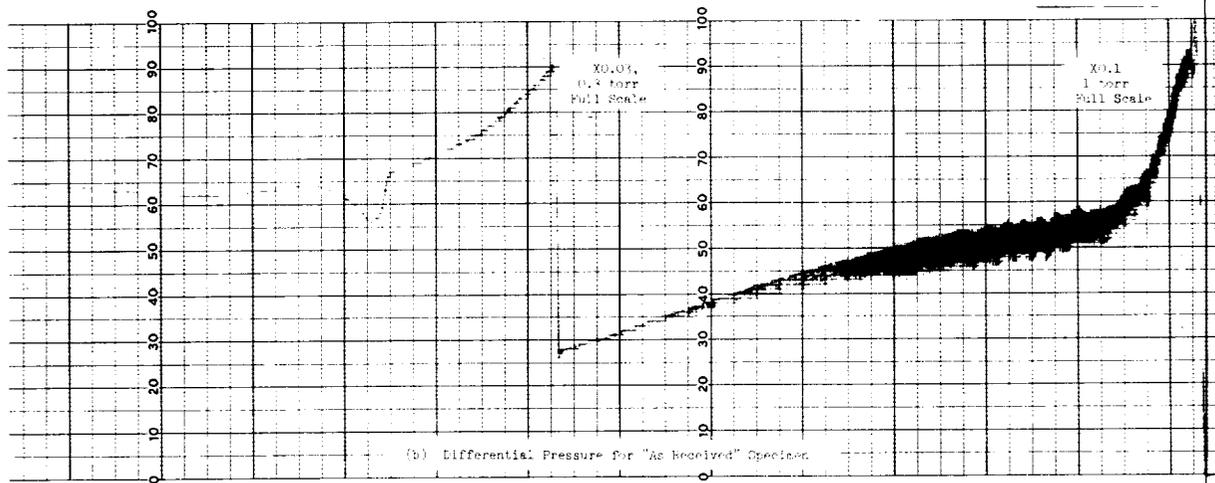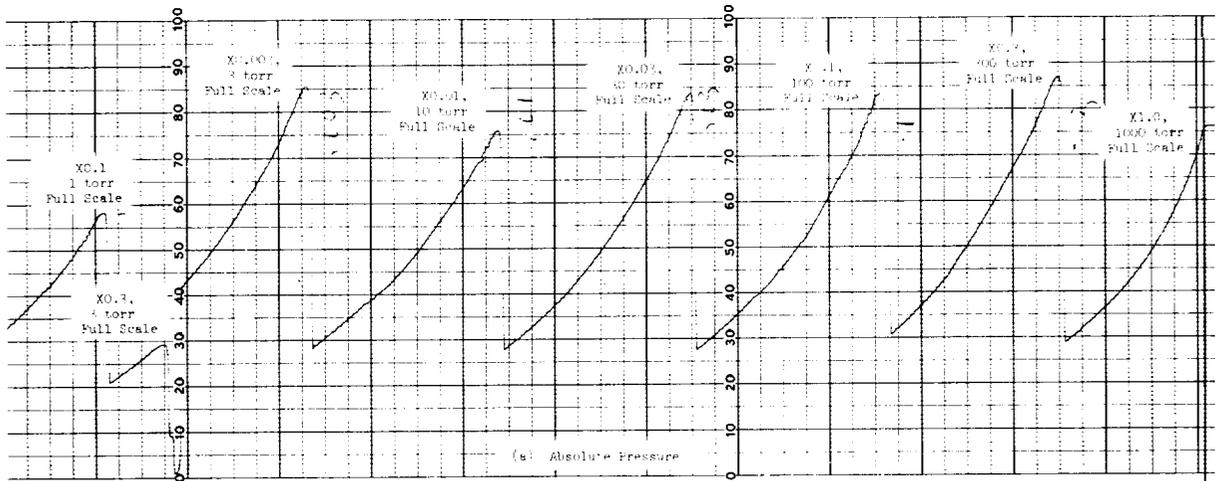
Fig. 5-14   Typical Stripchart Records as a Function of Time

LOCKHEED MISSILES & SPACE COMPANY

slowly diminishing value. Up to approximately one minute of evacuation time, the pressure oscillation induced in the chamber by the opening and closing of the reciprocating pump inlet valve is clearly shown. After approximately one minute of pumping time, the differential pressure began to decay, requiring switching to the X0.03 multiplier, and the trace became steadier as the absolute pressure was reduced. However, because of the initiation of outgassing with the reduction of the absolute pressure, the differential pressure ceased to diminish rapidly. At this point in time, the stripchart recorder was stopped and further data were taken manually. There was a very marked dip in differential pressure at a pumping time of about 12 minutes (not shown in the figure). This type of minimum was observed in all of the Task 2 data. It was most pronounced for helium, and less so for nitrogen and argon. A similar minimum was observed for the preliminary test without an insulation specimen in place, but it was much less pronounced. The minimum occured just before the flow enters the free molecule regime. Published data (Ref 26) have indicated that a minimum in conductance can be expected in this region, but the effect observed here indicates that a maximum in conductance was realized rather than a minimum. It is concluded that the effect is somehow related to the anamalous behavior previously observed at the high pressure end of the free molecule regime; however, a precise explanation cannot be advanced at this time.

Fig. 5-14(c) shows the differential pressure as a function of time for the specimen in a preconditioned state (i.e., with negligible outgassing). As shown, the pressure differential during the first minute of evacuation was virtually identical to that shown in Fig. 5-14(b), but at later times it continued to decrease rapidly to a constant value of about 5×10^{-4} torr. In fact, the accuracy of the transducer at low pressures following zeroing at high pressure is, according to the manufacturer, about $\pm$ 0.001 torr. Operating experience tended to confirm this figure. Thus, any data curve falling below 0.001 was automatically assumed to have reached zero within the accuracy of these measurements.

All of the data for all of the tests showed the same major characteristics as are shown in Fig. 5-14. It is possible to explain these characteristics semi-quantitatively, as follows.

The chamber was evacuated by a mechanical pump which is essentially a constant volume flow device over most of its pressure range. The continuity equation for evacuation of the chamber can thus be written

$$- \frac{V_c M}{R^o T} \frac{dP}{dt} = (\text{volumetric evacuation flow rate})(\frac{PM}{R^o T}) \qquad (5\text{-}45)$$

which implies that $(1/P)dP/dt$ = constant. This should result in an exponential pressure decay rate which is essentially independent of the gas being pumped (the nature of the gas affects only the flow resistance in the connecting lines, which was very low in this case, and the effect of recompression in the pump). The data confirm this fact. The absolute pressure data as a function of time are straight lines on a log-linear plot, and are within $\pm$ 4 percent for all purge gases (Ref Fig. 5-12).

It can be deduced from Section 5.1 that the flow conductance of any flow path can be written in the form $(A + BP)$ where A and B are constants. For the evacuation of the insulation, the pressure differential is very small and the pressure in the insulation is always very nearly equal to the pressure in the chamber. Therefore, it is possible to write an approximate continuity equation for the insulation as follows

$$- (\frac{V_I M}{R^o T}) \frac{dP}{dt} = (A + BP) \; \Delta P \qquad (5\text{-}46)$$

where V_I is the volume of the interstitial dead space. Since $(1/P)dP/dt$ is constant, according to the previous paragraph, it follows that

$$\left[\frac{A + BP}{P} \right] \Delta P = \text{a constant} \qquad (5\text{-}47)$$

and
$$\Delta P \cong \frac{P}{A \; + \; BP} \qquad (5\text{-}48)$$

When P is large, ΔP is essentially constant. When P is small, ΔP is proportional to P (i.e., it decays exponentially). Again, this behavior is observed in the data, with a single, notable departure. At the beginning of the evacuation, the differential pressure was higher for about four seconds. This was due to the large void volume in the evacuation line between the chamber valve and the pump inlet. When the valve was first opened, the chamber experienced a faster than equilibrium evacuation rate due to filling of this volume.

Experimental data obtained during Task 2 for each of the specimens described in Table 5-2 are presented in tabular form in Appendix B. The data are discussed and effects of each major test parameter are evaluated in the following section.

5.3 CORRELATION AND APPLICATION OF RESULTS

The foregoing sections describe the considerable amount of detailed analysis and testing performed under Task 2. The following paragraphs present and discuss a correlation of the results of these activities, a brief evaluation of the overall findings of Task 2, and the application of the gas evacuation analysis to the design of the Task 3 experiment, in particular, and to MLI systems in general.

5.3.1 Comparison of Analytical and Experimental Results

In order to assess the worth of the analysis, the predictions obtained from it must be compared with actual experimental data. In Task 2, the experimental variables were layer density, flow path length, purge gas species, temperature, perforation pattern, evacuation mode, insulation type, initial condition at test (i.e., "as received" or preconditioned), and evacuation time. The total number of different combinations of these test variables in the Task 2 work was considerable. An attempt to correlate the analysis with all of these cases would have consumed excessive computer time and, in addition, would have required some statistical analysis in order to isolate the effects of experimental uncertainties in each of the variables. This approach was avoided because of the excessive time and cost requirements* with very limited potential benefit. Instead, a systematic approach was used which quite adequately served the intended purposes of evaluating the data and of verifying the analytical models.

The general capability of the multiple-node analysis to predict differential pressure-time histories during evacuation is shown in Figs. 5-15, 5-16, and 5-17 for three typical cases. These data were obtained for two similar

---

* Computation time in the Task 2 analysis was inversely proportional to the maximum time step, ΔT, with the latter defined by Eq (5-11). Since ΔT is proportional to layer density squared, the total computation time required was excessive at the lower layer density values (i.e., 10 minutes to 1 hour per case for $\bar{N} < 39$ layers/cm, 100 layers/in.)

LOCKHEED MISSILES & SPACE COMPANY
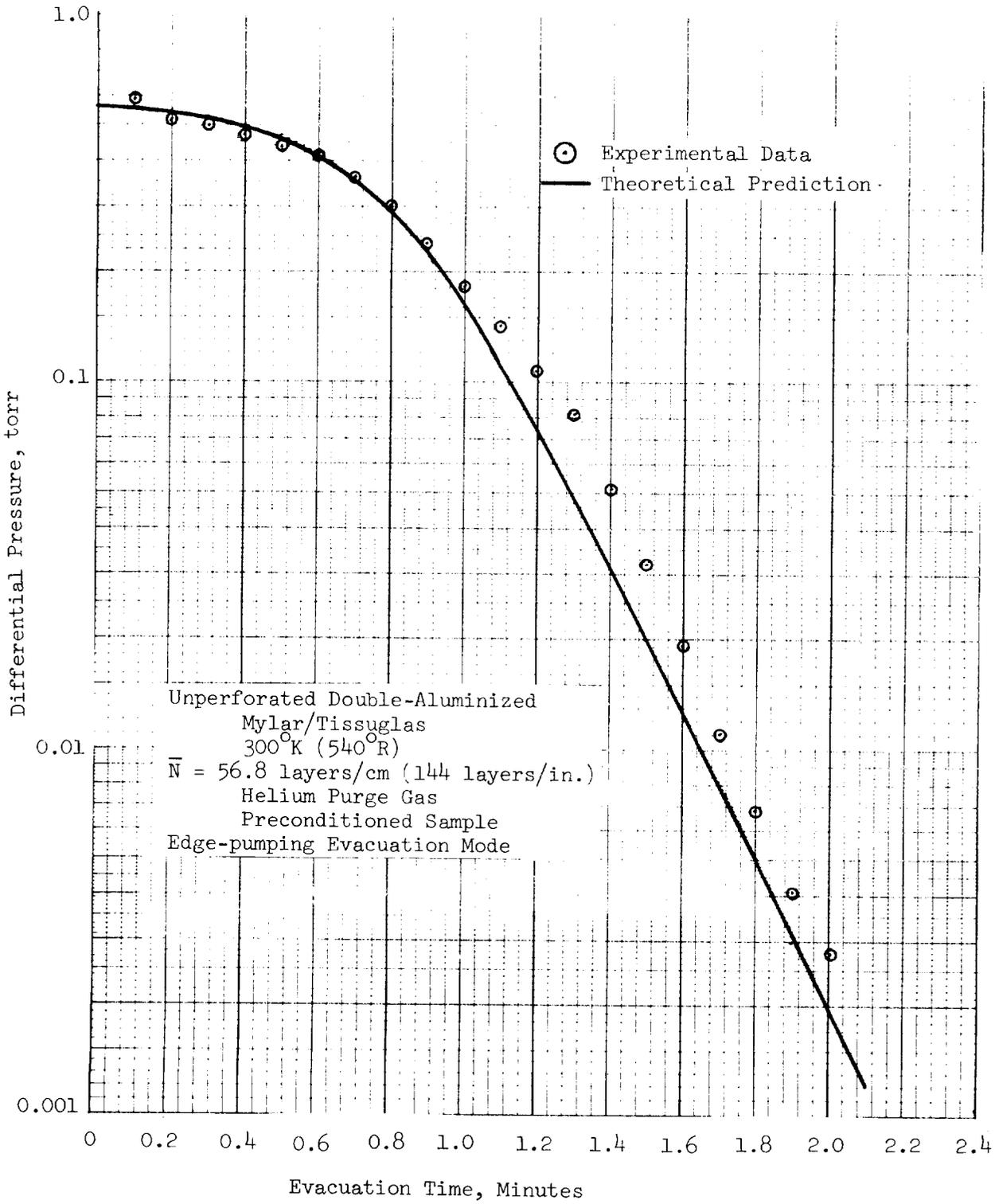
Fig. 5-15 Comparison of Analytical Prediction with Experimental Data for Specimen No. 4
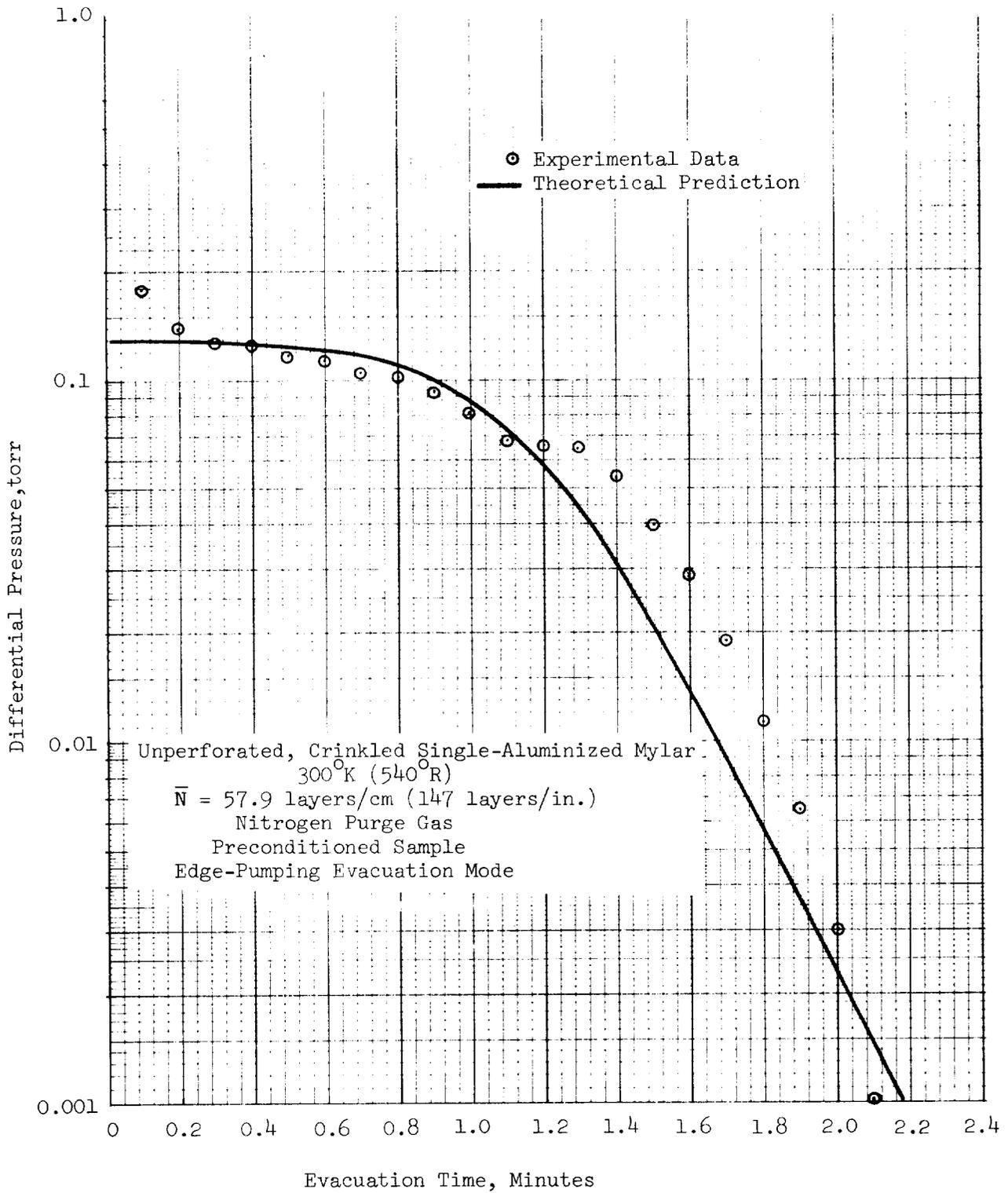
Fig. 5-16   Comparison of Analytical Prediction with Experimental Data for Specimen No. 21C

LOCKHEED MISSILES & SPACE COMPANY
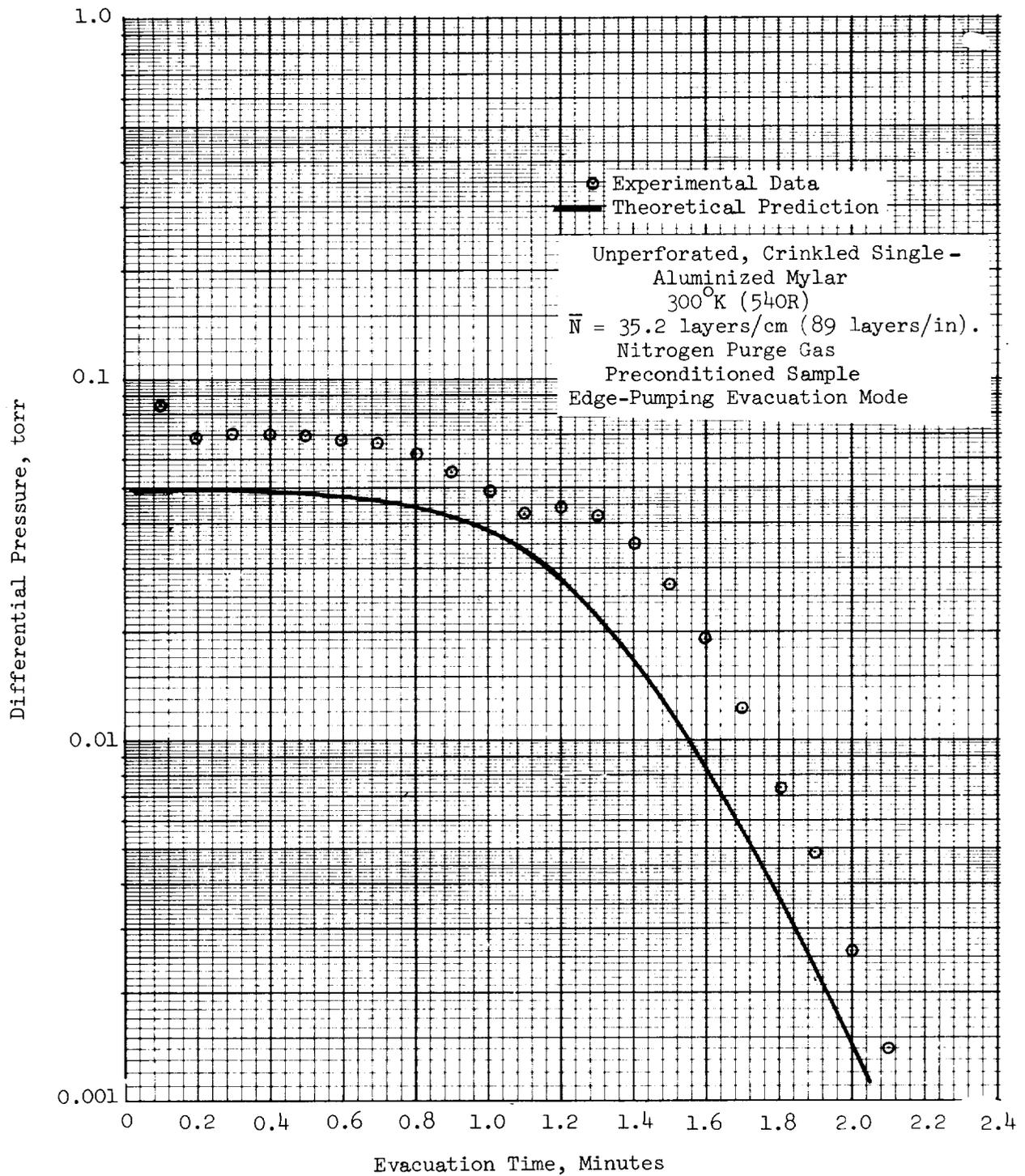
Fig. 5-17   Comparison of Analytical Prediction with Experimental Data for Specimen No. 21B

LOCKHEED MISSILES & SPACE COMPANY

layer densities with different purge gases, and for two different layer densities with the same purge gas. The experimental data were obtained from the tabulations of Appendix B. It can be readily seen that the qualitative agreement is generally good, and that the quantitative agreement improves as the layer density increases. The layer density effect is discussed in more detail later in this section. It was expected that the higher compressive loadings at the higher layer densities would create more contact points, thus causing an increase in the spring constant and reducing the tendency of the MLI system to form channels. With more uniform spacing, better agreement of the analytically-predicted and the experimental data was inevitable, since the analytical model assumes equal spacing.

In assessing the degree of correlation between the experimental and the analytically-predicted pressure differential histories, two important factors should be considered. First, the experimental data represent an early, if not the first, attempt to measure interstitial pressures for MLI as a function of time. Moreover, the plotted data have not been smoothed or otherwise processed. Second, the analytical procedure used is highly elementary inasmuch as an equally-spaced flat plate flow model has been assumed and a simple Newtonian integration technique has been used. It is noted that many obvious changes could be made to improve the model, such as use of an equivalent hydraulic diameter to account for the effect of spacers and crinkling. Also, a more sophisticated integration technique would undoubtedly increase the predictive accuracy. Nonetheless, although both the experimental data and the predictive technique could be significantly improved, the degree of correlation already obtained is most encouraging, and even now seems to be quite adequate for most engineering analysis.

It was noted at the beginning of this section that it was impractical to perform complete pressure-time history predictions for systems with low layer densities (i.e., $\overline{N} < 39$ layers/cm, 100 layers/in.) because of the excessive computer time required. Nevertheless, some comparison of the analytical and experimental data obtained for these lower layer density cases was desirable, and the following technique was devised. Using the analytical model, pressure

5-56

differential values at evacuation time zero were predicted for selected layer densities with a minimum of computer time. These predicted values are plotted in Fig. 5-18 as a function of layer density. The predictions were made for nitrogen purge gas at $300^\circ K$ ($540^\circ R$) with 68.6-cm- (27-in.-) diameter specimens. Also plotted in Fig. 5-18 are the experimental data for ΔP at time zero for the three selected types of insulation. These data were not actually measured at time zero, but were obtained by extrapolating the data for evacuation times greater than 0.2 minute back to time zero in order to exclude the initial transient effects which were not treated in developing the analytical model. In the Task 2 experiments, the evacuation rate was relatively high at time zero due to the influence of the previously evacuated volume of the line between the valve and the pump. Then, after the valve was opened, the evacuation rate quickly fell to a constant value characteristic of the pumping system conductance. The evacuation rate used in the analysis was this constant value, the initial transient value being neglected. Thus, to compare the experimental and analytical data on a similar basis at time zero, the effect of the void-volume-induced transient must be eliminated from the experimental data by back-extrapolating the data for the constant evacuation rate to time zero. As shown, the predicted values are, in general, close to the back-extrapolated experimental values. For one specimen of the double aluminized Mylar/Tissuglas system (i.e., Specimen No. 1), there appears to be no variation of initial ΔP with layer density. This apparent anomaly was probably caused by a channeling effect (i.e., a local non-uniform separation of the layers at one interlayer cavity). This result is discussed further later in this section. This material system was tested again as Specimen No. 4, using helium purge gas. The data for Specimen No. 4 also have been plotted in Fig. 5-18 after being corrected for the slight viscosity difference between nitrogen and helium. As shown, they were in good agreement with the prediction. It is seen again in Fig. 5-18 that the agreement of the experimental data with analytical predictions is better at the higher layer densities probably because the greater restraint upon the layers at the higher loadings reduces deviations from the flat plate model. It was also noted in evaluating the data shown in Fig. 5-18 that the analytical-experimental agreement is poorest for the insulation types which least resemble

5-57
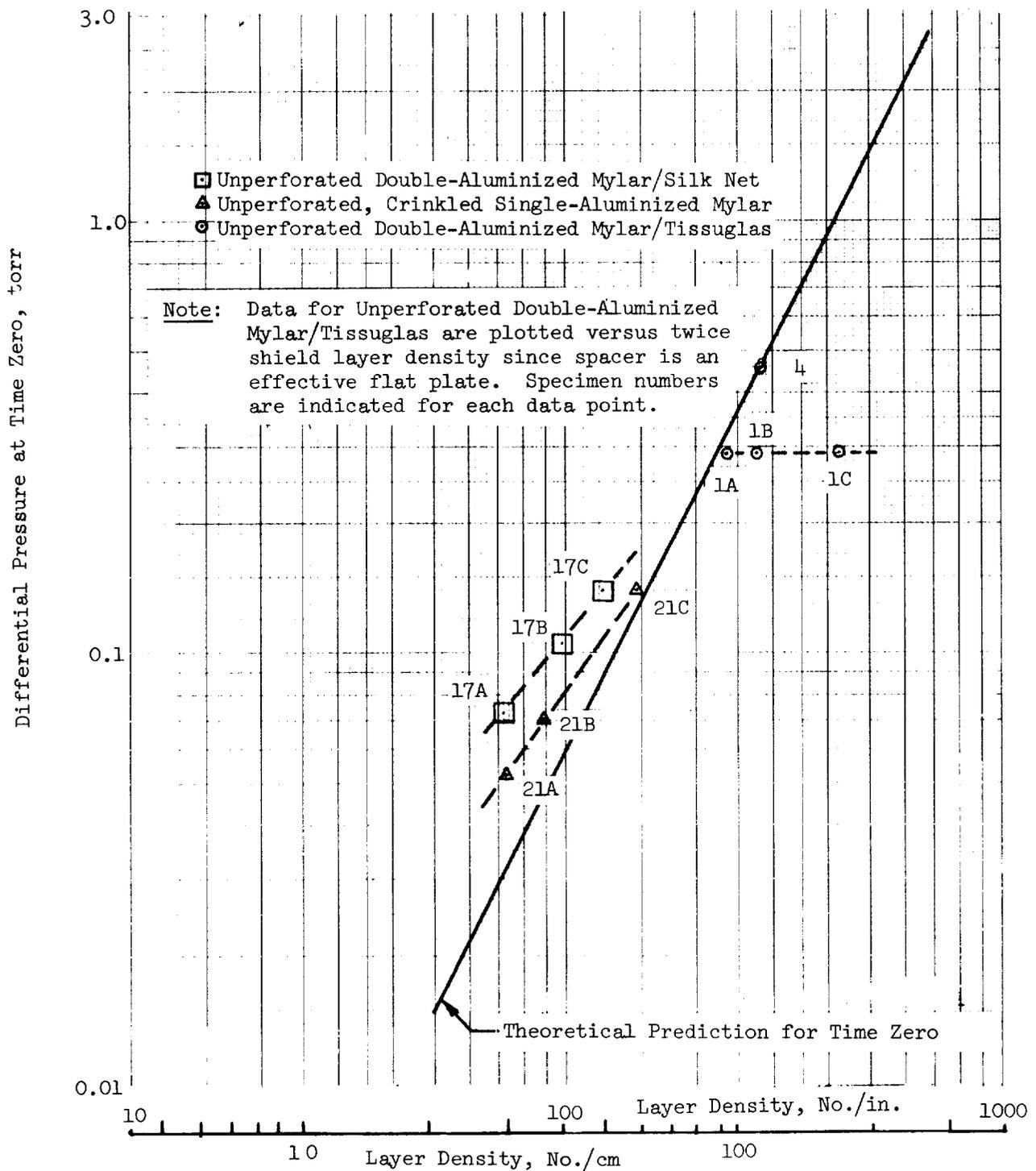
Fig. 5-18 Comparison of Analytically-Predicted and Experimental Data for Evacuation Time Zero

flat plates (i.e., double-aluminized Mylar/silk net and the crinkled, single-aluminized Mylar systems). This result is also discussed further later in this section.

The application of the full numerical analysis requires that the flow volumes and flow paths be subdivided into multiple smaller nodal elements. The governing equation is a general continuity equation describing the accumulation and flow into and out of a particular nodal volume. The parameters shown in the equation are pressures, the ratio of mass capacity to mass conductance for the node, the outgassing rate, and time. In principle, this equation can be written for a single-node system, in which the nodal mass capacitance (volume) equals that of the entire flow path, and the mass conductance is assessed from a mean point within the volume to the exterior. It can be shown that analysis of such a single-node system exhibits the same general dependence on the capacitance-to-conductance ratio and outgassing rate as the multiple-node case, but simply does not provide as accurate absolute values of pressure as a function of time. However, it is possible to investigate the influence of those parameters which affect the capacitance or conductance ratio or the outgassing rate by analysis using the single-node system. In the Task 2 data correlation, a single algebraic equation was written, and the resulting single-node approximation (hereinafter referred to as the simplified evacuation model) was used to assess the influence of all parameters other than time.

In applying the simplified evacuation model to the case of edge evacuation, the volume to be evacuated is the entire volume between two layers. The conductance from this volume to the exterior is based upon the distance between the average radius, $2/3\ r_o$, and the outer radius, r_o (average radius is defined as the integral of the area-radius product divided by the area). Thus, the simplified evacuation model equation for the edge-evacuation case can be expressed as

$$\left(\frac{2z_o\ \pi\ r_o^{\ 2}}{R^o\ T}\right)\ \frac{M dP}{dt} = -\ \Delta P\ \ C \tag{5-49}$$

5-59

where $C = \left(\dfrac{4\pi z_o^3}{3\mu}\right)\left(\dfrac{\overline{PM}}{R^oT}\right)\left[1 + \dfrac{4\mu v_a}{z_o P}\right]\Big/ \ln(3/2)$ 　　　　　　(5-50)

Combining these equations, and solving for the pressure differential yields

$$\Delta P = \left(\dfrac{-1}{P}\right)\left(\dfrac{dP}{dt}\right)\dfrac{(1.5\ln 1.5)\,\mu\, r_o^2}{z_o^2\left[1 + \dfrac{4\mu v_a}{z_o P}\right]} \qquad\qquad (5\text{-}51)$$

The simplified evacuation model can also be applied to the case of broadside evacuation. For this case, the volume to be evacuated is equal to the area associated with one shield perforation, multiplied by the layer separation and by the total number of layers in the system, N_{LT}. The conductance is based on the distance from the mid-thickness of the system to the exterior.

Based on these considerations, the simplified evacuation model equation for broadside evacuation is

$$(2z_o)(N_{LT})\left(\dfrac{\pi d_h^2}{4F_o}\right)\left(\dfrac{M}{R^oT}\right)\dfrac{dP}{dt} = -\Delta P\, C \qquad\qquad (5\text{-}52)$$

where $C = \left(\dfrac{4\pi z_o^3}{N_{LT}3\mu}\right)\left(\dfrac{\overline{PM}}{R^oT}\right)\left[1 + \dfrac{4\mu v_a}{z_o P}\right]\Big/ \ln\left(\dfrac{2}{3}\sqrt{\dfrac{1}{F_o}}\right)$ 　　(5-53)

Therefore, $\quad \Delta P = \left(\dfrac{-1}{P}\right)\left(\dfrac{dP}{dt}\right)\left(\dfrac{3\mu}{8}\right)\left(\dfrac{N_{LT}^2 d_h^2}{z_o^2 F_o}\right)\dfrac{\ln\left(\dfrac{2}{3}\sqrt{\dfrac{1}{F_o}}\right)}{\left[1 + \dfrac{4\mu v_a}{z_o P}\right]}$ 　(5-54)

These simplified equations are used extensively later in this section in the discussion of the influence of flow path length, layer separation, temperature, purge gas species, perforation pattern, and the effect of outgassing on the experimental data.

The manner in which layer density, flow path length, purge gas species, temperature, perforation size and open area, evacuation mode, multilayer

5-60

type, and outgassing each influence the gas evacuation characteristics of an MLI system was investigated using the experimental results at the conclusion of the Task 2 effort. The tabular data of Appendix B have been plotted systematically in Figs. 5-19 through 5-40 in order to illustrate these influences.

Since vacuum preconditioning in effect precludes outgassing, and since outgassing is difficult to predetermine analytically, the parameters listed above were investigated primarily for preconditioned specimens. These effects are shown in Figs. 5-19 through 5-30. However, since all specimens were initially evacuated in an off-shelf condition, considerable initial pump down data were also obtained. These latter data are presented in Figs. 5-31 through 5-40.

In analyzing the data, it is noted that the chamber evacuation rate was the same for all tests conducted with the sample and the chamber at 300°K (540°R). Consequently, the chamber evacuation rate was not a variable in any of the tests except those specifically designed to assess the effect of variable sample temperature. For the latter tests, where the sample was maintained at temperatures well below 300°K (540°R), the gas near the sample was initially cooled, thereby increasing the total mass present. Then, during evacuation, the cold gas was heated, thus increasing the effective volume to be removed. Also, it should be noted that differential pressure values below 0.002 torr are to be disregarded in the interpretation of parametric influences, since the zero error was of this approximate magnitude for these tests.

5.3.1.1 <u>Effect of Layer Density</u>. It can be inferred from Eq (5-51) that the pressure differential that develops across an MLI specimen during evacuation is inversely proportional to the second power of layer separation in the viscous flow regime, and to the first power of layer separation in the free molecule regime. The effect of varying layer density was investigated in tests 1A, 1B, and 1C for double-aluminized Mylar/Tissuglas; tests 17A, 17B,

5-61

and 17C for double-aluminized Mylar/silk net; and tests 21A, 21B, and 21C for crinkled, single-aluminized Mylar. The data obtained from these tests are presented in Figs. 5-19, 5-20, and 5-21, respectively. The data presented are for nitrogen purge gas. Inspection of Fig. 5-19 shows that ΔP did not vary significantly with layer density for Specimen No. 1. Also, based on the data tabulated in Appendix B for this specimen, no variation in ΔP as a function of layer density was observed where helium and argon purge gases were used. However, for Specimens No. 17 and 21, the variation of ΔP with layer density was approximately that expected from the theory. Both of these latter specimen tests clearly show that at lower layer densities, the ΔP was constant for a longer period of time (i.e., to a lower absolute chamber pressure). This indicates that a lower pressure is required to achieve the onset of free molecule flow for lower layer densities and hence higher inter-layer separation values. This is to be expected since free molecule flow occurs when the molecular mean free path, which is inversely proportional to pressure, is greater than the interlayer separation.

It is postulated that the apparent anomaly observed for Specimen No. 1 was due to "channeling" (i.e., local separation of the layers) which occurred during evacuation of this sample. It can be shown that gas flow over irregular flat surfaces produces forces which tend to magnify small deflec-tions (e.g., the fluttering of a flag in the wind). For MLI systems, lateral deflection of the individual layers is resisted only by the presence of the adjacent layers. A measure of the resistance which develops is the spring constant of the total multilayer stack or blanket, which is very low for double-aluminized Mylar/Tissuglas compared to either double-aluminized Mylar/ silk net or to crinkled, single-aluminized Mylar. This explains why the channeling effect was observed for Specimen No. 1, but not for Specimens No. 17 or 21.

LOCKHEED MISSILES & SPACE COMPANY
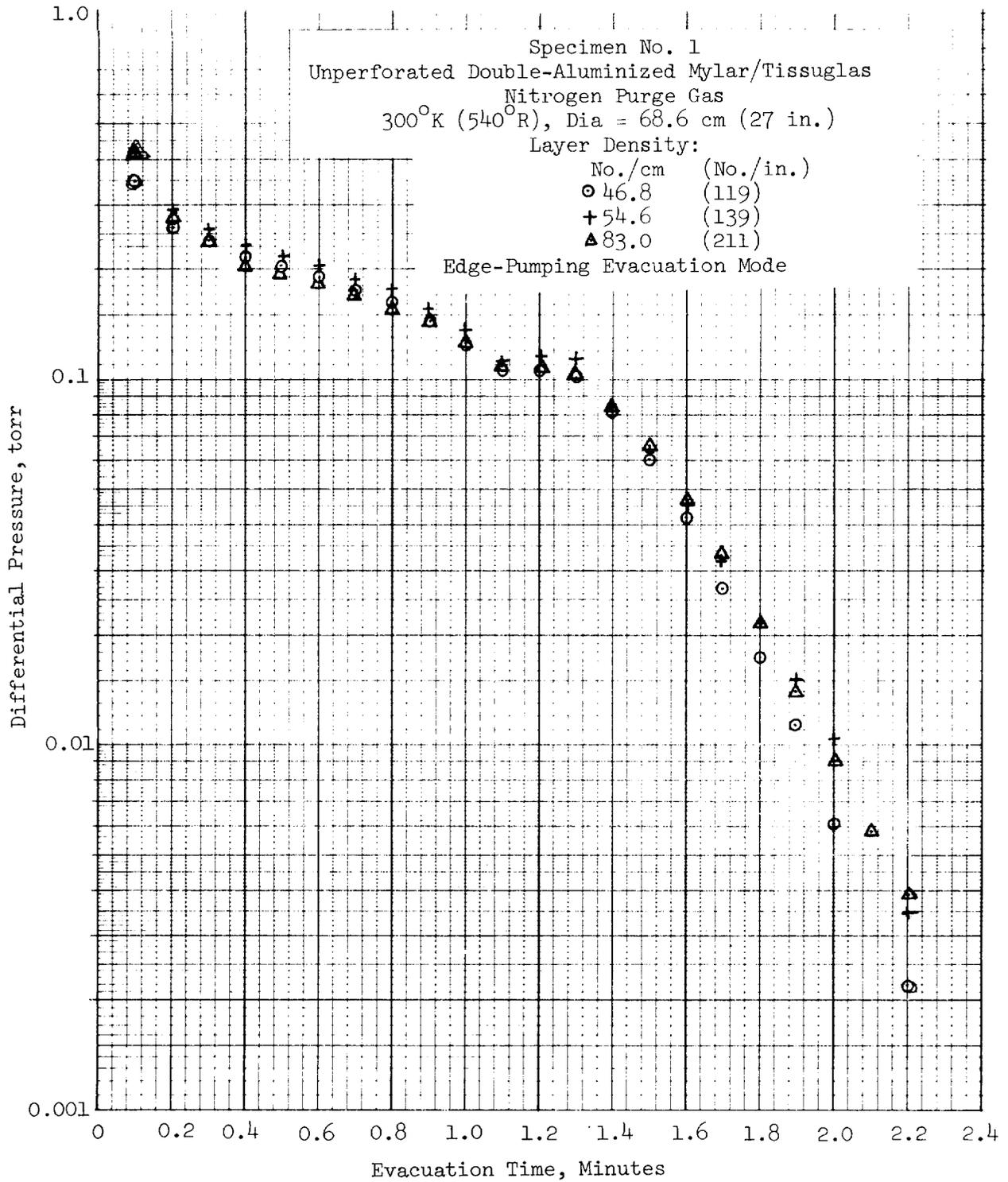
Fig. 5-19 Effect of Layer Density for
Double-Aluminized Mylar/Tissuglas

5-63
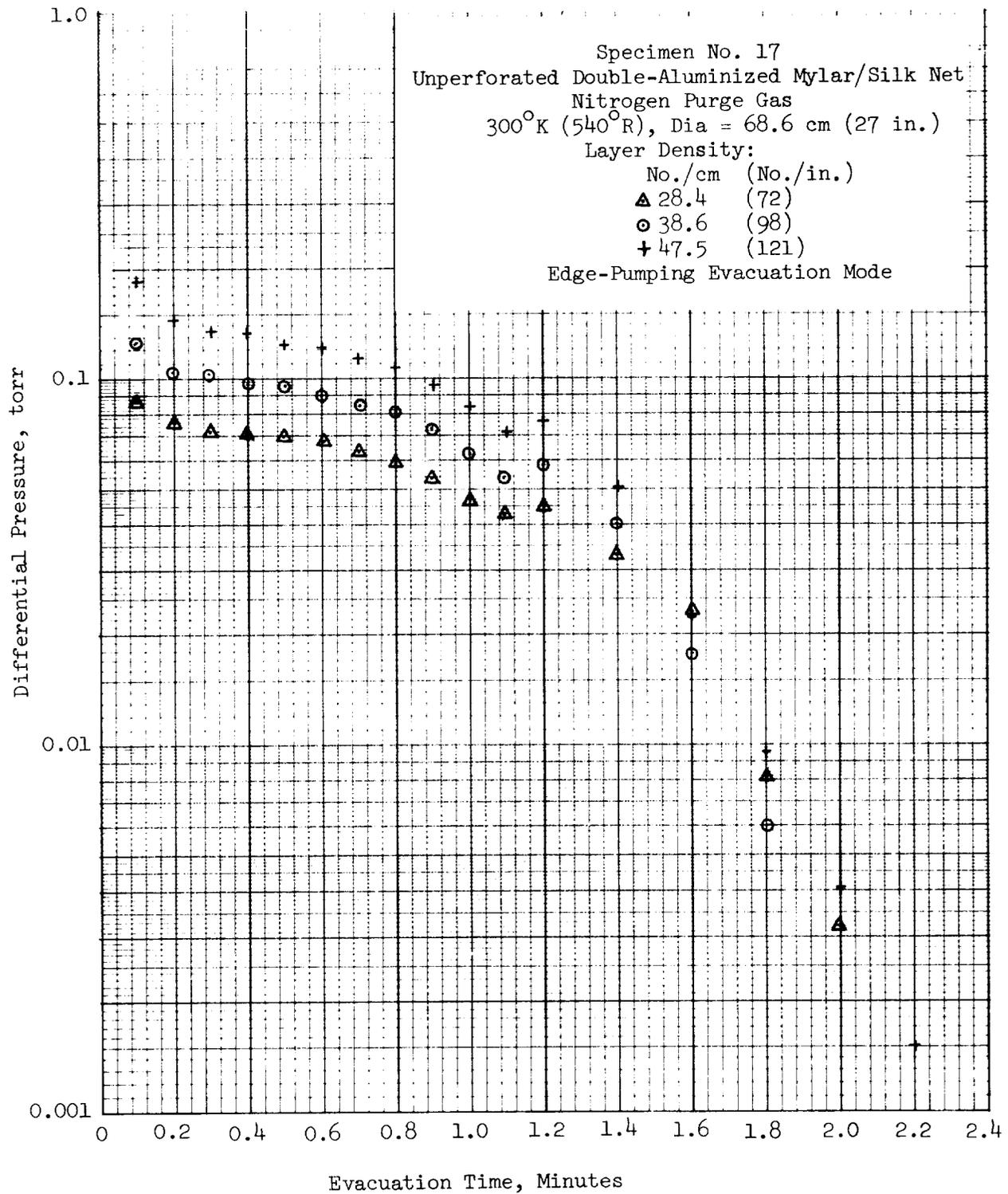
Fig. 5-20   Effect of Layer Density for
Double-Aluminized Mylar/Silk Net

5-64

LOCKHEED MISSILES & SPACE COMPANY
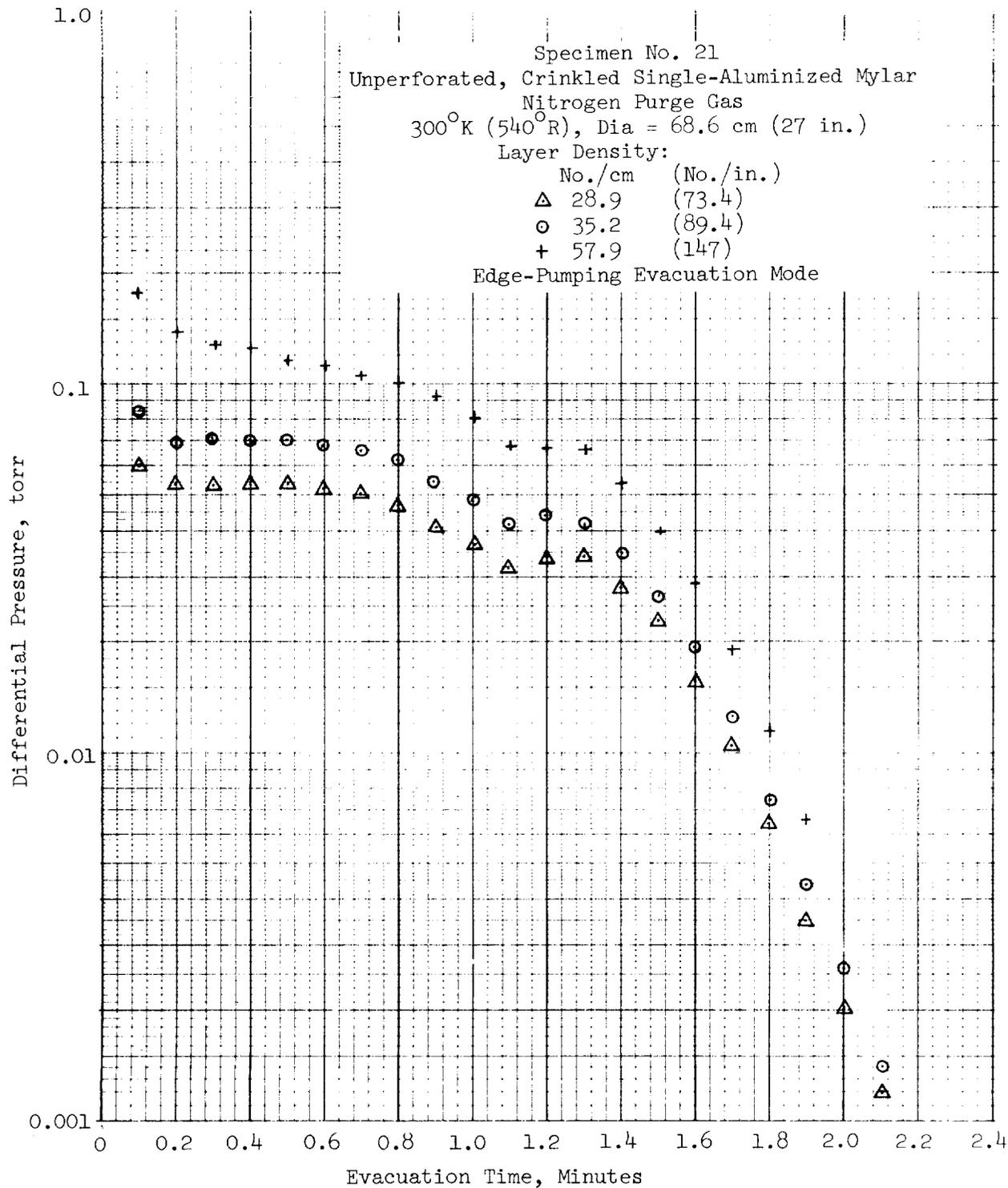
Fig. 5-21 Effect of Layer Density for
Crinkled, Single-Aluminized Mylar

5-65

Another factor that lends credence to the explanation presented above for the Specimen No. 1 anomaly is the result obtained from the tests of Specimen No. 4. These two specimens are similar, differing only in the total number of layers. However, the ΔP data obtained for Specimen No. 4 with helium purge gas at one layer density value were on the order of twice those obtained for Specimen No. 1. Since the data obtained for Specimen No. 4 are in good agreement with the theoretical analysis, and since the natural consequence of channeling would be pressure differentials lower than those predicted by the analysis, it appears that the Test No. 4 data are valid, and that those obtained for Test No. 1 should be disregarded in assessing the effect of layer density variations.

Analysis of the precise quantative variation of ΔP with layer density was very difficult since much of the test data obtained apply to the transition flow region where the influence of layer density should be passing from second- to first-power dependence. Inspection of the data obtained for Specimens No. 17 and 21 indicates that these data were within this range.

5.3.1.2 <u>Effect of Flow Path Length</u>. The effect of flow path length was investigated by varying the specimen diameter. This was done for double-aluminized Mylar/Tissuglas with Specimens No. 1B, 2 and 3, and for double-aluminized Mylar/silk net with Specimens No. 17B, 18, and 19. The purge gas was nitrogen, and the selected specimen diameters were 68.6 cm (27 in.), 50.8 cm (20 in.), and 38.1 cm (15 in.), respectively. The data are plotted in Figs. 5-22 and 5-23. Both sets of data show the expected increase of ΔP with radius.

Based on Eq (5-51), ΔP should vary in proportion to the specimen radius squared. The data obtained for Specimens No. 17B, 18, and 19 exhibit this dependency within a few percent. For example, at an evacuation time of 0.4
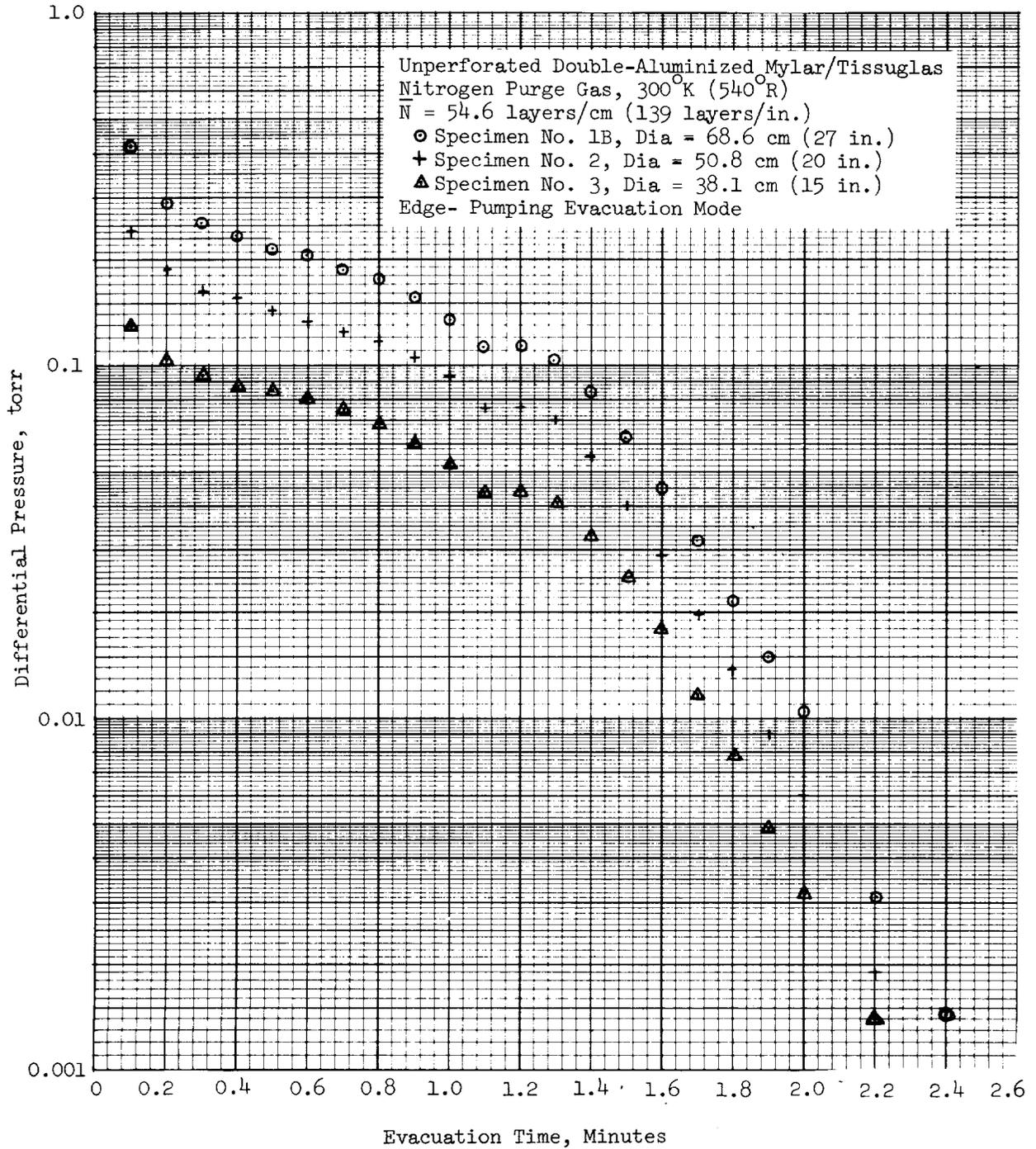
5-66

Fig. 5-22 Effect of Flow Path Length for
Double-Aluminized Mylar/Tissuglas

LOCKHEED MISSILES & SPACE COMPANY
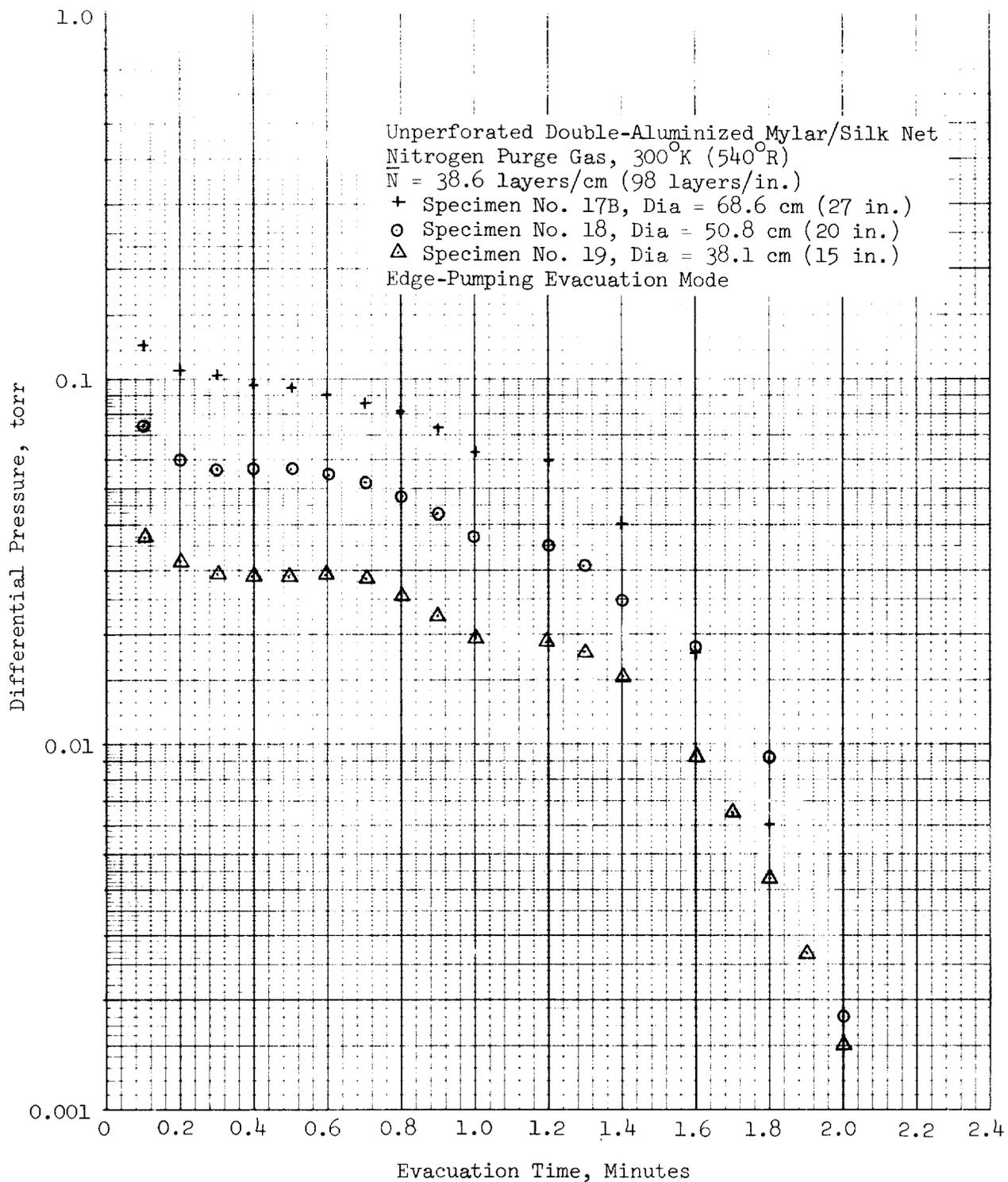
Fig. 5-23 Effect of Flow Path Length for
Double-Aluminized Mylar/Silk Net

5-68

min, the ΔP values obtained in Tests 17B, 18 and 19 are 0.097 torr, 0.057 torr, and 0.029 torr for radii of 34.3 cm (13.5 in.), 25.4 cm (10 in.), and 19.1 cm (7.5 in.), respectively. Referenced to the data for a radius of 34.3 cm (13.5 in.), the pressure ratios are 0.589 and 0.30, while the ratios for radius squared values are 0.55 and 0.31 for specimen radii of 25.4 cm (10 in.) and 19.1 cm (7.5 in.), respectively. For Tests 1B, 2, and 3, the relationship between data for Specimens No. 2 and 3 is good, but the Specimen 1B data are low by approximately 20 percent compared to the value expected from the analysis. It is noted that the data obtained for Specimen No. 1B are suspected to be in error due to channeling (Ref Section 5.3.1.1).

5.3.1.3 <u>Effect of Purge Gas Species</u>. The species of the purge gas used in evacuation testing was varied for Specimens No. 1A, 1B, 1C, and 20. Helium, nitrogen and argon gases were used. The data recorded for Specimen No. 20 are believed to be more reliable than those obtained for Specimens No. 1A, 1B, and 1C because of the channeling effect suspected for the latter (Ref Section 5.3.1.1). Consequently, only the data for Specimen No. 20 are presented for comparison in Fig. 5-24.

At early evacuation times, the gas evacuation flow is within the viscous regime, whereas free molecule flow governs at the later times. Within the viscous regime, the conductance depends upon viscosity. At $300^{\circ}K$ ($540^{\circ}R$), the viscosities of helium, nitrogen, and argon gases are 200×10^{-6} poise, 178×10^{-6} poise, and 228×10^{-6} poise, respectively. The differences between these values are slight, but, nonetheless, are clearly shown by the data which exhibit correlation with the analytical model within a few percent. In free molecule flow, the conductance is proportional to the square root of the molecular weight values, which are 2, 5.3, and 6.3 for helium, nitrogen, and argon, respectively. The test data obtained at the lower pressures do show the correct qualitative agreement with the model, although precise quantitative agreement was difficult to assess since most of the data are representative of the transient flow region.

5-69
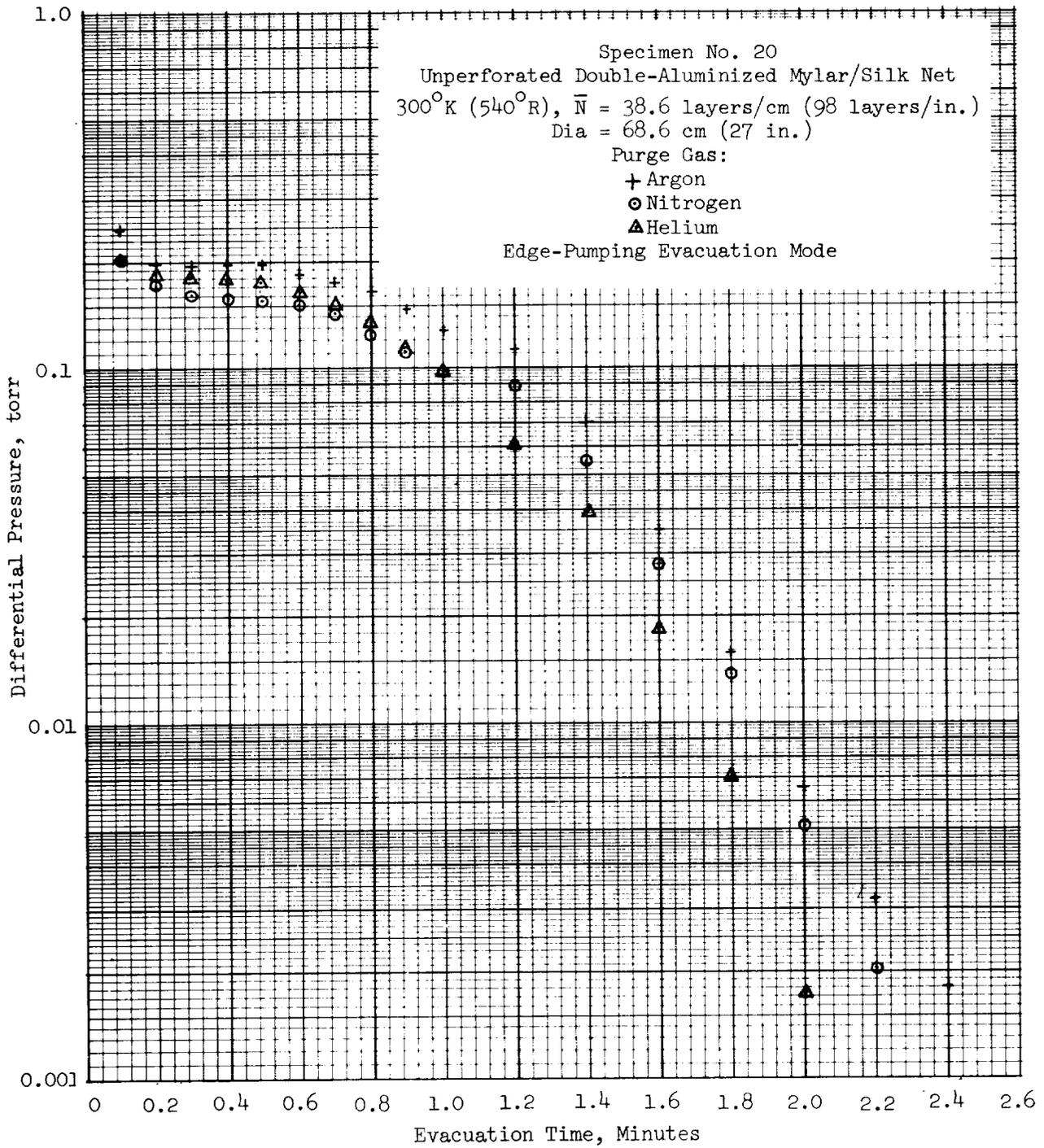
Fig. 5-24 Effect of Purge Gas Species for
Double-Aluminized Mylar/Silk Net

5.3.1.4 <u>Effect of Temperature</u>. The effect of temperature was investigated on Specimens No. 4 and 20 using helium as the initial purge gas. Evacuations were made at 300°K (540°R), 128°K (230°R), and several intermediate temperatures. The 128°K (230°R) temperature was the lowest value that could be attained within the insulation by circulating liquid nitrogen through the apparatus cooling coils. Differential pressure data obtained for these tests are plotted in Figs. 5-25 and 5-26. However, they should not be compared directly since the absolute pressure history of the evacuation chamber also varied with the specimen temperature. In order to make a valid comparison, some manipulation of the simplified evacuation model, Eq (5-51), is required.

By substituting the expression for v_a, as defined by Eq (5-21), into Eq (5-51), and by then extracting temperature and viscosity, Eq (5-51) can be rewritten as

$$\left(\frac{1}{T}\right)\left(\frac{dP}{dt}\right) = -\Delta P\left(\frac{P}{\mu T}\right)\left[A + \frac{B\mu T^{0.5}}{P}\right] \tag{5-55}$$

where A and B are constants. Inspection of the data shows that even though the absolute pressure history for the low temperature specimen case is different than it is for the ambient case, its form is similar (i.e., it is an exponential decay process). Thus, for any temperature, T, the absolute pressure history can be expressed as

$$\left(\frac{1}{P}\right)\left(\frac{dP}{dt}\right) = k_t \tag{5-56}$$

where k_t is a constant for a particular value of temperature.

Substituting Eq (5-56) into Eq (5-55) yields

$$\Delta P = \frac{k_t \mu}{A + \frac{B\mu T^{0.5}}{P}} \tag{5-57}$$
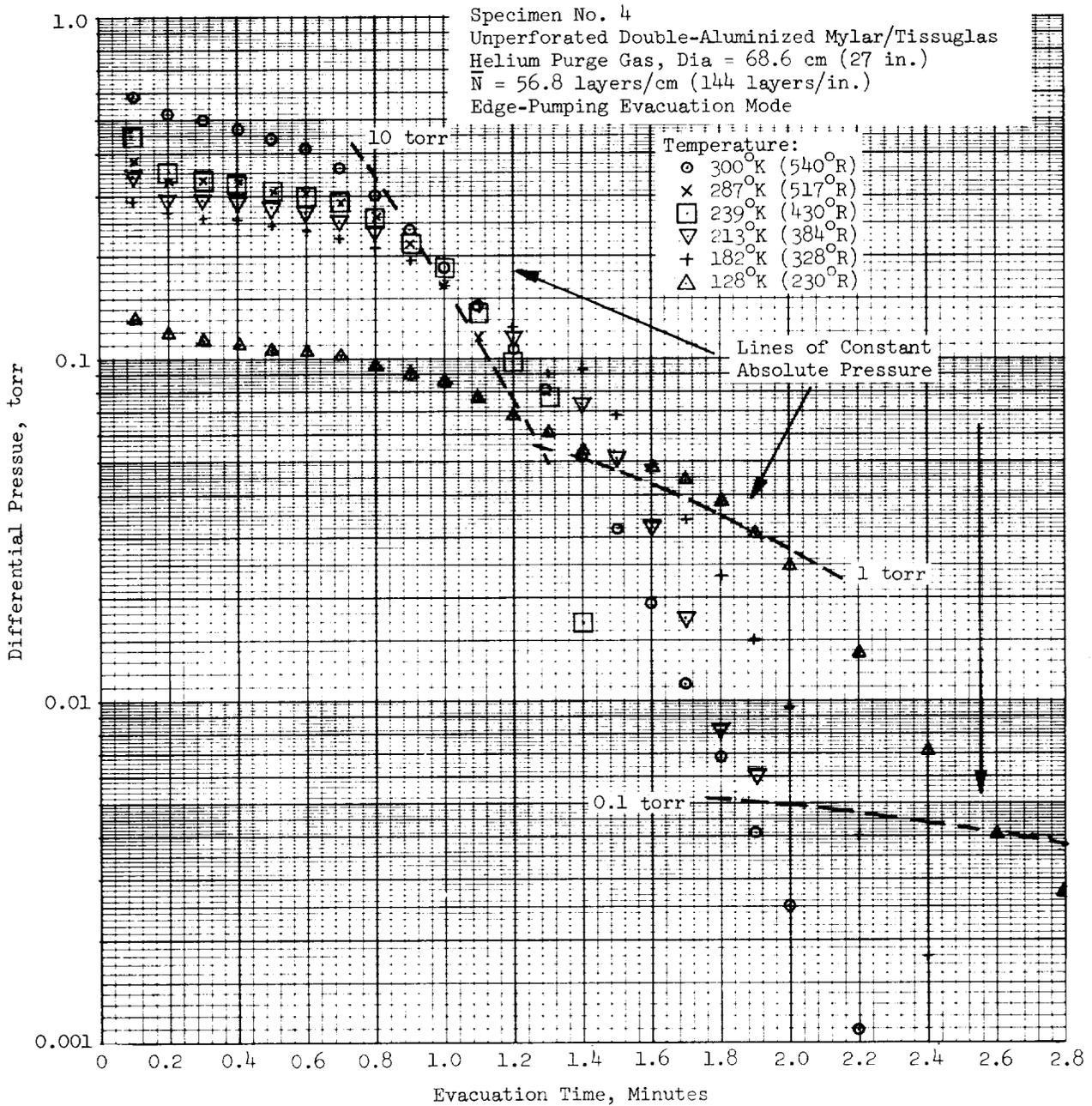
Fig. 5-25 Effect of Temperature for
            Double-Aluminized Mylar/Tissuglas

5-72
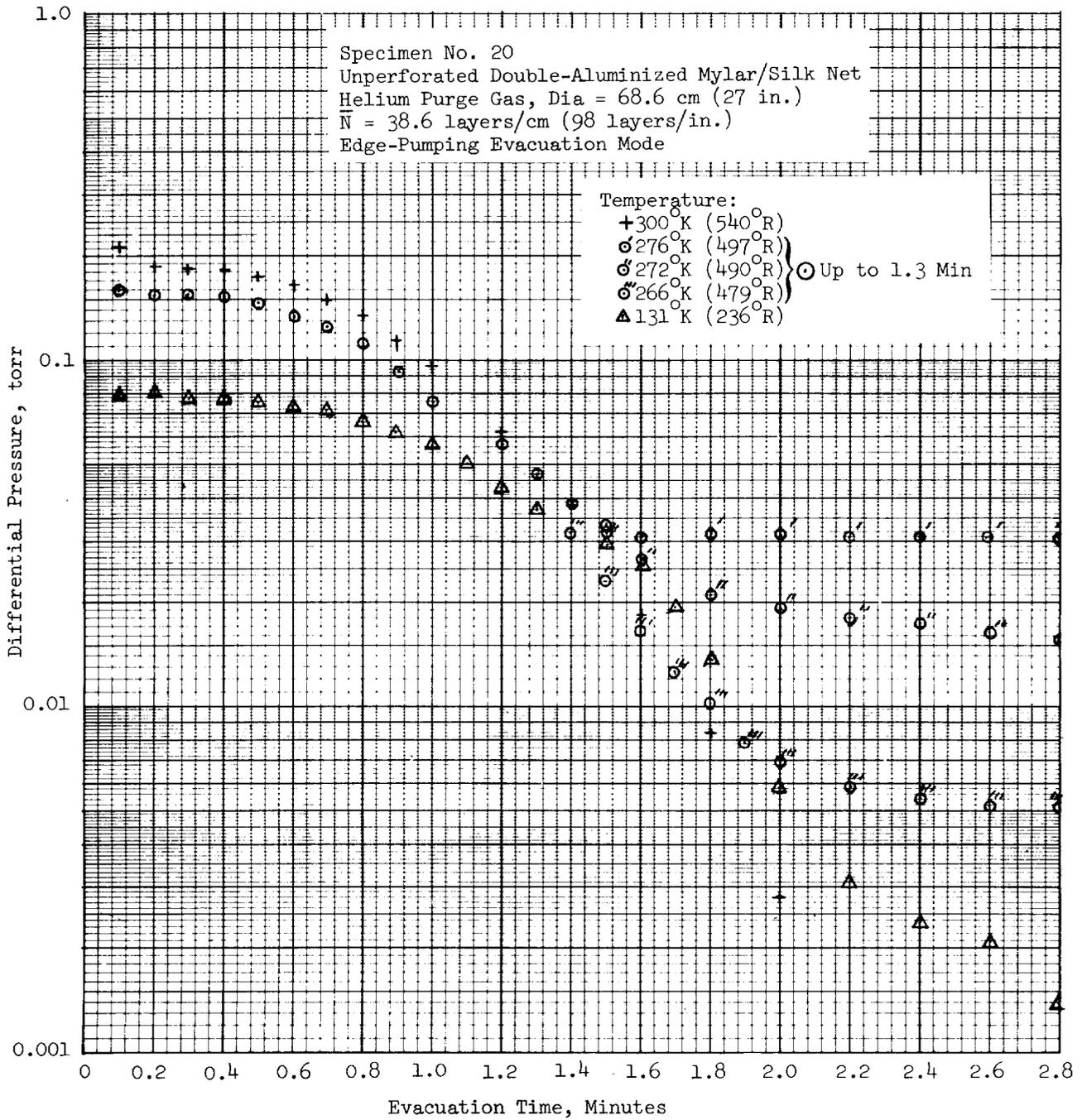
Fig. 5-26   Effect of Temperature for
            Double-Aluminized Mylar/Silk Net

LOCKHEED MISSILES & SPACE COMPANY

At high pressures, ΔP is proportional to $k_t \mu$. It would be tedious and not very informative to evaluate k_t for all of the low-temperature data. However, for illustration, a single comparison is made between the data obtained at $300°K$ ($540°R$) and $128°K$ ($230°R$).

A plot of the absolute pressure history as a function of evacuation time, as tabulated in Appendix B, on log-linear paper reveals values of k_t equal to 4.73 at $300°K$ ($540°R$) and 3.46 at $128°K$ ($230°R$). The viscosity of helium is proportional to temperature to the 0.647 power. Therefore, the ratio of $\Delta P_{(300°K)}/\Delta P_{(128°K)}$ should be approximately equal to 2.4 based on the analytical model.

For tests conducted on Specimen No. 20, the ratio of experimental values of ΔP at these same temperatures is approximately 2.3 for evacuation times less than 0.4 min when ΔP is essentially constant and the flow is clearly within the viscous regime. In the case of Specimen No. 4, the layer density is higher and the flow, even at early times, is already well into the transition flow regime. Therefore, the theoretical value of the ΔP ratio at $300°K$ ($540°R$) and $128°K$ ($230°R$) is difficult to determine. It can be seen that the ratio of 2.4 represents the limiting value for purely viscous flow. For purely free molecule flow, ΔP will be proportional to $k_t P/T^{0.5}$. The factor $(k_t/T^{0.5})$ is equal to values of 0.20 and 0.23 at temperatures of $300°K$ ($540°R$) and $128°K$ ($230°R$), respectively. Therefore, in the free molecule regime, the ΔP at $300°K$ ($540°R$) should be less than the ΔP at $128°K$ ($230°R$) for equal values of absolute pressure and with all other factors constant. Unfortunately, the data for this test do not extend to sufficiently low pressures for the evacuations at both temperatures to achieve pure free molecule flow, even for Specimen No. 4. However, in order to show that the data do exhibit the correct trend, a family of curves for constant absolute pressure values of 10 torr, 1 torr, and 0.1 torr are superimposed on the differential pressure curves of Fig. 5-25. Inspection of these data clearly shows that values of ΔP at $300°K$ ($540°R$) are decreasing with respect to those at $128°K$ ($230°R$) as the absolute pressure value is reduced. Based on this trend, it

5-74

appears that the ratio of $\Delta P_{(300^\circ K)} / \Delta P_{(128^\circ K)}$ at equilibrium (i.e., pure free molecule flow) would be very close to the predicted ratio of 0.20/0.23.

A qualitative comparison of the data obtained for Specimens No. 4 and 20 reveals another interesting and significant characteristic. For Specimen No. 4, tests were conducted for a wide range of intermediate temperatures including $287^\circ K$ ($517^\circ R$), $239^\circ K$ ($430^\circ R$), $213^\circ K$ ($384^\circ R$), and $182^\circ K$ ($328^\circ R$). For Specimen No. 20, three intermediate temperatures quite close to the ice point were used including $276^\circ K$ ($497^\circ R$), $272^\circ K$ ($490^\circ R$), and $266^\circ K$ ($479^\circ R$). The data obtained for the latter three evacuations were normal and essentially coincident for early evacuation times up to just over 1 min. After this time, the ΔP decayed very slowly with time, suggesting the influence of significant outgassing even though (a) the specimen was preconditioned, and (b) such an effect had not been observed in the prior $300^\circ K$ ($540^\circ R$) and $178^\circ K$ ($230^\circ R$) temperature evacuations of the same specimen. In the interim, the specimen was exposed only to helium.

Two factors are noted in explaining these results. First, the task 2 tests have shown that, even after extensive preconditioning, there will always be a certain quantity of sorbed gas remaining. Secondly, it can be shown experimentally that a material evacuated at a relatively high temperature will not outgas over an extended period because the high rate of desorption resulting from the ready availability of energy will rapidly reduce the sorbed gas concentration. On the other hand, a material evacuated at a relatively low temperature will not outgas because the desorbed gas will not be able to attain sufficient energy to escape the surface. Therefore, it can be anticipated that, at some intermediate temperatures, the concentration of outgas molecules will be high enough but the temperature will be low enough so that the outgassing rate will be finite, but very slow and persistent. Also, the temperatures at which this will occur can be expected to be near or below the normal condensation temperature for the particular sorbed gas. In the case of the data obtained for Specimen No. 20, there are clear indications that this phenomenum occurred at temperatures near the ice point because the outgas

component is predominately water vapor. By comparison with the data obtained for Specimen No. 4, it appears that $287^\circ K$ ($517^\circ R$) was too high a temperature, and that $213^\circ K$ ($430^\circ R$) was too low a temperature for this effect to occur.

5.3.1.5 <u>Effect of Perforation Pattern</u>. Five different shield perforation patterns and two spacers were used in the broadside evacuation tests. The two spacers used were Tissuglas and silk net. Of these, the silk net presented negligible lateral flow resistance, whereas the Tissuglas presented a finite but unknown resistance. Therefore, the influence of the shield perforation pattern alone is best assessed by analysis of the results obtained for the silk net spaced system. The data for these tests, which were conducted on Specimens No. 5, 6, 7, 8, and 9, are plotted in Fig. 5-27. For this case, the simplified broadside evacuation model, Eq (5-54), can be used to compare the analytical and experimental results. Assuming a constant temperature and layer density, Eq (5-54) can be reduced to

$$\Delta P = C \left(\frac{d_h^2}{F_o}\right) \ln\left(\frac{2}{3}\sqrt{\frac{1}{F_o}}\right) \tag{5-58}$$

where C is a constant. The variable function shown on the right side of this equation was evaluated for each of the five shield perforation patterns tested. The results are tabulated below.

d_h		F_o	$\left(\frac{d_h^2}{F_o}\right)\ln\left(\frac{2}{3}\sqrt{\frac{1}{F_o}}\right)$	
cm	(in.)		cm^2	$(in.^2)$
0.119	(0.047)	0.0107	2.53	(0.392)
0.119	(0.047)	0.0055	5.68	(0.88)
0.229	(0.090)	0.0099	9.94	(1.54)
0.119	(0.047)	0.0026	14.1	(2.18)
0.229	(0.090)	0.0048	24.6	(3.82)

It can be seen from inspection of Fig. 5-27 that the variable function tabulated above provides a good qualitative agreement with the major portion of the test data. However, in order to obtain an indication of the quantative agreement between Eq (5-58) and the test data, differential pressure values

LOCKHEED MISSILES & SPACE COMPANY
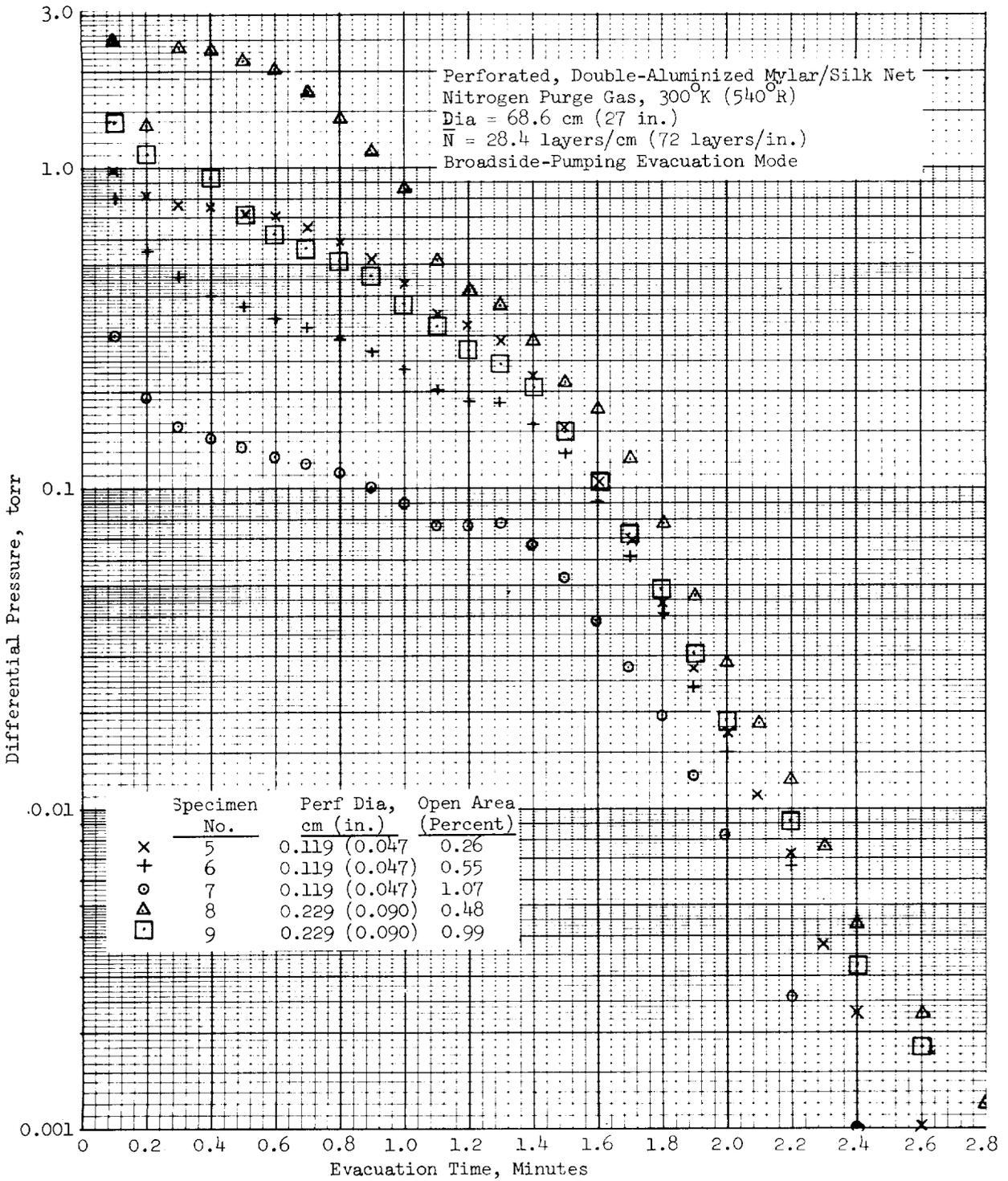
Fig. 5-27 Effect of Perforation Pattern on the Broadside
Evacuation of Double-Aluminized Mylar/Silk Net

5-77

LOCKHEED MISSILES & SPACE COMPANY

were extracted from Fig. 5-27 for pumping times of 0.8 and 2.2 min. These ΔP values are plotted as a function of the corresponding values of the tabulated function in Fig. 5-28. Straight lines of unity slope, which should result if Eq (5-58) is correct, were then fitted through the data points. It can be seen that the correlation is good for the earlier pumping time of 0.8 min when the flow was within the transition region between the viscous and free molecule regimes. A somewhat less satisfactory agreement was achieved for a pumping time of 2.2 min when the flow was within the free molecule regime, although the same general trend is shown. It was observed earlier (Ref Section 5.1.5.2) that the orifice flow resistance incurred during free molecule flow due to the shield perforations adds to the basic resistance due to flow between the layers. If the former were to constitute a significant portion of the total resistance, the geometric dependency described by Eq (5-58) would be inadequate. However, the degree of correlation achieved at 2.2 min of pumping time essentially confirms the assumption that the major resistance occurs due to flow between the layers, and the current analytical model seems to be quite adequate. For broadside evacuation, however, it should be noted that the ΔP induced by the flow tends to compress the MLI stack and thus to increase the ΔP value above that predicted by the analytical model. Also, the ΔP is distributed through the thickness so that the effect of the compression is not uniform. With regard to the Task 2 experiments, the outer (lower) layer of the stack was supported by the screen boundary and the effect of the ΔP was to move the inner layers away from the inner (upper) boundary plate. This created a relatively large void space which may have caused secondary interaction effects.

In order to qualitatively assess the effect of induced compression, a theoretical analysis was performed using load-deflection data from Task 1. The computer program was modified so that the interlayer separation was determined by the ΔP imposed across the MLI thickness. It was concluded as a result of this analysis that the deflections produced by the differential pressures were of the correct order of magnitude to explain the anomalies observed in the experimental results.
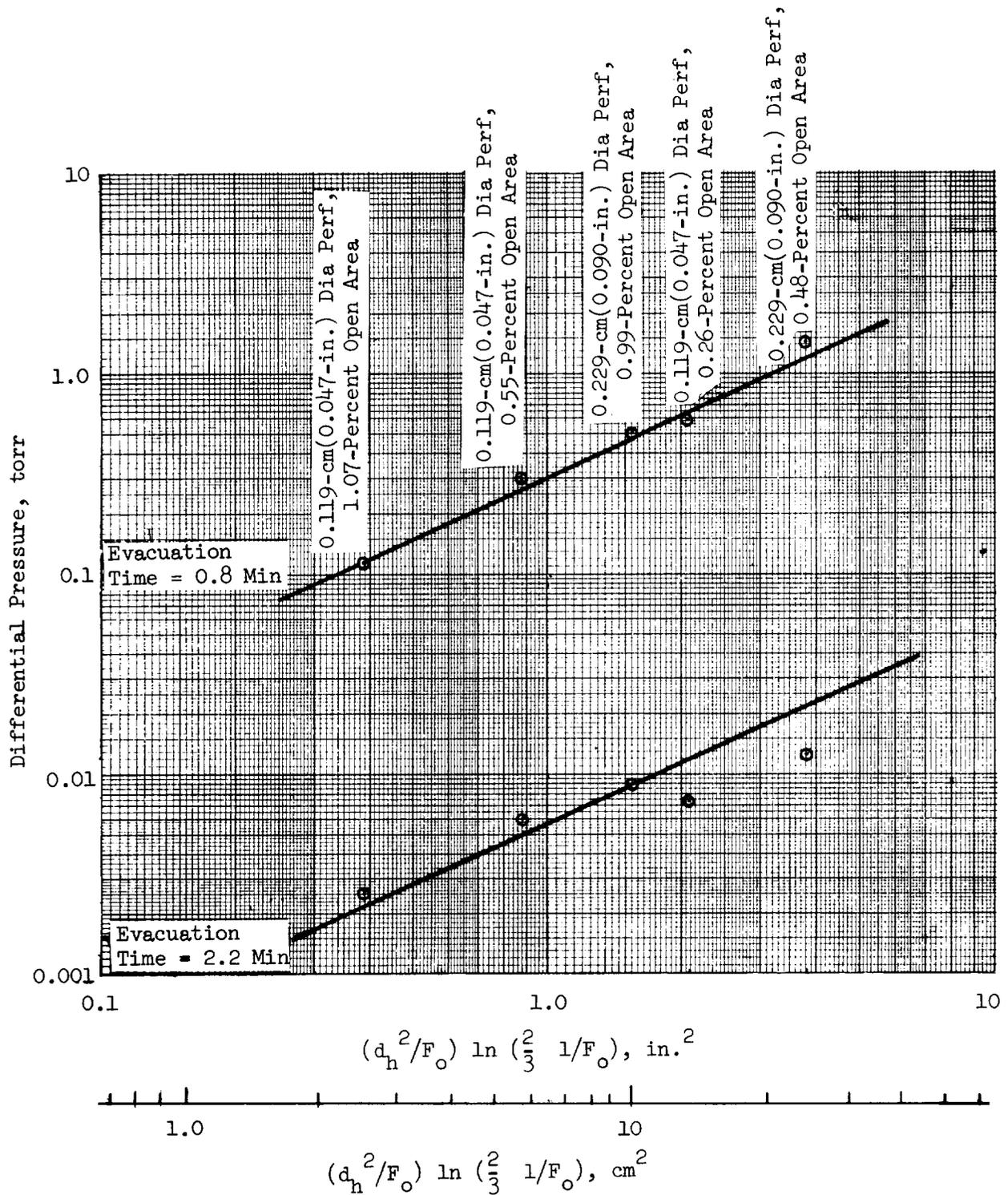
Fig. 5-28   Differential Pressure as a Function of Geometry
for Perforated Double-Aluminized Mylar/Silk Net

The test data obtained for broadside evacuation of the double-aluminized Mylar/
Tissuglas system are presented in Fig. 5-29. The layer density and the volume
of gas to be evacuated for this system were, respectively, approximately double
and one-half those of the silk net spaced system. Therefore, according to
Eq (5-54), the resulting pressure differential values should have been
approximately four times larger for the Tissuglas spaced system due to these
effects alone. In addition, the effect of the lateral flow resistance of the
porous but unperforated Tissuglas spacers should be included.

Since the Tissuglas spaced system has a very low compression spring constant
across the thickness, the effect of the relatively high differential pres-
sures imposed during the tests was to compress the MLI stack to the point
where evacuation was significantly impeded. The data obtained in the tests
show this effect very strongly. These specimens required by far the longest
evacuation period of any of the preconditioned specimens tested. The maximum
ΔP observed was not quite as high as that expected from the analysis, but it
occurred very late in the evacuation. This was because, in the early stages
of evacuation, the layers moved away from the upper boundary plate, thus
increasing the void volume and lowering the gas pressure by expansion. Analy-
sis shows that expansion ratios as high as 100 to 1 are possible for the
specimen geometry. Ultimately, however, no further pressure reduction was
achieved as a result of this effect and, subsequently, the pressure differen-
tials were governed by flow considerations only.

The general spread of the data obtained for specimens with different perfora-
tion patterns was similar to that observed for the silk net spaced system.
This indicates that the lateral flow resistance of the Tissuglas was not of
major significance.

It was noted that, after each series of evacuations conducted for a given
specimen, several of the Tissuglas spacers were torn and had to be replaced.
It was not determined conclusively whether this damage resulted directly from
the high differential pressures imposed or from the mechanical deformation of

5-80

Perforated, Double-Aluminized Mylar/Tissuglas
Nitrogen Purge Gas, 300°K (540°R)
$\underline{\text{Dia}} = 68.6$ cm (27 in.)
$\overline{\text{N}} = 58.2$ layers/cm (148 layers/in.)
Broadside-Pumping Evacuation Mode

10

1.0

0.1

0.01

0.001

Differential Pressure, torr

	Specimen No.	Perf Dia cm (in.)	Open Area (Percent)
⊙	11	0.119 (0.047)	0.26
△	12	0.119 (0.047)	0.55
◇	13	0.119 (0.047)	1.07
○	14	0.229 (0.090)	0.48
☐	15	0.229 (0.090)	0.99

0   1   2   3   4   5   6   7

Evacuation Time, Min
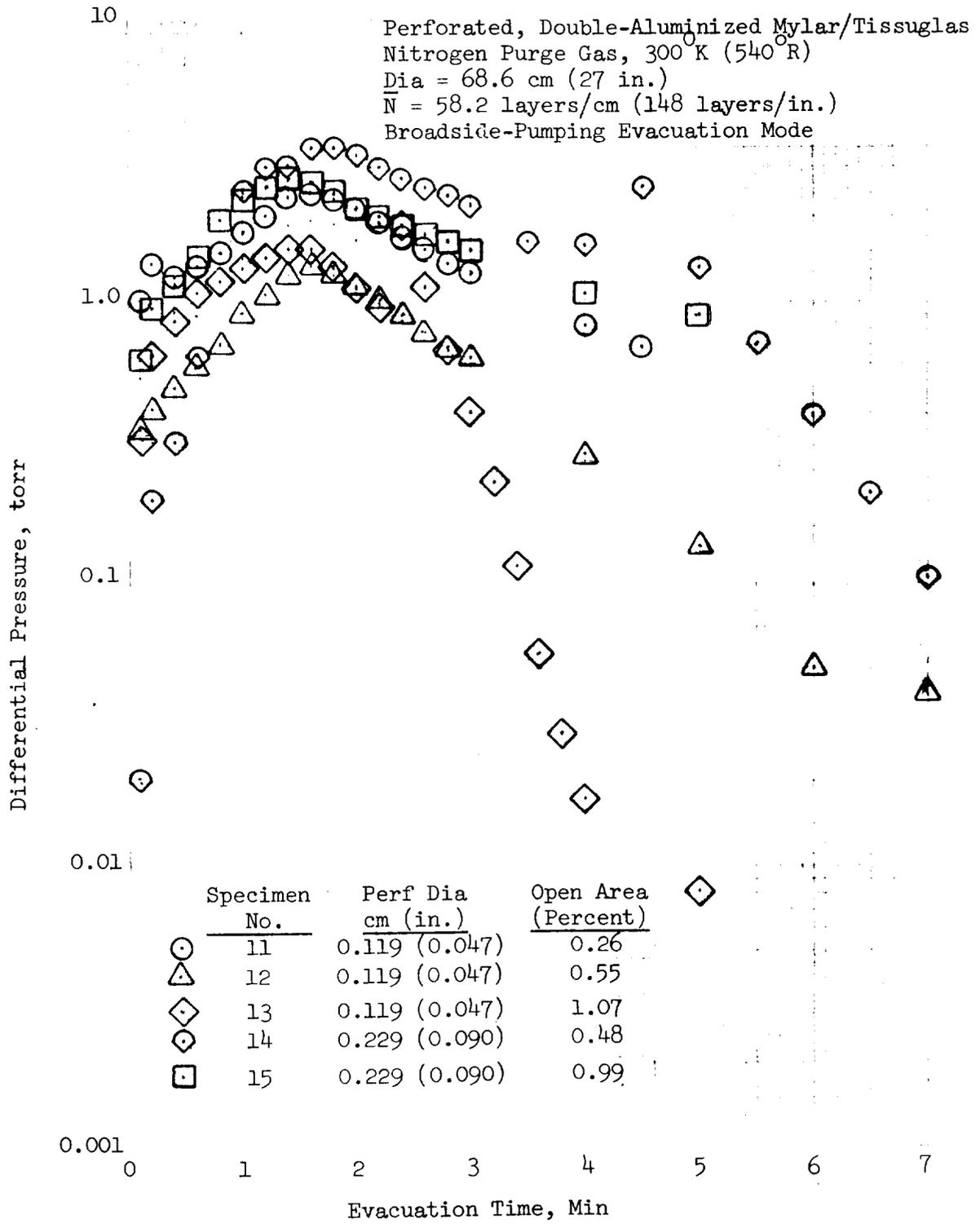
Fig. 5-29   Effect of Perforation Pattern on the Broadside Evacuation of
Double-Aluminized Mylar/Tissuglas

5-81

C-3.

the stack caused by these differentials. However, it was concluded that the latter case is more likely.

5.3.1.6 <u>Comparison of Edge and Broadside Evacuation</u>. One of the specific requirements of Tasks 1 and 2 was to select the best perforation pattern for study in Task 3. It became clear from tests conducted on Specimens No. 5 through 9 that the flow conductance of the 80-shield specimen was substantially lower in the broadside mode than it was in the edge-pumping mode. Therefore, in order to achieve any appreciable effect in raising the overall conductance for the case of combined edge- and broadside-pumping, it was necessary to select the perforation pattern with the highest conductance. This was the pattern used for Specimen No. 5 with a 0.119-cm-(0.047-in-) diameter perforation and a 1.07-percent open area. This pattern was tested as Specimen No. 10, with the outer clamp ring removed to permit edge as well as broadside flow. Fig. 5-30 shows the data obtained from this test compared with the data obtained for edge pumping alone from Specimen No. 20, and for broadside pumping alone from Specimen No. 7. As expected, the data show that the addition of shield perforations does not appreciably increase the effective conductance from the center of the insulation to the exterior for this particular set of dimensions. However, it is quite obvious that, for any particular perforation pattern, the ratio of edge pumping conductance to broadside pumping conductance will increase as the sample diameter decreases or as the number of layers in the stack increases. It can be seen from the analytical models that this ratio will vary as the square of either of these parameters.

5.3.1.7 <u>Comparison of Insulation Types</u>. The primary goal of the comparisons presented previously in this section was to show the degree of influence exerted by each parameter as predicted by the analysis and as evidenced by the experimental results. All comparisons of the effect of a particular parametric variation were made for a specific insulation type (i.e., material composite and configuration). However, the insulation type itself is a significant parameter. In the theoretical analysis it has been assumed that

5-82

LOCKHEED MISSILES & SPACE COMPANY
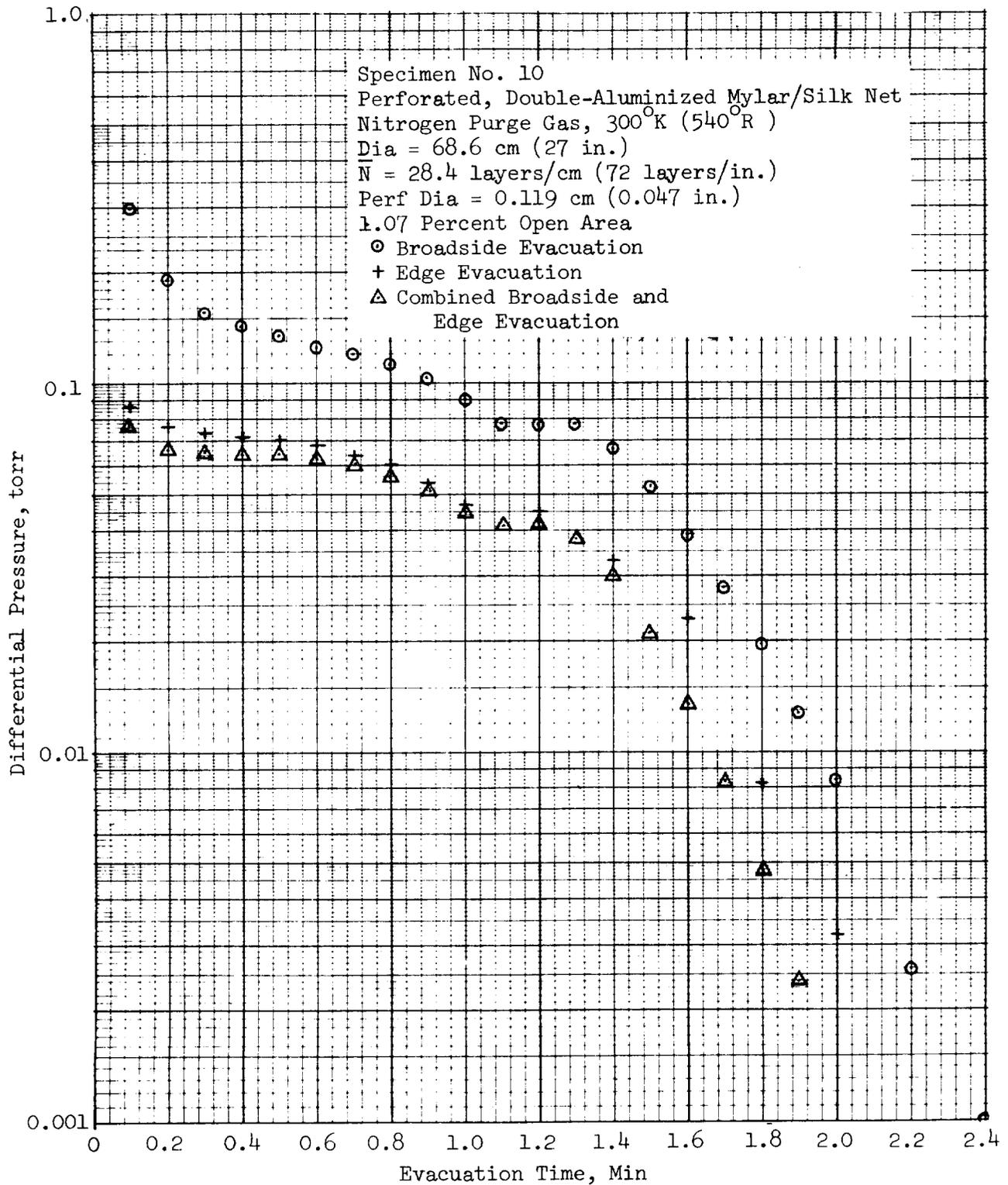
Fig. 5-30   Comparison of Edge and Broadside Evacuation
            Alone with Combined Evacuation

5-83

LOCKHEED MISSILES & SPACE COMPANY

evacuation flow conductances can be determined using the assumption of smooth, evenly-spaced flow plates. The double-aluminized Mylar/Tissuglas system can be modelled as flat plates, (assuming both shield and spacer to be separate plates), but the spacing is likely to be uneven and perhaps even time dependent. The double-aluminized Mylar/silk net system is likely to be more evenly spaced, but it is not obvious how to model the two silk net layers which are discontinuous. Clearly, they offer finite flow resistance, but of smaller magnitude than that for a continuous spacer. The crinkled, single-aluminized Mylar system is probably the most stable (i.e., it offers the highest compression spring rate) and contains no spacer, but some allowance must be made for the effect of the crinkled shields. In order to obtain a legitimate experimental comparison between insulation types, the data must be compared for cases where all other parameters are equal, including layer density. However, the layer density values tested for each composite type were selected from thermal performance considerations, and no general systematic comparison was possible. Therefore, investigation of the effect of the insulation type must be accomplished by comparison of experimental data with the predicted data using the flat plate model assumption. By determining the degree of correlation with the same model for each insulation type, the relationship between different composite types can be deduced.

By coincidence, one direct comparison can be made. Specimens No. 17A and 21A have very similar layer densities of 28.4 and 28.9 layers/cm (72 and 73.4 layers/in.), respectively. However, the ΔP values obtained for Specimen No. 17A (double-aluminized Mylar/silk net) are as much as 40 percent higher in the viscous regime than those obtained for Specimen No. 21A (crinkled, single-aluminized Mylar). Similarly, the ΔP values obtained for Specimen No. 17A were approximately 20 percent higher in the free molecule range. These data for a single comparison suggest that the effect of the two silk net spacers was to reduce the effective interlayer separation by about 20 percent.

5-84

One possible method of modifying the analysis to allow for departures from an ideal flat plate model is to use the concept of an equivalent hydraulic diameter in the flow equations. The hydraulic diameter, D_h, is defined as

$$D_h = \frac{4 \text{ (flow area)}}{\text{(wetted perimeter)}} \tag{5-59}$$

For flat parallel plates separated by a distance equal to $2z_o$, D_h is given by

$$D_h = \frac{4(2z_o)(\text{unit width})}{2 \text{ (unit width)}}$$

$$= 4z_o \tag{5-60}$$

Therefore, $z_o = \dfrac{D_h}{4}$ \hfill (5-61)

It is suggested that z_o be replaced in the conductance equations by $D_h/4$. For the case of the silk net spaced samples, D_h can be evaluated as

$$D_h = \frac{4 \text{ (flow area)}}{\text{(wetted perimeter of shields + spacers)}} \tag{5-62}$$

The silk net used contains approximately 38 cells/cm^2 (245 cells/in.^{2}), each with a length of approximately 0.56 cm. (0.22 in.) of silk fiber. The diameter of each silk fiber was approximately 0.0038 cm (0.0015 in.). Consequently, the total surface area of silk was 0.25 cm^2/cm^2 (0.25 in.^{2}/in.^{2}) of netting which is numerically equal to the wetted perimeter per unit length. Noting that two silk net spacers were used between each pair of shields, D_h is given by

$$D_h = \frac{4(2z_o)(1)}{(2 + 0.50)}$$

$$= 3.2z_o \tag{5-63}$$

5-85

Therefore, the modified or effective value for z_o, denoted z_o', to be used in the flat plate analysis is given by

$$z_o' = \frac{D_h}{4} = 0.8 z_o \tag{5-64}$$

It can be seen that these values almost exactly explain the discrepancy between the data for the silk net spaced and the unspaced systems for the same layer separation. While such good agreement is no doubt coincidental, it does appear that deviations from the ideal flat plate model can be treated by the use of an effective separation distance which is calculated as shown above.

5.3.1.8 <u>Influence of Outgassing</u>. Whenever the sample chamber was opened to the atmosphere during the Task 2 testing, it was necessary to then perform a preconditioning evacuation to lower the outgassing rate to a negligible value. (i.e., to a value that would not result in ΔP values greater than approximately 0.001 torr). The chamber was opened either to alter the layer density of a specimen already installed, or to install a new specimen. The preconditioning data obtained from installed specimens are of little interest because these specimens had been let back to one atmosphere with one of the purge gases and had minimal exposure to the atmosphere. The preconditioning evacuations of the new specimens, however, are of great practical interest. These data have been plotted in Figs. 5-31 through 5-39, together with the data for subsequent evacuation of the same specimens after preconditioning. The comparisons show the importance of preconditioning quite dramatically. It can be deduced from inspection of these figures that all of the original purge gas is rapidly removed from any MLI system during an evacuation, and that any gas present at longer duration times must originate from outgassing.

When outgassing is present, it is seen that the ΔP is approximately inversely proportional to time. This is to be expected, since the pressure differential is proportional to conductance and outgassing rate. In the region where outgassing predominates, the pressure is low enough for the flow to be free

5-86
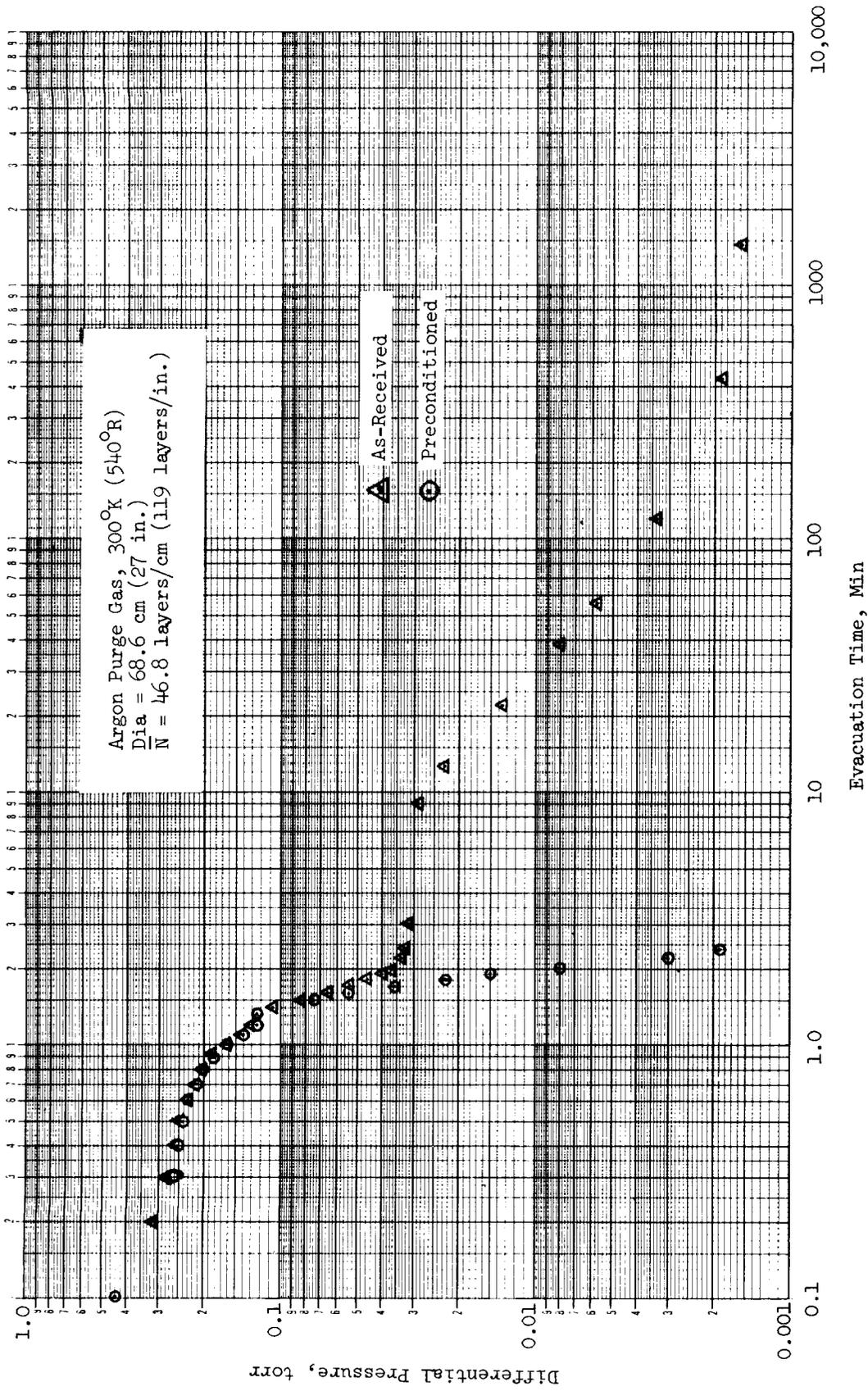
Fig. 5-31 Effect of Outgassing on Unperforated, Double-Aluminized Mylar/Tissuglas, Specimen No. 1A
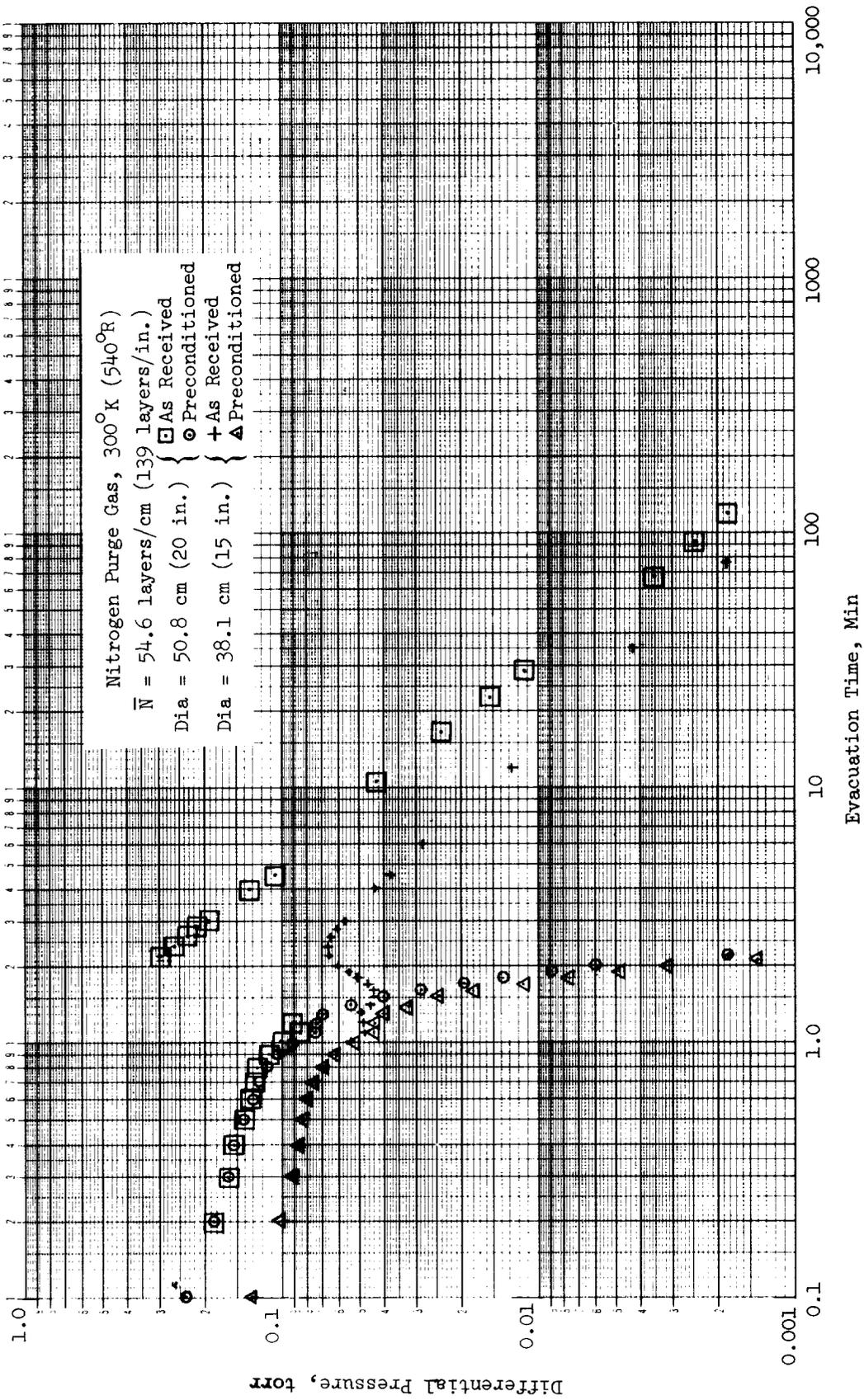
Fig. 5-32 Effect of Outgassing on Unperforated, Double-Aluminized Mylar/Tissuglas, Specimens No. 2 and 3

LOCKHEED MISSILES & SPACE COMPANY
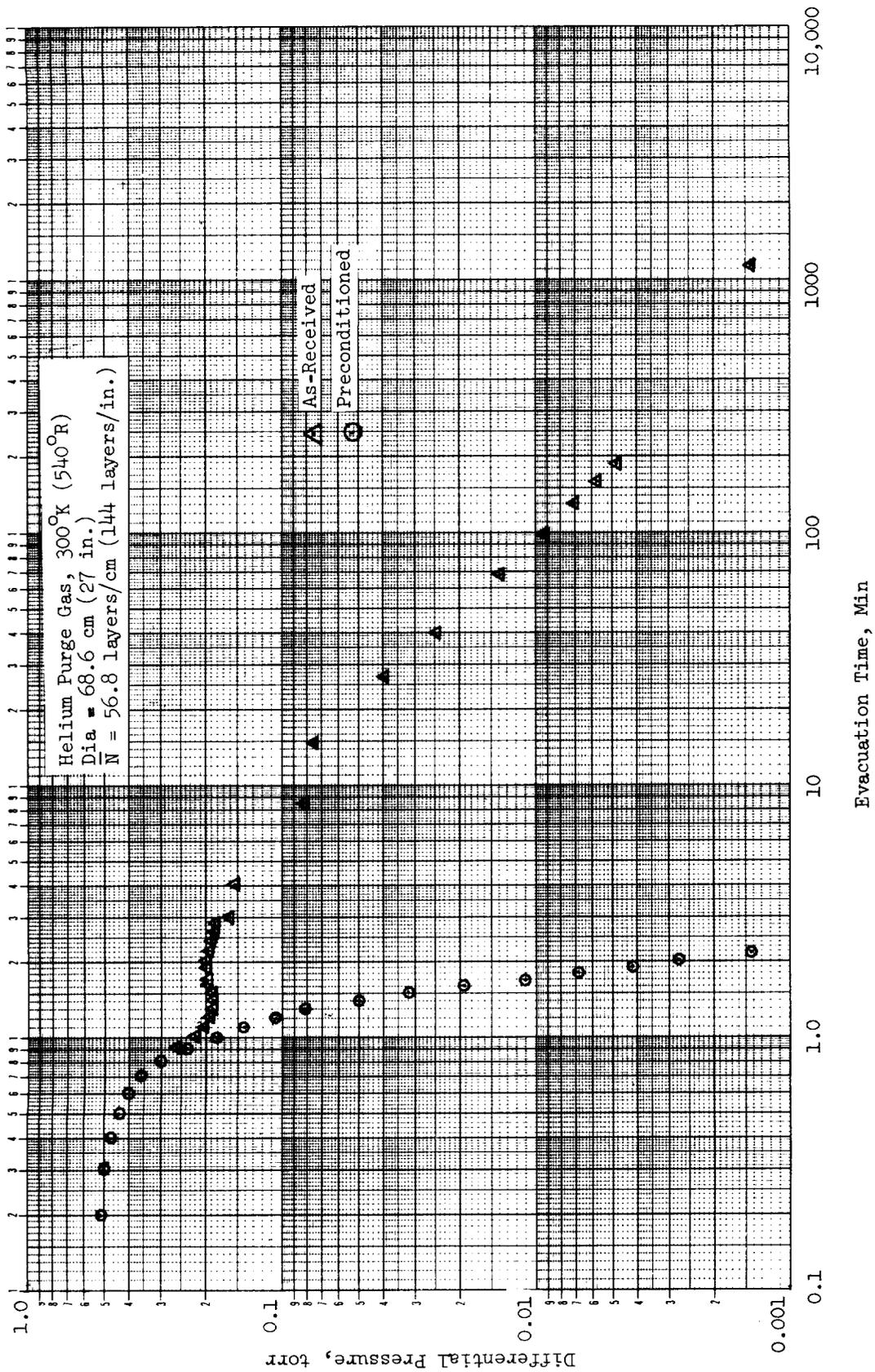
Fig. 5-33 Effect of Outgassing on Unperforated, Double-Aluminized Mylar/Tissuglas, Specimen No. 4

LOCKHEED MISSILES & SPACE COMPANY
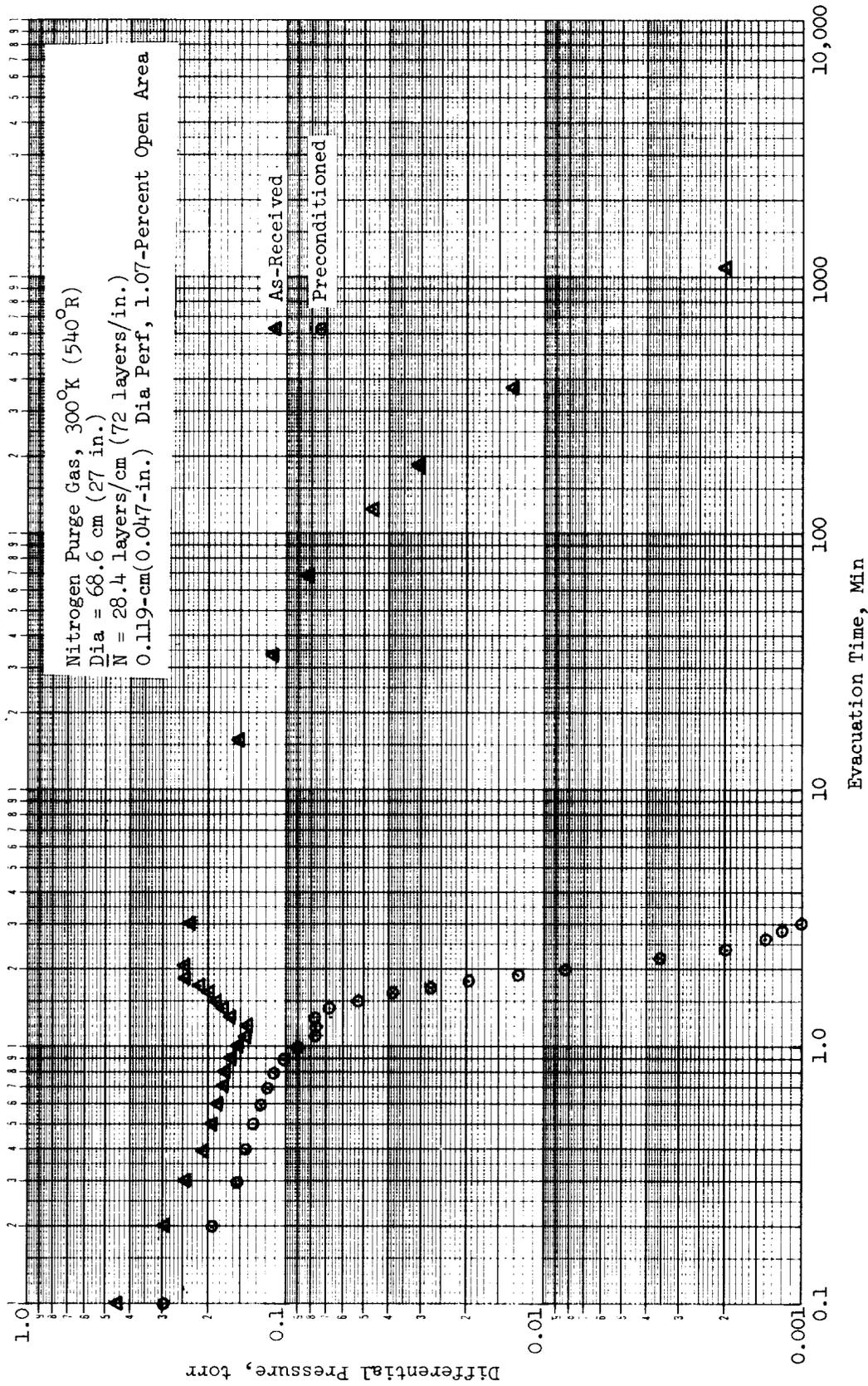
Fig. 5-34 Effect of Outgassing on Perforated, Double-Aluminized Mylar/Silk Net, Specimen No. 7

5-90
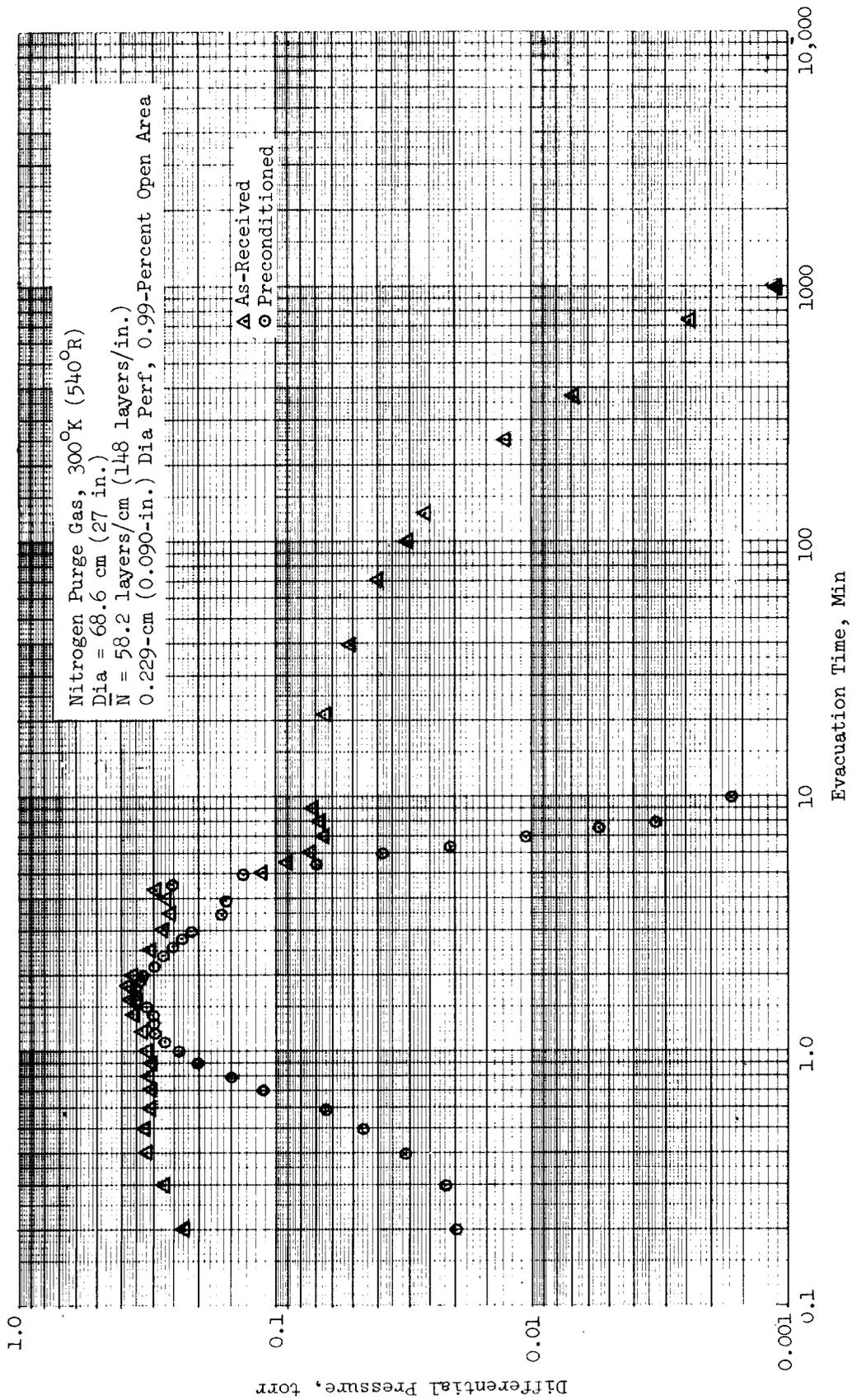
Fig. 5-35 Effect of Outgassing on Perforated, Double-Aluminized Mylar/Tissuglas, Specimen No. 15

Nitrogen Purge Gas, 300°K (540°R)
Dia = 68.6 cm (27 in.)
$\overline{N}$ = 58.2 layers/cm (148 layers/in.)
0.229-cm (0.090-in.) Dia Perf, 0.99-Percent Open Area

△ As-Received
⊙ Preconditioned

Evacuation Time, Min

Differential Pressure, torr

5-91
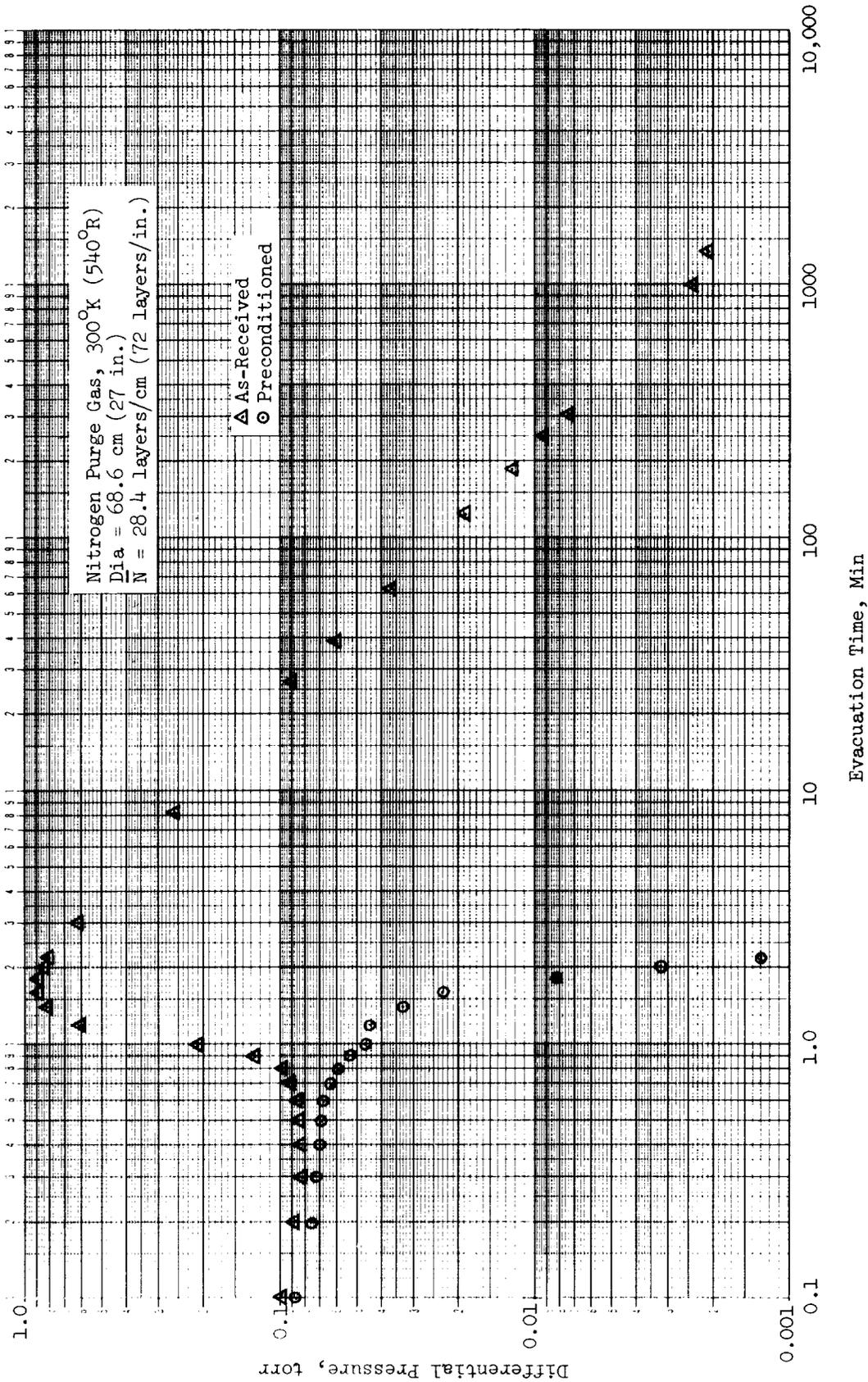
Fig. 5-36 Effect of Outgassing on Unperforated, Double-Aluminized Mylar/Silk Net, Specimen No. 17A

LOCKHEED MISSILES & SPACE COMPANY
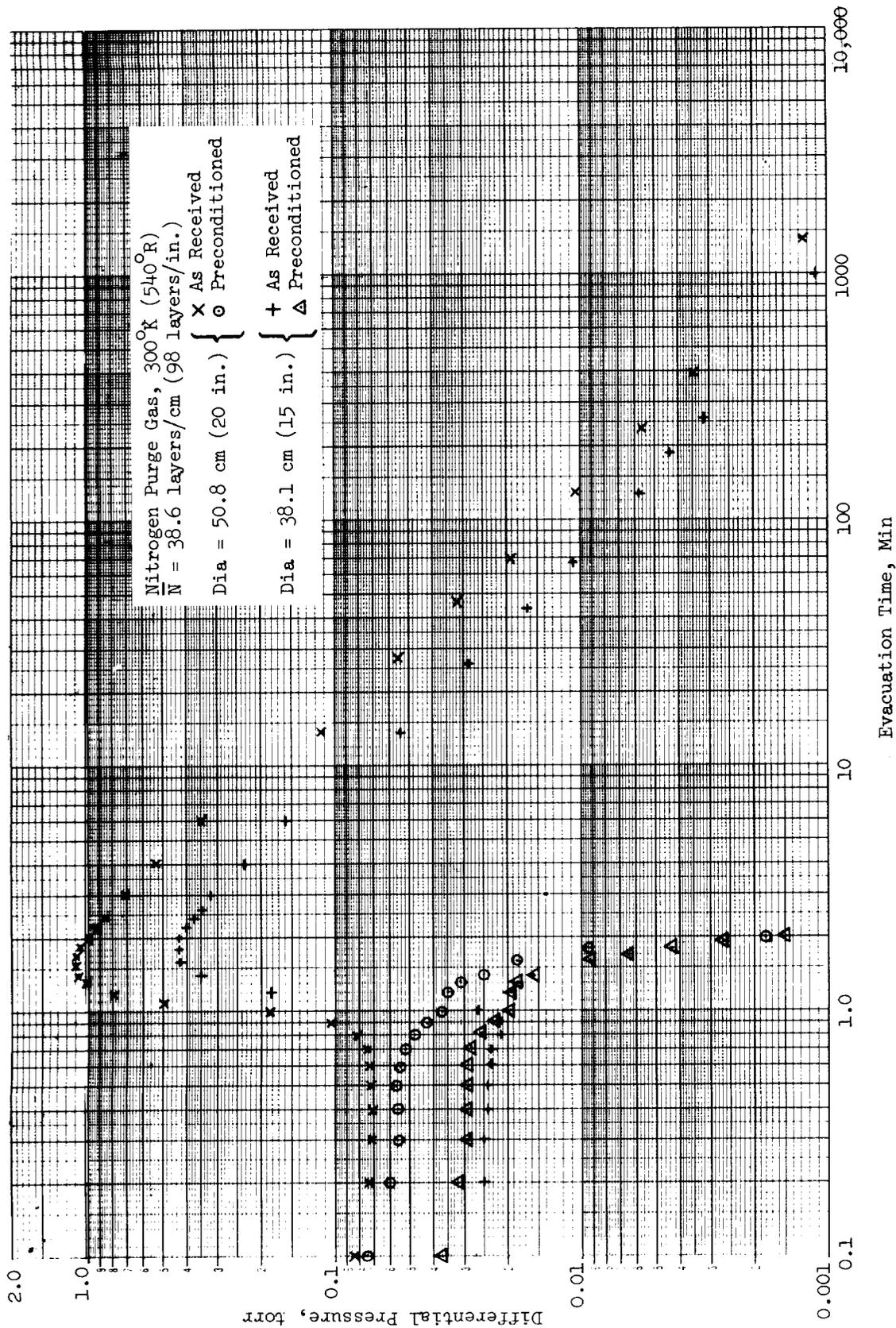
Fig. 5-37 Effect of Outgassing on Unperforated, Double-Aluminized Mylar/Silk Net, Specimens No. 18 and 19

5-93
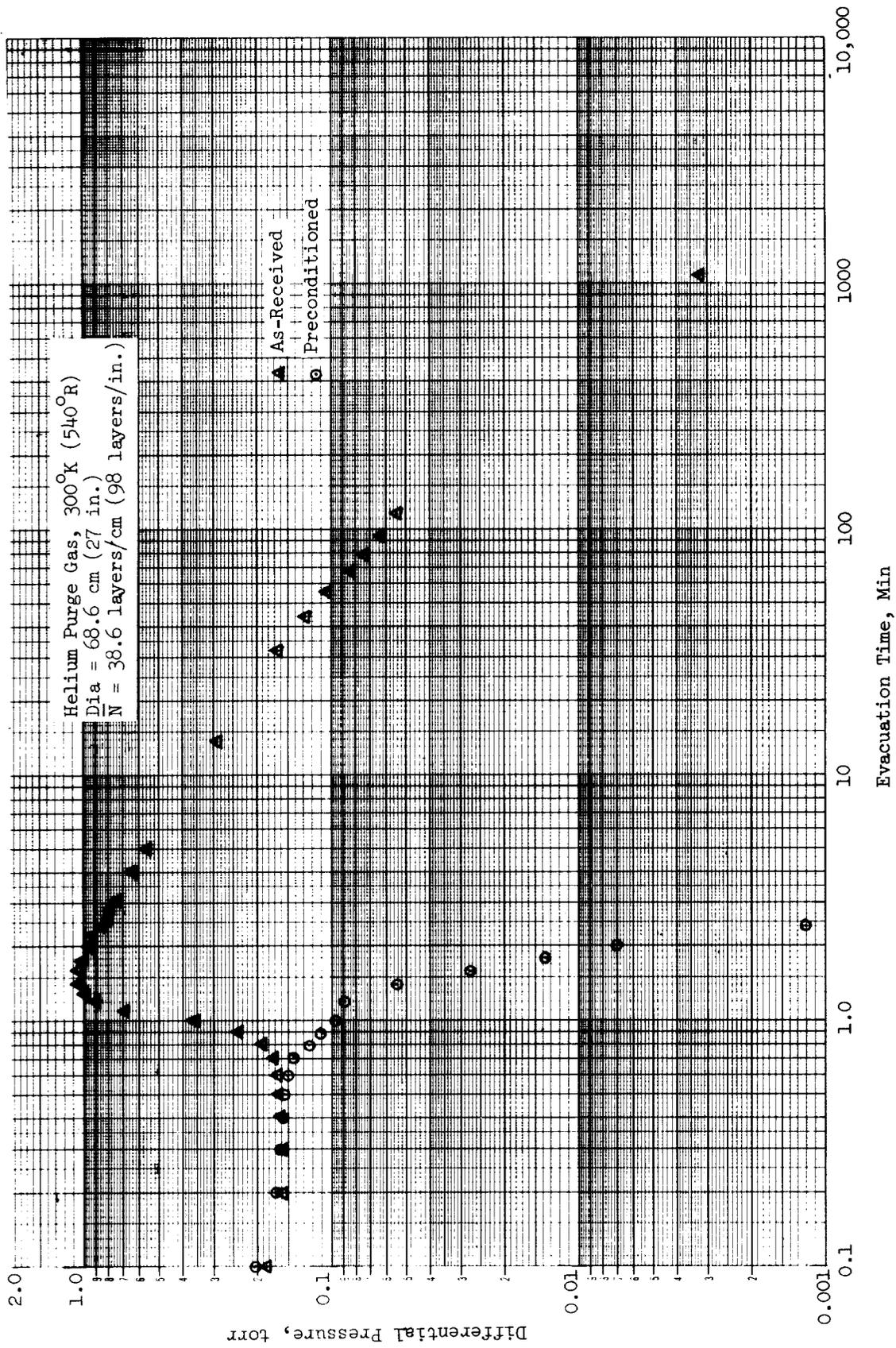
Fig. 5-38 Effect of Outgassing on Unperforated, Double-Aluminized Mylar/Silk Net, Specimen No. 20

5-94
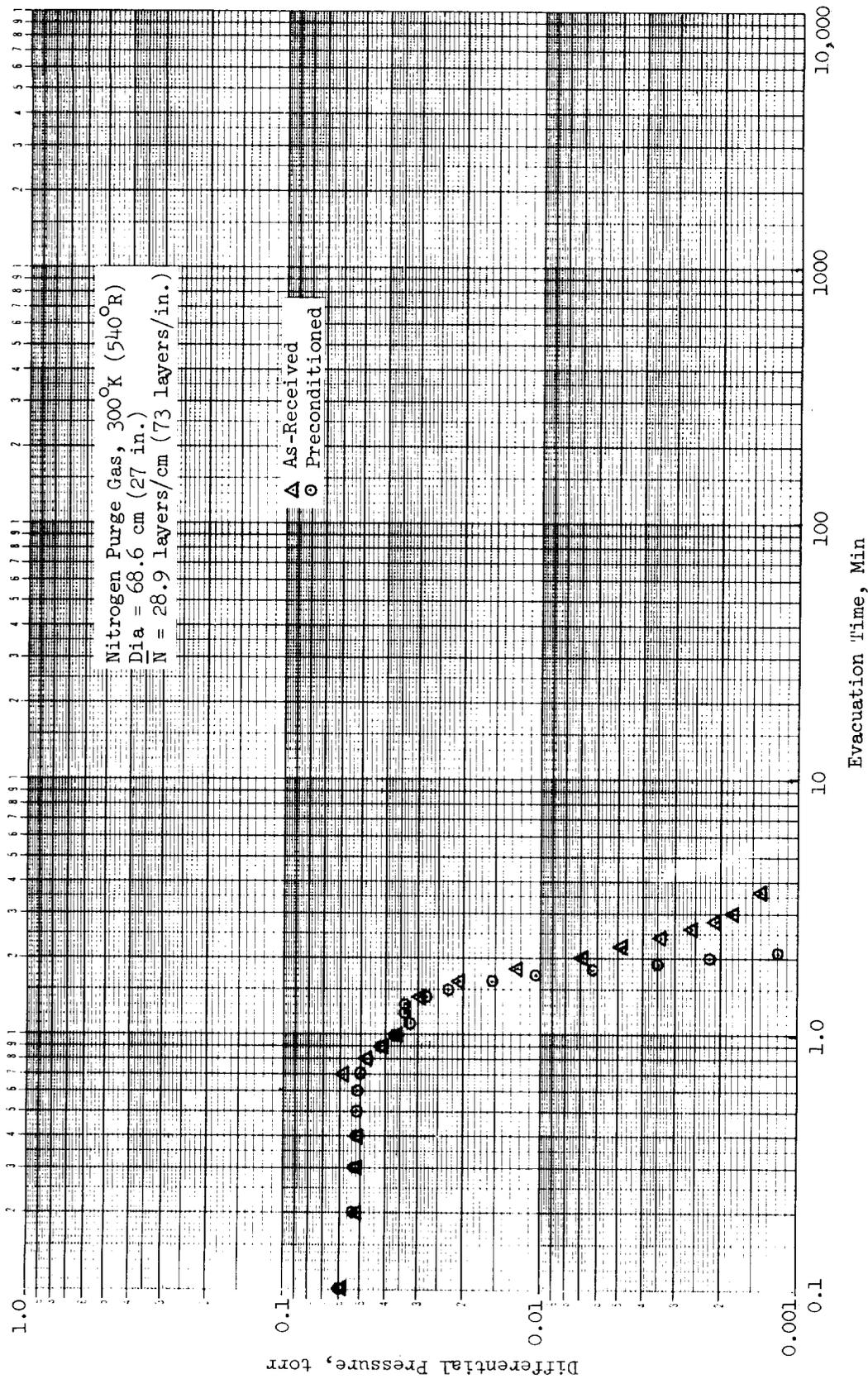
Fig. 5-39 Effect of Outgassing On Crinkled, Single-Aluminized Mylar, Specimen No. 21A

Nitrogen Purge Gas, 300°K (540°R)
Dia = 68.6 cm (27 in.)
N̄ = 28.9 layers/cm (73 layers/in.)

△ As-Received
⊙ Preconditioned

Evacuation Time, Min

Differential Pressure, torr

molecule and the conductance is constant. Thus, the ΔP has the same time dependence as the outgassing rate. Published data show that for most materials the outgassing rate is inversely proportional to time with an exponent close to unity.

For the silk net spaced systems (Ref Figs. 5-36, 5-37, and 5-38), the outgassing rate was very large because of the water spray preconditioning process used. For these cases, the ΔP was nearly constant for the first part of the evacuation where outgassing was minimal, and the evacuation process consisted primarily of removing the purge gas. At later times, the ΔP actually rose to a maximum and then declined at a rate governed by outgassing as noted previously. As the pressure was reduced, the conductance decreased until the constant free molecule value was reached. On the other hand, as the pressure was reduced, the outgassing rate increased to a maximum value for which the outgassing rate was no longer pressure sensitive. The maximum differential pressure achieved was a result of the interplay of these two effects, and can be explained quantitatively as follows.

The pressure differential can be considered as being due to the flow of two components (i.e., purge gas and outgas). If it is assumed that the influences of these two components are separable, the purge gas ΔP is that found for the preconditioned specimen, and the outgas ΔP is equal to the difference between the ΔP values obtained for the unpreconditioned and the preconditioned evacuations. This outgas pressure differential, ΔP_d, is proportional to the outgassing rate divided by the conductance, and can be expressed by

$$\Delta P_d \propto Q \left[\frac{(P_o - P)}{P_o} \right] \frac{1}{C} \tag{5-65}$$

Assuming an exponential pressure decay, $P = P_o e^{-kt}$ (Ref Eq. 5-8), and assuming that the outgassing rate is inversely dependent on time, then

$$\Delta P_d = K \left[\frac{(1-e^{-kt})}{t} \right] \frac{1}{C} \tag{5-66}$$

where K is a constant and C can be determined from Eq (5-37).

5-96

As an example, consider the evacuation of Specimen 17A. Substituting the correct values into Eq (5-66) for water vapor at $300^{\circ}K(540^{\circ}R)$ and a layer density of 28.4 layers/cm (72 layers/in.) yields the following expression for C using k = 0.080 for the chamber evacuation with t in seconds.

$$C = 8.82 \times 10^{-6} (e^{-kt} + 3.01 \times 10^{-3}) \frac{gm\text{-}cm^2}{sec\text{-}dynes} \qquad (5\text{-}67)$$

Substituting C into Eq (5-66) yields

$$\Delta P_d = K \left[\frac{1}{t} \left(\frac{1 - e^{-kt}}{e^{-kt} + .00301} \right) \right] \qquad (5\text{-}68)$$

For the $300^{\circ}K$ $(540^{\circ}R)$ evacuation in this program, k is 4.8 sec^{-1}. The variable term in Eq (5-68) is the portion in parentheses. This term has been evaluated and plotted in Fig. 5-40. Also plotted in this figure for comparison is the arithmetic difference between the as-received and preconditioned pressure differential data for Specimen No. 17A. It can be seen that the peaks occur at the same evacuation time and that the general form of the curves are similar. The constant of proportionality between the two curves is dependent upon the constant in the outgassing rate equation and, thus, cannot be derived analytically. It can be concluded from inspection of Fig. 5-40 that the explanation offered for the maxima observed in several of the ΔP curves for the as-received specimens is reasonable.

5.3.2 Evaluation of Results

The basic approach used in Task 2 was to determine both analytically and experimentally the pressure in a multilayer insulation system during evacuation of purge gas. Since it is difficult to measure pressure at even a single location, only the maximum pressure was determined, its location being constant and obvious from considerations of symmetry. The experimental data were measured by a diaphragm gauge of exceptional accuracy, reproducibility, and flexibility. The single limitation of the instrumentation was the absence of a means to rezero the gauge at low absolute pressure in the Task 2
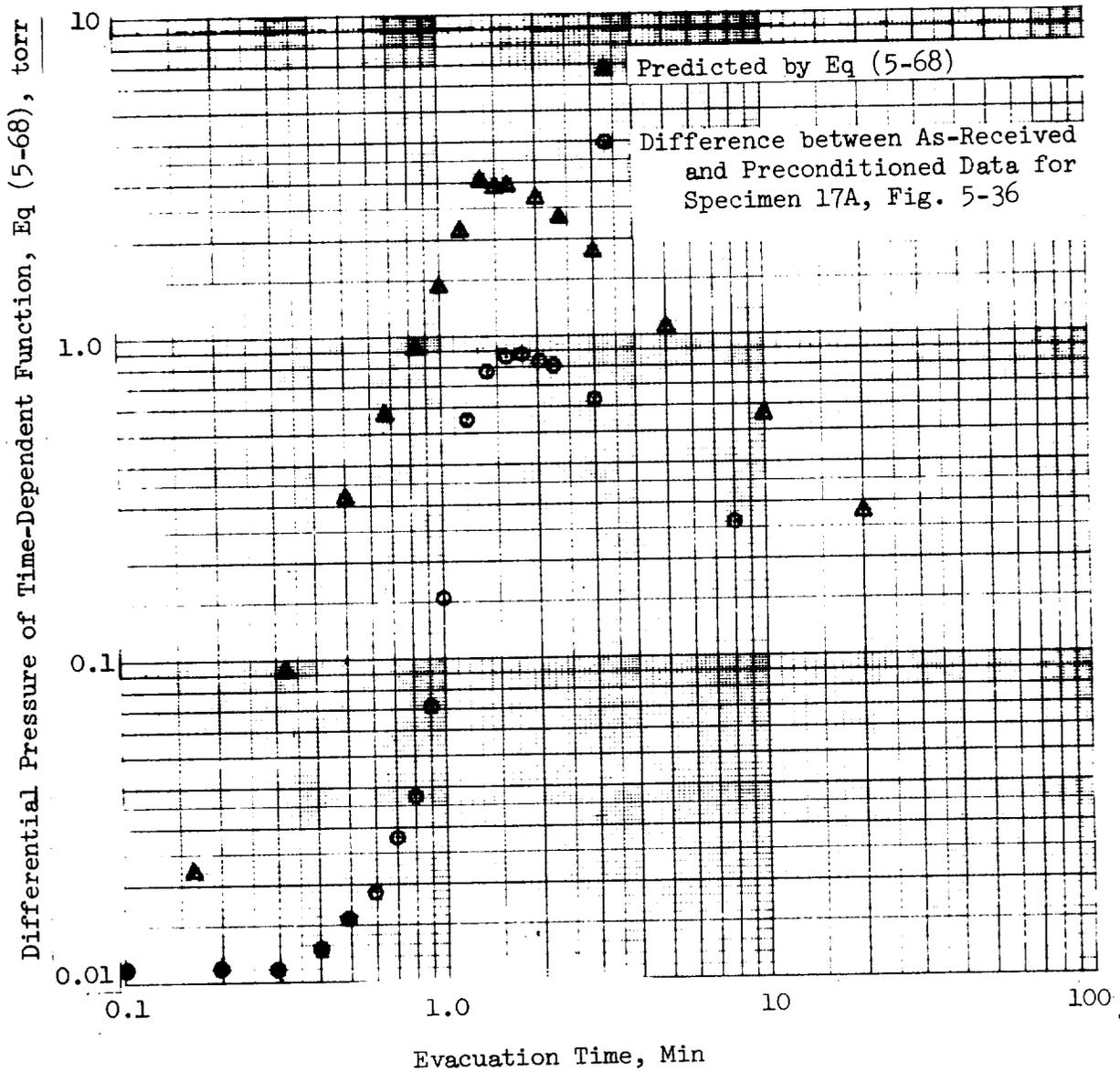
Fig. 5-40 Comparison of Pressure Differential Function Due to Outgassing
Obtained Experimentally and Analytically

installation. When zeroed at 760 torr, the possible error was about + 0.001 torr, so that no useful data could be obtained for absolute pressures below about 0.005 torr. However, the objectives of Task 2 were reached despite this limitation, which was understood and accepted at the outset of the program. The reason for not incorporating a low pressure rezeroing capability in Task 2 was to keep the tubulation between the transducer and the location to be monitored simple, in order to minimize possible associated errors. The extensive checkout of the instrumentation described in Section 5.2.3 indicated that these errors were indeed negligible. Finally, the techniques used for pressure tapping in both edge and broadside evacuation did not interfere with the insulation geometry. Hence, it was concluded that the experimental pressure-time data for Task 2 were highly reliable and that the same technique, with the addition of a rezeroing capability should be used in Task 3.

The analytical model was based on well established theory for viscous, slip, and free molecule flow. The dependence of these flow types on gas molecular weight, viscosity, and temperature have already been determined with great certainty, so the Task 2 experiments with these parameters as variables were to some extent trivial. The principal unknowns were the adequacy of the geometric model and of the Newtonian technique for solving the flow equation. For edge evacuation, the geometric model assumed the multilayers to be rigid, equally-spaced flat plates. Tissuglas spacers were assumed to be equivalent to shields, but silk net spacers were neglected. Crinkled surfaces were assumed to be flat. It was concluded from the program that the assumptions of rigidity and equal spacing were connected, and were more accurate with the high spring constant systems such as crinkled Mylar or silk net-spaced plain Mylar. The Tissuglas-spaced Mylar system was subject to lateral instability which seriously unbalanced the spacing and invalidated the model. However, for those cases where the Tissuglas system remained equally spaced, the agreement between experiment and analysis was very good, which is not surprising since this system most clearly resembles flat plates. For the silk net-spaced Mylar and the crinkled Mylar, the experimental data show higher pressure differentials than the analysis because of the effect of the silk net resistance and the crinkling, respectively. It was shown that these

influences can be allowed for by using an "equivalent spacing" in the analysis, based upon the total surface exposed to the flow. It was concluded, therefore, that if the analysis is used with this adjustment to the spacing satisfactory agreement with the experiment will be found (i.e., of the order of $\pm$ 15 percent). For a low spring constant system such as Tissuglas-spaced Mylar the measured pressure differential may be much less than the predicted value because of lateral instability and channelling.

For broadside evacuation an additional simplifying geometric assumption was made regarding the distribution of flow through successive perforations. This was found to be quite satisfactory. However, the assumption of rigid equally-spaced flat plates was inadequate for the early stages of evacuation when the induced pressure differentials were sufficiently large to compress the insulation system and reduce the interlayer separation significantly. The scope of the program was not sufficient to permit a full investigation of this effect, but a rough calculation using Task 1 spring rate data for silk net-spaced Mylar indicated that the effect of layer compression on pressure differential could be modelled with little difficulty. However, for the Tissuglas-spaced system, the spring constant was very small and the layer density was high, which exaggerated the compressive effect so severely that evacuation flow was all but shut off, and the analysis was unable to handle this extreme case without appropriate spring rate data. Fortunately, the experiment also indicated that this system was impractical so that no further work was needed. A second assumption used in the broadside evacuation model was that silk net has negligible lateral flow resistance, but that Tissuglas has finite lateral flow resistance. An analysis was developed to account for this lateral flow resistance, but again due to the impracticability of the Tissuglas system it was of no importance and has not been presented.

A numerical integration technique may be judged by its speed and its accuracy. The Newtonian technique is simple to use, but is neither as fast nor as accurate as other more sophisticated techniques. Its accuracy seems adequate for the present purposes, in view of the various uncertainties associated with the geometric model. However, the speed is impractically slow at the

lower layer densities and a faster integration technique such as the DuFort-Frankel technique should be used in future work.

It is generally concluded that, although further work would be desirable in some areas, it is possible to predict the evacuation rate of purge gas from an insulation system with accuracy sufficient for engineering purposes. The data show that the purge gas pressure follows the absolute pressure very closely and thus presents no long-term evacuation problem. The long-term problem is clearly due to outgassing alone, and this cannot be predicted unless outgassing data are available. The Task 2 program scope did not include generation of outgassing data, so this aspect was not fully investigated. Availability of such data are crucial to the usefulness of the analysis as an engineering design tool and further work is needed in this area. Unfortunately, techniques to determine outgassing data with the preciseness required for parametric analysis are not yet available. The evacuation data for these samples tested in both the as-received and the preconditioned states do indicate quite dramatically that a day of preconditioning evacuation, even without the application of heat, can be most effective in reducing the sorbed gas concentration to negligible values.

5.3.3 Application to MLI System Design

Two significant design problems are associated with the evacuation of multilayer insulation. In the early stages of evacuation the induced pressure differential can be quite high and may result in unacceptably high mechanical loading on the layers. Also, the attainment of pressures less than about 10^{-6} torr, necessary for complete elimination of gaseous heat conduction, may be delayed by outgassing from the layer surfaces. Clearly, both of these problems can be addressed using the techniques described in the preceding section. To do so it is necessary to develop a computer program based upon the equations presented, preferably using a faster integration technique. To perform the design analysis, data is needed for the expected variation of ambient pressure with time, and also for the outgassing rate of the materials to be used.

LOCKHEED MISSILES & SPACE COMPANY

In analyzing the data obtained in Task 2, it was shown that the evacuation could be represented approximately with a single equation by considering the insulation to consist of a single lumped node. This type of approximation can be used to estimate the pressure differential due to outgassing when the absolute pressure is small enough for the flow to be in the free molecule regime. In this regime the flow conductance is independent of absolute pressure and the pressure differential is a constant factor times the outgassing rate (Ref Eq 5-51 or Eq 5-54). To determine the time-maximum pressure differential does require the full multinode time-dependent analysis to be made. The Task 2 data show that this maximum could occur during early times, when purge gas evacuation predominates, or at later times, when outgassing predominates. Further, previous work (Ref 27) has shown that the shape of the ambient pressure history is of great significance in determining the magnitude and time of occurrence of the maximum pressure differential. There is one exception to the above, and that is the case where outgassing is negligible and where the ambient pressure history can be represented by an analytical function, such as the exponential decay associated with a constant-volume pumping system. In such a case an approximation similar to Eq (5-46) can be made.

In the special case of applying the Task 2 data to the Task 3 experiment design under this program, a slightly different design procedure was necessary. First, although a computer program was desireable, the one developed in Task 2 was admittedly too slow for a low layer density such as that specified for the Task 3 MLI system. Also, no outgassing data were available for the Mylar/water-preconditioned silk net system. The pressure-time history, therefore, was inferred from other data. Only the long-term effects were of principal interest. In Task 2, several similar Mylar/water-preconditioned silk net specimens were tested. It was assumed that the outgassing rate of all of these specimens was the same (although unknown), and that the pressure-time history for the Task 3 system could then be scaled from the Task 2 data according to the radius and layer separation relations presented in the preceding subsections. This was done, and the engineering conclusion obtained

was that vacuum preconditioning was essential in Task 3 if the interstitial pressures were to be reduced to acceptable values within reasonable times. Subsequent testing in Task 3 indicated that the extrapolated Task 2 data were within approximately 20 percent of the observed Task 3 data.

Section 6

TASK 3 - MULTILAYER INSULATION SYSTEM TESTS

The primary objective of Task 3 of the contract program was to verify
the analytical expressions developed in Tasks 1 and 2, respectively,
for predicting the evacuated thermal performance and the gas evacuation
characteristics of a selected MLI composite system installed on a 1.22-m-
(4-ft-) diameter tank calorimeter. The unperforated, double-aluminized
Mylar/water-preconditioned, double silk net composite system was selected
for this work.

Eight blankets of the selected MLI composite were fabricated and installed
on the tank. Each blanket contained 14 reflective shields and an equal
number of double silk net spacers, except that the blanket installed
directly on to the tank wall contained one additional double-net spacer.
Subsequent to installation, and again after each test series, the layer
density of this MLI system was assessed by obtaining tangential x-ray
exposures at 22 target locations distributed over the surface of the tank.
Thickness data and interstitial pressure measurements were also obtained during
the testing using unique instrumentation developed specifically for this
purpose.

During Task 3, three different heat flux tests and a single rapid evacuation
test were performed with the 112-shield system installed on the tank. Sub-
sequently, half of the MLI blankets were removed. One additional heat flux
test and a single gas evacuation test were then performed for the remain-
ing 56-shield system.

Details and results of the MLI fabrication, assembly, installation, and
testing are presented in this section.

6-1

6.1 INSULATION FABRICATION AND ASSEMBLY

6.1.1 Composite Material Selection

The double-aluminized Mylar/preconditioned silk net material system was
selected for the Task 3 tank tests from among the three basic material
composite candidates described in Section 3. The selection was based on
the results of the NAS 3-12025 contract program (Ref 28), as well as on results
of prior laboratory scale tests performed under Tasks 1 and 2 of this
contract program. The basic criteria used to make the selection are
as follows:

    (1)   Thermal performance and reproducibility of thermal performance.

    (2)   Adaptability to rapid evacuation without damage (edge-pumping
           or broadside-pumping modes).

    (3)   Forming and fabrication characteristics.

Initially, it was intended to fabricate and test two similar tank-installed
MLI systems of the selected material composite using first unperforated and
then perforated reflective shields. Prior to the tests conducted in Tasks
1 and 2, it had been anticipated that the perforated-shield system would
incur significantly higher radiative heat transfer, compared to the system
with unperforated shields, but that this would be partially or totally
offset by reduced conductive heat transfer due to an expected improvement
in gas evacuation characteristics. Results of the Task 1 heat transfer
tests showed that the system with the perforated shields did in fact
experience significantly higher radiative heat transfer. However, no
significant improvement in gas evacuation characteristics was observed
in the Task 2 tests of this system, even for the special case where the
circumferential edges were left unsealed in order to provide both broadside-
pumping and edge-pumping gas evacuation paths simultaneously. Thus, the
use of a perforated MLI system would be necessary only where some peculiarity
of the design or configuration required continuous taping of butt joints
of segments comprising a single MLI blanket.

LOCKHEED MISSILES & SPACE COMPANY

Based on these findings, only the unperforated system was tested in Task 3, although both composite systems were designed and fabricated. After fabrication, the perforated-shield system was protectively packaged and stored in the event that future testing of this particular system is warranted.

6.1.2 Molded Nylon Buttons

Button-pin attachments similar to those developed on a previous program (Ref 29) were used to assemble the tank MLI blankets in Task 3. The basic button stud was injection molded from Zytel 101*, a general purpose nylon resin molding powder. A GFE two-cavity injection molding tool was modified under the contract and used to produce these studs. During the modification, new inserts were machined in order to provide the required stud length of 0.508 cm (0.200 in.) and to replace the half-round stub shank end with a 0.953-cm-(0.375-in.-) long tapered extension. The purpose of the extension was to provide a means for holding the stud and preventing the shank from buckling during installation of the 1.27-cm-(0.5-in.-) diameter teflon retainer, which snaps into place in the detent groove on the shank. Subsequent to the installation, the shank extension was heated with a soldering tool and formed into a bead over the retainer to provide a permanent attachment. Details of the modified button stud are shown in Fig. 6-1.

Note: All dimensions in centimeters
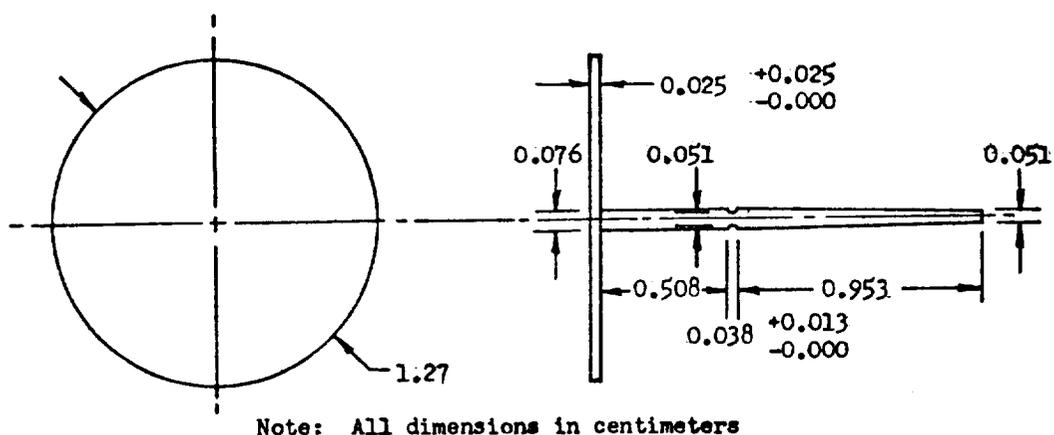
Fig. 6-1 Molded MLI Button Stud

* E. I. DuPont

6-3

6.1.3 Blanket Fabrication, Assembly, and Installation

The composite MLI system that was fabricated and installed on the tank calorimeter in Task 3 consists of eight multi-segment blankets. Each blanket is composed of unperforated, 0.0064-mm (0.25-mil), double-aluminized Mylar radiation shields alternated with water-preconditioned, double-thickness silk net spacers. The first blanket (i.e., that installed directly onto the tank wall) consists of 14 radiation shields and 15-double-net spacers (30 nets), with a spacer layer at each of the inner and outer blanket boundaries. Each of the seven remaining blankets contains 14 radiation shields and 14 double-net spacers (28 nets), and was assembled with a spacer layer at the outer blanket boundary only. The double-net spacer provided for the eighth (outermost) blanket was not required thermally, but served to contain and protect the MLI during handling.

For this MLI system, each blanket consists of a neck cylinder segment, an upper dome segment, a tank cylinder segment, and a lower dome segment. All of the cylinder segments were laid up in a flat pattern, whereas all of the dome segments were laid up over a contoured shop aid in order to achieve a more precise fit to the tank dome surfaces. The configuration of the tank calorimeter, prior to installation of the MLI, can be seen in the photograph of Fig. 6-2.

During layup of the dome blanket segments, radial slits were cut around the periphery of each radiation shield in order to fit it to the compound-curvature surface. These slits varied in length from 15.2 to 30.5 cm (6 to 12 in.) and were spaced at approximately 30-degree intervals around the circumference. Mating edges of the slits were overlapped and spot-taped with aluminized Mylar tape during the assembly.

Silk net spacers for cylinder blanket segments were prestretched over a rectangular, flat-pattern frame, sprayed with water, and were then air dried prior to assembly of the blankets. Similarly, the dome blanket net
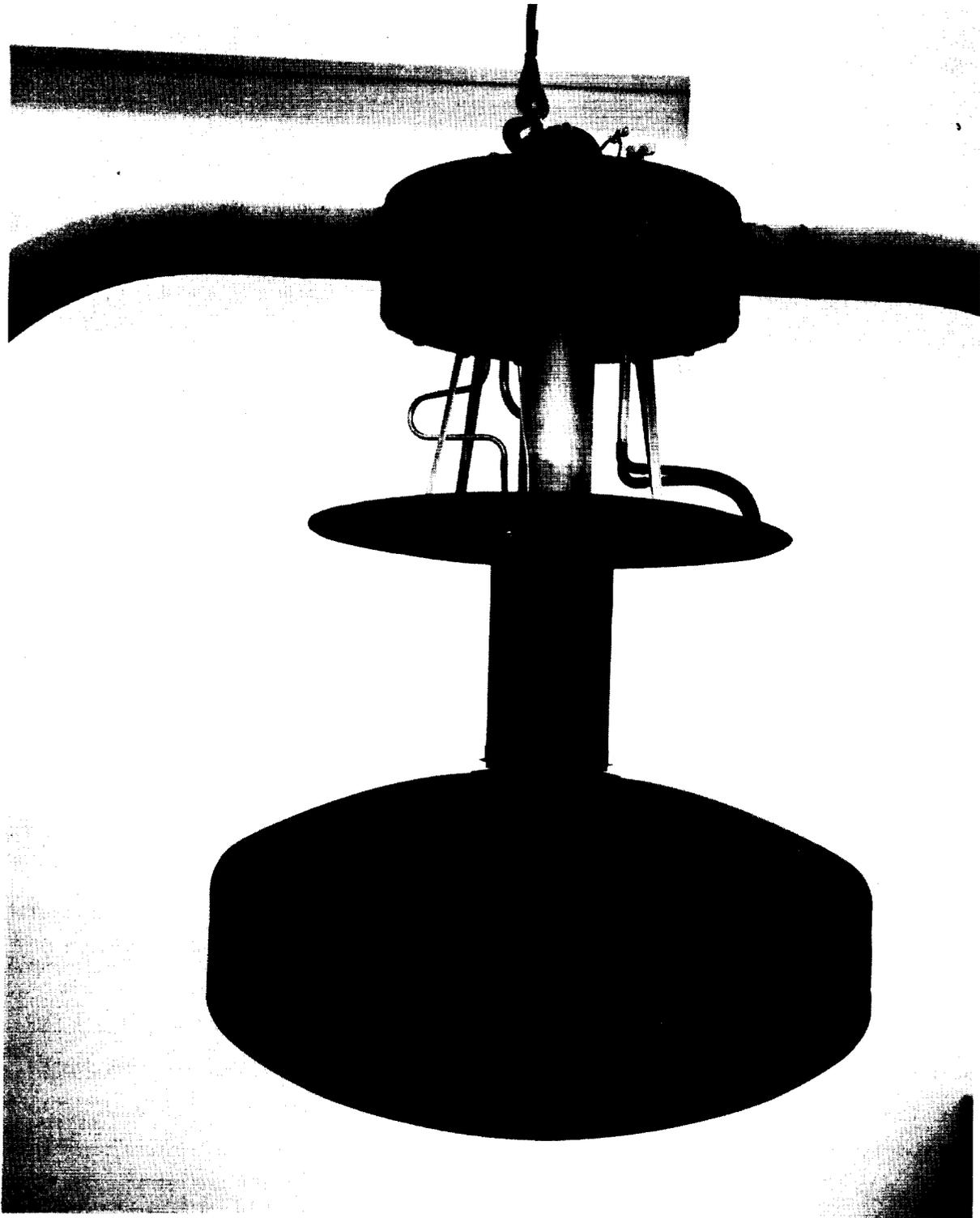
Fig. 6-2 Uninsulated Tank Calorimeter Supported in Handling Fixture

LOCKHEED MISSILES & SPACE COMPANY

spacers were preformed by water spraying over a contoured drying fixture. The primary purpose of this water-preconditioning process was to improve layer density control by eliminating wrinkles as well as to form to the desired surface contour as an aid in fabricating the blankets.

All cylinder and dome blanket segments were fabricated slightly oversize to permit trimming during assembly. Molded nylon buttons, spaced at approximately 10.2-cm (4-in.) centers along the edges with an edge distance of approximately 1.27 cm (0.5 in.), and at approximately 30.5-cm (12-in.) centers throughout the interior, were used to assemble each blanket segment. These buttons were sized to maintain a nominal blanket thickness of 0.508 cm (0.200 in.) based on a target design layer density value of 27.6 layers/cm (70 layers/in.).

During installation onto the tank, mating edges of the adjoining segments of each MLI blanket were match-trimmed in place in order to achieve a good fit at the intervening butt joints. The upper dome segment of each blanket was cut apart along a constant-meridian line to facilitate installation around the calorimeter neck. This resulted in a single longitudinal butt joint at the closure of this segment. Additional longitudinal butt joints also resulted where the ends of each of the neck and tank cylinder segments came together as they were wrapped around the tank. For each blanket, the neck cylinder segment was installed first, followed in sequence by the upper dome, tank cylinder, and lower dome segments. This sequence is illustrated by the photograph of Fig. 6-3 which was obtained after all but the lower dome segment of the first MLI blanket had been installed. After adjoining blanket segments were positioned on the tank and match-trimmed, both the longitudinal and circumferential butt joints were closed by lacing between the opposed rows of edge buttons using nylon monofilament. In addition, mating outer radiation shields of adjoining blanket segments were attached using short lengths of aluminized Mylar tape spaced at approximately 10- to 15-cm (4- to 6-in.) intervals. In applying the tape, care was exercised to ensure that no less than 40 percent of the joint was left untaped to provide a
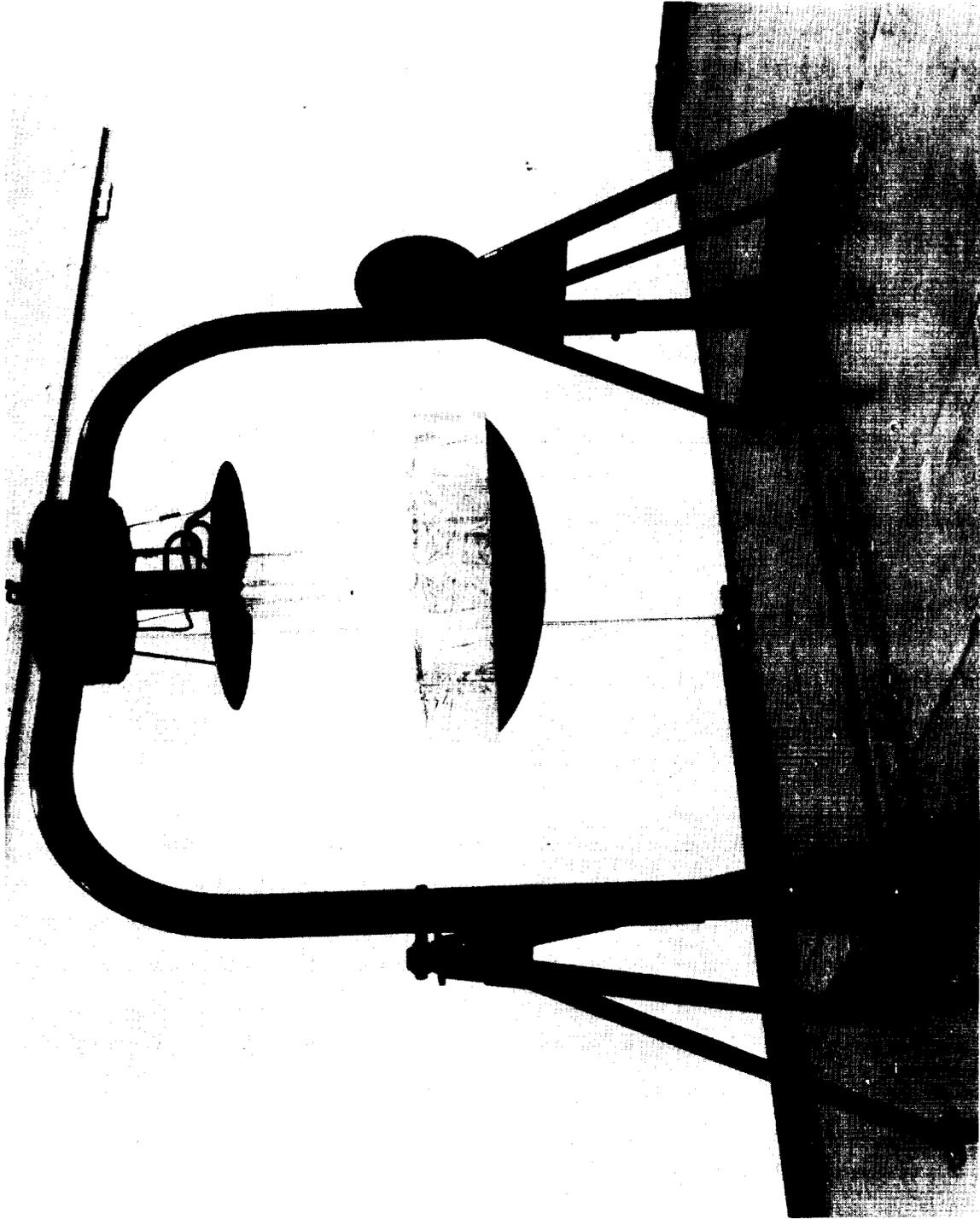
Fig. 6-3 MLI Blanket Installation Sequence

LOCKHEED MISSILES & SPACE COMPANY

sufficient path for evacuation of interstitial gas molecules. The lacing and the tape both serve to limit any inadvertant joint gaps, and thus minimize radiation penetration effects, as well as to provide structural integrity for support of the blanket around the tank. In this installation, no attachments were provided between successive blankets, and only minimal attachments (four small velcro fasteners located at 90° intervals on the lower dome) were provided between the tank wall and the first blanket.

Prior to installation of each MLI blanket onto the tank, 12 to 16 equally-spaced longitudinal slits, each 2.5 to 5.1 cm (1 to 2 in.) in length, were cut through the thickness at the lower edge of the neck cylinder segment. The rectangular tabs thus formed were extended radially outward onto the upper dome as the segment was positioned around the calorimeter neck. The resulting triangular gaps which opened between these tabs were then covered with short pieces of aluminized Mylar tape applied directly to the outer radiation shield of each neck blanket segment. After installation, a cat-gut draw string was tied lightly around the periphery of each neck blanket segment to control the circumference of the blanket, as well as to aid in controlling the layer density and the desired blanket contour in the neck/upper dome interface region. The installation of the MLI in this area can be seen in the photograph of Fig. 6-4.

During installation of some of the tank cylinder blanket segments, small pie-shaped sections (as required) were cut out and removed from both the upper and lower edges in order to fit these segments to the contour of the tank near the dome/cylinder interfaces. The resulting longitudinal slits, which varied in length from approximately 2.5 to 5.1 cm (1 to 2 in.) and were spaced at 20- to 30-cm (8- to 12-in.) intervals around the circumference, were closed and spot taped in a manner similar to that described above for the longitudinal butt joints.

As each succeeding MLI blanket was installed on the calorimeter tank, all longitudinal and circumferential butt joints were staggered by a distance

6-8
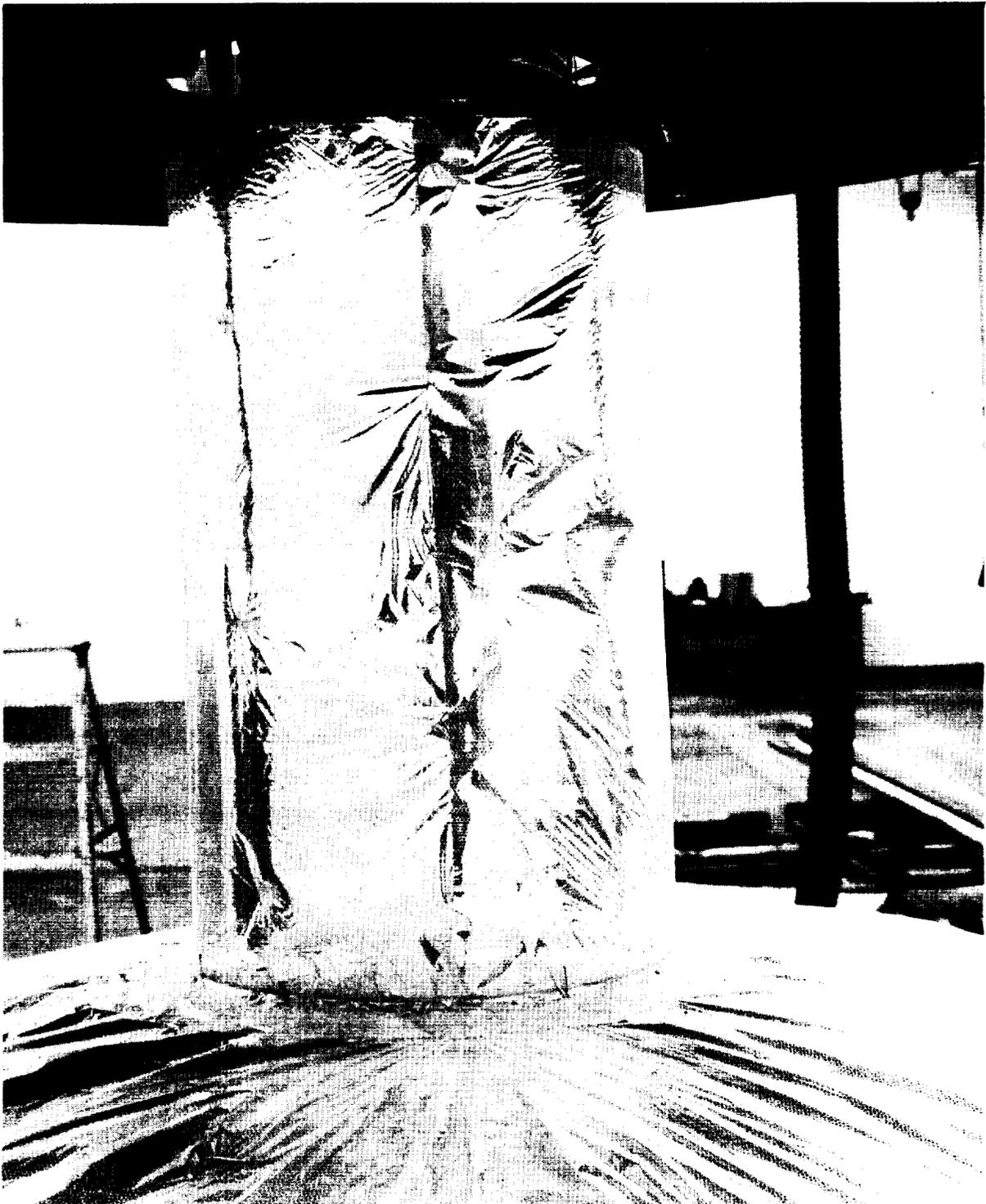
Fig. 6-4 Neck Cylinder/Upper Dome MLI Blanket Interface

LOCKHEED MISSILES & SPACE COMPANY

of approximately 2.5 to 5.1 cm (1 to 2 in.) with respect to those existing in the preceeding blanket. Particular attention was given to ensure that the slits introduced at the neck cylinder/upper dome segment interface, as well as those introduced at the tank cylinder/dome segment interfaces, were staggered from blanket-to-blanket through the thickness.

The tank calorimeter is shown in the photograph of Fig. 6-5 with seven of the eight MLI blankets already installed. Components of the lower dome segment for the eighth and final blanket of this system can be seen on the contoured shop aids in the foreground.

6.1.4 MLI Instrumentation

During fabrication and installation of the unperforated Mylar/silk net composite system, a total of 25 chromel-constantan thermocouples were installed at six different locations surrounding the tank as shown in Fig.6-6. In order to measure temperature profiles through the thickness of the MLI during the testing, two radial arrays of six thermocouples each were installed at selected locations on the upper and lower domes, and two additional radial arrays of four thermocouples each were added at separate locations on the upper dome and the tank cylinder. Individual thermocouples were installed on the neck cold guard coils and on the interstitial pressure sensor plenums to provide surface temperature data for these components.

Prior to installation of the first MLI blanket segments, a 0.318-cm-(0.125-in-) thick copper plate, approximately 10.2 cm (4 in.) long by 5.1 cm (2 in.) wide, was brazed to the outer surface of the lower dome. Thirty chromel-constantan reference thermocouple junctions were then installed by inserting each into a small-diameter hole pre-drilled into the edge of the copper plate and by peening the copper over it to achieve a good thermal contact. Subsequently each pair of reference thermocouple wires was attached to the tank surface at intervals of approximately

6-10
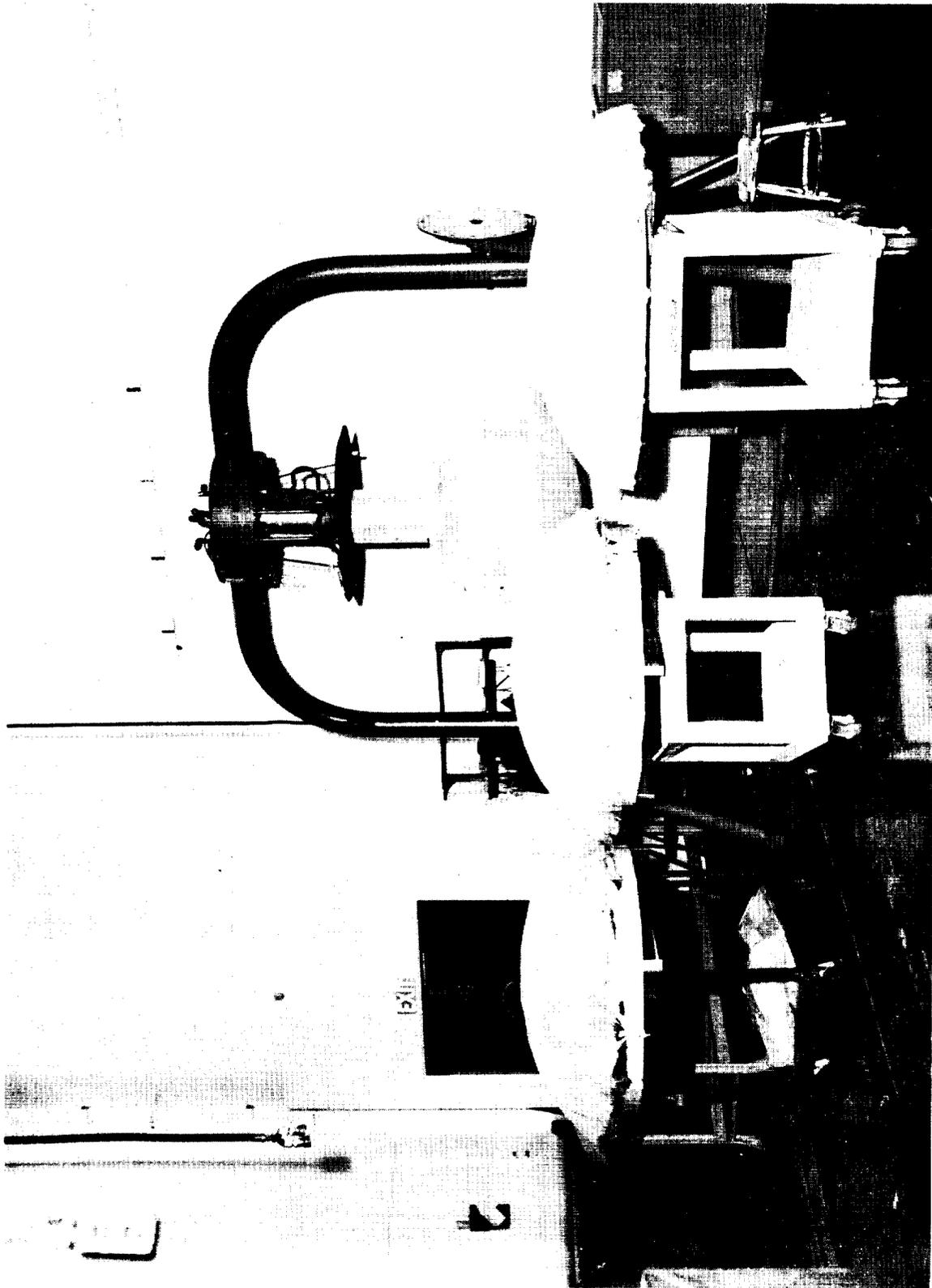
Fig. 6-5 Tank MLI Nearing Completion
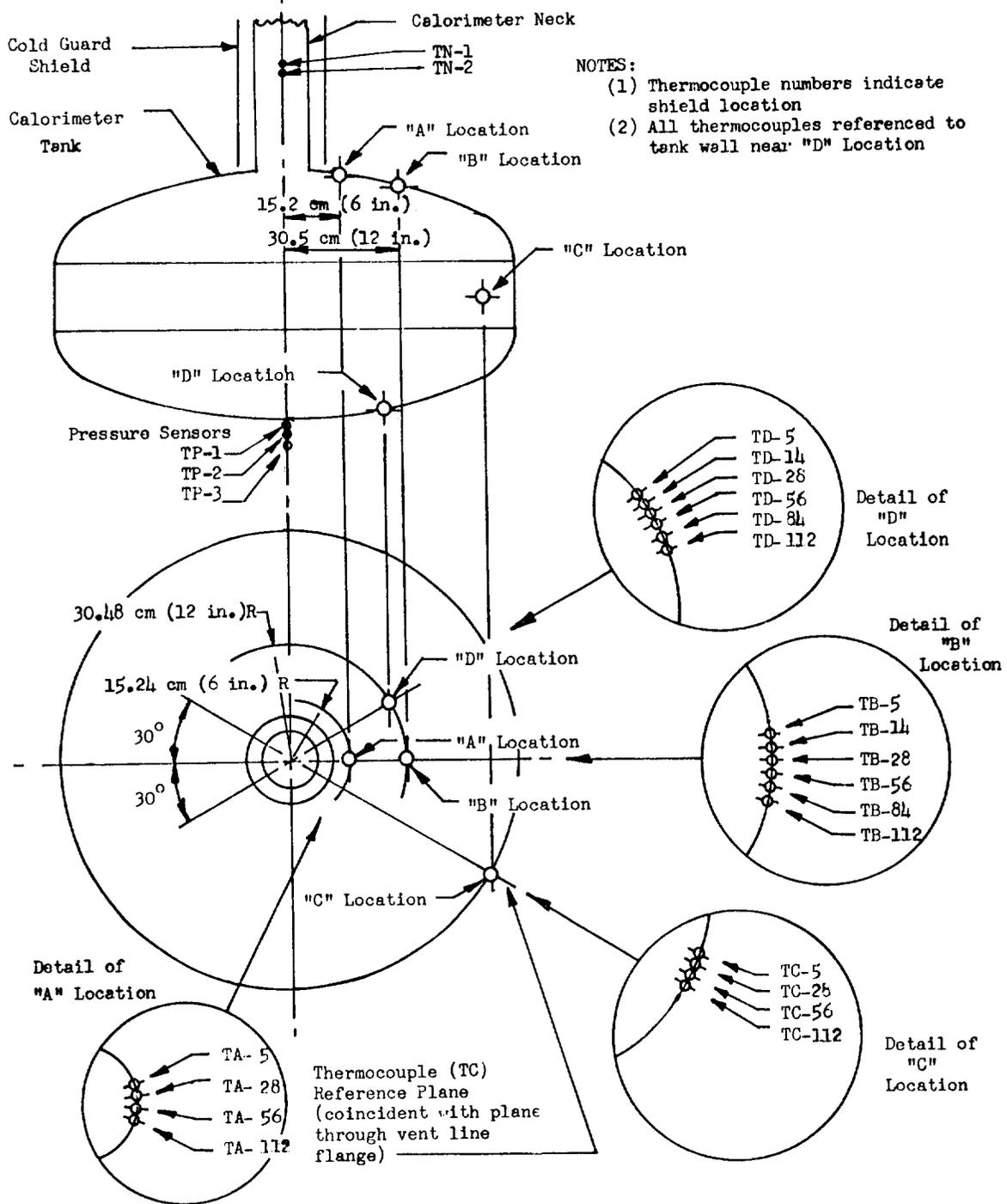
Fig. 6-6 Tank Calorimeter Thermocouple Locations

LOCKHEED MISSILES & SPACE COMPANY

30.5 cm (12 in.) along constant-meridian lines using small pieces of clear Mylar tape. The reference wires were routed to a point on the neck slightly above the cold guard coils for later connection to the measuring thermocouple leads as the MLI blankets were installed. These wires were taped to the guard coils in this region in order to intercept heat that might otherwise be conducted into the tank.

Chromel-constantan thermocouples were selected in preference to other types primarily because they exhibit greater sensitivity (i.e., higher output) at low temperatures near that of liquid hydrogen, and because the relatively low thermal conductivity of these materials, compared to copper in particular, results in minimum extraneous heat conduction into the system. In addition, thermocouples fabricated from these materials have been used with good reliability for previous applications with similar requirements.

Each of the MLI thermocouples was attached to the outer surface of the specified radiation shield at the location selected using a 1.27-cm-(0.5-in.-) square piece of clear, double-faced Mylar tape placed between the junction and the shield. Lead wires were routed along constant-meridian lines from the attachment point to the neck area where the MLI blankets were terminated. Short lengths of aluminized Mylar tape were used to attach the lead wires to the exterior surface of the shields at intervals of approximately 30.5 cm (12 inches). A continuous 30.5-cm (12-in.) length of the tape was then placed over the thermocouple junction and the adjacent portion of the lead wires to eliminate local gradients and thus ensure true shield temperature measurements.

Thermocouples attached to the calorimeter neck cold guard and to the interstitial pressure sensor plenums were bonded in place using silver-filled epoxy to ensure good thermal contact. Lead wires for the cold guard thermocouples were spot-taped to the neck, whereas those for the pressure sensor plenums were routed along and spot-taped to the MLI radiation shields in a manner similar to that described above for the MLI thermocouples.

LOCKHEED MISSILES & SPACE COMPANY

Lead wires for the pressure sensor plenum thermocouples and all MLI thermo-couples, except those attached to the fifth radiation shield, were routed along and spot-taped to the outer shield of the particular blanket in which they were installed. Those for the fifth shield thermocouples were routed along and spot-taped to the fifth radiation shield, but only within the blanket segment (i.e., lower dome, tank cylinder, etc.) in which they were installed. At the point where these leads reached the circumferential butt joint between that segment and the next higher one, they were routed radially out through the joint and, thereafter, were routed along and spot-taped to the fourteenth radiation shield (i.e., the outer shield for the first blanket).

During assembly of the unperforated Mylar/silk net composite system, a total of 120 lead tape x-ray markers were installed at 20 different locations sur-rounding the tank as shown in Fig. 6-7. These markers were provided as an aid to assess blanket-to-blanket layer density distribution through the thickness of the MLI from pre-test and post-test x-ray data. Each is approx-imately 2.5 cm (1 in.) long by 0.64 cm (0.25 in.) wide by 0.13 mm (5 mil) thick, and is attached with a pressure-sensitive adhesive backing directly to the MLI radiation shield at the location indicated in the figure. The marker thickness selection was based on results obtained from a preliminary experimental study. In this study, it was determined that the x-ray image obtained for thinner markers was not sufficiently distinct for a large number of MLI layers. Since the surface area of the markers was small compared to the total shield surface area, the degradation of emissivity due to their presence was insignificant.

In addition to the thermocouples and x-ray markers described above, three small plastic interstitial pressure sensor plenums were also installed at the center of the lower dome segments for the first, third, and seventh MLI blankets (numbered in sequence from the tank wall). Since each lower dome blanket segment is circular (i.e., radially symmetrical), the plenums were placed at the center to ensure measurement of pressures precisely at the no-flow boundary point during evacuation and repressurization cycles.

6-14
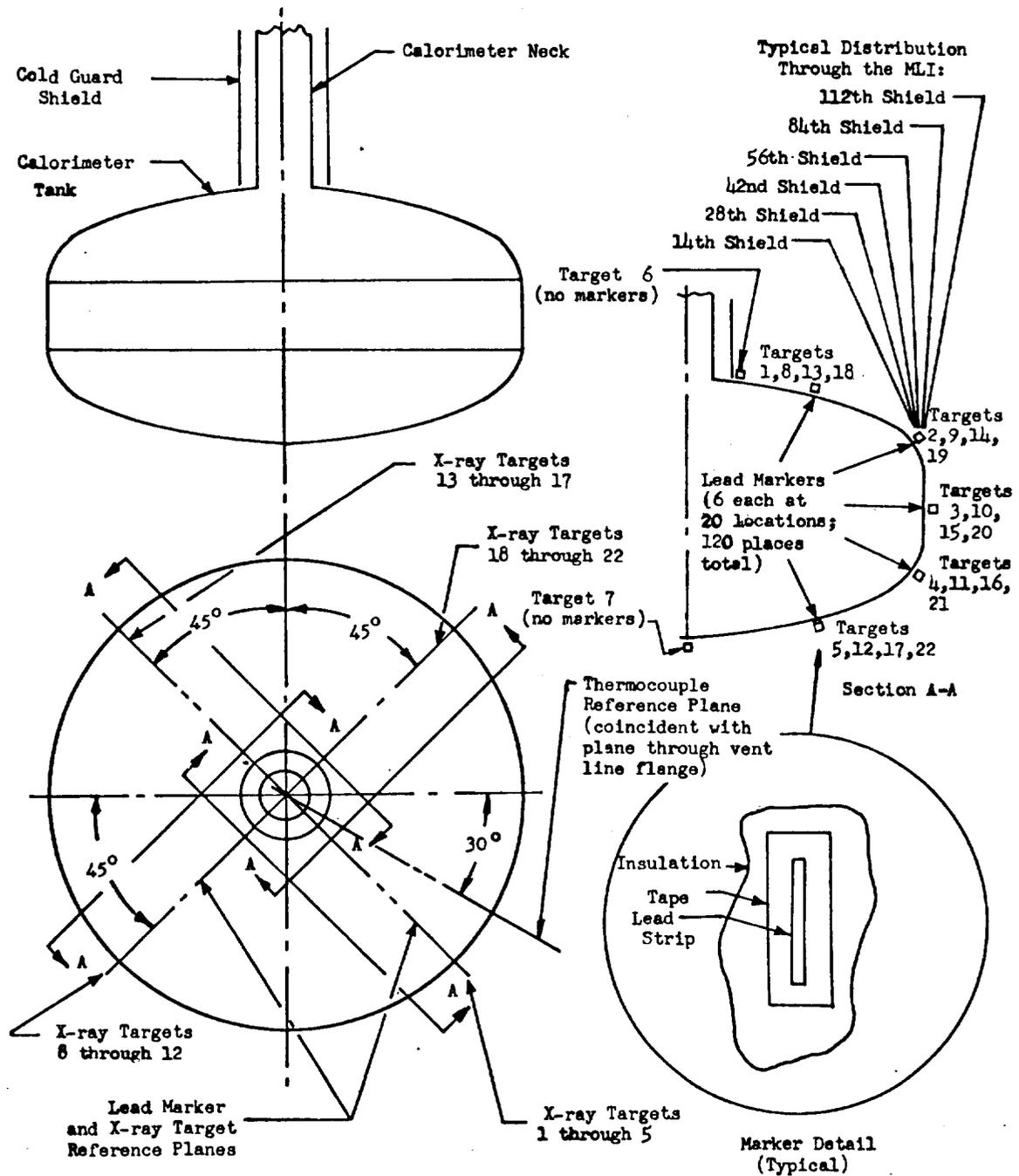
Fig. 6-7   Tank Calorimeter X-Ray Marker and Exposure Target Locations

6-15

Consequently, the plenums are concentric with the longitudinal axis of the tank, and are directly superimposed, one over the other, through the thickness of the MLI system.

Each plenum consists of a 0.508-cm-(0.2-in.-) long, 2.54-cm-(1-in.-) diameter, 0.051-cm-(0.020-in.-) thick cylindrical shell bonded to flat end-closure discs. The diameter of the outer disc matches that of the cylinder, whereas the inner disc was cut to a 5.72-cm (2.25-in.) diameter and overlaps the cylinder in order to provide a mounting flange for the MLI. Twelve 0.25-cm-(0.10-in.-) diameter holes, equally spaced at 30-degree intervals around the circumference of the cylinder, permit free communication of trapped interstitial gas molecules between the blanket segment multilayers and the plenum. A pressure sensing tube, approximately 30.5 cm (12 in.) long by 0.203 cm (0.080 in.) I.D., connects each plenum with the externally-mounted pressure transducer system. A typical sensor plenum is shown in the cut-away view of Fig. 6-8.

The pressure sensing tubes were mounted parallel to the longitudinal axis of tank (i.e., normal to the insulation multilayers) in order to obtain a relatively short, relatively large-diameter sensing path. Previous work has shown that longer, capillary-sized sensing tubes do not provide adequate response within the free molecular flow regime as the system is evacuated to lower pressures. The tubes are offset by approximately 1.0 cm (0.4 in.), with respect to each other, to form a triangular-pattern bundle as they emerge from the insulation. Pass-through tubes were installed as required to accommodate penetration of the third-blanket plenum by the first-blanket sensing tube, and penetration of the seventh-blanket plenum by sensing tubes from the first- and third-blanket plenums. For each penetration, 0.64-cm-(0.25-in.-) diameter holes were cut through each end-closure disc, and a 0.51-cm-(0.2-in.-) long, 0.64-cm-(0.25-in.-) diameter pass through tube was bonded in place to seal the plenum cavity. Details of the total installation are shown in Figs. 6-9 and 6-10.

6-16

5.72-cm-(2.25-in.-) Dia by 0.025-cm-(0.010-in.-) Thick
Teflon End Closure

2.54-cm-(1.0-in.-) Dia by 0.46-cm-(0.18-in.-) Long
by 0.064-cm-(0.025-in.-) Thick Teflon Plenum Cyl Pre-Drilled
with Twelve 0.254-cm-(0.10-in.-) Dia Holes at 30° Intervals

Aluminized Mylar Tape

MLI Blanket

2.54-cm-(1.0-in.-) Dia by 0.025-cm-
(0.010-in.-) Thick
Teflon End Closure

0.279-cm-(0.110-in.-) O.D. by
0.038-cm-(0.015-in.-) Wall
by 25.4-cm-(10-in.-) Long
Teflon Sensing Tube

Notes:

1. All mating parts cleaned and
   etched with Tetra-Etch,
   W. L. Gove and Assoc., Inc.
   1505 N. 4th St., Flagstaff, Ariz.

2. Assembled with Epibond 123,
   Curing Agent 9615-10,
   Furane Plastics, 16 Spielman Rd.,
   Fairfield, New Jersey.

3. Outgassed in Thermal-Vacuum
   Oven at 25 Microns and 93.3°C (200°F)
   for 24 hours.

0.318-cm-(0.125-in.-) Dia
Stainless Steel Tube Stub

Fig. 6-8 Cut-Away View of Broadside-Flow Pressure Sensor

6-17

LOCKHEED MISSILES & SPACE COMPANY

Tank Wall

MLI
Blanket

No.

1
2
3
4
5
6
7
8

Ten 2.54-cm-(1.0-in.-) Dia
by 2.54-cm-(1.0-in.-) Thick
Cylindrical Core Segments
of Opacified Fiberglass Bat-
ting, Pre-Punched to Fit
Over Sensor Tubes

Tube MLI Blankets Individually
Split, Faired, and Spot-Taped
to Tank MLI

Four 3-wrap Cylindrical
Blankets of Aluminized Mylar

Tube MLI Blankets Individually
Split, Faired, and Spot-Taped
Around Sensor Tubes

Sensor No. 2

Sensor No. 3

Sensor No. 1

Fig. 6-9   Section Through Pressure Sensor System Installation

LOCKHEED MISSILES & SPACE COMPANY
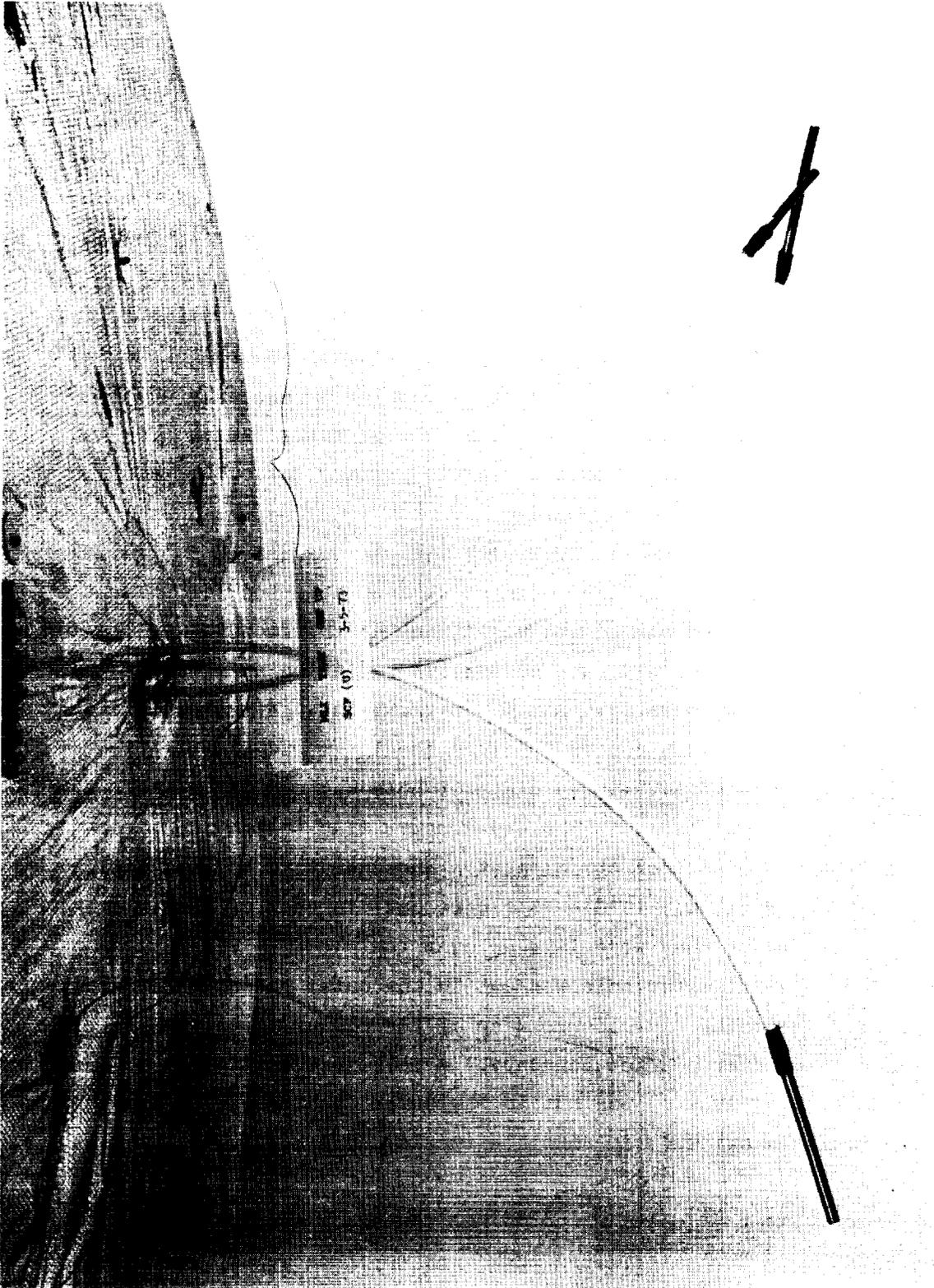
Fig. 6-10 View of Lower Dome Showing Uninsulated Pressure Sensor Leads

LOCKHEED MISSILES & SPACE COMPANY

Component parts of each pressure sensor plenum were cut from teflon tube and sheet stock. This material was selected primarily because it offers exceptionally low thermal conductivity as well as minimum outgassing characteristics. Low thermal conductivity is essential to this particular design in order to minimize heat conduction into the MLI system. Minimum outgassing is required not only to permit adequate evacuation of the plenums but also to minimize pressure measurement errors due to whatever residual outgassing does occur at low pressures. During fabrication, component parts of each plenum were pre-etched and then were bonded together using a low-temperature epoxy adhesive. Subsequently, the assemblies were cured and thoroughly outgassed in a thermal-vacuum oven prior to assembly of the MLI blanket assemblies (Ref Fig. 6-8 for details concerning the etching and bonding materials, and the procedures used to prepare, assemble, and outgas these plenums).

During assembly of each lower dome blanket segment selected for interstitial pressure measurements, the plenum was positioned at the longitudinal center-line of the contoured shop aid, and successive radiation shields and spacer layer nets were laid up over it. A 5.72-cm-(2.25-in.-) diameter hole was cut in the inner double-net spacer to clear the inner end-closure disc of the plenum. Then a 4.45-cm-(1.75-in.-) diameter hole was cut in the inner radiation shield, and it was taped to the end-closure disc to provide a gas-tight seal at the inner boundary of the blanket. Subsequently, holes slightly larger than 2.54 cm (1 in.) in diameter were cut in each of the interior shields and spacers as they were laid up over the plenum. Finally, a 1.91-cm-(0.75-in.-) diameter hole was cut in the outer radiation shield, and it was taped to the outer end-closure disc of the plenum to provide a gas-tight seal at the outer blanket boundary. A hole just sufficient to clear the pressure sensing tube(s) was cut in the outer double-net spacer, and it was placed over the assembly to complete the lay up.

As lower dome blanket segments which do not contain pressure sensor plenums were installed onto the calorimeter tank, one to three 0.318-cm-(0.125-in.-)

6-20

diameter holes (as required) were punched through the multilayers at the center of the segments to accommodate pressure sensing tubes from the inboard blankets.

Subsequent to installation of the tank MLI system, the three pressure sensing tubes were insulated collectively for a distance of approximately 25.4 cm (10 in.) below the outer blanket surface (Ref. Fig. 6-9). This insulation consists of a 2.54-cm-(1-in.-) diameter core of opacified fiberglass batting covered with 12 layers of double aluminized Mylar. The core is composed of ten 2.54-cm-(1-in.-) diameter circular discs which were cut from 2.54-cm-(1-in.-) thick batting material, penetrated with three 0.318-cm-(0.125-in.-) diameter holes, and then slipped in succession over the sensing tubes. The Mylar covering was applied in four individual blankets of three wraps each. During installation, the upper end of each three-wrap blanket was slit, the resulting tabs were faired onto the outer surface of the tank MLI, and all joints were spot-taped using aluminized Mylar tape. In a similar manner, the lower end of each three-wrap blanket was also slit, faired over the lower end of the core batting, and taped in place around the sensing tubes.

6.2 APPARATUS AND FACILITY PREPARATION

After installation of the 112-layer, unperforated Mylar/silk net MLI system on the calorimeter tank, the apparatus was transported to the Santa Cruz Test Base (SCTB) site where it was installed into the 4.88-m-(16-ft-) diameter vacuum chamber and prepared for Task 3 testing. A schematic diagram showing the general arrangement of the apparatus within the chamber, as well as the approximate location and inter-relationship of primary instrumentation sensors and plumbing components, is presented in Fig. 6-11. Referring to this figure, the general operation of the apparatus during a nominal test run is described in the following paragraphs.

Initially, the vacuum chamber is pumped down using the mechanical roughing pumps, the Roots blower system, and the 122-cm-(48-in.-) diameter diffusion pumps in sequence. Chamber pressure is monitored during the successive phases

LOCKHEED MISSILES & SPACE COMPANY

Instrumentation Sensors:

1. PTU-1
2. PTU-2
3. PVC-1
4. PVC-2, PVC-3
5. PI-1, PI-2, PI-3
6. FB
7. DI-1 through DI-6
8. TV
9. TLO
10. TGO
11. TGI
12. TB
13. TS-1, TS-2, TS-3

Plumbing Connections:

A. LH_2 Fill
B. LH_2 Overflow
C. H_2 Vent
D. GHe or GN_2 Backfill
E. LH_2 Cold Guard Inlet
F. LH_2 Cold Guard Outlet
G. Tap Water Supply
H. Chilled Water Supply
I. Hot Water Supply
J. Water Overboard
K. Chilled Water Return

Vacuum Chamber

Hot Boundary Shroud

Hot Boundary Baffle

Support Flange

MLI

LH_2

Calorimeter Tank

Quartz Heat Lamps
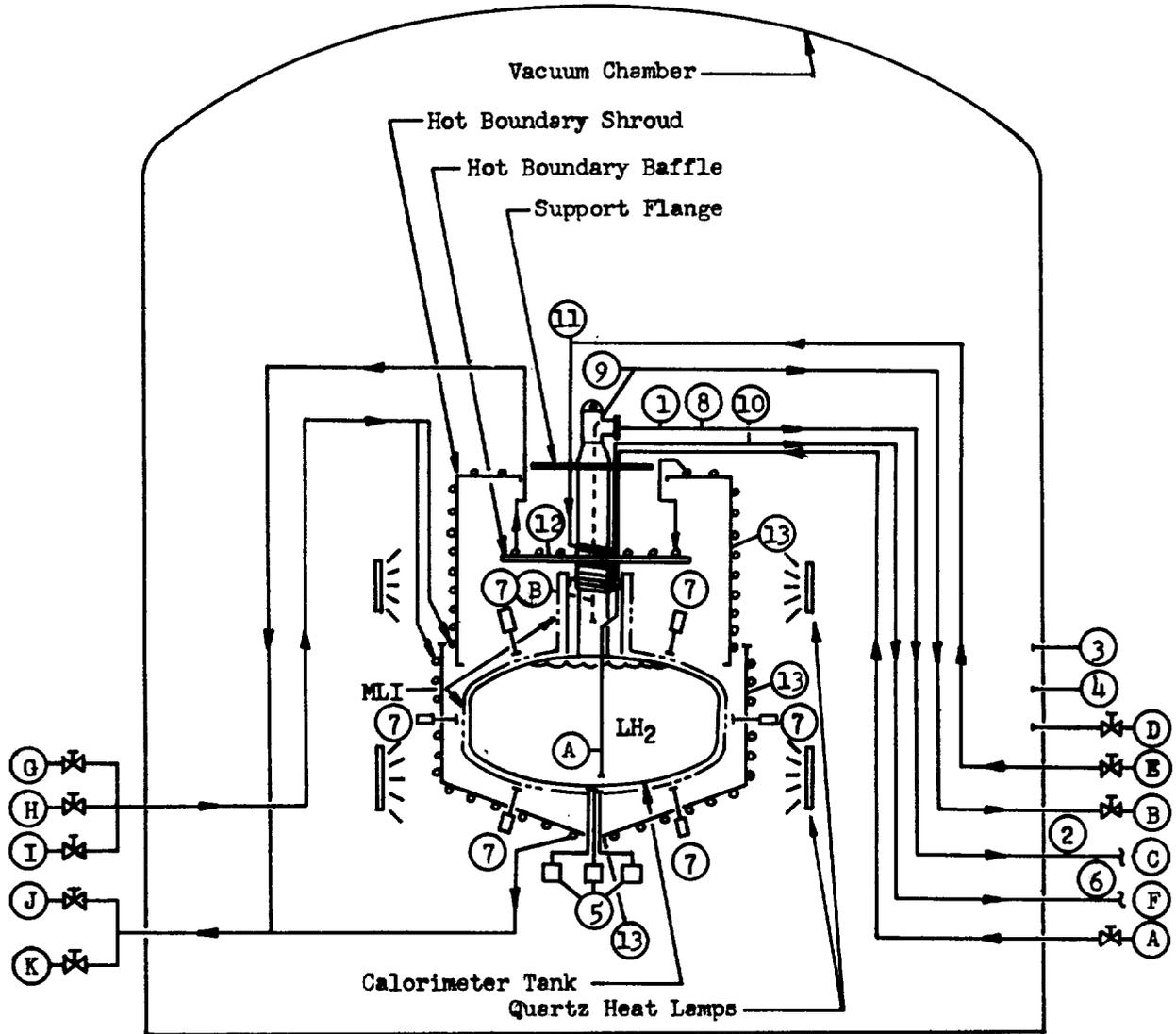
Fig. 6-11 Schematic of Tank Calorimeter Test Apparatus

6-22

LOCKHEED MISSILES & SPACE COMPANY

of the pumpdown using a strain gauge transducer PVC-1, a thermocouple gauge PVC-2, and an ionization gauge PVC-3. The latter is also used to monitor and record vacuum chamber pressures during the test run. When it is desired to backfill the system with GHe or GN_2, either to prepare for a rapid pumpdown test or to raise the chamber pressure back to one atmosphere after a test run, a throttling valve located in the backfill connection line D is used.

At a convenient point in the pre-test operations (usually just prior to filling the tank), the desired hot boundary temperature is established for the planned test run. Tap water at approximately $292^{\circ}K$ ($525^{\circ}R$), chilled water at approximately $278^{\circ}K$ ($500^{\circ}R$), or hot water at temperatures ranging from $306^{\circ}K$ ($550^{\circ}R$), to $361^{\circ}K$ ($650^{\circ}R$) (the latter supplied from the steam ejector system boiler) is supplied to the hot boundary shroud and baffle through connections G, H, or I, respectively. An array of quartz heat lamps, which surrounds the apparatus in the chamber, can be used where desired to trim the specified hot boundary temperature, or to adjust it to achieve inter-mediate values. Copper constantan thermocouples, referenced to a $65.6^{\circ}C$ ($150^{\circ}F$) source located outside of the chamber, were installed to monitor and record the baffle temperature TB and the shroud temperature at three points TS-1, TS-2, and TS-3. The water is circulated at a constant, relatively high flow rate to maintain a uniform temperature over the baffle and shroud surface using a 1.58-liter/sec (25-gpm) pump.

Water returning to the facility from the baffle and shroud heat exchangers is normally dumped overboard through the plumbing connection J. However, where chilled water is supplied to achieve a low hot boundary temperature, the return flow is recirculated through the connection K to the facility chiller in order to reduce refrigeration heat load requirements. For closed-loop operation where chilled water is supplied, the output signal from the shroud temperature sensor TS-2 is used through an automatic controller to activate the chiller. Where either tap water or hot water from the boiler is supplied in an open-loop operation, valve settings and boiler heater power settings are controlled manually in conjunction with visual monitoring of the shroud and baffle temperatures.

The calorimeter tank is chilled down and then filled by supplying liquid cryogen (LH_2 for this contract program) from the storage dewar through the fill line A. During the chilldown and fill process, boiloff gas is expelled through the vent line C and through the liquid overflow line B to the facility. When the liquid level has risen to the point in the calorimeter neck where it covers the inlet to the liquid overflow line (i.e., just below the neck cold guard), liquid is expelled through the overflow line. The temperature of the fluid being expelled through the overflow line B is monitored using a probe-type platinum resistance thermometer TLO. When this sensor indicates a LH_2-temperature fluid overflow, the fill process is terminated by closing shutoff valves in the fill and liquid overflow lines located just outside of the vacuum chamber wall. During the test program, special care is taken to ensure that the tank is completely filled prior to each test series in order to minimize the size of the ullage volume and, therefore, minimize any inherent thermal stratification, as well as to avoid boiling the tank dry during very long test durations.

At the time the fill process is terminated, and the fill and liquid overflow line valves are closed, the desired tank ullage pressure (to be maintained throughout the duration of the test) is established. In order to ensure that the fluid in the tank is completely saturated at this time, the tank ullage pressure is set to a value 1.4×10^4 to 3.4×10^4 N/m^2 (2 to 5 psia) below that maintained during loading, and 3.4×10^4 to 6.9×10^4 N/m^2 (5 to 10 psia) below that maintained in the storage dewar prior to loading. Vigorous bulk boiling is thus induced in the tank during the fill process and as the selected test ullage pressure value is established. A temperature compensated pressure transducer PTU-1, located in the vent line C just downstream of the calorimeter neck, and a backup transducer PTU-2 located in the vent line just outside of the vacuum chamber wall, are used to monitor and record tank ullage pressure throughout the duration of the test.

The absolute accuracy of these pressure transducers is approximately $\pm 3.4 \times 10^3$ N/m^2 ($\pm$ 0.5 psia); however, minute fluctuations in tank pressure on the order of $\pm$ 69 N/m^2 ($\pm$ 0.01 psia) can be detected by monitoring the output of

the recording digital voltmeter used for test data acquisition. From the time the tank fill cycle has been completed until after thermal equilibrium boil-off flow data are obtained at the end of the test run, an automatic control valve and back-pressure regulator system is used to maintain the desired test tank ullage pressure value. This system is shown schematically in Fig. 6-12. During operation, the Moore Controller senses any slight changes in tank pressure, as detected by the pressure transducer, and then generates compensating control signals to maintain a constant value by opening or closing the electro-hydraulic regulator valve as required. Using this system, tank pressure control within the $\pm$ 69 N/m^2 ($\pm$ 0.01 psia) sensitivity range of the measurement transducer was readily achieved during each of the Task 3 tests.
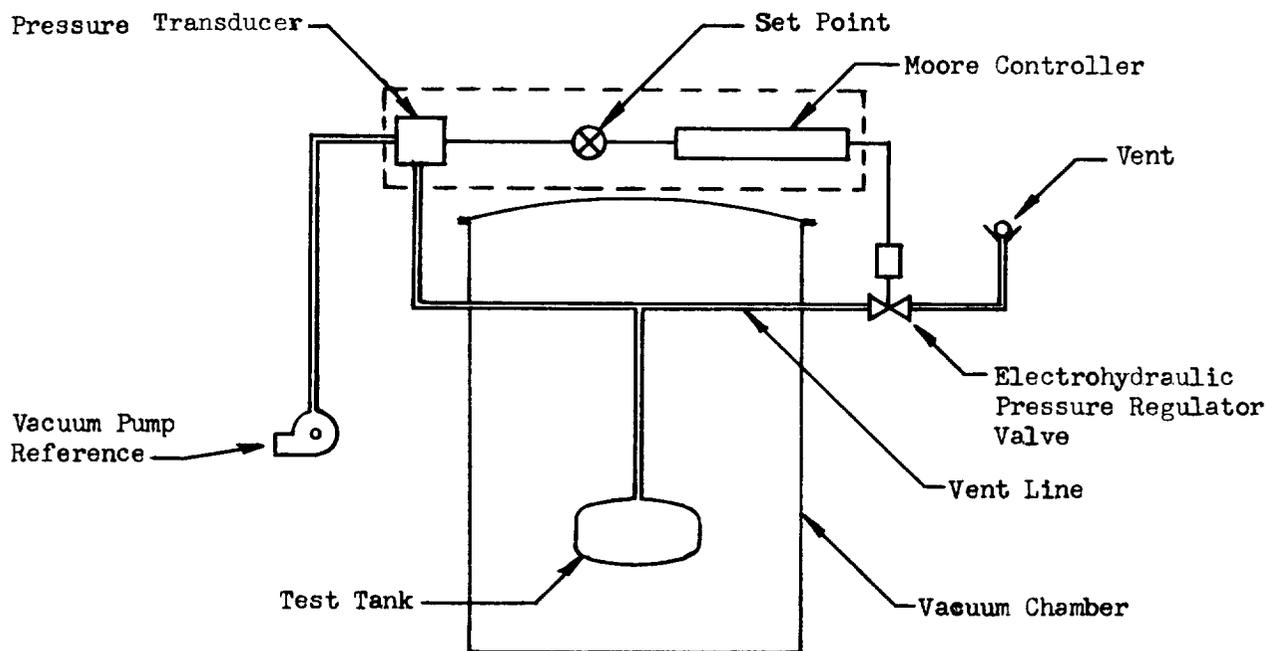
Fig. 6-12 Schematic of Test Tank Pressure Control System

The temperature of the boiloff gas as it flows out of the calorimeter neck is monitored and recorded by a second probe-type platinum resistance thermometer TV. Boiloff flowrate values are also monitored and recorded by

6-25

selecting any one of three thermal mass flowmeters FB which are located in
parallel loops of the vent line C downstream of the vacuum chamber pass-
through.

Using the procedure developed during the NAS 3-12025 contract program (Ref 28,
Page 3-54), the calorimeter neck cold guard is operated only during the 2- to
4-hr period immediately preceeding the time when the equilibrium boiloff flow
data is to be obtained for any given test run. Liquid cryogen (LH_2) is supplied
through the cold guard inlet line E and expelled through the outlet line F to
the facility vent system. Since it is vented to the atmosphere, the guard
system pressure is maintained at values just above atmospheric pressure.
Due to the relatively high flow resistance where the 1.27-cm- (0.5-in.-)
diameter cold guard heat-exchanger line is coiled around the neck, an appre-
ciable pressure drop is incurred at this point in the flow path. Thus, the
location along the cold guard flow path where significant vaporization occurs
is highly dependent upon the storage dewar (driving) pressure, the degree of
throttling introduced at the inlet supply valve E, and the heat load on the
calorimeter neck. When flashing, accompanied by substantial two-phase flow,
does occur within the guard coils, the pressure and temperature oscillations
which result, in turn, induce small pressure and temperature fluctuations of
the boiloff gas within the neck   These fluctuations not only make precise
control of the tank pressure very difficult, but also cause small fluctuations
in the neck heat load. Consequently, during operation of the cold guard,
considerable care is exercised to ensure that the flow is sufficient to maintain
liquid well downstream of the guard coils. In addition to the neck thermo-
couples (Ref. Section 6.1.4), two probe-type platinum resistance thermometers
TGI and TGO are installed in the guard inlet and outlet lines, respectively,
to monitor and record the guard fluid temperatures for this purpose.

In setting the pressure of the supply dewar and the percent-open position of
the inlet throttling valve during operation of the cold guard, an additional
precaution is taken to ensure that the temperature of the guard fluid is
always maintained at a value slightly above that of the tank boiloff gas as

measured by the vent line thermometer TV. This precludes the possibility of condensing the boiloff gas in the neck and thus introducing an error in the boiloff flow measurement FB.

During the entire test period (including initial evacuation, high-vacuum hold, and repressurization operations), interstitial pressures are monitored and recorded using the differential pressure transducer system coupled to the plenum sensors PI-1, PI-2, and PI-3 located in the first, third, and seventh MLI blankets, respectively. The arrangement of the three-way, solenoid-operated, selection valve, the pressure transducer, and the connecting plumbing can be seen below the lower hot boundary shroud in Fig. 6-13. The MLI shown immediately below the pressure transducer system had been removed for access when this photograph was obtained, but was reinstalled prior to initiating the next test series.

Changes in total insulation thickness, incurred primarily during evacuation and repressurization cycles, are monitored and recorded at six locations surrounding the tank using electromechanical thickness measurement trans-ducers DI-1 through DI-6. Those installed on the lower dome and one of the tank cylinder locations can also be seen in the Fig. 6-13 photograph. Data from these transducers are used in conjunction with pre-test and post-test x-ray data to determine MLI layer density values over the surface of the tank during the thermal performance and gas evacuation testing.

During the apparatus preparation period, all instrumentation transducers to be used in the Task 3 test program were calibrated against traceable standards. Thermal mass flowmeters were calibrated against both a wet test meter and a rotameter.

Prior to installation of the tank calorimeter test apparatus into the vacuum chamber, the insulated tank and the two-piece hot boundary control shroud were suspended from the upper cross beams of a welded tubular stand such that the center of the tank was supported approximately 1.22 m (4 ft) above floor level. Fig. 6-14 shows the apparatus assembly partially completed outside

Fig. 6-13 Interstitial Pressure and Thickness Measurement Transducer Installations

LOCKHEED MISSILES & SPACE COMPANY
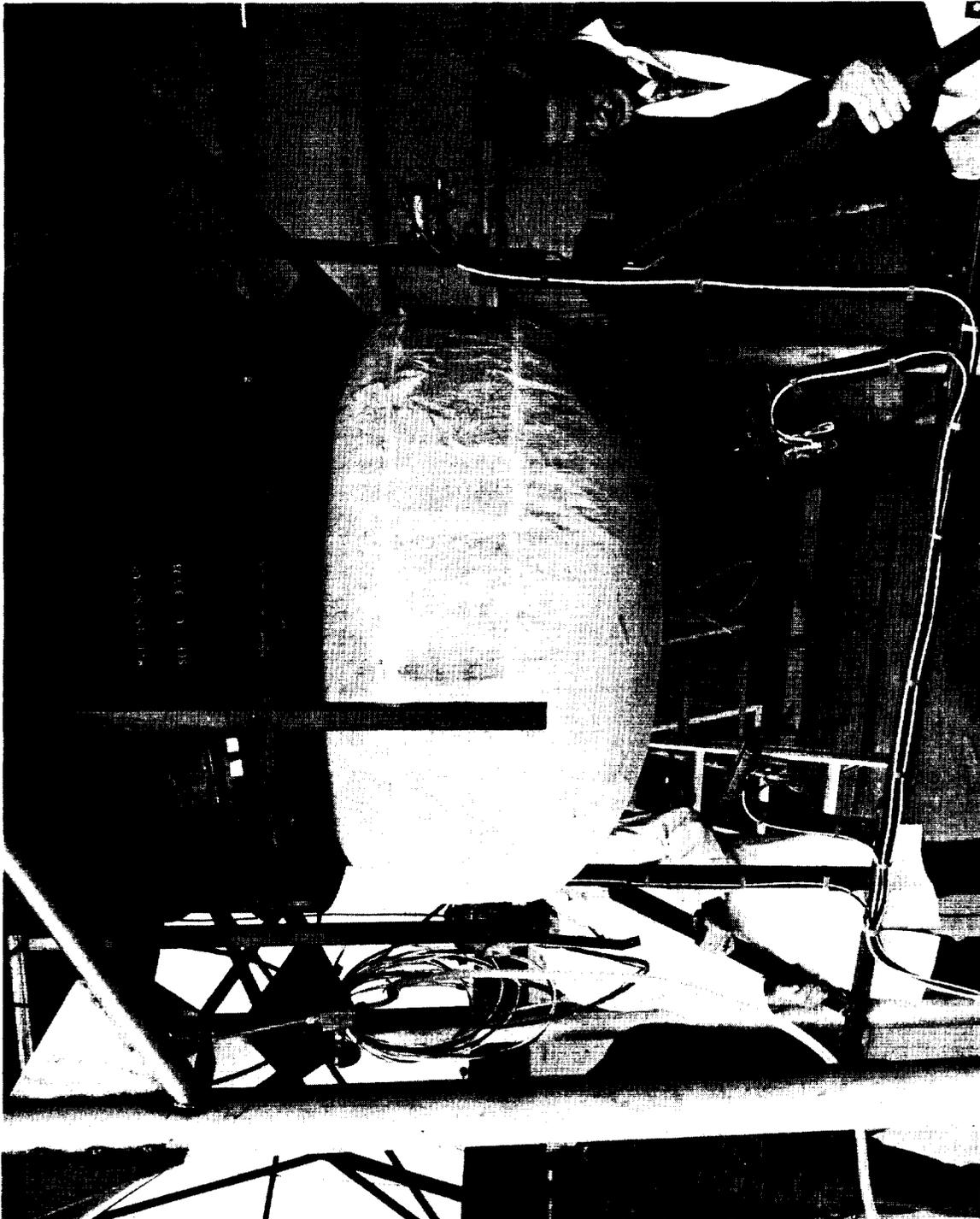
Fig. 6-14 Partial Assembly of the Apparatus Outside of the Vacuum Chamber

LOCKHEED MISSILES & SPACE COMPANY

of the vacuum chamber. In this photograph, the structural frame provided to support the cylinder and lower dome electromechanical thickness measurement transducers is being hand-held slightly below its final position with respect to the tank. Note that the lower hot boundary shroud is not yet in place.

Subsequent to completion of the entire assembly, the apparatus was lifted into the vacuum chamber, plumbing lines were connected, and instrumentation and control wiring harnesses were installed. Prior to installation of the lower hot boundary shroud inside of the chamber, the initial set of x-ray thickness measurements was obtained. Typical x-ray exposures are shown in Fig. 6-15. A view looking down on the apparatus after installation in the vacuum chamber is presented in Fig. 6-16.

After installation, the calorimeter tank and all associated plumbing systems were leak-checked using GHe, and a complete functional checkout was conducted to verify proper operation of all instrumentation and control systems. Finally, the vacuum chamber was closed up and sealed to complete preparations for the first planned test series.

A summary of the test instrumentation requirements applicable during the tank calorimeter test program is presented in Table 6-1.

6.3 TANK CALORIMETER TEST PROGRAM

In Task 3, planned heat transfer and gas evacuation tests were conducted on the unperforated, double-aluminized Mylar/silk net composite MLI system, as installed on the 1.22-m-(4-ft-) diameter tank calorimeter. A summary of requirements for these tests is presented in Table 6-2.

LOCKHEED MISSILES & SPACE COMPANY

0.5-IN. STEEL
SCALE

TANK
WALL
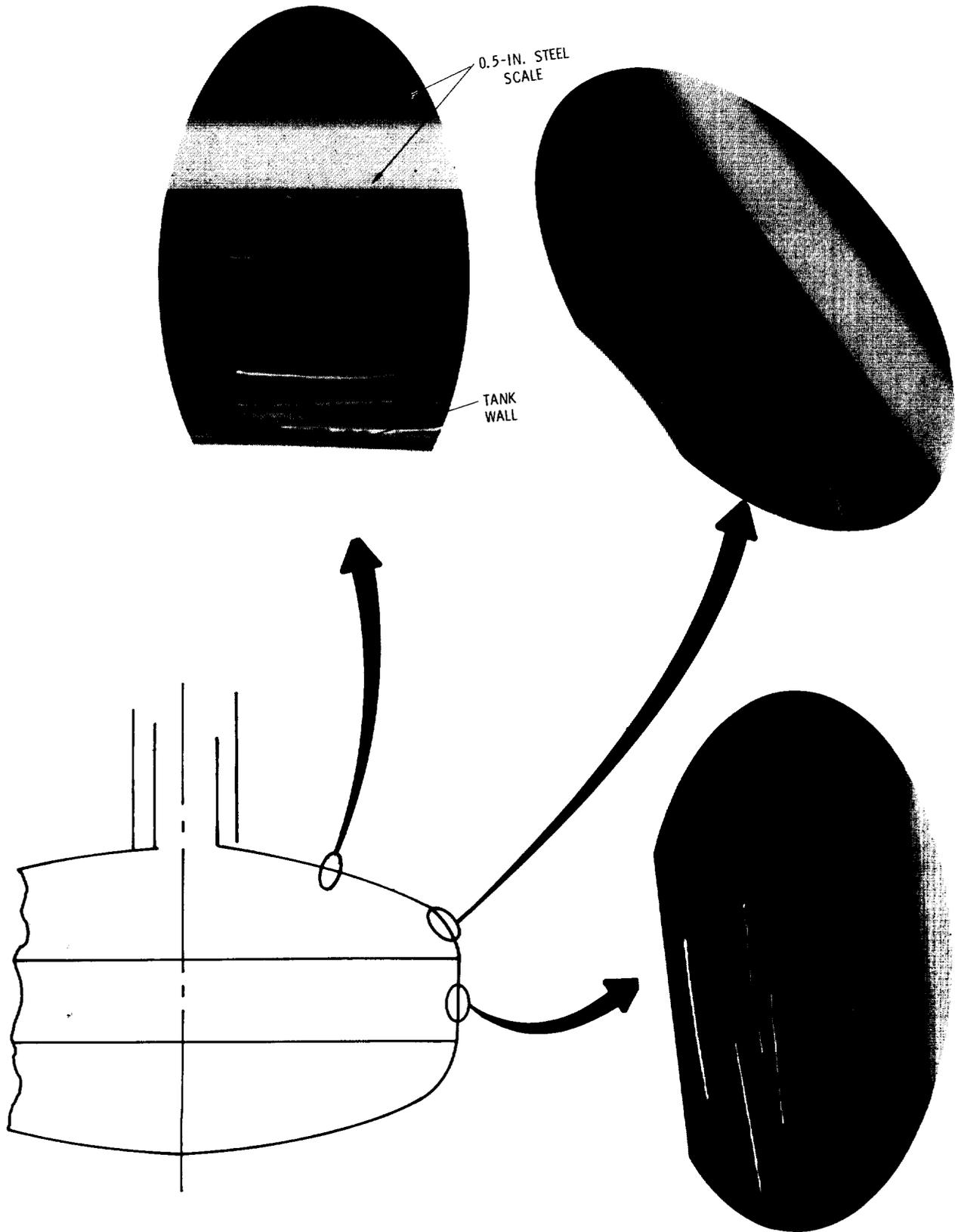
Fig. 6-15   Typical X-Ray Details

6-31

LOCKHEED MISSILES & SPACE COMPANY
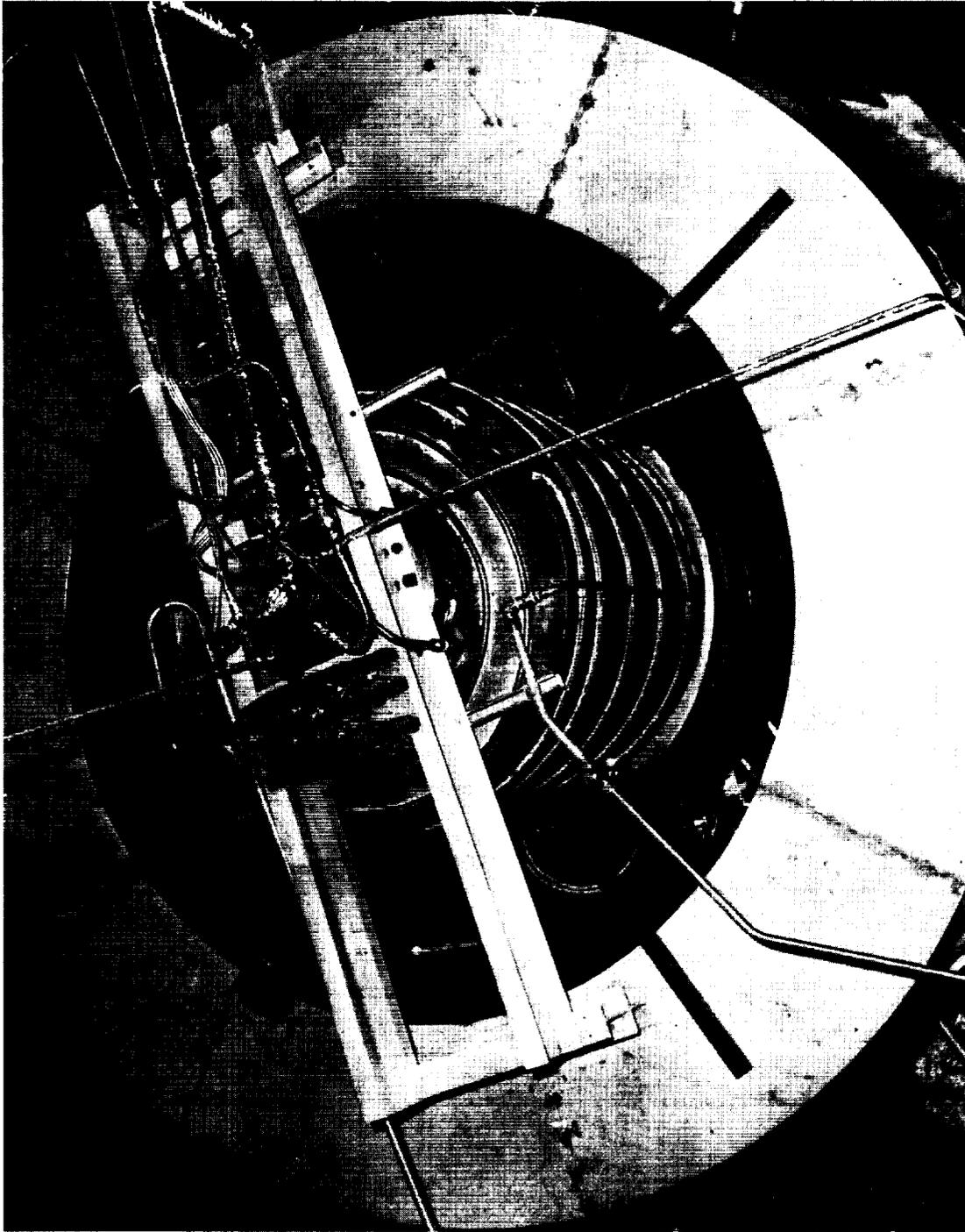
Fig. 6-16 View Looking Down on the Apparatus After Installation in the Vacuum Chamber

Table 6-1

SUMMARY OF TASK 3 TEST INSTRUMENTATION REQUIREMENTS

Instrumentation Function	Code	Sensor Description			Sensor Range	Estimated Accuracy	Required Test Range
		Type	Manufacturer	Model			
Pressure, Tank Ullage	PTU-1	Strain Gauge Transducer	Statham	PA 285 TC	0 to 1.7×10^5 N/m^2 (0 to 25 psia)	$\pm 3.4 \times 10^3$ N/m^2 [a] (± 0.5 psia)	8.3×10^4 to 1.4×10^5 N/m^2 (12 to 20 psia)
	PTU-2						
Pressure, Vacuum Chamber	PVC-1			PA 203 TC	0 to 1.03×10^5 N/m^2 (0 to 15 psia)		0 to 9.45×10^4 N/m^2 (0 to 13.7 psia)
	PVC-2	TC Gauge	Fredericks	3A	5×10^{-2} to 1 torr	± 13.5 percent of reading	5×10^{-2} to 1 torr
	PVC-3	Ion Gauge			10^{-6} to 10^{-3} torr	± 2 (ea. decade)	10^{-6} to 10^{-3} torr
Pressure, Insulation[d]	PI-1	Differential Capacitance Manometer	Data Metrics	521	0 to 1 torr	$\pm 5 \times 10^{-5}$ torr [b]	10^{-5} to 1 torr
	PI-2			510	0 to 10 torr		10^{-5} to 10 torr
	PI-3			510	0 to 10 torr		
Flowrate, Boiloff	FB-1	Linear Mass Flowmeter	Teledyne Hastings-Raydist	ALL-500	0 to 500 sccm	± 1 percent of range	500 to 5000 sccm
				ALL-5K	0 to 5000 sccm		
	FB-2	Wet Test Meter	Precision-Scientific		0 to 3930 sccs	± 1 percent of reading	
Deflection, Insulation	DI-1	Electro-Mech Transducer	LMSC	N/A	0 to 1.27 cm (0 to 0.5 in.)	± 0.005 cm (± 0.002 in.)	0 to 1.27 cm (0 to 0.5 in.)
	DI-2						
	DI-3						
	DI-4						
	DI-5						
	DI-6						
Temperature, Vent Line	TV	Platinum RTB	Rosemont	150 MA 10	19.4 to 100°K (35 to 180°R)	± 0.33°K (± 0.6°R)	19.4 to 100°K (35 to 180°R)
Temp, Liquid Overflow	TLO						
Temp, Guard Outlet	TGO						
Temp, Guard Inlet	TGI						
Temp, Baffle	TB						
Temp, Shroud	TS-1	Chrml-Con TC	N/A	N/A	19.4 to 367°K (35 to 660°R)	± 1.1°K[c] (± 2°R)	19.4 to 367°K (35 to 660°R)
	TS-2						
	TS-3						
Temp, Neck Guard	TN-1						
	TN-2						
Temp, Pressure Plenum	TP-1						
	TP-2						
	TP-3						
Temp, Insulation Location A	TA-5						
	TA-28						
	TA-56						
	TA-112						
Temp, Insulation Location B	TB-5						
	TB-14						
	TB-28						
	TB-56						
	TB-84						
	TB-112						
Temp, Insulation Location C	TC-5						
	TC-28						
	TC-56						
	TC-112						
Temp, Insulation Location D	TD-5						
	TD-14						
	TD-28						
	TD-56						
	TD-84						
Temp, Insulation Location D	TD-112	Chrml-Con TC	N/A	N/A	19.4 to 367°K (35 to 660°R)	± 1.1°K[c] (± 2°R)	19.4 to 367°K (35 to 660°R)

NOTES:
(a) Estimated system sensitivity = ± 69 N/m^2 (± 0.01 psi)
(b) Estimated for remote rezeroing at low pressure
(c) Varies with differential temperature between TC and reference
(d) These three transducers replaced with a single 0 to 1 torr MKS Baratron transducer subsequent to Second Evacuation (See Section 6.3.4)

Table 6-2

SUMMARY OF TASK 3 TEST REQUIREMENTS

Run No.	No. of Shields, N_S [a]	Test Description	Boundary Temperatures	
			T_H °K (°R)	T_C °K (°R)
1	112	Heat Flux	278 (500)	20.6 (37)
2	112	Heat Flux	319 (575)	20.6 (37)
3	112	Heat Flux	361 (650)	20.6 (37)
4	112	Rapid Evacuation	(b)	20.6 (37)
5	56	Heat Flux	361 (650)	20.6 (37)
6	56	Slow Evacuation	(b)	20.6 (37)

NOTES: (a) Total number of layers = N_S + 1, since the first blanket contains one additional double-net spacer placed at the tank wall interface.

(b) Hot-side boundary temperature was allowed to seek its own level during gas evacuation testing.

Runs 1 through 4 were performed first, with the entire 8-blanket, 112-shield system installed on the tank. Subsequently, the outer four blankets were removed, and Runs 5 and 6 were then performed with the 4-blanket, 56-shield system in place.

Initial attempts to conduct Test Run 1 failed when it was determined that extraneous heat leaks into the calorimeter tank had resulted in a boiloff flowrate more than an order of magnitude higher than that predicted by analysis. An investigation was launched immediately to determine the source of these heat leaks. Although the precise cause was not established conclusively until the testing was resumed later, the apparatus was modified based on results of the investigation. Subsequently, the test program was completed as planned, and no further significant problems were encountered.

Details of the initial gas evacuation, the pre-modification testing, the high heat rate investigation, the resulting modification of the test apparatus,

LOCKHEED MISSILES & SPACE COMPANY

the post-modification testing, and the correlation of experimental results with analytical predictions are presented in this section.

6.3.1 Initial Gas Evacuation

During the first pumpdown of the system, the vacuum chamber was evacuated from atmospheric pressure to a value of approximately 1.9×10^{-1} torr in two hours using the mechanical roughing pumps only. These pumps were operated overnight (approximately 17 hours) prior to activating the Roots blower and the two 122-cm-(48-in.-) diameter diffusion pumps. Then, using the combined mechanical/diffusion pumping system, the chamber pressure was reduced to approximately 6×10^{-4} torr in one-half hour of additional pumping time. Thereafter, the rate of pressure decrease fell off sharply, indicating the probability of a significant air leak into the system. Although the combined high-vacuum pumping system was operated for an additional 24-hour period, the chamber pressure could not be reduced below a value of 4×10^{-4} torr. Consequently, the pumps were shut off, and a check of the rate of increase in chamber pressure with time confirmed the fact that a significant air leak did in fact exist. Subsequently, a series of GHe leak checks was performed to locate the source of the leak. Ultimately, these checks revealed that a small crack had developed in an LN_2 cold wall supply line bellows located inside of the chamber. The chamber was then let up to atmospheric pressure with dry nitrogen, the cracked line was repaired, and the chamber was again closed and sealed to prepare for a second pumpdown.

Data obtained during the initial vacuum pumpdown indicated that the MLI interstitial pressure measurement system was operating properly. After approximately 45 minutes of pumping time, with a chamber pressure of 1 torr, the differential pressure between the third-blanket MLI sensor and the chamber was approximately 3×10^{-1} torr. The differential pressure decreased steadily after this time until, at 31.3 hours of pumping time, the third-blanket value was approximately 1.7×10^{-2} torr with a chamber pressure of approximately 6×10^{-4} torr. The slope of the differential pressure curve, plotted

as a function of pumping time on log-log paper, was essentially constant at a value of -1 during this interval. The pressure-time relationship observed was expected based on the results of the Task 2 gas evacuation studies.

During the initial vacuum pumpdown, it was found that only four of the six electro-mechanical transducers, developed and installed to obtain MLI thickness data, were operating. Data obtained from these four transducers (located on the tank cylinder and lower dome) show an increase in MLI thickness of 0.13 to 0.38 mm (5 to 15 mils) (approximately 0.4 to 1.0 percent of the initial thickness values) as the chamber pressure was reduced from one atmosphere to 7.24×10^4 N/m^2 (10.5 psia). Subsequent to this time, the indicated thickness values at each of the four locations showed a decrease until, at a chamber pressure of 3.45×10^3 N/m^2 (0.5 psia), they ranged from 0.64 to 4.6 mm (25 to 180 mils) (1.1 to 7.2 percent) less than the pre-test thickness values. Later in the program, it was found that the operating mechanisms for these transducers had failed and that these latter values were erroneous (see Section 6.3.4).

Results of the second evacuation showed that the air leak had been repaired successfully. Chamber pressure was reduced from one atmosphere to a value of 1×10^{-4} torr in approximately two hours using the mechanical pumps in combination with the Roots blower system and the diffusion pumps. Subsequently, the blower and diffusion pumps were shutoff, resulting in an increase in pressure, and the chamber pressure was maintained at a value of approximately 1.5×10^{-1} torr for an additional 3 hours using the mechanical pumps only. After day-shift personnel came on duty, the high-vacuum pumps were restarted and the vacuum chamber pressure was reduced to a value of 5×10^{-5} torr in approximately three hours (8 hours total pumping time). Thereafter, the chamber pressure was maintained at or below the 5×10^{-5} torr value for the duration of this test series.

A plot of the interstitial differential pressure data obtained during the second evacuation is presented as a function of vacuum pumping time in Fig. 6-17. As shown, the system was pumped with the hot boundary shroud (and the
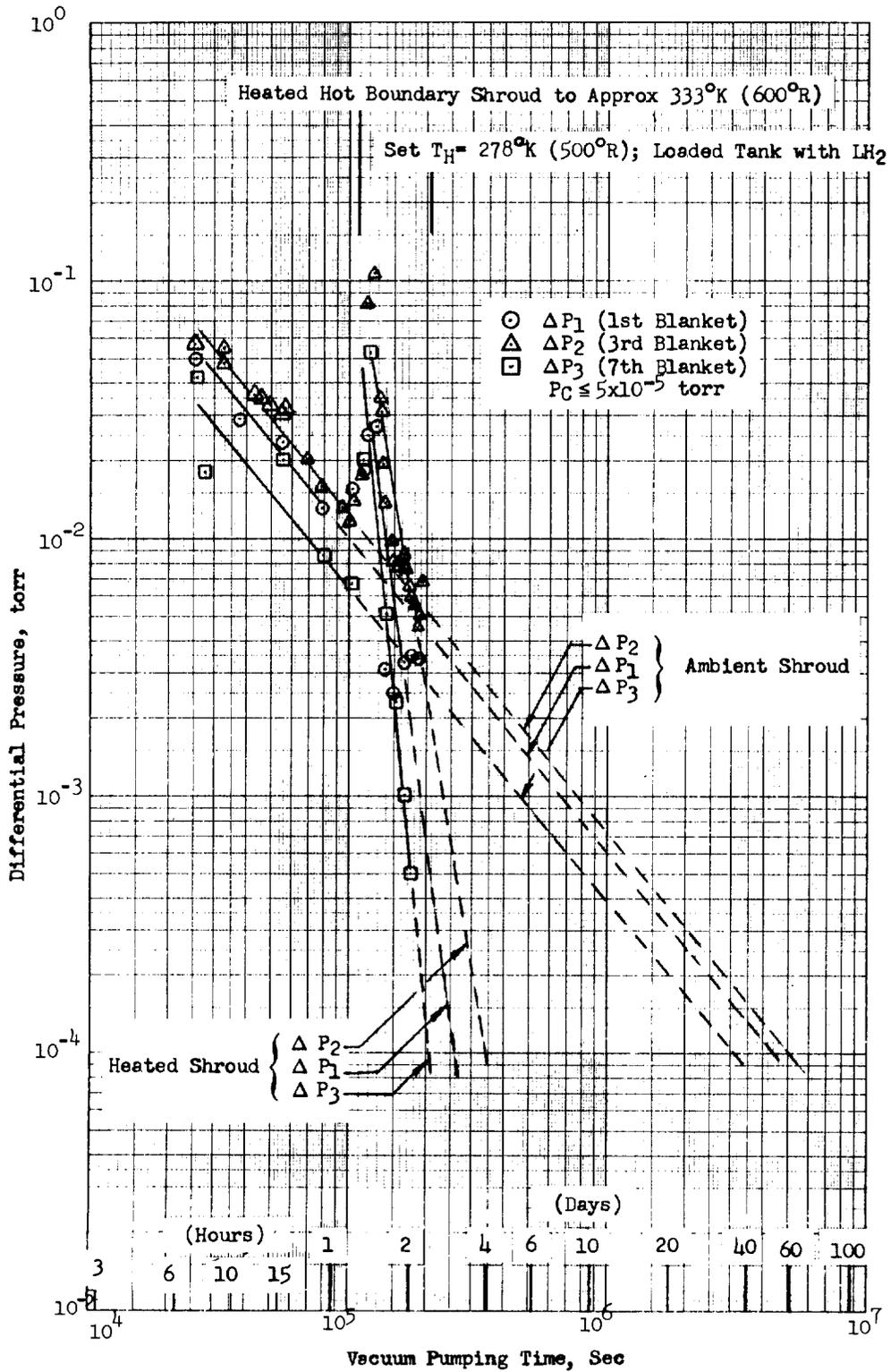
Fig. 6-17 Interstitial Pressure History During Second Evacuation

6-37

MLI) at ambient temperatures up to approximately 30 hours of pumping time. The best fit of these data is a family of straight-line curves, each with a slope of approximately -1, as observed previously during the Task 2 work and again during the first pumpdown in Task 3. The data also show a variation of interstitial pressures through the thickness, with the maximum value observed in the third blanket and the minimum in the seventh blanket. It is hypothesized that the third-blanket pressure was higher than that in the first blanket because of a higher installed layer density in this region (see Section 6.3.6.1).

Extrapolation of the ambient-shroud interstitial pressure data curves shows that continued high-vacuum pumping would be required for 6 to 10 days in order to reduce the interstitial differential pressures to a value of 1×10^{-3} torr, and for 40 to 60 days in order to reduce these pressures to a value of 1×10^{-4} torr. Within the free molecule flow regime, the differential pressure values vary directly with outgassing rate and inversely with the conductance of the system. Therefore, the differential pressure values achieved are independent of the absolute chamber pressure provided the latter is sufficiently low to maintain outgassing.

A simplified analysis was then performed to assess the effect of loading the tank with LH_2, assuming that the MLI contained only water vapor at interstitial pressures ranging from 1 to 10^{-4} torr. It was further assumed that the total mass of water vapor initially present within the insulation at any given interstitial pressure would cryopump onto the outer surface of the tank and an indeterminate number of the adjacent cold radiation shields soon after the tank was filled with LH_2. Based on these assumptions, the total calculated thickness of cryodeposited ice ranges from approximately 400 $\overset{o}{A}$ for an initial pressure of 1 torr to approximately 0.04 $\overset{o}{A}$ for a 10^{-4} torr initial pressure. Based on an extrapolation of previous work (Ref 30), it was estimated that the shield emittance could degrade significantly for a cryodeposit of ice approximately 100 $\overset{o}{A}$ or more in thickness. Also, the cryodeposited ice could contribute to an increase in solid conduction, although no quantative estimate is possible without further experimental

6-38

data. Since there are many uncertainties inherent in this analysis, it was
concluded that the tank should not be loaded with LH_2 until the measured
interstitial pressure had been decreased to a value of 2.5×10^{-3} torr or
lower, corresponding to a calculated total ice cryodeposit thickness of
approximately 1 $\overset{\circ}{A}$. However, due to the large number of analytical uncer-
tainties, no estimate was made of the potential degradation of thermal
performance if the tank were to be loaded at higher interstitial pressure
values.

Based on results of the preliminary cryopumping analysis, a decision was
made to heat the MLI by raising the temperature of the hot boundary shroud.
This was done and the test was continued with all other factors held constant.
It was anticipated that this heating would accelerate outgassing of the
water vapor and, thereby, decrease the vacuum pumping time required to
achieve acceptable interstitial pressures prior to loading the tank. Hot
water was circulated through the shroud and baffle heat exchangers to raise
the hot boundary temperature to approximately $333^{\circ}K$ ($600^{\circ}R$) for this purpose.

As shown in Fig. 6-17, the outgassing rate was significantly increased by
the application of heat in conjunction with the high-vacuum pumping. Again,
the best fit of the interstitial differential pressure data obtained is a
family of straight-line curves, although the slope of these curves is much
steeper than that of the ambient-shroud curves. As seen by extrapolating
the heated-shroud curves, only two to four days of high-vacuum pumping would
have been required to achieve an interstitial differential pressure value of
1×10^{-4} torr. However, based on a tradeoff of the cost of continued pumping
versus the degree of potential thermal performance degradation, it was decided
to load the tank and proceed with the testing after approximately 2.4 days
of vacuum pumping.

During the second evacuation of the MLI system, no data were obtained from
the electro-mechanical thickness transducers, since they had become inoper-
ative immediately after initiating the vacuum pumping sequence.

LOCKHEED MISSILES & SPACE COMPANY

6.3.2 Pre-modification Testing

Based on pretest calculations , the time constant (i.e., the time required to chill the MLI from ambient to equilibrium temperatures) was estimated to be approximately 6 to 8 days at high-vacuum conditions. Consequently, just prior to filling the calorimeter tank with LH_2, the vacuum pumps were shutoff and the chamber was backfilled to a pressure of approximately 5×10^{-2} torr with GHe. The purpose of this backfilling was to establish a high heat transfer rate through the MLI during the fill, and thus obtain a quick chill-down of the multilayers. It was hoped that this technique would significantly reduce the long hold time that would otherwise be required to achieve thermal equilibrium.

The calorimeter tank was then filled with LH_2 and the desired ullage pressure value was established without vacuum pumping. Soon thereafter, the vacuum pumps were restarted in order to reduce the high heat rate into the tank as the test was continued. During the subsequent 3-day operation, the tank calorimeter and vacuum chamber pressures were maintained at constant values of approximately 9.38×10^4 N/m^2 (13.6 psia) and 6×10^{-6} torr, respectively. On the third day, insulation temperature data indicated that the tank had boiled dry. It was apparent that the high heat rate established prior to loading had resulted in only partial filling of the tank and/or had been maintained for too long a period of time after the fill. In either case, it was necessary to refill the tank and restart the test.

During the second fill process, the GHe backfill technique was modified. In this instance, the chamber was maintained highly evacuated as the tank was filled and the desired ullage pressure value was established. Then, with the vacuum pumps operating continuously, a backflow of GHe was throttled through

a needle valve to achieve a constant chamber pressure of approximately 1.5×10^{-2} torr. Insulation temperature data were monitored closely during as well as after the fill so that the backflow of GHe could be terminated and the chamber could be re-evacuated as soon as the MLI was chilled sufficiently. Although the resulting temperature profile established through the MLI was significantly different in shape than that predicted for equilibrium at high-vacuum conditions, the best approximation of the high-vacuum profile was achieved in approximately 3.5 hours. Subsequently, the backflow of GHe was terminated, and the vacuum chamber pressure was again reduced to the 6×10^{-6} torr value in less than 20 minutes.

Testing at constant tank pressure and high-vacuum conditions was continued for an additional period of approximately 6 days in order to achieve near-equilibrium MLI temperatures. During this time, the rate of change of temperatures within the MLI system was extremely slow, although the total change in temperature required at any given point was much less with the initial GHe backfilling than it would have been with the MLI continuously evacuated. Since there was no apparent reduction in the total time required to achieve equilibrium, it was concluded that the chilldown process is dependent only on the thermal capacitance of the multilayers (i.e., the time constant), and not the initial temperature profile. Consequently, the GHe backfill technique was not used again for any of the subsequent tests and is not recommended for future work.

During the entire 10-day period of pre-modification testing, tank pressure, boiloff flowrate, and MLI temperature data were monitored and recorded at nominal 400-sec intervals. Chamber pressure values also were monitored and recorded, nominally at 2000-sec intervals. However, shortly after the initial tank fill, both the Barocell pressure manometers and the electro-mechanical thickness transducers became inoperative, and no further MLI interstitial pressure or thickness data were obtained during this test sequence.

When near-equilibrium temperatures were achieved within the MLI system, the LH_2 cold guard was operated to eliminate any heat leak through the

calorimeter neck. The total heat rate into the tank prior to operation of
the guard, based on boiloff flow measurements, was approximately 11.2 w
(38.2 Btu/hr). With operation of the guard, this value was reduced by
2.0 w (6.7 Btu/hr) to a net value of approximately 9.2 w (31.5 Btu/hr).
The heat rate value predicted during the pre-test analysis was approx-
imately 0.76 w (2.6 Btu/Hr)˙ (i.e., 0.19 w/m^2 or 0.06 Btu/hr ft^2 multiplied
by 4.01 m^2 or 43.2 ft^2) based on an assumed average layer density of 27.6
layers/cm (70 layers/in.) and negligable gas conduction heat transfer (Ref
Fig. 4-29). Thus, the measured heat rate value for Run 1 was approximately
12 times higher than that predicted by analysis.

Preliminary calculations, based on measured temperature data, showed that
the maximum (worst-case) extraneous heat leaks which could have been incurred
due to thermal shorting of the MLI on the neck and near the interstitial
pressure sensor plenums were 0.82 and 0.29 w (2.8 and 1.0 Btu/hr), respect-
ively. Even allowing for these extraneous effects, the net measured heat
rate into the tank was still approximately 7.3 w (24.9 Btu/hr), or nearly
an order of magnitude higher than the predicted value.

6.3.3 High Heat Rate Investigation

Once it was determined during the initial test series that the measured heat
rate into the tank was unacceptably high, a detailed investigation was
launched to determine the source of the excess heating. Possible sources
which were identified early in the investigation include: (1) leakage of
GH$_2$ through the fill line valve, after closure, from the supply dewar into
the tank, (2) leakage of GHe, GN$_2$, on air from some higher-pressure source
into the tank or vent line, (3) inadvertent damage or slippage of the MLI
to create a local high-radiation heat leak, (4) inadvertent thermal shorting
of the 22.9-cm- (9-in.-) diameter, copper, cylindrical neck shield to the
upper dome of the tank, (5) local compression or damage of the MLI by one or
more of the inoperative electro-mechanical thickness transducers, or (6) a
pressure instability (thermal oscillation) within the column of stratified

gas in either the fill line or the liquid overflow line after closure of the shutoff valves in these lines.

The possibility that the excessive heat rate might have resulted from a thermal oscillation (item 6 above) could not be investigated until the fill and liquid overflow lines had been modified to install pressure monitoring transducers. However, the investigation of all of the other possible sources listed above was begun immediately.

Initially, a series of inspections and leak checks, conducted at test conditions, ruled out the possibility of leakage into the tank (items 1 and 2 above). Subsequently, the hot boundary temperature was raised to 361°K (650°R), and the possibility of a large radiation heat leak into the tank (item 3) was also eliminated, since the resulting increase in total measured heat rate did not reflect a strong T_H^4 influence. Then, warm GHe was bled through the cold guard heat exchanger, with the hot boundary temperature maintained at 361°K (650°R), in an effort to determine whether or not the cylindrical neck shield was in fact thermally shorted to the tank surface (item 4). Results of this test were inconclusive, since the flow of warm GHe induced a rather severe oscillation of the boiloff flowrate.

When no apparent cause for the abnormally-high heat rate could be found from these initial inspections and leak checks, test operations were terminated. Subsequently, the vacuum chamber was let up to atmospheric pressure with dry GN_2, and the chamber was opened in order to continue the investigation. Although the apparatus was partially disassembled and inspected, no evidence was found to indicate that the MLI had been damaged or degraded in any way (items 3 and 5).

At this point, a procedure was devised to determine conclusively whether or not the cylindrical neck shield was thermally shorted to the tank wall (item 4). This was done by removing the circumferential row of attachment screws, located near the top of the shield, and by then allowing the shield to slip vertically downward (inside of the neck MLI blankets) until it came

6-43

into direct contact with the upper dome of the tank. Access to the attachment screws was gained by cutting a number of short, longitudinal slits through the neck MLI at the top, and by then folding the multilayers down for a distance of approximately 5 cm (2 inches). Using this procedure, it was shown that a gap of approximately 0.318 cm (0.125 in.) did in fact exist between the bottom edge of the cylindrical shield and the upper dome of the tank. Subsequently, the shield was lifted up to its proper position, the attachment screws were replaced, and the neck MLI blankets were repaired. As the individual multilayers were repositioned around the top of the cylindrical shield, strips of aluminized Mylar tape were applied to every fifth radiation shield to cover the slits which had been cut to gain access. Modification of the neck shield/cold guard region of the tank, as well as other modifications to the apparatus accomplished concurrently with the high heat rate investigation, are described in the following section.

6.3.4 Modification of the Test Apparatus

Although no specific source for the excessive heat rate into the tank was identified conclusively during the high heat rate investigation, every component of the apparatus and MLI was thoroughly inspected. The system was then modified based on conclusions reached as a result of the investigation. Major modifications included: (1) the addition of a copper guard ring to augment the existing cold guard on the neck, (2) the installation of three additional thermocouples on the neck and the cylindrical neck shield, (3) the installation of a radial array of four additional thermocouples through the thickness of the neck MLI blankets, (4) the removal of the electro-mechanical thickness transducers, and (5) the installation of fittings and shut off valves to accommodate pressure monitoring transducers in the tank fill and liquid overflow lines.

Details of the copper guard ring and the additional thermocouples installed in the neck shield/cold guard region of the tank are shown in Fig. 6-18. Other existing details of the apparatus are also shown in this sketch. The guard ring was added to intercept extraneous heat leaks which would otherwise

Fig. 6-18 Schematic of Tank Calorimeter Neck and Cold Guard

LOCKHEED MISSILES & SPACE COMPANY

be conducted into the system through the relatively short, relatively thick neck insulation. The thermocouples were added to provide additional temperature measurements in this region of the tank. The data obtained during subsequent tests were used to verify proper operation of the cold guard and the cylindrical neck shield, as well as to correct the boiloff flow data for the heat extracted from the neck MLI blankets by the guard ring.

Although no direct evidence was found during the high heat rate investigation to indicate that the inoperative electro-mechanical thickness transducers had caused the excessive heat input to the tank (i.e., by local compression of the multilayers), a decision was made to remove them anyway prior to the next test sequence. Since the source of the excessive heat input was not yet known, it was concluded that the benefit of any thickness data which might be obtained was not worth the risk that this might prove to be the source.

During the modification period, fittings and shutoff valves were installed in the tank fill and liquid overflow lines at a point just outboard of the vacuum chamber wall. Fast-response pressure transducers were then installed in each of these lines in order to monitor the pressures during steady-state testing (subsequent to tank fill). An oscilloscope was set up to obtain a visual display of the transducer outputs, since it was anticipated that the amplitude of any thermally-induced oscillation would be small. The shut off valves were provided to permit installation of an accumulator to either or both lines (or to interconnect them) in order to damp out any oscillation that was found to exist during testing.

Concurrent with the high heat rate investigation and the resulting modification of the test apparatus, an investigation was also conducted to determine the cause of failure of the interstitial pressure and the electro-mechanical thickness measurement systems. Inspection of the Barocell pressure heads and the associated wiring indicated that these instruments had been severely damaged by high-voltage corona discharge during the previous testing. Further investigation revealed that high-voltage electrical power was supplied to the switching bus terminal for the quartz heat lamp array located inside of the

6-46

vacuum chamber during the time that the chamber was backfilled with GHe. Although the lamps were not being operated at the time, the potential at the switching terminal was apparently sufficient to cause the discharge with the chamber pressure in a critical range.

During the modification period, a single 0-to 1-torr Baratron pressure sensor head was installed to replace the three damaged Barocell heads. The Baratron head was connected independently, through a solenoid-valve selection system, to each of the three interstitial pressure sensor plenums previously installed in the lower dome tank MLI blankets.

Because of the corona discharge problem, the quartz heat lamps were disconnected and were not used during subsequent tests.

Visual inspection of the electro-mechanical thickness measurement transducers revealed that these units had failed because the nylon cord actuators provided to connect the MLI contact probes to the electrical motor drive assemblies had stretched and, in some cases, broken. When these transducers were installed originally, the high-strength nylon cord was used primarily because of its flexibility and low thermal conductivity. During early bench testing of the system, conducted in an atmospheric environment, the nylon performed extremely well. However, the cords had become extremely dry and brittle during prolonged exposure to the high-vacuum test environment (heat generated by the corona discharge also may have been a contributing factor). It was concluded that the apparent decrease in measured MLI thickness during the latter portion of the initial pump down of the vacuum chamber (Ref Section 6.3.1) was in fact due to the failure of these nylon actuator cords. Consequently, when four of the six transducers were reinstalled later for use during the 56-shield test series, stainless steel wires were provided to eliminate this problem.

6.3.5 Post-Modification Testing

After the high heat rate investigation was completed and the test apparatus was modified, the vacuum chamber was again closed and re-evacuated in order

to resume the planned test program. A summary of sequential test operations performed during this period is presented in Table 6-3. As noted, post-test x-rays for the 112-shield MLI system*, as well as pre-test x-rays for the 56-shield system, were obtained during the interim between test runs 4 and 5 while the vacuum chamber was opened to the atmosphere in order to remove the outer insulation blankets. Subsequent to completion of the 56-shield tests, post-test x-rays were again obtained for this system.

In order to determine MLI layer density values which existed during each test run as precisely as possible, insulation thickness measurements obtained from both pre-test and post-test x-rays were used in conjunction with either measured or calculated ** thickness variations incurred during evacuation of the system.

6.3.5.1 <u>Heat Flux Testing - Runs 1 thru 3</u>. When modifications to the test apparatus resulting from the high heat rate investigation had been completed, the high-vacuum pumps were used to evacuate the system during a 68-hr period prior to loading the tank with LH_2. This was the third vacuum pumpdown of the system conducted since the Task 3 test program was undertaken. Initially, the chamber was evacuated from ambient pressure to a value of approximately 1.8×10^{-4} torr in 2.6 hours using the mechanical roughing pumps only. After operating with the roughing pumps overnight, the pressure was further reduced to a value of approximately 6×10^{-5} torr in slightly less than 3 hours using the Roots blower and diffusion pumping systems. Hot water at approximately 339°K (610°R) was circulated through the hot boundary shroud and baffle, after a total of approximately 22 hours of vacuum pumping, in order to heat the MLI and thereby accelerate outgassing of interstitial water vapor. The heating and high-vacuum pumping were continued for an

---

* Pre-test x-rays (not identified in Table 3) had been obtained for the 112 shield MLI system prior to the pre-modification test series described earlier in this report.

** Since the electro-mechanical thickness measurement transducers were not used during the 112-shield test series, thickness variation values proportionate to those measured during the 56-shield tests were calculated and used in the post-test analysis.

Table 6-3

SUMMARY OF TASK 3 POST-MODIFICATION TEST OPERATIONS

Test Run No.	Description of Operations
1 through 3	Closed Vacuum Chamber; Evacuated MLI System (Third Evacuation); Loaded Tank with LH_2 Conducted Heat Flux Tests for 112-Shield MLI System; Identified Thermal Oscillation as Source of High Heat Rate Into Tank.
4	Backfilled Vacuum Chamber to Atmospheric Pressure with GHe; Refilled and Topped Tank with LH_2; Conducted Rapid Evacuation Test (Fourth Evacuation) for 112-shield MLI System Repressurized Vacuum Chamber with Dry GN_2 and Opened to Atmosphere; Obtained Post-Test X-Rays for 112-Shield MLI System; Removed Outer 4 MLI Blankets; Obtained Pre-Test X-Rays for 56-Shield MLI system. Closed Vacuum Chamber; Evacuated MLI System; (Fifth Evacuation); Loaded Tank with LH_2)
5	Conducted Heat Flux Test for 56-Shield MLI System
6	Backfilled Vacuum Chamber to Atmospheric Pressure with GHe; Refilled and Topped Tank with LH_2; Conducted Slow Evacuation Test (Sixth Evacuation) for 56-Shield MLI System Repressurized Vacuum Chamber with Dry GN_2 and Opened to Atmosphere; Obtained Post-Test X-Rays for 56-Shield MLI System

additional period of approximately 46 hours. Then, the hot boundary temperature was reset to a nominal value of 278°K (500°R), as required for Test Run 1, and the tank was filled.

Interstitial differential pressure data are plotted in Fig. 6-19 as a function of vacuum pumping time for the third pumpdown sequence. As for the previous pumpdown (Ref Section 6.3.1), the best fit of the data is again a family of straight-line curves. Extrapolation of these curves shows that continued high-vacuum pumping would have been required for 12 to 16 days prior to loading the tank in order to reduce the interstitial differential pressure values to 1 x 10^{-4} torr. This is significantly longer than the 2- to 4-day period required to achieve this pressure value during the second pumpdown when the MLI was also heated. Since the rate of decrease of the interstitial pressure is strongly dependent upon the amount of outgassing, it is apparent that the MLI had absorbed significantly more water vapor prior to this (third) pumpdown than was initially present during the second pumpdown. This was to be expected since the system was completely exposed to the atmosphere for a period of approximately two weeks during the high heat rate investigation and modification. Prior to the second pumpdown, the system was exposed to the atmosphere only briefly (i.e., between the first and second evacuations) while the chamber leak was repaired.

During the third pumpdown, the interstitial differential pressure data shown in Fig. 6-19 were evaluated to determine when sufficient outgassing had occurred so that the tank could be loaded in order to proceed with the test. As shown in the figure, loading of LH_2 was initiated after approximately 3 days of pumping when the average interstitial differential pressure had decreased to a value of approximately 3 x 10^{-3} torr. This was somewhat higher than the interstitial pressure value achieved prior to loading during the second evacuation sequence. However, it was based on a tradeoff of the increasing test time and cost against decreasing improvement of the ultimate high-vacuum thermal performance of the MLI as more of the water vapor was removed.

6-50
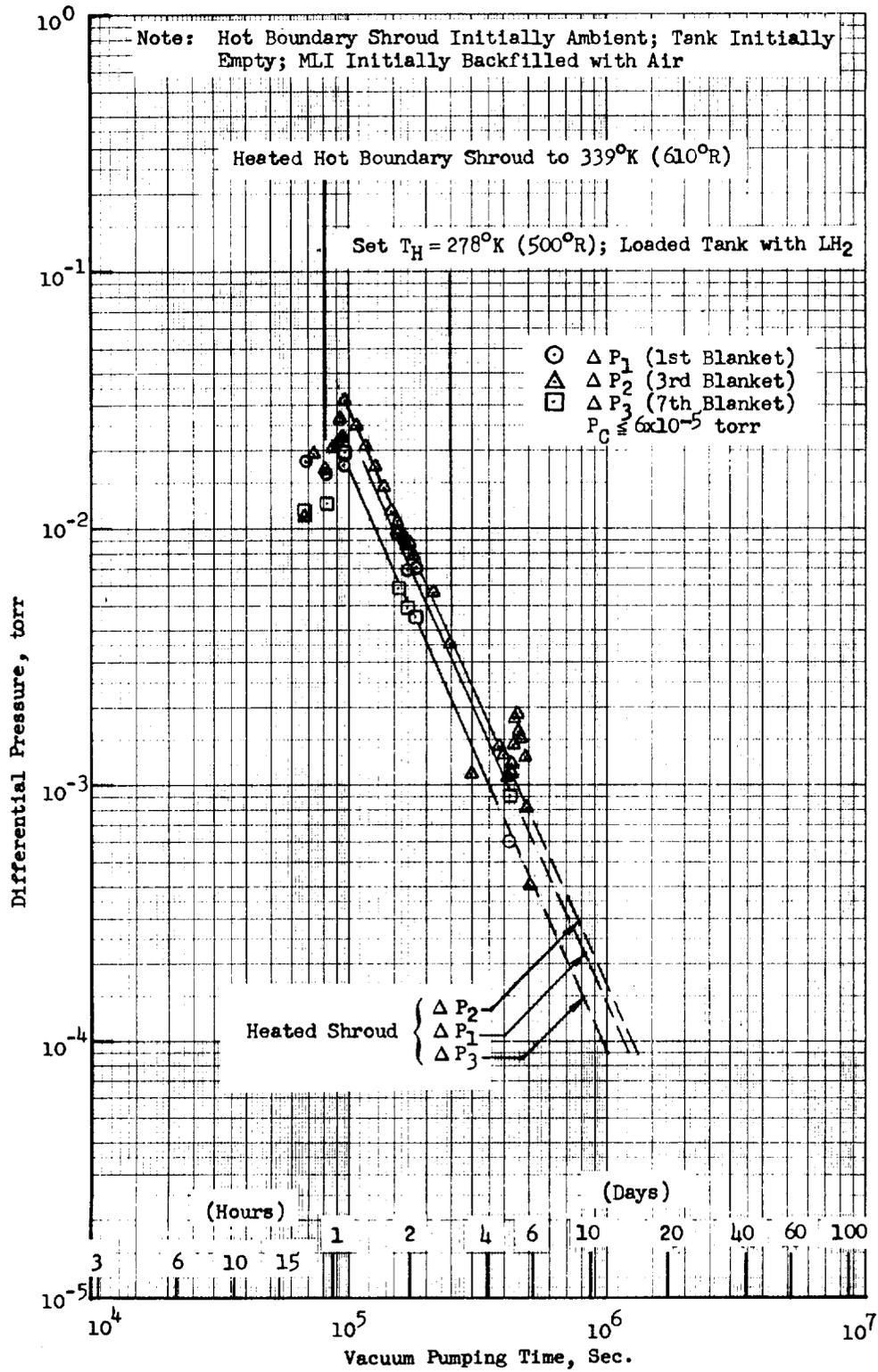
Fig. 6-19 Interstitial Pressure History During Third Evacuation

6-51

Shortly after the tank was filled with LH_2 and the valve in the fill line was closed, the output of the pressure transducer installed to monitor fill line pressure revealed that a relatively low-frequency, low-amplitude thermal oscillation did in fact exist within the column of stratified vapor contained in this line. The magnitude of the oscillation was approximately 483 N/m^2 (0.07 psia) peak to peak, with a frequency of approximately 2 hz. As soon as the presence of the oscillation was confirmed, a short jumper line was installed between fittings in the fill and liquid over-flow lines (i.e., those installed during the modification), and the lines were interconnected by opening the associated shut off valves. The effect of this interconnection was both immediate and dramatic. Not only did the oscillation cease, but the heat rate into the tank decreased by nearly an order of magnitude as indicated by boiloff flowrate measurements of approximately 0.104 kg/hr (0.23 lbm/hr) and 0.011 kg/hr (0.025 lbm/hr) obtained before and after the interconnection, respectively. The primary effect of coupling these two lines at the warm (ambient) ends was to eliminate any potential for developing or sustaining a pressure difference between them. However, in addition, the tank ullage effectively provided an accumulator volume of gas to modify the natural frequency of the column of highly-stratified vapor within the fill line, and thus served to dampen out the oscillation which had occurred.

Later, during Test Run 3, an experiment was conducted to determine whether or not the thermal oscillation which had occurred was self-inducing (i.e., whether or not it would recur) with the lines again isolated as they had been previously. Results of this experiment are presented in Fig. 6-20. As shown, the oscillation did recur within approximately 1 second after the interconnection valve was closed. After slight initial fluctuations, both the magnitude and the frequency of the oscillation matched those observed earlier. The experiment was continued for approximately 51 sec, after which the interconnection valve was reopened. Again, as shown, the oscillation was dampened out completely within approximately 5 seconds. During this experiment, the initial and final boiloff flowrate values, obtained with the lines interconnected, were both approximately 0.017 kg/hr (0.038 lbm/hr). The intervening boiloff flowrate, obtained with the fill line isolated, was approximately 0.10 kg/hr (0.22 lbm/hr).

6-52

Fill Line and Liquid
Overflow Line
Disconnected
(Valves Closed)

Fill Line and Liquid
Overflow Line
Reconnected
(Valves Opened)

Time Reference:

1 Sec

Elapsed Time (Sec)	t < 0	t=0 to 51	t > 51
Valve Position	Open	Closed	Open
Tank Ullage Pres, N/m² (psia)	1.12×10^5 (16.20)	1.12×10^5 (16.20)	1.12×10^5 (16.20)
Overflow Line Pres, N/m² (psia)	1.12×10^5 (16.20)	1.12×10^5 (16.20)	1.12×10^5 (16.20)
Fill Line Pres, N/m² (psia)	1.12×10^5 (16.20)	$1.12 \times 10^5 \pm 241$ (16.20±0.035)	1.12×10^5 (16.20)
Boiloff Flowrate, kg/hr (lbm/hr)	0.017 (0.038)	0.10 (0.22)	0.017 (0.038)

Actual Trace of
Strip Chart Record

$483 N/m^2$ (0.07 psia)

t=0 Sec

t=51 Sec

Fig. 6-20 Trace of Fill Line Pressure During Thermal Oscillation

6-53

After the thermal oscillation problem was identified as the source of the excessive heat rate into the tank, and after it was eliminated as described above, the planned Task 3 test program was conducted with only minor additional difficulties.

Approximately 5 days of around-the-clock test operations were required to achieve near-equilibrium conditions for Test Run 1 after the tank was loaded with LH$_2$. Subsequently, the cold guard was operated for a period of approximately 4.6 hours, and steady-state boiloff flowrate data were recorded. Then the nominal hot boundary temperature was reset to 319°K (575°R) to initiate Test Run 2. This test required approximately 4 days of continuous operation to achieve near-equilibrium insulation temperatures, operate the cold guard, and record the steady-state boiloff flowrate data. Finally, a nominal 361°K (650°R) hot boundary temperature was established, and the testing was continued for approximately 5 more days in order to achieve near-equilibrium conditions, operate the cold guard, and record the steady-state boiloff flowrate data. A summary of system measurements obtained near equilibrium for the 112-shield test runs is presented in Table 6-4.

Table 6-4

SUMMARY OF SYSTEM MEASUREMENTS OBTAINED NEAR EQUILIBRIUM
FOR THE 112-SHIELD TESTS

Test Run No.	1	2	3
Hot Boundary Temp at 112th Shield, T_H, °K(°R) Nominal / Av.Meas.	278(500) / 275.6(496.1)	319(575) / 317.3(571.1)	361(650) / 358.7(645.7)
Vac Chamber Pressure, PVC, Torr	4.0 x 10^{-5}	3.8 x 10^{-5}	3.1 x 10^{-5}
Tank Pressure, PTU, N/m^2 (psia)	1.116 x 10^{-5} (16.18)	1.115 x 10^{-5} (16.17)	1.114 x 10^{-5} (16.15)
Tank Liquid Temp., TTL, °K(°R)	20.7(37.2)	20.7(37.2)	20.7(37.2)
Av. Guard Fluid Temp., TG, °K(°R)	21.9(39.5)	22.1(39.7)	22.4(40.4)
Boiloff Flowrate, FB, kg/hr (lbm/hr)	0.005012 (0.01105)	0.00600 (0.01323)	0.00918 (0.02024)
Meas. Heat Rate, Q_M, w (Btu/hr)	0.6163 (2.105)	0.7379 (2.520)	1.129 (3.856)

During each of the 112-shield system test runs, temperatures of the hot boundary shroud and baffle were maintained at values approximately 3.9 to 5.0°K (7 to 9°R) higher than those obtained at the 112th shield (i.e., the average measured hot boundary temperature values). This was necessary in order to satisfy a total heat balance from the shroud and baffle to the outer shield, and from that shield to the tank wall. The 3.9 to 5.0°K (7 to 9°R) temperature difference compares to average increments of approximately 1.7, 5.6, and 11.1°K (3, 10, and 20°R) observed for 20-, 10-, and 5- shield MLI systems, respectively, during the NAS 3-12025 contract program (Ref 28, Tables 3-6, 3-7, and 3-8).

When the cold guard was operated to minimize neck heat leaks during the last 4 to 6 hours of each test run, the flow of LH_2 was carefully adjusted to minimize consumption as planned (Ref Section 6.2). However, for each test run, near-liquid guard fluid temperatures were achieved at both the inlet and outlet sensor probe locations. As equilibrium was approached during each of the runs, it was found that the outlet fluid temperature TGO was approximately 1.1°K (2°R) lower than that at the inlet TGI. This was expected, since it simply reflected the pressure drop incurred across the guard coils, resulting in some flashing and cooling of the guard fluid. This same effect was observed during the previous contract program (Ref 28, page 3-55).

Another phenomenon observed during these tests, which had also been encountered during the previous contract, was the apparent oscillation of the boiloff flowrates (Ref 28, page 3-54). The oscillation was somewhat more pronounced during the time when the guard was operated. Flowrate values used to calculate the near-equilibrium heat rates into the tank were obtained in each case by averaging from 300 to 600 discrete flow data points sampled at 1-sec intervals. Additional averages of 300 to 600 data points each were obtained approximately once each hour as thermal equilibrium was approached.

Profiles of the MLI radiation shield and pressure sensor plenum temperatures through the thickness, obtained from thermocouple measurements at 6 locations

on the tank and neck insulation, are presented in Figs. 6-21, 6-22 and 6-23 for Test Runs 1, 2, and 3, respectively. For clarity in each of these figures, the best curve fit of the data is shown for the lower dome location only, although discrete data points are included for each of the other 4 locations. It can be seen from the data presented that the temperatures measured on the outer surface of each of the pressure sensor plenums generally correlate well with those measured on corresponding lower dome radiation shields. The maximum deviation observed during any of the runs is approximately $11.1^{\circ}K$ $(20^{\circ}R)$ for the sensor mounted in the first MLI blanket (i.e., that corresponding to shield 14).

In general, the shape of all of the measured temperature profile curves obtained for the 112-shield MLI system indicate that near-equilibrium conditions were achieved, and that the MLI was evacuated to the 10^{-5} torr pressure decade or lower. It is also apparent from inspection of these temperature data that the layer density of the MLI on the lower dome was significantly less than that achieved on the upper dome. This observation was also confirmed by the x-ray measurement data (see discussion under Section 6.3.6, "Post-Test Analysis and Data Correlation").

Data points shown in Figs. 6-21 through 6-23 indicate that appreciable local temperature depressions were experienced within the interior neck MLI blankets near the cold guard. Consequently, some heat was extracted from the neck MLI, during operation of the cold guard, which otherwise would have contributed to the total heat input into the tank. Using the temperature data shown, estimates of the heat flow out of the neck MLI were calculated analytically, and were then used to correct the gross heat rate into the tank as determined from the boiloff flowrate measurements.

6.3.5.2 <u>Rapid Evacuation Testing-Run 4</u>. At the conclusion of the 112-shield MLI system heat flux tests, the vacuum chamber was let up slowly with dry GHe to atmospheric pressure. Concurrently, the steam ejector system boiler
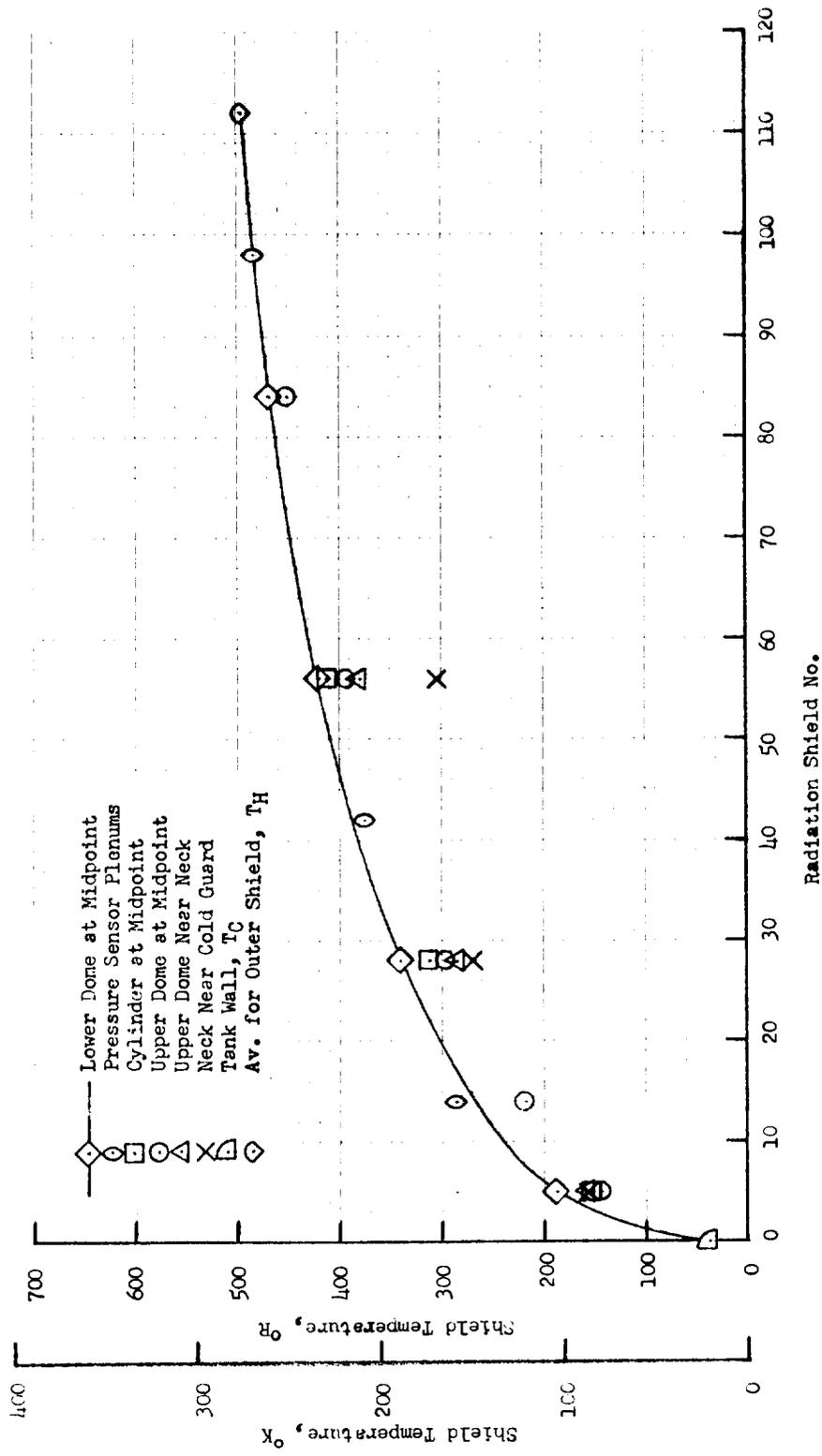
Fig. 6-21 Measured MLI Temperature Profile for Test Run 1

LOCKHEED MISSILES & SPACE COMPANY
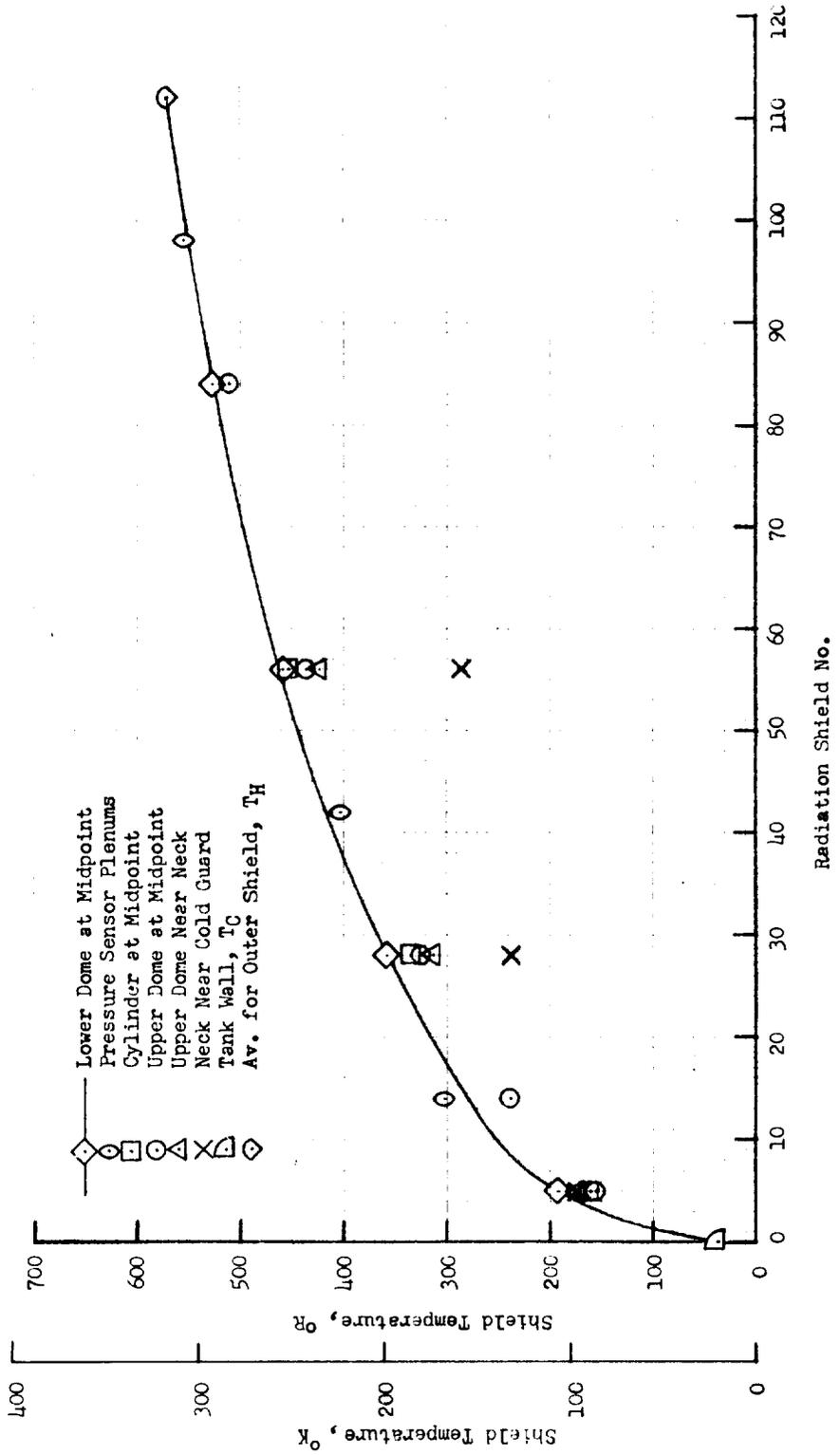
Fig. 6-22 Measured MLI Temperature Profile for Test Run 2

LOCKHEED MISSILES & SPACE COMPANY
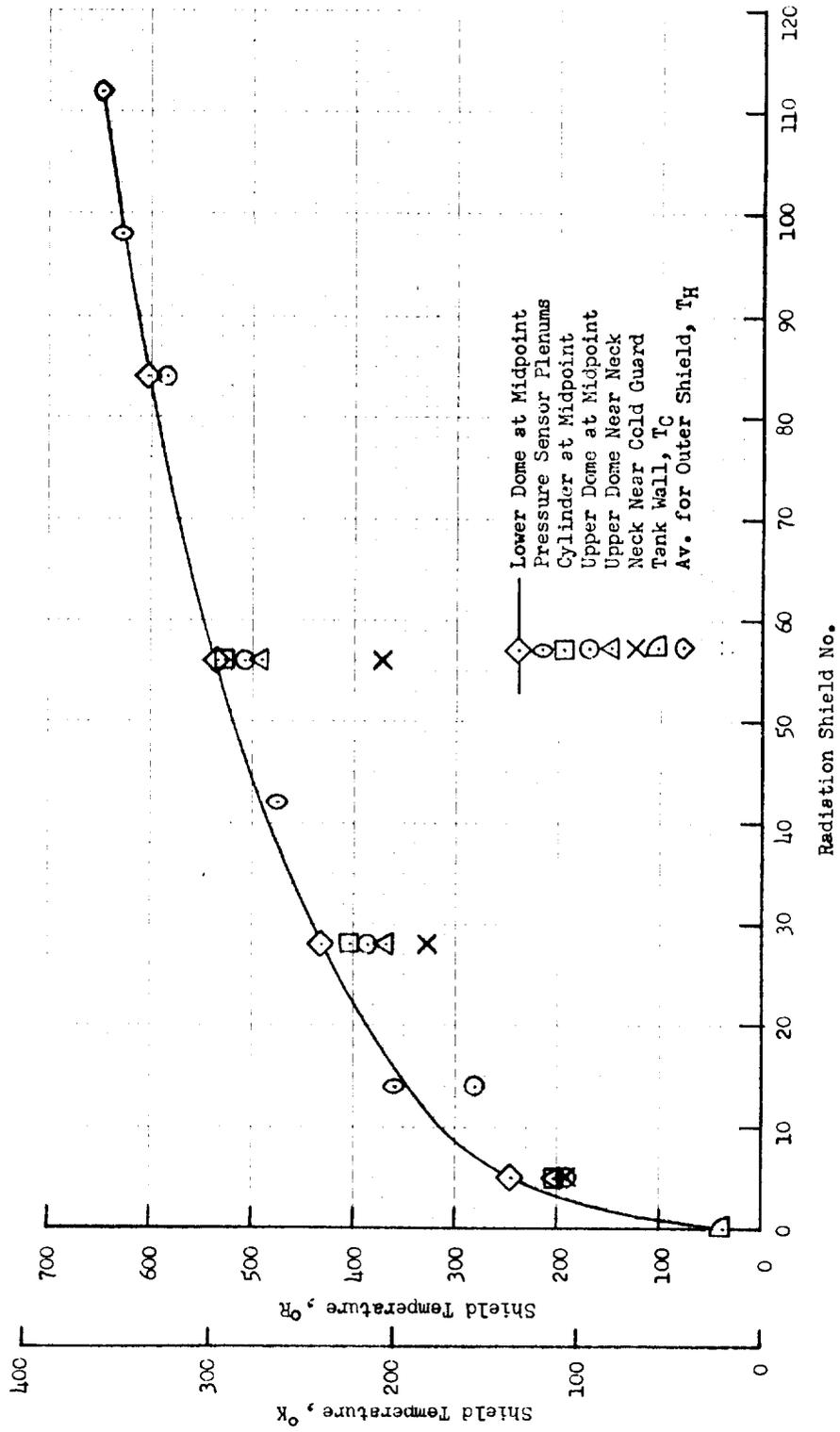
Fig. 6-23 Measured MLI Temperature Profile for Test Run 3

LOCKHEED MISSILES & SPACE COMPANY

was heated to prepare for the rapid evacuation test, and the hot boundary temperature was reset to a nominal value of $278^{\circ}K$ ($500^{\circ}R$). Just prior to initiation of the rapid pump down test, the tank was refilled with LH_2.

During the rapid evacuation test sequence (i.e., the fourth evacuation since the Task 3 program was initiated), the vacuum chamber was pumped down from atmospheric pressure to a value of approximately 0.3 torr in approximately 75 seconds. In an attempt to maintain the corresponding constant evacuation rate of 1379 N/m^2-sec (0.2 psid/sec)* throughout the early portion of the test, the throttling valve in the line connecting the vacuum chamber to the steam ejector pumps was controlled manually. The average evacuation rate achieved during the early pump down period was approximately equal to the desired value, thus very satisfactorily demonstrating the structural integrity of the MLI and its attachments. However, manual control of the throttling valve proved to be quite unsatisfactory, since the resulting chamber pressure-time history was very unsteady. As a consequence, the correlation of predicted and measured interstitial pressure data was difficult.

In addition to the difficulty of achieving a smooth chamber pressure decay history, the throttling valve closure mechanism failed to reseat the valve properly as the chamber pressure was reduced to approximately 10 torr. This failure resulted in backfilling of the chamber to approximately 5.5×10^4 N/m^2 (8 psia) with moist air. Even though the valve was subsequently closed and reseated manually, the chamber pressure could not be reduced below approximately 0.3 torr after more than 4 hours of continuous pumping. The test sequence was then terminated, the tank was drained, and the chamber was let up to atmospheric pressure with dry GN_2 in order to gain access for the post-test x-rays and removal of the outer MLI blankets.

6.3.5.3 Heat Flux Testing-Run 5. Subsequent to completion of the 112-shield MLI tests, the outer 4 blankets were removed from the tank calorimeter apparatus.

---

*This value corresponds to the maximum evacuation rate that would be imposed on a tank-mounted MLI system during a typical Saturn V launch trajectory.

In order to accomplish this, the apparatus was partially disassembled and the insulation installed locally around the bundle of interstitial pressure sensing tubes were removed. During this activity, it was found that the epoxy bond attaching the sensing tube to the first pressure sensor plenum (i.e., that installed in the first MLI blanket immediately adjacent to the tank wall) had failed. Although the exact cause of failure could not be determined conclusively, it was probably due to the severe thermal cycling imposed during the three previous tank fill sequences. Consequently, this sensing tube was removed, as was that attached to the third sensor plenum (seventh MLI blanket), and the single remaining tube for the second sensor plenum (third MLI blanket) was reinsulated in a manner similar to that employed earlier for the 3-tube bundle.

As noted previously (Ref Table 6-3), post-test x-rays were obtained for the 112-shield MLI system prior to removal of the outer 4 blankets. After removal of these blankets and reinsulation of the remaining pressure sensing tube, the pre-test x-rays were obtained for the 56-shield MLI system. Since it had been determined during the 112-shield system tests that the electro-mechanical thickness measurement transducers apparently had not contributed to the high heat leak, four of these transducers were reinstalled in order to obtain thickness measurements on the tank cylinder and lower dome blankets. Then, the apparatus was reassembled, leak and functional checks were performed, and the planned 56-shield system tests were initiated.

Vacuum pumpdown of the system (the fifth conducted in Task 3) was accomplished in two phases. During the first of these, with the hot boundary shroud heated continuously to approximately 361^OK (650^OR), the vacuum chamber pressure was reduced from one atmosphere to approximately 0.4 torr in 1.6 hours using the mechanical roughing pumps and the Roots blower system. After overnight pumping with the mechanical pumps only, the pressure was further reduced to approximately $3x10^{-5}$ torr over a 31.8- hr period using the roughing pumps, the blower, and the diffusion pumps in combination. At this time, the measured interstitial pressure value was approximately $8x10^{-4}$ torr, indicating that most of the water vapor had been desorbed and outgassed from the MLI system. Subsequently,

6-61

the pumps were shut down, and the vacuum chamber was backfilled to atmospheric pressure with dry GN_2 in order to ensure that no water vapor could be re-absorbed by the MLI during the following 3-day holiday period when the facility was shut down and secured.

After the holiday period, the facility was reactivated and the second phase of the vacuum pumpdown was conducted. Initially in this phase, the vacuum chamber pressure was reduced from one atmosphere to approximately 2.0×10^{-5} torr in 2.8 hours using the combined high-vacuum pumping systems in sequence. At this time, the measured interstitial differential pressure value was found to be approximately 7.2×10^{-4} torr. Shortly thereafter, the tank was filled with LH_2 to initiate Test Run 5.

A plot of interstitial differential pressure data obtained during the fifth vacuum pumpdown sequence is presented in Fig. 6-24 as a function of vacuum pumping time. In order to determine the net effective pumping time, the 86.6-hr holiday period was deleted from the total elapsed time as shown. A straightline curve was found to provide the best fit of the data, as observed for previous evacuations. Inspection of the data presented shows that the interstitial differential pressure was reduced to a value of approximately 4×10^{-4} torr prior to loading the tank with LH_2. This required only approximately 1.5 days of vacuum pumping, whereas approximately 3 days of pumping had been required to achieve an interstitial differential pressure value of approximately 3×10^{-3} torr (after which the tank was loaded) during the third evacuation with the 112-shield system installed (Ref Fig. 6-19). The shorter pumpdown time may have been due in part to the fact that heat was applied to the MLI (through the hot boundary shroud) throughout the pumpdown sequence. In addition, it should be noted that half of the MLI blankets had been removed prior to the fifth evacuation, thus reducing the potential quantity of water vapor initially present and slightly shortening the length of the outgas flow path* for the inner MLI blankets.

----

* Since the unperforated-shield MLI system is evacuated by edge pumping, the length of the flow path is similar for all blankets through the thickness. However, due to the staggering of butt joints between adjacent blankets, the inner blanket flow paths are slightly longer than those for the outer blankets.
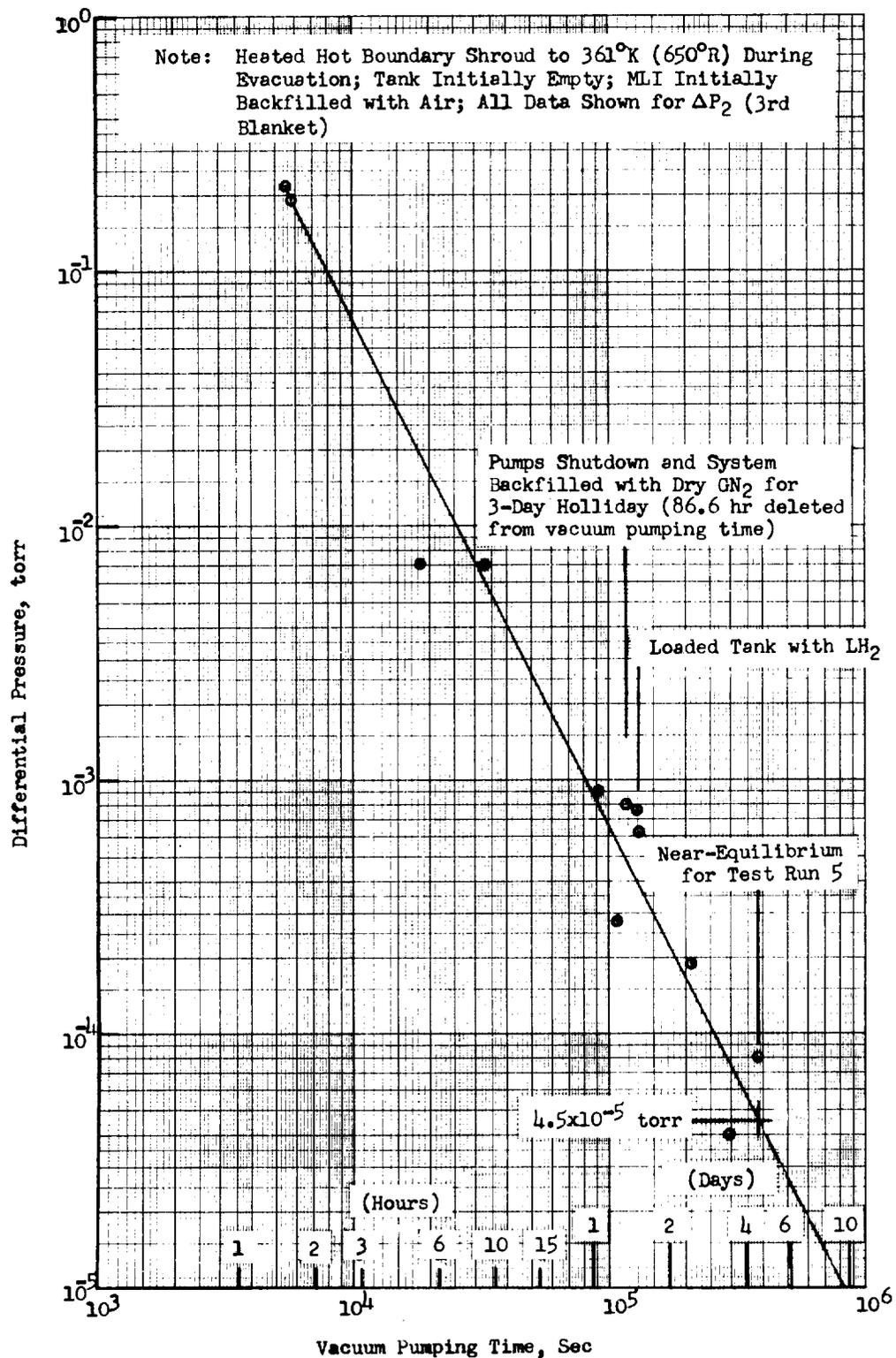
Fig. 6-24 Interstitial Pressure History During Fifth Evacuation

6-63

Subsequent to loading the tank with LH_2, around-the-clock testing was continued for approximately 3 additional days in order to achieve near-equilibrium MLI shield temperature and boiloff flowrate values. The cold guard was then operated for approximately 6.5 hours, and steady-state boiloff flowrate data were recorded. System measurements obtained near equilibrium for this 56-shield MLI test are summarized in Table 6-5.

During Test Run 5, the hot boundary shroud and baffle were maintained at a temperature approximately $3.0^{\circ}K$ $(5.4^{\circ}R)$ higher than that of the 56th MLI shield. When the guard was operated to obtain near-equilibrium boiloff flowrate values, the flow was again regulated to achieve near-liquid temperatures at the guard inlet and outlet sensor probes, with minimum consumption of LH_2. Data recorded at near-equilibrium conditions show that the fluid temperature at the guard outlet probe TGO was approximately $1.3^{\circ}K$ $(2.4^{\circ}R)$ lower than that maintained at the inlet probe TGI. Again, as for the 112-shield system tests, boiloff flowrate values were sampled and recorded at 1-sec intervals for 5- to 10- min. periods approximately once each 30 minutes as thermal equilibrium was approached.

Table 6-5

SUMMARY OF SYSTEM MEASUREMENTS OBTAINED NEAR EQUILIBRIUM
FOR THE 56-SHIELD TEST (RUN NO. 5)

Hot Boundary Temp. at $\}$ Nominal 56th Shield, T_H, $^{\circ}K(^{\circ}R)$ $\}$ Av. Meas.	361 (650) 358.2 (644.8)
Vac. Chamber Pressure, PVC (Torr)	1.9×10^{-6}
Tank Pressure, PTU, N/m^2 (psia)	1.08×10^5 (15.64)
Tank Liquid Temp., TTL, $^{\circ}K$ $(^{\circ}R)$	20.5 (36.9)
Av. Guard Fluid Temp., T_G, $^{\circ}K$ $(^{\circ}R)$	22.4 (40.3)
Boiloff Flowrate, FB, kg/hr (lbm/hr)	0.01579 (0.03481)
Meas. Heat Rate, Q_M, W (Btu/Hr)	1.945 (6.642)

LOCKHEED MISSILES & SPACE COMPANY

Fig. 6-25 shows measured MLI radiation shield temperatures near thermal equilibrium for Test Run 5. These were obtained from the thermocouple sensors at each of the 6 locations described previously. For clarity, the best curve fit of the data for the lower dome location is again the only one included in the figure. As shown, the temperatures measured on the outer surface of the pressure sensor plenums installed in the first and third MLI blankets correlated well with those for the corresponding shields in the lower dome blankets. The shape of the temperature profile curve is quite similar to that obtained in the 112-shield system tests, and indicates that near-equilibrium, high-vacuum conditions were achieved. In general, it can be seen that the layer density achieved for the lower dome blankets was somewhat less than that realized at other locations on the tank. Also, it is shown that the temperatures of the neck MLI shields were depressed locally by the cooling effect of the neck cold guard operation. An estimate of the heat flow out of the neck MLI, based on the measured temperature values, was calculated and used to correct the total heat rate into the tank, as determined by boiloff flowrate measurements.

Data obtained from the electro-mechanical thickness measurement transducers during the fifth evacuation sequence and Test Run 5 are presented in Fig. 6-26. As shown, total MLI thickness values at the four indicated probe locations increased significantly during the initial pumpdown sequence. These increases to the initial thickness values, with the latter based on pre-test x-rays, ranged from 0.41 to 0.66 cm (0.16 to 0.26 in.) (13.7 to 22.3 percent, respectively). During subsequent test operations, the measured total MLI thickness values fluctuated somewhat until near thermal equilibrium conditions, they showed net increases over the pre-test thickness values ranging from 0.236 to 0.551 cm (0.093 to 0.217 in.) (8.0 to 18.6 percent, respectively). The average increase in pre-test thickness values, based on measurements obtained from all four thickness probes, was approximately 0.386 cm (0.152 inches). This corresponds to an increase of approximately 10 percent in the average total MLI thickness, based on pre-test x-rays at 20 points over the tank surface.

6-65
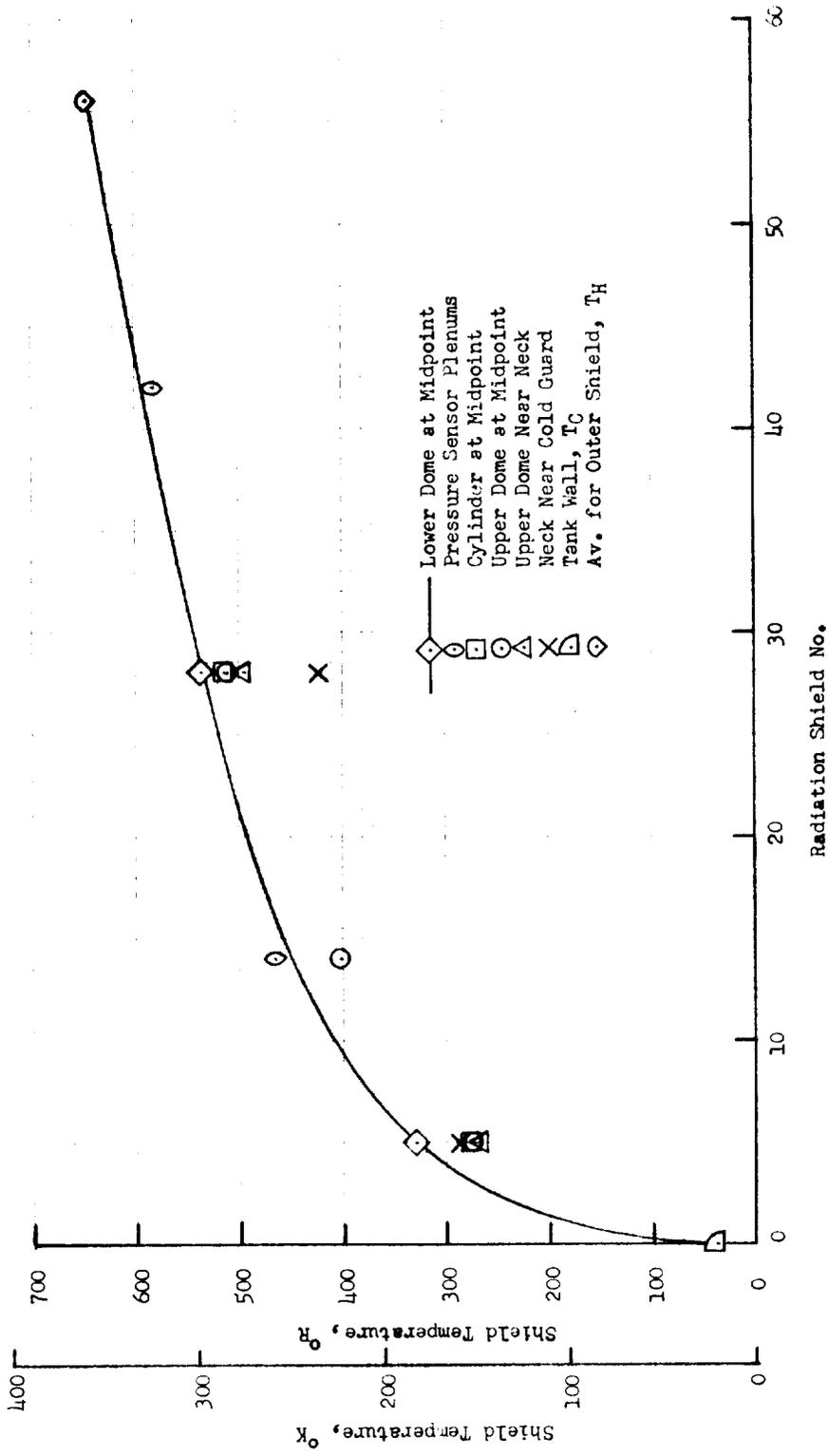
Fig. 6-25 Measured MLI Temperature Profile for Test Run 5
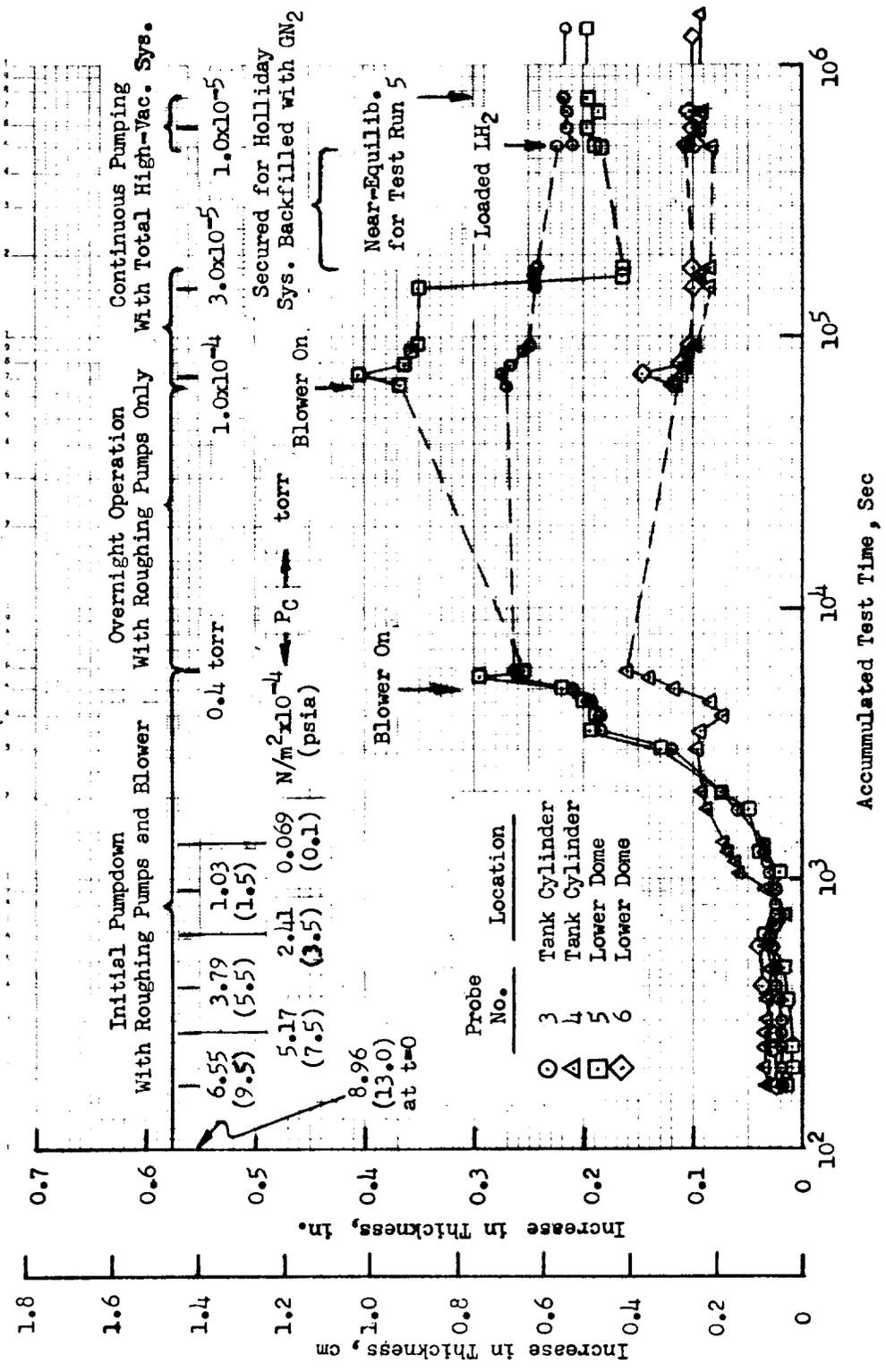
Fig. 6-26 Thickness Variation for 56-Shield MLI System During Test Run 5

6.3.5.4 Slow Evacuation Testing - Run 6. Subsequent to completion of the
56-shield MLI system thermal testing, dry GHe was introduced slowly to raise
the vacuum chamber and MLI interstitial pressures back to one atmosphere in
order to prepare for the final evacuation test sequence. Because the rapid
evacuation test procedures employed for Run 4 had resulted in an unsteady
chamber pressure decay-time history, and because the structural capability
of this MLI system had already been demonstrated during Test Run 4, the deci-
sion was made to conduct this evacuation test more slowly using only the
mechanical pumps, the blower, and the diffusion pumps in combination. Prior
to initiating the test sequence, the tank was topped off with LH_2, and
throughout the test the hot boundary shroud temperature was maintained at a
nominal value of $361^{\circ}K$ $(650^{\circ}R)$.

During the slow evacuation test sequence (the sixth and final evacuation of the
Task 3 program), the vacuum chamber was pumped down from atmospheric pressure
to a value of approximately 5×10^{-6} torr in approximately 2.2 hours. Inter-
stitial differential pressure data obtained from measurements taken during the
test are plotted in Fig. 6-27 as a function of vacuum pumping time. A straight-
line curve fit through the data shows that the GHe was readily evacuated from
the dry MLI system, with an interstitial differential pressure value of 1×10^{-4}
torr achieved in approximately 2.5 hours of pumping time. The straight-line
extrapolation of this curve shows that the interstitial differential pressure
could be expected to decay further to a value of 1×10^{-5} torr after approxi-
mately 6 hours of pumping time.

Early in Test Run 6, two of the four electro-mechanical thickness measurement
transducers (which had been used successfully in Test Run 5) ceased to operate.
However, representative data were still obtained, since one of the two remain-
ing transducers was located on the tank cylinder while the other was located
on the lower dome. Data obtained from these two transducers during Test Run 6
are presented in Fig. 6-28. For each transducer, the reference position of
the probe (i.e., the position corresponding to a zero increase in total MLI

LOCKHEED MISSILES & SPACE COMPANY
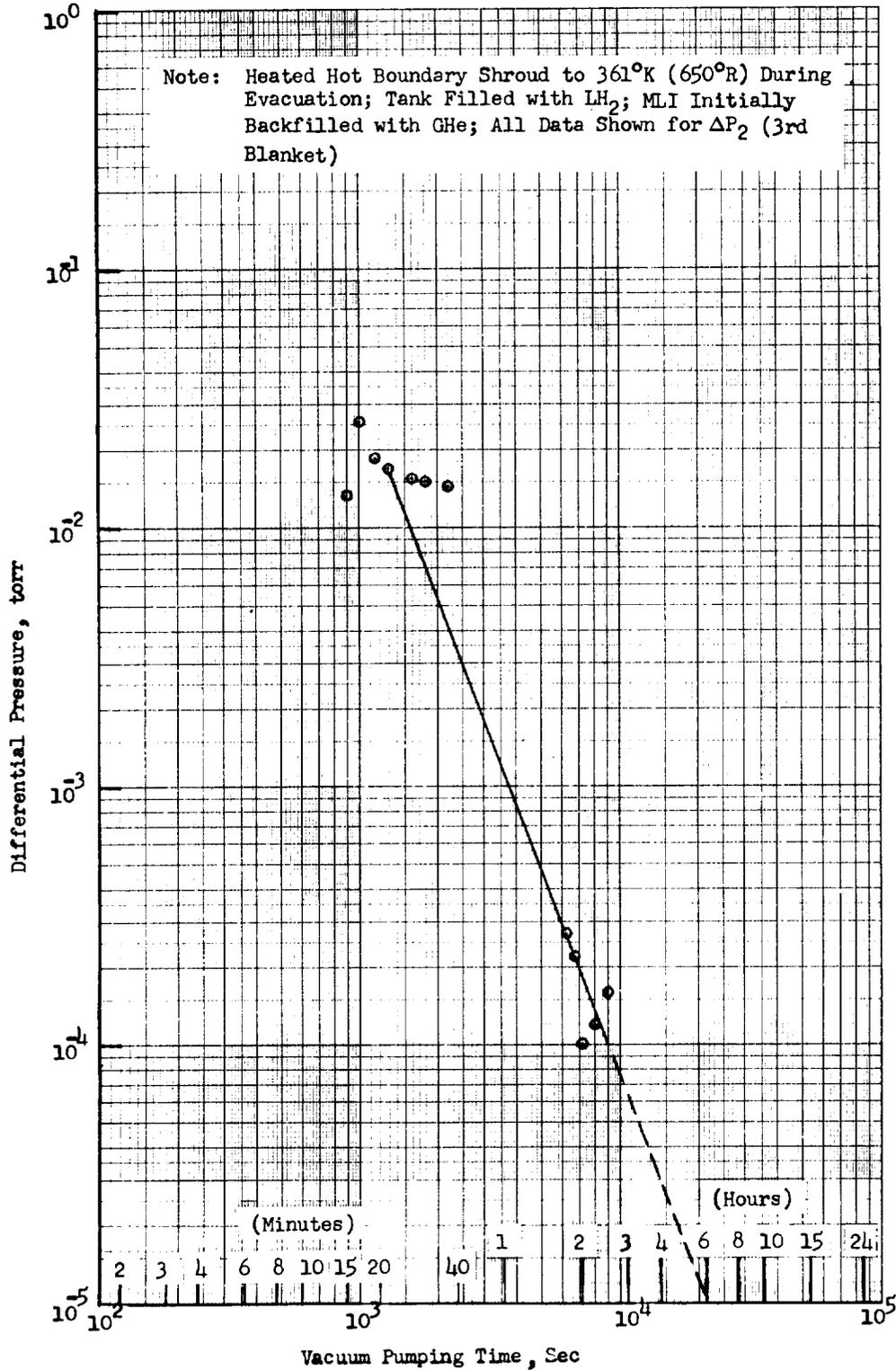
Fig. 6-27   Interstitital Pressure History During Sixth Evacuation
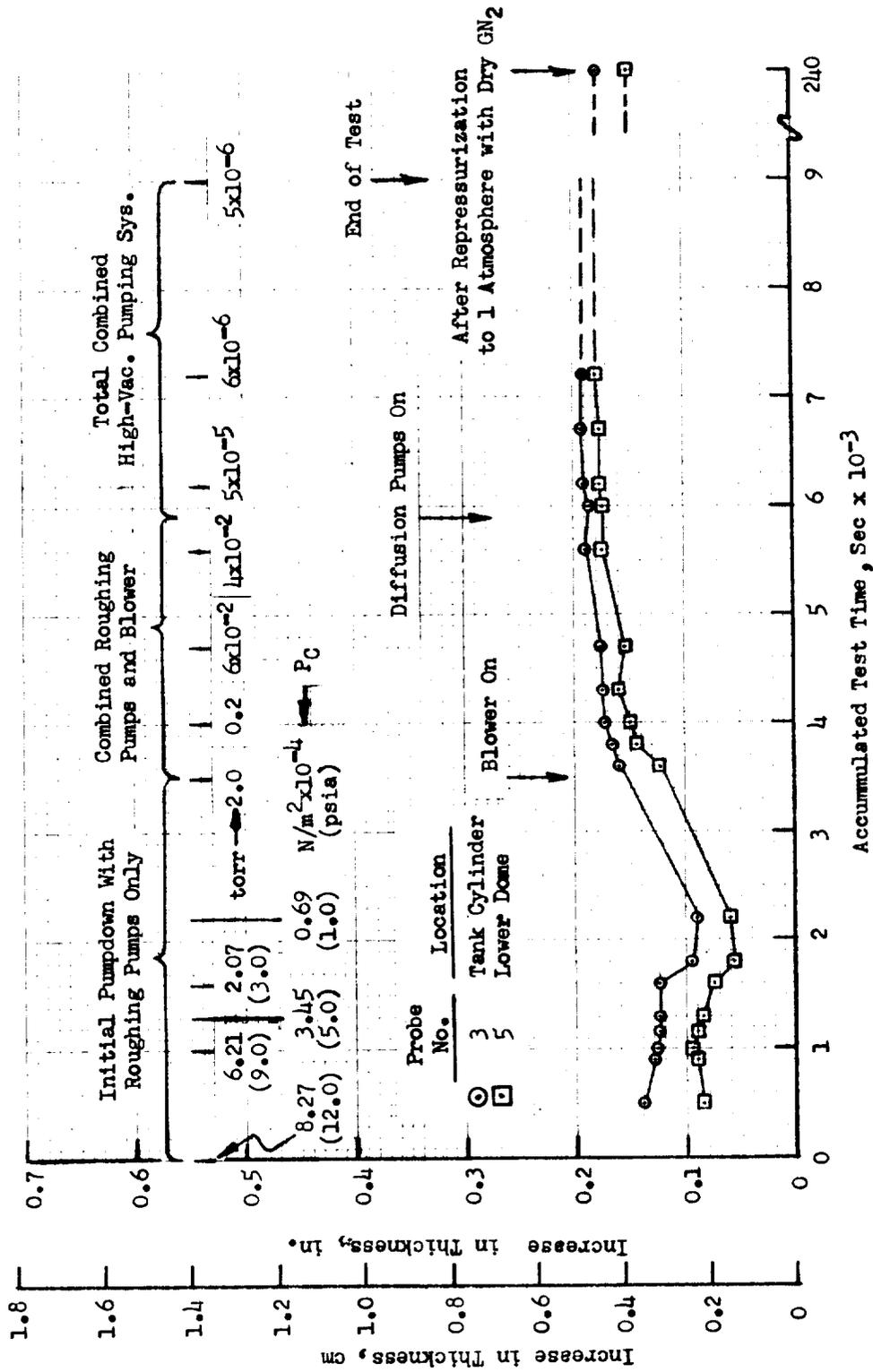
Fig. 6-28 Thickness Variation for 56-Shield MLI System During Test Run 6

thickness) was the same as the reference used for Test Run 5 data (Ref Fig. 6-26) as established from the pre-test x-rays for the 56-shield MLI system.

As shown in Fig. 6-28, total MLI thickness values measured at the tank cylinder and lower dome locations shortly after the beginning of the pumpdown for Test Run 6 were 0.356 and 0.216 cm (0.140 and 0.085 in.) (12.0 and 3.2 percent), respectively , greater than those obtained from the pre-test x-rays. During the successive evacuation sequence, the measured data show a decrease followed by an increase in the total thickness at each location. Maximum total thickness increases of 0.488 and 0.457 cm (0.192 and 0.180 in.) (16.5 and 6.7 percent) for the tank cylinder and lower dome locations, respectively, were recorded near the end of the test with the vacuum chamber pressure reduced to a value of less than 1×10^{-5} torr. The average MLI thickness increase at the end of the test for these two locations was 0.472 cm (0.186 in.), or approximately 12.0 percent of the average total MLI thickness based on pre-test x-ray measurements at 20 locations over the surface of the tank.

After completion of Test Run 6, the vacuum chamber pressure was let up slowly with dry GN_2 in order to complete the the Task 3 test program and secure the facility. Final thickness probe measurements, obtained approximately 3 days after the repressurization but prior to the post-test x-rays, show net increases over the pre-test thickness values of 0.455 and 0.381 cm (0.179 and 0.150 in.) (15.4 and 5.6 percent) for the tank cylinder and lower dome locations, respectively. Since these values are somewhat different than the 0.356- and 0.216-cm (0.140- and 0.085-in.) measurements recorded at the beginning of Test Run 6 (i.e., the end of Test Run 5), it appears that the degree of MLI compression which resulted from the repressurization gas flow process was not very reproducible from run to run. This was to be expected, since the rate of repressurization depends upon a bleed valve setting and, consequently, is difficult to reproduce precisely.

6-71

6.3.6 Post-Test Analysis and Data Correlation

Subsequent to completion of the Task 3 test program, an extensive analysis
was performed in order to correlate the data obtained during the test with
those predicted using the analytical heat transfer and gas evacuation models
developed in Tasks 1 and 2. ·Details of the post-test analysis and data cor-
relation activities are presented in the following paragraphs.

6.3.6.1 MLI Thickness Measurements. In order to assess the effect of var-
iable layer density on heat transfer, MLI thickness measurements obtained
from pretest and post-test x-rays at 20 locations over the surface of the
tank were correlated with those obtained during testing using the electro-
mechanical thickness measurement transducers previously installed at 4 of
the 20 locations* (Ref Figs. 6-7 and 6-11). As shown in Fig. 6-29, the tank
surface area was divided into five zones (A through E), with each zone divided
further into four equal quadrants for a total of 20 area segments. These area
segments were selected so that their centroids coincide with the x-ray expos-
ure target points and the locations of the electro-mechanical thickness
measurement transducer probes. Values of incremental tank zone surface
area, and the percent of area increase at mid-thickness per unit of total MLI
thickness are tabulated in the figure for each zone.

Pre-test and post-test x-ray thickness values were determined using the tech-
niques developed under Contract NAS 3-12025 (Ref 28, Section 3.3.1). How-
ever, during this program, only a 1.27-cm- (0.5-in.-) wide steel scale was
used to obtain true dimensions in each of the x-ray exposures. Summaries of
the MLI thickness data and the corresponding layer density values obtained
from the pre-test and post-test x-ray measurements for the 112-shield and the
56-shield composite systems are presented in Tables 6-6 thru 6-9, respectively.
In each of these tables, values of average MLI thickness, layer density, MLI
area (at mid-thickness), and area-thickness product were calculated for each

*Thickness data obtained from x-rays at 20 of the 22 target locations were used
 in this analysis (x-rays of the upper and lower polar regions of the tank were
 not used). In addition, data obtained from electro-mechanical thickness meas-
 urement transducers installed on the tank cylinder and lower dome (4 of the 6
 initially installed) were used during the 56-shield system tests only.

LOCKHEED MISSILES & SPACE COMPANY

Surface Area Zone	Tank Surface Area,		Area Increase, Percent Per Unit of Thickness,
	m^2 (ft^2)	percent	per cm (per in.)
A	0.973 (10.473)	26.23	0.430 (1.079)
B	0.436 (4.689)	11.74	5.396 (13.820)
C	0.851 (9.164)	22.95	0.818 (2.084)
D	0.436 (4.689)	11.74	5.396 (13.820)
E	1.014 (10.915)	27.34	0.412 (1.035)
Total	3.710 (39.930)	100.00	1.680 Av. (4.290)
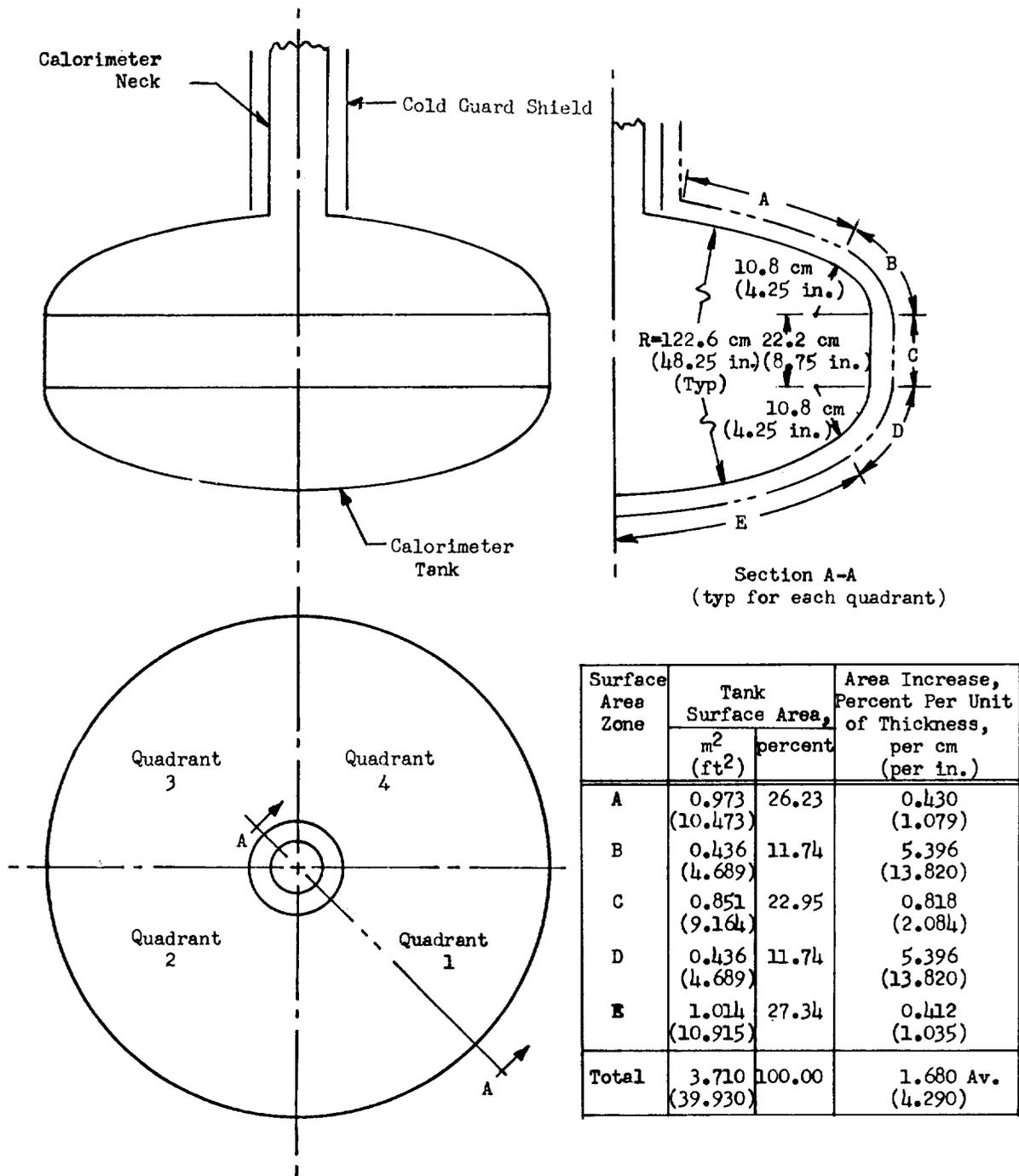
Fig. 6-29   Tank Calorimeter and MLI Surface Areas

LOCKHEED MISSILES & SPACE COMPANY

Table 6-6

PRE-TEST X-RAY THICKNESS AND LAYER DENSITY
VALUES FOR THE 112-SHIELD COMPOSITE MLI SYSTEM

Tank Zone	Zone Area m^2 (ft^2)	Quadrant	MLI Thickness cm (in.)	Layer Density layers/cm(layers/in.)	MLI Area m^2 (ft^2)	Area Thickness Product m^2-cm $(ft^2$-in.)
A	0.973 (10.473)	1 2 3 4 Av	3.99 (1.57 3.89 (1.53) 4.06 (1.60) 4.37 (1.72) 4.077(1.605)	27.7 (70.4)	0.990 (10.654)	4.036 (17.089)
B	0.436 (4.689)	1 2 3 4 Av	4.47 (1.76) 3.05 (1.20) 3.18 (1.25) 3.51 (1.38) 3.551(1.398)	31.8 (80.8)	0.520 (5.594)	1.847 (7.820)
C	0.851 (9.164)	1 2 3 4 Av	4.19 (1.65) 3.61 (1.42) 4.24 (1.67) 4.17 (1.64) 4.051(1.595)	27.9 (70.8)	0.880 (9.469)	3.565 (15.113)
D	0.436 (4.689)	1 2 3 4 Av	4.78 (1.88) 4.67 (1.84) 4.32 (1.70) 4.37 (1.72) 4.534(1.785)	24.9 (63.3)	0.543 (5.845)	2.462 (10.427)
E	1.014 (10.915)	1 2 3 4 Av	6.35 (2.50) 7.26 (2.86) 7.62 (3.00) 7.09 (2.79) 7.082(2.788)	15.9 (40.5)	1.043 (11.230)	7.387 (31.309)
Totals	3.710 (39.930)	Overall Av	4.853(1.911)[a]	23.3 (59.1)[b]	3.976 (42.792)	19.297 (81.758)

NOTES: (a) Effective Thickness = Σ Area-Thickness Product/ Σ MLI Area
(b) Effective Layer Density = N_s + 1/Effective Thickness

Table 6-7

POST-TEST X-RAY THICKNESS AND LAYER DENSITY VALUES
FOR THE 112-SHIELD COMPOSITE MLI SYSTEM

Tank Zone	Zone Area m^2 (ft^2)	Quadrant	MLI Thickness cm (in.)	Layer Density layers/cm(layers/in.)	MLI Area m^2 (ft^2)	Area Thickness Product m^2-cm (ft^2-in.)
A	0.973 (10.473)	1 2 3 4 Av	4.19 (1.65) 4.22 (1.66) 4.32 (1.70) 4.75 (1.87) 4.369 (1.720)	25.8 (65.6)	0.991 (10.668)	4.330 (18.370)
B	0.436 (4.689)	1 2 3 4 Av	3.76 (1.48) 3.12 (1.23) 3.94 (1.55) 3.94 (1.55) 3.691 (1.453)	30.6 (77.8)	0.523 (5.631)	1.930 (8.182)
C	0.851 (9.164)	1 2 3 4 Av	4.72 (1.86) 4.57 (1.80) 5.36 (2.11) 5.03 (1.98) 4.923 (1.938)	23.0 (58.3)	0.886 (9.534)	4.362 (18.486)
D	0.436 (4.689)	1 2 3 4 Av	5.38 (2.12) 5.66 (2.23) 5.94 (2.34) 4.90 (1.93) 5.474 (2.155)	20.6 (52.4)	0.565 (6.086)	3.093 (13.115)
E	1.014 (10.915)	1 2 3 4 Av	7.59 (2.99) 8.43 (3.32) 9.98 (3.93) 8.41 (3.31) 8.606 (3.388)	13.1 (33.4)	1.049 (11.297)	9.028 (38.252)
Totals	3.710 (39.930)	Overall Av	5.666 (2.231)[a]	19.9 (50.6)[b]	4.014 (43.216)	22.743 (96.405)

NOTES: (a) Effective Thickness = Σ Area-Thickness Product/Σ MLI Area
(b) Effective Layer Density = N_s + 1/Effective Thickness

C-4.

LOCKHEED MISSILES & SPACE COMPANY

Table 6-8

PRE-TEST X-RAY THICKNESS AND LAYER DENSITY VALUES
FOR THE 56-SHIELD COMPOSITE MLI SYSTEM

Tank Zone	Zone Area m² (ft²)	Quadrant	MLI Thickness cm (in.)	Layer Density layers/cm(layers/in.)	MLI Area m² (ft²)	Area Thickness Product m²-cm (ft²-in.)
A	0.973 (10.473	1 2 3 4 Av.	2.57 (1.01) 2.90 (1.14) 2.90 (1.14) 2.46 (0.97) 2.705 (1.065)	21.1 (53.6	0.984 (10.593)	2.662 (11.271)
B	0.436 (4.689	1 2 3 4 Av.	2.39 (0.94) 2.13 (0.84) 2.69 (1.06) 2.31 (0.91) 2.380 (0.937)	24.0 (61.0)	0.492 (5.295)	1.171 (4.951)
C	0.851 (9.164)	1 2 3 4 Av.	28.4 (1.12) 2.72 (1.07) 3.05 (1.20) 3.20 (1.26) 2.954 (1.163)	19.3 (49.0)	0.872 (9.387)	2.576 (10.926)
D	0.436 (4.689	1 2 3 4 Av.	2.77 (1.09) 3.15 (1.24) 3.53 (1.39) 3.40 (1.34) 3.213 (1.265)	17.7 (45.0)	0.512 (5.510)	1.645 (6.981)
E	1.014 (10.915)	1 2 3 4 Av.	-- 6.83 (2.69) -- -- 6.830 (2.690)	8.3 (21.2)	1.042 (11.218)	7.117 (30.176)
Totals	3.710 (39.930)	Overall Av.	3.888 (1.531)[a]	14.7 (37.2)[b]	3.902 (42.003)	15.171 (64.305)

NOTES: (a) Effective Thickness = Σ Area-Thickness Product/ Σ MLI Area

(b) Effective Layer Density = N_S + 1/Effective Thickness

LOCKHEED MISSILES & SPACE COMPANY

Table 6-9

POST-TEST X-RAY THICKNESS AND LAYER DENSITY VALUES
FOR THE 56-SHIELD COMPOSITE MLI SYSTEM

Tank Zone	Zone Area m² (ft²)	Quadrant	MLI Thickness cm (in.)		Layer Density layers/cm (layers/in.)	MLI Area m² (ft²)	Area Thickness Product m²-cm (ft²-in.)
A	0.973 (10.473)	1	2.90	(1.14)			
		2	2.90	(1.14)			
		3	3.43	(1.35)			
		4	2.84	(1.12)			
		Av.	3.018	(1.188)	18.90 (48.0)	0.985 (10.607)	2.973 (12.601)
B	0.436 (4.689)	1	2.03	(0.80)			
		2	2.16	(0.85)			
		3	2.51	(0.99)			
		4	2.62	(1.03)			
		Av.	2.329	(0.917)	24.5 (62.2)	0.491 (5.283	1.144 (4.845)
C	0.851 (9.164)	1	3.15	(1.24)			
		2	2.82	(1.11)			
		3	3.25	(1.28)			
		4	3.20	(1.26)			
		Av.	3.106	(1.223)	18.3 (46.6)	0.873 (9.398)	2.712 (11.494)
D	0.436 (4.689)	1	2.92	(1.15)			
		2	3.28	(1.29)			
		3	3.43	((1.35)			
		4	3.20	(1.26)			
		Av.	3.208	(1.263)	17.8 (45.1)	0.512 (5.510)	1.642 (6.959)
E	1.014 (10.915	1	7.37	(2.90)			
		2	7.90	(3.11)			
		3	7.09	(2.79)			
		4	8.20	(3.23)			
		Av.	7.640	(3.008)	7.4 (18.9)	1.045 (11.254)	7.984 (33.852)
Totals	3.710 (39.930)	Overall Av.	4.213 (1.659)[a]		13.5 (34.4)[b]	3.906 (42.052)	16.455 (69.751)

NOTES: (a) Effective Thickness = Σ Area-Thickness Product/Σ MLI Area

(b) Effective Layer Density = N_s + 1/Effective Thickness

LOCKHEED MISSILES & SPACE COMPANY

tank surface zone. The average layer density and MLI area values for each zone were then used later in calculating the integrated solid conduction heat transfer term for each test run. Overall average MLI thickness and layer density values for the total tank-mounted system were also calculated for comparison of the pre-test and post-test x-ray data with the electro-mechanical thickness measurement transducer data obtained during testing for the 56-shield composite system. These overall average thickness and layer density values are shown at the bottom of each table.

It can be seen by inspection of the x-ray data presented in the tables that, in general, post-test layer density values for any given tank surface zone or for the total composite system are significantly lower than the corresponding pre-test values. For example, overall average layer density values for the 112-shield composite system were 19.9 and 23.3 layers/cm (50.6 and 59.1 layers/in.), as obtained from the post-test and pre-test x-rays, respectively. These values indicate a reduction in layer density during testing of approximately 14 percent. Similarly, for the 56-shield composite system, overall average layer density values of 13.5 and 14.7 layers/cm (34.4 and 37.2 layers/in.) were obtained from the post-test and pre-test x-rays, respectively, evidencing a reduction during testing of approximately 7.5 percent. These in-test layer density reductions were simply the result of the gas evacuation process experienced during pumpdown of the two MLI systems. Although some post-test compaction of the MLI was also observed in each case, due to repressurization gas forces imposed as the vacuum chamber pressure was let back up to one atmosphere after testing, this effect was much less pronounced than the expansion of the MLI noted during the pre-test evacuations.

Comparison of the magnitude of the layer density reduction values experienced during testing of the 56-shield composite MLI system, based on electro-mechanical thickness measurement transducer data and x-ray data, shows generally good correlation where overall averages are used, but less satisfactory correlation where values for specific tank area zones are used. For example, the average in-test layer density reduction obtained using the data from electro-mechanical

6-78

thickness measurement transducer probes 3 and 5, after repressurization of the system with dry GN_2 (Ref Fig. 6-28), was approximately 10.5 percent (i.e., 15.3 and 5.6 percent for probes 3 and 5, respectively). The over-all average layer density reduction obtained from the pre-test and post-test x-rays (Ref Tables 6-8 and 6-9) was approximately 8.4 percent for 20 x-ray locations, but was 5.1 percent for the tank cylinder (Zone C, corresponding to probe 3) and was 11.8 percent for the lower dome (Zone E, corresponding to probe 5).

During reduction of the pre-test and post-test x-ray data, an attempt was made to assess the distribution of layer density through the thickness of the MLI, as indicated by the lead-strip markers installed at pre-selected locations (Ref Fig. 6-7). In general, good qualitative data was obtained, but quantative data determined for specific locations was of questionable value. The major problem encountered was one of interpretation of the x-ray data. In many instances, no conclusive determination could be made as to whether the apparent spacing between markers at a particular location resulted from true separation of the layers or from improper positioning of the markers. In addition, the markers were often warped, twisted, or otherwise misaligned with respect to the x-ray line of sight so that selection of the true plane of the marker was difficult. However, based on a qualitative assessment of these data, it was concluded that the average layer density of the inner blankets was some-what less than that of the outer blankets. This conclusion was substantiated by comparing the over-all average layer densities obtained from the x-rays for the 56-shield and 112-shield composite systems; i.e., 14.7 and 23.3 layers/ cm (37.2 and 59.1 layers/in.), respectively, based on pre-test x-ray data; and 13.5 and 19.9 layers/cm (34.4 and 50.6 layers/in.), respectively, based on post-test x-ray data.

Comparison of the layer density values obtained from the Task 3 x-ray measure-ments, for both the 56-shield and 112-shield composite MLI systems, with the minimum stacking layer density value obtained from Task 1 tests, for an unloaded flat specimen of this composite system, shows that significant gaps did exist (on the lower dome in particular), either within the tank-mounted systems or between the inner boundary of the MLI and the tank wall. Since the tank-mounted

6-79

systems were installed in 14-shield blankets, with the maximum blanket thickness
controlled by button-stud attachments, any large gaps within the MLI could have
existed only between adjacent blankets. In Task 1 studies of the double-
aluminized Mylar/preconditioned silk net composite system, an average minimum
stacking layer density value of 28.5 layers/cm (72.5 layers/in.) was estab-
lished during compressive pressure tests of four flat, 30.5-cm-(12-in.-) square,
80-shield specimens (Ref Table 3-5). Inspection of the data presented in
Tables 6-6 through 6-9 shows that the average layer density values achieved
on the upper dome and tank cylinder zones for the tank-mounted systems ranged
from approximately 3 percent to 35 percent lower than this minimum stacking
layer density. Further, the average values achieved on the lower dome zone
of the tank varied between approximately 44 percent and 74 percent lower than
the minimum stacking value.

Based on an evaluation of all of the layer density data obtained during the
Task 3 test program, it was concluded that the best assessment of solid con-
duction heat transfer for each test run would be that attained by integrating
average layer density and MLI area values for each tank surface area zone from
the post-test x-rays. Although in-test data obtained from the electro-mechanical
thickness measurement transducers would, theoretically, be better for this
purpose, the number of measurements obtained was insufficient to provide
adequate coverage over the total surface of the tank (no useable data at all
were obtained for the 112-shield system). Moreover, generally good correlation
was demonstrated between over-all average layer density values obtained from
the post-test x-rays and those obtained from the electro-mechanical trans-
ducers for the 56-shield composite system. Accordingly, the integrated post-test
x-ray values were used for the final heat transfer correlations presented
later in this section.

6.3.6.2 Interstitial Pressure Measurements. Data on gas evacuation obtained
from the Task 3 tests were analyzed during the post-test analysis in order to
determine the magnitude and distribution of interstitial gas pressures through
the thickness of the MLI. Results of this analysis were then used to compute

6-80

gas conduction heat transfer components near thermal equilibrium in order to correlate theoretical and measured values of total heat flux.

Plots of total pressure as a function of vacuum pumping time are presented in Figs. 6-30 and 6-31 for the 112-shield and 56-shield composite MLI system tests, respectively. The total interstitial pressure values shown are simply the sum of the vacuum chamber pressure values P_C and the interstitial differential pressure values presented previously (Ref Figs. 6-19 and 6-24). The location of each interstitial pressure sensor plenum and that of the vacuum chamber pressure sensor, with respect to the tank wall and the MLI blanket boundary shields, are shown within the insert in each figure. Significant events which occurred during the test sequences (e.g., shroud heating, tank loading, thermal equilibrium, etc.) are identified in time on the plots.

It has been shown previously under Contract NAS 8-20758 (Ref 29 , page 5-1) that, subsequent to initial evacuation, the predominant interstitial gas specie within any MLI system is water vapor. Accordingly, plots of the vapor pressure of ice*, which correspond to the temperature-time history of pertinent MLI shields, are superimposed over the measured interstitial pressure-time history plots in each figure. In general then, due to cryo-pumping of the water vapor molecules, the maximum interstitial gas pressure that can be sustained within any given interlayer cavity is the vapor pressure of ice corresponding to the temperature of the shield at the colder inner boundary. However, the maximum sustainable gas pressure within the first, third, and seventh MLI blankets (i.e., those which contain the interstitial pressure sensor plenums) tends toward the vapor pressure of ice corresponding to the temperature of the shield at the inner blanket boundary (i.e., the tank wall, shield 28, and shield 84, respectively)**.

---

* Temperature profiles through the MLI for each Task 3 test run (Ref Figs. 6-21, 6-22, 6-23, and 6-25) show that all shields between the tank wall and a point at mid-thickness or greater were maintained at temperatures below the freezing point of water; i.e., 273°K (492°R).

** Interstitial gas pressures tend to equalize for all inter-layer cavities of MLI blankets which contain the interstitial pressure sensor plenums, since these cavities are allowed to communicate freely with each other at the plenum location.
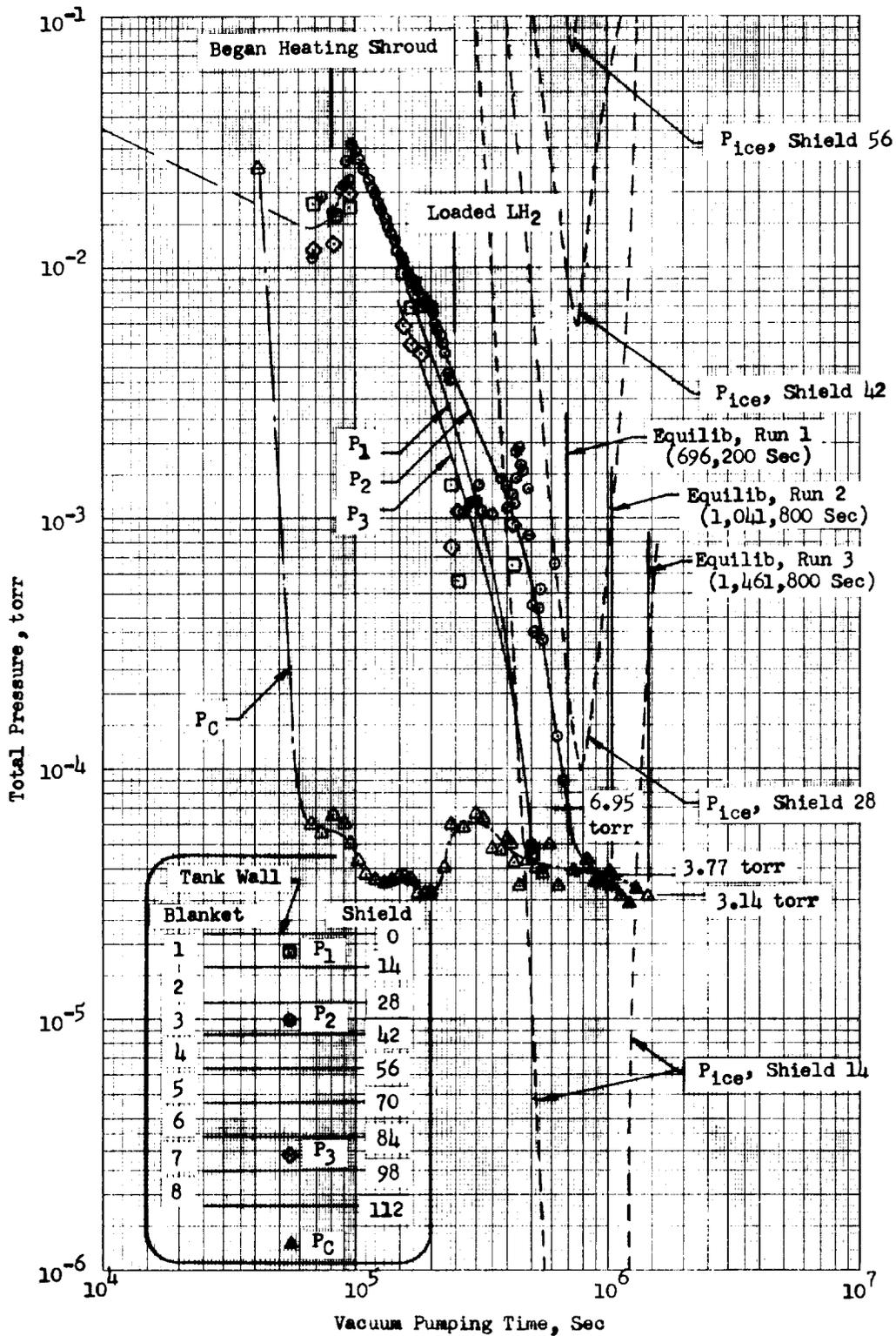
Fig. 6-30 Interstitial Pressure History for 112-Shield Composite System Tests

LOCKHEED MISSILES & SPACE COMPANY
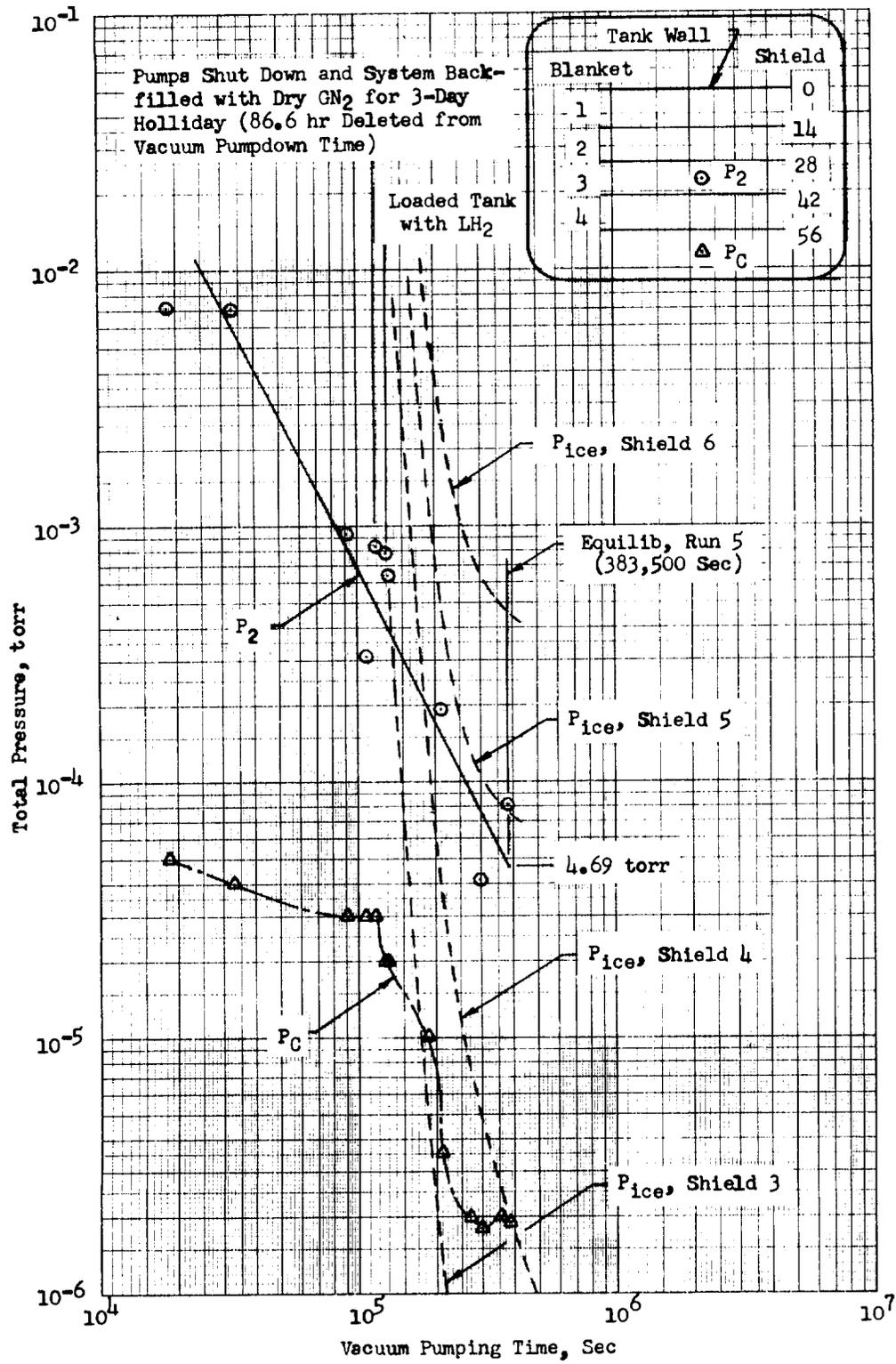
Fig. 6-31 Interstitial Pressure History for 56-Shield Composite System Tests

6-83

Fig. 6-30 shows that the vacuum chamber pressure achieved near equilibrium for the 112-shield composite system tests ranged from approximately 4×10^{-5} torr (Test Run 1) to approximately 3.14×10^{-5} torr (Test Run 3). As shown, the interstitial gas pressures P_1, P_2, and P_3 decreased according to the best fit of the measured data, and then were assumed to level off at the chamber pressure value, since no differential pressure potential existed (due to vacuum pumping) to cause further decay. However, the data presented on the vapor pressure of ice, corresponding to shield temperature-time histories, clearly indicates that the interstitial pressures did in fact decay further due to cryopumping for the cold inner layers close to the tank wall. Close inspection of Fig. 6-30 shows that the interstitial gas pressure was reduced to a negligible value (e.g., $< 1 \times 10^{-6}$ torr) from a point somewhere in blanket 2 inboard to the tank wall. The precise theoretical location for each of the 112-shield composite system tests was determined in the heat flux correlation analysis presented in the following section.

Similar conclusions can be drawn from inspection of the data presented in Fig. 6-31 for the 56-shield composite system tests. In this case, the vacuum chamber pressure value achieved near thermal equilibrium for Test Run 5 was approximately 1.9×10^{-6} torr. At this time, the interstitial pressure P_2 had not yet been reduced to the chamber pressure value. However, due to cryopumping, the interstitial pressures for all of the inter-layer cavities inboard of shield 5 were reduced to values well below that of P_2. Again, the exact theoretical location where the vapor pressure was reduced to the value below 1×10^{-6} torr was determined during the heat flux correlation analysis.

6.3.6.3 <u>Heat Flux Correlations</u>. The analytical model developed in Task 1 to predict heat flux for the tank-mounted MLI system tested in Task 3 assumes a uniform distribution of interstitial gas pressures through the thickness of the insulation (Ref Fig. 4-29 and Equation 4-56). However, it has been shown by the evaluation of Task 3 test data (Ref Section 6.3.6.2) that interstitial pressures not only vary in magnitude through the thickness, but in fact become negligibly small in the cold inner layers due to cryopumping of

water vapor. Consequently, the resulting gas conduction heat transfer term is actually discontinuous across the thickness, and the analytical model must be revised accordingly.

A summary of interstitial gas pressures within blankets 1, 3, and 7, obtained from the 112-shield and 56-shield composite MLI system test data (Ref Fig. 6-30 and 6-31, respectively), is presented in Table 6-10. Inspection of these data shows that interstitial pressures through the warmer outer layers can be reasonably approximated by the arithmetic average of the measured values (i.e., $(P_2 + P_3)/2$) for the 112-shield system, and simply by P_2 for the 56-shield system. It can also be seen that the vapor pressure of ice, corresponding to the temperature of the cold inner layers, is negligibly small compared to the pressures within the outer layers and, therefore, can be assumed to be zero for some distance outboard of the tank wall.

Table 6-10

SUMMARY OF INTERSTITIAL PRESSURE DATA

(All Pressure Values in Torr)

Test Run No.	1	2	3	5
No. Shields	112	112	112	56
P_1, Shields 0-14[a]	$< 2.2 \times 10^{-8}$	$< 1.45 \times 10^{-7}$	$< 3.14 \times 10^{-5}$	(b)
P_2, Shields 28-42	6.95×10^{-5}	3.77×10^{-5}	3.14×10^{-5}	4.69×10^{-5}
P_3, Shields 84-98	3.95×10^{-5}	3.76×10^{-5}	3.14×10^{-5}	--
$P_o = (P_2+P_3)/2$	5.45×10^{-5}	3.76×10^{-5}	3.14×10^{-5}	4.69×10^{-5}

Notes: (a) Values shown correspond to the measured interstitial pressure P_1 or to P_{ice} for Shield 14, whichever is smaller; however, the maximum sustainable pressure within this blanket tends toward $P_{ice} < 1 \times 10^{-22}$, corresponding to the tank wall temperature of $20.6°K$ ($37°R$).

(b) No measured value obtained for P_1; P_{ice} for Shield 14 = 5.4×10^{-1}.

In the final analysis of the Task 3 test data, a total heat balance was performed between the outer layers and the inner layers in order to determine the point through the thickness where gas conduction heat transfer became negligibly small for each test run. In this analysis, gas conduction heat transfer was assumed to be negligible for interstitial pressure values below 1×10^{-6} torr (Ref Fig. 4-29).

The over-all heat balance performed in the analysis can be expressed as

$$Q_{so} + Q_{go} + Q_{ro} = Q_{si} + Q_{ri} \qquad (6\text{-}1)$$

where s indicates solid conduction, g indicates gas conduction, r indicates radiation, o indicates the multilayers outboard of a point x defined by $T_x = 162^{\circ}K$ ($292^{\circ}R$) (corresponding to $P_{ice} = 1 \times 10^{-6}$ torr), and i indicates the multilayers inboard of that point. The terms of Equation (6-1) are defined as follows, with x equal to the distance from the tank wall to point x and δ equal to the total insulation thickness:

$$Q_{so} = \frac{C_s \, T_{mo} \, (T_H - T_x)}{N_s(1 - x/\delta)} \, \Sigma \, A_n (\bar{N}_n)^{2.56} \qquad (6\text{-}2)$$

where $C_s = 8.95 \times 10^{-8}$ for T in $^{\circ}K$, A in m^2, and $\bar{N}$ in layers/cm

$\qquad = 8.06 \times 10^{-10}$ for T in $^{\circ}R$, A in ft^2, and $\bar{N}$ in layers/in.

$$Q_{go} = \frac{C_g \, P_o \, (T_H^{0.52} - T_x^{0.52}) \, A}{N_s(1 - x/\delta)} \qquad (6\text{-}3)$$

where $C_g = 1.46 \times 10^4$ for P_o in torr, T in $^{\circ}K$, and A in m^2

$\qquad = 3.44 \times 10^3$ for P_o in torr, T in $^{\circ}R$, and A in ft^2

$$Q_{ro} = \frac{C_r \, \sigma \, (T_H^{4.67} - T_x^{4.67}) \, A}{N_s(1 - x/\delta)} \qquad (6\text{-}4)$$

where $C_r = 2.95 \times 10^{-4}$ for σ in $w/m^2 \; ^{\circ}K^4$, T in $^{\circ}K$, and A in m^2

$\qquad = 1.99 \times 10^{-4}$ for σ in $Btu/hr \; ft^2 \; ^{\circ}R^4$, T in $^{\circ}R$, and A in ft^2

$$Q_{si} = \frac{C_s \, T_{mi} \, (T_x - T_C)}{N_s(x/\delta)} \, \Sigma \, A_n (\bar{N}_n)^{2.56} \qquad (6\text{-}5)$$

where C_s is as defined above for Eq (6-2)

6-86

$$Q_{ri} = \frac{C_r \, \sigma \, (T_x^{4.67} - T_C^{4.67}) \, A}{N_S(x/\delta)} \qquad (6\text{-}6)$$

where C_r is as defined above for Eq (6-4)

Substituting these component heat transfer terms into Eq (6-1), with the numerator of each term represented as Q^*, and then solving for the ratio of the inner layer thickness to the outer layer thickness yields

$$\frac{(x/\delta)}{(1-x/\delta)} = \frac{Q^*_{si} + Q^*_{ri}}{Q^*_{so} + Q^*_{go} + Q^*_{ro}} \qquad (6\text{-}7)$$

Finally, substituting Q^{**} for the right side of Eq (6-7), the ratio x/δ is given by

$$x/\delta = \frac{Q^{**}}{1+Q^{**}} \qquad (6\text{-}8)$$

After the location of point x has been determined from Eq (6-8), each of the terms of Eq (6-1) can be evaluated numerically. However, in order to determine the relative contributions of solid conduction, gas conduction, and radiation to the total heat transfer (i.e., that through the total MLI thickness), values of Q_s and Q_r must be calculated, based on the extreme temperature boundaries, as follows:

$$Q_s = \frac{C_s \, T_m \, (T_H - T_C)}{N_S} \; \Sigma \, A_n(\bar{N}_n)^{2.56} \qquad (6\text{-}9)$$

$$Q_r = \frac{C_r \, \sigma \, (T_H^{4.67} - T_C^{4.67}) A}{N_S} \qquad (6\text{-}10)$$

where C_s and C_r are as defined above for Eq (6-2) and (6-4), respectively.

The average gas conduction heat transfer through the total MLI thickness can then be determined as

$$Q_g = Q_{so} + Q_{go} + Q_{ro} - Q_s - Q_r \qquad (6\text{-}11)$$

Results of the final heat transfer analysis, and the correlation of measured heat flux values with those obtained from the analysis, are presented in Table 6-11. Values of N_x shown in the table were determined as the product

6-87

Table 6-11

SUMMARY OF PREDICTED AND MEASURED HEAT FLUX DATA

Test Run No.	1	2	3	5
N_s	112	112	112	56
N_x	24.05	17.39	12.38	4.30
Av. $\bar{N}$, layers/cm(layers/in.)	19.9 (50.6)	19.9 (50.6)	19.9 (50.6)	13.5 (34.4)
Av. T_H, $^\circ K$ ($^\circ R$)	275.6 (496.1)	317.3 (571.1)	358.7 (645.7)	358.2 (644.8)
Av. P_o (torr)	5.45×10^{-5}	3.76×10^{-5}	3.14×10^{-5}	4.69×10^{-5}
Q_s, w(Btu/hr)	0.368 (1.257)	0.488 (1.668)	0.625 (2.134)	0.621 (2.120)
Q_g, w(Btu/hr)	0.129 (0.439)	0.117 (0.398)	0.119 (0.408)	0.346 (1.181)
Q_r, w(Btu/hr)	0.149 (0.510)	0.288 (0.984)	0.511 (1.745)	0.988 (3.374)
Q_{neck}, w(Btu/hr)	-0.132 (-0.450)	-0.205 (-0.700)	-0.252 (-0.860)	-0.135 (-0.460)
$Q_{pres\ tap}$, w(Btu/hr)	0.059 (0.200)	0.070 (0.240)	0.138 (0.470)	0.217 (0.740)
$Q_P{}^{(a)}$, w(Btu/hr)	0.573 (1.956)	0.758 (2.590)	1.141 (3.897)	2.036 (6.955)
FB, kg/hr (lbm/hr)	0.00501 (0.01105)	0.00600 (0.01323)	0.00918 (0.02024)	0.01579 (0.03481)
$Q_M{}^{(b)}$, w(Btu/hr)	0.616 (2.105)	0.738 (2.520)	1.129 (3.856)	1.945 (6.642)
$100 \left(\dfrac{Q_M}{Q_P} - 1\right)$ (percent)	+7.6	-2.7	-1.1	-4.5

Notes: (a) $Q_P = Q_s + Q_g + Q_r + Q_{neck} + Q_{pres\ tap}$

(b) $Q_M = \lambda\ FB$ (where λ = 442.7 joules/gm or 190.5 Btu/lbm)

of x/δ, Ref Eq (6-8), and N_S, and indicate the theoretical point (shield no.) through the thickness where gas conduction becomes negligible. Values of Q_{neck} shown in the table were calculated using the measured temperature distributions at locations A, B, and E (Ref Fig. 6-18). They include both parallel conduction along the multilayer shields and radiation tunneling through the inter-layer cavities. Values of $Q_{pres\ tap}$ shown in the table were calculated assuming radiation heat transfer only* between the inboard edge of the pressure sensor plenum for blanket 1 and the tank wall. An emittance value of 1 was assumed for the plenum surface.

In the analysis, estimates were made of the degree of thermal equilibrium achieved during each test run. These estimates were based on the thermal capacitance of the MLI mass and the rate of change of measured shield temperatures approaching equilibrium. Results of the analysis showed that the data obtained for each of the 112-shield tests (Runs 1, 2, and 3) were within 10 percent of true equilibrium, and that those obtained for the 56-shield test (Run 5) were within 5 percent of the ultimate equilibrium value. Since the measured insulation temperatures were still decreasing for Run 1, and were still increasing for Runs 2 and 3, when the boiloff measurements were obtained, the percentage variations between measured and calculated values shown in Table 6-11 would decrease further at true thermal equilibrium conditions. Conversely, since the measured insulation temperatures were still decreasing when the boiloff data were obtained for Run 5, the percentage variation shown would increase at true equilibrium. However, the correlation between measured and calculated heat flux values, including the effects of not achieving absolute equilibrium shield temperatures, is well within ± 10 percent for all of the test runs.

---

* X-rays of the lower polar region of the tank clearly show that there was no physical contact between the inner surface of the plenum and the tank wall during any of the test runs.

Section 7

DISCUSSION OF RESULTS

The objectives which were identified for each program task in previous sections of this report were achieved during the contract effort. In Task 1 the analytical heat transfer model originally developed for selected MLI composites under Contract NAS 3-12025 was modified for an extended range of applicable boundary temperatures using a higher number of shields in a given test specimen. Although gas conduction heat transfer was negligible for the Task 1 work, an analytical expression was developed for gas conduction considering either helium or nitrogen at various pressure levels within the MLI composite. In addition, an independent analytical model was developed under Task 2 in order to investigate gas evacuation and outgassing characteristics of these same MLI composites. Finally in Task 3, these analytical models were used to predict the thermal performance of both a 112-shield and a 56-shield MLI composite system as installed on a 1.22-m-(4 ft-) diameter tank calorimeter. The predictions were correlated with the experimental data obtained during testing within approximately $\pm$ 8 percent.

7.1 COMPOSITE MATERIAL INVESTIGATIONS

Early in the program, a water-spray technique was developed for preconditioning of the silk net spacers to be used in preparing MLI specimens for all tasks. This technique was found to be superior to complete immersion and soaking of the netting in that inherent wrinkles were smoothed out and layer density control was significantly improved without removing a major portion of the sizing. Typically the "as received" silk net material contains approximately 4.5 percent water by weight and an unknown percentage of sizing. Using the water-spray preconditioning process, the initial weight was reduced by approximately 7 percent, whereas complete immersion and soaking resulted in a weight loss of approximately 35 percent of the initial value. The water content after

7-1

preconditioning and air-drying was essentially the same as that for "as received" netting regardless of whether the netting was water-sprayed or soaked to accomplish the preconditioning.

Subsequent to selection of the water-spray preconditioning process, a series of laboratory-scale tests were performed to assess the layer density characteristics of double-aluminized Mylar/preconditioned silk net composite specimens as a function of applied compressive loading. Three 0.093 m^2 (1.0 ft^2) specimens each of 10, 20, and 80 shields (22, 42, and 162 layers of net, respectively) were tested on a compression testing machine. Results of the tests were compared with those obtained for similar specimens composed of double-aluminized Mylar with "as received" silk net spacers. It was found that the spacer preconditioning process resulted in a higher layer density value for any given value of compressive pressure, but that the specimen-to-specimen layer density reproducibility was significantly improved for the specimens containing preconditioned rather than "as received" net spacers. For example, at low values of compressive pressure, the maximum variation in layer density observed for specimens with preconditioned spacers was 6 percent, whereas a 26 percent difference was noted for specimens with "as received" net spacers. At the highest values of compressive pressure, these variations in layer density decreased to approximately 2 percent and 10 percent, respectively. The significance of the layer density variations is best understood by noting the resulting effect on conduction heat transfer (e.g., a 15-percent uncertainty in layer density corresponds to a 50-percent uncertainty in conduction heat transfer).

Additional efforts conducted early in the contract program included the selection of five suitable reflective shield perforation patterns, procurement of MLI shield and spacer materials, and assessment of shield optical properties by obtaining representative emittance and reflectance measurements. The total hemispherical emittance measured at 297°K (535°R) for a single sample of the smooth, unperforated double-aluminized Mylar was 0.031 $\pm$ 0.001, with a corresponding near-normal reflectance value of 0.977. Average reflectance values

obtained for samples of the large hole-spacing patterns (i.e., S-602, S-603, 937, and 937S) ranged from 0.959 to 0.967, indicating that some degradation of the optical properties was incurred due to handling encountered during the perforation process. The relatively low average reflectance value of 0.950 obtained for the small hole-spacing S-604 pattern was most likely caused by the close spacing of the perforations and the size of the reflectometer entrance aperature, since the exposed edges of the perforations decrease the reflectance viewed through the aperature even though the shield is backed by a first surface aluminum mirror.

7.2 TASK 1 HEAT TRANSFER INVESTIGATIONS

In Task 1, heat flux measurements were obtained on a 61-cm-(24-in.-) diameter flat plate calorimeter for specimens of 20 and 80 reflective shields each for three different MLI composites over a wide range of boundary temperatures and layer density values. Since the anticipated heat flux values were impractically low for measurement using conventional boiloff calorimetry, an electrical power input difference method was selected. With this method, cryogens were used only to maintain a constant sink temperature, and heat flux was determined as the difference in electrical energy required to maintain thermal equilibrium for a calibration condition and the actual test condition. Cold boundary temperatures were varied from $40^{\circ}K$ ($72^{\circ}R$) to $300^{\circ}K$ ($540^{\circ}R$), while hot boundary temperatures applied during these tests ranged from $70^{\circ}K$ ($126^{\circ}R$) to $390^{\circ}K$ ($702^{\circ}R$). Thus, the differential temperature values achieved during the testing ranged from $30^{\circ}K$ ($54^{\circ}R$) to $350^{\circ}K$ ($630^{\circ}R$). Layer density values were varied from 52 layers/cm (132 layers/in.) to 91 layers/cm (230 layers/in.) for double-aluminized Mylar/Tissuglas specimens, and from 28 layers/cm (71 layers/in.) to 48 layers/cm (122 layers/in.) for double-aluminized Mylar/preconditioned silk net specimens.

Results of the tests performed on double-aluminized Mylar/Tissuglas specimens show that a significantly better correlation was achieved between predicted and measured heat flux values when the analytical model was revised to include a more realistic, non-linear temperature dependence of the Tissuglas spacers.

7-3

The revised model predicts a higher conduction heat transfer value at lower temperatures because of the non-linear variation of the glass thermal conductivity with temperature. Although the previous linear-dependency model does predict satisfactory values for hot boundary temperatures of $200^{\circ}K$ ($360^{\circ}R$) or higher, where the thermal conductivity of the glass does behave in a nearly linear manner with temperature, the revised model given by Eq (4-11) is recommended for general design applications.

Evaluation of the test results obtained for double-aluminized Mylar/preconditioned silk net composite specimens with both unperforated and perforated reflective shields shows that the previously-derived form of the analytical model, which employs a linear temperature dependence of the silk net spacers, provides a correlation between predicted and experimental values which is generally within $\pm$ 10 percent. The coefficients and exponents of the solid conduction term were reevaluated independently for specimens with unperforated and with perforated shields using the technique developed during the previous NAS 3-12025 contract program. The resulting heat flux prediction equations, which are recommended for all design applications employing these respective shield and spacer composites, are as follows:

> Unperforated Double-Aluminized Mylar/Preconditioned Double Silk Net, Eq (4-14)
>
> Perforated Double-Aluminized Mylar (Pattern S-602)/Preconditioned Double Silk Net, Eq (4-16)
>
> Perforated Double-Aluminized Mylar (Pattern S-603)/Preconditioned Double Silk Net, Eq (4-17)
>
> Perforated Double-Aluminized Mylar (Pattern S-604)/Preconditioned Double Silk Net, Eq (4-18)
>
> Perforated Double-Aluminized Mylar (Pattern 937-S)/Preconditioned Double Silk Net, Eq (4-19)
>
> Perforated Double-Aluminized Mylar (Pattern 937)/Preconditioned Double Silk Net, Eq (4-20)

Comparison of the solid conduction term of Eq (4-14), for the unperforated double-aluminized Mylar/preconditioned silk net composite, with that of Eq (4-15), which was developed under Contract NAS 3-12025 for the similar

composite system using "as received" spacers, shows somewhat better thermal performance at low layer density values for the untreated-net composite. However, at high layer density values, the preconditioned-net system provides lower predicted heat flux values and, in addition, provides a much smaller uncertainty in thermal performance over the entire range of layer density values tested. For a layer density value of 29 layers/cm (70 layers/in.), Eq (4-15) yields a solid conduction heat flux value approximately 35 percent lower than that obtained from Eq (4-14). At a layer density value of 43 layers/cm (110 layers/in.), both equations yield approximately equal values of solid conduction heat flux. Finally, for a layer density value of 51 layers/cm (130 layers/in.), Eq (4-15) provides a solid conduction heat flux value approximately 20 percent greater than that achieved using Eq (4-14).

An evaluation of the influence of shield perforations on radiative heat transfer was also performed in Task 1. Results of this analysis show that the radiative heat transfer values obtained for systems with perforated shields compared to those obtained for unperforated-shield composites ranged from approximately 9 percent higher, for an open area of 0.26 percent, to approximately 32 percent higher for an open area of 1.07 percent. No significant difference in radiative heat flux was noted for the two perforation sizes studied at any given value of open area percentage.

For the double-aluminized Mylar/preconditioned silk net composite, a comparison of solid conduction plus radiation heat flux values was also performed for perforated-shield and unperforated-shield systems assuming that both were highly evacuated and that the gas conduction heat transfer component was negligible. It was found from this comparison that the heat flux values predicted for the perforated-shield system (i.e., the S-604 pattern with 1.07 percent open area) were higher in every case, ranging from an increase of approximately 13 percent, for boundary temperatures of $278^{\circ}K$ ($500^{\circ}R$) to $22^{\circ}K$ ($40^{\circ}R$) and for a layer density of 39 layers/cm (100 layers/in.), to an increase of approximately 30 percent for boundary temperatures of $361^{\circ}K$ ($650^{\circ}R$) to $22^{\circ}K$ ($40^{\circ}R$) and for a layer density of 28 layers/cm (70 layers/in.).

Finally in Task 1, an analysis was performed to evaluate the effect of gas conduction on the total predicted heat transfer for both nitrogen and helium interstitial gas species at pressures of 10^{-3} torr or less. A gas conduction component term was derived and added to the basic heat flux prediction model for this analysis. As interstitial pressures were increased above 10^{-6} torr, the influence of the gas conduction heat transfer was found to be increasingly significant. The additional heat transfer, calculated with nitrogen as the assumed interstitial gas, was found to be approximately double that computed for helium at a given interstitial pressure value. For the perforated, double-aluminized Mylar/preconditioned silk net system, with nitrogen as the interstitial gas and with a layer density of 28 layers/cm (70 layers/in.), the predicted ratio of gas conduction to the sum of solid conduction and radiation ranged from 0.004, for boundary temperatures of $361^{\circ}K$ ($650^{\circ}R$) to $22^{\circ}K$ ($40^{\circ}R$) and for an interstitial pressure value of 10^{-6} torr, to 8.08 for boundary temperatures of $278^{\circ}K$ ($500^{\circ}R$) and $22^{\circ}K$ ($40^{\circ}R$) and for an interstitial pressure of 10^{-3} torr. Similarly, for the same composite system with unperforated shields and with the same interstitial gas species and layer density, the ratio ranged from 0.006 to 9.62 for the same respective boundary temperatures and interstitial pressures.

7.3 TASK 2 GAS EVACUATION INVESTIGATIONS

Initially in Task 2, an analysis was performed to develop the theoretical models needed to predict interstitial gas pressures as a function of time, perforation size and open area, flow path length, specimen temperature, purge gas species, and layer density. The resulting models which were developed during this analysis, for both the edge-pumping and the broadside-pumping modes of evacuation, were quite similar in form, but varied in the manner in which the detailed computations were accomplished. For accurate prediction of interstitial pressure histories during evacuation (i.e., within $\pm$ 15 percent), a multinode model was developed which requires solution of a series of equations for evaluation. Since one of these is a non-linear first order partial differential equation which cannot be solved by any simple closed-form

method, a computerized numerical technique was used. The general model is defined by Equations (5-1) through (5-9). Flow conductance parameters, which are different in detail for different evacuation modes, are obtained from Equations (5-37) and (5-44) for the edge-evacuation and broadside-evacuation modes, respectively.

In order to obtain approximate interstitial pressure values for preliminary design of an MLI system or for preliminary correlation of analytical and experimental results, simplified single-node models were also developed in the Task 2 program for the edge and broadside evacuation modes. These simplified models, given by Equations (5-51) and (5-54), respectively, were found to predict interstitial pressure values typically 50 to 100 percent higher than those obtained using the corresponding multinode computer models.

Subsequently, gas evacuation tests were performed using a 68.6-cm-(27- in.-) diameter flat plate apparatus for specimens of 20 and 80 reflective shields each for five different MLI composites over a wide range of perforation characteristics, flow path lengths, test temperatures, purge gas species, and layer density values. The perforation size and open area values and the layer density values used in the Task 2 tests were identical to those previously described and used in Task 1. Flow path lengths were varied from 19.1 cm (7.5 in.) to 34.3 cm (13.5 in.), while test temperatures ranged from 128°K (230°R) to 300°K (540°R). Helium, nitrogen, and argon purge gases were used.

In general, the data obtained during the first pumpdown of any given specimen included the effects of significant outgassing of water vapor. Data obtained subsequently during the second and third pumpdowns of each specimen were essentially identical and evidenced little or no outgassing effects.

During post-test analysis of the data, good qualitative correlations were obtained between the predicted and experimental results for variation of each major flow parameter. Good quantative correlations were also obtained for some of the parametric variations. However, in many cases, results of the

LOCKHEED MISSILES & SPACE COMPANY

analyses and tests could not be properly compared, since the evacuation flow was often within the transient region between the purely viscous and the purely free molecule flow regimes where the flow characteristics are not as well defined or understood.

Early in the Task 2 program, it was found that the vacuum pumping rate achieved from test to test varied only with temperature. Consequently, the data required correction for the variation of pumping rate due to temperature effects for only 2 of the 20 specimens tested.

During preliminary evacuations of the empty apparatus, it was established that the absolute accuracy of the interstitial pressure measurements which could be achieved using the Barocell differential measurement transducer system as installed was approximately ± 0.0005 torr. In the Task 2 application, the transducer was mounted inside the vacuum chamber, a compensating tube was installed on the reference port of the transducer head, and the system was zeroed only prior to initiating the pumpdown (i.e., at 760 torr). However, these preliminary test results indicated that the greater accuracy needed for Task 3 testing could be achieved by installing a 3-way solenoid-operated valve within the pressure sensing line in order to rezero the transducer as the chamber pressure was reduced.

In the theoretical analysis, it was shown that the differential pressure which exists across the specimen multilayers during evacuation is inversely proportional to the second power of layer separation in the viscous flow regime, and to the first power of the layer separation in the free molecule flow regime. Test data confirmed this relationship qualitatively, although a precise quantative correlation could not be obtained since much of the test data were obtained within the transition flow regime where the influence of layer density was passing from second- to first-power dependence.

Test data obtained where the specimen diameter was varied to study the influence of flow path length showed the expected variation in differential pressure with the square of the specimen radius for both the viscous and the free molecule flow regimes.

7-8

The effect of the purge gas species was also investigated in the Task 2 tests. It was found that the differential pressure varies inversely with viscosity within the viscous flow regime, and inversely with the square root of molecular weight within the free molecule flow regime. Test data obtained at early evacuation times showed good quantitative correlation with the theory for viscous flow. Data obtained at later times were again within the transient flow region, however, so that only a qualitative correlation could be obtained between those data and the model.

In evaluating the effect of temperature on gas evacuation flow character-istics, an excellent correlation was obtained at high pressures where the differential pressure is proportional to the product of a temperature dependent constant and viscosity. For example, the ratio of differential pressure values within the viscous flow regime for temperatures of 300°K (540°R) and 128°K (230°R) was found to be 2.3, based on the test data, compared to 2.4 based on the theoretical model. At lower pressures within the free molecule regime, a good qualitative correlation was obtained, but again an exact numerical comparison was precluded since purely free molecule flow was not achieved in these particular Task 2 tests.

With regard to temperature effects, it was also noted during the Task 2 test-ing that outgassing of water vapor was experienced over much longer evacua-tion times for specimens maintained near the ice-point temperature of 273°K (492°R) than for those which were either appreciably colder or warmer. Al-though this result had not been anticipated prior to the tests, it is not surprising since outgassing is essentially precluded by cryopumping for tempera-tures below the ice point, but is greatly accelerated due to the increased energy levels maintained for higher temperature specimens.

During the investigation of broadside evacuation of MLI using specimens with perforated shields, good correlation was obtained between the test data and the model regarding the effect of perforation size and open area on differential pressure. However, the test data confirmed the analytical prediction that the

flow conductance of an unperforated-shield specimen using edge evacuation would be significantly better than that for any one of the perforated-shield specimens using broadside evacuation. Consequently, the S-604 perforation pattern, which offers the highest open area percentage with the smallest perforation size, was selected for the testing of combined edge-and broadside-evacuation. As expected, the test data obtained show that little additional benefit was realized from the addition of the shield perforations. For example, at 1.4 minutes of pumping time, the differential pressure value obtained with edge evacuation alone was lower than that obtained with broadside evacuation alone by approximately 51 percent. When combined edge- and broadside evacuation modes were employed, the resulting differential pressure value was approximately 55 percent lower than that obtained by broadside evaucation alone for a typical specimen.

Comparison of the test data obtained for specimens of different MLI composite systems, where all other flow parameters were kept the same, showed that the insulation type itself can exert a significant influence on evacuation flow characteristics. For example, analysis of the test data obtained for specimens of the double-aluminized Mylar/preconditioned silk net composite system showed that the effect of the double silk net spacers was to reduce the effective interlayer (shield) separation by approximately 20 percent. It was shown in the analysis that the use of the "hydraulic diameter", defined as proportional to the cross-sectional flow area divided by the wetted perimeter, rather than the interlayer separation per se can be used successfully to assess the effects of such unique physical characteristics.

Finally in the Task 2 program, comparison of the test results obtained from the initial evacuation of a given specimen with those obtained during subsequent evacuations shows that outgassing of water vapor exerts a very strong influence on evacuation flow characteristics. For example, approximately 1500 minutes (i.e., 25 hours) of evacuation time were required to achieve a differential pressure of 2×10^{-3} torr during the first pumpdown of Specimen No. 17A (Ref Fig. 5-37), compared to approximately 2.1 minutes required to

achieve the same differential pressure during a subsequent pumpdown. This result, which is typical for all of the specimens tested in Task 2, very dramatically emphasizes the need for adequate preconditioning to remove the adsorbed water vapor from MLI systems. Moreover, it illustrates that the original purge gas is very rapidly removed from any MLI system during evacuation, and that any gas present at later times must originate from outgassing.

7.4 TASK 3 MLI SYSTEM TESTS

In Task 3, gas evacuation and thermal performance tests were performed on a 112-shield, unperforated, double-aluminized Mylar/preconditioned silk net composite system as installed on a 1.22-m-(4-ft-) diameter tank calorimeter. The insulation was fabricated and installed as eight segmented blankets of 14 shields each. Radial thermocouple arrays were installed at five locations over the surface of the tank in order to obtain measured temperature profiles during the testing. A series of three interstitial pressure measurement plenums were installed within the blankets at the bottom of the tank in order to obtain differential pressure measurements during the tests. In addition, x-ray measurements were obtained at 22 locations over the surface of the tank before and after each series of tests, and electromechanical thickness measurement transducers were installed at 6 of these 22 locations in order to assess MLI layer density values during the tests.

During the first test series, three thermal performance tests and a rapid evacuation test were run with the total 112-shield composite system installed. Hot boundary temperatures were set at nominal values of 278°K (500°R), 319°K (575°R), and 361°K (650°R), and a cold boundary temperature of 21°K (37°R) was established using liquid hydrogen as the calorimetric fluid. Subsequently, the outer four MLI blankets were removed, and one additional thermal performance test plus a slow evacuation test were performed with the 56-shield system installed on the tank. During this thermal performance testing, the hot boundary was set at a nominal temperature value of 361°K (650°R).

LOCKHEED MISSILES & SPACE COMPANY

Early in the test program, a cold leak was encountered within the vacuum chamber plumbing system. Subsequently, the leak was repaired and the chamber was then successfully evacuated. However, it was determined that the measured heat rate into the tank during the first thermal performance test run was more than an order of magnitude higher than that predicted by the analysis. An investigation revealed that the high heat rate was caused by a thermal oscillation wich had occurred within the liquid fill line. The apparatus was then modified to eliminate the thermal oscillation, as well as to provide additional temperature measurements for use during the post-test analysis. No additional difficulties were encountered during the remainder of the Task 3 testing.

Post-test analysis of interstitial pressure measurements obtained during the Task 3 tests showed that the pressure profile across the thickness of the insulation was not uniform, as had been assumed in developing the analytical heat transfer model. For example, at a given time during the second evacuation of the ambient MLI system, prior to loading the tank with LH_2, the measured differential pressure within the third MLI blanket was approximately 20 percent higher than that obtained within the first blanket (i.e., that immediately adjacent to the tank wall). At the same time, the measured differential pressure within the seventh MLI blanket was approximately 35 percent lower than the first blanket reference value. Similar relative differential pressure values were also observed in later pumpdowns of the ambient or heated-shroud systems. Since there was no significant temperature profile imposed across the thickness of the MLI during these times, and since the variation in differential pressure across the thickness was not consistent with any slight differences in flow path length due to staggering of the butt joints for successive outer MLI blankets, it was concluded that the pressure differentials observed were most likely due to variations in layer density through the thickness. This conclusion was substantiated somewhat during the post-test analysis of X-ray thickness data.

Subsequent to evacuation of the MLI and loading of the tank for each test series conducted in Task 3, the variation in measured differential pressure values across the MLI thickness was significantly magnified. Here, the

7-12

pressure within the cold inner layers close to the tank wall was shown to
be negligible due to cryopumping of the outgassed water vapor. Outboard of
the shield location where the MLI temperatures exceeded the ice point of
$273^{\circ}K$ $(492^{\circ}R)$, interstitial pressures were found to be in the mid 10^{-5} torr
decade. From the measurements, it was determined that the pressure near the
warm outer boundary was still somewhat lower than that near mid-thickness.

Based on these results, the heat transfer model was revised to assume negligi-
ble interstitial pressure for the multilayers in-board of a point through the
thickness where the vapor pressure of ice, corresponding to the local shield
temperature, is equal to 10^{-6} torr. Outboard of this point, a constant inter-
stitial pressure value equal to the average of the measured pressure values
was assumed. The solid conduction and radiation heat transfer mechanisms
were then assumed to be continuous through the entire thickness, and total
heat transfer was evaluated by performing a heat balance between the inner
and outer layers. Results of this analysis showed excellent correlation
between the theoretical predictions and the experimentally measured values
as summarized in Table 7-1 below.

Table 7-1

SUMMARY OF TASK 3 HEAT FLUX CORRELATIONS[a]

Test Run No.	1	2	3	5
N_s	112	112	112	56
T_H, $^{\circ}K$ ($^{\circ}R$)	275.6 (496.1)	317.3 (571.1)	358.7 (645.7)	358.2 (644.8)
Q Predicted, w (Btu/hr)	0.573 (1.956)	0.758 (2.590)	1.141 (3.897)	2.036 (6.955)
Q Measured, w (Btu/hr)	0.616 (2.105)	0.738 (2.520)	1.129 (3.856)	1.945 (6.642)
Percent Deviation[b]	+7.6	-2.7	-1.1	-4.5

Notes: (a) Ref Table 6-11

(b) Percent Deviation = $100 \left(\dfrac{Q_M}{Q_P} - 1 \right)$

For example, for Test Run No. 1, the total heat rate into the tank predicted using the revised model was 0.573 w (1.956 Btu/hr). This compares to a measured heat rate of 0.616 w (2.105 Btu/hr), which exceeds the predicted value by 7.6 percent. Results obtained for the other thermal performance test runs were similar, with all of the data correlating within ± 8 percent.

A summary of MLI layer density values, obtained from analysis of Task 3 x-ray data is presented in Table 7-2.

Table 7-2

SUMMARY OF MLI LAYER DENSITY VALUES
FROM X-RAY DATA[a]

N_s	112	56
Pretest Values, layers/cm (layers/in.)	23.3 (59.1)	14.6 (37.2)
Post-Test Values[b], layers/cm (layers/in.)	19.9 (50.6)	13.5 (34.4)

Notes: (a) Ref Tables 6-6 through 6-9

(b) These post-test x-ray values used in predicting heat flux values for the Task 3 tests

Evaluation of pre-test x-ray measurements for the 112-shield system showed that as-installed average MLI layer density values ranged from approximately 15.9 layers/cm (40.5 layers/in.) on the lower dome of the tank to 31.8 layers/cm (80.8 layers in.) near the intersection of the upper dome and the cylinder. The area-weighted overall average layer density value based on pretest measurements was 23.3 layers/cm (59.1 layers/in.).

Similar x-ray measurements obtained for the 112-shield system subsequent to testing revealed that the MLI was significantly loosened and expanded due to the evacuation process. The area-weighted overall average layer density value determined from analysis of these data was 19.9 layers/cm (50.6 layers/in.).

7-14

LOCKHEED MISSILES & SPACE COMPANY

Corresponding layer density values were also assessed from the pre-test and post-test x-ray measurements obtained for the 56-shield MLI system. The area-weighted overall average values determined for these cases were 14.6 layers/cm (37.2 layers/in.) and 13.5 layers/cm (34.4 layers/in.), respectively. The substantial reduction in the measured layer density values for the 56-shield system compared to those obtained for the 112-shield system was attributed primarily to the human factors involved in fabrication and installation of the MLI. This result of the Task 3 work clearly shows the need for careful assessment of as-installed layer density values since this parameter cannot be controlled precisely within the current state-of-the-art.

Evaluation of the data obtained during evacuation and testing of the 56-shield composite system, using the electromechanical thickness transducers installed at selected locations over the tank surface, shows generally good correlation with the thickness data obtained from the post-test x-rays. For example, the average in-test reduction of layer density obtained from the electromechanical transducer measurements after repressurization of the system with dry GN_2 was approximately 10.5 percent. The corresponding reduction in average layer density, based on pre-test and post-test x-ray measurements, was 8.4 percent.

LOCKHEED MISSILES & SPACE COMPANY

Section 8

CONCLUSIONS

The conclusions which were evolved from results of the analytical and experimental studies conducted during the NAS 3-14377 contract program are as follows:

1. Interstitial pressures up to three orders of magnitude higher than those maintained within the surrounding vacuum environment can exist in composite MLI systems for relatively long times (i.e., for days or even weeks) due to continued outgassing of water vapor.

2. Outgassing of water vapor from a tank-mounted MLI system can be accelerated significantly by increasing the temperature of the MLI while exposed to a high-vacuum environment prior to loading the tank with a cryogenic fluid.

3. Interstitial gas evacuation is essentially independent of blanket position through the thickness provided adequate edge venting paths are established.

4. Pretest calculations show that a cryogenic tank should not be loaded with a cryogenic fluid before the interstitial differential pressure has been reduced to a value of approximately 2.5×10^{-3} torr or less.

5. Gas conduction heat transfer through composite MLI systems becomes significant at interstitial pressures above 10^{-6} torr.

6. The presence of interstitial water vapor and/or frost due to inadequate vacuum preconditioning was the most probable cause of the anomalous thermal performance observed during previous tests of relatively thick composite MLI systems where measured heat transfer rates were significantly higher than those predicted.

7. Perforated reflective shields offer little benefit with regard to improving the gas evacuation characteristics of an MLI system, and in fact result in degraded thermal performance due to higher radiative heat transfer.

8. Radiation heat transfer through perforated-shield MLI systems is a direct function of the percent open area, and is independent of perforation size for perforations up to 0.229-cm (0.090-in.) in diameter.

9. Use of perforated shields to improve gas evacuation characteristics of an MLI system would be necessary only where the configuation required continuous taping of butt joints between adjacent panels comprising a single MLI blanket.

10. The as-installed layer density of a relatively thick composite MLI system must be measured by tangential x-rays (or by equivalent means) at representative locations over the insulated surface in order to obtain good thermal performance predictions. Within the current state-of-the-art, adequate layer density control during installation is precluded by the non-reproducibility of available MLI materials and by human factors, even where the highest standards of workmanship and inspection are maintained.

11. Where relatively long, isolated (i.e., nonflowing) plumbing lines are maintained in direct communication with liquid hydrogen, and in particular where such lines are routed into the top of an insulated cryogen container, low-frequency, low-amplitude thermal oscillations can develop within the resulting column of highly-stratified vapor. These oscillations can be detected only by sensitive instrumentation, but can increase the gross heat transfer into the tank by an order of magnitude or more. They can be eliminated by cross-connection of the warm end of the line with the tank ullage space, or by connection of an accumulator volume in order to modify the natural frequency of the stratified column of gas.

12. Composite MLI systems which employ water-preconditioned silk net spacers provide superior reproducibility of layer density and thermal performance when compared to those using as-received silk net spacers.

13. The water-spray silk net preconditioning process is superior to complete immersion and soaking in that most of the sizing is retained. This sizing imparts both stiffness and fire-retardent properties to the netting.

14. A flat plate calorimeter using cryogens only as cold sinks and using differences in electrical heater power levels to maintain the hot and cold surfaces at specified calibration and test temperatures is an effective technique of experimentally measuring low-flux thermal performance.

15. At low layer density values, the solid conduction heat transfer through a double-aluminized Mylar/preconditioned silk net MLI system can be up to 35 percent higher than that experienced for the same composite with as-received net spacers. However, due to the improved reproducibility of the system, the effective thermal performance penalty will be much less. Moreover, at higher layer density values, the thermal performance of the preconditioned-net-spaced system will be superior to that for the system using as-received net spacers.

16. The thermal performance of tank-mounted composite MLI systems using water-preconditioned silk net or Tissuglas spacers, regardless of the number of layers, can be predicted within approximately ± 10 percent, but only if the following requirements are met:

     a. The MLI must be thoroughly vacuum-dried to remove absorbed water vapor prior to exposure to a cryogenic cold boundary temperature.

LOCKHEED MISSILES & SPACE COMPANY

b. The as-installed layer density must be carefully assessed at representative locations over the surface.

c. The total hemispherical emittance of representative reflective shield surfaces must be assessed.

d. The boundary temperatures must be precisely defined and maintained.

e. The system must be installed in multi-blanket butt-jointed segments to provide adequate gas evacuation paths. The blanket joints must be staggered and overlapped through the thickness of the MLI, and joint gaps must be adequately defined and controlled.

17. The interstitial gas pressure which will exist within an MLI system can be predicted within approximately $\pm$ 15 percent as a function of evacuation rate and time, perforation size and open area (if any), flow path length, specimen temperature, purge gas species, and layer density* using the multi-node analytical model(s) and the test data developed during this program. Predictions from 50 to 100 percent higher can be obtained using the simplified single-node model. However, since outgassing of MLI composites cannot be accurately predicted within the current state-of-the-art, prediction of interstitial pressures within the accuracy stated above requires thorough outgas preconditioning of the system by vacuum-drying at 10^{-6} torr or less until an interstitial pressure of approximately 2.5×10^{-3} torr or less is achieved. This requires vacuum pumping for approximately 240 hours at near room temperature, or for approximately 72 hours at $335^{\circ}K$ $(603^{\circ}R)$, for a typical tank-mounted MLI system.

---

*In order to achieve this degree of accuracy, the hydraulic diameter concept must be used to determine the effective layer density, since the multilayers of current insulations are not the precisely-spaced flat plates assumed in the analytical model.

LOCKHEED MISSILES & SPACE COMPANY

18. The time required to achieve an equilibrium temperature distribution through an evacuated composite MLI system is determined primarily by the thermal capacitance of the multilayer mass, and cannot be significantly shortened by initial backfilling of the system with helium in order to achieve a straight-line temperature distribution.

19. Tissuglas spacers tend to rupture and tear when subjected to a broadside gas evacuation pumping mode.

Appendix A

PURCHASE SPECIFICATIONS FOR PERFORATED OR UNPERFORATED METALLIZED MYLAR[*]

1.0 SCOPE

This specification establishes the requirements to be met by suppliers of vacuum-deposited aluminum and gold on 2.5×10^{-4}-in.- $(6.4 \times 10^{-4}$-cm-) thick Mylar (Polyethylene terephthalate) film for use in studies of cryogenic multilayer insulations. The coated material is designated as follows:

Type A: Vacuum-deposited aluminum on one side only, film crinkled
Type B: Vacuum-deposited aluminum on both sides, film smooth
Type C: Vacuum-deposited gold on both sides, film smooth

2.0 REQUIREMENTS

2.1 Materials

The film material shall be "as supplied" by the film substrate supplier. The metal and deposition conditions shall be such as to achieve the emittance values specified in Section 2.2.1.

2.2 Properties

2.2.1 Radiative Properties - Emittance of the metallized surfaces at room temperature, 530 to 550°R (294 to 306°K), shall be as given in Table A-1. Near-normal spectral reflectance measurements may be performed in lieu of emittance determination (Table A-1).

2.2.2 Adhesion - The metallized surface shall not be removed by normal handling during shipping or fabrication of the insulation assemblies.

_____

[*] Tradename, E. I. DuPont

LOCKHEED MISSILES & SPACE COMPANY

2.3 Perforations

The openings shall be of uniform size and shape and shall be uniformly spaced throughout the entire roll of material. No tears or snags shall be acceptable. The metallized surface shall be free of scratches or areas of metal coating removal. All openings shall be free of film material (slugs) and all slugs shall be removed from the roll prior to shipment.

Table A-1

METALLIZED SURFACE RADIATIVE PROPERTIES

Material Type	Emittance	Reflectance
A and B	≤0.030 average with no single measurement >0.035	5.0 to 25.0 μm, 0.975
C	≤0.020 average with no single measurement >0.025	5.0 to 25.0 μm, 0.985

3.0 TEST METHODS

3.1 Radiative Properties

Room temperature, 530 to 550°R (294 to 306°K), emittance measurements will be made with a Lion Research Corporation Model 25 Emissometer using standards supplied to the vendor by LMSC. These are a low range (ϵ = 0.030) and a mid-range (ϵ = 0.59) standard. The total hemispherical emittance of these standards has been measured by LMSC to provide correlation with the emittance as measured by the Lion Emissometer.

In order to assure that the specimen and standard are at the same temperatures and that the temperature remains constant during the measurements, both the standards and the metallized film shall be placed upon a suitable plate of high thermal mass; i.e., a ½-in.- (1.27-cm-) thick by 4-in.- (10.2-cm-) square aluminum plate. Measurements of standard and specimen shall be made with the emissometer head in the same position (horizontal, inverted).

LOCKHEED MISSILES & SPACE COMPANY

In lieu of emissometer measurements, near-normal spectral reflectance may be measured from 5.0 to 25.0 μm (Gier-Dunkle Model HC-300 heated cavity reflectometer or equivalent). Apparatus and procedures for this method shall be reviewed by LMSC before approval is granted for this method.

3.2 Adhesion

No evidence of metal surface removal shall be evident during re-rolling for packaging.

4.0 SAMPLING

All specimens taken for the optical properties measurements shall be supplied to LMSC at the time of shipment of the finished material.

4.1 Aluminized Material

Three test specimens shall be cut across the web from each end of the lot (a total of six). The specimens shall be taken 6 in. (15.2 cm) from each end of the web and at the center.

4.2 Gold-Coated Material

Specimens shall be taken across the web as per 4.1. These shall be cut at the start of the roll and at 100-ft (30.5-m) intervals along the roll to the end.

A-3

Appendix B

TABULATED GAS EVACUATION TEST RESULTS

Results of each of the Gas Evacuation tests conducted during the Task 2 program are presented in this appendix. Each tabulated page represents one particular test run, as described by the introductory data at the top. All of these data were obtained from a standard data reduction and print-out computer program adapted for this specific application.

The data presented herein were obtained from stripchart records for the early evacuation times (i.e., up to approximately 3 min.), and from hand recorded summaries thereafter.

LOCKHEED MISSILES & SPACE COMPANY

DOUBLE ALUMINIZED MYLAR/TISSUGLAS   SPECIMEN NO. 1A

EDGE EVACUATION- OFFSHELF SAMPLE
PURGE GAS= ARGON
TEMPERATURE =540. DEG R
SAMPLE DIAMETER = 27.0 INS   SAMPLE HEIGHT = .160 INS
TOTAL NUMBER OF SHIELDS = 20.0   LAYERS/INCH =119.0

| VACUUM CHAMBER PRESSURE HISTORY | | DIFFERENTIAL PRESSURE ACROSS SAMPLE | |
| TIME | PRESSURE | TIME | PRESSURE |
MIN	TORR	MIN	TORR
.1	410.000000	.1	.4400
.2	243.000000	.2	.3200
.3	153.000000	.3	.2800
.4	96.000000	.4	.2610
.5	62.000000	.5	.2460
.6	40.000000	.6	.2340
.7	25.200000	.7	.2160
.8	16.200000	.8	.2040
.9	10.500000	.9	.1890
1.0	7.000000	1.0	.1680
1.1	5.000000	1.1	.1440
1.2	3.500000	1.2	.1320
1.3	2.160000	1.3	.1290
1.4	1.440000	1.4	.1080
1.5	.960000	1.5	.0840
1.7	.290000	1.6	.0660
1.9	.117000	1.7	.0540
2.0	.078000	1.8	.0460
2.1	.054000	1.9	.0400
2.2	.039000	2.0	.0370
2.3	.028000	2.2	.0340
2.4	.021300	2.4	.0330
2.5	.016800	2.6	.0330
2.6	.013200	2.8	.0330
2.7	.010800	3.0	.0330
2.8	.009000	9.0	.0290
2.9	.007400	12.5	.0225
3.0	.006400	22.0	.0135
5.0	.001200	39.0	.0080
8.0	.000530	55.0	.0058
12.0	.000260	120.0	.0034
15.0	.000150	439.0	.0019
20.0	.000090	1428.0	.0016
42.0	.000038		
78.0	.000022		
120.0	.000012		

B-2

DOUBLE ALUMINIZED MYLAR/TISSUGLAS   SPECIMEN NO. 1A

EDGE EVACUATION-PRECONDITIONED SAMPLE
PURGE GAS- ARGON
TEMPERATURE =540. DEG R
SAMPLE DIAMETER = 27.0 INS   SAMPLE HEIGHT = .160 INS
TOTAL NUMBER OF SHIELDS = 20.0   LAYERS/INCH =119.0

| VACUUM CHAMBER PRESSURE HISTORY | | DIFFERENTIAL PRESSURE ACROSS SAMPLE | |
| TIME | PRESSURE | TIME | PRESSURE |
MIN	TORR	MIN	TORR
.1	400.000000	.1	.4500
.2	243.000000	.2	.3100
.3	159.000000	.3	.2700
.4	103.500000	.4	.2580
.5	66.000000	.5	.2460
.6	42.500000	.6	.2310
.7	27.000000	.7	.2130
.8	17.400000	.8	.2010
.9	11.400000	.9	.1860
1.0	7.500000	1.0	.1650
1.1	5.100000	1.1	.1410
1.2	3.400000	1.2	.1260
1.3	2.250000	1.3	.1260
1.4	1.440000	1.4	.1020
1.6	.450000	1.5	.0750
1.7	.290000	1.6	.0540
1.8	.183000	1.7	.0360
1.9	.120000	1.8	.0225
2.0	.081000	1.9	.0150
2.1	.052000	2.0	.0080
2.2	.042000	2.2	.0030
2.3	.031500	2.4	.0019
2.4	.024000	2.6	.0011
2.5	.019500	2.8	.0008
2.6	.016000	3.0	.0006
2.7	.013000	3.5	.0004
2.8	.011000		
2.9	.009500		
3.0	.008500		
5.7	.000200		
12.0	.000160		
23.0	.000078		
33.0	.000052		
49.0	.000038		
55.0	.000028		
70.0	.000028		
95.0	.000028		
120.0	.000024		

DOUBLE ALUMINIZED MYLAR/TISSUGLAS   SPECIMEN NO. 1A

EDGE EVACUATION-PRECONDITIONED SAMPLE
PURGE GAS- NITROGEN
TEMPERATURE =540. DEG R
SAMPLE DIAMETER = 27.0 INS   SAMPLE HEIGHT = .160 INS
TOTAL NUMBER OF SHIELDS = 20.0   LAYERS/INCH =119.0

VACUUM CHAMBER PRESSURE HISTORY		DIFFERENTIAL PRESSURE ACROSS SAMPLE	
TIME MIN	PRESSURE TORR	TIME MIN	PRESSURE TORR
.1	390.000000	.1	.3500
.2	237.000000	.2	.2600
.3	150.000000	.3	.2370
.4	99.000000	.4	.2190
.5	60.000000	.5	.2040
.6	37.000000	.6	.1890
.7	24.000000	.7	.1770
.8	15.600000	.8	.1650
.9	10.000000	.9	.1470
1.0	6.700000	1.0	.1260
1.1	4.600000	1.1	.1080
1.2	3.100000	1.2	.1080
1.3	2.000000	1.3	.1020
1.4	1.300000	1.4	.0810
1.5	.690000	1.5	.0600
1.6	.410000	1.6	.0420
1.7	.242000	1.7	.0270
1.8	.162000	1.8	.0175
1.9	.105000	1.9	.0114
2.0	.069000	2.0	.0061
2.1	.048000	2.2	.0022
2.2	.035000	2.4	.0007
2.3	.026000	2.6	.0002
2.4	.020000		
2.5	.015300		
2.6	.012000		
2.7	.009900		
2.8	.008400		
2.9	.007000		
3.0	.006000		
3.5	.003200		
4.0	.002000		
6.3	.000260		
8.0	.000140		
12.0	.000080		
23.0	.000042		
42.0	.000024		
75.0	.000018		
120.0	.000018		

DOUBLE ALUMINIZED MYLAR/TISSUGLAS   SPECIMEN NO.   1A

EDGE EVACUATION-PRECONDITIONED SAMPLE
PURGE GAS- HELIUM
TEMPERATURE =540. DEG R
SAMPLE DIAMETER = 27.0 INS   SAMPLE HEIGHT = .160 INS
TOTAL NUMBER OF SHIELDS = 20.0   LAYERS/INCH =119.0

VACUUM CHAMBER PRESSURE HISTORY		DIFFERENTIAL PRESSURE ACROSS SAMPLE	
TIME MIN	PRESSURE TORR	TIME MIN	PRESSURE TORR
.1	400.000000	.1	.2500
.2	240.000000	.2	.2220
.3	153.000000	.3	.2190
.4	96.000000	.4	.2130
.5	60.000000	.5	.2040
.6	37.000000	.6	.1890
.7	22.800000	.7	.1710
.8	14.400000	.8	.1500
.9	9.300000	.9	.1260
1.0	6.000000	1.0	.1050
1.1	4.000000	1.1	.0800
1.2	2.600000	1.2	.0710
1.3	1.650000	1.3	.0520
1.4	1.050000	1.4	.0350
1.5	.540000	1.5	.0230
1.7	.204000	1.6	.0140
1.8	.132000	1.7	.0087
1.9	.087000	1.8	.0054
2.0	.057000	1.9	.0034
2.1	.040000	2.0	.0022
2.2	.027300	2.2	.0011
2.3	.019500	2.4	.0007
2.4	.014100	2.6	.0005
2.5	.010500	2.8	.0003
2.6	.007800		
2.7	.005800		
2.8	.004300		
2.9	.003300		
3.0	.002200		
3.5	.000400		
5.0	.000300		
7.6	.000130		
10.0	.000079		
15.0	.000049		
23.0	.000034		
38.0	.000024		
61.0	.000019		
120.0	.000012		

DOUBLE ALUMINIZED MYLAR/TISSUGLAS   SPECIMEN NO. 1B

EDGE EVACUATION-PRECONDITIONED SAMPLE
PURGE GAS- ARGON
TEMPERATURE =540. DEG R
SAMPLE DIAMETER = 27.0 INS   SAMPLE HEIGHT = .137 INS
TOTAL NUMBER OF SHIELDS = 20.0   LAYERS/INCH =139.0

VACUUM CHAMBER PRESSURE HISTORY		DIFFERENTIAL PRESSURE ACROSS SAMPLE	
TIME MIN	PRESSURE TORR	TIME MIN	PRESSURE TORR
.1	410.000000	.1	.4700
.2	237.000000	.2	.3200
.3	162.000000	.3	.2820
.4	108.000000	.4	.2610
.5	68.000000	.5	.2460
.6	43.000000	.6	.2310
.7	26.400000	.7	.2160
.8	17.700000	.8	.2010
.9	11.700000	.9	.1860
1.0	7.500000	1.0	.1650
1.1	5.200000	1.1	.1410
1.2	3.500000	1.2	.1360
1.3	2.100000	1.3	.1230
1.4	1.350000	1.4	.0990
1.5	.900000	1.5	.0720
1.7	.273000	1.6	.0510
1.8	.177000	1.7	.0340
1.9	.114000	1.8	.0216
2.0	.077000	1.9	.0129
2.1	.057000	2.0	.0068
2.2	.042000	2.2	.0018
2.3	.033000	2.4	.0004
2.4	.025500		
2.5	.020700		
2.6	.017400		
2.7	.014700		
2.8	.012900		
2.9	.011250		
3.0	.010200		
5.5	.000700		
7.0	.000430		
9.0	.000300		
12.0	.000200		
17.0	.000150		
22.0	.000110		
25.0	.000090		
31.0	.000074		
36.0	.000064		
57.0	.000041		
85.0	.000032		
100.0	.000030		
120.0	.000028		

B-6

DOUBLE ALUMINIZED MYLAR/TISSUGLAS   SPECIMEN NO.   1B

EDGE EVACUATION-PRECONDITIONED SAMPLE
PURGE GAS- NITROGEN
TEMPERATURE =540. DEG R
SAMPLE DIAMETER = 27.0 INS   SAMPLE HEIGHT = .137 INS
TOTAL NUMBER OF SHIELDS = 20.0   LAYERS/INCH =139.0

VACUUM CHAMBER PRESSURE HISTORY		DIFFERENTIAL PRESSURE ACROSS SAMPLE	
TIME MIN	PRESSURE TORR	TIME MIN	PRESSURE TORR
.1	390.000000	.1	.4200
.2	237.000000	.2	.2900
.3	153.000000	.3	.2550
.4	99.000000	.4	.2310
.5	60.000000	.5	.2160
.6	38.000000	.6	.2010
.7	24.500000	.7	.1890
.8	15.900000	.8	.1770
.9	9.900000	.9	.1560
1.0	6.800000	1.0	.1350
1.1	4.700000	1.1	.1110
1.2	3.200000	1.2	.1140
1.3	2.040000	1.3	.1050
1.4	1.210000	1.4	.0850
1.5	.870000	1.5	.0630
1.7	.252000	1.6	.0450
1.8	.165000	1.7	.0320
1.9	.105000	1.8	.0216
2.0	.070000	1.9	.0150
2.1	.049000	2.0	.0102
2.2	.035000	2.2	.0057
2.3	.026500	2.4	.0042
2.0	.020100	2.6	.0035
2.5	.015900	2.8	.0031
2.6	.012900	3.0	.0030
2.7	.010500	3.5	.0028
2.8	.009000		
2.9	.007700		
3.0	.006700		
6.3	.000300		
8.3	.000160		
10.0	.000120		
14.0	.000094		
18.0	.000072		
22.0	.000060		
26.0	.000051		
36.0	.006040		
45.0	.000036		
60.0	.000030		
90.0	.000026		
120.0	.000024		

DOUBLE ALUMINIZED MYLAR/TISSUGLAS   SPECIMEN NO. 1B

EDGE EVACUATION-PRECONDITIONED SAMPLE
PURGE GAS- HELIUM
TEMPERATURE =540. DEG R
SAMPLE DIAMETER = 27.0 INS   SAMPLE HEIGHT = .137 INS
TOTAL NUMBER OF SHIELDS = 20.0   LAYERS/INCH =139.0

VACUUM CHAMBER PRESSURE HISTORY		DIFFERENTIAL PRESSURE ACROSS SAMPLE	
TIME MIN	PRESSURE TORR	TIME MIN	PRESSURE TORR
.1	430.000000	.1	.2600
.2	260.000000	.2	.2280
.3	162.000000	.3	.2250
.4	162.000000	.4	.2160
.5	64.000000	.5	.2070
.6	41.000000	.6	.1950
.7	25.500000	.7	.1770
.8	15.900000	.8	.1560
.9	10.200000	.9	.1290
1.0	6.500000	1.0	.1050
1.1	4.300000	1.1	.0870
1.2	2.900000	1.2	.0710
1.3	1.800000	1.3	.0530
1.4	1.020000	1.4	.0360
1.5	.580000	1.5	.0240
1.6	.340000	1.6	.0150
1.7	.222000	1.7	.0093
1.8	.141000	1.8	.0058
1.9	.093000	1.9	.0036
2.0	.061000	2.0	.0024
2.1	.042000	2.2	.0012
2.2	.031000	2.4	.0007
2.3	.021300	2.6	.0006
2.4	.015600	2.8	.0005
2.5	.011700	3.0	.0005
2.6	.009000		
2.7	.007000		
2.8	.005400		
2.9	.004300		
3.0	.003600		
6.0	.000500		
8.0	.000130		
11.0	.000080		
17.0	.000061		
25.0	.000046		
31.0	.000039		
43.0	.000033		
60.0	.000028		
90.0	.000024		
120.0	.000024		

DOUBLE ALUMINIZED MYLAR/TISSUGLAS   SPECIMEN NO.   IC

EDGE EVACUATION-PRECONDITIONED SAMPLE
PURGE GAS- ARGON
TEMPERATURE =540. DEG R
SAMPLE DIAMETER = 27.0 INS   SAMPLE HEIGHT = .090 INS
TOTAL NUMBER OF SHIELDS = 20.0   LAYERS/INCH =211.0

VACUUM CHAMBER PRESSURE HISTORY		DIFFERENTIAL PRESSURE ACROSS SAMPLE	
TIME MIN	PRESSURE TORR	TIME MIN	PRESSURE TORR
.1	400.000000	.1	.4900
.2	246.000000	.2	.3200
.3	159.000000	.3	.2790
.4	102.000000	.4	.2550
.5	65.000000	.5	.2370
.6	43.000000	.6	.2280
.7	27.000000	.7	.2130
.8	17.700000	.8	.2010
.9	11.400000	.9	.1860
1.0	7.400000	1.0	.1650
1.1	5.100000	1.1	.1440
1.2	3.500000	1.2	.1350
1.3	2.250000	1.3	.1290
1.4	1.440000	1.4	.1080
1.5	.960000	1.5	.0850
1.6	.650000	1.6	.0620
1.8	.190000	1.7	.0430
2.0	.084000	1.8	.0300
2.1	.058000	1.9	.0200
2.2	.043000	2.0	.0135
2.3	.032000	2.2	.0065
2.4	.024900	2.4	.0039
2.5	.020100	2.6	.0027
2.6	.016500	2.8	.0023
2.7	.013800	3.0	.0020
2.8	.011700	3.5	.0019
2.9	.010200		
3.0	.009000		
3.5	.005600		
4.0	.004100		
7.0	.000350		
9.0	.000210		
15.0	.000110		
20.0	.000091		
31.0	.000064		
48.0	.000050		
120.0	.000036		

DOUBLE ALUMINIZED MYLAR/TISSUGLAS   SPECIMEN NO. 1C

EDGE EVACUATION-PRECONDITIONED SAMPLE
PURGE GAS- NITROGEN
TEMPERATURE =540. DEG R
SAMPLE DIAMETER = 27.0 INS   SAMPLE HEIGHT = .090 INS
TOTAL NUMBER OF SHIELDS = 20.0   LAYERS/INCH =211.0

VACUUM CHAMBER PRESSURE HISTORY		DIFFERENTIAL PRESSURE ACROSS SAMPLE	
TIME MIN	PRESSURE TORR	TIME MIN	PRESSURE TORR
.1	380.000000	.1	.4200
.2	230.000000	.2	.2730
.3	147.000000	.3	.2310
.4	93.000000	.4	.2070
.5	58.000000	.5	.1950
.6	37.000000	.6	.1830
.7	23.400000	.7	.1710
.8	15.600000	.8	.1590
.9	9.900000	.9	.1440
1.0	6.600000	1.0	.1260
1.1	4.600000	1.1	.1080
1.2	3.100000	1.2	.1080
1.3	1.980000	1.3	.1020
1.5	.640000	1.4	.0840
1.6	.390000	1.5	.0660
1.7	.246000	1.6	.0470
1.8	.159000	1.7	.0330
1.9	.102000	1.8	.0216
2.0	.068000	1.9	.0141
2.1	.048000	2.0	.0090
2.2	.035000	2.1	.0058
2.3	.026100	2.2	.0039
2.4	.020100	2.3	.0028
2.5	.015900	2.4	.0019
2.6	.013800	2.6	.0012
2.7	.011100	2.8	.0007
2.8	.009300	3.0	.0006
2.9	.008100	3.5	.0005
3.0	.007100		
3.5	.004400		
4.0	.003400		

DOUBLE ALUMINIZED MYLAR/TISSUGLAS   SPECIMEN NO. IC

EDGE EVACUATION-PRECONDITIONED SAMPLE
PURGE GAS- HELIUM
TEMPERATURE =540. DEG R
SAMPLE DIAMETER = 27.0 INS   SAMPLE HEIGHT = .090 INS
TOTAL NUMBER OF SHIELDS = 20.0   LAYERS/INCH =211.0

VACUUM CHAMBER PRESSURE HISTORY		DIFFERENTIAL PRESSURE ACROSS SAMPLE	
TIME MIN	PRESSURE TORR	TIME MIN	PRESSURE TORR
.1	415.000000	.1	.2300
.2	260.000000	.2	.2070
.3	156.000000	.3	.2010
.4	99.000000	.4	.1980
.5	61.000000	.5	.1890
.6	38.000000	.6	.1800
.7	23.700000	.7	.1620
.8	15.000000	.8	.1410
.9	9.600000	.9	.1230
1.0	6.100000	1.0	.0990
1.1	4.100000	1.1	.0770
1.2	2.670000	1.2	.0720
1.3	1.650000	1.3	.0540
1.4	1.050000	1.4	.0370
1.5	.540000	1.5	.0250
1.6	.310000	1.6	.0160
1.7	.201000	1.7	.0096
1.8	.129000	1.8	.0063
1.9	.084000	1.9	.0043
2.0	.056000	2.0	.0032
2.1	.039000	2.2	.0019
2.2	.027300	2.4	.0015
2.3	.019800	2.6	.0012
2.4	.014400	2.8	.0010
2.5	.010800		
2.6	.008100		
2.7	.006300		
2.8	.004900		
2.9	.003850		
3.0	.003100		
3.5	.001100		
5.0	.000300		
7.0	.000120		
11.0	.000080		
20.0	.000041		
46.0	.000031		
60.0	.000031		
90.0	.000031		
90.0	.000029		
120.0	.000027		

DOUBLE ALUMINIZED MYLAR/TISSUGLAS   SPECIMEN NO.   2

EDGE EVACUATION- OFFSHELF SAMPLE
PURGE GAS- NITROGEN
TEMPERATURE =540. DEG R
SAMPLE DIAMETER = 20.0 INS   SAMPLE HEIGHT = .137 INS
TOTAL NUMBER OF SHIELDS = 20.0   LAYERS/INCH =139.0

VACUUM CHAMBER PRESSURE HISTORY		DIFFERENTIAL PRESSURE ACROSS SAMPLE	
TIME MIN	PRESSURE TORR	TIME MIN	PRESSURE TORR
.1	400.000000	.1	.2450
.2	250.000000	.2	.1890
.3	150.000000	.3	.1620
.4	99.000000	.4	.1560
.5	62.000000	.5	.1440
.6	40.000000	.6	.1350
.7	24.900000	.7	.1290
.8	16.500000	.8	.1230
.9	10.800000	.9	.1110
1.0	7.100000	1.0	.0990
1.1	4.900000	1.2	.0900
1.2	3.400000	2.2	.2910
1.3	2.220000	2.4	.2610
1.4	1.530000	2.6	.2340
1.5	.720000	2.8	.2130
1.6	.450000	3.0	.1950
1.7	.294000	4.0	.1350
1.8	.210000	4.5	.1080
1.9	.156000	10.5	.0430
2.0	.120000	16.5	.0240
2.1	.096000	22.5	.0156
2.2	.080000	28.5	.0114
2.3	.069000	54.5	.0082
2.4	.062000	67.0	.0035
2.5	.056000	91.0	.0025
2.6	.051000	120.0	.0019
2.7	.047500		
2.8	.044000		
2.9	.042000		
3.0	.040000		
8.0	.001300		
10.0	.001000		
13.0	.000800		
21.0	.000500		
27.0	.000360		
35.0	.000270		
67.0	.000120		
90.0	.000090		
120.0	.000080		

DOUBLE ALUMINIZED MYLAR/TISSUGLAS   SPECIMEN NO.   2

EDGE EVACUATION-PRECONDITIONED SAMPLE
PURGE GAS- NITROGEN
TEMPERATURE =540. DEG R
SAMPLE DIAMETER = 20.0 INS   SAMPLE HEIGHT = .137 INS
TOTAL NUMBER OF SHIELDS = 20.0   LAYERS/INCH =139.0

VACUUM CHAMBER PRESSURE HISTORY		DIFFERENTIAL PRESSURE ACROSS SAMPLE	
TIME	PRESSURE	TIME	PRESSURE
MIN	TORR	MIN	TORR
.1	420.000000	.1	.2400
.2	250.000000	.2	.1860
.3	159.000000	.3	.1620
.4	102.000000	.4	.1530
.5	64.000000	.5	.1410
.6	40.000000	.6	.1320
.7	25.800000	.7	.1260
.8	16.800000	.8	.1170
.9	10.800000	.9	.1050
1.0	7.100000	1.0	.0930
1.1	4.800000	1.1	.0760
1.2	3.300000	1.2	.0755
1.3	2.100000	1.3	.0700
1.5	.690000	1.4	.0550
1.6	.420000	1.5	.0400
1.7	.270000	1.6	.0290
1.8	.168000	1.7	.0198
1.9	.108000	1.8	.0138
2.0	.072000	1.9	.0090
2.1	.051000	2.0	.0060
2.2	.037000	2.2	.0032
2.3	.028000	2.4	.0022
2.4	.022000	2.6	.0017
2.5	.017400	2.8	.0016
2.6	.014100	3.0	.0015
2.7	.012000	4.0	.0014
2.8	.010200		
2.9	.009000		
3.0	.007700		
5.0	.000360		
7.0	.000180		
11.0	.000120		
19.0	.000088		
28.0	.000071		
43.0	.000060		
81.0	.000050		
96.0	.000044		
120.0	.000041		

DOUBLE ALUMINIZED MYLAR/TISSUGLAS   SPECIMEN NO.   3

EDGE EVACUATION- OFFSHELF SAMPLE
PURGE GAS- NITROGEN
TEMPERATURE =540. DEG R
SAMPLE DIAMETER = 15.0 INS   SAMPLE HEIGHT = .137 INS
TOTAL NUMBER OF SHIELDS = 20.0   LAYERS/INCH =139.0

VACUUM CHAMBER PRESSURE HISTORY		DIFFERENTIAL PRESSURE ACROSS SAMPLE	
TIME MIN	PRESSURE TORR	TIME MIN	PRESSURE TORR
.1	410.000000	.1	.1250
.2	250.000000	.2	.0990
.3	150.000000	.3	.0910
.4	97.000000	.4	.0870
.5	63.000000	.5	.0830
.6	39.000000	.6	.0790
.7	26.000000	.7	.0740
.8	16.200000	.8	.0680
.9	10.800000	.9	.0615
1.0	7.000000	1.0	.0540
1.1	4.900000	1.1	.0475
1.2	3.300000	1.2	.0490
1.3	2.100000	1.3	.0490
1.5	.700000	1.4	.0460
1.6	.440000	1.5	.0440
1.7	.270000	1.6	.0440
1.8	.180000	1.7	.0470
1.9	.123000	1.8	.0510
2.0	.090000	1.9	.0560
2.1	.066000	2.0	.0610
2.2	.052000	2.2	.0660
2.3	.043000	2.4	.0660
2.4	.037000	2.6	.0640
2.5	.032500	2.8	.0610
2.6	.028800	3.0	.0570
6.0	.013800	4.0	.0430
9.0	.010950	4.5	.0380
12.0	.009500	6.0	.0282
16.0	.000900	12.0	.0129
24.0	.000520	35.0	.0043
36.0	.000360	76.0	.0019
59.0	.000230	120.0	.0013
76.0	.000190		
105.0	.000160		

DOUBLE ALUMINIZED MYLAR/TISSUGLAS   SPECIMEN NO.   3

EDGE EVACUATION-PRECONDITIONED SAMPLE
PURGE GAS- NITROGEN
TEMPERATURE =540. DEG R
SAMPLE DIAMETER = 15.0 INS   SAMPLE HEIGHT = .137 INS
TOTAL NUMBER OF SHIELDS = 20.0   LAYERS/INCH =139.0

VACUUM CHAMBER PRESSURE HISTORY		DIFFERENTIAL PRESSURE ACROSS SAMPLE	
TIME MIN	PRESSURE TORR	TIME MIN	PRESSURE TORR
.1	400.000000	.1	.1300
.2	240.000000	.2	.1020
.3	150.000000	.3	.0930
.4	99.000000	.4	.0880
.5	63.000000	.5	.0850
.6	39.500000	.6	.0805
.7	25.200000	.7	.0760
.8	15.600000	.8	.0695
.9	10.200000	.9	.0610
1.0	6.900000	1.0	.0530
1.1	4.700000	1.1	.0440
1.2	3.200000	1.2	.0440
1.3	2.040000	1.3	.0410
1.5	.680000	1.4	.0330
1.6	.420000	1.5	.0250
1.7	.255000	1.6	.0180
1.8	.165000	1.7	.0117
1.9	.105000	1.8	.0078
2.0	.072000	1.9	.0049
2.1	.051000	2.0	.0032
2.2	.036500	2.2	.0014
2.3	.026700	2.4	.0006
2.4	.021000	2.6	.0003
2.5	.016800	2.8	.0001
2.6	.013500	3.0	.0000
2.7	.011400		
2.8	.009600		
2.9	.008300		
3.0	.007300		
4.0	.003400		
6.0	.004000		
8.0	.001600		
10.0	.000140		
14.0	.000100		
20.0	.000090		
30.0	.000088		
63.0	.000070		
120.0	.000060		

DOUBLE ALUMINIZED MYLAR/TISSUGLAS   SPECIMEN NO. 4

EDGE EVACUATION- OFFSHELF SAMPLE
PURGE GAS- HELIUM
TEMPERATURE =540. DEG R
SAMPLE DIAMETER = 27.0 INS   SAMPLE HEIGHT = .548 INS
TOTAL NUMBER OF SHIELDS = 80.0   LAYERS/INCH =144.0

VACUUM CHAMBER PRESSURE HISTORY		DIFFERENTIAL PRESSURE ACROSS SAMPLE	
TIME MIN	PRESSURE TORR	TIME MIN	PRESSURE TORR
.1	410.000000	.1	.5900
.2	255.000000	.2	.5300
.3	162.000000	.3	.5000
.4	102.000000	.4	.4700
.5	62.000000	.5	.4500
.6	38.000000	.6	.4100
.7	24.000000	.7	.3600
.8	15.600000	.8	.3100
.9	9.900000	.9	.2610
1.0	6.500000	1.0	.2220
1.1	4.200000	1.1	.2010
1.2	2.700000	1.2	.1920
1.3	1.770000	1.3	.1875
1.4	.960000	1.4	.1860
1.5	.590000	1.5	.1900
1.6	.380000	1.6	.1950
1.7	.250000	1.7	.1980
1.8	.183000	1.8	.2010
1.9	.138000	1.9	.2010
2.0	.108000	2.0	.2010
2.1	.090000	2.2	.1980
2.2	.078000	2.4	.1920
2.3	.071000	2.6	.1860
2.4	.065000	2.8	.1860
2.5	.062000	3.0	.1620
2.6	.058000	4.0	.1530
2.7	.056000	8.6	.0810
2.8	.055000	14.6	.0750
2.9	.054000	26.6	.0390
3.0	.052500	40.0	.0249
5.0	.003800	68.6	.0138
15.0	.003400	98.6	.0093
21.0	.002000	128.6	.0070
37.0	.001100	158.6	.0058
47.0	.000900	188.6	.0049
115.0	.004600	1133.0	.0014
209.0	.000260		
1134.0	.000059		

DOUBLE ALUMINIZED MYLAR/TISSUGLAS   SPECIMEN NO. 4

EDGE EVACUATION-PRECONDITIONED SAMPLE
PURGE GAS- HELIUM
TEMPERATURE =540. DEG R
SAMPLE DIAMETER = 27.0 INS   SAMPLE HEIGHT = .548 INS
TOTAL NUMBER OF SHIELDS = 80.0   LAYERS/INCH =144.0

VACUUM CHAMBER PRESSURE HISTORY .		DIFFERENTIAL PRESSURE ACROSS SAMPLE	
TIME MIN	PRESSURE TORR	TIME MIN	PRESSURE TORR
.1	410.000000	.1	.5900
.2	255.000000	.2	.5200
.3	165.000000	.3	.5000
.4	102.000000	.4	.4700
.5	63.000000	.5	.4400
.6	39.000000	.6	.4100
.7	24.300000	.7	.3600
.8	15.900000	.8	.3000
.9	10.200000	.9	.2400
1.0	6.400000	1.0	.1830
1.1	4.200000	1.1	.1410
1.2	2.800000	1.2	.1080
1.3	1.770000	1.3	.0810
1.4	.960000	1.4	.0510
1.5	.550000	1.5	.0320
1.6	.350000	1.6	.0192
1.7	.220000	1.7	.0111
1.8	.140000	1.8	.0069
1.9	.096000	1.9	.0041
2.0	.061000	2.0	.0028
2.1	.043000	2.2	.0145
2.2	.031000	2.4	.0009
2.3	.021900	2.6	.0006
2.4	.016200	2.8	.0005
2.5	.012000	3.0	.0004
2.6	.009300	4.0	.0004
2.7	.007300	8.0	.0003
2.8	.005800		
2.9	.004600		
3.0	.003800		
5.0	.000240		
10.0	.000110		
20.0	.000086		
34.0	.000079		
45.0	.000074		
63.0	.000073		
83.0	.000069		
94.0	.000070		
120.0	.000069		

DOUBLE ALUMINIZED MYLAR/TISSUGLAS   SPECIMEN NO.   4

EDGE EVACUATION-PRECONDITIONED SAMPLE
PURGE GAS- HELIUM
TEMPERATURE =230. DEG R
SAMPLE DIAMETER = 27.0 INS   SAMPLE HEIGHT = .548 INS
TOTAL NUMBER OF SHIELDS = 80.0   LAYERS/INCH =144.0

VACUUM CHAMBER PRESSURE HISTORY		DIFFERENTIAL PRESSURE ACROSS SAMPLE	
TIME MIN	PRESSURE TORR	TIME MIN	PRESSURE TORR
.1	430.000000	.1	.1650
.2	290.000000	.2	.1560
.3	192.000000	.3	.1470
.4	132.000000	.4	.1410
.5	90.000000	.5	.1330
.6	59.000000	.6	.1290
.7	41.000000	.7	.1200
.8	28.000000	.8	.1140
.9	18.900000	.9	.1050
1.0	13.500000	1.0	.0945
1.1	9.750000	1.1	.0860
1.2	6.900000	1.2	.0750
1.3	4.800000	1.3	.0665
1.4	3.500000	1.4	.0550
1.5	2.490000	1.5	.0530
1.6	1.680000	1.6	.0400
1.7	1.200000	1.7	.0300
1.8	.870000	1.8	.0213
1.9	.630000	1.9	.0147
2.0	.495000	2.0	.0102
2.2	.330000	2.2	.0057
2.4	.255000	2.4	.0034
2.6	.052000	2.6	.0017
2.8	.025200	2.8	.0007
3.0	.015000	3.0	.0002
3.5	.006300		
4.0	.003500		

DOUBLE ALUMINIZED MYLAR/TISSUGLAS   SPECIMEN NO.   4

EDGE EVACUATION-PRECONDITIONED SAMPLE
PURGE GAS- HELIUM
TEMPERATURE =230. DEG R
SAMPLE DIAMETER = 27.0 INS   SAMPLE HEIGHT = .548 INS
TOTAL NUMBER OF SHIELDS = 80.0   LAYERS/INCH =144.0

VACUUM CHAMBER PRESSURE HISTORY .		DIFFERENTIAL PRESSURE ACROSS SAMPLE	
TIME MIN	PRESSURE TORR	TIME MIN	PRESSURE TORR
.1	460.000000	.1	.1500
.2	320.000000	.2	.1320
.3	219.000000	.3	.1275
.4	159.000000	.4	.1200
.5	111.000000	.5	.1140
.6	81.000000	.6	.1080
.7	54.000000	.7	.0990
.8	38.000000	.8	.0930
.9	28.000000	.9	.0900
1.0	20.500000	1.0	.0830
1.1	14.400000	1.1	.0750
1.2	10.800000	1.2	.0670
1.3	7.800000	1.3	.0580
1.4	6.200000	1.4	.0460
1.5	4.900000	1.5	.0430
1.6	3.750000	1.6	.0445
1.7	2.900000	1.7	.0455
1.8	2.100000	1.8	.0410
1.9	16.500000	1.9	.0340
2.0	1.050000	2.0	.0270
2.2	.640000	2.1	.0150
2.4	.440000	2.2	.0072
2.6	.320000	2.3	.0032
2.8	.258000	2.4	.0014
3.0	.222000	2.5	.0004
3.5	.174000		
4.0	.147000		
5.0	.102000		
8.0	.003000		
11.0	.001000		
14.0	.000760		
16.0	.000120		
21.0	.000090		
36.0	.000089		
81.0	.000085		
91.0	.000086		

DOUBLE ALUMINIZED MYLAR/TISSUGLAS   SPECIMEN NO.   4

EDGE EVACUATION-PRECONDITIONED SAMPLE
PURGE GAS- HELIUM
TEMPERATURE =230. DEG R
SAMPLE DIAMETER = 27.0 INS   SAMPLE HEIGHT = .548 INS
TOTAL NUMBER OF SHIELDS = 80.0   LAYERS/INCH =144.0

VACUUM CHAMBER PRESSURE HISTORY		DIFFERENTIAL PRESSURE ACROSS SAMPLE	
TIME MIN	PRESSURE TORR	TIME MIN	PRESSURE TORR
.1	470.000000	.1	.1400
.2	330.000000	.2	.1320
.3	225.000000	.3	.1260
.4	156.000000	.4	.1230
.5	114.000000	.5	.1140
.6	80.000000	.6	.1050
.7	59.000000	.7	.0930
.8	43.000000	.8	.0820
.9	34.000000	.9	.0680
1.0	28.000000	1.0	.0540
1.1	22.800000	1.1	.0370
1.2	19.500000	1.2	.0210
1.3	17.400000	1.3	.0070
1.4	16.200000		
1.5	15.000000		
1.6	14.400000		
1.7	13.800000		
1.8	13.500000		
1.9	13.200000		
2.0	12.900000		
2.2	12.750000		
2.4	12.500000		
2.6	12.300000		
2.8	12.100000		
3.0	12.000000		

DOUBLE ALUMINIZED MYLAR/TISSUGLAS   SPECIMEN NO. 4A

EDGE EVACUATION- OFFSHELF SAMPLE
PURGE GAS- HELIUM
TEMPERATURE =540. DEG R
SAMPLE DIAMETER = 27.0 INS   SAMPLE HEIGHT = .548 INS
TOTAL NUMBER OF SHIELDS = 80.0   LAYERS/INCH =144.0

VACUUM CHAMBER PRESSURE HISTORY		DIFFERENTIAL PRESSURE ACROSS SAMPLE	
TIME MIN	PRESSURE TORR	TIME MIN	PRESSURE TORR
.1	410.000000	.1	.5900
.2	255.000000	.2	.5300
.3	162.000000	.3	.5000
.4	102.000000	.4	.4700
.5	62.000000	.5	.4500
.6	38.000000	.6	.4100
.7	24.000000	.7	.3600
.8	15.600000	.8	.3100
.9	9.900000	.9	.2610
1.0	6.500000	1.0	.2220
1.1	4.200000	1.1	.2010
1.2	2.700000	1.2	.1920
1.3	1.770000	1.3	.1875
1.4	.960000	1.4	.1860
1.5	.590000	1.5	.1900
1.6	.380000	1.6	.1950
1.7	.250000	1.7	.1980
1.8	.183000	1.8	.2010
1.9	.138000	1.9	.2010
2.0	.108000	2.0	.2010
2.1	.090000	2.2	.1980
2.2	.078000	2.4	.1920
2.3	.071000	2.6	.1860
2.4	.065000	2.8	.1860
2.5	.062000	3.0	.1620
2.6	.058000	4.0	.1530
2.7	.056000	8.6	.0810
2.8	.055000	14.6	.0750
2.9	.054000	26.6	.0390
3.0	.052500	40.0	.0249
5.0	.003800	68.6	.0138
15.0	.003400	98.6	.0093
21.0	.002000	128.6	.0070
37.0	.001100	158.6	.0058
47.0	.000900	188.6	.0049
115.0	.004600	1133.0	.0014
209.0	.000260		
1134.0	.000059		

DOUBLE ALUMINIZED MYLAR/TISSUGLAS   SPECIMEN NO. 4A

EDGE EVACUATION-PRECONDITIONED SAMPLE
PURGE GAS- HELIUM
TEMPERATURE =540. DEG P
SAMPLE DIAMETER = 27.0 INS   SAMPLE HEIGHT = .548 INS
TOTAL NUMBER OF SHIELDS = 80.0   LAYERS/INCH =144.0

VACUUM CHAMBER PRESSURE HISTORY		DIFFERENTIAL PRESSURE ACROSS SAMPLE	
TIME	PRESSURE	TIME	PRESSURE
MIN	TORR	MIN	TORR
.1	410.000000	.1	.5900
.2	255.000000	.2	.5200
.3	165.000000	.3	.5000
.4	102.000000	.4	.4700
.5	63.000000	.5	.4400
.6	39.000000	.6	.4100
.7	24.300000	.7	.3600
.8	15.900000	.8	.3000
.9	10.200000	.9	.2400
1.0	6.400000	1.0	.1830
1.1	4.200000	1.1	.1410
1.2	2.800000	1.2	.1080
1.3	1.770000	1.3	.0810
1.4	.960000	1.4	.0510
1.5	.550000	1.5	.0320
1.6	.350000	1.6	.0192
1.7	.220000	1.7	.0111
1.8	.140000	1.8	.0069
1.9	.096000	1.9	.0041
2.0	.061000	2.0	.0028
2.1	.043000	2.2	.0145
2.2	.031000	2.4	.0009
2.3	.021900	2.6	.0006
2.4	.016200	2.8	.0005
2.5	.012000	3.0	.0004
2.6	.009300	4.0	.0004
2.7	.007300	8.0	.0003
2.8	.005800		
2.9	.004600		
3.0	.003800		
5.0	.000240		
10.0	.000110		
20.0	.000086		
34.0	.000079		
45.0	.000074		
63.0	.000073		
83.0	.000069		
94.0	.000070		
120.0	.000069		

DOUBLE ALUMINIZED MYLAR/TISSUGLAS   SPECIMEN NO. 4B

EDGE EVACUATION-PRECONDITIONED SAMPLE
PURGE GAS- HELIUM
TEMPERATURE =230. DEG R
SAMPLE DIAMETER = 27.0 INS   SAMPLE HEIGHT = .548 INS
TOTAL NUMBER OF SHIELDS = 80.0   LAYERS/INCH =144.0

VACUUM CHAMBER PRESSURE HISTORY		DIFFERENTIAL PRESSURE ACROSS SAMPLE	
TIME MIN	PRESSURE TORR	TIME MIN	PRESSURE TORR
.1	430.000000	.1	.1650
.2	290.000000	.2	.1560
.3	192.000000	.3	.1470
.4	132.000000	.4	.1410
.5	90.000000	.5	.1330
.6	59.000000	.6	.1290
.7	41.000000	.7	.1200
.8	28.000000	.8	.1140
.9	18.900000	.9	.1050
1.0	13.500000	1.0	.0945
1.1	9.750000	1.1	.0860
1.2	6.900000	1.2	.0750
1.3	4.800000	1.3	.0665
1.4	3.500000	1.4	.0550
1.5	2.490000	1.5	.0530
1.6	1.680000	1.6	.0400
1.7	1.200000	1.7	.0300
1.8	.870000	1.8	.0213
1.9	.630000	1.9	.0147
2.0	.495000	2.0	.0102
2.2	.330000	2.2	.0057
2.4	.255000	2.4	.0034
2.6	.052000	2.6	.0017
2.8	.025200	2.8	.0007
3.0	.015000	3.0	.0002
3.5	.006300		
4.0	.003500		

DOUBLE ALUMINIZED MYLAR/TISSUGLAS   SPECIMEN NO. 4B

EDGE EVACUATION-PRECONDITIONED SAMPLE
PURGE GAS- HELIUM
TEMPERATURE =230. DEG R
SAMPLE DIAMETER = 27.0 INS   SAMPLE HEIGHT = .548 INS
TOTAL NUMBER OF SHIELDS = 80.0   LAYERS/INCH =144.0

| VACUUM CHAMBER PRESSURE HISTORY | | DIFFERENTIAL PRESSURE ACROSS SAMPLE | |
TIME MIN	PRESSURE TORR	TIME MIN	PRESSURE TORR
.1	460.000000	.1	.1300
.2	330.000000	.2	.1200
.3	234.000000	.3	.1140
.4	168.000000	.4	.1110
.5	117.000000	.5	.1080
.6	81.000000	.6	.1050
.7	57.000000	.7	.1020
.8	41.000000	.8	.0960
.9	29.000000	.9	.0900
1.0	20.400000	1.0	.0870
1.1	14.700000	1.1	.0780
1.2	10.800000	1.2	.0690
1.3	8.100000	1.3	.0610
1.4	6.000000	1.4	.0540
1.5	4.500000	1.5	.0430
1.6	3.300000	1.6	.0480
1.7	2.300000	1.7	.0440
1.8	1.740000	1.8	.0380
1.9	1.080000	1.9	.0310
2.0	.750000	2.0	.0250
2.2	.380000	2.2	.0138
2.4	.200000	2.4	.0072
2.6	.113000	2.6	.0041
2.8	.074000	2.8	.0028
3.0	.052000	3.0	.0020
3.5	.003400		
5.5	.003500		
8.0	.002400		
11.0	.001500		
14.0	.001100		
20.0	.000450		
26.0	.000240		
29.0	.000160		
34.0	.000080		

DOUBLE ALUMINIZED MYLAR/TISSUGLAS   SPECIMEN NO. 4B

EDGE EVACUATION-PRECONDITIONED SAMPLE
PURGE GAS- HELIUM
TEMPERATURE =230. DEG R
SAMPLE DIAMETER = 27.0 INS   SAMPLE HEIGHT = .548 INS
TOTAL NUMBER OF SHIELDS = 80.0   LAYERS/INCH =144.0

VACUUM CHAMBER PRESSURE HISTORY		DIFFERENTIAL PRESSURE ACROSS SAMPLE	
TIME MIN	PRESSURE TORR	TIME MIN	PRESSURE TORR
.1	460.000000	.1	.1500
.2	320.000000	.2	.1320
.3	219.000000	.3	.1275
.4	159.000000	.4	.1200
.5	111.000000	.5	.1140
.6	81.000000	.6	.1080
.7	54.000000	.7	.0990
.8	38.000000	.8	.0930
.9	28.000000	.9	.0900
1.0	20.500000	1.0	.0830
1.1	14.400000	1.1	.0750
1.2	10.800000	1.2	.0670
1.3	7.800000	1.3	.0580
1.4	6.200000	1.4	.0460
1.5	4.900000	1.5	.0430
1.6	3.750000	1.6	.0445
1.7	2.900000	1.7	.0455
1.8	2.100000	1.8	.0410
1.9	16.500000	1.9	.0340
2.0	1.050000	2.0	.0270
2.2	.640000	2.1	.0150
2.4	.440000	2.2	.0072
2.6	.320000	2.3	.0032
2.8	.258000	2.4	.0014
3.0	.222000	2.5	.0004
3.5	.174000		
4.0	.147000		
5.0	.102000		
8.0	.003000		
11.0	.001000		
14.0	.000760		
16.0	.000120		
21.0	.000090		
36.0	.000089		
81.0	.000085		
91.0	.000086		

DOUBLE ALUMINIZED MYLAR/TISSUGLAS   SPECIMEN NO. 4B

EDGE EVACUATION-PRECONDITIONED SAMPLE
PURGE GAS- HELIUM
TEMPERATURE =230. DEG R
SAMPLE DIAMETER = 27.0 INS   SAMPLE HEIGHT = .548 INS
TOTAL NUMBER OF SHIELDS = 80.0   LAYERS/INCH =144.0

VACUUM CHAMBER PRESSURE HISTORY		DIFFERENTIAL PRESSURE ACROSS SAMPLE	
TIME MIN	PRESSURE TORR	TIME MIN	PRESSURE TORR
.1	470.000000	.1	.1400
.2	330.000000	.2	.1320
.3	225.000000	.3	.1260
.4	156.000000	.4	.1230
.5	114.000000	.5	.1140
.6	80.000000	.6	.1050
.7	59.000000	.7	.0930
.8	43.000000	.8	.0820
.9	34.000000	.9	.0680
1.0	28.000000	1.0	.0540
1.1	22.800000	1.1	.0370
1.2	19.500000	1.2	.0210
1.3	17.400000	1.3	.0070
1.4	16.200000		
1.5	15.000000		
1.6	14.400000		
1.7	13.800000		
1.8	13.500000		
1.9	13.200000		
2.0	12.900000		
2.2	12.750000		
2.4	12.500000		
2.6	12.300000		
2.8	12.100000		
3.0	12.000000		

DOUBLE ALUMINIZED MYLAR/TISSUGLAS   SPECIMEN NO.   4C

EDGE EVACUATION-PRECONDITIONED SAMPLE
PURGE GAS- HELIUM
TEMPERATURE =430. DEG R
SAMPLE DIAMETER = 27.0 INS   SAMPLE HEIGHT = .548 INS
TOTAL NUMBER OF SHIELDS = 80.0   LAYERS/INCH =144.0

VACUUM CHAMBER PRESSURE HISTORY		DIFFERENTIAL PRESSURE ACROSS SAMPLE	
TIME MIN	PRESSURE TORR	TIME MIN	PRESSURE TORR
.1	420.000000	.1	.4500
.2	261.000000	.2	.3500
.3	171.000000	.3	.3300
.4	111.000000	.4	.3200
.5	68.000000	.5	.3100
.6	44.000000	.6	.2940
.7	29.000000	.7	.2820
.8	18.900000	.8	.2550
.9	12.600000	.9	.2190
1.0	8.400000	1.0	.1830
1.1	5.900000	1.1	.1380
1.2	4.200000	1.2	.0990
1.3	3.000000	1.3	.0780
1.4	2.100000	1.4	.0170
1.5	1.500000		
1.6	.870000		

DOUBLE ALUMINIZED MYLAR/TISSUGLAS   SPECIMEN NO. 4C

EDGE EVACUATION-PRECONDITIONED SAMPLE
PURGE GAS- HELIUM
TEMPERATURE =384. DEG R
SAMPLE DIAMETER = 27.0 INS   SAMPLE HEIGHT = .548 INS
TOTAL NUMBER OF SHIELDS = 80.0   LAYERS/INCH =144.0

VACUUM CHAMBER PRESSURE HISTORY		DIFFERENTIAL PRESSURE ACROSS SAMPLE	
TIME MIN	PRESSURE TORR	TIME MIN	PRESSURE TORR
.1	435.000000	.1	.3400
.2	280.000000	.2	.2900
.3	186.000000	.3	.2910
.4	117.000000	.4	.2850
.5	75.000000	.5	.2790
.6	50.000000	.6	.2700
.7	32.500000	.7	.2520
.8	21.300000	.8	.2310
.9	14.100000	.9	.2010
1.0	9.300000	1.0	.1680
1.1	6.500000	1.1	.1380
1.2	4.400000	1.2	.1140
1.3	3.100000	1.3	.0900
1.4	2.100000	1.4	.0740
1.5	1.800000	1.5	.0510
1.6	.750000	1.6	.0320
1.7	.490000	1.7	.0174
1.8	.320000	1.8	.0081
1.9	.210000	1.9	.0060
2.0	.140000		
2.2	.075000		

DOUBLE ALUMINIZED MYLAR/TISSUGLAS   SPECIMEN NO. 4C

EDGE EVACUATION-PRECONDITIONED SAMPLE
PURGE GAS- HELIUM
TEMPERATURE =328. DEG R
SAMPLE DIAMETER = 27.0 INS   SAMPLE HEIGHT = .548 INS
TOTAL NUMBER OF SHIELDS = 80.0   LAYERS/INCH =144.0

VACUUM CHAMBER PRESSURE HISTORY		DIFFERENTIAL PRESSURE ACROSS SAMPLE	
TIME MIN	PRESSURE TORR	TIME MIN	PRESSURE TORR
.1	440.000000	.1	.2900
.2	290.000000	.2	.2700
.3	192.000000	.3	.2580
.4	129.000000	.4	.2520
.5	84.000000	.5	.2460
.6	56.000000	.6	.2370
.7	37.000000	.7	.2250
.8	24.900000	.8	.2100
.9	17.100000	.9	.1905
1.0	11.400000	1.0	.1680
1.1	8.300000	1.1	.1440
1.2	5.500000	1.2	.1230
1.3	3.900000	1.3	.0900
1.4	2.700000	1.4	.0930
1.5	1.860000	1.5	.0690
1.6	1.260000	1.6	.0490
1.7	.000000	1.7	.0340
1.8	.460000	1.8	.0230
1.9	.300000	1.9	.0150
2.0	.204000	2.0	.0096
2.2	.099000	2.2	.0040
2.4	.052000	2.4	.0018
2.6	.030000	2.6	.0011
2.8	.018300	2.8	.0009
3.0	.012300		
3.5	.005800		
4.0	.000000		

DOUBLE ALUMINIZED MYLAR/TISSUGLAS   SPECIMEN NO. 4C

EDGE EVACUATION-PRECONDITIONED SAMPLE
PURGE GAS- HELIUM
TEMPERATURE =517. DEG R
SAMPLE DIAMETER = 27.0 INS   SAMPLE HEIGHT = .548 INS
TOTAL NUMBER OF SHIELDS = 80.0   LAYERS/INCH =144.0

VACUUM CHAMBER PRESSURE HISTORY		DIFFERENTIAL PRESSURE ACROSS SAMPLE	
TIME MIN	PRESSURE TORR	TIME MIN	PRESSURE TORR
.1	410.000000	.1	.3800
.2	270.000000	.2	.3300
.3	168.000000	.3	.3300
.4	105.000000	.4	.3200
.5	66.000000	.5	.3100
.6	42.000000	.6	.3050
.7	28.000000	.7	.2880
.8	17.400000	.8	.2550
.9	11.700000	.9	.2130
1.0	7.600000	1.0	.1620
1.1	5.300000	1.1	.1170
1.2	3.800000	1.2	.0690
1.3	2.600000	1.3	.0480
1.4	1.650000	1.4	.0105
1.5	1.170000		
1.6	.850000		
1.7	.660000		
1.8	.530000		
1.9	.450000		

DOUBLE ALUMINIZED MYLAR/SILK NET   SPECIMEN NO.   5

BROADSIDE EVACUATION- OFFSHELF SAMPLE
PURGE GAS- NITROGEN
TEMPERATURE =540. DEG R
SAMPLE DIAMETER = 27.0 INS   SAMPLE HEIGHT =1.124 INS
TOTAL NUMBER OF SHIELDS = 80.0   LAYERS/INCH = 72.0
PERFORATION DIAMETER = .047 INS   PER CENT OPEN AREA = .26

VACUUM CHAMBER PRESSURE HISTORY		DIFFERENTIAL PRESSURE ACROSS SAMPLE	
TIME MIN	PRESSURE TORR	TIME MIN	PRESSURE TORR
.1	410.000000	.1	1.0200
.2	250.000000	.2	.8300
.3	162.000000	.3	.7900
.4	102.000000	.4	.7700
.5	64.000000	.5	.7500
.6	41.000000	.6	.7150
.7	26.400000	.7	.6700
.8	16.800000	.8	.6150
.9	11.100000	.9	.5400
1.0	7.400000	1.0	.4700
1.1	5.100000	1.1	.4000
1.2	3.600000	1.2	.3600
1.3	2.250000	1.3	.3600
1.4	1.380000	1.4	.3100
1.5	.750000	1.5	.2700
1.6	.510000	1.6	.2400
1.7	.350000	1.8	.2190
1.8	.243000	2.0	.2220
1.9	.186000	3.0	.2110
2.0	.147000	6.0	.1470
2.2	.099000	30.0	.0910
2.4	.086000	60.0	.0610
2.6	.078000	120.0	.0405
2.8	.072000	180.0	.0320
3.0	.069000	300.0	.0234
4.0	.059000	500.0	.0159
12.0	.039000	1434.0	.0012
24.0	.030000		
18.0	.004600		
58.0	.002600		
118.0	.001900		
147.0	.001500		
175.0	.001100		
248.0	.000900		
280.0	.000900		
414.0	.000720		
499.0	.000620		
1433.0	.000060		

DOUBLE ALUMINIZED MYLAR/SILK NET   SPECIMEN NO.   5

BROADSIDE EVACUATION-PRECONDITIONED SAMPLE
PURGE GAS- NITROGEN
TEMPERATURE =540. DEG R
SAMPLE DIAMETER = 27.0 INS   SAMPLE HEIGHT =1.124 INS
TOTAL NUMBER OF SHIELDS = 80.0   LAYERS/INCH = 72.0
PERFORATION DIAMETER = .047 INS   PER CENT OPEN AREA = .26

VACUUM CHAMBER PRESSURE HISTORY		DIFFERENTIAL PRESSURE ACROSS SAMPLE	
TIME MIN	PRESSURE TORR	TIME MIN	PRESSURE TORR
.1	400.000000	.1	.9900
.2	240.000000	.2	.8200
.3	159.000000	.3	.7750
.4	99.000000	.4	.7600
.5	63.000000	.5	.7350
.6	39.000000	.6	.7000
.7	24.900000	.7	.6550
.8	16.200000	.8	.5900
.9	10.500000	.9	.5200
1.0	7.000000	1.0	.4400
1.1	4.700000	1.1	.3500
1.2	3.300000	1.2	.3250
1.3	2.130000	1.3	.2900
1.4	1.230000	1.4	.2220
1.5	.710000	1.5	.1560
1.6	.420000	1.6	.1050
1.7	.270000	1.7	.0690
1.8	.174000	1.8	.0440
1.9	.114000	1.9	.0276
2.0	.076000	2.0	.0171
2.2	.038000	2.1	.0111
2.4	.021900	2.2	.0072
2.6	.013200	2.3	.0052
2.8	.009600	2.4	.0037
3.0	.007400	2.5	.0032
5.0	.000320	2.6	.0025
15.0	.000120	2.8	.0019
43.0	.000089	3.0	.0017
56.0	.000080	3.5	.0015
70.0	.000087		
90.0	.000082		
120.0	.000078		

DOUBLE ALUMINIZED MYLAR/SILK NET   SPECIMEN NO.   6

BROADSIDE EVACUATION- OFFSHELF SAMPLE
PURGE GAS- NITROGEN
TEMPERATURE =540. DEG R
SAMPLE DIAMETER = 27.0 INS   SAMPLE HEIGHT =1.124 INS
TOTAL NUMBER OF SHIELDS = 80.0   LAYERS/INCH = 72.0
PERFORATION DIAMETER = .047 INS   PER CENT OPEN AREA = .55

VACUUM CHAMBER PRESSURE HISTORY		DIFFERENTIAL PRESSURE ACROSS SAMPLE	
TIME MIN	PRESSURE TORR	TIME MIN	PRESSURE TORR
.1	490.000000	.1	1.7700
.2	280.000000	.2	1.5300
.3	180.000000	.3	1.4700
.4	114.000000	.4	1.4400
.5	72.000000	.5	1.3500
.6	45.000000	.6	1.2900
.7	29.000000	.7	1.2000
.8	19.200000	.8	1.0800
.9	12.000000	.9	.9600
1.0	8.100000	1.0	.8100
1.1	5.500000	1.2	.6800
1.2	3.500000	1.4	.7000
1.3	2.550000	1.6	.7200
1.4	1.590000	1.8	.7600
1.5	.900000	2.0	.7600
1.6	.610000	3.0	.6700
1.7	.430000	4.0	.6000
1.8	.320000	5.0	.5400
1.9	.252000	35.0	.1530
2.0	.213000	65.0	.1020
2.2	.168000	95.0	.0710
2.4	.150000	218.0	.0290
2.6	.138000	338.0	.0160
3.0	.123000	578.0	.0070
4.0	.105000	818.0	.0040
6.0	.084000	986.0	.0031
10.0	.071000		
22.0	.047000		
42.0	.033000		
46.0	.010000		
69.0	.004400		
84.0	.002800		
98.0	.002300		
115.0	.002000		
986.0	.001400		

DOUBLE ALUMINIZED MYLAR/SILK NET   SPECIMEN NO.   6

BROADSIDE EVACUATION-PRECONDITIONED SAMPLE
PURGE GAS- NITROGEN
TEMPERATURE =540. DEG R
SAMPLE DIAMETER = 27.0 INS   SAMPLE HEIGHT =1.124 INS
TOTAL NUMBER OF SHIELDS = 80.0   LAYERS/INCH = 72.0
PERFORATION DIAMETER = .047 INS   PER CENT OPEN AREA = .55

VACUUM CHAMBER PRESSURE HISTORY		DIFFERENTIAL PRESSURE ACROSS SAMPLE	
TIME MIN	PRESSURE TORR	TIME MIN	PRESSURE TORR
.1	390.000000	.1	.8000
.2	240.000000	.2	.5500
.3	153.000000	.3	.4600
.4	99.000000	.4	.4000
.5	61.000000	.5	.3700
.6	39.000000	.6	.3400
.7	24.900000	.7	.3200
.8	16.500000	.8	.2940
.9	10.800000	.9	.2670
1.0	6.900000	1.0	.2340
1.1	4.800000	1.1	.2010
1.2	3.300000	1.2	.1890
1.3	2.100000	1.3	.1860
1.4	1.140000	1.4	.1590
1.5	.690000	1.5	.1290
1.6	.430000	1.6	.0900
1.7	.280000	1.7	.0610
1.8	.174000	1.8	.0420
1.9	.114000	1.9	.0270
2.0	.078000	2.0	.0183
2.2	.039000	2.2	.0096
2.4	.021900	2.4	.0060
2.6	.014400	2.6	.0047
2.8	.010000	2.8	.0042
3.0	.007700	3.0	.0039
4.0	.000400	3.5	.0032
10.0	.000240	120.0	.0028
23.0	.000180		
34.0	.000120		
56.0	.000120		
83.0	.000120		
90.0	.000100		
120.0	.000100		

DOUBLE ALUMINIZED MYLAR/SILK NET   SPECIMEN NO.   7

BROADSIDE EVACUATION- OFFSHELF SAMPLE
PURGE GAS- NITROGEN
TEMPERATURE =540. DEG R
SAMPLE DIAMETER = 27.0 INS   SAMPLE HEIGHT =1.124 INS
TOTAL NUMBER OF SHIELDS = 80.0   LAYERS/INCH = 72.0
PERFORATION DIAMETER = .047 INS   PER CENT OPEN AREA =1.07

VACUUM CHAMBER PRESSURE HISTORY		DIFFERENTIAL PRESSURE ACROSS SAMPLE	
TIME MIN	PRESSURE TORR	TIME MIN	PRESSURE TORR
.1	420.000000	.1	.4500
.2	260.000000	.2	.2900
.3	159.000000	.3	.2400
.4	102.000000	.4	.2100
.5	65.000000	.5	.1920
.6	42.000000	.6	.1830
.7	27.000000	.7	.1770
.8	17.700000	.8	.1710
.9	11.400000	.9	.1650
1.0	7.500000	1.0	.1530
1.1	5.300000	1.1	.1440
1.2	3.700000	1.2	.1440
1.3	2.500000	1.3	.1620
1.4	1.650000	1.4	.1740
1.5	.900000	1.5	.1860
1.6	.610000	1.6	.1980
1.7	.440000	1.8	.2130
1.8	.350000	2.0	.2430
1.9	.291000	3.0	.2370
2.0	.258000	15.2	.1500
2.2	.222000	33.2	.1110
2.4	.204000	63.2	.0810
2.6	.195000	123.2	.0460
2.8	.187500	183.2	.0300
3.0	.180000	363.2	.0130
63.4	.126000	1080.0	.0020
183.4	.096000		
243.4	.087500		
363.4	.076000		
720.0	.056000		
1080.0	.042000		
1440.0	.038000		
1800.0	.032500		
2160.0	.025000		
2520.0	.025000		

DOUBLE ALUMINIZED MYLAR/SILK NET   SPECIMEN NO.   7

BROADSIDE EVACUATION-PRECONDITIONED SAMPLE
PURGE GAS- NITROGEN
TEMPERATURE =540. DEG R
SAMPLE DIAMETER = 27.0 INS   SAMPLE HEIGHT =1.124 INS
TOTAL NUMBER OF SHIELDS = 80.0   LAYERS/INCH = 72.0
PERFORATION DIAMETER = .047 INS   PER CENT OPEN AREA =1.07

VACUUM CHAMBER PRESSURE HISTORY		DIFFERENTIAL PRESSURE ACROSS SAMPLE	
TIME	PRESSURE	TIME	PRESSURE
MIN	TORR	MIN	TORR
.1	410.000000	.1	.3000
.2	250.000000	.2	.1920
.3	153.000000	.3	.1590
.4	99.000000	.4	.1440
.5	63.000000	.5	.1350
.6	40.000000	.6	.1260
.7	25.200000	.7	.1200
.8	16.200000	.8	.1110
.9	10.500000	.9	.1020
1.0	7.200000	1.0	.0900
1.1	5.000000	1.1	.0780
1.2	3.300000	1.2	.0780
1.3	2.100000	1.3	.0780
1.4	1.170000	1.4	.0670
1.5	.730000	1.5	.0530
1.6	.450000	1.6	.0390
1.7	.280000	1.7	.0280
1.8	.180000	1.8	.0198
1.9	.117000	1.9	.0129
2.0	.081000	2.0	.0084
2.2	.040000	2.2	.0036
2.4	.023400	2.4	.0020
2.6	.015600	2.6	.0014
2.8	.011400	2.8	.0012
3.0	.008700	3.0	.0010
5.0	.000370		
10.0	.000150		
20.0	.000090		
31.0	.000620		
59.0	.000050		

DOUBLE ALUMINIZED MYLAR/SILK NET   SPECIMEN NO.   8

BROADSIDE EVACUATION- OFFSHELF SAMPLE
PURGE GAS- NITROGEN
TEMPERATURE =540. DEG R
SAMPLE DIAMETER = 27.0 INS   SAMPLE HEIGHT =1.124 INS
TOTAL NUMBER OF SHIELDS = 80.0   LAYERS/INCH = 72.0
PERFORATION DIAMETER = .090 INS   PER CENT OPEN AREA = .48

VACUUM CHAMBER PRESSURE HISTORY		DIFFERENTIAL PRESSURE ACROSS SAMPLE	
TIME MIN	PRESSURE TORR	TIME MIN	PRESSURE TORR
.1	405.000000	.1	2.6100
.2	240.000000	.2	2.2200
.3	150.000000	.3	2.2800
.4	99.000000	.4	2.3400
.5	60.000000	.5	2.2500
.6	38.000000	.6	2.0100
.7	24.000000	.7	1.7700
.8	15.600000	.8	1.4700
.9	10.200000	.9	1.2000
1.0	7.000000	1.0	.9000
1.1	4.800000	1.1	.6500
1.2	3.200000	1.2	.5800
1.3	2.040000	1.4	.5000
1.4	1.140000	1.6	.4000
1.5	.720000	1.8	.3750
1.6	.480000	2.0	.3700
1.7	.330000	4.0	.2880
1.8	.240000	12.2	.1920
1.9	.189000	34.0	.1380
2.0	.156000	64.0	.0870
2.2	.123000	124.0	.0480
2.4	.108000	304.0	.0135
2.6	.099000	484.0	.0060
2.8	.093000		
3.0	.090000		
5.3	.069000		
13.3	.047500		
21.3	.040000		
29.3	.002600		
42.0	.002200		
64.0	.002100		

DOUBLE ALUMINIZED MYLAR/SILK NET   SPECIMEN NO.   8

BROADSIDE EVACUATION-PRECONDITIONED SAMPLE
PURGE GAS- NITROGEN
TEMPERATURE =540. DEG P

SAMPLE DIAMETER = 27.0 INS   SAMPLE HEIGHT =1.124 INS
TOTAL NUMBER OF SHIELDS = 80.0   LAYERS/INCH = 72.0
PERFORATION DIAMETER = .090 INS   PER CENT OPEN AREA = .48

VACUUM CHAMBER PRESSURE HISTORY		DIFFERENTIAL PRESSURE ACROSS SAMPLE	
TIME MIN	PRESSURE TORR	TIME MIN	PRESSURE TORR
.1	410.000000	.1	2.5800
.2	243.000000	.2	1.3800
.3	156.000000	.3	2.3700
.4	99.000000	.4	2.3400
.5	63.000000	.5	2.1900
.6	40.000000	.6	2.0100
.7	25.200000	.7	1.7400
.8	16.500000	.8	1.4400
.9	10.800000	.9	1.1400
1.0	7.100000	1.0	.8700
1.1	5.000000	1.1	.5200
1.2	3.400000	1.2	.4200
1.3	2.130000	1.3	.3750
1.4	1.170000	1.4	.2900
1.5	.750000	1.5	.2190
1.6	.460000	1.6	.1770
1.7	.290000	1.7	.1230
1.8	.180000	1.8	.0780
1.9	.120000	1.9	.0470
2.0	.080000	2.0	.0290
2.2	.041000	2.1	.0186
2.4	.023100	2.2	.0123
2.6	.015000	2.3	.0077
2.8	.010500	2.4	.0056
3.0	.008400	2.6	.0035
5.0	.000640	2.8	.0025
10.0	.000220	3.0	.0020
20.0	.000100	9.0	.0016
30.0	.000094	30.0	.0012
55.0	.000076		
85.0	.000072		
100.0	.000070		
120.0	.000068		

DOUBLE ALUMINIZED MYLAR/SILK NET   SPECIMEN NO.   9

BROADSIDE EVACUATION- OFFSHELF SAMPLE
PURGE GAS- NITROGEN
TEMPERATURE =540. DEG R
SAMPLE DIAMETER = 27.0 INS   SAMPLE HEIGHT =1.124 INS
TOTAL NUMBER OF SHIELDS = 80.0   LAYERS/INCH = 72.0
PERFORATION DIAMETER = .090 INS   PER CENT OPEN AREA = .99

VACUUM CHAMBER PRESSURE HISTORY		DIFFERENTIAL PRESSURE ACROSS SAMPLE	
TIME MIN	PRESSURE TORR	TIME MIN	PRESSURE TORR
.1	420.000000	.1	2.1900
.2	252.000000	.2	1.7700
.3	162.000000	.3	1.6500
.4	105.000000	.4	1.5300
.5	63.000000	.5	1.4100
.6	41.000000	.6	1.2600
.7	27.000000	.7	1.1100
.8	17.400000	.8	.9600
.9	11.400000	.9	.8000
1.0	7.400000	1.0	.6700
1.1	5.200000	1.1	.5500
1.2	3.600000	1.2	.4900
1.3	2.370000	1.3	.4700
1.4	1.440000	1.4	.4200
1.5	.840000	1.6	.3500
1.6	.550000	1.8	.3320
1.7	.370000	2.0	.3300
1.8	.270000	3.0	.2850
1.9	.201000	4.0	.2490
2.0	.159000	10.0	.1680
2.2	.117000	18.0	.1260
2.4	.099000	34.0	.0960
3.0	.078500	64.0	.0610
4.5	.064000	124.0	.0390
8.5	.048000	170.0	.0300
20.5	.034000	290.0	.0189
39.0	.004400	410.0	.0126
71.0	.002000	530.0	.0084
103.0	.001600	710.0	.0030
168.0	.001000	1115.0	.0022
1114.0	.000140		

DOUBLE ALUMINIZED MYLAR/SILK NET   SPECIMEN NO.   9

BROADSIDE EVACUATION-PRECONDITIONED SAMPLE
PURGE GAS- NITROGEN
TEMPERATURE =540. DEG R
SAMPLE DIAMETER = 27.0 INS   SAMPLE HEIGHT =1.124 INS
TOTAL NUMBER OF SHIELDS = 80.0   LAYERS/INCH = 72.0
PERFORATION DIAMETER = .090 INS   PER CENT OPEN AREA = .99

VACUUM CHAMBER PRESSURE HISTORY		DIFFERENTIAL PRESSURE ACROSS SAMPLE	
TIME MIN	PRESSURE TORR	TIME MIN	PRESSURE TORR
.1	400.000000	.1	1.3800
.2	240.000000	.2	1.1100
.3	150.000000	.3	.9300
.4	99.000000	.4	.8300
.5	62.000000	.5	.7200
.6	40.000000	.6	.6300
.7	25.200000	.7	.5700
.8	15.900000	.8	.5100
.9	9.900000	.9	.4600
1.0	7.100000	1.0	.3800
1.1	4.800000	1.1	.3200
1.2	3.300000	1.2	.2700
1.3	2.130000	1.3	.2490
1.4	1.200000	1.4	.2070
1.5	.720000	1.5	.1500
1.6	.450000	1.6	.1050
1.7	.270000	1.7	.0720
1.8	.180000	1.8	.0480
1.9	.114000	1.9	.0300
2.0	.054000	2.0	.0186
2.2	.040000	2.2	.0090
2.4	.023000	2.4	.0052
2.6	.014700	2.6	.0038
2.8	.010200	2.8	.0032
3.0	.007800	3.0	.0028
5.0	.000480	4.0	.0027
12.0	.000180	64.0	.0021
20.0	.000150	124.0	.0020
35.0	.000120		
50.0	.000100		
95.0	.000100		

DOUBLE ALUMINIZED MYLAR/SILK NET   SPECIMEN NO. 10

COMBINED EDGE AND BROADSIDE EVACUATION
PRECONDITIONED SAMPLE
PURGE GAS= NITROGEN
TEMPERATURE =540. DEG R

SAMPLE DIAMETER = 27.0 INS   SAMPLE HEIGHT =1.124 INS
TOTAL NUMBER OF SHIELDS = 80.0   LAYERS/INCH = 72.0
PERFORATION DIAMETER = .047 INS   PER CENT OPEN AREA =1.07

VACUUM CHAMBER PRESSURE HISTORY		DIFFERENTIAL PRESSURE ACROSS SAMPLE	
TIME MIN	PRESSURE TORR	TIME MIN	PRESSURE TORR
.1	400.000000	.1	.0770
.2	240.000000	.2	.0660
.3	150.000000	.3	.0650
.4	96.000000	.4	.0650
.5	60.000000	.5	.0640
.6	38.000000	.6	.0630
.7	24.000000	.7	.0600
.8	15.600000	.8	.0560
.9	10.200000	.9	.0510
1.0	6.700000	1.0	.0450
1.1	4.600000	1.1	.0410
1.2	3.200000	1.2	.0420
1.3	2.000000	1.3	.0380
1.4	1.320000	1.4	.0300
1.5	.930000	1.5	.0210
1.6	.400000	1.6	.0138
1.7	.261000	1.7	.0084
1.8	.180000	1.8	.0048
1.9	.126000	1.9	.0024
2.0	.091000	2.0	.0007
2.1	.072000		
2.2	.059000		

DOUBLE ALUMINIZED MYLAR/SILK NET   SPECIMEN NO. 10

COMBINED EDGE AND BROADSIDE EVACUATION
PRECONDITIONED SAMPLE
PURGE GAS- NITROGEN
TEMPERATURE =540. DEG R
SAMPLE DIAMETER = 27.0 INS   SAMPLE HEIGHT =1.124 INS
TOTAL NUMBER OF SHIELDS = 80.0   LAYERS/INCH = 72.0
PERFORATION DIAMETER = .047 INS   PER CENT OPEN AREA =1.07

| VACUUM CHAMBER PRESSURE HISTORY | | DIFFERENTIAL PRESSURE ACROSS SAMPLE | |
TIME MIN	PRESSURE TORR	TIME MIN	PRESSURE TORR
.1	400.000000	.1	.0780
.2	240.000000	.2	.0700
.3	144.000000	.3	.0670
.4	96.000000	.4	.0660
.5	59.000000	.5	.0650
.6	37.000000	.6	.0650
.7	24.000000	.7	.0620
.8	15.000000	.8	.0580
.9	10.200000	.9	.0520
1.0	6.500000	1.0	.0440
1.1	4.400000	1.1	.0390
1.2	2.900000	1.2	.0390
1.3	1.740000	1.3	.0290
1.4	1.110000	1.4	.0150
1.5	.680000	1.5	.0021
1.6	.450000		
1.7	.310000		
1.8	.219000		
1.9	.171000		

DOUBLE ALUMINIZED MYLAR/TISSUGLAS   SPECIMEN NO. 11

BROADSIDE EVACUATION- OFFSHELF SAMPLE
PURGE GAS- NITROGEN
TEMPERATURE =540. DEG R
SAMPLE DIAMETER = 27.0 INS   SAMPLE HEIGHT = .548 INS
TOTAL NUMBER OF SHIELDS = 80.0   LAYERS/INCH =148.0
PERFORATION DIAMETER = .047 INS   PER CENT OPEN AREA = .26

VACUUM CHAMBER PRESSURE HISTORY		DIFFERENTIAL PRESSURE ACROSS SAMPLE	
TIME MIN	PRESSURE TORR	TIME MIN	PRESSURE TORR
.1	400.000000	.1	.0300
.2	240.000000	.2	.0300
.3	150.000000	.3	.1100
.4	96.000000	.4	.1700
.5	60.000000	.5	.3000
.6	39.000000	.6	.4300
.7	25.000000	.7	.6300
.8	15.900000	.8	1.3800
.9	10.800000	.9	1.6200
1.0	7.200000	1.0	1.8600
1.1	5.200000	1.1	1.9800
1.2	3.600000	1.2	2.1000
1.3	2.430000	1.3	2.2800
1.4	1.710000	1.4	2.4300
1.5	.960000	1.5	2.5200
1.6	.640000	1.6	2.5800
1.7	.450000	1.7	2.5500
1.8	.340000	1.8	2.4900
1.9	.264000	1.9	2.4000
2.0	.213000	2.0	2.3100
2.2	.156000	2.2	2.1600
2.4	.123000	2.4	2.0100
2.6	.105000	2.6	1.8600
2.8	.090000	2.8	1.7100
3.0	.081000	3.0	1.5900
4.0	.055000	4.0	1.2000
6.5	.036000	6.0	.8600
12.0	.003750	37.0	.3800
15.0	.002600	67.0	.2900
21.0	.002000	127.0	.2100
26.0	.001700	187.0	.1560
50.0	.001100	367.0	.0840
80.0	.000860	547.0	.0630
120.0	.000640	727.0	.0420
990.0	.000540	990.0	.0330

B-43

DOUBLE ALUMINIZED MYLAR/TISSUGLAS   SPECIMEN NO. 11

BROADSIDE EVACUATION-PRECONDITIONED SAMPLE
PURGE GAS- NITROGEN
TEMPERATURE =540. DEG R

SAMPLE DIAMETER = 27.0 INS   SAMPLE HEIGHT = .548 INS
TOTAL NUMBER OF SHIELDS = 80.0   LAYERS/INCH =148.0
PERFORATION DIAMETER = .047 INS   PER CENT OPEN AREA = .26

VACUUM CHAMBER PRESSURE HISTORY		DIFFERENTIAL PRESSURE ACROSS SAMPLE	
TIME MIN	PRESSURE TORR	TIME MIN	PRESSURE TORR
.1	405.000000	.1	1.0200
.2	250.000000	.2	1.3800
.3	156.000000	.3	1.2900
.4	99.000000	.4	1.2300
.5	63.000000	.5	1.2600
.6	41.000000	.6	1.3500
.7	26.100000	.7	1.3800
.8	16.800000	.8	1.5000
.9	11.400000	.9	1.6500
1.0	7.500000	1.0	1.7700
1.1	5.500000	1.1	1.8900
1.2	3.900000	1.2	2.0100
1.3	2.550000	1.3	2.1600
1.4	1.740000	1.4	2.3400
1.5	1.020000	1.5	2.4200
1.6	.670000	1.6	2.4300
1.7	.470000	1.7	2.4000
1.8	.330000	1.8	2.3400
1.9	.240000	1.9	2.2200
2.0	.189000	2.0	2.1300
2.2	.126000	2.2	1.9200
2.4	.093000	2.4	1.6800
2.6	.073000	2.6	1.5300
2.8	.061000	2.8	1.3800
3.0	.052500	3.0	1.2900
6.0	.001300	4.0	.8300
10.0	.000240	4.5	.6900
18.0	.000140	9.3	.0470
39.0	.000100	10.5	.0300
51.0	.000070	11.7	.0267
61.0	.000058	41.7	.0255
84.0	.000050	71.7	.0252
99.0	.000046	101.7	.0246
120.0	.000044		

DOUBLE ALUMINIZED MYLAR/TISSUGLAS   SPECIMEN NO. 12

BROADSIDE EVACUATION- OFFSHELF SAMPLE
PURGE GAS- NITROGEN
TEMPERATURE =540. DEG R

SAMPLE DIAMETER = 27.0 INS   SAMPLE HEIGHT = .548 INS
TOTAL NUMBER OF SHIELDS = 80.0   LAYERS/INCH =148.0
PERFORATION DIAMETER = .047 INS   PER CENT OPEN AREA = .55

VACUUM CHAMBER PRESSURE HISTORY		DIFFERENTIAL PRESSURE ACROSS SAMPLE	
TIME MIN	PRESSURE TORR	TIME MIN	PRESSURE TORR
.1	400.000000	.1	.2000
.2	240.000000	.2	.2500
.3	150.000000	.3	.2700
.4	96.000000	.4	.3300
.5	61.000000	.5	.4400
.6	39.000000	.6	.5300
.7	24.900000	.7	.6300
.8	16.200000	.8	.7400
.9	10.500000	.9	.8500
1.0	7.200000	1.0	.9600
1.1	5.100000	1.1	1.0500
1.2	3.500000	1.2	1.2300
1.3	2.310000	1.3	1.4700
1.4	1.380000	1.4	1.5900
1.5	.840000	1.5	1.6200
1.6	.550000	1.6	1.5900
1.7	.370000	1.7	1.5700
1.8	.270000	1.8	1.5000
1.9	.198000	1.9	1.4100
2.0	.156000	2.0	1.3200
2.2	.105000	2.2	1.1400
2.4	.080000	2.4	.9900
2.6	.066000	2.6	.8100
2.8	.056000	2.8	.7100
3.0	.049000	3.0	.6000
4.0	.031500	4.0	.3200
4.5	.027000	5.0	.1590
6.0	.001700	6.0	.1020
11.3	.000800	13.0	.0780
23.0	.000800	25.0	.0500
30.0	.000440	67.0	.0345
56.0	.000260	157.0	.0240
76.0	.000200	367.0	.0144
94.0	.000170	727.0	.0063
135.0	.000100	1087.0	.0039
1096.0	.000020		

BROADSIDE EVACUATION-PRECONDITIONED SAMPLE
PURGE GAS- NITROGEN
TEMPERATURE =540. DEG R
SAMPLE DIAMETER = 27.0 INS   SAMPLE HEIGHT = .548 INS
TOTAL NUMBER OF SHIELDS = 80.0   LAYERS/INCH =148.0
PERFORATION DIAMETER = .047 INS   PER CENT OPEN AREA = .55

VACUUM CHAMBER PRESSURE HISTORY		DIFFERENTIAL PRESSURE ACROSS SAMPLE	
TIME MIN	PRESSURE TORR	TIME MIN	PRESSURE TORR
.1	400.000000	.1	.3600
.2	240.000000	.2	.4200
.3	150.000000	.3	.4800
.4	99.000000	.4	.5000
.5	63.000000	.5	.5400
.6	39.000000	.6	.6000
.7	25.000000	.7	.6600
.8	16.500000	.8	.7200
.9	10.800000	.9	.8300
1.0	7.200000	1.0	.9200
1.1	5.000000	1.1	.9900
1.2	3.500000	1.2	1.0800
1.3	2.310000	1.3	1.1700
1.4	1.530000	1.4	1.2600
1.5	.880000	1.5	1.3200
1.6	.540000	1.6	1.3400
1.7	.360000	1.7	1.3200
1.8	.249000	1.8	1.2600
1.9	.180000	1.9	1.2000
2.0	.135000	2.0	1.1400
2.2	.084000	2.2	1.0200
2.4	.060000	2.4	.9000
2.6	.046000	2.6	.7800
2.8	.038000	2.8	.6900
3.0	.031500	3.0	.0630
5.0	.000620	4.0	.2900
8.0	.000140	5.0	.1380
31.0	.000038	6.0	.0500
76.0	.000026	7.0	.0405
120.0	.000024	30.0	.0390

DOUBLE ALUMINIZED MYLAR/TISSUGLAS   SPECIMEN NO. 13

BROADSIDE EVACUATION- OFFSHELF SAMPLE
PURGE GAS- NITROGEN
TEMPERATURE =540. DEG P
SAMPLE DIAMETER = 27.0 INS   SAMPLE HEIGHT = .548 INS
TOTAL NUMBER OF SHIELDS = 80.0   LAYERS/INCH =148.0
PERFORATION DIAMETER = .047 INS   PER CENT OPEN AREA =1.07

VACUUM CHAMBER PRESSURE HISTORY		DIFFERENTIAL PRESSURE ACROSS SAMPLE	
TIME MIN	PRESSURE TORR	TIME MIN	PRESSURE TORR
.1	420.000000	.1	.5400
.2	250.000000	.2	.7200
.3	159.000000	.3	1.0200
.4	102.000000	.4	.9300
.5	63.000000	.5	.8400
.6	41.000000	.6	.9000
.7	26.000000	.7	.9900
.8	16.800000	.8	1.0800
.9	11.100000	.9	1.2300
1.0	7.800000	1.0	1.4400
1.1	5.300000	1.1	1.5000
1.2	3.700000	1.2	1.5900
1.3	2.520000	1.3	1.7700
1.4	1.680000	1.4	1.8900
1.5	.930000	1.5	1.9500
1.6	.620000	1.6	1.9500
1.7	.430000	1.7	1.9500
1.8	.320000	1.8	1.8900
1.9	.246000	1.9	1.8000
2.0	.198000	2.0	1.6800
2.2	.147000	3.0	1.2750
2.4	.120000	4.0	1.0200
2.6	.105000	5.0	.9900
2.8	.094500	36.0	.4000
3.0	.087000	66.0	.2700
4.0	.067000	96.0	.1920
6.2	.049000	126.0	.1140
10.2	.001500	366.0	.0510
20.0	.003400	726.0	.0300
30.0	.002000	944.0	.0270
71.0	.001000		
90.0	.000800		
121.0	.000600		
944.0	.000030		

DOUBLE ALUMINIZED MYLAR/TISSUGLAS   SPECIMEN NO. 13

BROADSIDE EVACUATION-PRECONDITIONED SAMPLE
PURGE GAS- NITROGEN
TEMPERATURE =540. DEG F
SAMPLE DIAMETER = 27.0 INS   SAMPLE HEIGHT = .548 INS
TOTAL NUMBER OF SHIELDS = 80.0   LAYERS/INCH =148.0
PERFORATION DIAMETER = .047 INS   PER CENT OPEN AREA =1.07

VACUUM CHAMBER PRESSURE HISTORY		DIFFERENTIAL PRESSURE ACROSS SAMPLE	
TIME MIN	PRESSURE TORR	TIME MIN	PRESSURE TORR
.1	410.000000	.1	.3300
.2	240.000000	.2	.6600
.3	156.000000	.3	.6900
.4	99.000000	.4	.8700
.5	63.000000	.5	.9900
.6	41.000000	.6	1.0950
.7	26.000000	.7	1.1100
.8	16.500000	.8	1.2000
.9	10.800000	.9	1.2600
1.0	7.200000	1.0	1.3200
1.1	5.100000	1.1	1.4100
1.2	3.500000	1.2	1.4400
1.3	2.280000	1.3	1.5000
1.4	1.350000	1.4	1.5600
1.5	.840000	1.5	1.5750
1.6	.520000	1.6	1.5300
1.7	.340000	1.7	1.4100
1.8	.225000	1.8	1.3200
1.9	.156000	1.9	1.2300
2.0	.081000	2.0	1.1400
2.2	.065000	2.2	.9900
2.4	.043000	2.4	1.8600
2.6	.032000	2.6	1.1400
2.8	.024000	2.8	.6900
3.0	.018600	3.0	.4100
3.5	.099000	3.2	.2300
4.0	.057000	3.4	.1170
7.0	.000220	3.6	.0570
15.0	.000090	3.8	.0300
20.0	.000078	4.0	.0174
30.0	.000060	5.0	.0082
42.0	.000050	10.0	.0080
61.0	.000042	30.0	.0078
75.0	.000038	120.0	.0075
120.0	.000036		

DOUBLE ALUMINIZED MYLAR/TISSUGLAS   SPECIMEN NO. 14

BROADSIDE EVACUATION- OFFSHELF SAMPLE
PURGE GAS- NITROGEN
TEMPERATURE =540. DEG R
SAMPLE DIAMETER = 27.0 INS   SAMPLE HEIGHT = .548 INS
TOTAL NUMBER OF SHIELDS = 80.0   LAYERS/INCH =148.0
PERFORATION DIAMETER = .090 INS   PER CENT OPEN AREA = .48

VACUUM CHAMBER PRESSURE HISTORY		DIFFERENTIAL PRESSURE ACROSS SAMPLE	
TIME MIN	PRESSURE TORR	TIME MIN	PRESSURE TORR
.1	410.000000	.1	1.2000
.2	249.000000	.2	2.3000
.3	162.000000	.3	2.8000
.4	105.000000	.4	3.2000
.5	65.000000	.5	3.3000
.6	41.000000	.6	3.1500
.7	27.000000	.7	3.1000
.8	17.700000	.8	3.0500
.9	11.400000	.9	3.1000
1.0	7.800000	1.0	3.2000
1.1	5.600000	1.2	3.3500
1.2	4.100000	1.4	3.6000
1.3	2.800000	1.6	3.8000
1.4	1.860000	1.8	3.9000
1.5	1.080000	2.0	3.7000
1.8	.740000	2.5	3.1500
1.7	.540000	3.0	2.8000
1.8	.400000	3.5	2.6700
1.9	.310000	4.0	2.6700
2.0	.250000	4.3	2.9800
2.2	.180000	4.5	2.5500
2.4	.141000	5.0	1.1400
2.6	.117000	5.5	.9000
2.8	.102000	6.0	.7400
3.0	.090000	7.0	.6600
4.0	.060000	8.0	.6900
6.0	.035000	9.0	.7400
13.0	.002300	21.0	.0640
19.0	.001400	39.0	.5100
26.0	.001100	69.0	.3900
40.0	.000800	99.0	.3100
55.0	.000600	129.0	.2610
74.0	.000500	249.0	.1260
86.0	.000500	369.0	.0690
109.0	.000520	729.0	.0240
125.0	.000460	1135.0	.0120
172.0	.000360		
1135.0	.000030		

DOUBLE ALUMINIZED MYLAR/TISSUGLAS   SPECIMEN NO. 14

BROADSIDE EVACUATION-PRECONDITIONED SAMPLE
PURGE GAS- NITROGEN
TEMPERATURE =540. DEG R
SAMPLE DIAMETER = 27.0 INS   SAMPLE HEIGHT = .548 INS
TOTAL NUMBER OF SHIELDS = 80.0   LAYERS/INCH =148.0
PERFORATION DIAMETER = .090 INS   PER CENT OPEN AREA = .48

VACUUM CHAMBER PRESSURE HISTORY		DIFFERENTIAL PRESSURE ACROSS SAMPLE	
TIME MIN	PRESSURE TORR	TIME MIN	PRESSURE TORR
.1	420.000000	.1	.0200
.2	250.000000	.2	.2000
.3	160.000000	.3	.2200
.4	99.000000	.4	.3200
.5	64.000000	.5	.4600
.6	41.000000	.6	.6500
.7	26.100000	.7	1.1200
.8	16.800000	.8	1.5000
.9	11.100000	.9	2.0000
1.0	7.500000	1.0	2.4500
1.1	5.300000	1.1	2.7500
1.2	3.700000	1.2	3.0000
1.3	2.500000	1.3	3.0000
1.4	1.620000	1.4	3.0500
1.5	1.140000	1.5	3.2000
1.6	.600000	1.6	3.5000
1.7	.420000	1.7	3.5000
1.8	.290000	1.8	3.5000
1.9	.216000	1.9	3.4000
2.0	.168000	2.0	3.3000
2.2	.114000	2.2	3.0000
2.4	.084000	2.4	2.7500
2.6	.068000	2.6	2.5200
2.8	.057000	2.8	2.3700
3.0	.048000	3.0	2.1900
3.5	.035000	3.5	1.6200
7.0	.000320	4.0	1.5900
10.0	.000140	4.5	2.5500
18.0	.000080	5.0	1.3200
23.0	.000080	5.5	.7000
28.0	.000060	6.0	.3900
32.0	.000060	6.5	.2100
47.0	.000058	7.0	.1050
65.0	.000044	7.5	.0550
73.0	.000044	8.0	.0330
89.0	.000042	10.0	.0162
101.0	.000041	70.0	.0156
120.0	.000041	120.0	.0153

DOUBLE ALUMINIZED MYLAR/TISSUGLAS   SPECIMEN NO. 15

BROADSIDE EVACUATION- OFFSHELF SAMPLE
PURGE GAS- NITROGEN
TEMPERATURE =540. DEG R
SAMPLE DIAMETER = 27.0 INS   SAMPLE HEIGHT = .548 INS
TOTAL NUMBER OF SHIELDS = 80.0   LAYERS/INCH =148.0
PERFORATION DIAMETER = .090 INS   PER CENT OPEN AREA = .99

VACUUM CHAMBER PRESSURE HISTORY		DIFFERENTIAL PRESSURE ACROSS SAMPLE	
TIME MIN	PRESSURE TORR	TIME MIN	PRESSURE TORR
.1	400.000000	.1	1.4000
.2	250.000000	.2	1.4000
.3	153.000000	.3	1.4000
.4	99.000000	.4	1.6000
.5	62.000000	.5	1.8000
.6	40.000000	.6	2.1000
.7	26.000000	.7	2.4000
.8	16.500000	.8	2.7000
.9	11.100000	.9	2.9000
1.0	7.500000	1.0	2.8000
1.1	5.300000	1.1	2.8000
1.2	3.900000	1.2	2.8000
1.3	2.700000	1.3	3.0000
1.4	1.800000	1.4	3.1500
1.5	1.080000	1.5	3.2000
1.6	.720000	1.6	3.2500
1.7	.530000	1.7	3.2000
1.8	.400000	1.8	3.2000
1.9	.310000	1.9	3.1000
2.0	.255000	2.0	3.0000
2.2	.189000	2.2	2.8000
2.4	.150000	2.4	2.5500
2.6	.126000	2.6	2.3400
2.8	.108000	2.8	2.1300
3.0	.096000	3.0	1.9800
4.0	.062000	4.0	1.4100
5.0	.041000	5.0	1.0800
6.0	.002300	6.0	.7700
10.0	.002100	37.0	.2400
13.0	.002000	127.0	.1560
18.0	.001500	247.0	.1140
27.0	.001200	367.0	.0840
35.0	.001000	727.0	.0375
55.0	.000850	1126.0	.0270
77.0	.000700		
100.0	.000580		
122.0	.000500		
175.0	.000400		
1126.0	.000043		

DOUBLE ALUMINIZED MYLAR/TISSUGLAS   SPECIMEN NO. 15

BROADSIDE EVACUATION-PRECONDITIONED SAMPLE
PURGE GAS- NITROGEN
TEMPERATURE =540. DEG R

SAMPLE DIAMETER = 27.0 INS   SAMPLE HEIGHT = .548 INS
TOTAL NUMBER OF SHIELDS = 80.0   LAYERS/INCH =148.0
PERFORATION DIAMETER = .090 INS   PER CENT OPEN AREA = .99

VACUUM CHAMBER PRESSURE HISTORY		DIFFERENTIAL PRESSURE ACROSS SAMPLE	
TIME MIN	PRESSURE TORR	TIME MIN	PRESSURE TORR
.1	410.000000	.1	.6300
.2	243.000000	.2	.9600
.3	156.000000	.3	1.0500
.4	99.000000	.4	1.1700
.5	62.000000	.5	1.2900
.6	40.000000	.6	1.4700
.7	26.000000	.7	1.7100
.8	16.500000	.8	1.9500
.9	11.100000	.9	2.1600
1.0	7.500000	1.0	2.3400
1.1	5.300000	1.1	2.4300
1.2	3.800000	1.2	2.5500
1.3	2.600000	1.3	2.6700
1.4	1.680000	1.4	2.7300
1.5	.990000	1.5	2.7300
1.6	.660000	1.6	2.6700
1.7	.470000	1.7	2.4900
1.8	.340000	1.8	2.4000
1.9	.249000	1.9	2.2200
2.0	.198000	2.0	2.1600
2.2	.135000	2.2	2.0100
2.4	.099000	2.4	1.8900
2.6	.081000	2.6	1.7400
2.8	.068000	2.8	1.6200
3.0	.058000	3.0	1.5300
3.5	.042500	4.0	1.0800
7.0	.000900	5.0	.9000
11.0	.000160	23.2	.0240
20.0	.000100	120.0	.0240
54.0	.000064		
74.0	.000060		
120.0	.000060		

CRINKLED SINGLE ALUMINIZED MYLAR   SPECIMEN NO. 17A

EDGE EVACUATION- OFFSHELF SAMPLE
PURGE GAS- NITROGEN
TEMPERATURE =540. DEG R
SAMPLE DIAMETER = 27.0 INS   SAMPLE HEIGHT = .292 INS
TOTAL NUMBER OF SHIELDS = 20.0   LAYERS/INCH = 72.0

VACUUM CHAMBER PRESSURE HISTORY		DIFFERENTIAL PRESSURE ACROSS SAMPLE	
TIME MIN	PRESSURE TORR	TIME MIN	PRESSURE TORR
.1	400.000000	.1	.0990
.2	243.000000	.2	.0870
.3	150.000000	.3	.0840
.4	96.000000	.4	.0850
.5	61.000000	.5	.0860
.6	39.000000	.6	.0880
.7	24.600000	.7	.0910
.8	15.900000	.8	.0980
.9	10.500000	.9	.1260
1.0	7.200000	1.0	.2070
1.1	5.200000	1.2	.6000
1.2	3.700000	1.4	.8200
1.3	2.700000	1.6	.8800
1.4	1.910000	1.8	.8800
1.5	1.590000	2.0	.8400
1.6	1.290000	2.2	.8000
1.7	1.110000	8.2	.2600
1.8	.960000	26.2	.0900
1.9	.840000	38.2	.0600
2.0	.795000	62.2	.0370
2.1	.780000	122.2	.0190
2.2	.750000	182.2	.0123
2.3	.710000	242.2	.0093
2.8	.380000	302.2	.0075
2.9	.365000	1306.0	.0021
3.0	.350000		
4.0	.240000		
44.0	.004500		
56.0	.002000		
130.0	.001300		
152.0	.000700		
326.0	.000320		
1306.0	.000360		

CRINKLED SINGLE ALUMINIZED MYLAR   SPECIMEN NO. 17A

EDGE EVACUATION-PRECONDITIONED SAMPLE
PURGE GAS- NITROGEN
TEMPERATURE =540. DEG R
SAMPLE DIAMETER = 27.0 INS   SAMPLE HEIGHT = .292 INS
TOTAL NUMBER OF SHIELDS = 20.0   LAYERS/INCH = 72.0

| VACUUM CHAMBER PRESSURE HISTORY | | DIFFERENTIAL PRESSURE ACROSS SAMPLE | |
TIME MIN	PRESSURE TORR	TIME MIN	PRESSURE TORR
.1	400.000000	.1	.0870
.2	245.000000	.2	.0760
.3	150.000000	.3	.0730
.4	975.000000	.4	.0710
.5	61.000000	.5	.0700
.6	38.000000	.6	.0680
.7	25.000000	.7	.0640
.8	15.000000	.8	.0600
.9	9.600000	.9	.0540
1.0	6.300000	1.0	.0470
1.1	4.200000	1.2	.0450
1.2	2.650000	1.4	.0330
1.3	1.620000	1.6	.0230
1.4	1.020000	1.8	.0081
1.5	.630000	2.0	.0032
1.6	.380000	2.2	.0013
1.7	.240000	2.4	.0005
1.8	.150000	2.6	.0003
1.9	.099000	2.8	.0001
2.0	.066000		
2.1	.048000		
2.2	.036000		
2.3	.027000		
2.4	.021300		
2.5	.016500		
2.6	.014400		
2.7	.012300		
2.8	.010800		
2.9	.009400		
3.0	.008500		

DOUBLE ALUMINIZED MYLAR/SILK NET   SPECIMEN NO. 17B

EDGE EVACUATION-PRECONDITIONED SAMPLE
PURGE GAS- NITROGEN
TEMPERATURE =540. DEG R
SAMPLE DIAMETER = 27.0 INS   SAMPLE HEIGHT = .214 INS
TOTAL NUMBER OF SHIELDS = 20.0   LAYERS/INCH = 98.0

VACUUM CHAMBER PRESSURE HISTORY		DIFFERENTIAL PRESSURE ACROSS SAMPLE	
TIME MIN	PRESSURE TORR	TIME MIN	PRESSURE TORR
.1	400.000000	.1	.1260
.2	240.000000	.2	.1050
.3	150.000000	.3	.1020
.4	93.000000	.4	.0970
.5	59.000000	.5	.0950
.6	38.000000	.6	.0900
.7	24.000000	.7	.0850
.8	15.000000	.8	.0810
.9	9.600000	.9	.0730
1.0	6.300000	1.0	.0630
1.1	4.200000	1.2	.0590
1.2	2.650000	1.4	.0400
1.3	1.575000	1.6	.0177
1.4	1.020000	1.8	.0060
1.5	.620000	2.0	.0008
1.6	.380000		
1.7	.240000		
1.8	.160000		
1.9	.105000		
2.0	.075000		
2.1	.055000		
2.2	.042000		

DOUBLE ALUMINIZED MYLAR/SILK NET   SPECIMEN NO. 17C

EDGE EVACUATION-PRECONDITIONED SAMPLE
PURGE GAS- NITROGEN
TEMPERATURE =540. DEG R
SAMPLE DIAMETER = 27.0 INS   SAMPLE HEIGHT = .173 INS
TOTAL NUMBER OF SHIELDS = 20.0   LAYERS/INCH =121.0

VACUUM CHAMBER PRESSURE HISTORY		DIFFERENTIAL PRESSURE ACROSS SAMPLE	
TIME MIN	PRESSURE TORR	TIME MIN	PRESSURE TORR
1.0	400.000000	.1	.1830
.2	245.000000	.2	.1470
.3	150.000000	.3	.1350
.4	96.000000	.4	.1320
.5	60.000000	.5	.1260
.6	38.000000	.6	.1200
.7	24.000000	.7	.1140
.8	15.000000	.8	.1080
.9	9.600000	.9	.0960
1.0	6.300000	1.0	.0840
1.1	4.200000	1.2	.0760
1.2	2.650000	1.4	.0510
1.3	1.560000	1.6	.0222
1.4	1.020000	1.8	.0096
1.5	.620000	2.0	.0040
1.6	.380000	2.2	.0015
1.7	.240000		
1.8	.156000		
1.9	.105000		
2.0	.072000		
2.1	.054000		
2.2	.041000		
2.3	.033500		
2.4	.028000		
2.5	.024000		
2.6	.021000		
2.7	.019000		
2.8	.017400		
2.9	.016200		
3.0	.015300		
3.5	.012750		

DOUBLE ALUMINIZED MYLAR/SILK NET   SPECIMEN NO. 18

EDGE EVACUATION- OFFSHELF SAMPLE
PURGE GAS- NITROGEN
TEMPERATURE =540. DEG R

SAMPLE DIAMETER = 20.0 INS   SAMPLE HEIGHT = .214 INS
TOTAL NUMBER OF SHIELDS = 20.0   LAYERS/INCH = 98.0

VACUUM CHAMBER PRESSURE HISTORY		DIFFERENTIAL PRESSURE ACROSS SAMPLE	
TIME MIN	PRESSURE TORR	TIME MIN	PRESSURE TORR
.1	410.000000	.1	.0840
.2	250.000000	.2	.0730
.3	153.000000	.3	.0710
.4	97.500000	.4	.0710
.5	61.000000	.5	.0720
.6	38.000000	.6	.0730
.7	24.000000	.7	.0750
.8	16.000000	.8	.0830
.9	9.900000	.9	.1050
1.0	6.600000	1.0	.1890
1.1	4.500000	1.1	.5100
1.2	3.000000	1.2	.8000
1.3	2.000000	1.3	1.0200
1.4	1.600000	1.4	1.1100
1.5	1.110000	1.6	1.1400
1.6	.850000	1.8	1.1100
1.7	.690000	2.0	1.0400
1.8	.580000	2.2	.9450
1.9	.490000	2.4	.8700
2.0	.430000	3.0	.7100
2.1	.380000	4.0	.5400
2.2	.350000	6.0	.3500
2.3	.330000	13.8	.1140
2.4	.300000	27.8	.0560
2.5	.280000	45.8	.0320
2.6	.265000	69.8	.0198
2.7	.263000	129.8	.0105
2.8	.237000	236.0	.0056
2.9	.225000	390.0	.0035
3.0	.213000	1337.0	.0013
6.0	.093000		
20.0	.003300		
60.0	.000700		
105.0	.000400		
135.0	.000030		
236.0	.000170		
286.0	.000120		
390.0	.000100		
1337.0	.000017		

DOUBLE ALUMINIZED MYLAR/SILK NET   SPECIMEN NO. 18

EDGE EVACUATION-PRECONDITIONED SAMPLE
PURGE GAS- NITROGEN
TEMPERATURE =540. DEG R
SAMPLE DIAMETER = 20.0 INS   SAMPLE HEIGHT = .214 INS
TOTAL NUMBER OF SHIELDS = 20.0   LAYERS/INCH = 98.0

VACUUM CHAMBER PRESSURE HISTORY		DIFFERENTIAL PRESSURE ACROSS SAMPLE	
TIME MIN	PRESSURE TORR	TIME MIN	PRESSURE TORR
.1	400.000000	.1	.0750
.2	234.000000	.2	.0600
.3	150.000000	.3	.0570
.4	97.500000	.4	.0570
.5	60.000000	.5	.0570
.6	38.000000	.6	.0550
.7	24.000000	.7	.0520
.8	15.300000	.8	.0480
.9	9.750000	.9	.0430
1.0	6.300000	1.0	.0370
1.1	4.100000	1.1	.0360
1.2	2.520000	1.2	.0350
1.3	1.560000	1.3	.0310
1.4	.990000	1.4	.0250
1.5	.620000	1.6	.0186
1.6	.360000	1.8	.0093
1.7	.230000	2.0	.0018
1.8	.141000	2.2	.0002
1.9	.096000		
2.0	.064000		
2.1	.046000		
2.2	.034000		
2.3	.025500		
2.4	.020400		
2.5	.016800		

DOUBLE ALUMINIZED MYLAR/SILK NET   SPECIMEN NO.   19

EDGE EVACUATION- OFFSHELF SAMPLE
PURGE GAS- NITROGEN
TEMPERATURE =540. DEG R
SAMPLE DIAMETER = 15.0 INS   SAMPLE HEIGHT = .214 INS
TOTAL NUMBER OF SHIELDS = 20.0   LAYERS/INCH = 98.0

| VACUUM CHAMBER PRESSURE HISTORY | | DIFFERENTIAL PRESSURE ACROSS SAMPLE | |
| TIME | PRESSURE | TIME | PRESSURE |
MIN	TORR	MIN	TORR
.1	400.000000	.1	.0270
.2	250.000000	.2	.0250
.3	150.000000	.3	.0250
.4	93.000000	.4	.0240
.5	59.000000	.5	.0240
.6	38.000000	.6	.0234
.7	24.000000	.7	.0231
.8	15.000000	.8	.0216
.9	9.900000	.9	.0213
1.0	6.500000	1.0	.0267
1.1	4.500000	1.2	.1860
1.2	3.100000	1.4	.3500
1.3	2.000000	1.6	.4250
1.4	1.320000	1.8	.4350
1.5	.990000	2.0	.4300
1.6	.740000	2.2	.4000
1.7	.580000	2.4	.3750
1.8	.460000	2.6	.3500
1.9	.380000	3.0	.3200
2.0	.330000	4.0	.2370
2.1	.290000	6.0	.1590
2.2	.260000	13.9	.0550
2.3	.235000	25.9	.0290
2.4	.213000	43.9	.0165
2.5	.198000	67.9	.0108
2.6	.186000	127.9	.0058
4.0	.105000	187.9	.0043
6.0	.067000	256.0	.0032
13.0	.004300	1497.0	.0020
20.0	.001750		
35.0	.000940		
57.0	.000620		
94.0	.000360		
122.0	.000280		
221.0	.000160		
302.0	.000120		
497.0	.000086		
1438.0	.000018		

DOUBLE ALUMINIZED MYLAR/SILK NET   SPECIMEN NO. 19

EDGE EVACUATION-PRECONDITIONED SAMPLE
PURGE GAS- NITROGEN
TEMPERATURE =540. DEG R
SAMPLE DIAMETER = 15.0 INS   SAMPLE HEIGHT = .214 INS
TOTAL NUMBER OF SHIELDS = 20.0   LAYERS/INCH = 98.0

VACUUM CHAMBER PRESSURE HISTORY		DIFFERENTIAL PRESSURE ACROSS SAMPLE	
TIME MIN	PRESSURE TORR	TIME MIN	PRESSURE TORR
.1	400.000000	.1	.0370
.2	231.000000	.2	.0320
.3	147.000000	.3	.0291
.4	96.000000	.4	.0291
.5	58.000000	.5	.0291
.6	37.000000	.6	.0291
.7	24.000000	.7	.0282
.8	14.400000	.8	.0255
.9	9.300000	.9	.0228
1.0	6.000000	1.0	.0198
1.1	4.000000	1.2	.0191
1.2	2.500000	1.3	.0180
1.3	1.440000	1.4	.0153
1.4	.960000	1.6	.0093
1.5	.580000	1.7	.0065
1.6	.360000	1.8	.0043
1.7	.230000	1.9	.0027
1.8	.141000	2.0	.0015
1.9	.093000	2.1	.0008
2.0	.062000	2.2	.0003
2.1	.045000		
2.2	.034000		
2.3	.026000		
2.4	.020000		
2.5	.016000		

C-5

DOUBLE ALUMINIZED MYLAR/SILK NET   SPECIMEN NO. 20

EDGE EVACUATION= OFFSHELF SAMPLE
PURGE GAS= NITROGEN
TEMPERATURE =540. DEG R
SAMPLE DIAMETER = 27.0 INS   SAMPLE HEIGHT = .826 INS
TOTAL NUMBER OF SHIELDS = 80.0   LAYERS/INCH = 98.0

VACUUM CHAMBER PRESSURE HISTORY		DIFFERENTIAL PRESSURE ACROSS SAMPLE	
TIME MIN	PRESSURE TORR	TIME MIN	PRESSURE TORR
.1	410.000000	.1	.1860
.2	250.000000	.2	.1650
.3	156.000000	.3	.1600
.4	96.000000	.4	.1650
.5	60.000000	.5	.1650
.6	36.000000	.6	.1680
.7	25.000000	.7	.1740
.8	16.000000	.8	.1950
.9	9.900000	.9	.2400
1.0	6.600000	1.0	.3700
1.1	4.900000	1.1	.7000
1.2	3.700000	1.2	.9100
1.3	2.900000	1.4	1.0500
1.4	2.400000	1.6	1.0500
1.5	2.010000	1.8	1.0200
1.6	1.740000	2.0	.9600
1.7	1.680000	2.2	.9300
1.8	1.530000	2.4	.0860
1.9	1.400000	2.6	.8250
2.0	1.290000	2.8	.7900
2.1	1.200000	3.0	.0760
2.2	1.140000	4.0	.6500
2.3	1.070000	5.0	.5750
2.4	1.010000	13.8	.2900
2.5	.950000	31.8	.1650
2.6	.900000	43.8	.1290
2.7	.870000	55.8	.1050
2.8	.830000	67.8	.0840
2.9	.790000	79.8	.0750
3.0	.755000	91.8	.0640
6.0	.400000	115.8	.0550
12.0	.235000	1067.0	.0000
25.0	.132000		
45.0	.081000		
65.0	.059000		
75.0	.052000		
128.0	.003400		
135.0	.003000		
1067.0	.000900		

DOUBLE ALUMINIZED MYLAR/SILK NET   SPECIMEN NO. 20

EDGE EVACUATION-PRECONDITIONED SAMPLE
PURGE GAS- NITROGEN
TEMPERATURE =540. DEG R
SAMPLE DIAMETER = 27.0 INS   SAMPLE HEIGHT = .826 INS
TOTAL NUMBER OF SHIELDS = 80.0   LAYERS/INCH = 98.0

VACUUM CHAMBER PRESSURE HISTORY		DIFFERENTIAL PRESSURE ACROSS SAMPLE	
TIME MIN	PRESSURE TORR	TIME MIN	PRESSURE TORR
.1	410.000000	.1	.2020
.2	240.000000	.2	.1710
.3	153.000000	.3	.1620
.4	99.000000	.4	.1590
.5	60.000000	.5	.1560
.6	38.000000	.6	.1500
.7	24.000000	.7	.1410
.8	16.000000	.8	.1260
.9	9.900000	.9	.1110
1.0	6.600000	1.0	.0975
1.1	4.500000	1.2	.0900
1.2	2.900000	1.4	.0550
1.3	1.860000	1.6	.0280
1.4	.990000	1.8	.0138
1.5	.660000	2.0	.0070
1.6	.360000	2.2	.0047
1.7	.220000	2.4	.0038
1.8	.144000	2.6	.0034
1.9	.096000	2.8	.0026
2.0	.065000		
2.1	.047000		
2.2	.036000		
2.3	.028000		
2.4	.023000		
2.5	.018600		

DOUBLE ALUMINIZED MYLAR/SILK NET   SPECIMEN NO. 20

EDGE EVACUATION-PRECONDITIONED SAMPLE
PURGE GAS- HELIUM
TEMPERATURE =540. DEG R
SAMPLE DIAMETER = 27.0 INS   SAMPLE HEIGHT = .826 INS
TOTAL NUMBER OF SHIELDS = 80.0   LAYERS/INCH = 98.0

VACUUM CHAMBER PRESSURE HISTORY		DIFFERENTIAL PRESSURE ACROSS SAMPLE	
TIME MIN	PRESSURE TORR	TIME MIN	PRESSURE TORR
.1	410.000000	.1	.2100
.2	250.000000	.2	.1860
.3	156.000000	.3	.1830
.4	96.000000	.4	.1830
.5	60.000000	.5	.1740
.6	37.000000	.6	.1650
.7	23.000000	.7	.1500
.8	14.100000	.8	.1350
.9	9.100000	.9	.1140
1.0	5.900000	1.0	.0960
1.1	4.000000	1.1	.0800
1.2	2.500000	1.2	.0610
1.3	1.550000	1.4	.0395
1.4	1.050000	1.6	.0186
1.5	.700000	1.8	.0084
1.6	.480000	2.0	.0040
1.7	.340000	2.2	.0022
1.8	.120000	2.4	.0014
1.9	.078000	2.6	.0013
2.0	.053000		
2.1	.038000		
2.2	.027000		
2.3	.019000		
2.4	.014400		
2.5	.011100		
2.6	.008400		
2.7	.007000		
4.0	.000200		
10.0	.000074		
15.0	.000062		
38.0	.000048		
52.0	.000046		
76.0	.000044		

DOUBLE ALUMINIZED MYLAR/SILK NET   SPECIMEN NO. 20

EDGE EVACUATION-PRECONDITIONED SAMPLE
PURGE GAS- ARGON
TEMPERATURE =540. DEG R
SAMPLE DIAMETER = 27.0 INS   SAMPLE HEIGHT = .826 INS
TOTAL NUMBER OF SHIELDS = 80.0   LAYERS/INCH = 98.0

VACUUM CHAMBER PRESSURE HISTORY		DIFFERENTIAL PRESSURE ACROSS SAMPLE	
TIME MIN	PRESSURE TORR	TIME MIN	PRESSURE TORR
.1	400.000000	.1	.2450
.2	250.000000	.2	.1980
.3	156.000000	.3	.1950
.4	105.000000	.4	.1950
.5	65.000000	.5	.1890
.6	41.000000	.6	.1830
.7	27.000000	.7	.1740
.8	18.000000	.8	.1620
.9	11.100000	.9	.1470
1.0	7.500000	1.0	.1290
1.1	5.000000	1.2	.1110
1.2	3.200000	1.4	.0700
1.3	2.100000	1.6	.0350
1.4	1.400000	1.8	.0156
1.5	.900000	2.0	.0066
1.6	.640000	2.2	.0032
1.7	.490000	2.4	.0018
1.8	.400000	2.6	.0013
1.9	.120000	2.8	.0009
2.0	.081000	3.0	.0007
2.1	.060000	3.2	.0003
2.2	.046000	3.4	.0002
2.3	.037000		
2.4	.031000		
2.5	.026000		
2.6	.022000		
2.7	.019000		
2.8	.017700		
2.9	.016200		
5.0	.000500		
10.0	.000200		
16.0	.000120		
49.0	.000056		

DOUBLE ALUMINIZED MYLAR/SILK NET   SPECIMEN NO. 20

EDGE EVACUATION-PRECONDITIONED SAMPLE
PURGE GAS- HELIUM
TEMPERATURE =497. DEG R
SAMPLE DIAMETER = 27.0 INS   SAMPLE HEIGHT = .826 INS
TOTAL NUMBER OF SHIELDS = 80.0   LAYERS/INCH = 98.0

VACUUM CHAMBER PRESSURE HISTORY		DIFFERENTIAL PRESSURE ACROSS SAMPLE	
TIME MIN	PRESSURE TORR	TIME MIN	PRESSURE TORR
.1	420.000000	.1	.1600
.2	260.000000	.2	.1560
.3	162.000000	.3	.1560
.4	102.000000	.4	.1530
.5	63.000000	.5	.1470
.6	39.000000	.6	.1350
.7	24.600000	.7	.1260
.8	15.900000	.8	.1110
.9	10.200000	.9	.0930
1.0	6.600000	1.0	.0760
1.1	4.300000	1.1	.0530
1.2	2.400000	1.2	.0570
1.3	1.770000	1.3	.0470
1.4	1.080000	1.4	.0390
1.5	.660000	1.5	.0335
1.6	.440000	1.6	.0210
1.7	.310000	1.7	.0300
1.8	.220000	1.8	.0305
1.9	.156000	1.9	.0310
2.0	.120000	2.0	.0315
2.2	.082000	2.2	.0310
2.4	.066000	2.4	.0310
2.6	.057500	2.6	.0310
2.8	.053000	2.8	.0305
3.0	.050000	3.0	.0300
3.5	.050000	3.5	.0300
4.0	.050000	4.0	.0300

DOUBLE ALUMINIZED MYLAR/SILK NET   SPECIMEN NO. 20

EDGE EVACUATION-PRECONDITIONED SAMPLE
PURGE GAS- HELIUM
TEMPERATURE =479. DEG R
SAMPLE DIAMETER = 27.0 INS   SAMPLE HEIGHT = .826 INS
TOTAL NUMBER OF SHIELDS = 80.0   LAYERS/INCH = 98.0

VACUUM CHAMBER PRESSURE HISTORY		DIFFERENTIAL PRESSURE ACROSS SAMPLE	
TIME MIN	PRESSURE TORR	TIME MIN	PRESSURE TORR
.1	415.000000	.1	.1600
.2	250.000000	.2	.1560
.3	159.000000	.3	.1530
.4	102.000000	.4	.1500
.5	62.500000	.5	.1440
.6	39.000000	.6	.1350
.7	24.000000	.7	.1245
.8	15.900000	.8	.1080
.9	10.200000	.9	.0915
1.0	6.600000	1.0	.0780
1.1	4.500000	1.1	.0500
1.2	3.000000	1.2	.0550
1.3	1.890000	1.3	.0430
1.4	1.020000	1.4	.0320
1.5	.630000	1.5	.0230
1.6	.380000	1.6	.0165
1.7	.243000	1.7	.0126
1.8	.165000	1.8	.0101
1.9	.111000	1.9	.0079
2.0	.076000	2.0	.0069
2.2	.041000	2.2	.0059
2.4	.024000	2.4	.0054
2.6	.018600	2.6	.0051
2.8	.015000	2.8	.0050
3.0	.012900	3.0	.0049
3.5	.010800	3.5	.0045
4.0	.102000	4.0	.0045
4.5	.010000	4.5	.0045
5.0	.009450	.0	.0000

DOUBLE ALUMINIZED MYLAR/SILK NET   SPECIMEN NO. 20

EDGE EVACUATION-PRECONDITIONED SAMPLE
PURGE GAS= HELIUM
TEMPERATURE =490. DEG R
SAMPLE DIAMETER = 27.0 INS   SAMPLE HEIGHT = .826 INS
TOTAL NUMBER OF SHIELDS = 80.0   LAYERS/INCH = 98.0

VACUUM CHAMBER PRESSURE HISTORY		DIFFERENTIAL PRESSURE ACROSS SAMPLE	
TIME MIN	PRESSURE TORR	TIME MIN	PRESSURE TORR
.1	400.000000	.1	.1700
.2	250.000000	.2	.1620
.3	153.000000	.3	.1590
.4	99.000000	.4	.1500
.6	38.000000	.6	.1380
.7	24.000000	.7	.1260
.8	15.600000	.8	.1110
.9	10.200000	.9	.0945
1.0	6.500000	1.0	.0630
1.1	4.400000	1.1	.0520
1.2	3.000000	1.2	.0595
1.3	1.900000	1.3	.0480
1.4	1.300000	1.4	.0390
1.5	.870000	1.5	.0320
1.6	.390000	1.6	.0270
1.7	.250000	1.7	.0235
1.8	.162000	1.8	.0210
1.9	.114000	1.9	.0200
2.0	.081000	2.0	.0192
2.2	.047000	2.2	.0180
2.4	.033000	2.4	.0171
2.6	.026000	2.6	.0162
2.8	.022500	2.8	.0156
3.0	.020700	3.0	.0150
3.5	.019500	3.5	.0141
4.0	.018300	4.0	.0132
5.0	.017250	5.0	.0132

DOUBLE ALUMINIZED MYLAR/SILK NET   SPECIMEN NO. 20

EDGE EVACUATION- OFFSHELF SAMPLE
PURGE GAS- HELIUM
TEMPERATURE =236. DEG R
SAMPLE DIAMETER = 27.0 INS   SAMPLE HEIGHT = .826 INS
TOTAL NUMBER OF SHIELDS = 80.0   LAYERS/INCH = 98.0

VACUUM CHAMBER PRESSURE HISTORY		DIFFERENTIAL PRESSURE ACROSS SAMPLE	
TIME MIN	PRESSURE TORR	TIME MIN	PRESSURE TORR
.1	460.000000	.1	.0800
.2	310.000000	.2	.0810
.3	210.000000	.3	.0780
.4	147.000000	.4	.0780
.5	102.000000	.5	.0760
.6	69.000000	.6	.0730
.7	47.000000	.7	.0720
.8	34.000000	.8	.0670
.9	23.500000	.9	.0620
1.0	17.000000	1.0	.0570
1.1	11.700000	1.1	.0500
1.2	8.400000	1.2	.0430
1.3	6.000000	1.3	.0375
1.4	4.600000	1.4	.0270
1.5	3.400000	1.5	.0300
1.6	2.250000	1.6	.0260
1.7	1.560000	1.7	.0195
1.8	1.110000	1.8	.0138
1.9	.750000	1.9	.0090
2.0	.510000	2.0	.0058
2.2	.250000	2.2	.0031
2.4	.126000	2.4	.0023
2.6	.066000	2.6	.0021
2.8	.037000	2.8	.0014
3.0	.023000	3.0	.0006
3.5	.007600	3.5	.0001
4.0	.003500		

DOUBLE ALUMINIZED MYLAR/SILK NET   SPECIMEN NO. 20A

EDGE EVACUATION- OFFSHELF SAMPLE
PURGE GAS- NITROGEN
TEMPERATURE =540. DEG R
SAMPLE DIAMETER = 27.0 INS   SAMPLE HEIGHT = .826 INS
TOTAL NUMBER OF SHIELDS = 80.0   LAYERS/INCH = 98.0

VACUUM CHAMBER PRESSURE HISTORY		DIFFERENTIAL PRESSURE ACROSS SAMPLE	
TIME MIN	PRESSURE TORR	TIME MIN	PRESSURE TORR
.1	410.000000	.1	.1860
.2	250.000000	.2	.1650
.3	156.000000	.3	.1600
.4	96.000000	.4	.1650
.5	60.000000	.5	.1650
.6	36.000000	.6	.1680
.7	25.000000	.7	.1740
.8	16.000000	.8	.1950
.9	9.900000	.9	.2400
1.0	6.600000	1.0	.3700
1.1	4.900000	1.1	.7000
1.2	3.700000	1.2	.9100
1.3	2.900000	1.4	1.0500
1.4	2.400000	1.6	1.0500
1.5	2.010000	1.8	1.0200
1.6	1.740000	2.0	.9600
1.7	1.680000	2.2	.9300
1.8	1.530000	2.4	.0860
1.9	1.400000	2.6	.8250
2.0	1.290000	2.8	.7900
2.1	1.200000	3.0	.0760
2.2	1.140000	4.0	.6500
2.3	1.070000	5.0	.5750
2.4	1.010000	13.8	.2900
2.5	.950000	31.8	.1650
2.6	.900000	43.8	.1290
2.7	.870000	55.8	.1050
2.8	.830000	67.8	.0840
2.9	.790000	79.8	.0750
3.0	.755000	91.8	.0640
6.0	.400000	115.8	.0550
12.0	.235000	1067.0	.0000
25.0	.132000		
45.0	.081000		
65.0	.059000		
75.0	.052000		
128.0	.003400		
135.0	.003000		
1067.0	.000900		

DOUBLE ALUMINIZED MYLAR/SILK NET   SPECIMEN NO. 20A

EDGE EVACUATION-PRECONDITIONED SAMPLE
PURGE GAS- NITROGEN
TEMPERATURE =540. DEG R
SAMPLE DIAMETER = 27.0 INS   SAMPLE HEIGHT = .826 INS
TOTAL NUMBER OF SHIELDS = 80.0   LAYERS/INCH = 98.0

VACUUM CHAMBER PRESSURE HISTORY		DIFFERENTIAL PRESSURE ACROSS SAMPLE	
TIME MIN	PRESSURE TORR	TIME MIN	PRESSURE TORR
.1	410.000000	.1	.2020
.2	240.000000	.2	.1710
.3	153.000000	.3	.1620
.4	99.000000	.4	.1590
.5	60.000000	.5	.1560
.6	38.000000	.6	.1500
.7	24.000000	.7	.1410
.8	16.000000	.8	.1260
.9	9.900000	.9	.1110
1.0	6.600000	1.0	.0975
1.1	4.500000	1.2	.0900
1.2	2.900000	1.4	.0550
1.3	1.860000	1.6	.0280
1.4	.990000	1.8	.0138
1.5	.660000	2.0	.0070
1.6	.360000	2.2	.0047
1.7	.220000	2.4	.0038
1.8	.144000	2.6	.0034
1.9	.096000	2.8	.0026
2.0	.065000		
2.1	.047000		
2.2	.036000		
2.3	.028000		
2.4	.023000		
2.5	.018600		

DOUBLE ALUMINIZED MYLAR/SILK NET   SPECIMEN NO. 20A

EDGE EVACUATION-PRECONDITIONED SAMPLE
PURGE GAS- HELIUM
TEMPERATURE =540. DEG R
SAMPLE DIAMETER = 27.0 INS   SAMPLE HEIGHT = .826 INS
TOTAL NUMBER OF SHIELDS = 80.0   LAYERS/INCH = 98.0

VACUUM CHAMBER PRESSURE HISTORY		DIFFERENTIAL PRESSURE ACROSS SAMPLE	
TIME MIN	PRESSURE TORR	TIME MIN	PRESSURE TORR
.1	410.000000	.1	.2100
.2	250.000000	.2	.1860
.3	156.000000	.3	.1830
.4	96.000000	.4	.1830
.5	60.000000	.5	.1740
.6	37.000000	.6	.1650
.7	23.000000	.7	.1500
.8	14.100000	.8	.1350
.9	9.100000	.9	.1140
1.0	5.900000	1.0	.0960
1.1	4.000000	1.1	.0800
1.2	2.500000	1.2	.0610
1.3	1.550000	1.4	.0395
1.4	1.050000	1.6	.0186
1.5	.700000	1.8	.0084
1.6	.480000	2.0	.0040
1.7	.340000	2.2	.0022
1.8	.120000	2.4	.0014
1.9	.078000	2.6	.0013
2.0	.053000		
2.1	.038000		
2.2	.027000		
2.3	.019000		
2.4	.014400		
2.5	.011100		
2.6	.008400		
2.7	.007000		
4.0	.000200		
10.0	.000074		
15.0	.000062		
38.0	.000048		
52.0	.000046		
76.0	.000044		

DOUBLE ALUMINIZED MYLAR/SILK NET   SPECIMEN NO. 20A

EDGE EVACUATION-PRECONDITIONED SAMPLE
PURGE GAS- ARGON
TEMPERATURE =540. DEG R
SAMPLE DIAMETER = 27.0 INS   SAMPLE HEIGHT = .826 INS
TOTAL NUMBER OF SHIELDS = 80.0   LAYERS/INCH = 98.0

VACUUM CHAMBER PRESSURE HISTORY		DIFFERENTIAL PRESSURE ACROSS SAMPLE	
TIME MIN	PRESSURE TORR	TIME MIN	PRESSURE TORR
.1	400.000000	.1	.2450
.2	250.000000	.2	.1980
.3	156.000000	.3	.1950
.4	105.000000	.4	.1950
.5	65.000000	.5	.1890
.6	41.000000	.6	.1830
.7	27.000000	.7	.1740
.8	18.000000	.8	.1620
.9	11.100000	.9	.1470
1.0	7.500000	1.0	.1290
1.1	5.000000	1.2	.1110
1.2	3.200000	1.4	.0700
1.3	2.100000	1.6	.0350
1.4	1.400000	1.8	.0156
1.5	.900000	2.0	.0066
1.6	.640000	2.2	.0032
1.7	.490000	2.4	.0018
1.8	.400000	2.6	.0013
1.9	.120000	2.8	.0009
2.0	.081000	3.0	.0007
2.1	.060000	3.2	.0003
2.2	.046000	3.4	.0002
2.3	.037000		
2.4	.031000		
2.5	.026000		
2.6	.022000		
2.7	.019000		
2.8	.017700		
2.9	.016200		
5.0	.000500		
10.0	.000200		
16.0	.000120		
49.0	.000056		

DOUBLE ALUMINIZED MYLAR/SILK NET   SPECIMEN NO. 20B

EDGE EVACUATION-PRECONDITIONED SAMPLE
PURGE GAS- HELIUM
TEMPERATURE =497. DEG R
SAMPLE DIAMETER = 27.0 INS   SAMPLE HEIGHT = .826 INS
TOTAL NUMBER OF SHIELDS = 80.0   LAYERS/INCH = 98.0

VACUUM CHAMBER PRESSURE HISTORY		DIFFERENTIAL PRESSURE ACROSS SAMPLE	
TIME MIN	PRESSURE TORR	TIME MIN	PRESSURE TORR
.1	420.000000	.1	.1600
.2	260.000000	.2	.1560
.3	162.000000	.3	.1560
.4	102.000000	.4	.1530
.5	63.000000	.5	.1470
.6	39.000000	.6	.1350
.7	24.600000	.7	.1260
.8	15.900000	.8	.1110
.9	10.200000	.9	.0930
1.0	6.600000	1.0	.0760
1.1	4.300000	1.1	.0530
1.2	2.400000	1.2	.0570
1.3	1.770000	1.3	.0470
1.4	1.080000	1.4	.0390
1.5	.660000	1.5	.0335
1.6	.440000	1.6	.0210
1.7	.310000	1.7	.0300
1.8	.220000	1.8	.0305
1.9	.156000	1.9	.0310
2.0	.120000	2.0	.0315
2.2	.082000	2.2	.0310
2.4	.066000	2.4	.0310
2.6	.057500	2.6	.0310
2.8	.053000	2.8	.0305
3.0	.050000	3.0	.0300
3.5	.050000	3.5	.0300
4.0	.050000	4.0	.0300

DOUBLE ALUMINIZED MYLAR/SILK NET   SPECIMEN NO. 20B

EDGE EVACUATION-PRECONDITIONED SAMPLE
PURGE GAS- HELIUM
TEMPERATURE =479. DEG R
SAMPLE DIAMETER = 27.0 INS   SAMPLE HEIGHT = .826 INS
TOTAL NUMBER OF SHIELDS = 80.0   LAYERS/INCH = 98.0

VACUUM CHAMBER PRESSURE HISTORY		DIFFERENTIAL PRESSURE ACROSS SAMPLE	
TIME MIN	PRESSURE TORR	TIME MIN	PRESSURE TORR
.1	415.000000	.1	.1600
.2	250.000000	.2	.1560
.3	159.000000	.3	.1530
.4	102.000000	.4	.1500
.5	62.500000	.5	.1440
.6	39.000000	.6	.1350
.7	24.000000	.7	.1245
.8	15.900000	.8	.1080
.9	10.200000	.9	.0915
1.0	6.600000	1.0	.0780
1.1	4.500000	1.1	.0500
1.2	3.000000	1.2	.0550
1.3	1.890000	1.3	.0430
1.4	1.020000	1.4	.0320
1.5	.630000	1.5	.0230
1.6	.380000	1.6	.0165
1.7	.243000	1.7	.0126
1.8	.165000	1.8	.0101
1.9	.111000	1.9	.0079
2.0	.076000	2.0	.0069
2.2	.041000	2.2	.0059
2.4	.024000	2.4	.0054
2.6	.018600	2.6	.0051
2.8	.015000	2.8	.0050
3.0	.012900	3.0	.0049
3.5	.010800	3.5	.0045
4.0	.102000	4.0	.0045
4.5	.010000	4.5	.0045
5.0	.009450	.0	.0000

DOUBLE ALUMINIZED MYLAR/SILK NET   SPECIMEN NO. 20B

EDGE EVACUATION-PRECONDITIONED SAMPLE
PURGE GAS- HELIUM
TEMPERATURE =490. DEG R
SAMPLE DIAMETER = 27.0 INS   SAMPLE HEIGHT = .826 INS
TOTAL NUMBER OF SHIELDS = 80.0   LAYERS/INCH = 98.0

VACUUM CHAMBER PRESSURE HISTORY		DIFFERENTIAL PRESSURE ACROSS SAMPLE	
TIME MIN	PRESSURE TORR	TIME MIN	PRESSURE TORR
.1	400.000000	.1	.1700
.2	250.000000	.2	.1620
.3	153.000000	.3	.1590
.4	99.000000	.4	.1500
.6	38.000000	.6	.1380
.7	24.000000	.7	.1260
.8	15.600000	.8	.1110
.9	10.200000	.9	.0945
1.0	6.500000	1.0	.0630
1.1	4.400000	1.1	.0520
1.2	3.000000	1.2	.0595
1.3	1.900000	1.3	.0480
1.4	1.300000	1.4	.0390
1.5	.870000	1.5	.0320
1.6	.390000	1.6	.0270
1.7	.250000	1.7	.0235
1.8	.162000	1.8	.0210
1.9	.114000	1.9	.0200
2.0	.081000	2.0	.0192
2.2	.047000	2.2	.0180
2.4	.033000	2.4	.0171
2.6	.026000	2.6	.0162
2.8	.022500	2.8	.0156
3.0	.020700	3.0	.0150
3.5	.019500	3.5	.0141
4.0	.018300	4.0	.0132
5.0	.017250	5.0	.0132

DOUBLE ALUMINIZED MYLAR/SILK NET   SPECIMEN NO. 20C

EDGE EVACUATION- OFFSHELF SAMPLE
PURGE GAS- HELIUM
TEMPERATURE =236. DEG R
SAMPLE DIAMETER = 27.0 INS   SAMPLE HEIGHT = .826 INS
TOTAL NUMBER OF SHIELDS = 80.0   LAYERS/INCH = 98.0

VACUUM CHAMBER PRESSURE HISTORY		DIFFERENTIAL PRESSURE ACROSS SAMPLE	
TIME MIN	PRESSURE TORR	TIME MIN	PRESSURE TORR
.1	460.000000	.1	.0800
.2	310.000000	.2	.0810
.3	210.000000	.3	.0780
.4	147.000000	.4	.0780
.5	102.000000	.5	.0760
.6	69.000000	.6	.0730
.7	47.000000	.7	.0720
.8	34.000000	.8	.0670
.9	23.500000	.9	.0620
1.0	17.000000	1.0	.0570
1.1	11.700000	1.1	.0500
1.2	8.400000	1.2	.0430
1.3	6.000000	1.3	.0375
1.4	4.600000	1.4	.0270
1.5	3.400000	1.5	.0300
1.6	2.250000	1.6	.0260
1.7	1.560000	1.7	.0195
1.8	1.110000	1.8	.0138
1.9	.750000	1.9	.0090
2.0	.510000	2.0	.0058
2.2	.250000	2.2	.0031
2.4	.126000	2.4	.0023
2.6	.066000	2.6	.0021
2.8	.037000	2.8	.0014
3.0	.023000	3.0	.0006
3.5	.007600	3.5	.0001
4.0	.003500		

CRINKLED SINGLE ALUMINIZED MYLAR   SPECIMEN NO. 21A

EDGE EVACUATION- OFFSHELF SAMPLE
PURGE GAS- NITROGEN
TEMPERATURE =540. DEG R
SAMPLE DIAMETER = 27.0 INS   SAMPLE HEIGHT = .286 INS
TOTAL NUMBER OF SHIELDS = 20.0   LAYERS/INCH = 73.4

| VACUUM CHAMBER PRESSURE HISTORY | | DIFFERENTIAL PRESSURE ACROSS SAMPLE | |
| TIME | PRESSURE | TIME | PRESSURE |
MIN	TORR	MIN	TORR
.1	420.000000	.1	.0600
.2	260.000000	.2	.0510
.3	165.000000	.3	.0520
.4	102.000000	.4	.0520
.5	63.000000	.5	.0520
.6	41.000000	.6	.0510
.7	26.100000	.7	.0590
.8	16.800000	.8	.0460
.9	11.100000	.9	.0420
1.0	7.200000	1.0	.0370
1.1	5.000000	1.2	.0340
1.2	3.500000	1.4	.0300
1.3	2.220000	1.6	.0210
1.4	1.440000	1.8	.0126
1.5	.730000	2.0	.0070
1.6	.440000	2.2	.0049
1.7	.290000	2.4	.0034
1.8	.189000	2.6	.0026
1.9	.126000	2.8	.0021
2.0	.087000	3.0	.0018
2.1	.063000	3.6	.0014
2.2	.049000	4.2	.0034
2.3	.039000	4.4	.0027
2.4	.032500	10.4	.0004
2.5	.027000		
2.6	.023700		
2.7	.021300		
2.8	.019500		
2.9	.018300		
3.0	.017100		
9.0	.000800		
11.0	.000600		
17.0	.000430		
24.0	.000300		
27.0	.000280		
51.0	.000160		
85.0	.000110		
104.0	.000090		

CRINKLED SINGLE ALUMINIZED MYLAR   SPECIMEN NO. 21A

EDGE EVACUATION-PRECONDITIONED SAMPLE
PURGE GAS- NITROGEN
TEMPERATURE =540. DEG R
SAMPLE DIAMETER = 27.0 INS   SAMPLE HEIGHT = .286 INS
TOTAL NUMBER OF SHIELDS = 20.0   LAYERS/INCH = 73.4

VACUUM CHAMBER PRESSURE HISTORY		DIFFERENTIAL PRESSURE ACROSS SAMPLE	
TIME MIN	PRESSURE TORR	TIME MIN	PRESSURE TORR
.1	400.000000	.1	.0600
.2	250.000000	.2	.0540
.3	153.000000	.3	.0530
.4	99.000000	.4	.0530
.5	60.000000	.5	.0530
.6	38.000000	.6	.0520
.7	24.600000	.7	.0500
.8	15.600000	.8	.0470
.9	10.200000	.9	.0410
1.0	6.800000	1.0	.0370
1.1	4.700000	1.1	.0320
1.2	3.200000	1.2	.0340
1.3	2.040000	1.3	.0340
1.4	1.110000	1.4	.0280
1.5	.670000	1.5	.0230
1.6	.400000	1.6	.0156
1.7	.249000	1.7	.0105
1.8	.159000	1.8	.0063
1.9	.105000	1.9	.0035
2.0	.070000	2.0	.0022
2.1	.049000	2.1	.0012
2.2	.036000	2.2	.0006
2.3	.027300	2.3	.0002
2.4	.021000		
2.5	.017100		
2.6	.013800		
2.7	.012000		
2.8	.010200		
2.9	.009000		
3.0	.008000		
4.0	.004500		
6.0	.000400		
8.0	.000200		
14.0	.000120		
23.0	.000100		
41.0	.000093		
78.0	.000082		
120.0	.000076		

CRINKLED SINGLE ALUMINIZED MYLAR   SPECIMEN NO. 21B

EDGE EVACUATION-PRECONDITIONED SAMPLE
PURGE GAS- NITROGEN
TEMPERATURE =540. DEG R
SAMPLE DIAMETER = 27.0 INS   SAMPLE HEIGHT = .235 INS
TOTAL NUMBER OF SHIELDS = 20.0   LAYERS/INCH = 89.4

VACUUM CHAMBER PRESSURE HISTORY		DIFFERENTIAL PRESSURE ACROSS SAMPLE	
TIME MIN	PRESSURE TORR	TIME MIN	PRESSURE TORR
.1	400.000000	.1	.0850
.2	240.000000	.2	.0690
.3	150.000000	.3	.0710
.4	96.000000	.4	.0700
.5	61.000000	.5	.0700
.6	40.000000	.6	.0680
.7	25.000000	.7	.0660
.8	15.600000	.8	.0620
.9	10.200000	.9	.0550
1.0	6.700000	1.0	.0490
1.1	4.600000	1.1	.0425
1.2	3.100000	1.2	.0440
1.3	2.010000	1.3	.0420
1.4	1.110000	1.4	.0350
1.5	.670000	1.5	.0270
1.6	.410000	1.6	.0192
1.7	.255000	1.7	.0126
1.8	.162000	1.8	.0074
1.9	.105000	1.9	.0044
2.0	.075000	2.0	.0026
2.1	.051000	2.1	.0014
2.2	.037000	2.2	.0007
2.3	.028000	2.3	.0003
2.4	.021900		
2.5	.017700		
2.6	.014700		
2.7	.012600		
2.8	.010800		
2.9	.009600		
3.0	.008700		
4.0	.000700		
6.0	.000450		
8.0	.000260		
16.0	.000180		
30.0	.000140		
120.0	.000140		

CRINKLED SINGLE ALUMINIZED MYLAR   SPECIMEN NO. 21C

EDGE EVACUATION-PRECONDITIONED SAMPLE
PURGE GAS- NITROGEN
TEMPERATURE =540. DEG R
SAMPLE DIAMETER = 27.0 INS   SAMPLE HEIGHT = .143 INS
TOTAL NUMBER OF SHIELDS = 20.0   LAYERS/INCH =147.0

VACUUM CHAMBER PRESSURE HISTORY		DIFFERENTIAL PRESSURE ACROSS SAMPLE	
TIME MIN	PRESSURE TORR	TIME MIN	PRESSURE TORR
.1	395.000000	.1	.1800
.2	240.000000	.2	.1400
.3	157.000000	.3	.1290
.4	100.000000	.4	.1260
.5	62.000000	.5	.1170
.6	40.000000	.6	.1110
.7	25.000000	.7	.1050
.8	16.300000	.8	.1020
.9	10.000000	.9	.0930
1.0	6.800000	1.0	.0810
1.1	4.600000	1.1	.0680
1.2	3.200000	1.2	.0670
1.3	1.920000	1.3	.0660
1.4	1.170000	1.4	.0540
1.5	.700000	1.5	.0400
1.6	.430000	1.6	.0290
1.7	.260000	1.7	.0190
1.8	.160000	1.8	.0114
1.9	.105000	1.9	.0066
2.0	.069000	2.0	.0030
2.1	.047000	2.1	.0010
2.2	.034000		
2.3	.024000		
2.4	.018000		
2.5	.015600		
2.6	.012600		
2.7	.010800		
2.8	.009300		
2.9	.008300		
3.0	.007500		
5.0	.000500		
9.0	.000320		
12.0	.000260		
30.0	.000200		
62.0	.000180		
90.0	.000180		
120.0	.000160		

Appendix C

TEMPERATURE-TIME HISTORIES

During the Task 3 testing, MLI temperature profiles were obtained using radial thermocouple arrays installed at five different locations over the surface of the calorimeter tank (Ref. Figs. 6-6 and 6-18 for these locations). Subsequent to setting the desired hot boundary temperature and filling the cryogen tank to initiate any particular test run, temperature data for each thermocouple were sampled and recorded at nominal 400-sec intervals.

Figs. C-1 and C-2 show the MLI temperature data obtained from the D-location (i.e., the lower dome) thermocouples during Test Run No. 1. The data shown are for representative reflective shields through the thickness, and were reduced and plotted using an existing computer program. Data obtained for shields 5 and 28 are shown in Fig. C-1, while those obtained for shields 56 and 84 are presented in Fig. C-2. The temperature measured for shield 112 and that for the tank wall are not shown, since these temperatures were maintained at the hot and cold boundary values, respectively, throughout the duration of the test.

As shown in these figures for Test Run 1, the MLI was initially at ambient (room) temperature prior to setting the hot and cold boundary values. Consequently, the entire mass of the insulation was slowly chilled to achieve the near-equilibrium values shown at the end of the test. The 5-day period · required to achieve these near-equilibrium temperature values appears to be directly related to the time constant of this particular number of multilayers (Ref. discussion in Section 6.3.2). However, the data shown in the figures provide an excellent graphical representation of the chilldown process.

Similar temperature-time history curves are presented in Figs. C-3 and C-4 for the data obtained by the same D-location thermocouples during Test Run No. 3. Here, the data obtained for shields 5 and 28 are shown in Fig. C-3, whereas those obtained for shields 56 and 84 are given in Fig. C-4.

Fig. C-1   Temperature-Time History Data for Reflective Shields 5 and 28 During Test Run No. 1

C-2

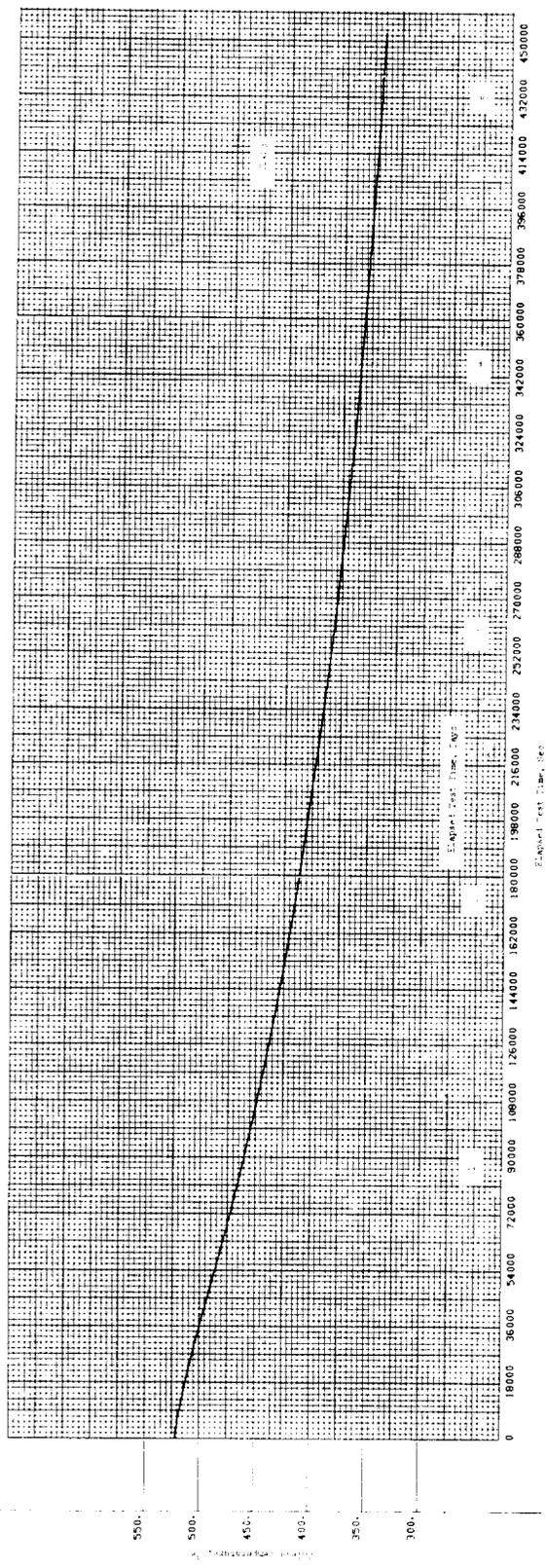Fig. C-2 Temperature-Time History Data for Reflective Shields 56 and 84 During Test Run No. 1

C-3
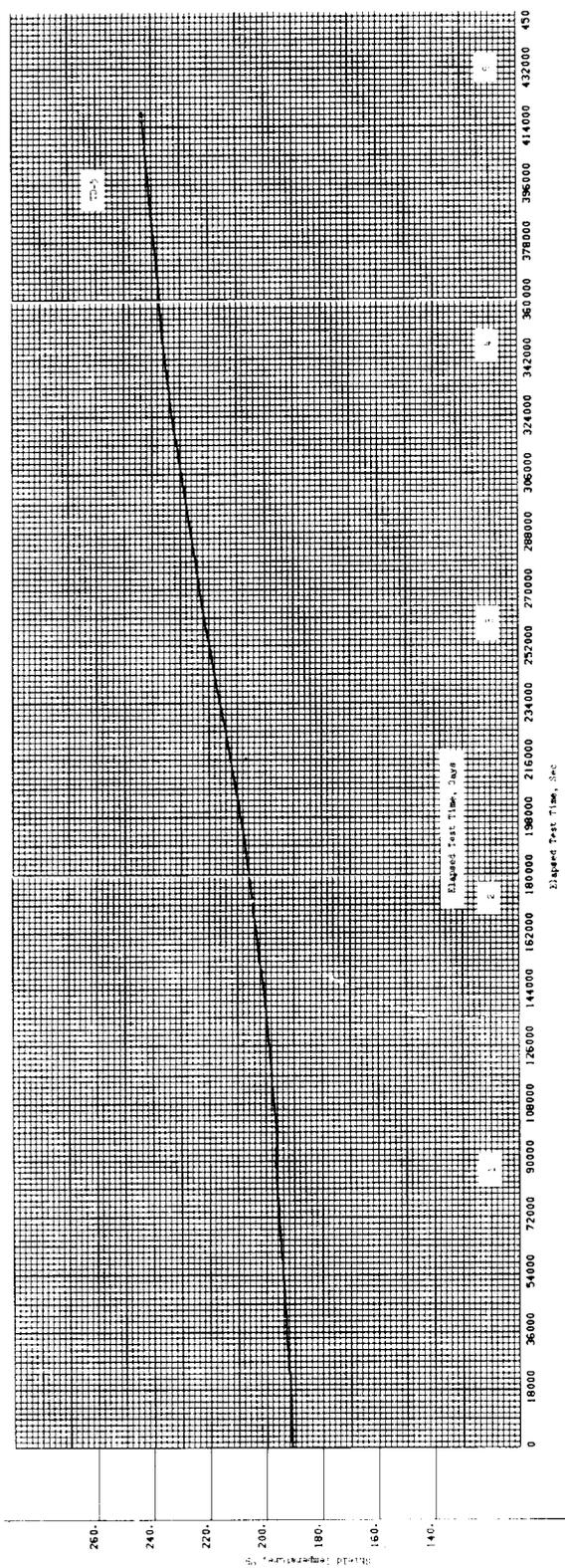
Fig. C-3 Temperature-Time History Data for Reflective Shields 5 and 28 During Test Run No. 3
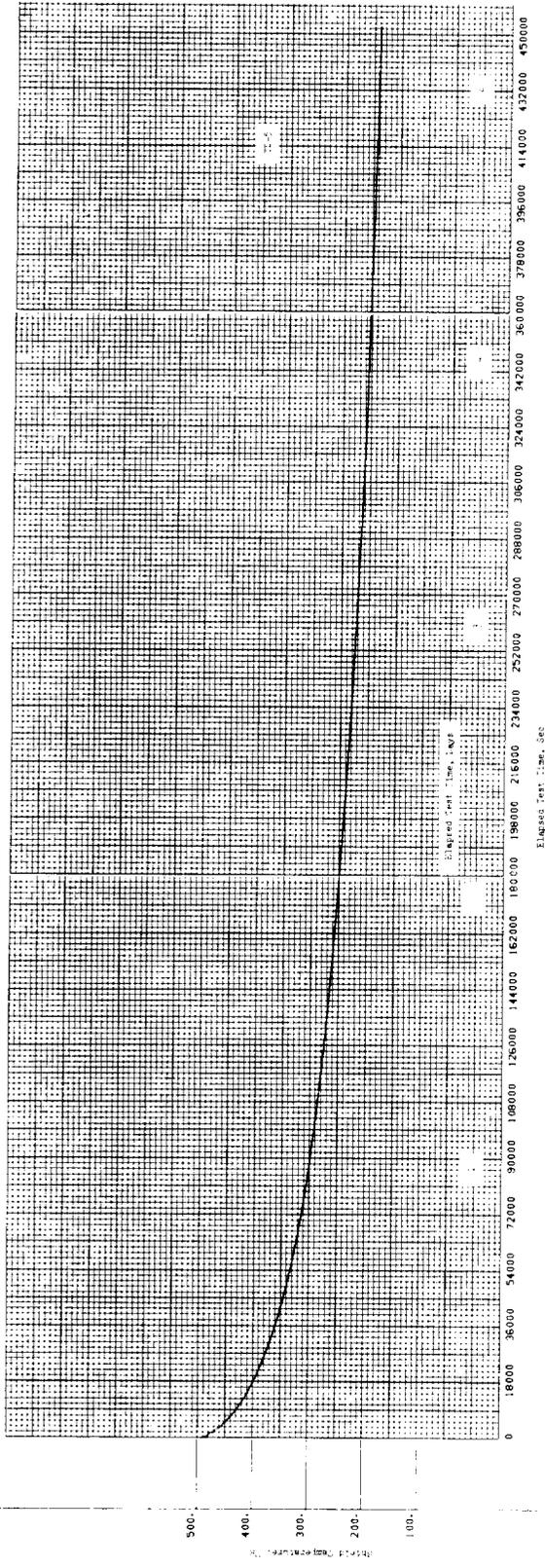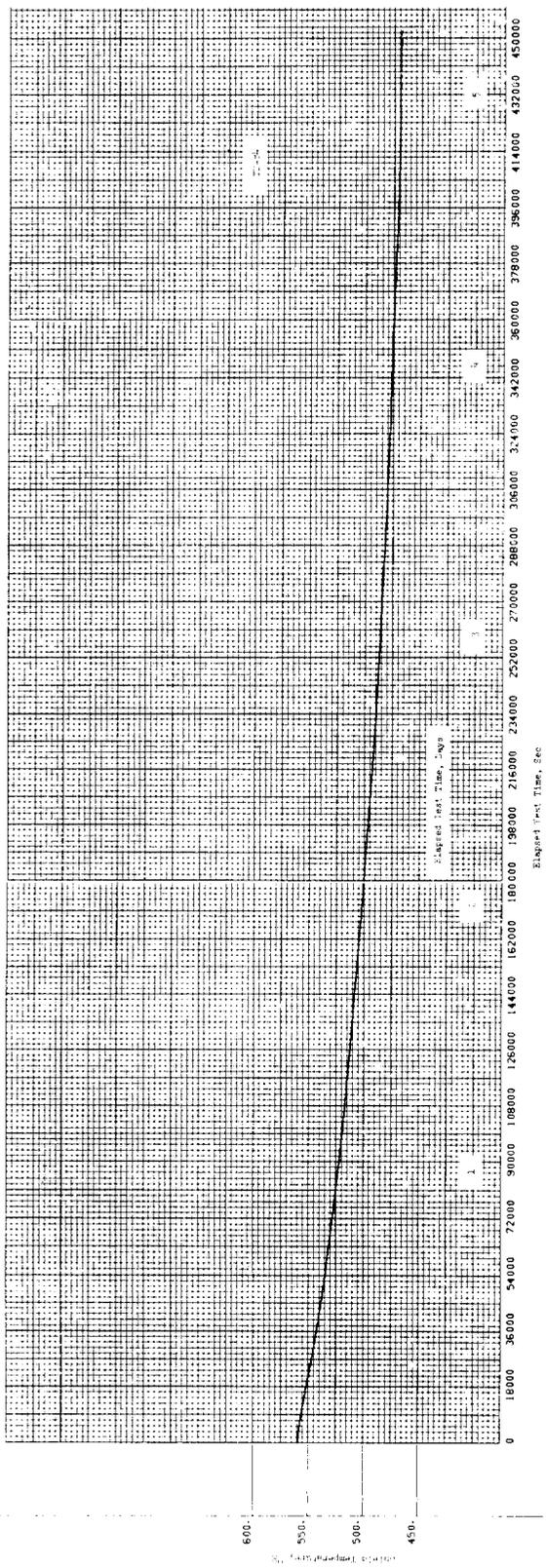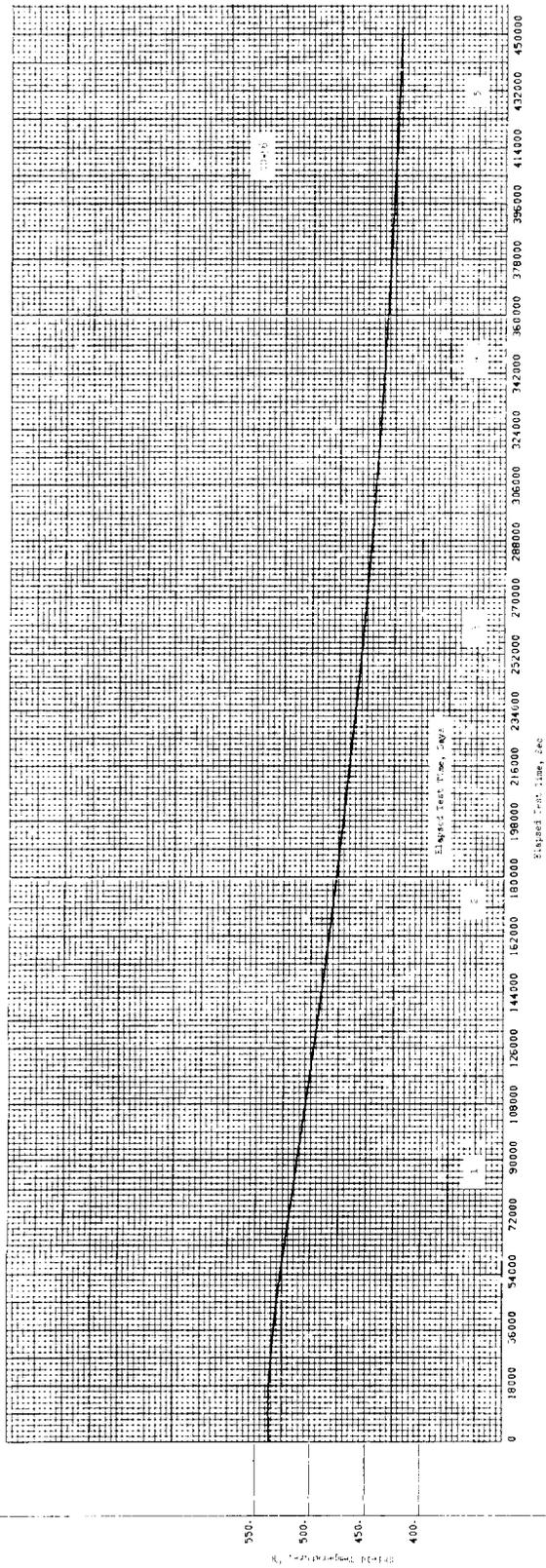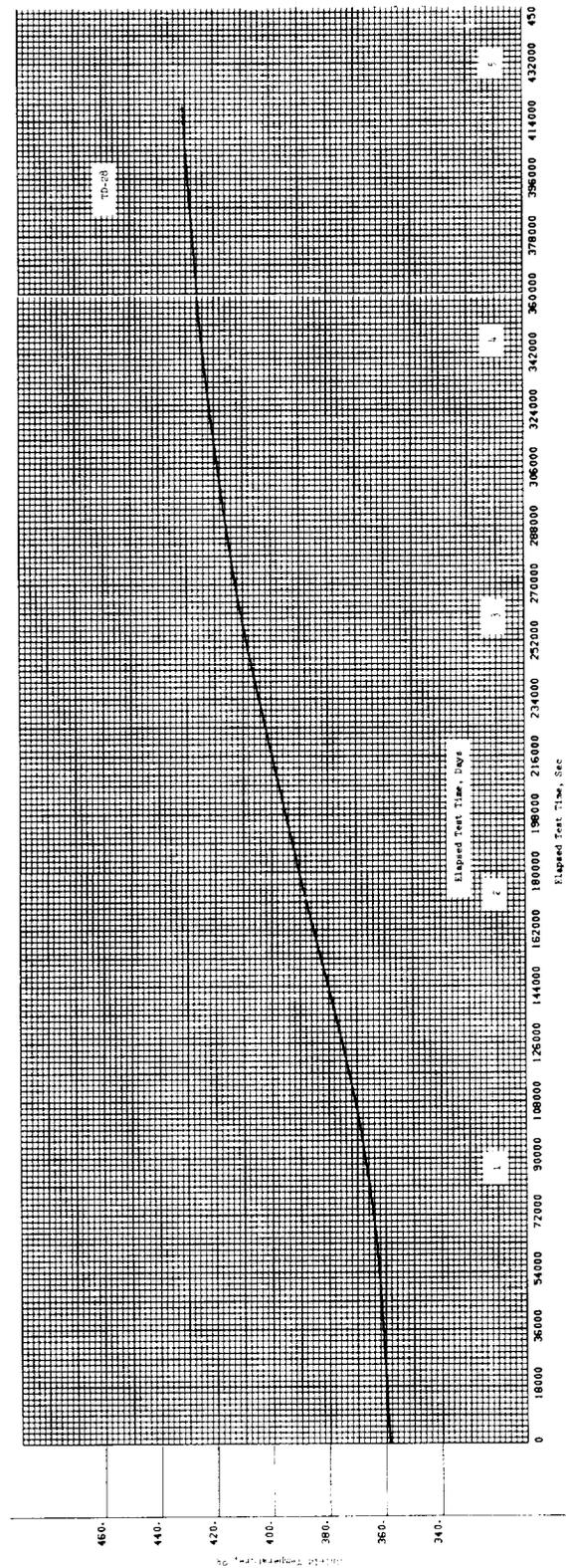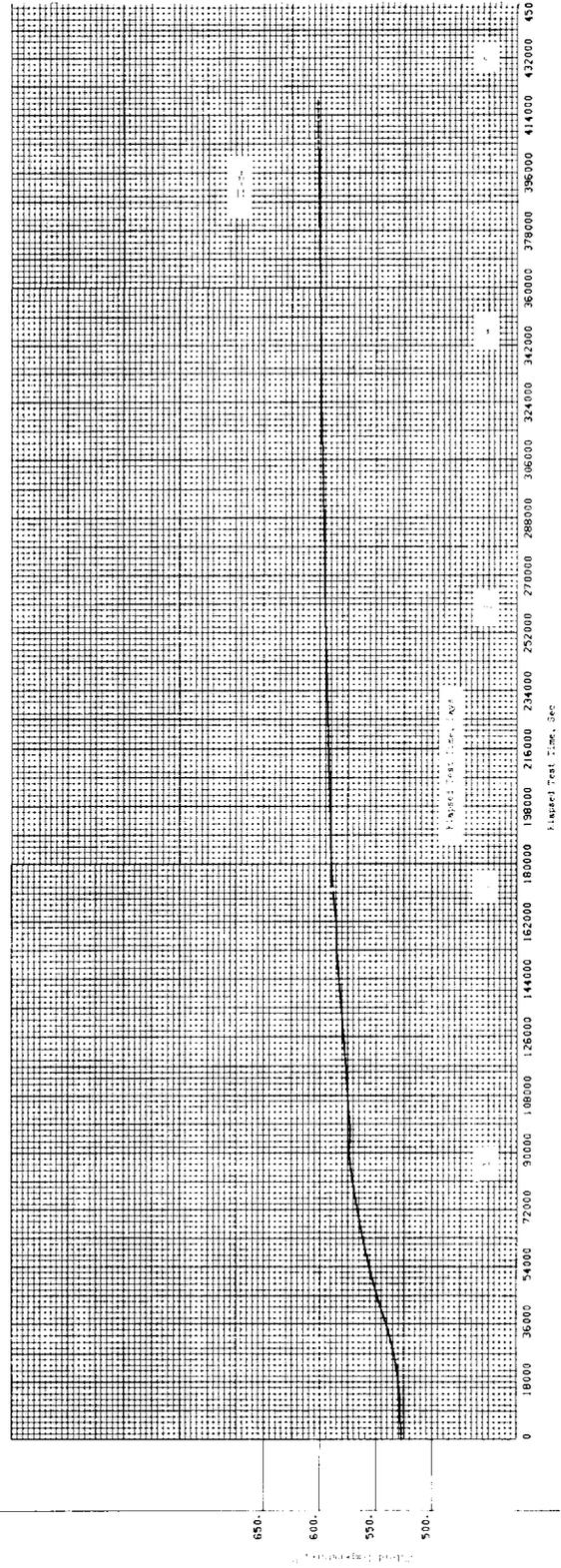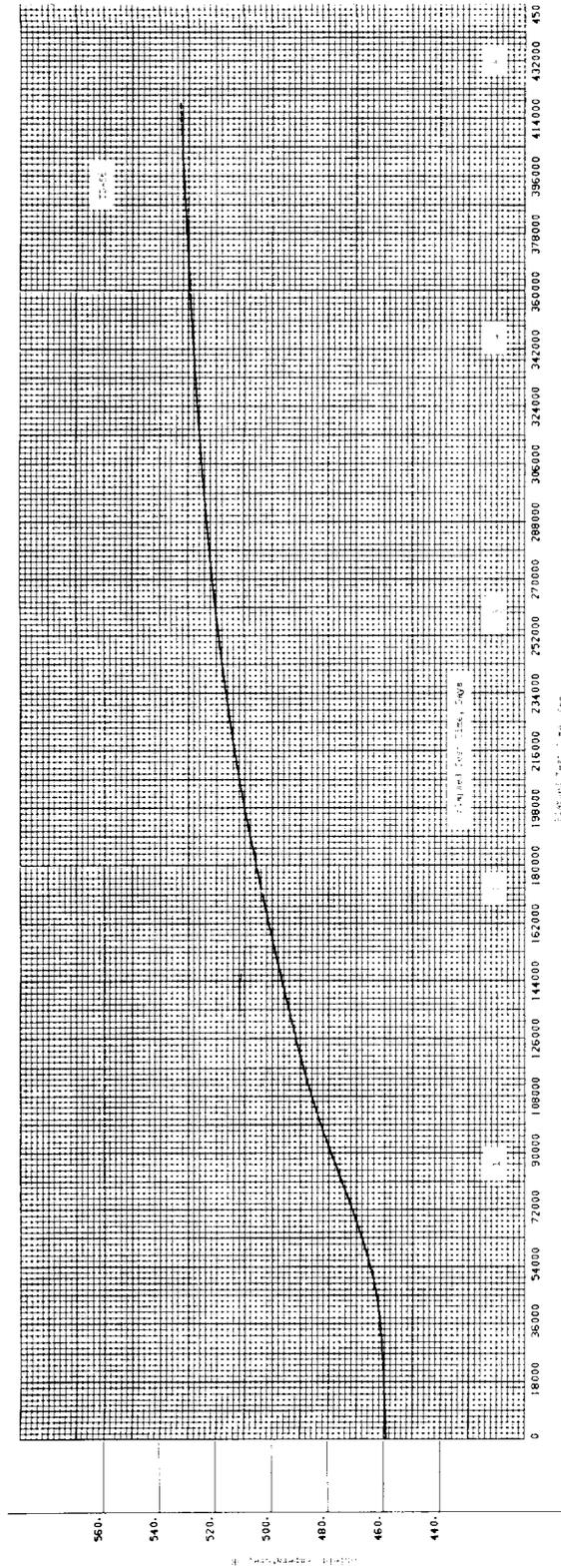
Fig. C-4 Temperature-Time History Data for Reflective Shields 56 and 84 During Test Run No. 3

LOCKHEED MISSILES & SPACE COMPANY

Inspection of the temperature data presented in these figures for Test Run
No. 3 shows that, in this case, the mass of the MLI was slowly being heated
from the previous near-equilibrium temperature values obtained for Test Run
No. 2. Again, nearly 5 days of elapsed test time were required in order to
achieve the new near-equilibrium values, although the total temperature change
experienced by any particular shield was somewhat less than that observed
earlier for Test Run No. 1. This serves to illustrate the fact that the time
required to achieve temperature equilibrium conditions within an MLI system
is primarily dependent upon the time constant of that particular insulation
mass, and is not significantly influenced by the initial conditions.

Appendix D

NOMENCLATURE

BASIC SYMBOLS:

A	surface area, m^2 (ft^2)
A_m	surface area of measuring plate, m^2 (ft^2)
A_s	effective shield surface area for each perforation, m^2 (ft^2)
C	conductance of interstitial gas flow path, kg m^2/N sec (lbm/psi sec)
C_v	molar specific heat, joules/kg mole $^{\circ}K$ (Btu/lbm mole $^{\circ}R$
D_h	equivalent hydraulic diameter, cm (in.)
E	modulus of elasticity (Young's modulus), N/m^2 (psi)
$\bar{E}$	effective modulus of elasticity for two materials in contact
E_n	emissive power of the nth shield, $^{\circ}K/m^2$ ($^{\circ}R/ft^2$)
E_o	emissive power of the cold boundary surface, $^{\circ}K/m^2$ ($^{\circ}R/ft^2$)
F	force, N (lbf)
F_o	fraction open area for a perforated shield, dimensionless
K	a constant, dimensionless
K	effective thermal conductivity of a composite MLI system, w/cm$^{\circ}K$ (Btu/hr ft $^{\circ}R$)
L	characteristic length of the interstitial gas layer (i.e., the vacuum spacing), cm (in.)
M	molecular weight, gm/mole (lbm/mole)
$\bar{N}$	layer density, layers/cm (layers/in.)
N_L	number of layers per node, dimensionless
N_{LT}	total number of layers, dimensionless
N_o	total number of layers, dimensionless
N_s	number of reflective shields, dimensionless
P	electrical power, w (Btu/hr)
P	effective contact pressure, N/m^2 (psi)
P	gas pressure, N/m^2 (psi) or torr
$\bar{P}$	average pressure, N/m^2 (psi) or torr
ΔP	difference in pressure between the interstitial void space and the external environment, N/m^2 (psi) or torr

D-1

P_C	electrical power supplied to the measuring plate heater during the steady state calibration condition, w (Btu/hr)
P_H	electrical power supplied to the measuring plate heater during the steady state test condition, w (Btu/hr)
Q	local outgassing rate per unit area, kg/m^2 (lbm/ft^2)
Q_{FM}	gas conduction heat rate within the free molecular flow regime, w (Btu/hr)
Q_M	measured heat flow rate, w (Btu/hr)
Q_P	predicted heat flow rate, w (Btu/hr)
R^O	molar gas constant, joules/kg mole ^{O}K (ft lbf/lbm mole ^{O}R)
R_c	resistance to heat transfer between two circular contact areas, ^{O}K/w (^{O}R hr/Btu)
R_n	resistance to heat transfer for n shields, ^{O}K/w (^{O}R hr/Btu)
R_s	resistance across a spacer layer, ^{O}K/w (^{O}R hr/Btu)
R_T	total resistance between adjacent MLI shields, ^{O}K/w (^{O}R hr/Btu)
T	temperature, ^{O}K (^{O}R)
T_1	temperature of the measuring plate, ^{O}K (^{O}R)
T_2	temperature of the guard plate, ^{O}K (^{O}R)
T_3	temperature of the warm boundary plate, ^{O}K (^{O}R)
T_C	cold boundary temperature, ^{O}K (^{O}R)
T_E	temperature of the edge guard ring, ^{O}K (^{O}R)
T_H	hot boundary temperature, ^{O}K (^{O}R)
T_S	temperature of the cryogen sink, ^{O}K (^{O}R)
T_m	mean temperature, ^{O}K (^{O}R)
ΔT	temperature difference across a given set of boundaries (i.e., $T_H - T_C$), ^{O}K (^{O}R)
V	volume, m^3 (ft^3)
V_c	volume of vacuum chamber, m^3 (ft^3)
V_I	volume of the interstitial void space, m^3 (ft^3)
Z	an empirical constant used to describe the characteristic gas flow within a round tube corresponding to minimum conductance, dimensionless
a	Tube radius, cm (in.)
$\bar{c}$	mean molecular speed, m/sec (ft/sec)
c_v	constant-volume specific heat, joules/kg mole ^{O}K (Btu/lbm mole ^{O}R)

LOCKHEED MISSILES & SPACE COMPANY

d_A diameter of equivalent circular shield surface area per perforation, cm (in.)

d_h perforation diameter, cm (in.)

f specular reflection coefficient, dimensionless

h multilayer shield spacing (i.e., the reciprocal of layer density), cm (in.)

k thermal conductivity, w/cm $^\circ$K (Btu/hr ft $^\circ$R)

k_b thermal conductivity of a bulk metal, w/cm $^\circ$K (Btu/hr ft $^\circ$R)

k_f thermal conductivity of a thin metal film, w/cm $^\circ$K (Btu/hr ft $^\circ$R)

k_g thermal conductivity of a gas, w/cm $^\circ$K (Btu/hr ft $^\circ$R)

$k_g{}'$ effective thermal conductivity of an interstitial gas at reduced pressures, w/cm $^\circ$K (Btu/hr ft $^\circ$R)

k_s thermal conductivity of a spacer, w/cm $^\circ$K (Btu/hr ft $^\circ$R)

$\bar{k}_s$ effective thermal conductivity of two materials in contact, w/cm $^\circ$K (Btu/hr ft $^\circ$R)

ℓ characteristic dimension of the contact geometry for adjacent MLI shields and spacers, m(ft)

ℓ mean free path of molecular collisions, cm(in.)

ℓ composite MLI total thickness, cm(in.)

ℓ' effective mean free path of molecular collisions, cm(in.)

k electron mean free path for thermal conductivity, $\overset{\circ}{\text{A}}$

$\dot{m}$ mass flow rate, kg/sec (lbm/sec)

n number of reflective shields in an MLI system, dimensionless

p probability of specular electron reflection, dimensionless

q or q_i heat flux through a given MLI system, w/m^2 (Btu/hr ft^2)

q_C gas conduction heat flux within the continuum flow regime, w/m^2 (Btu/hr ft^2)

q_{FM} gas conduction heat flux within the free molecular flow regime, w/m^2 (Btu/hr ft^2)

q_r radiation heat flux w/m^2 (Btu/hr ft^2)

q_{ro} radiation heat flux for reference MLI system with unperforated shields, w/m^2 (Btu/hr ft^2)

q_s solid conduction heat flux, w/m^2 (Btu/hr ft^2)

q_{sp} solid conduction heat flux for MLI with perforated shields, w/m^2 (Btu/hr ft^2)

q_{su} solid conduction heat flux for MLI with unperforated shields, w/m^2 (Btu/hr ft^2)

q_t	total heat flux, w/m^2 (Btu/hr ft^2)
q_x	gas conduction heat flux through one element of a system composed of many elements, w/m^2 (Btu/hr ft^2)
r	characteristic dimension of a contact surface, m (ft)
r_c	radius of a circular contact area, m (ft)
r_o	outer radius, m (ft)
r_s	radius of a spherical contacting element, m (ft)
t	spacer transmittance, dimensionless
t	thickness of a thin metal film, $\overset{o}{A}$
v_a	mean molecular velocity, m/sec (ft/sec)
v_o	velocity of gas flow at the wall of the flow channel, m/sec (ft/sec)
v_r	radial flow velocity, m/sec (ft/sec)
$\overline{v}_r$	average radial flow velocity, m/sec (ft/sec)
z_o	one-half of the distance between adjacent layers of an MLI system, cm (in.)
Φ	increment of solid conduction heat transfer normalized with respect to the number of layers and the boundary temperatures, $w/m^2 \, {}^oK^2$ (Btu/hr $ft^2 \, {}^oR^2$)
α	thermal accommodation coefficient, dimensionless
$\overline{\alpha}$	effective thermal accommodation coefficient, dimensionless
γ	specific heat ratio for an interstitial gas, dimensionless
ϵ or ϵ_s	reflective shield emittance, dimensionless
ϵ_{TH}	total hemispherical emittance dimensionless
ϵ_{TN}	total normal emittance, dimensionless
ϵ_{TR}	total hemispherical emittance at room temperature, dimensionless
ζ	slip coefficient describing gas flow at the channel wall, dimensionless
μ	Poisson's ratio, dimensionless
μ	gas viscosity, poise
$\overline{\mu}$	effective Poisson's ratio for two materials in contact, dimensionless
ρ	density, kg/m^3 (lbm/ft^3)
ρ_N	near-normal reflectance, dimensionless
σ	Steffan-Boltzmann constant equal to $5.669 \times 10^{-8} \, w/m^2 \, {}^oK^4$ (1.713×10^{-9} Btu/hr $ft^2 \, {}^oR^4$)

LOCKHEED MISSILES & SPACE COMPANY

τ	fraction of open shield surface area due to perforations, dimensionless
τ	shear stress at the wall for a gas flowing within a channel N/m^2 (psi)

CORRELATION CONSTANTS:

Coefficients (dimensional or dimensionless)

A, B, C , C_g, C_r, C_s , C_{s1}, C_{s2}, a, a', a_0, a_1, a_2, b, ϕ

Exponents (dimensionless)

M, N, S, k, m, n, o

ABBREVIATIONS:

A	argon
DI	deflection of the insulation surface
FB	boiloff mass flowrate
H_2	hydrogen
He	helium
LH_2	liquid hydrogen
LMSC	Lockheed Missiles and Space Company
LVDT	linear variable differential transducer
MLI	multilayer insulation
N_2	nitrogen
PI	interstitial pressure
PRT	platinum resistance thermometer
PTU	tank ullage pressure
PVC	vacuum chamber pressure
SCTB	Santa Cruz Test Base
TB	hot boundary baffle temperature
TGI	guard inlet fluid temperature
TGO	guard outlet fluid temperature
TLO	liquid overflow fluid temperature
TS	hot boundary shroud temperature
TTL	tank bulk liquid temperature
TV	vent gas temperature

Appendix E

REFERENCES

1. Cunnington, G.R., Keller, C.W., and Bell, G.A., "Thermal Performance of Multilayer Insulations," Interim Report for Contract NAS3-12025, NASA- CR 72605, Lockheed Missiles and Space Company, Sunnyvale, California, 1971

2. Hinckley, R.B., "Liquid Propellant Losses During Space Flight," Final Report for Contract NAS w-615, Report No. 65008-00-04, Arthur D. Little, Inc., Cambridge, Massachusetts, 1964

3. Burkley, R.A., et al, "Development of Materials and Materials Application Concepts for Joint Use as Cryogenic Insulation and Micrometeoroid Bumpers," Annual Summary Report for Contract NAS8-11747, Report No. GER 11679 S/47, Goodyear Aerospace Corporation, Akron, Ohio, 1968

4. Holm, R., Electric Contacts Handbook, 3rd Edition, Springer-Verlag, Germany, 1958

5. Timoshenko, S., Theory of Elasticity, McGraw-Hill, 1958

6. Tien, C.L., et al, Thermal Conductivity, C. Y. Ho and R. E. Taylor, Editors, Plenum Press, New York, 1969

7. Lucks, C.F., and Bing, G.F., "Experimental Measurements of Thermal Conductivity, Specific Heats, and Density of Metallic Transports and Protective Materials," AFTR-6145, Part II, p 32, Contract AF33(038) 20558, 1952

8. Keller, C.W., "Fiberglass Supports for Cryogenic Tanks," Final Report for Contract NAS3-12037, NASA-CR 120937, p 3-42, Lockheed Missiles and Space Company, Sunnyvale, California, 1972

9. Tien, C.L., and Cunnington, G.R., "Radiation Heat Transfer in Multilayer Insulations Having Perforated Shields," to be published in Progress in Astronautics and Aeronautics, 1974

10. Kreith, F., Principles of Heat Transfer, 2nd Edition, International Textbook Company, Scranton, Pennsylvania, 1965

11. Springer, G.S., Advances in Heat Transfer, Vol 7, p 157, 1971

12. Corruccini, R.J., Advances in Cryogenic Engineering, Vol 3, p 353, Plenum Press, New York, 1960

13. Tien, C.L., and Lienhard, J.H., Statistical Thermodynamics, Chapter 11, Holt, Rinehard, and Winston, Inc., New York, 1971

14. Dushman, Saul, Scientific Foundations of Vacuum Technology, p 49, John Wiley and Sons, Inc., New York, 1962

REFERENCES (Cont'd)

15. Scott, R.B., Cryogenic Engineering, p 147, D. Van Norstrand Company,
    Inc., Princeton, New Jersey, 1960.

16. Mikhal 'Chenko, R.S., et al, "Cryogenic Engineering, Present Status
    and Future Development," Proceedings of the First International Cryo-
    genic Engineering Conference, p 34, Heywood-Temple Publications,
    London, England, 1968.

17. Verschoor, J.D., and Greebler, P. Transactions ASME 74, p 961-968, 1952.

18. Schneider, P.J., Conduction Heat Transfer, 1st Edition, Chapter 12,
    p 294, Addison-Wesley, Reading, Massachusetts , 1955.

19. Gambill, W.E., "To Get Viscosity for a Gas Mixture," Chemical Engineer-
    ing, Vol 65, No. 23, p 157-160, 1958.

20. "Reporting of Outgassing Data," Standard AVS-9, American Vacuum Society,
    Boston, Massachusetts, 1963.

21. Rohsenow, W.M., and Choi, H., Heat, Mass, and Momentum Transfer, 1st
    Edition, Chapter 3, p 47-52, Prentice-Hall, Englewood Cliffs, New
    Jersey, 1961.

22. Loeb, L.B., The Kinetic Theory of Gases, 3rd Edition, Chapter 7, p 284,
    Dover, New York, 1961.

23. Dushman, S., Foundations of Vacuum Technique, 2nd Edition, Chapter 1,
    p 9, John Wiley and Sons, Inc., New York, 1962.

24. Dushman, S., Foundations of Vacuum Technique, 2nd Edition, Chapter 2,
    p 87, John Wiley and Sons, Inc., New York, 1962.

25. Dushman, S., Foundations of Vacuum Technique, 2nd Edition, Chapter 2,
    p 106, John Wiley and Sons, Inc., New York, 1962

26. Loeb, L.B., The Kinetic Theory of Gases, 3rd Edition, Chapter 7, p 295,
    Dover, New York, 1961

27. Glassford, A.P.M., "Prediction of Pressure During Evacuation of Multi-
    layer Insulation," Journal of Spacecraft and Rockets, Vol 9, No. 5,
    p 378-381, 1972

28. Keller, C.W., "Thermal Performance of Multilayer Insulation," Final
    Report for Contract NAS3-12025, NASA-CR 72747, Lockheed Missiles and
    Space Company, Sunnyvale, California, 1971

29. "Investigations Regarding Development of a High-Performance Insulation
    System," Final Report for Contract NAS8-20758, Report No. K-17-68-5,
    p 3-64 through 3-72, Lockheed Missiles and Space Company, Sunnyvale,
    California, 1968

30. Wood, B.E., Smith, A.M., Roux, J.A., and Seiber, B.A., "Spectro Infra-
    red Reflectance of H_2O Condensed on LN_2-Cooled Surfaces in Vacuum,"
    AIAA Journal, Vol 9, No. 9, p 1836-1842, 1971

Appendix F

DISTRIBUTION LIST

Copies   National Aeronautics & Space Administration
                Lewis Research Center
                21000 Brookpark Road
                Cleveland, Ohio 44135

   1   Attn: Contracting Officer, MS 500-313
   5   E. A. Bourke, MS 500-205
   1   Technical Utilization Office, MS 3-16
   1   Technical Report Control Office, MS 5-5
   2   AFSC Liaison Office, MS 501-3
   2   Library MS 60-3
   1   Office of Reliability & Quality Assurance, MS 500-211
   1   N. T. Musial, MS 500-113
  25   W. R. Johnson, Project Manager, MS 500-204

   1   Director, Manned Space Technology, RS
                Office of Aeronautics & Space Technology
                NASA Headquarters
                Washington, D.C. 20546

   1   Director Space Prop. and Power, RP
                Office of Aeronautics & Space Technology
                NASA Headquarters
                Washington, D.C. 20546

   1   Director, Launch Vehicles & Propulsion, SV
                Office of Space Science
                NASA Headquarters
                Washington, D.C. 20546

   1   Director, Materials & Structures Div., RW
                Office of Aeronautics & Space Technology
                NASA Headquarters
                Washington, D.C. 20546

   1   Director, Advanced Missions, MT
                Office of Manned Space Flight
                NASA Headquarters
                Washington, D.C. 20546

   1   Director, Physics and Astronomy Programs, SG
                Office of Space Science
                NASA, Headquarters
                Washington, D.C. 20546

LOCKHEED MISSILES & SPACE COMPANY

Copies

1	Director, Planetary Programs, SL Office of Space Science NASA, Headquarters Washington, D.C. 20546
1	Office of Aeronautics & Space Technology, R NASA, Headquarters Washington, D.C. 20546
1	National Aeronautics & Space Administration Ames Research Center Moffett Field, California 94035 Attn: Library
1	National Aeronautics & Space Administration Flight Research Center P. O. Box 273 Edwards, California 93523 Attn: Library
1	Director, Technology Utilization Division Office of Technology Utilization NASA Headquarters Washington, D.C. 20546
1	Office of the Director of Defense Research & Engineering Washington, D.C. 20301 Attn: Office of Asst. Dir. (Chem Technology)
10	NASA Scientific and Technical Information Facility P. O. Box 33 College Park, Maryland 20740 Attn: NASA Representative
1	National Aeronautics & Space Administration Goddard Space Flight Center Greenbelt, Maryland 20771 Attn: Library
1	National Aeronautics & Space Administration Langley Research Center Langley Station Hampton, Virginia 23365 Attn: Library
1	National Aeronautics & Space Administration John F. Kennedy Space Center Cocoa Beach, Florida 32931 Attn: Library

F-2

Copies

1	National Aeronautics & Space Administration Manned Spacecraft Center Houston, Texas 77001 Attn: Library
1	National Aeronautics & Space Administration George C. Marshall Space Flight Center Huntsville, Alabama 35912 Attn: Library
1	Jet Propulsion Laboratory 4800 Oak Grove Drive Pasadena, California 91103 Attn: Library
1	Defense Documentation Center Cameron Station Building 5 5010 Duke Street Alexandria, Virginia 22314 Attn: TISIA
1	RTD (RTNP) Bolling Air Force Base Washington, D.C. 20332
1	Arnold Engineering Development Center Air Force Systems Command Tullahoma, Tennessee 37389 Attn: Library
1	Advanced Research Projects Agency Washington, D.C. 20525 Attn: Library
1	Aeronautical Systems Division Air Force Systems Command Wright-Patterson Air Force Base, Dayton, Ohio Attn: Library
1	Air Force Missile Test Center Patrick Air Force Base, Florida Attn: Library
1	Air Force Systems Command Andrews Air Force Base Washington, D.C. 20332 Attn: Library

LOCKHEED MISSILES & SPACE COMPANY

Copies

1   Commander
U. S. Naval Missile Center
Point Mugu, California 93041
Attn: Technical Library

1   Commander
U. S. Naval Weapons Center
China Lake, California 93557
Attn: Library

1   Commanding Officer
Naval Research Branch Office
1030 E. Green Street
Pasadena, California 91101
Attn: Library

1   Director (Code 6180)
U. S. Naval Research Laboratory
Washington, D.C. 20390
Attn: Library

1   Picatinny Arsenal
Dover, New Jersey 07801
Attn: Library

1   Air Force Aero Propulsion Laboratory
Research & Technology Division
Air Force Systems Command
United States Air Force
Wright-Patterson AFB, Ohio 45433
Attn: APRP (Library)

1   Electronics Division
Aerojet-General Corporation
P.O. Box 296
Azusa, California 91703
Attn: Library

1   Space Divison
Aerojet-General Corporation
9200 East Flair Drive
El Monte, California 91734
Attn: Library

1   Aerojet Ordance and Manufacturing
Aerojet-General Corporation
11711 South Woodruff Avenue
Fullerton, California 90241
Attn: Library

LOCKHEED MISSILES & SPACE COMPANY

1   Aerojet Liquid Rocket Company
P. O. Box 15847
Sacramento, California 95813
Attn: Technical Library 2484-2015A

1   Aeronutronic Division of Philco Ford Corp.
Ford Road
Newport Beach, California 92663
Attn: Technical Information Department

1   Aerospace Corporation
2400 E. El Segundo Blvd.
Los Angeles, California 90045
Attn: Library-Documents

1   Arthur D. Little, Inc.
20 Acorn Park
Cambridge, Massachusetts 02140
Attn: Library

1   Astropower Laboratory
McDonnell-Douglas Aircraft Company
2121 Paularino
Newport Beach, California 92163
Attn: Library

1   ARO, Incorporated
Arnold Engineering Development Center
Arnold AF Station, Tennessee 37389
Attn: Library

1   Susquehanna Corporation
Atlantic Research Division
Shirley Highway & Edsall Road
Alexandria, Virginia 22314
Attn: Library

1   Battelle Memorial Institute
505 King Avenue
Columbus, Ohio 43201
Attn: Report Library, Room 6A

1   Beech Aircraft Corporation
Boulder Facility
Box 631
Boulder, Colorado
Attn: Library

Copies

1   Bell Aerosystems, Inc.
Box 1
Buffalo, New York 14240
Attn: Library

1   Instruments & Life Support Division
Bendix Corporation
P.O. Box 4508
Davenport, Iowa 52808
Attention: Library

1   Boeing Company
Space Division
P.O. Box 868
Seattle, Washington 98124
Attn: Library

1   Boeing Company
1625 K Street, N.W.
Washington, D.C 20006

1   Boeing Company
P.O. Box 1680
Huntsville, Alabama 35801

1   Chemical Propulsion Information Agency
Applied Physics Laboratory
8621 Georgia Avenue
Silver Spring, Maryland 20910

1   Chrysler Corporation
Missile Division
P.O. Box 2628
Detroit, Michigan
Attn: Library

1   Chrysler Corporation
Space Division
P.O. Box 29200
New Orleans, Louisiana 70129
Attn: Librarian

1   Curtiss-Wright Corporation
Wright Aeronautical Division
Woodridge, New Jersey
Attn: Library

LOCKHEED MISSILES & SPACE COMPANY

Copies

1   University of Denver
     Denver Research Institute
     P.O. Box 10127
     Denver, Colorado 80210
     Attn: Security Office

1   Fairchild Stratos Corporation
     Aircraft Missiles Division
     Hagerstown, Maryland
     Attn: Library

1   Research Center
     Fairchild Hiller Corporation
     Germantown, Maryland
     Attn: Library

1   Republic Aviation
     Fairchild Hiller Corporation
     Farmington, Long Island
     New York

1   General Dynamics/Convair
     P.O. Box 1128
     San Diego, California 92112
     Attn: Library

1   Missiles and Space Systems Center
     General Electric Company
     Valley Forge Space Technology Center
     P.O. Box 8555
     Philadelphia, Pa. 19101
     Attn: Library

1   General Electric Company
     Flight Propulsion Lab. Department
     Cincinnati, Ohio
     Attn: Library

1   Grumman Aircraft Engineering Corporation
     Bethpage, Long Island, New York
     Attn: Library

1   Hercules Powder Company
     Allegheny Ballistics Laboratory
     P.O. Box 210
     Cumberland, Maryland 21501
     Attn: Library

LOCKHEED MISSILES & SPACE COMPANY

<u>Copies</u>

1   Honeywell Inc.
Aerospace Division
2600 Ridgeway Road
Minneapolis, Minnesota
Attn: Library

1   IIT Research Institute
Technology Center
Chicago, Illinois 60616
Attn: Library

1   Kidde Aerospace Division
Walter Kidde & Company, Inc.
567 Main Street
Belleville, New Jersey 07109

1   Ling-Temco-Vought Corporation
P.O. Box 5907
Dallas, Texas 75222
Attn: Library

1   Lockheed Missiles and Space Company
P.O. Box 504
Sunnyvale, California 94087
Attn: Library

1   Lockheed Propulsion Company
P.O. Box 111
Redlands, California 92374
Attn: Library, Thackwell

1   Marquardt Corporation
16555 Saticoy Street
Box 2013 - South Annex
Van Nuys, California 91409

1   Denver Division
Martin-Marietta Corporation
P.O. Box 179
Denver, Colorado 80201
Attn: Library

1   Orlando Division
Martin-Marietta Corporation
Box 5827
Orlando, Florida
Attn: Library

LOCKHEED MISSILES & SPACE COMPANY

Copies

1	Western Division McDonnell Douglas Astronautics 5301 Bolsa Ave Huntington Beach, California 92647 Attn: Library
1	McDonnell Douglas Aircraft Corporation P.O. Box 516 Lambert Field, Missouri 63166 Attn: Library
1	Rocketdyne Division North American Rockwell, Inc. 6633 Canoga Avenue Canoga Park, California 91304 Attn: Library, Department 596-306
1	Space & Information Systems Division North American Rockwell 12214 Lakewood Blvd Downey, California Attn: Library
1	Northrop Space Laboratories 3401 West Broadway Hawthorne, California Attn: Library
1	Purdue University Lafayette, Indiana 47907 Attn: Library (Technical)
1	Radio Corporation of America Astro-Electronics Products Princeton, New Jersey Attn: Library
1	Rocket Research Corporation Willow Road at 116th Street Redmond, Washington 98052 Attn: Library
1	Stanford Research Institute 333 Ravenswood Avenue Menlo Park, California 94025 Attn: Library

LOCKHEED MISSILES & SPACE COMPANY

Copies

1   Thiokol Chemical Corporation
     Redstone Division
     Huntsville, Alabama
     Attn: Library

1   TRW Systems Inc.
     1 Space Park
     Redondo Beach, California 90278
     Attn: Tech. Lib. Doc. Acquisitions

1   TRW
     TAPCO Division
     23555 Euclid Avenue
     Cleveland, Ohio 44117

1   United Aircraft Corporation
     Corporation Library
     400 Main Street
     East Hartford, Connecticut 06108
     Attn: Library

1   United Aircraft Corporation
     Pratt & Whitney Division
     Florida Research & Development Center
     P.O. Box 2691
     West Palm Beach, Florida 33402
     Attn: Library

1   United Aircraft Corporation
     United Technology Center
     P.O. Box 358
     Sunnyvale, California 94038
     Attn: Library

1   Vickers Incorporated
     Box 302
     Troy, Michigan

1   Vought Astronautics
     Box 5907
     Dallas, Texas
     Attn: Library

LOCKHEED MISSILES & SPACE COMPANY